Zooming in on star formation in the brightest galaxies of the early universe discovered with the Planck and Herschel satellites

Raoul Cañameras Cañameras

To cite this version:

Raoul Cañameras Cañameras. Zooming in on star formation in the brightest galaxies of the early universe discovered with the Planck and Herschel satellites. Cosmology and Extra-Galactic Astrophysics [astro-ph.CO]. Université Paris Saclay (COmUE), 2016. English. NNT : 2016SACLS237 . tel-01416000

HAL Id: tel-01416000
https://theses.hal.science/tel-01416000

Submitted on 13 Dec 2016

NNT : 2016SACLS237

THÈSE DE DOCTORAT
DE
L'UNIVERSITÉ PARIS-SACLAY
PRÉPARÉE À
L'UNIVERSITÉ PARIS-SUD

INSTITUT D'ASTROPHYSIQUE SPATIALE

ECOLE DOCTORALE N° 127
Astronomie et Astrophysique d'Île-de-France

Spécialité Sciences de l'Univers

Par

Raoul CAÑAMERAS

Zooming in on star formation in the brightest galaxies of the early Universe discovered with the Planck and Herschel satellites

Thèse présentée et soutenue à Orsay, le 26 septembre 2016

Composition du Jury

Pr. Laurent VERSTRAETE	Professeur (Institut d'Astrophysique Spatiale)	Président du jury
Pr. Véronique BUAT	Professeur (Laboratoire d'Astrophysique de Marseille)	Rapporteure
Dr. Carlos DE BREUCK	Astronome Associé (European Southern Observatory)	Rapporteur
Dr. David ELBAZ	Ingénieur-Chercheur (Service d'Astrophysique – CEA Saclay)	Examinateur
Dr. Alessandro BOSELLI	Directeur de Recherche (Laboratoire d'Astrophysique de Marseille)	Examinateur
Dr. Nicole NESVADBA	Chargée de Recherche (Institut d'Astrophysique Spatiale)	Directrice de thèse

Titre : Zoom sur la formation stellaire au sein des galaxies les plus brillantes de l'univers jeune découvertes avec les satellites Planck et Herschel

Mots clés : galaxies lointaines, formation stellaire, lentillage gravitationnel

Résumé : Les galaxies amplifiées par lentillage gravitationnel fort offrent une opportunité exceptionnelle pour caractériser la formation stellaire intense au sein des galaxies poussiéreuses les plus distantes. Dans les cas les plus favorables, il est possible d'étudier les mécanismes qui régissent la formation stellaire jusqu'aux échelles des régions de formation d'étoiles individuelles. Les alignements fortuits entre ces galaxies actives et des structures d'avant-plan produisant des facteurs d'ampli-fication par lentillage gravitationnel >>10 restent néanmoins très rares. L'échantillon des Planck's Dusty GEMS (Gravitationally Enhan-ced subMillimeter Sources), découvert par le relevé de ciel complet du satellite Planck dans le domaine sub-millimétrique, contient onze galaxies à haut décalage spectral extrêmement brillantes. Leurs densités de flux à 350 microns se situent entre 300 et 1000 mJy, au-delà de la plupart des sources lentillées précédemment découvertes par les relevés en infrarouge lointain et sub-millimétrique. Six d'entre elles dépassent la limite en complétude à 90% du catalogue de sources ponctuelles détectées par Planck (PCCS), indiquant qu'elles sont parmi les plus brillantes sources lointaines sélection-nées par leur formation stellaire intense. Cette thèse s'intègre dans le suivi multi-longueur d'onde de cet échantillon exceptionnel, destiné à sonder les propriétés globales des sources d'arrière-plan et à contraindre les configurations de lentillage. Premièrement, j'utilise de l'imagerie et de la spectroscopie en visible et en infrarouge proche et moyen pour caractériser les structures formant la lentille et pour construire des modèles de lentillage gravitationnel complets. J'en déduis que les onze GEMS sont effectivement alignées avec des surdensités de matière en avant-plan, soit des galaxies massives et isolées, soit des groupes ou amas de galaxies. Ces objets amplifiants contiennent des populations d'étoiles évoluées et âgées de plusieurs milliards d'années, indiquant qu'il s'agit de galaxies précoces. De plus, la modélisation détaillée de l'effet de lentillage vers les GEMS suggère que les amplifications atteignent systématiquement des facteurs >10, et >20 pour certaines lignes de visée. Deuxièmement, nous observons dans les domaines infrarouge lointain et millimétrique pour caractériser les sources d'arrière-plan. Les données en interférométrie de l'IRAM et du SMA à des résolutions inférieures à la seconde d'arc montrent que les GEMS ont des morphologies très déformées, preuve de fortes distorsions gravitationnelles. J'obtiens des températures de poussières de 33 à 50 K et des luminosités atteignant 2x10^{14} luminosités solaires en infrarouge lointain, sans corriger du facteur d'amplification. La relation entre températures de poussières et luminosités infrarouge confirme également que, pour une température donnée, les GEMS sont plus brillantes que les galaxies similaires non lentillées. Je conclus qu'à ces longueurs d'onde, le chauffage des poussières semble être dominé par l'activité de formation stellaire avec une contamination par d'éventuels noyaux actifs systématiquement inférieure à 30%. Nous trouvons des décalages vers le rouge compris entre 2.2 et 3.6 grâce à la détection d'au moins deux raies d'émission du gaz atomique ou moléculaire par source. Finalement, je cible les trois sources lentillées de l'échantillon ayant les propriétés les plus remarquables. En particulier, la plus brillante d'entre elles s'avère être un sursaut présentant des densités de formation stellaire proches de la limite d'Eddington, et permet de sonder la naissance des étoiles dans ses phases les plus extrêmes.

ÉCOLE DOCTORALE
Astronomie
et Astrophysique
d'Île-de-France

Title : Zooming in on star formation in the brightest galaxies of the early universe discovered with the Planck and Herschel satellites

Keywords : distant galaxies, star formation, gravitational lensing

Abstract : Strongly gravitationally lensed galaxies offer an outstanding opportunity to characterize the most intensely star-forming galaxies in the high-redshift universe. In the most extreme cases, one can probe the mechanisms that underlie the intense star formation on the scales of individual star-forming regions. This requires very fortuitous gravitational lensing configurations offering magnification factors >>10, which are particularly rare toward the high-redshift dusty star-forming galaxies. The Planck's Dusty GEMS (Gravitationally Enhanced subMilli-meter Sources) sample contains eleven of the brightest high-redshift galaxies discovered with the Planck sub-millimeter all-sky survey, with flux densities between 300 and 1000 mJy at 350 microns, factors of a few brighter than the majority of lensed sources previously discovered with other surveys. Six of them are above the 90% completeness limit of the Planck Catalog of Compact Sources (PCCS), suggesting that they are among the brightest high-redshift sources on the sky selected by their active star formation. This thesis comes within the framework of the extensive multi-wavelength follow-up programme designed to determine the overall properties of the high-redshift sources and to probe the lensing configurations. Firstly, to characterize the intervening lensing structures and calculate lensing models, I use optical and near/mid-infrared imaging and spectroscopy. I deduce that our eleven GEMS are aligned with intervening matter overdensities at intermediate redshift, either massive isolated galaxies or galaxy groups and clusters. The foreground sources exhibit evolved stellar populations of a few giga years, characteristic of early-type galaxies. Moreover, the first detailed models of the light deflection toward the GEMS suggest magnification factors systematically >10, and >20 for some lines-of-sight. Secondly, we observe the GEMS in the far-infrared and sub-millimeter domains in order to characterize the background sources. The sub-arcsec resolution IRAM and SMA interferometry shows distorded morphologies which definitively confirm that the eleven sources are strongly lensed. I obtain dust temperatures between 33 and 50 K, and outstanding far-infrared luminosities of up to $2x10^{14}$ solar luminosities before correcting for the gravitational magnification. The relationship between dust temperatures and far-infrared luminosities also confirms that the GEMS are brighter than field galaxies at a given dust temperature. I conclude that dust heating seems to be strongly dominated by the star formation activity with an AGN contamination systematically below 30%. We find secure spectroscopic redshifts between 2.2 and 3.6 for the eleven targets thanks to the detection of at least two CO emission lines per source. Finally, I focus on the three gravitationally lensed sources showing the most remarkable properties including the brightest GEMS, a maximal starburst with star formation surface densities near the Eddington limit.

Remerciements

J'aimerais tout d'abord remercier une nouvelle fois mes rapporteurs, Véronique Buat et Carlos De Breuck, d'avoir consacré du temps à la relecture du manuscrit et pour leurs commentaires constructifs sur les résultats de cette thèse et leur présentation. Merci à mes examinateurs, Laurent Verstraete, David Elbaz et Alessandro Boselli, d'avoir accepté d'évaluer ce travail. Je voudrais également exprimer ma gratitude envers l'ensemble des membres de mon jury pour leurs questions très constructives et leurs commentaires encourageants pendant la soutenance.

Je tiens à remercier tout particulièrement Nicole pour toute la confiance qu'elle a pu m'accorder et pour son soutien, ses précieux conseils et son enthousiasme communicatif durant cette thèse. L'ensemble des interactions que nous avons pu avoir au sujet des galaxies lointaines ont rendu ces trois années scientifiquement passionnantes, et m'ont grandement incité à poursuivre en post-doctorat sur ce sujet.

Merci aux permanents de l'IAS, en particulier à ceux de l'équipe MIC et du groupe cosmologie, avec qui j'ai pu avoir des discussions enrichissantes tout au long de cette période. Je suis particulièrement reconnaissant envers Guillaume, Mathieu, Zahia, ainsi que Jacques, pour leur suivi et pour leurs conseils. Je voudrais également adresser mes remerciements à Marceau pour nos interactions entamées durant la deuxième année, qui m'ont beaucoup appris.

Bien d'autres membres du personnel de l'IAS ont contribué à rendre cette période au laboratoire si agréable. Et j'aimerais adresser en particulier un grand merci à l'équipe administrative et au service informatique pour leur gentillesse.

Merci aux doctorants et post-doctorants pour cette l'atmosphère si sympathique jour après jour ! Merci pour votre bonne humeur communicative. Nos pauses – de durées variables selon les personnes environnantes (!) – ont été les bienvenues, notamment lors des périodes de travail les plus intenses. Ces excellents moments se sont souvent prolongés hors du laboratoire et j'espère qu'ils se prolongeront également dans le futur, à Orsay ou autre part sur le globe !

Je continuerai avec ma famille qui a été extrêmement présente à mes côtés pendant ces trois années. J'adresse en particulier d'immenses remerciements à ma mère, ma grand-mère et ma soeur. Il est très difficile de résumer ce que j'aimerais exprimer pour vous montrer que cette thèse est aussi la vôtre !

Un grand merci, Anne-Marie pour ces excellents moments en ta compagnie et pour tes encouragements, et Sylvie pour l'envoi Colissimo de produits Pyrénéens et pour ton soutien. Merci Inès pour tant de bonne humeur, de musique et de courage. Que de fierté d'être ton frérot ! Une grosse pensée pour mon grand-père avec qui j'aurais aimé discuter de ces galaxies amplifiées par lentille gravitationnelle. Je garde une grande place dans cette page de remerciements pour mon père, qui a largement participé à dévier mon intérêt débordant pour le football (voir ci-dessous) vers des domaines plus divers tels que les sciences et l'astronomie. Ce travail acharné n'aurait pas pu aboutir s'il ne m'avait pas appris à travailler avec acharnement !

Comment ne pas vous remercier vous tous – amis de promo, colocs, amis parisiens ou de contrées plus ensoleillées – qui m'avez fait passer de super moments durant ces trois années (mais pas seulement) et m'avez souvent permis de déconnecter totalement des étoiles et des galaxies. Je n'écrirais pas de noms, de peur d'oublier quelqu'un, mais je sais que vous vous reconnaîtrez et je tiens à vous remercier bien fort. Merci Raphaël pour cette amitié par-delà les âges et les pays (la France et la Catalogne plus précisément) qui t'a amené jusqu'à la salle 1-2-3 le 26/09/16.

Un bref mot de gratitude au RER B pour les émotions si fortes qu'il a pu me procurer. Mais j'adresserai plutôt mes remerciements à Pierre, Clément, Maud et Marie-Co pour leur gentillesse. Grâce à vous j'ai évité de prendre le Noctilien un bon nombre de soirs !

Les semaines auraient été bien longues sans les coupures sportives, et en particulier les coupures footballistiques du mercredi. Chers Oranges, notre groupe me manquera beaucoup, mais je resterai à jamais Orange dans l'âme. Je vous remercie à tous pour votre rigueur défensive, et surtout pour l'ensemble de ces moments de détente. Merci également aux courageux coureurs, compagnons des rares pauses déjeuner pendant lesquelles j'ai réussi à prendre mon courage à deux mains et à prendre mes jambes à mon coup pour me joindre à eux ! Un merci tout particulier à Pierre et Marco, compères d'entraînement en première année, avec qui je me suis engagé dans un grand défi loin de la vallée de Chevreuse.

Et bien sûr, pour terminer, un immense merci est particulièrement réservé à Pascaline qui m'a donné un courage incommensurable pour traverser cette période intense qu'est la thèse. Je me contenterai d'un smiley car les 228 pages suivantes ne seraient pas suffisantes pour te remercier dignement ;-)

Résumé

Durant cette thèse, je me suis intéressé aux mécanismes de formation stellaire au sein des galaxies poussiéreuses à grand décalage spectral[1], en exploitant le phénomène de lentille gravitationnelle forte. Lors d'alignements fortuits, des galaxies isolées, groupes, ou amas massifs d'avant-plan peuvent jouer le rôle de télescope gravitationnel en accroissant la brillance et la taille apparente de ces galaxies actives et lointaines. De telles configurations offrent une opportunité exceptionnelle pour caractériser la formation stellaire intense au sein de l'Univers jeune et, dans les cas les plus favorables, des facteurs d'amplification par lentille gravitationnelle $\gg$10 permettent d'accéder aux échelles des régions de formation stellaire individuelles.

Contexte et sélection de l'échantillon

Cette thèse présente une première caractérisation des "Planck's Dusty GEMS" (Gravitationally Enhanced sub-Millimetre Sources, Cañameras et al. 2015), un petit échantillon de sources extrêmement brillantes situées à z $\sim 2-3$ et découvertes à l'aide du relevé de ciel complet du satellite Planck dans le domaine (sub-)millimétrique. Il s'agit de onze galaxies présentant des densités de flux de 300 à 1000 mJy à 350 μm, plus brillantes que la majorité des sources lentillées découvertes jusqu'à présent lors des relevés de grande envergure menés avec Herschel (Eales et al. 2010; Oliver et al. 2012) et le South Pole Telescope (Vieira et al. 2013). Cet échantillon ouvre donc une fenêtre intéressante sur la naissance des étoiles autour du pic de l'histoire cosmique de la formation stellaire (voir Fig.1.1 Madau & Dickinson 2014), au sein de galaxies atteignant des activités prodigieuses.

Sa sélection est basée sur l'identification de candidats à haut redshift dans les données de l'instrument HFI (High Frequency Instrument), installé à bord du satellite Planck, grâce à des critères de couleur à 350, 550 et 850 μm (voir Planck Collaboration et al. 2015d). A ces longueurs d'onde, Planck offre des résolutions angulaires de 4-5$'$ correspondant typiquement aux tailles angulaires d'amas de galaxies à z $\sim 2-3$, et ne permet donc pas de déterminer la nature astrophysique de ces candidats. De ce fait, c'est un suivi aux mêmes longueurs d'onde et à plus haute résolution angulaire mené avec l'instrument SPIRE, à bord de l'observatoire spatial Herschel, qui a permis d'isoler de potentielles sources lentillées. Il en résulte 11 cibles situées dans des zones inexplorées du ciel extragalactique et directement observables à partir de l'hémisphère nord. Il s'agit de sources ponctuelles, brillantes et isolées dans les cartes de SPIRE à 250 μm et à une résolution d'environ $18''$, ayant les couleurs typiques de galaxies poussiéreuses à haut redshift. Six d'entre elles proviennent du catalogue de sources compactes de Planck (PCCS, Planck Collaboration et al. 2014b) et dépassent la limite de complétude à 90% d'environ 600 mJy dans les bandes de fréquences les plus élevées. Cela suggère qu'elles appartiennent aux sources les plus brillantes de l'Univers jeune, sélectionnées par leur formation stellaire intense, sur 50% du ciel présentant une faible contamination par l'émission des poussières Galactiques. Les cinq autres ont été initialement détectées lors d'une recherche de sources froides dans le fond cosmique infrarouge observé par Planck (Planck Collaboration et al. 2015c).

---

[1] par abréviation de *décalage spectral vers le rouge*, également désigné par *redshift* ou simplement par z dans la suite de ce résumé

CFHT

ALMA

IRAM/30m

HST

Nécessité d'un suivi multi-longueurs d'onde

Cette thèse aborde d'une part l'analyse des configurations de lentille gravitationnelle, et d'autre part la caractérisation des pouponnières d'étoiles dans les sources sub-millimétriques détectées avec Planck et Herschel. Une telle étude nécessite un suivi multi-longueurs d'onde, et le chapitre 3 présente l'ensemble des observations menées durant ce suivi avec des instruments au sol ou dans l'espace. Globalement, l'émission des réservoirs de poussière chauffés par la formation stellaire au sein des sources d'arrière-plan domine à grande longueur d'onde, au-delà de l'infrarouge moyen. Comme les GEMS sont des sources poussiéreuses, elles sont nécessairement fortement obscurcies et donc très ténues à plus courte longueur d'onde. En conséquence, les domaines optique et infrarouge proche sont nettement dominés par les populations stellaires des galaxies d'avant-plan, appartenant au potentiel gravitationnel amplifiant.

D'une part, l'émission des poussières dans les GEMS est analysée à partir de l'imagerie de SCUBA-2 au JCMT et de GISMO au 30-m de l'IRAM, à 850 μm et 2-mm respectivement, en complément des trois bandes photométriques de SPIRE à 250, 350 et 500 μm. J'inclus également les densités de flux ou bien les limites supérieures des relevés IRAS à 60 et 100 μm, et WISE à 22 μm. Pour sa part, le spectrographe large bande EMIR sur l'antenne de 30 mètres de l'IRAM permet d'observer les raies d'émission de plusieurs traceurs du gas atomique et moléculaire tels que le CO, le [CI] ou H_2O. Nous basons également l'étude sur des observations de l'interféromètre SMA, en configuration COM et VEXT, de manière à résoudre l'émission continuum des poussières dans les GEMS. L'interférométrie du Plateau de Bure et d'ALMA atteint des résolutions angulaires sous la seconde d'arc et offre une vue détaillée des conditions physiques de la matière interstellaire au sein de sources individuelles.

D'autre part, l'imagerie optique et infrarouge proche est essentielle pour identifier les lentilles et caractériser leur profil radial, leur décalage vers le rouge, ainsi que leur masse projetée. Dans cette thèse, j'utilise les caméras MegaCam et WIRCam au CFHT, FORS2 et HAWK-I au VLT, et IRAC à bord du satellite Spitzer pour sonder la distribution de matière en avant-plan sur des régions d'environ $5' \times 5'$. A 3.6 et 4.5 μm, IRAC est également sensible aux populations stellaires des composantes à haut redshift. En complément, la spectroscopie X-Shooter permet de déterminer précisément le redshift de la galaxie à l'origine de l'amplification gravitationnelle vers la source sub-mm la plus lumineuse de l'échantillon.

Réservoirs de poussière et formation stellaire intégrée dans les GEMS

Les propriétés globales de l'échantillon obtenues à partir du suivi infrarouge lointain et sub-mm sont présentées dans une publication (Cañameras et al. 2015) ainsi qu'au chapitre 4. La mesure des redshifts spectroscopiques des GEMS est effectuée avec le spectrographe EMIR qui permet d'observer la bande à 3-mm avec une couverture spectrale étendue (environ 16 GHz par réglage de fréquence). Pour chaque source, notre stratégie d'observation comportant deux réglages de fréquence successifs inclut au moins une raie d'émission du CO, pour un décalage spectral $z \gtrsim 1.1$. La détection d'au moins deux transitions par GEMS (soit CO(3-2) et CO(4-3), soit CO(4-3) et CO(5-4)) garantit des redshifts spectroscopiques robustes, dans l'intervalle $z = 2.2 - 3.6$.

J'ajuste ensuite un corps noir modifié sur la photométrie infrarouge lointain et sub-mm pour caractériser les réservoirs de poussière froide. Des ajustements avec une composante unique suggèrent des températures de poussière dans l'intervalle $T_d = 33 - 50$ K, en accord avec la caractérisation d'autres galaxies poussiéreuses à haut décalage spectral (e.g., Greve et al. 2012; Weiß et al. 2013). De telles températures sont observées aussi bien dans des galaxies sub-mm à sursaut de formation stellaire intense que dans des galaxies poussiéreuses distantes à formation stellaire plus régulière, sur la séquence principale. Ces mêmes ajustements permettent d'évaluer les masses de poussière et les luminosités infrarouge lointain des GEMS, de $M_d = (3.5 - 11) \times 10^9\ \mu^{-1}\ M_\odot$ et $L_{FIR} = (4.6 - 27) \times 10^{13}\ \mu^{-1}\ M_\odot$ respectivement. Des telles luminosités suggèrent des taux de formation stellaire intégrée dans l'intervalle $8000 - 46000\ \mu^{-1}\ M_\odot\ yr^{-1}$, d'après le facteur de conversion de Kennicutt (1998). Néanmoins, il est important de rappeler que ces dernières grandeurs sont déduites des densités de flux boostées par lentille gravitationnelle et doivent, par conséquent, être corrigées par les facteurs d'amplification.

L'analyse des distributions spectrale d'énergie illustrée par la Figure 4.9, ainsi que les données du relevé FIRST à 1.4 GHz, prouvent que les GEMS n'abritent pas de noyau actif puissant participant au chauffage des poussières de manière significative. Au contraire, ce chauffage produisant des températures de poussière inférieures à 50 K semble totalement dominé par la formation stellaire. D'autre part, de nombreux arguments empiriques tels que les morphologies résolues du continuum des poussières et du gaz moléculaire, ou la relation entre T_d et L_{FIR}, confirment clairement la nature lentillée de chaque GEMS. Notamment, certaines de ces sources rouges se révèlent compactes à des résolutions angulaires de $2''$, tandis que la plupart forment des arcs gravitationnels étendus (Fig.4.6).

Nous caractérisons également la corrélation infrarouge lointain radio pour notre échantillon et trouvons des valeurs du paramètre q_{IR} très dispersées. Certaines sources atteignent $q_{IR} \sim 2.7$, indiquant un excès considérable d'émission infrarouge lointain par rapport à l'émission synchrotron. Un tel régime peut être la conséquence de mouvements turbulents dans le milieu interstellaire, comme également suggéré par les profils élargis des raies d'émission du CO. Les GEMS présentent des rapports L'_{CO}/M_d de 40-140, compatibles avec un faible facteur de conversion α_{CO} (e.g., Downes & Solomon 1998), tel qu'attendu pour des galaxies massives et poussiéreuses ayant des métallicités élevées (Magdis et al. 2011; Genzel et al. 2012). Ces arguments suggèrent des masses de gaz moléculaire de $(2 - 10) \times 10^{11}\ \mu^{-1}\ M_\odot$. Enfin, la loi de Schmidt-Kennicutt intégrée tracée en Figure 4.12 prouve que cet échantillon contient des galaxies à sursaut de formation stellaire ordinaires (par comparaison, en particulier, avec les échantillons de Daddi et al. 2010) et bénéficiant d'amplifications gravitationnelles élevées.

Distribution de la masse intervenant le long de chaque ligne de visée

Notre modélisation du phénomène de lentille gravitationnelle forte est basée sur une approche paramétrique et requiert, au préalable, une caractérisation des potentiels gravitationnels d'avant-plan. Afin de contraindre la distribution de matière le long des lignes de visée vers chaque GEMS, j'utilise l'imagerie optique et infrarouge proche obtenue au CFHT et au VLT ainsi que les redshifts spectroscopiques disponibles dans les catalogues publics du Sloan Digital Sky Survey ou issus de nos propres observations. L'analyse détaillée basée sur ce jeu de données est présentée au chapitre 5 et suit trois étapes. Tout d'abord, j'estime les comptages de galaxies dans l'infrarouge proche, puis je mesure les redshifts photométriques des galaxies d'avant-plan pour enfin effectuer une recherche aveugle de la séquence rouge dans l'optique et l'infrarouge proche.

Premièrement, l'algorithme AKDE (Adaptive Kernel Density Estimate, Pisani 1996; Valtchanov et al. 2013) permet d'estimer la densité de galaxies par unité de surface dans un champ de référence, pour en déduire la position et la significativité des surdensités de sources dans la bande K. En second lieu, je combine cette analyse bidimensionelle avec les quelques redshifts spectroscopiques disponibles (3.3.2 ou SDSS-DR12, Alam et al. (2015)) et nos propres redshifts photométriques estimés avec le code BPZ (Bayesian Photometric Redshifts, Benítez 2000), afin d'identifier sans équivoque les structures de

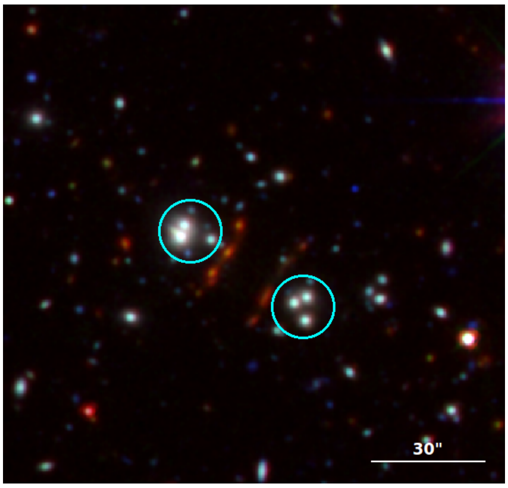

Figure 1: Image trois couleurs d'une source de l'échantillon "Planck's Dusty GEMS" utilisant les bandes r et K de MegaCam et WIRCam, respectivement, et le canal à 4.5 μm d'IRAC. Sur ce champ de vue, les arcs gravitationnels détectés par Planck et Herschel dans les domaines infrarouge lointain et sub-millimétrique ont des couleurs très rouges et une morphologie fragmentée. Ils se situent à $z = 2.24$, derrière deux groupes de galaxies à $z = 0.35$ (cercles bleus) produisant la majeure partie de l'amplification gravitationnelle.

galaxies en direction des GEMS. Notre suivi en imagerie couvre la discontinuité à 4000 Å ($D_n(4000)$, Connolly et al. 1995) – une discontinuité spectrale nettement marquée dans les galaxies passives – pour des galaxies à décalage spectral intermédiaire, augmentant ainsi la fiabilité de nos redshifts photométriques. Troisièmement, j'utilise la séquence rouge en tant que sonde des environnements denses (Gladders & Yee 2000) pour localiser les amas de galaxies les plus massifs. Après avoir calibré nos modèles sur l'amas de Coma à $z = 0.023$, j'effectue une recherche aveugle de cette séquence à $z < 1.0$ dans les diagrammes couleur-magnitude.

Comme résumé au 5.5 et sur la Figure 5.11, cette caractérisation montre que chaque source sub-mm de notre échantillon est alignée avec une structure d'avant-plan responsable de l'amplification gravitationnelle, généralement située à $z < 1$. La moitié d'entre elles sont associés à des galaxies isolées, tandis que seules trois d'entre elles sont clairement lentillées par des groupes ou amas de galaxies mis en évidence par l'analyse de surdensité et la distribution en redshift. Pour deux GEMS, nos modèles de séquence rouge sont compatibles avec les excès de sources rouges et passives détectés dans les diagrammes couleur-magnitude, suggérant des conglomérats de galaxies particulièrement denses au sein de ces potentiels gravitationels.

Modélisation de l'effet de lentille gravitationnelle forte avec LENSTOOL

La modélisation détaillée de l'effet de lentille forte est menée à l'aide du logiciel LENSTOOL (Kneib 1993; Jullo et al. 2007), dans le but de déduire les masses intégrées le long des lignes de visée et les facteurs d'amplifications précis. LENSTOOL est un code public qui adopte le formalisme bayésien pour optimiser la distribution de masse responsable du potentiel gravitationnel, à partir des caractéristiques structurales de la lentille et de la position et multiplicité des images lentillées. La Figure 6.1 présente une telle association d'images multiples permettant de contraindre le modèle. Les incertitudes sont calculées suivant une méthode de Monte-Carlo par chaînes de Markov (MCMC).

Seules quatre sources de l'échantillon présentant des contraintes observationnelles suffisantes sont modélisées de la sorte. Tout d'abord, je me focalise sur la GEMS la plus brillante résolue, par le SMA et ALMA, en un anneau d'Einstein quasi-complet de $1.4''$ de diamètre (Fig.6.1). Je déduis du modèle de lentille qu'elle se trouve derrière une galaxie isolée produisant des amplifications de $\mu \sim 10 - 20$.

Cela suggère que les propriétés apparentes de cette GEMS tracent des activités de formation stellaire intenses perçues au travers d'un télescope cosmique particulièrement puissant. La masse intégrée le long de la ligne de visée produisant de telles amplifications et distorsions vaut $(3.7 \pm 0.5) \times 10^{11}$ $M_\odot$, à l'intérieur de l'anneau formé par les arcs sub-mm. Le modèle me permet également de reconstruire la morphologie intrinsèque de cette GEMS dans le plan source et, bien sûr, d'utiliser le facteur μ pour corriger l'ensemble des propriétés déterminées dans le Chapitre 4. Dans un deuxième temps, je dérive le modèle de lentille de chaque GEMS associée à un groupe ou amas de galaxies d'avant-plan, nécessitant d'introduire un halo de matière noire de grande échelle (Kneib et al. 1996).

Etude détaillée de trois sources de l'échantillon

Durant notre suivi de l'échantillon complet – notamment avec l'interféromètre de l'IRAM au Plateau de Bure, le SMA et ALMA – trois sources se sont avéré posséder des propriétés particulièrement remarquables. Tout d'abord le *Malachite*, une GEMS à z = 2.6 et à formation stellaire modérée, présente une morphologie intéressante dans le plan image. Elle comprend trois composantes distribuées le long d'une ligne critique de 12″ de diamètre, dont deux images multiples d'une région intrinsèquement compacte et un arc étendu sur plus de 5″. J'utilise les observations du CO(3-2) à une résolution angulaire inférieure à la seconde d'arc pour étudier la cinématique perturbée du gaz moléculaire dans cette source. Les offsets en vitesse atteignent 600 km s^{-1} entre chaque extrémité des composantes compactes, suggérant qu'elles tracent une région de recouvrement entre deux galaxies en interaction, comme observé par le passé dans d'autres sources sub-mm.

Ensuite, nous utilisons la raie de structure fine [CII] observée avec l'interféromètre ALMA à une résolution de 0.3″, pour sonder les propriétés du gaz interstellaire dans le *Grenat* (Nesvadba et al. 2016). Nous caractérisons uniquement l'une des quatre composantes de la source d'arrière-plan. Nous présentons d'une part les cinématiques résolues au sein de cette composante, déduites du [CII] observé en émission. Mais nous présentons surtout la première détection d'une caractéristique d'absorption du [CII] hors de la Voie Lactée (Fig.7.9). En général, de telles raies d'absorption du [CII] tracent le milieu interstellaire diffus de notre Galaxie (e.g., Gerin et al. 2015) et sont détectées en direction de régions de formation stellaire produisant une émission continuum brillante. Dans notre cas, nous attribuons cette caractéristique spectrale à un réservoir de matière gazeuse situé entre l'observateur et la source de continuum sub-mm, et en train de chuter vers cette dernière. Pour cette raison, le *Garnet* offre une opportunité rare pour étudier le gaz dans une galaxie à grand décalage spectral, en dehors des régions de formation stellaire intenses. Ces résultats, combinés aux rapports $L_{[CII]}/L_{FIR}$, montrent que la détection de cette raie de structure fine à haute redshift sonde une large gamme d'environnements, du gaz dense aux réservoirs plus diffus et étendus.

Finalement, je caractérise la source la plus brillante de notre échantillon, le *Ruby*. Cette source à sursaut de formation stellaire possède des propriétés extrêmes dans le plan image. Elle est lentillée par une seule galaxie d'avant-plan et forme un anneau d'Einstein quasi-complet d'environ 1.4″ de diamètre. Nous mesurons des intensités de formation stellaire exceptionnelles, de 1000 à 5000 $M_\odot$ yr^{-1} kpc^{-2}, au sein des amas de formation stellaire distribués le long des arcs sub-mm et résolus avec le SMA. J'utilise la distribution spectrale d'énergie en optique et infrarouge pour distinguer les populations stellaires évoluées provenant de l'avant-plan et les populations plus jeunes et atténuées émises par le *Ruby* en arrière-plan. Cela me permet de déduire une masse stellaire $M_* = (2.5 - 3.0) \times 10^{11}$ $M_\odot$ pour la galaxie amplifiante qui se situe à un décalage spectral étonnamment élevé (z = 1.52, comparable aux lentilles gravitationnelles les plus distantes, van der Wel et al. 2013; Wong et al. 2014).

Une caractérisation préliminaire des conditions du gaz moléculaire et des processus de formation stellaire dans cette GEMS est obtenue grâce à l'interférométrie CO(4-3) d'ALMA, à une résolution de 0.1″. Ce cube de données confirme que l'émission du CO(4-3) et du continuum des poussières à

3-mm ont une morphologie fragmentée (voir Fig.7.15). La majeure partie de l'émission provient en réalité d'un total de dix noeuds, présentant des offsets en vitesse élevés (de -600 à +200 km s^{-1}) et un intervalle de dispersions de vitesse très large (25-330 km s^{-1}). Finalement, après avoir déduit une masse dynamique $M_{\rm dyn} = 3 \times 10^{10}$ $M_{\odot}$, je sonde la relation de Schmidt-Kennicutt résolue à la Figure 7.16. Cette figure met clairement en évidence une efficacité de formation stellaire accrue dans le *Ruby*, en comparaison avec les galaxies actives proches (e.g., Andrews & Thompson 2011) et les nuages moléculaires géants les plus denses de notre Galaxie. L'analyse suggère que pour chaque noeud, environ 30% du gaz est transformé en étoiles par temps de chute libre. Il s'agit d'une valeur bien supérieure aux 1% mesurés habituellement dans l'univers local (e.g., Krumholz & Tan 2007). Elle est cependant comparable aux efficacités mesurées dans les régions internes des nuages moléculaires géants de la Voie Lactée (Alves et al. 2007). Ces résultats suggèrent donc que les régions de formation stellaire dans les galaxies poussiéreuses à grand décalage spectral pourraient ressembler à des coeurs de nuages moléculaires géants étendus sur plusieurs dizaines de parsecs (voir aussi Stacey et al. 2010; Swinbank et al. 2011).

Cette GEMS est également idéale pour déterminer les processus limitant la formation stellaire dans ses phases les plus extrêmes. En particulier, les dispersions de vitesse mesurées avec le cube de données ALMA suggèrent que la turbulence pourrait compenser l'effondrement gravitationnel, et donc limiter la formation des étoiles dans le *Ruby*. Au §7.3.6, nous discutons des processus physiques potentiellement capables de produire une telle turbulence. Cependant, les intensités de formation stellaire maximales présentées à la Figure 7.16 montrent que le *Ruby* tombe dans le régime des sursauts de formation stellaire proches de la limite d'Eddington et régulés par la pression de radiation. Cela signifie donc que le processus de rétroaction lié à la naissance des étoiles – dû à la pression de rayonnement exercée par les populations les plus jeunes et massives – pourrait permettre à la formation stellaire d'être auto-régulée dans cette GEMS.

Contents

List of Figures

List of Tables

Chapter 1

High-redshift star formation in the context of galaxy evolution

Contents

1.1 Introduction

Understanding the cosmic structure formation from the Big-Bang to the present day requires studying the processes that underlie the growth of gravitationally bound structures from the near homogeneous initial state. It is now well established that the small temperature inhomogeneities of the cosmic microwave background probed by several ground or space-based missions, including the Planck satellite, provide the adequate initial conditions for the characterization of mass assembly. A global picture of galaxy evolution has been obtained from a large number of multi-wavelength surveys, and from the detailed characterization of specific populations at different cosmic epochs. However, the formation of the first galaxies and their evolution throughout cosmic time remains an active area of research in observational cosmology. Several studies of distant galaxies are naturally based on observations of low or intermediate redshift slices of the universe and attempt to determine the similarities and fundamental differences between each population. Generally, focusing on the high-redshift universe allows to probe the physical mechanisms that led to the formation of the large scale structures and produced the great diversity of galaxies seen at low redshift.

In the framework of the Λ-CDM paradigm, it appears that the dark energy (Λ) and Cold Dark Matter (CDM) components play a substantial role for the formation and evolution of galaxies and that the gradual mass assembly constrain their growth, sometimes through gas-rich mergers. In the hierarchical model of galaxy formation and evolution, these occasional and violent events have a significant role in the increase of their size and stellar mass over cosmic time. In addition, the continuous accretion of diffuse gas from the cosmic web filaments can also replenish the interstellar medium of galaxies, fuel the active star formation, and affect their global evolution (Kereš et al. 2005). In contrast, strong galactic winds from young stellar populations or mass accretion onto the central supermassive black holes can result in large-scale outflows that eject the gas from the gravitational potential of the host galaxy (Heckman et al. 1990). These competing effects result in a decrease of the molecular gas fractions from about 50% at $z \sim 2$ (Tacconi et al. 2013) to about 5% locally.

1.2 Why do we need to probe the universe at z∼2 ?

The time evolution of the cosmic star formation rate (SFR) density was probed in several studies during the last two decades, in multiple wavelength regimes from the rest-frame UV to the FIR. A consensus has emerged from these studies according to which most of the stars have been formed during a peak of star formation at $1 < z < 3$ (e.g. Madau et al. 1996; Hopkins et al. 2006; Madau & Dickinson 2014). Figure 1.1 shows that the volume averaged star formation rate density at this cosmic epoch was an order of magnitude higher than today. This means that about half of the stars we see today were already in place by $z \sim 2$ (Dickinson et al. 2003). Probing the formation mechanisms at $z \sim 2$ is therefeore crucial to constrain the stellar mass build up in early galaxies and their overall evolution. This also implies that the cosmic epoch corresponding to lookback times of about 10 Gyr has a direct influence on the stellar populations and overall properties of local galaxies.

Moreover, the range $z \sim 2-3$ probes the rapid phase of mass assembly for the most massive elliptical galaxies with $M_* \gtrsim 10^{11}$ $M_\odot$ seen in the local universe. Consequently, it is associated with the time interval where the strong color bimodality between red early-type and blue late-type galaxies was implemented. This critical phase of particularly intense star formation activity can be characterized directly in the sub-millimeter regime, through the population of bright dust-enshrouded galaxies which will be further described in this introduction (Magnelli et al. 2012). For these reasons, $z \sim 2-3$ corresponds to a turnover epoch in galaxy evolution and has solicited special efforts in the field of extragalactic astronomy, also facilitated by ever-improved long wavelength instrumentation. In this section, I will focus on the most interesting processes occuring at these redshifts and addressed in this thesis. Some of them remain poorly understood such as, for instance, the drop of star formation density observed at $z < 2$.

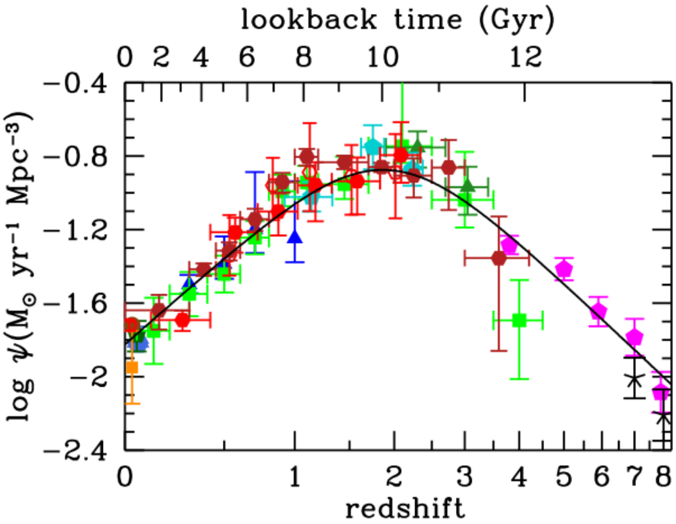

Figure 1.1: The cosmic evolution of the star formation rate volume density of Madau & Dickinson (2014) (their Figure 9), obtained from a compilation of multiple surveys selected from the rest-frame ultraviolet (grey, blue, light green, dark green, turquoise, magenta and black points) or the infrared (brown, orange, light red and dark red points). The best-fitting model is plotted as a black line and shows a strong peak at z $\sim$ 2.

1.2.1 The quenching of star formation

Given the extreme environments observed at z $\sim 2-3$, the evolutionary models predict a higher proportion of massive Star-Forming Galaxies (SFGs) at low redshift than actually observed. Thus, the minimal gas masses observed in the most massive local galaxies suggest a rapid quenching of the star formation at old lookback times. There is also growing evidence that this process differs in disks and ellipticals, involving different timescales (Schawinski et al. 2014). A large range of powerful mechanisms have been proposed in the literature, from Active Galactic Nuclei (AGN) feedback (Springel et al. 2005), strong tidal perturbations or galaxy mergers (Sanders & Mirabel 1996; Hopkins et al. 2006), to an abrupt change in the mode of gas accretion (Kereš et al. 2005). It is also widely recognized that, if strong gas outflows can remove sufficient amounts of gas from the host galaxy, the overall growth of the structure can be stopped and the star formation can be efficiently quenched. On the one hand, molecular gas outflows are commonly detected in nearby ULIRGs (e.g., Cicone et al. 2014; Feruglio et al. 2015; García-Burillo et al. 2015) and are either attributed to negative feedback from the AGN activity, to winds or intense radiation pressure from massive newborn stars (i.e. directly associated with the recent star formation), or to both effects. On the other hand, the discovery of massive gas-poor and quiescent galaxies at z $\sim$ 2 (e.g., Daddi et al. 2005) suggest that this process also takes place in the distant universe, amongst other arguments. In fact, fast ionized outflows are commonly detected in z $\sim 2-3$ SFGs (Carniani et al. 2015) and also seem to be driven by the intense star formation (Newman et al. 2012) or, when present, by the central AGN (Genzel et al. 2014).

1.2.2 The main sequence of star formation and the starburst mode

As a general rule, it is established that dusty galaxies with higher gas masses form stars at higher rates. However, the stellar mass build up and overall growth of galaxies is actually governed by two distinct modes of star formation clearly illustrated in Figure 1.2 :

- a steady mode in normal disks that define a tight correlation in the SFR-M_* plane called the main sequence of star formation,

- a more rapid starburst mode containing outliers of this sequence and generally assumed to be driven by mergers.

The tight correlation between star formation rate and stellar mass

The main sequence of star formation plays an important role in determining the physical nature of star formation in galaxies. It was characterized in several local studies using extensive UV/optical samples, such as subsets of the Sloan Digital Sky Survey with no AGN contamination (Brinchmann et al. 2004; Salim et al. 2005). A similar correlation was found in the Extended Groth Strip by Noeske et al. (2007) and in GOODS by Elbaz et al. (2007) at $z \sim 1$, showing that this sequence was already in place when the universe was about half of its current age. Furthermore one can probe the main sequence out to $z \sim 2$ by selecting moderately star forming galaxies (Rodighiero et al. 2011), for instance with their photometry in the B, z and K bands (the BzK criteria, Daddi et al. 2004). Daddi et al. (2007) use deep multi-wavelength observations of $1.5 < z < 2.5$ galaxies in the GOODS field and apply this criteria to build a complete sample of SFGs without quiescent sources. They also detect a tight $\mathrm{SFR} - \mathrm{M}_*$ correlation for the galaxies showing counterparts in their 24 μm imaging. Consequently, the detection of this feature up to $z \sim 2.5$ suggests that galaxies falling on the main sequence have formed their stars gradually and during long timescales, probably thanks to the fueling of several gas rich inflows.

The slope of the main sequence is shallower than unity and strongly depends both on the sample selection and the SFR estimate. At $z \lesssim 1.3$, the slope varies at a characteristic mass $\sim 10^{10}$ $\mathrm{M}_\odot$ and the $\mathrm{SFR} - \mathrm{M}_*$ relation tends to flatten at higher stellar masses (Lee et al. 2015). The normalization of the correlation is a more crucial parameter and obviously increases from $z \sim 0$ to $z \sim 2$ (Elbaz et al. 2007; Daddi et al. 2007; Kurczynski et al. 2016). This means that, for a given mass, a $z \sim 2$ galaxy falling on the fitted main sequence would form about 4 and 30 times more stars per unit time than similar sources at $z \sim 1$ and $z \sim 0$, respectively (Daddi et al. 2007). This trend probably highlights that the average star formation rate in galaxies declines steadily with decreasing redshift due to lower gas fractions, while the impact of starburst frequency and feedback efficiency is probably minor (Noeske et al. 2007). The dispersion of the $\mathrm{SFR} - \mathrm{M}_*$ correlation is constant out to $z \sim 1$ (Noeske et al. 2007) and the scatter does not seem to increase as would be expected in less massive galaxies with M_* as low as $\sim 10^7$ $\mathrm{M}_\odot$ (Kurczynski et al. 2016). In fact, interpreting this trend remains challenging because SED fitting methods used to derive the SFRs and M_* are probably averaging the variations over timescales <100 Myr, that are typical for the underlying physical processes.

The population of extreme starbursts

Dusty starbursting galaxies are optically thick in the UV and they are therefore usually selected in the FIR regime where the star formation rates can be directly measured. This population both includes local ULIRGs and a fraction of the high redshift SMGs. Compared to the best-fitting main sequence they show much higher integrated star formation rates, up to 4-10 times higher for a given stellar mass (see Fig.1.2). Consequently, the specific star formation rates ($\mathrm{SFR}/\mathrm{M}_*$) of starbursts are significantly offset compared to more gradually star-forming galaxies on the main sequence, and this physical parameter can be used to distinguish the two populations. For instance, these outliers amount to a significant portion of the large sample of sub-millimeter bright galaxies of Magnelli et al. (2012) characterized with the Herschel satellite.

The extreme star formation activity observed in these sources has been usually attributed to the tidal perturbations during gas rich mergers. This type of interaction could result in gaseous inflows along with strong concentration of gas and, consequently, in major burst of star formation. This scenario is supported by hydrodynamical simulations (e.g. Mihos & Hernquist 1996), but only about one third of the star-forming galaxies at $z \sim 1 - 3$ show clear signatures of mergers or tidal interactions in their spatially-resolved gas kinematics (e.g. Förster Schreiber et al. 2009). Thus, alternative modes of triggering of extreme star formation activity have been considered in the literature, as further described in 1.3.1.

These two modes in the global picture of star formation

Rodighiero et al. (2011) first quantified the relative contribution of the two modes of star formation, during the $1.5 < z < 2.5$ epoch that dominates the cosmic history of star formation (Fig.1.2). Using the Herschel/PACS follow up of the COSMOS and GOODS-S fields, they find that starburst galaxies have a minor role in the formation of stars since they only account for about 10% of the cosmic star formation rate density at $z \sim 2$. The contribution of the starburst population only becomes significant when considering the SFR > 1000 $M_\odot$ yr^{-1} regime. In addition, these starbursts – and particularly those that are driven by major mergers – are expected to play a crucial role on the quenching of star formation and the morphological transformation of galaxies.

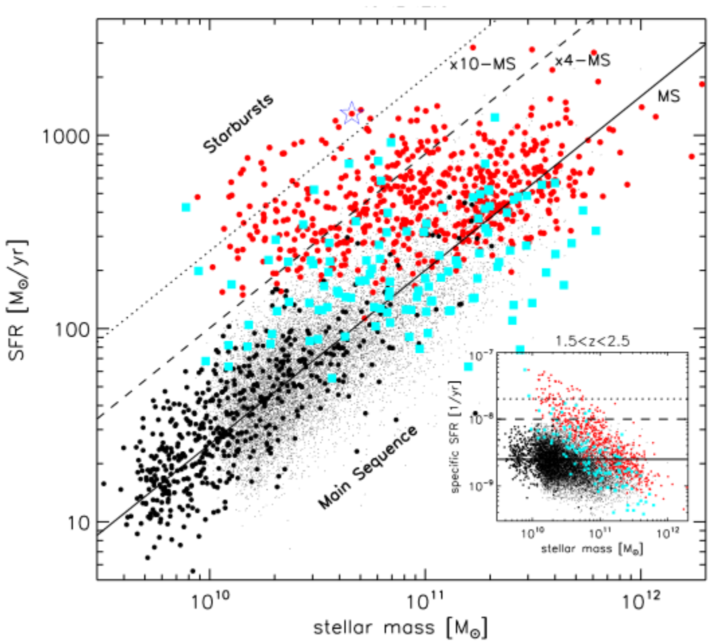

Figure 1.2: The star formation main sequence of Rodighiero et al. (2011) presented in the SFR-M_* plane using four samples of galaxies at $1.5 < z < 2.5$. The figure includes Herschel/PACS observations of the COSMOS (red circles) and GOODS-S fields (cyan squares), as well as BzK galaxies in COSMOS (black dots) and GOODS-S (black filled circles). The solid black line is the best-fitting main sequence of Daddi et al. (2007), at $z \sim 2$. The inset panel shows a similar relation for the specific star formation rate (i.e. SFR/M_*).

1.2.3 Resolved Schmidt-Kennicutt law at high-redshift

The Schmidt-Kennicutt law

The Schmidt-Kennicutt empirical law between the gas mass surface density and star formation rate density was first derived in the Milky Way by M. Schmidt, who found a power law relation $\Sigma_{\rm SFR} \propto \Sigma_{\rm gas}^{\rm n}$. Combining an analysis of young nearby stars and white dwarfs, with measurements of Helium abundance, he deduced a power in the range $\rm n \sim 1 - 3$ and recommended to adopt $\rm n = 2$ (Schmidt 1959). Then, Kennicutt (1998) calibrated the relation using 61 local spirals and 36 infrared-luminous galaxies, finding a slope of 1.4 ± 0.15 in the log-space. He derived averaged gas mass surface densities from the neutral and molecular components and neglected the atomic gas in the infrared starbursts. This work confirms that in the local universe, gas mass surface density seems to be the major parameter determining the star formation intensity over several orders of magnitude. A mix of physical mechanisms could also put this tight correlation in place and no clear consensus has emerged yet. Subsequent studies have nonetheless shown that it holds over scales of around 100 pc to entire galaxies.

It is worth mentioning that the star formation observed in nearby galaxies is quite inefficient, with only 1% of gas collapsing per free-fall time. This is probably due to a combination of several processes that prevent the gravitational collapse. Turbulence enhanced by interstellar shocks must play a major role by stabilizing the gas clouds on large scales. Other energetic processes such as the radiation pressure from young massive stars, or galactic winds can significantly perturb the properties and structure of star-forming clouds. The ultraviolet photons indeed alter the atomic to molecular transition phase and heat the interstellar medium, while Jeans instability only occurs if this radiation is efficiently shielded (Krumholz et al. 2012). Star formation can become more efficient in strongly compressed gas reservoirs located, for instance, in the overlap region between merging galaxies (e.g., Genzel et al. 2010).

Challenges of the distant star formation

Star formation feedback seems to play a crucial role on the activity and global evolution of galaxies in the early universe. This ingredient and the main other processes observed at low-redshift have been characterized during the last two decades, with a major breakthrough occuring since the last few years due to the advent of a new generation of long-wavelength facilities. At the present time, it remains to be established whether the same mix of processes regulates the star formation efficiency and hence the star formation law at low and high-redshift. The higher stellar and gas mass surface densities observed in distant galaxies could have a great impact, but different heating mechanisms by UV radiation or cosmic rays might also be considered.

Several studies have emphasized that not all galaxies may strictly obey the same empirical star formation law. Genzel et al. (2010) find similar relations between total molecular gas mass and averaged star formation in normal star-forming galaxies at low and high redshift ($1 < z < 3$), and independent of the environment. However, at a given gas mass and both for local and distant sources, starbursts show 4-10 times greater star formation rates than these normal disks. They interpret this effect either as a result of a top-heavy initial mass functions in these systems (Baugh et al. 2005), or as evidence for merger-driven star formation or higher gas fractions. Daddi et al. (2010) also highlight these two regimes in the Schmidt-Kennicutt diagram which can be associated with a more rapid star formation mode for starbursts than normal disks (or higher dynamical timescales in disks). These results demonstrate the need to interpret the star formation efficiencies of these extremely star-forming sources and to disentangle the influence of dynamical instabilities and molecular gas fractions. This is particularly important at high-redshift where this population shows the most outstanding properties and where the environments differ significantly from the local universe. For example, one could consider that their interstellar medium contains more star-forming clouds than in more quiescent high-redshift galaxies (Lehnert et al. 2013), or the star formation efficiency per free-fall time could be higher (Dekel et al. 2009).

It is generally accepted that distant galaxies comprise dense star-forming clumps accross a more diffuse disk. Thus, a better understanding of the high-redshift star formation requires resolved observations of these compact regions, ideally including the gas, dust and stellar components. From such constraints, one can determine if star formation is fundamentally different in gas-rich galaxies at $z \sim 2$ and in quiescent Milky Way like disks at $z \sim 0$. These data enable us to compare the properties of low and high-redshift starbursts and, finally, to conclude whether the populations of low and high-redshift sources follow common or separate modes of star formation. Unfortunately, the limited angular resolutions make it extremely difficult to probe these spatial scales and to resolve the Schmidt-Kennicutt relation at high-redshift.

1.3 The populations of dusty galaxies at high-redshift

Understanding the star formation processes in the global context of galaxy evolution requires the analysis of the most massive high-redshift starbursts. They could be the progenitors of the giant ellipticals seen in high-density regions of the local universe (Lilly et al. 1999; Swinbank et al. 2006; Hickox et al. 2012) because the stellar populations observed in the bulge of these ellipticals seem to have formed very rapidly and at high lookback times. The dusty starburst galaxies are expected to dominate the cosmic star formation rate density in the redshift range $z \sim 1-3$ (Dole et al. 2006). They should also account for more than half of the energy produced by star formation in the entire universe (Hauser & Dwek 2001). Originally, the study of these distant galaxies in the sub-mm regime was initiated by the development of the high-sensitivity SCUBA camera and its deep fields (Smail et al. 1997). However, the beam sizes of the JCMT of about $14''$ did not allow to resolve these sources and the identification of their extremely faint optical counterparts was extremely challenging. Fortunately, during the following decade, major instrumental progresses have allowed to enhance the characterization of this population and suggested that it plays a pivotal role in the global picture of galaxy evolution.

1.3.1 Overall properties

This population of massive dusty high-redshift galaxies are sometimes referred to as SubMillimeter Galaxies (SMGs) when selected with (sub-)mm imaging. They are the most highly star-forming sources accross the history of the universe, with prodigious star formation rates between a few hundred $M_\odot yr^{-1}$ (Smail et al. 1997) and 1000 $M_\odot yr^{-1}$, about an order of magnitude higher than the most intense starbursts in the nearby universe (e.g. the Arp 220 merger at about 75 Mpc Engel et al. 2011). Their massive dust reservoirs are heated by the intense star formation during a rapid initial growth phase associated with extreme FIR/sub-mm luminosities (typically in the regime of hyperluminous infrared galaxies). However this tremendous activity only holds during a limited amount of time until the gas reservoirs get depleted. For this reason, their high sub-millimeter emission is rather short with typical timescales of $\lesssim 100$ Myr, making this population extremely uncommon in the local universe. More precisely, the intrinsic volume density of the SMG population increases by 3 orders of magnitude from $z = 0$ to $z \sim 2.5$ (Blain et al. 2002), and declines above $z \sim 3$ (Chapman et al. 2005).

These galaxies exhibit typical stellar and dynamical masses of a few times 10^{10-11} $M_\odot$ (Smail et al. 2004; Swinbank et al. 2006; Nesvadba et al. 2007). During the last decade, the advent of the new generation of mm/radio interferometers has allowed detailed studies of their cold molecular gas (Daddi et al. 2010; Tacconi et al. 2013). At $z \sim 2$, this reveals extensive gas reservoirs of about 10 kpc and high gas fractions of 20-80% (Daddi et al. 2010; Tacconi et al. 2010). At a given redshift, the most massive and starbursting SMGs nonetheless have lower gas fractions than more quiescent disks on the main sequence (Geach et al. 2011), suggesting that this population is observed during a relatively evolved phase. It is also generally accepted that their insterstellar medium is highly turbulent (Lehnert et al. 2009) which might be caused by a number of processes related to galaxy assembly and the associated gas heating (merging, gas accretion, fragmentation of gaseous disks, feedback from star formation or AGN).

1.3.2 Morphology and kinematics

High-resolution optical imaging available for these sources reveal clumpy and irregular morphologies. However, with such data it is not immediately clear whether this clumpiness indicates the preferred sites of star formation or results from an irregular dust extinction. Molecular gas emission traced by the intermediate rotational levels of CO also reveal compact clumps in high-redshift star-forming galaxies (Swinbank et al. 2011), suggesting that the fuel for star formation is mainly distributed in several high-mass concentrations. The formation of these clumps in high-redshift galaxies seems to result from strong dynamical instabilities. These perturbations could fragment the dense and turbulent interstellar medium into massive concentrations of 10^{8-9} $M_\odot$ (Elmegreen 2007). This mechanism differs from the continuous energy dissipation and the condensation of giant molecular clouds observed in local disks.

Some studies reveal complex molecular gas kinematics, which they attribute either to signatures of ongoing gas-rich mergers or to very dense star-forming disks (Tacconi et al. 2006, 2008). In the latter case, the perturbed observed kinematics may be the consequence of the relative motions between star-forming clumps distributed accross globally rotating disks (Förster Schreiber et al. 2006). Shapiro et al. (2008) present a criterion to determine if such galaxies are dominated by turbulent or rotational motions. They suggest to perform a Fourier analysis of the irregularities of the velocity field, to conclude if a given distant galaxy observed with enough spatial resolution elements is more likely a disk or a merger.

1.3.3 Contribution of active galactic nuclei

The spectroscopic characterizations conducted from the NIR to the X-ray domains have shown that starbursts are the main source of dust heating in SMGs (Engel et al. 2010). However, active galactic nuclei are detected in a large fraction of SMGs with deep X-ray observations. Alexander et al. (2003) suggests that about 30-50% of the bright SMGs with $S_{850} > 5$ mJy contain this major source of dust heating. Subsequent studies have found a large range of AGN contributions to the bolometric infrared luminosities of SMGs, from 8% to 35% (Swinbank et al. 2004; Alexander et al. 2005, 2008). Accordingly, these results demonstrate that the outstanding luminosities of SMGs do not guarantee that they probe only the extremely star-forming environments. Selecting the most intensely star-forming galaxies at high-redshift requires a careful identification of AGN dominated sources.

1.4 The help of strong gravitational lensing

Even the most outstanding high-redshift galaxies are very faint and have small projected sizes of 1-2$''$ or even less. Fortunately, the strong gravitational lensing effect enables to naturally zoom in onto the distant universe and to characterize the dusty star formation at high-redshift with spatial resolutions approaching those accessible in local galaxies.

Gravitational lensing involves the deflection of light paths by a massive foreground astronomical object located between the emitter and the observer, a phenomenon which was already considered by Newton although its description of light and gravity did not allow a proper understanding of the process. Private notes from John Mitchell were discovered during the nineteenth century and showed that, in 1783, this astronomer suggested to use this effect to measure the mass of stars. The first paper predicting the deflection of light paths near the sun within the framework of Newtonian gravity was published by Johann Georg von Soldner in 1801. Einstein repeated the calculation by using the principle of equivalence and subsequently derived the equations of General Relativity (GR) in 1916 which allowed him to find a new prediction, two times higher (Einstein 1916). A few years later, Arthur Stanley Eddington confirmed Einstein's result by measuring the angular position of background stars during a total solar eclipse (Eddington 1919). The light deflection produced by the sun therefore became one of the most important tests confirming the validity of the GR.

In addition, Fritz Zwicky considered strong gravitational lensing by entire galaxies and suggested that their light deflection could produce multiple images of a given background source with angular separations detectable for an observer on Earth (Zwicky 1937a,b). The first detection of a gravitationally lensed object was obtained decades later by Denis Walsh, Robert F. Carswell and Ray J. Weymann who discovered a pair of quasars separated by 5.7$''$, 0957+561 A and B, at $z = 1.406$ (Walsh et al. 1979). The two spectra were perfectly matching which lead the authors to conclude that they were observing two multiple images of a single quasar produced by a foreground lensing potential. Other studies subsequently detected the lensing galaxy and thereby rejected the hypothesis of an intrinsically double quasar. Then, the discovery of the first giant gravitational arcs produced by foreground massive galaxy clusters of 10^{14-15} $M_\odot$ marked the start of a new era for this research field. These clusters indeed form cosmic lenses of about 2 million light-years of transversal size which focus the light toward the observer and therefore increase the overall brightness of background galaxies that would otherwise appear extremely faint. Their apparent angular size are also increased and, since the light paths are bended by the gravitational potential, the effect distorts their morphology and generates multiple images of individual sources. The first detection of this type of extended and luminous gravitational arcs was obtained beyond the cluster Abell 370 by Soucail et al. (1987a,b). This demonstrated that, as a whole, these cosmic structures are dense enough to produce significant deflections and that they thereby contain a large amount of dark matter. Over the last few years, the number of known lensed galaxies has gradually increased and today forms statistically significant samples with independent selections, such as the SDSS Quasar Lens Search (SQLS, Oguri et al. 2006), the Sloan Lens Advanced Camera for Surveys (SLACS, Bolton et al. 2006), or more recent surveys conducted in the (sub-)mm (see §1.4.3).

I start this section by defining the theoretical framework of strong gravitational lensing and its fundamental properties, in order to lay solid foundations on the discussions presented throughout this thesis. For a more comprehensive overview, the interested reader is referred to the reviews of Meylan et al. (part B of 2006) and Treu (2010) and to the lecture notes of M. Meneghetti[1], which partly served as a basis to write the following introduction on the strong lensing phenomenon. I will then describe the greatest advantages offered by this natural effect to observe the high-redshift universe and I will finally introduce a subset of the recent surveys targeting gravitationally lensed sub-mm sources.

1.4.1 The theoretical framework

General context

In the framework of general relativity, the light rays emitted by distant sources undergo multiple deflections due to the local deformations of the space-time induced by the mass overdensities. This contrasts with a perfectly homogeneous and isotropic universe where the photons would travel in straight lines. The successive gravitational potentials along the light paths will perturb the trajectories, implying that the apparent properties of the low-to-high-redshift sources observed from earth are all affected in a more or less pronounced way. In the linear regime, when the light deflections are small, this effect produces slight distorsions in the source morphologies which only become perceptible with statistical studies. This is called weak gravitational lensing. However, when a foreground massive structure such as an isolated galaxy or a galaxy cluster is adequately positioned, we enter into the specific non-linear regime of strong gravitational lensing. From an observational viewpoint, one can consider that the strong lensing regime is achieved when the deflector is able to produce significant distorsions and multiple images of the background source.

The characterization of astrophysical structures magnified by strong gravitational lensing requires a robust cosmological framework to deduce the relevant physical scales. The standard cosmological Λ-CDM model further tested by the Planck mission (Planck Collaboration et al. 2014c) and the Friedmann-Lemaître-Robertson-Walker (FLRW) metric are assumed to describe properly these fundamental distances.

All the matter overdensities between the source and the observer produce deflections. However, for simplicity, the theoretical modelisation usually assume that only the main gravitational potential is dominating. This approximation therefore allows to consider a thin lens, with a dimension along the line-of-sight negligible with respect to the relative distances between the source, the lens, and the observer. This setup is valid for most of the astronomical objects susceptible to act as a gravitational

---

[1] http://www.ita.uni-heidelberg.de/ massimo/sub/Lectures/gl$_{a}$*ll.pdf*

lens, from single galaxies to groups and clusters. Only the rare, very fortuitous configurations require a different approximation. For instance, this happens when two gravitationally unconnected potential wells lie at different redshifts along the line-of-sight and produce equivalent deflection angles. Secondly, assuming a space-time locally flat near the image plane greatly simplifies the modelisation. This requires a weak perturbation of the space-time metric by the Newtonian gravitational potential of the lens, ϕ, and namely that $\phi \ll \mathrm{c}^2$. Within these limits, the lensing potential produces small deflection angles which allows to linearize the lensing equation. These approximations lead to define the image plane at the redshift of the main deflector. Similarly, the source plane designates the projection of the background source onto a plane, assuming there is no deflector.

The lensing effect does not depend on the energy of the emitted photons but only on the total mass creating the gravitational potential. It is therefore achromatic. The fluxes of multiple images are expected to depend on the strong lensing magnification but not on the wavelength. However, several differential astrophysical effects can produce misleading colour changes for the observer. For instance, if the dust content of the lensing structure strongly differs between each path taken by the light rays, some lensed images will appear redder than the others (Nadeau et al. 1991).

The lens equation

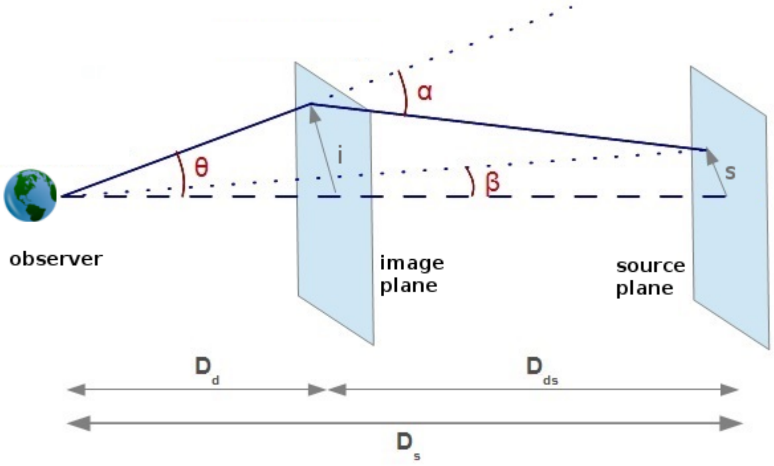

Figure 1.3: Schematic illustration of the geometric angles and angular diameter distances involved in the lens equation (Treu 2010, and references therein). The positions of the image and source planes correspond to a single background source and assume a thin gravitational lens.

Similarly to geometrical optics, light deflections can be deduced from the Fermat's principle (Blandford & Narayan 1992). In fact, searching for the cosmic paths which minimize the light travel time between the emitter and the observer gives results equivalent to the complete calculation of geodesics in the general relativity. This allows to find more easily the angular positions where the lensed images form. In particular, Figure 1.3 shows that the following relation between the image and source planes holds for small intervening angles

$$\theta \mathrm{D_s} = \beta \mathrm{D_s} + \alpha(\theta) \mathrm{D_{ds}} \tag{1.1}$$

where $\mathrm{D_s}$ and $\mathrm{D_{ds}}$ are the angular diameter distances between the observer and the source planes, and between the image and the source planes, respectively. α is the single deflection angle experienced by the light path in the thin lens approximation. It can be converted into a reduced angle according to $\widehat{\alpha}(\theta) = \frac{\mathrm{D_{ds}}}{\mathrm{D_s}}\alpha(\theta)$. This transformation results in the lens equation relating the angular position of the source shifted by the lensing potential, θ, to the position that would be observed with a perfectly homogeneous universe without any foreground deflector, β,

$$\theta = \beta + \widehat{\alpha}(\theta) \tag{1.2}$$

In the strong lensing regime, θ has multiple solutions which indicate the two-dimensional angular position of each image of the background source. Deducing the expression of the two-dimensional lensing potential, ϕ, from the Newtonian gravitational potential then allows to relate its gradient, $\triangledown\phi$, to the deflection angle

$$\alpha = \frac{\mathrm{D_s}}{\mathrm{D_{ds}}} \triangledown \phi \tag{1.3}$$

This means that, for a given foreground mass distribution at a fixed redshift, the strong gravitational lensing effect will produce higher deflections for light rays emitted at higher redshifts due to the $\frac{\mathrm{D_s}}{\mathrm{D_{ds}}}$ term. Finally, since the lensing equation simply becomes $\theta = \beta + \triangledown\phi$, the number of multiple images and their position clearly depend on the profile of the foreground distribution of dark matter through the lensing potential, but also on the relative alignement between the source and the deflector.

The three-dimensional density of the deflector, $\rho(\mathrm{R}, \mathrm{z})$, is converted to the projected surface density, $\Sigma(\mathrm{R})$, at the redshift of the image plane by

$$\Sigma(\mathrm{R}) = \int \rho(\mathrm{R}, \mathrm{z})\mathrm{dz} \tag{1.4}$$

Multiple images can appear if $\Sigma(\mathrm{R})$ exceeds the critical surface density, Σ_{crit}, at least for one line-of-sight crossing the image plane at a radial distance $\mathrm{R} \sim \mathrm{D_d}\theta$ from the center of the lens. Following Treu (2010), this characteristic surface density is defined as

$$\Sigma_{\mathrm{crit}} = \frac{\mathrm{c}^2}{4\pi \mathrm{G}} \frac{\mathrm{D_s}}{\mathrm{D_d D_{ds}}} \tag{1.5}$$

where $\mathrm{D_d}$ is the third angular diameter distance, between the observer and the image plane. This leads to define the convergence, κ, which provides the total surface density of the lens in units of Σ_{crit}

$$\kappa(\theta) = \frac{\Sigma(\mathrm{D_d}\theta)}{\Sigma_{\mathrm{crit}}} \tag{1.6}$$

According to the Poisson equation, the convergence is merely half the Laplacian of the potential, $\kappa = \triangledown^2\phi/2$.

The magnification factor

The Jacobian matrix between the source plane and image plane two-dimensional coordinates is

$$\frac{\partial \beta_\mathrm{i}}{\partial \theta_\mathrm{j}} = \delta_{\mathrm{ij}} - \frac{\partial \alpha_\mathrm{i}}{\partial \theta_\mathrm{j}} = \delta_{\mathrm{ij}} - \frac{\partial^2 \phi}{\partial \theta_\mathrm{i} \partial \theta_\mathrm{j}} \tag{1.7}$$

where one can introduce the convergence, κ, and the dimensionless shear, γ, to find

$$\frac{\partial \beta_\mathrm{i}}{\partial \theta_\mathrm{j}} = \begin{pmatrix} 1 - \kappa - \gamma_1 & -\gamma_2 \\ -\gamma_2 & 1 - \kappa + \gamma_1 \end{pmatrix} \tag{1.8}$$

The shear vector $\gamma = \gamma_1 + \mathrm{i}\gamma_2$ models the distorsion of the source, without any contribution from the convergence factor. This implies that the angular distorsions of gravitational arcs observed in telescope images directly indicate the direction of the shear.

The Jacobian is also designated as the inverse amplification tensor, A^{-1}, and determines the apparent magnification of a given background point-source, in each direction. Its determinant provides the local absolute magnification factor μ,

$$\mu = \frac{1}{\det\left(\mathrm{A}^{-1}\right)} = \frac{1}{(1-\kappa)^2 - |\gamma^2|} \tag{1.9}$$

Since the surface brightness of the source is preserved by strong gravitational lensing, μ indicates the factor by which the apparent area is increased and also corresponds to the total boost of its integrated flux. For an isotropic stretching one would therefore expect a linear magnification of $\sqrt{\mu}$. However, this factor depends both on the convergence and shear components, κ and γ, which demonstrates that strong gravitational magnifications are anisotropic. The presence of a preferential amplification axis explains the distorded morphologies observed in the image plane. Linear magnifications are therefore generally highly anisotropic, with values much larger than $\sqrt{\mu}$ in the radial or tangential direction with respect to the center of the deflector and lower than $\sqrt{\mu}$ in the perpendicular direction.

Although the point-source approximation is often valid when observing lensed galaxies at high-redshift, it is also necessary to mention the differences arising for extended sources. In such cases, the surface brightness of the source also influences the calculation of the local magnification factor in each line-of-sight.

The critical and caustic lines

For $1 - \kappa = \pm\gamma$, the determinant of the inverse amplification matrix equals to zero and the magnification factor formally goes to infinity. The positions of the image plane that meet this condition form closed and non-overlapping curves called the critical lines. These lines are divided in two categories associated with different apparent distorsions. Firstly, the internal critical lines correspond to radial stretching and, secondly, the external ones identify the position of the gravitational images that undergo tangential distorsions. However, in practice the most compact astrophysical sources lying near these curves will have high magnifications of up to $\mu \sim 100$ and finite apparent fluxes.

The transformation of the critical lines in the source plane are referred to as caustics. In addition to specifying the positions in the source plane which will result in high magnifications, they also delineate separate regions where the number of multiple images formed remains constant. For a simple non-singular elliptical mass acting as a lens, a source outside the external caustic produces a single image, while a source within this curves is divided into three separate images with different magnifications and including a radial arc. Similarly, crossing the internal caustic will produce two additional images. Moreover, in a given system, the position of the background emitter with respect to the caustic lines will determine the morphological transformations of the lensed images. For the same elliptical lens, sources lying near the sharp-edged caustic undergo a tangential stretching and can produce the typical fold and cusp catastrophes. The second caustic curve induces radial distorsions on the sky, and both lines can either be internal or external depending on the foreground mass distribution.

The Einsein radius

We turn next to an essential parameter, the Einstein radius θ_{e}, which defines the projected area in the image plane enclosing a surface density equal to the critical density of the universe. For a lens with spherical symmetry, this means that $\mathrm{M}(\mathrm{R_e}) = \pi\Sigma_{\mathrm{crit}}\theta_{\mathrm{e}}^2$. This characteristic angle indicates the typical separations between different lines-of-sight with maximal lensing magnifications and, consequently, the angular separations between the multiple images. θ_{e} depends not only on the lensing mass, but also on the redshifts of the image and source planes. Accordingly, this parameter is well constrained observationally and, in combination with detailed models, it allows accurate measurements of the total mass enclosed within the lensed images.

The Einstein radius reduces to simple expression for a lensing mass supposed to be concentrated on a single point. Firstly, in this case the deflection angle writes as follows

$$\alpha(\mathrm{R}) = \frac{4\mathrm{GM}}{\mathrm{c}^2\mathrm{R}} \tag{1.10}$$

with, for small angles, $\mathrm{R} \sim \mathrm{D_d}\theta$. Thus, if the lens is strictly aligned with the background source from the viewpoint of the observer, the lens equation becomes

$$\theta \mathrm{D_s} = 0 + \mathrm{D_{ds}} \frac{4\mathrm{GM}}{\mathrm{c}^2 \theta \mathrm{D_d}} \tag{1.11}$$

with, in this configuration, the angle θ equal to θ_e. The gravitational image formed by the point mass is therefore a continuous circle centered on the lens, with a radius

$$\theta_\mathrm{e} = \sqrt{\frac{4\mathrm{GM}}{\mathrm{c}^2} \frac{\mathrm{D_{ds}}}{\mathrm{D_d D_s}}} \tag{1.12}$$

This typical apparent morphology is known as an Einstein ring. More generally, a similar distorsion can be obtained for all types of gravitational lenses with circular symmetry, providing that the source remains perfectly aligned with the center of the mass distribution.

The angular diameter distance

The lens equation involves angular diameter distances defined, in a given metric, as the ratio of the physical transverse separation to the angular size directly measured in sky images (Hogg 1999). The mathematical expression of the angular diameter distance is based on the transverse comoving distance, which is given in the FLRW metric and for a given redshift z by

$$\mathrm{D_M}(\mathrm{z}) = \begin{cases} \mathrm{D_H} \frac{1}{\sqrt{\Omega_\mathrm{K}}} \sinh\left(\sqrt{\Omega_\mathrm{K}} \int_0^\mathrm{z} \frac{\mathrm{dz}'}{\mathrm{E}(\mathrm{z}')}\right) & \text{for } \Omega_\mathrm{K} > 0 \\ \mathrm{D_H} \int_0^\mathrm{z} \frac{\mathrm{dz}'}{\mathrm{E}(\mathrm{z}')} & \text{for } \Omega_\mathrm{K} = 0 \\ \mathrm{D_H} \frac{1}{\sqrt{|\Omega_\mathrm{K}|}} \sin\left(\sqrt{|\Omega_\mathrm{K}|} \int_0^\mathrm{z} \frac{\mathrm{dz}'}{\mathrm{E}(\mathrm{z}')}\right) & \text{for } \Omega_\mathrm{K} < 0 \end{cases} \tag{1.13}$$

where E(z) is a function of Ω_M, Ω_Λ and Ω_K the matter, dark energy and curvature density parameters, $\mathrm{E}(\mathrm{z}) = \sqrt{\Omega_\mathrm{M}(1+\mathrm{z})^3 + \Omega_\mathrm{K}(1+\mathrm{z})^2 + \Omega_\Lambda}$. $\mathrm{D_H}$ is the Hubble distance defined as $\mathrm{D_H} = \mathrm{c}/\mathrm{H_0}$, for the present value of the Hubble constant.

The angular diameter distance to redshift z is then given by

$$\mathrm{D_A}(\mathrm{z}) = \frac{\mathrm{D_M}(\mathrm{z})}{1+\mathrm{z}} \tag{1.14}$$

In contrast to other cosmological distance indicators, $\mathrm{D_A}$ does not diverge at increasing redshifts but passes through a maximum at $\mathrm{z} \sim 1-2$, according to the values of the cosmological parameters. Beyond this threshold and for a fixed intrinsic size, more distant sources will therefore have larger angular sizes in telescope images and a smaller angular diameter distance.

In strong gravitational lensing systems, the angular diameter distance between the lens and the source is defined for an observer at the position of the lens. This implies that $\mathrm{D_A}(\mathrm{z_l}, \mathrm{z_s}) \neq \mathrm{D_A}(\mathrm{z_s}) - \mathrm{D_A}(\mathrm{z_l})$, with $\mathrm{z_l}$ and $\mathrm{z_s}$ the redshifts of the lens and the source, respectively. For $\Omega_\mathrm{K} \geq 0$, $\mathrm{D_A}(\mathrm{z_l}, \mathrm{z_s})$ can be expressed as

$$\mathrm{D_A}(\mathrm{z_l}, \mathrm{z_s}) = \frac{1}{1+\mathrm{z_s}} \left[\mathrm{D_M}(\mathrm{z_s}) \sqrt{1 + \Omega_\mathrm{K} \frac{\mathrm{D_M^2}(\mathrm{z_l})}{\mathrm{D_H^2}}} - \mathrm{D_M}(\mathrm{z_l}) \sqrt{1 + \Omega_\mathrm{K} \frac{\mathrm{D_M^2}(\mathrm{z_s})}{\mathrm{D_H^2}}}\right] \tag{1.15}$$

where $\mathrm{D_M}(\mathrm{z_l})$ and $\mathrm{D_M}(\mathrm{z_s})$ are the transverse comoving distances at the lens and source redshifts, respectively. Following the recent results from the Planck mission we assume $\Omega_\mathrm{K} \sim 0$ (Planck Collaboration et al. 2015b), thereby reducing the above equation.

1.4.2 Major astrophysical applications of strongly lensed systems

Magnifying the high-redshift universe

Gravitational lensing greatly facilitate the characterization of the inner properties of intrinsically bright sources at redshifts of 2-3, near the peak of the cosmic star formation history. The most powerful of these natural telescopes can boost their apparent brightness and increase their apparent size by factors of up to 10-50. This opens an outstanding window towards fine spatial scales within these galaxies ($\lesssim 1$ kpc) and pushes back the resolution limits of the HST and mm/radio interferometers in non-lensed studies. Such magnifications help decreasing the substantial integration times involved in follow-up spectroscopic observations with, for instance, $\mu = 10$ corresponding to an observing time divided by a factor 100. One can therefore determine the resolved morphology, size, kinematics of their individual star forming regions and probe the local physical properties of their ISM with modest amounts of telescope time. Moreover, the intrinsic properties of these sources corrected for the strong lensing amplifications and distorsions can also be reconstructed with adequate lensing models. At the same time, lensing conserves the intrinsic surface brightness and the quantities expressed per unit area are therefore independent of the large uncertainties inherent to these models. Given these obvious advantages, a small set of individual sources with interesting lensing configurations have been extensively followed-up and characterized by independent teams. As a matter of example, one can cite the "Cosmic Horseshoe" at z = 2.38 (Belokurov et al. 2007), the "Cosmic Eye" at z = 3.07 (Smail et al. 2007) or the "Cosmic Eyelash" at z = 2.33 (Swinbank et al. 2010).

However, these well-known sources exhibit very outstanding properties. They are essentially very massive, intrinsically bright and cover extreme star formation laws within or near the starburst regime. In particular, it has been shown that lensed galaxies exhibit enriched interstellar environments just below the solar metallicity (e.g., Pettini et al. 2000) while other unlensed populations at similar redshifts – such as the damped Lyα systems detected through absorption features in the spectra of background quasars – suggest lower metallicities (Wolfe et al. 2005). Fortunately, strong gravitational lensing also enables to probe less massive galaxies at $z = 2-3$ which are more numerous and more representative of the overall population at this cosmic epoch. This offers a perspective to extend the study of the bright end of the luminosity function toward the fainter, bluer and smaller objects which are expected to form the building blocks of the most massive galaxies observed in the local universe. This brightness regime would otherwise be accessible with the next generation of extremely large ground-based telescopes.

In addition, the most massive lensing clusters are capable of producing dramatic deflection angles of $10-50''$. In particular, the ~50 most massive of them which are reported in the literature and produce significant magnifications have been used to push back the scientific boundaries. They serve as natural telescopes allowing to unveil extremely distant galaxies that would otherwise remain below the sensitivity limit of the most powerful facilities. The enhanced brightness enables to break several records in the search for the most distant sources near the epoch of reionization, and to probe the high-redshift universe with unprecedented details (Richard et al. 2008, 2009; Bouwens et al. 2009). In particular, such studies have extended the luminosity functions toward higher redshifts and showed that, at high lookback times, galaxies with moderate intrinsic luminosities could be more numerous than expected. This population could therefore play a significant role in the cosmic reionization (e.g., Bouwens et al. 2012). Moreover, among the very highest redshift candidates collected across the sky thanks to gravitational lensing, the ones exceptionally magnified by massive foreground clusters can even be confirmed spectroscopically (e.g., Finkelstein et al. 2013; Oesch et al. 2016).

Mapping the mass distribution in the lens

Strongly gravitationally lensed arcs are the only astrophysical observables which allow to recover the total distribution of matter in the foreground potential well. Other methods that seek to estimate the total masses of individual galaxies or large-scale gravitationally bound structures conveniently account for their baryonic content through the light fluxes received in all the wavelength regimes. However, they hardly model the integrated mass of dark matter and even less its spatial distribution and homogeneity. In turn, strong lensing is sensitive to variations in the mass profiles down to the sub-kiloparsec scales where baryons exhibit crucial motions. For instance, Hezaveh et al. (2016) use ALMA long-baseline observations of the well-studied SMG H-ATLAS J090311.6+003906 (SDP.81) at $z = 3.042$ to investigate the properties of the dark matter sub-halos in the lensing galaxy at $z \sim 0.3$. The effect therefore allows to probe the gravitational interplay between dark matter and baryons within internal regions of galaxies.

In the case of strong lensing by galaxy clusters, the detection of large sets of multiple images of background sources enable to invert the lens equation and to model the distribution of dark matter from the inner regions of the cluster to the outskirts. This provides an outstanding opportunity to probe the global profiles and the dark matter sub-structures using multi-scale mass reconstructions. Approximately, one mass concentration of this type per ∼50 square degree is supposed to act as a strong gravitational lens. Extremely detailed modelisations have been conducted as part of the Hubble Frontier Field program, and are based on very deep exposures of massive lensing clusters detecting more than 150 multiple images (Jauzac et al. 2014, 2015). These mass reconstructions are usually combined with X-ray observations tracing the hot gas within the clusters, and with weak lensing studies probing lower gravitational deflections in their outskirts (Limousin et al. 2007b).

Other cosmological applications

The position of the multiple images or their flux ratios which are directly observable from earth are directly related to the angular diameter distances, which in turn are a function of the adopted metric of the universe. In this way, strong lensing opens a window on the overall geometry of the universe. In terms of pioneering studies, Refsdal (1964) proposed to use the time delay between multiple images in a given strong lensing system to estimate the Hubble constant. This technique was subsequently applied to several lensed quasars. In addition, Refsdal (1966) also worked on the test of cosmological theories with strong lensing observables. Finally, dedicated strong lensing configurations comprising multiple source planes have improved the constraints on the total matter density of the universe, $\Omega_{\rm M}$, and the equation of state of dark energy (e.g., Collett & Auger 2014).

1.4.3 Former surveys targeting lensed SMGs

The strongly lensed dusty high-redshift galaxies are particularly important for the purpose of this thesis. We summarize the most important progress made recently concerning their selection and show the most promising samples collected so far.

In a first instance, it is worth noticing that a large number of very bright gravitationally lensed SMGs have been discovered serendipitously. Such is case, for instance, of the "Cosmic Eyelash" at $z = 2.326$ (Swinbank et al. 2010; Ivison et al. 2010a). This extremely bright source reaches flux densities of about 400 mJy at 350 μm and is magnified by extreme factors of up to $\mu \lesssim 40$. Its resolved dust morphology reveals 8 compact clumps distributed across an extended arc of $\sim 4''$ which forms a total of 220 ± 50 $\rm M_\odot$ $\rm yr^{-1}$. The strong gravitational magnifications produced by the foreground massive galaxy cluster MACSJ2135-010217 at $z = 0.325$ project the typical scales of individual star-forming regions, ∼100 pc, onto $0.75''$ in the image plane. In the source plane, this corresponds to intrinsic separations of ~ 1.5 kpc between the clumps. This source therefore demonstrates the benefit of strong gravitational lensing and it has been widely discussed in the literature during the last few years.

In addition, the identification of lensed SMGs have been conducted with different ground or space-based facilities. We can mention a sub-mm survey of 720 arcmin^2 with the SCUBA camera on the James Clerk Maxwell Telescope probing down rms noises of 2 mJy (Coppin et al. 2006), and a survey covering the 400 arcmin^2 of the Extended Chandra Deep Field South (ECDFS) with the Large Apex BOlometer Camera (LABOCA) on the APEX telescope and with slightly higher depth (Weiß et al. 2009). However, as explained in the next section, Negrello et al. (2010) subsequently showed that the identification of lensed and unlensed SMGs should be much easier at very high sub-mm flux densities. Unfortunately, we can not expect to find more than one of these bright sources per square degree on the sky. The coverage of these SCUBA and LABOCA surveys is therefore too limited to effectively select small sets of lensed source candidates and several tens of square degrees are more suitable.

The most outstanding samples of high-redshift lensed star-forming galaxies have been collected with a new generation of wide-field surveys performed in the FIR/mm regime with the Herschel satellite and the South Pole Telescope (SPT). The Herschel Astrophysical Terahertz Large Area Survey (H-ATLAS, Eales et al. 2010) and the Herschel Multi-tiered Extragalactic Survey (HerMES, Oliver et al. 2012) both conducted with the SPIRE imager and the SPT survey (Harris et al. 2012; Greve et al. 2012; Vieira et al. 2013) total about 550, 380 and 80 square degrees, respectively. Taken together, they cover more than 1000 deg^2 on the extragalactic sky. For this area, the modeled number counts predict the detection of about 250 lensed high-redshift SMGs of 500 μm flux densities between 100 and 200 mJy (Negrello et al. 2010; Bussmann et al. 2013). Wardlow et al. (2013) are able to confirm that only one galaxy among their set of 13 lensed source candidates identified in HerMES is not gravitationally lensed, but has typical properties of a distant HyLIRG. Their results suggest that, for these flux densities, very luminous unlensed sources are indeed very rare compared to lensed SMGs, which validates the selection method recommended by Negrello et al. (2010). In addition, most of the sources identified in the SPT survey are amplified by single massive galaxies and they exhibit typical Einstein radii of $1-2''$. They reach flux densities of $\mathrm{S}_{350} = 100-200$ mJy, with only one source exceeding 500 mJy at 350 μm (Vieira et al. 2013), and Hezaveh et al. (2013) measure typical magnification factors of $5-20$. Concerning the H-ATLAS lensed sources, Bussmann et al. (2013) find lower magnification factors which implies high intrinsic luminosities in the regime of ULIRGs or HyLIRGs. This sample contains 30 sources with $\mathrm{S}_{350} = 100-200$ mJy, and 6 with $\mathrm{S}_{350} > 350$ mJy. Finally, these results prove that such wide-field sub-mm surveys are only able to identify low numbers of lensed sources with dust continuum peaking above 200 mJy.

1.5 Zooming in on the intense star formation at z∼2-3

1.5.1 The need for spatially-resolved observations

The brightest SMGs and ULIRGs at $z \sim 2-3$ are ideal laboratories to study the intense star formation in high gas and stellar mass systems. However, this process is regulated by the local conditions within the individual star-forming regions (Elmegreen 1999) which are inaccessible for unlensed high-redshift objects. Even the outstanding resolutions of $\lesssim 0.1''$ offered by ALMA suffer from the low surface brightness of these field SMGs. For these reasons, the mechanisms underlying the star formation in $z \sim 2-3$ dusty galaxies are still actively debated in the literature. In particular, the respective roles of high gas mass surface densities and gas fractions, strong feedback from star formation or active galactic nuclei, and powerful shocks from supernovae explosions, remain quite unclear. These sources have no similar counterparts in the local universe and must be examined directly at high-redshift. Thus, further progresses require resolved observations of their individual star-forming regions in order to characterize the physical processes acting on the gas on these scales.

Fortunately, strong gravitational lensing offers a wonderful opportunity to overcome the faintness and limited apparent size of distant SMGs. We showed previously how fortuitous configurations can provide an outstanding boost in spatial resolution and apparent integrated brightness. In fact this natural effect becomes particularly interesting for dusty star-forming sources because their strong attenuation makes the identification of low wavelengths counterparts extremely challenging.

The typical scales of star-forming regions in nearby late-type galaxies are of order 100 pc in the source plane. Without gravitational magnification, this would correspond to angular resolutions of $0.01''$ for a dusty star-forming galaxy at $z \sim 2-3$. This is an order of magnitude below the typical beam sizes offered by ALMA, or current optical facilities (HST, VLT). In the most favourable cases, foreground galaxies or galaxy clusters can provide magnification factors of up to 20-60 (e.g., Swinbank et al. 2011). These configurations are much scarcer than the ones producing moderate values of μ, but they are the only ones able to fill the gap in angular resolution and to give access to sufficient spatial details. In this end, the most extreme gravitational magnifications allow us to reach the physical scales of individual star-forming regions where the local processes dominate over the rotational gas support (Toomre 1964) and which are otherwise only accessible in very nearby galaxies . The most important processes setting the efficiency of gas conversion can then be characterized at local scales (Danielson et al. 2011; Swinbank et al. 2011; Combes et al. 2012). Consequently, strong lensing can unveil the fundamental differences between the star formation mechanisms at low and high-redshift and support or reject the specific mode at high-redshift (Genzel et al. 2010; Daddi et al. 2010). In fact, given the current state of astronomical technologies, this remains the only way to draw a complete understanding of intense star formation during the peak of the star formation history.

1.5.2 Toward an all-sky survey in the FIR/sub-mm

The identification of the brightest gravitationally lensed dusty star-forming galaxies at $z \sim 2-3$ can rely on the conclusions from theoretical studies. For instance, Negrello et al. (2007) show that these sources can be effectively selected at 500 μm flux densities above 100 mJy. In this regime, they are indeed expected to dominate the integrated high-redshift number counts compared to the unlensed populations. Independently from this work, Béthermin et al. (2012) use a simple empirical model distinguishing starburst from main sequence galaxies to predict the number counts from the MIR to radio wavelengths. They confirm a significant contribution of strongly lensed sources to the sub-mm counts. Including both low and high-redshift objects, at flux densities of 100 mJy their contribution amounts to about 8% and 25% at 350 and 500 μm, respectively. At first sight, their selection seems to be an easy task but it nevertheless encounters some difficulties.

In fact, very bright dusty high-redshift sources are extremely massive systems and their intense star formation activities reduce their evolutionary timescales. Their gas reservoirs are very rapidly depleted, in a few tens of Myr, and their bright FIR/sub-mm emission lasts relatively briefly compared to main sequence galaxies. For these reasons, this type of sources appear to be very rare on the sky and, consequently, their selection becomes rather challenging. Several studies predict number densities in the high flux regime, suggesting less than one candidate per square degree in the FIR/sub-mm sky. Negrello et al. (2010) find densities lower than ~ 0.5 deg^{-2} for $S_{500} > 100$ mJy, and even lower than ~ 0.01 deg^{-2} for $S_{500} > 300$ mJy. For their part, the models of Lapi et al. (2012) assuming magnification factors of 20-30 predict surface densities of about $0.003 - 0.1$ deg^{-2} for $S_{500} > 400$ mJy. Thus, these studies confirm that we can expect to find only a few of these sources on the extragalactic sky.

For these reasons, identifying samples of bright strongly lensed star-forming galaxies at high-redshift require a large scale survey covering a significant portion of the sky in the sub-mm. As shown previously, the mapped area has been substantially increased by recent surveys with Herschel and the South Pole Telescope. Taken together, the 80 deg^2 and 550 deg^2 mapped by the SPT survey and H-ATLAS, respectively, correspond to $\lesssim 5\%$ of the surface of the sky. Ideally, it would be appropriate to extend this coverage toward the entire surface observable from Earth, with the purpose of performing a systematic selection of extremely bright high-redshift sources. Fortunately, during the last few years, Planck has conducted the first all-sky survey with the depth and angular resolution necessary to achieve this goal. The 90% completeness limit of the Planck Catalogue of Compact Sources (PCCS) corresponds to $L_{IR} \sim 6 \times 10^{13}$ $L_\odot$ for a typical ULIRG at $z = 2$ (Planck Collaboration et al. 2014b). This means that this survey probes the extreme end of the luminosity function where the modeled number counts predict only few detections for the entire sky (Negrello et al. 2010; Lapi et al. 2012). By way of confirmation, Herranz et al. (2013) find very few candidates during their dedicated search in the Early Release Catalogue of Compact Sources (ERCSC, Planck Collaboration et al. 2011b). However, even though the Planck all-sky survey is confusion limited in the highest frequency bands (Blain et al. 1998), a careful selection of bright sources with FIR/sub-mm colors matching those of high-redshift galaxies can identify a small set of gravitationally lensed source candidates.

1.5.3 Our approach : characterizing a small set of outstanding lensed sources

This thesis focuses on the characterization of the extraordinary sample of extremely bright dusty star-forming galaxies that could be selected with the Planck all-sky survey. Unlike the targeted FIR/mm surveys that attempt to build robust samples with controled selection functions, this work probes the most outstanding lensed high-redshift sources detected in the cleanest regions of the extragalactic sky. With this small set of strongly gravitationally lensed SMGs, we seek to increase our understanding of the gas and dust conditions and the star formation mechanisms at $z \sim 2-3$. In particular, since we study these physical processes in the brightest distant sources currently known, we cover essentially the high-mass regime of $M \gtrsim 10^{10}$ $M_\odot$.

After deriving the global dust properties of this sample, we conduct case studies of the individual sources that exhibit the most favourable lensing configurations and particularly interesting properties both in the image and source planes. In fact, we aim at obtaining maximum benefit from the boost in sensitivity and spatial resolution offered by these natural gravitational telescopes. This approach was also adopted to characterize other individual lensed galaxies discovered serendipitously, such as the "Cosmic Eyelash" (Swinbank et al. 2010). For these reasons, this thesis relies primarily on comprehensive studies of exceptionally bright starbursting sources to constrain the resolved gas and dust properties as well as the star formation mechanisms in the high-redshift universe.

1.6 Thesis outline

This thesis begins with a comprehensive description of the selection of our sample, the Planck's Dusty Gravitationally Enhanced subMillimetre Sources (GEMS). In Chapter 2, we present our search for high-redshift candidates in the all-sky survey of the High Frequency Instrument on-board the Planck satellite. Then we describe how this subset of lensed source candidates was identified based on follow-up imaging with the Spectral and Photometric Imaging Receiver on-board the Herschel space observatory. In Chapter 3, we present the multi-wavelength observations that were conducted during this thesis with several ground or spaced-based facilities, with the aim of characterizing the main astrophysical components in our sources.

In Chapter 4, we determine the global properties of our sample, taken as a whole. After describing the blind redshift search in the millimeter regime, we probe the spatially-integrated dust reservoirs in these targets and rule out a significant contribution of an active galactic nucleus to the overall dust heating. We provide a range of compelling arguments in favour of the strongly gravitationally lensed nature of each source. Then, we characterize the far-infrared-radio correlation, the molecular gas masses and the integrated Schmidt-Kennicutt law in the sample.

In Chapter 5, we perform a detailed analysis of the foreground mass distribution toward each dusty high-redshift emitter. We derive galaxy number counts in the near-infrared, measure photometric redshifts and conduct a blind search for the galaxy red sequence in the optical and near-infrared.

Together with a small set of available spectroscopic redshift, these results unambiguously determine the astrophysical structures magnifying the Planck's Dusty GEMS. Then, Chapter 6 is dedicated to the modelisation of the strong lensing effect with LENSTOOL, in order to deduce the total masses enclosed in the lensing potentials and accurate magnification factors.

Finally, in Chapter 7, we focus on the three gravitationally lensed sources showing the most remarkable properties. Firstly, we use high-resolution interferometry to study the perturbed kinematics of the molecular gas in a gradually star-forming source showing a particular morphology in the image plane. Secondly, we rely on the [CII] fine structure line to trace the properties of the interstellar gas in a bright multiply imaged starbursting clump. We present not only the resolved kinematics of the [CII] emission, but also the first extragalactic detection of a [CII] absorption feature which suggests infalling gaseous material. Thirdly, we characterize the brightest source in our sample, a maximal starburst magnified by a single foreground galaxy and forming a near-complete Einstein ring in the image plane. We deblend the contribution from the foreground and background stellar populations to the optical-to-MIR spectral energy distribution and discuss the outstanding properties of its lensing galaxy. We also characterize the physical state of the molecular gas in the lensed component, and the extreme gas and star formation surface densities in the individual star-forming clumps.

Chapter 2

The Planck's Dusty GEMS : Sample selection

Contents

2.1 Searching for bright star-forming galaxies at high-redshift

The spectral energy distribution of strongly lensed galaxies at $z \sim 2-3$ that experience an active phase of star formation peaks around 100 μm in the rest-frame. The dust continuum in the FIR/sub-mm dominates their bolometric emission, while the extreme levels of attenuation make them extremely faint at optical/NIR wavelengths. Thus, this type of candidates should be selected in the sub-mm regime around the position of their redshifted dust peak ($\sim 300-400$ μm). Until the last decade, distant star-forming galaxies have been mostly identified from the ground, in the atmospheric transmission windows around 0.8 and 1 mm, or even 2 mm. Without satellite data, their selection has been by necesity conducted at higher wavelengths than the emission peak of galaxies caught during the most active phase of cosmic star formation history.

Between 2009 and 2013, the Planck satellite has observed the whole sky in a large spectral range between 350 μm and 1 cm with 9 photometric bands (Planck Collaboration et al. 2014a). It has therefore covered the wavelengths corresponding to the redshifted emission from dust heated by the intense star formation in galaxies at $z \sim 2-3$. Planck has a very low spatial resolution of nearly $5'$, which is not sufficient to identify these high-redshift sources. However, this could be overcome with follow-up observations with the Herschel satellite which was launched simultaneously and covers a similar wavelength range (55-670 μm) at $20''$ beam resolution. The SPIRE imager on-board Herschel also reaches a sufficient sensitivity to identify the brightest of these sources on the sky. This is the strategy that was used to collect the sample of this thesis, the "Planck's Dusty GEMS" (Gravitationally Enhanced sub-Millimetre Sources).

In this chapter, we will focus on the selection of the high-redshift source candidates with the Planck satellite and their follow-up with Herschel. We will also describe the identification of our independent sample of strongly gravitationally lensed source candidates that will be characterized throughout the thesis.

2.1.1 The help of the negative k-correction

Statistical studies have shown that the volume density of bright SMGs increases by a factor ∼1000 between the present epoch and $z \gtrsim 2$, but their selection also benefit from a second, less intuitive effect. In fact, dusty galaxies observed in the sub-millimeter and millimeter wavebands benefit from a strong negative k-correction which implies that, for $z \gtrsim 1$, their observed brightness remains nearly constant as their redshift increases. In general, the k-correction enables us to convert the magnitude observed for a source at redshift z to a rest-frame magnitude, while taking into account the shape of its redshifted Spectral Energy Distribution (SED). It is defined as the K(z) term in the following equation (Oke & Sandage 1968; Blanton & Roweis 2007),

$$\mathrm{m} = \mathrm{M} + 5\,(\log \mathrm{D_L} - 1) + \mathrm{K(z)} \tag{2.1}$$

This type of correction depends also on the filter transmission curve. It is negative when an increasing redshift also leads to a brightening of the object. In case of the dust SED, the slope of the Rayleigh-Jeans tail almost cancels cosmological surface brightness dimming. Figure 2.1 shows that, for broad-band observations above 250 μm, the SED of dusty star-forming galaxies balances the flux drop with the inverse square of the luminosity distance. Therefore, the effect of k-corrections is a great advantage for the identification of such high-redshift sources because it makes their flux density roughly stable in a large range above $z \sim 1$. Especially, for the broadband filters centered above 850 μm and below the radio regime, the k-corrections can take very negative values which imply a slight increase in flux density as the sources move away from the observer.

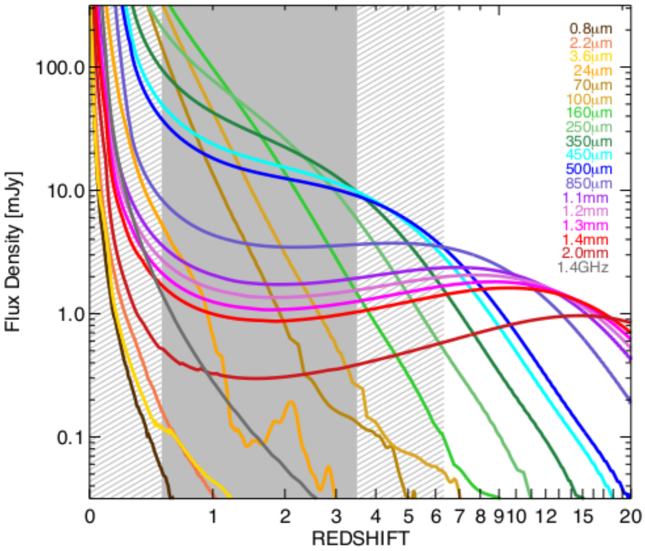

Figure 2.1: Flux densities measured in several photometric bands as a function of redshift, for a template of ultra-luminous infrared galaxy. This figure is taken from Casey et al. (2014) and demonstrates the effect of the very negative k-corrections in several (sub-)mm bands, for $z \gtrsim 1$. The flux densities in the photometric bands centered above 24 μm are computed from the SMG template of Pope et al. (2008), while the empirical SED of Arp 220 is used in the optical and NIR regimes.

2.2 The Planck selection of high-redshift candidates

2.2.1 The Planck all-sky survey

The Planck satellite observed the fluctuations of the cosmic microwave background (CMB) in 9 frequency bands, covering the whole sky every 6 months (Tauber et al. 2010; Planck Collaboration et al. 2011a). It comprises two different instruments, the Low Frequency Instrument (LFI, Valenziano et al. 2007) targeting three wide bands centered at 30, 40 and 70 GHz, and the High Frequency Instrument (HFI, Planck HFI Core Team et al. 2011) working in six other bands at 100, 143, 217, 353, 545 and 857 GHz. LFI observed the synchrotron radiation from the Galactic plane together with the CMB during 4 complete years, corresponding to 8 scans of the full sky. However, this instrument covers lower frequencies than the redshifted dust peak of star-forming galaxies at $z \sim 2-3$ and our selection is therefore based solely on the HFI maps.

The relatively high sensitivity of HFI (about 600 times that of COBE) is made possible by its unique cryogenic system which cools down the bolometers around 100 mK. However, these instrumental constraints also limited the lifetime of the instrument to 5 complete sky surveys (3 observations less than LFI). At the nominal frequencies of HFI, the FWHM of the Point Spread Function (PSF) of Planck increases from $4.22'$ at 857 GHz, to $9.66'$ at 100 GHz (Planck Collaboration et al. 2015a). This FWHM is sampled with a pixel scaling of $1'$ pix^{-1} in the released maps.

2.2.2 Selection of the candidates in the HFI maps

In this section, we describe the selection of 234 Planck high-redshift candidates with two independent methods. This analysis was conducted prior to this thesis work by collaborators in Orsay and Toulouse, as part of the Planck consortium (Planck Collaboration et al. 2015d). The first of those two approaches is based on the extraction of the CIB component from the Planck/HFI maps. Then it consists in applying a color criteria to identify a set of high-redshift cold sources candidates. For its part, the

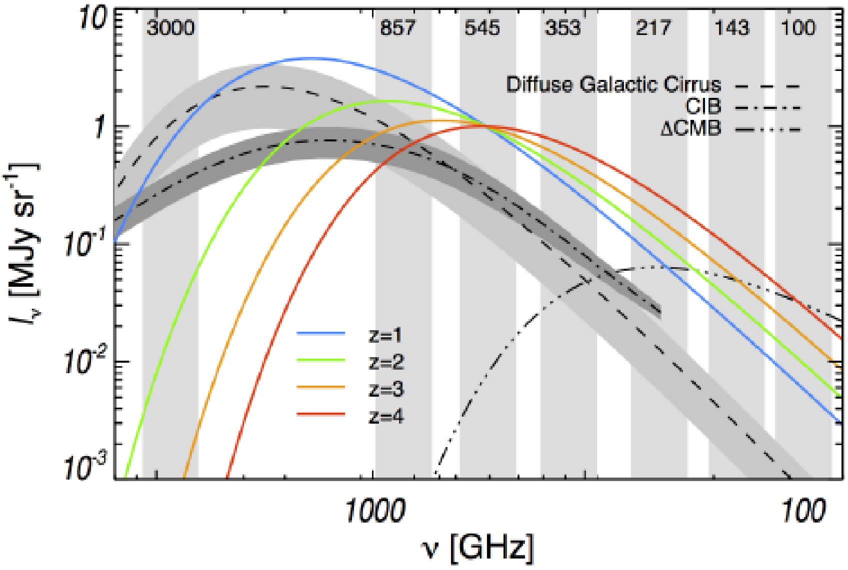

Figure 2.2: Spectral energy distribution of the main astrophysical components in the (sub-)millimeter domain, including the CMB, the CIB and Galactic cirrus (black dotted lines). Their surface brightness is measured at high Galactic latitude and compared to idealized SEDs of high-redshift dusty starbursts, modeled with a single greybody of $T_d = 30$ K and $\beta = 1.5$ (colored solid lines, from z = 1 to z = 4). Vertical grey-shaded regions indicate the position of the 6 Planck/HFI bands and the IRAS/IRIS band at 100 μm. For z > 2, high-redshift starbursts dominate the cosmic infrared and microwave backgrounds as well as the foreground Galactic dust in 3 or 4 HFI bands. The figure is taken from Planck Collaboration et al. (2015c).

second approach seeks to conduce a complementary selection from the Planck Catalogue of Compact Sources (PCCS, Planck Collaboration et al. 2014b).

Dedicated search for cold sources in the CIB

The first part of the selection was performed with the combination of Planck/HFI maps and a publicly available lower-wavelength data set from the Improved Reprocessing of the InfraRed Astronomical Satellite (IRAS) Survey (IRIS, Miville-Deschênes & Lagache 2005). This search for high-redshift candidates combines spectral and angular criteria, according to the recipe described in Montier et al. (2010) or Planck Collaboration et al. (2015d) and briefly summarized below. It probes fainter sources than the second approach and focuses on the 26% of the sky showing a lower contamination from Galactic cirrus at 857 GHz.

To begin, the cleaning algorithm removes the contribution of the CMB to the HFI maps. Since this component dominates at 143 GHz, its contribution is measured in this frequency band and it is subsequently extrapolated and subtracted from the 5 other HFI bands. Secondly, the residual emission from Galactic cirrus at high latitudes is estimated from the IRAS/IRIS map at 100 μm, usually considered as a template for the warm component of Galactic dust. The result is also extrapolated to a wider frequency range, with the purpose of removing this second component from each of the 6 HFI bands. This provides a set of cleaned maps where the CIB fluctuations can be identified.

More precisely, the detection of point sources in the CIB is performed with a 5σ threshold in excess maps at 545 GHz (the construction of these maps is described in Planck Collaboration et al. 2015c). Since this detection is based on a single band, an additional search for counterparts in the cleaned maps at 353, 545 and 857 GHz increases its reliability. Then, the synchrotron sources showing a flux excess at low frequencies are removed by requiring a 5σ non-detection in the HFI map at 100 GHz.

The selection is derived from the photometry of the 5 cleaned maps, by applying colour cuts consistent with the spectral shape of exceptionally bright, intensely star-forming high-redshift galaxies. Figure 2.2 shows that, for $z > 2$, the FIR continuum of these sources is significantly different from the spectral shape of the cosmic infrared and microwave backgrounds as well as the foreground Galactic dust in 3 or 4 HFI bands. Thanks to different drops in their respective SEDs between 545 and 857 GHz, the red high-redshift starbursts can be distinguished from the diffuse Galactic cirrus with the criteria $S_{857}/S_{545} < 2$. A second color criteria, $S_{353}/S_{545} < 0.9$, allows to keep the high-redshift candidates while eliminating the SZ sources. Another class of interlopers that mimic the spectral signature of dusty high-redshift galaxies remains, which are the Galactic dusty sources. They can be removed by matching the final Planck catalog with the Planck Galactic Cold Clump catalogue (PGCC, Planck Collaboration et al. 2014b). This selection in the Planck/HFI maps results in more than two thousand candidates over the "extragalactic" sky outside the Milky Way plane.

Candidates in the Planck catalogue of compact sources

We also searched for high-redshift candidates in the first version of the PCCS published in 2013. This catalogue contains the detections found independently in the nine frequency bands of LFI and HFI, and over the full sky. It contains bright Galactic and extragalactic sources with, for instance, a 90% completeness limit of about 600 mJy at 545 and 857 GHz (Planck Collaboration et al. 2014b). To begin, we mask the Galactic plane in order to remove the cold cores and the diffuse dust emission in the Milky Way that could easily meet the selection criteria and degrade our final sample. We apply the mask derived in the highest frequency band of HFI, where the Galactic emission is the most extended (i.e. at 857 GHz) (Planck Collaboration et al. 2013). The process filters the sources from the PCCS falling in 48% of the sky. In order to avoid redundancy with competing groups, we also remove the regions of the sky already targeted by wide-field surveys carried out with Herschel (H-ATLAS, HerMES) and the South-Pole Telescope (Vieira et al. 2013).

Then, we search for very bright high-redshift candidates applying the same color and flux cuts as in Negrello et al. (2010). This means that we include the sources with $S/N > 4$ at 550 μm and the red sources satisfying the two criteria, $S_{857}/S_{545} < 1.5$ and $S_{217}/S_{353} < 1.0$. This selection therefore results in a higher flux threshold than the first approach.

Finally, it is necessary to identify and remove the main interlopers with muliwavelength criteria. Firstly, below 500 μm the bright end of the luminosity function is dominated by local sources rather than dusty strongly lensed galaxies at high-redshift (Negrello et al. 2007; Wardlow et al. 2013). Fortunately, these low-redshift late-type galaxies and the Galactic cirrus can be easily identified in the optical (or at 60 μm) with publicly available catalogs from wide-field surveys. Similarly, the numerous blazars satisfying our color selection are necesarily bright and detected in the existing radio surveys. We perform this cleaning thanks to the NASA/IPAC Extragalactic Database (NED) and the public data from IRAS and ALADIN. This results in the rejection of about 50% of the sources initially selected from the PCCS.

Characteristics of the Planck sample

In conclusion, the overall sample of high-redshift candidates from Planck/HFI is primarily selected in three spectral windows centered at 350, 550, 850 μm. These data probe the FIR/sub-mm emission from each source with very low angular resolutions of $4-5'$, corresponding to the typical scale of galaxy clusters at $z \sim 2-3$. Thus, Planck alone does not allow to determine the astrophysical nature of the detections. It also does not provide accurate flux measurements, because of strong confusion noise in the large Planck beam and the various fore and backgrounds. The colors are less affected because the spectral shape of the fore and background components is extremely well known. Nevertheless, the rediscovery of known high-redshift sources presented in §2.4.3 led us to believe that this strategy is suitable to systematically detect the brightest high-redshift sources on the sky with peak fluxes between 100 and 300 mJy.

2.3 Sample follow-up with Herschel/SPIRE

A total of 234 promising candidates have been subsequently followed-up with Herschel/SPIRE at higher angular resolutions and with a 10 times greater depth.

2.3.1 Description of the instrument

The Spectral and Photometric Imaging REceiver (SPIRE, Griffin et al. 2010) on board the Herschel satellite (Pilbratt et al. 2010) includes two modules. Firstly, a spectrometer covers the wavelength ranges between 194 and 313 μm, and between 303 and 671 μm, with three different spectral resolutions. It is not used in the present analysis to follow-up our candidates, contrary to the second imaging module which includes three observing bands centered at 250, 350, and 500 μm. The latter performs the detection with three independent bolometer arrays cooled to a temperature of about 0.3 K. It offers total fields-of-view of about $4' \times 8'$, sampled with pixel sizes ranging between $6''$ and $14''$. Finally, the primary mirror of the Herschel satellite reaches 3.5 meters in diameter which translates into beam sizes of about 18, 25 and $36''$ at 250, 350, and 500 μm, respectively[1]. Thus, the SPIRE imager allows to characterize the Planck candidates in the same wavelength regime but with higher sensitivities and with angular resolutions about 20 times higher. This implies that the compact sources detected by Planck potentially correspond to several counterparts in SPIRE maps, and therefore require a careful identification.

2.3.2 Follow-up observations and photometry

Herschel/SPIRE observations at 250, 350, and 500 μm were carried out between December 2012 and March 2013. The follow-up consisted of three parts. The OT1 (PI : L. Montier) and OT2 (PI : H. Dole) subsamples were obtained in response to the Herschel first and second Open Time calls, respectively. The OT1 and OT2 contain 10 and 70 sources, respectively, essentially detected as fluctuations of the CIB with HFI and IRAS. Their observations were conducted with slightly different strategies. The third subsample, the Herschel and Planck All-Sky Survey legacy Snapshot (HPASSS) was obtained as a "Must-Do" Director's Discretionary Time program. It includes 126 candidates from the dedicated search with HFI, 28 sources selected in the PCCS, and another set that will not be considered in this thesis. The parameters of these three follow-up programs (e.g. total integration times and map sizes) are presented in Planck Collaboration et al. (2015d).

The Herschel/SPIRE observations only identify 4 interlopers associated with diffuse emission from Galactic cirrus among the 234 fields targeted during the three follow-up programmes. This very low level of contamination demonstrates the effectiveness of the cleaning process applied in the Planck maps. After removing 4 other fields (repeated observations and calibration fields), the sample reduces to a total of 228 Herschel/SPIRE candidates.

Its preliminary characterization relies on the photometry measured in the three SPIRE bands by David Guéry, with two different procedures. To summarize, the sources are detected independently at 250, 350, and 500 μm with StarFinder (Diolaiti et al. 2000). Then, this algorithm integrates over the point spread function measured directly from the maps. It is therefore more suitable for the SPIRE data which are dominated by confusion noise than classical aperture photometry. In addition, a second band-merging procedure applies a prior on the catalog at 350 μm. Generally, whatever the method adopted, SPIRE photometry confirms that the selected sources indeed have the typical sub-mm colours of high-redshift infrared and sub-mm galaxies. Further details on the reduction of

---

[1] See the SPIRE Handbook 2014, http://herschel.esac.esa.int/Docs/SPIRE/spire_handbook.pdf

the SPIRE data set and the statistical analysis of the photometric catalogs are available in Planck Collaboration et al. (2015d).

2.4 Identification of the strongly lensed source candidates

For the purpose of this thesis, we focus on the search for bright isolated point sources in the SPIRE sample which could be consistent with being strongly gravitationally lensed high-redshift galaxies. In the next section, I present an efficient method developed in the literature in order to identify this population.

2.4.1 The search for high-redshift lensed galaxies

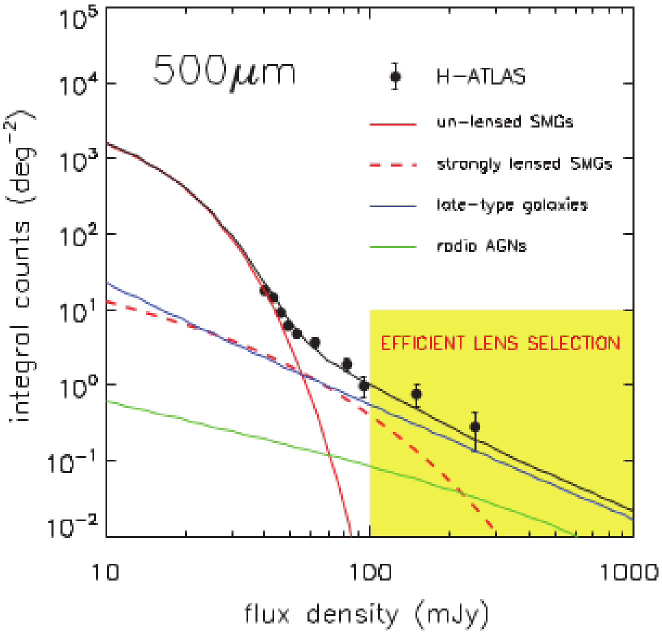

Figure 2.3: Number counts at 500 μm predicted for the main populations of sources observable in the sub-mm regime, namely high-redshift SMGs (solid and dotted red lines), local late-type galaxies (blue line) and radio sources (green line). These counts are derived from the physical and phenomenological galaxy evolution models described in Negrello et al. (2007). The observed number counts obtained for a region of ~14 sq. deg. in the Herschel-ATLAS survey are also plotted (black points, Clements et al. 2010). The yellow region shows the flux regime where the population of gravitationally lensed SMGs can be efficiently selected. The figure is taken from Negrello et al. (2010).

The number counts of unlensed SMGs show a steep decrease at very high flux densities while, in this regime, gravitationally lensed sources at high-redshift contribute to a large fraction of the observed populations (Negrello et al. 2010). This trend can be partly interpreted with the probability of finding strong lensing configurations as a function of the redshift of the background source. In fact, this probability increases very quickly between z = 0 and z = 2 provided that, in the meantime, the intrinsic size of dusty galaxies is not varying (Hezaveh & Holder 2011; Weiß et al. 2013). Figure 2.3 from Negrello et al. (2010) clearly illustrates that a significant fraction of extremely bright high-redshift SMGs are strongly lensed. It shows that the vast majority of extragalactic sources with 500 μm flux densities above 100 mJy are either isolated high-redshift SMGs with apparent fluxes boosted by gravitational lensing, groups of SMGs blended in the telescope beam or late-type galaxies at lower redshift and radio emitting AGNs.

In this context, Negrello et al. (2007) presented a method to select these lensed sources, taking advantage of the large negative k-correction. To begin, they use a combination of physical and phenomenological models to predict number counts of lensed sources in the sub-mm and compare with other dominant populations. These predictions show that the unlensed star-forming SMGs almost entirely reproduce the number counts at 850 μm from SCUBA. They also extend the findings of Figure 2.3 to the wavelength regime covered by the SPIRE bands, showing that the fraction of strongly lensed SMGs is rapidly increasing at high fluxes. Consequently, lensed sources could be selected in this regime after removing the main interlopers with multi-wavelength data sets. As already mentioned, blazars can be selected with their radio counterparts and, similarly, low-redshift starbursts and late-type galaxies can be identified with publicly available surveys in the optical or at 60 μm. Finally, Negrello et al. (2007) recommend to select the lensed SMGs at 500 and 850 μm, well above 100 mJy because the contribution of unlensed sources to the number counts becomes negligible. This cleaning and flux selection has already proven successful for HerMES and H-ATLAS surveys (Negrello et al. 2010; Wardlow et al. 2013).

2.4.2 Classification of the sources detected with Herschel/SPIRE

A similar procedure can be applied to the Planck/HFI sample followed-up with Herschel/SPIRE. In a nutshell, we apply a simple classification to the overall SPIRE sample, in order to distinguish a small set of high-redshift lensed source candidates from several overdensities of sub-mm sources. The classification combines flux and color criteria. Firstly, a color criteria selects the SPIRE counterparts of Planck sources with the peak falling either at 350 or 500 μm. This removes the bluer targets peaking in the 250 μm band which probably lie at $z < 1.5$, and to keep only the higher-redshift candidates. Secondly, a flux threshold at 350 μm enables to distinguish bright and single point sources which are potentially gravitationally lensed, from overdensities of fainter sources. Since the Galactic cirrus and low-redshift galaxies have been carefully removed previously, the isolated counterparts of Planck sources satisfying $S_{350} > 400$ mJy are presumably strongly gravitationally lensed (see Fig.2.3). A careful inspection of the individual SPIRE maps provide another handful of candidates with peak fluxes a few tens of mJy below this threshold.

To summarize, our selection is based both on the small angular size and the outstanding sheer brightness of these detections. The resulting set of candidates corresponds to a very small minority of the overall sample (about 5%). The by far largest subsample are agglomerates of multiple sources with high-redshift like colors, perhaps forming galaxy proto-clusters. Although our selection is based on the 350 μm flux densities, the lensed source candidates exceed 100 mJy at 850 μm and therefore satisfy the thresholds of Negrello et al. (2007)[2]. Our candidates are unresolved point sources in the $18''$ beam of SPIRE, which corresponds to about 120 kpc at $z \sim 2$. This strongly suggests that SPIRE maps probe physical scales associated with a single background emitter benefitting from a significant gravitational magnification. Nevertheless, in principle this angular resolution also leaves scope for a few outstanding concentrations of multiple unlensed high-redshift galaxies (Ivison et al. 2013). This makes extensive follow-up observations essential.

As a result, the Planck all-sky survey in the sub-millimeter combined with the Herschel/SPIRE follow-up at similar wavelengths and higher angular resolutions result in the identification of 15 gravitationally lensed source candidates with extraordinary brightness. Their flux densities range between 294 mJy and 1054 mJy at 350 μm, and between 270 mJy and 800 mJy at 500 μm, with typical uncertainties of 5-10 mJy. This is close to the confusion level in the SPIRE maps (Nguyen et al. 2010) but does not include the systematic uncertainty of 7% inherent to the SPIRE photometry. Their complete

---

[2] This might also imply that we are missing sets of multiple, but fainter gravitationally lensed objects that would have been identified as overdensities.

photometry in SPIRE bands is presented in Table 3.5 and has been published in Cañameras et al. (2015) and Planck Collaboration et al. (2015d).

2.4.3 Detection of lensed sources from the literature

This complete sample includes two lensed galaxies already studied in the literature and first presented by Fu et al. (2012) and Combes et al. (2012), respectively. The first one, PLCKERC857 PLCK_G270.59+58.52, is part of the Planck Early Release Catalogue of Compact Sources (ERCSC, Planck Collaboration et al. 2011b) and is fortuitously within the sky coverage of the H-ATLAS survey. Fu et al. (2012) confirmed its astrophysical nature with the detection of multiple images and obtained a spectroscopic redshift z = 3.259. This source of $S_{500} \sim 300$ mJy has been subsequently characterized by Herranz et al. (2013) and Bussmann et al. (2013). The second one, HLS 091828.6+514223, reaches $S_{500} \sim 200$ mJy and was detected by the Herschel Lensing Survey (Egami et al. 2010). It is located behind the massive galaxy cluster Abell 773 at z = 0.22, with an isolated galaxy at z = 0.63 producing most of the gravitational deflection. Its resolved morphology exhibits a near complete Einstein ring of about $1.5''$ diameter (Rawle et al. 2014). The delensed properties of this source are those of a ULIRG, with kinematics suggesting star formation potentially triggered by a merger (Combes et al. 2012).

The last one falls at a spectroscopic redshift of z = 5.243 (Combes et al. 2012), significantly higher than the other photometric redshifts deduced from our SPIRE photometry. The extensive spectroscopic follow-up presented in Chapter 4 will confirm this discrepancy. However, at the same time, we find no other fundamental difference between the properties of the two published sources and the rest of the sample.

2.4.4 The final sample of gravitationally enhanced sub-millimeter sources

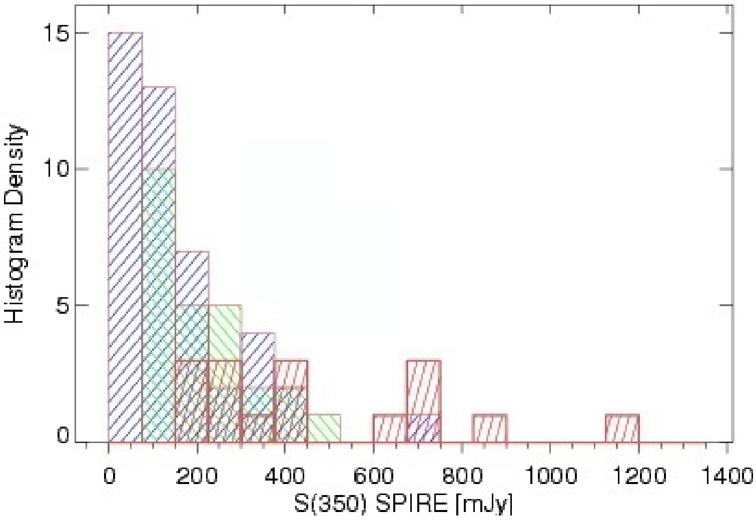

Figure 2.4: Histogram comparing the 350 μm flux densities of our 11 Planck's Dusty Gravitationally Enhanced sub-Millimetre Sources (GEMS) (red) with other samples from the literature. The external samples include the strongly lensed dusty star-forming galaxies from H-ATLAS (green, Harris et al. 2012) and from the SPT survey (blue, Greve et al. 2012; Weiß et al. 2013). The 90% completeness limit of the PCCS is ~600 mJy at the highest frequencies of HFI.

In this thesis, I focus on the characterization of 11 sources in this sample, the so-called "Planck's Dusty Gravitationally Enhanced sub-Millimetre Sources (GEMS)". This subset of the parent sample of 15 candidates excludes the two lensed sources selected independently and already widely characterized in the literature. In this analysis, I also exclude two candidates located too far in the south to be followed-up with the northern observing facilities. The remaining 11 are directly observable from the northern hemisphere, allowing us to measure a robust spectroscopic redshift with the EMIR broadband receiver on the IRAM 30-m telescope. A detailed description of this redshift search is provided in Chapter 4. In other words, I focus on the sources that are unambiguously confirmed to be at high-redshift. Six of them are originally from the PCCS and the five other have been detected during the search of CIB sources in Planck maps (see the full list in Table 1 of Cañameras et al. 2015).

Given the unprecedented sky coverage of the original sample identified with Planck, we can affirm that these are among the brightest high-redshift galaxies on the sky outside of the Galactic plane. The histogram of the 350 μm flux densities from Herschel/SPIRE presented in Figure 2.4 indeed shows that our candidates are brighter than similar lensed sources detected with the SPT and previous wide-field Herschel surveys. The flux threshold applied during the selection implies that our sources are above $S_{350} \sim 300$ mJy. Moreover, the flux densities of six Planck's Dusty GEMS even exceed the 90% completeness limit of the PCCS in the 545 and 857 GHz bands of 570 and 680 mJy, respectively (Table 1 of Planck Collaboration et al. 2014b). At 350 μm, one of them exhibits $S_{350} = 1054 \pm 10$ mJy, nearly two times higher than the previous brightest record-holder and three times higher than the well-studied Cosmic Eyelash (Swinbank et al. 2010). The complete Herschel/SPIRE photometry of our sample is presented in Table 3.5.

Throughout this thesis, I will take advantage of our multi-wavelength follow-up to further show that these galaxies are strongly gravitationally lensed. I will also determine whether their intrinsic delensed properties indeed correspond to the most actively star-forming environments in the early universe. The Planck's Dusty GEMS will be named according to their galactic coordinates as is custom for sources discovered with Planck and, for the sake of simplicity, we will frequently use their galactic longitude only. For instance, the brightest source will be referred to as either PLCK_G244.8+54.9 or G244.8.

Chapter 3

Follow-up observations and data reduction

Contents

3.1 The need for a multiwavelength analysis

Characterizing the very active star forming regions in the GEMS requires to combine multi-wavelength observations. At long wavelengths above the mid-infrared (MIR) regime, we are sensitive the redshifted and magnified emission of interstellar gas and dust from the background source. Since the dusty GEMS are strongly obscured, they contribute very little to shorter wavelengths and the optical/NIR regime is therefore dominated by the foreground galaxies that are members of the lensing structures. Collecting extensive follow-up observations in the following regimes is therefore primordial to obtain a complete picture of our targets.

Optical/near-infrared imaging is essential to identify and characterize the foreground lensing structures that magnify our high-redshift SMGs. Estimating the radial profile, redshift and projected mass of the gravitational lens is indeed mandatory to derive robust strong lensing models. This requires to identify the isolated galaxies or cluster members forming the lenses, to measure their photometric redshifts and to use their mass and apparent morphology as a proxy of the underlying dark matter potential. In the rest-frame UV/optical we can probe these foreground galaxies with their stellar populations. However these wavelengths also target the rest-frame optical counterparts of the GEMS themselves and constrain their Spectral Energy Distribution (SED). For the high-redshift SMGs with moderate extinction, such observations could even enable to characterize the stellar populations of the background star-forming galaxies. In this section we describe the observations that provided us with optical and NIR imaging.

Optical/near-infrared spectroscopy is also pivotal to better constrain the main lensing sources and therefore to improve the accuracy of the strong lensing models toward the GEMS. It allows us to measure the spectroscopic redshifts of these foreground galaxies which are either isolated or members of extended structures like low-mass clusters. These redshifts are more robust ($\Delta z/z \sim 0.1$ with photometry and $\Delta z/z \sim 10^{-3}$ with spectroscopy) and enable us to confirm their group/cluster membership inferred from imaging. With this data we can therefore better understand the overall structure of the lens by constraining the mass profile of the foreground dark-matter halos and finding dark-matter substructures along some lines-of-sight. Optical/NIR spectroscopy also provides velocity dispersions which can be used as a proxy of mass.

Far-IR/submillimeter imaging and spectroscopy probes the redshifted thermal dust emission and the molecular and atomic interstellar gas tracers in our background dusty galaxies. For instance, the CO molecule emits bright rotational transitions and efficiently trace the cold molecular gas clouds. Along with other elements, CO probes the star formation at galactic scales as well as the gas heating mechanisms or the kinematics and physical state of the gas reservoirs. By observing dedicated transitions we can disentangle the spatial distribution of the diffuse and dense molecular gas components in our high-redshift galaxies. Moreover, high resolution interferometry is able to resolve our bright star forming sources and to map the star formation and gas mass surface densities down to fine spatial details. Interferometry is therefore primordial to resolve the morphologies and kinematics of the overall sample and to constrain the local star formation mechanisms.

3.2 Photometry

3.2.1 CFHT and VLT optical/NIR photometry

The Canada-France-Hawaii Telescope and its wide field cameras

Since 1979, the Canada-France-Hawaii observatory is located on top of the Mauna Kea volcano on Hawaii's Big Island, at 4200 meters above see level. Its optical/infrared telescope has a primary mirror

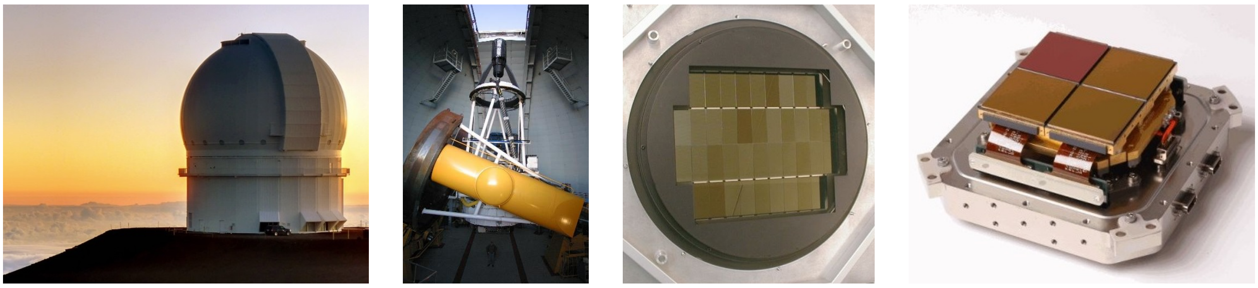

Figure 3.1: The CFHT near the summit of Mauna Kea moutain (*left*), the prime focus MegaPrime at the top end of the telescope (*center-left*), the 40 CCDs MegaCam (*center-right*) and the 4 detectors of WIRCam (*right*).

of 3.6 meters in diameter and became an intermediate size instrument after the commissioning of 8-meter class telescopes such as the Keck or the VLT. In particular, the Canada-France-Hawaii telescope (CFHT) hosts high resolution wide field imaging facilities since 2003.

The four instruments of the CFHT are directly settled on the prime focus due to the Cassegrain configuration of the telescope, and the two imagers as well as the high resolution and the multi-object spectrographs are interchangeable. We will essentially describe the wide field imagers that were used in this thesis.

First of all, the large optical/near-infrared camera MegaCam (Boulade et al. 1998) is connected to the prime focus with MegaPrime. This system at the upper end of the telescope includes an image stabilisation unit providing corrections of ± $1''$ in the focal plane, and two independent CCD detectors tracking the positions of guide stars to keep accurate pointings. A secondary unit automatically corrects the focus from the influence of temperature variations. MegaCam is itself sensitive to optical/near-infrared wavelengths with eight interchangeable filters and covers very wide fields-of-view of about 1×1 square degree. The camera is a CCD mosaic of 40 CCDs (36 are currently in working order) totalling about 340 Megapixels. The remarkable data stream generated during the acquisition is read in about 30 seconds with a read noise below 5 electrons. The dark current in the detector is strongly attenuated by a cryogenic cooling system working at -120 °C. Each pixel in the mosaic measures 13.5 μm which corresponds to a projected scale of 0.187 $''$/pixel on sky. Since the weather conditions on the Mauna Kea throughout the year offer an atmospheric seeing in the range $0.7 - 1.0''$ at these wavelengths, this pixel size properly samples the seeing disc.

Secondly, WIRCam (Puget et al. 2004) is a near-infrared (NIR) imager that was implemented in 2006, with the purpose of extending MegaCam sensitivity towards higher wavelengths. It operates up to 2.2 μm in several narrow and wide wavebands, including the usual J, H and Ks spectral bands in the NIR atmospheric windows. Eight lenses distribute the light beam in the focal plane over the four CCD detectors of WIRCam. Each of these CCDs comprise 2048×2048 pixels for a total of 16 Megapixels over the camera, and are cooled to 80 °C. The total field-of-view of WIRCam is 20 square arcmin with a pixel scale of 0.30 $''$/pixel. This scaling was chosen to conveniently sample seeing discs of diameters close to $0.8''$, the median value in the NIR, or above. However the site sometimes enjoys exceptionnal seeing conditions of about $0.5''$ and the point spread function (PSF) therefore becomes undersampled. An image stabilisation unit is available for these circumstances, and the image sampling can be reduced to 0.15 $''$/pixel. As will see below, this particular setup was not required in our proposal to observe the GEMS foregrounds with WIRCam.

The FORS2 and HAWK-I imagers on the Very Large Telescope

The FOcal Reducer/low dispersion Spectrograph (FORS2, Appenzeller et al. 1998) and the High Acuity Wide field K-band Imager (HAWK-I, Pirard et al. 2004; Casali et al. 2006; Kissler-Patig et al.

2008) are mounted on the Very Large Telescope (VLT) of the European Southern Observatory (ESO). These instrument are located on the focus of two different Unit Telescopes (UT1 and UT4) with main mirrors of 8.2 diameter. With such a large aperture, resolutions of $\sim 0.1''$ are theoretically achievable and the quality of astronomical images obtained at the VLT are therefore limited by the atmospheric turbulence (seeing).

The FORS2 instrument operates in the optical domain, in the wavelength range 330-1100 nm. It includes several observing modes from long-slit and multi-object spectroscopy to polarimetry, imaging, and also a high time resolution mode available for imaging and spectroscopy. In this thesis, we only use the imaging mode of FORS2. Its detector has a pixel size of 0.25 "/pix in the standard resolution mode corresponding to $6.8' \times 6.8'$ projected fields.

HAWK-I is a NIR wide-field imager installed on the VLT in the course of 2007. Its four detectors cooled to 80 °K contain 2048×2048 pixels and cover an on-sky field-of-view of $7.5' \times 7.5'$. The pixel size of HAWK-I mosaics is 0.106 "/pix.

Observation strategy

In order to probe the foreground light distribution and properly characterize the gravitational lensing structures toward the GEMS, we requested CFHT imaging in four bands for the nine sources in the northern hemisphere. These nine fields-of-view were observed with MegaCam and WIRCam in the r, z, J and Ks photometric bands, as summarized in Table 3.1. In the four programs 13AD98, 13BF07, 14AF06, 14BF07 (PI : N. Nesvadba), we requested a moderate atmospheric seeing of $0.8'' - 1.0''$ in r, z and J, and a better seeing in the Ks-band (about $0.6'' - 0.7''$) to match the expected resolution of the background sources followed-up with sub-mm interferometry. The observations were carried out in the Queued Service Observing mode by the telescope staff between March 2013 and March 2015. In optical bands, we estimated an approximate integration time per source allowing to detect typical L^* galaxies at $z = 1.0$ (Fassbender et al. 2011) — since the majority of galaxies in the lensing potentials should lie at redshifts below 1.0 — with a SNR about 5. In the NIR, we derived integration times intended to probe down to the expected magnitude of the high redshift sources. Individual frames had exposure times of about 300s in the optical and 15s in the NIR to limit the thermal noise in the detector and the tracking errors. The total exposure times and the detailed atmospheric conditions are reported in Table 3.1 for each field-of-view and each photometric band.

The data from MegaCam were then pre-processed and calibrated in astrometry and photometry with the Elixir system, and eventually released to the PI. WIRCam near-infrared frames were pre-processed with the 'I'iwi pipeline, and then coadded and sky-subtracted by N. Nesvadba.

For the last two GEMS lying at equatorial or southern declinations, G242.3 and G244.8, we obtained FORS2 imaging in three optical bands using the default V_{High}, R_{Special} and I_{Bessel} broad band filters. Observations were carried out in May 2013 and January 2014 as part of program 090.A-0896 and DDT program 291.A-5014, respectively (PI : N. Nesvadba). These optical frames were combined with HAWK-I observations taken in May and October 2013 using J and Ks filters with very similar transmissions to those of WIRCam. NIR frames include 60s individual exposures with a dithering pattern of $20''$. Optical exposures were taken in dark or grey time with an airmass ranging from 1.4 to 1.8 whereas we did not require any specific lunar phase in the NIR. The total integration times per bands are itemized in Table 3.1. The VLT images are deeper than their CFHT equivalents since we requested detections of L^* galaxies at $z = 2.0$ with reasonable SNR.

Individual frames from FORS2 and HAWK-I were pre-processed by ESO pipelines and subsequently coadded and sky-substracted by the PI.

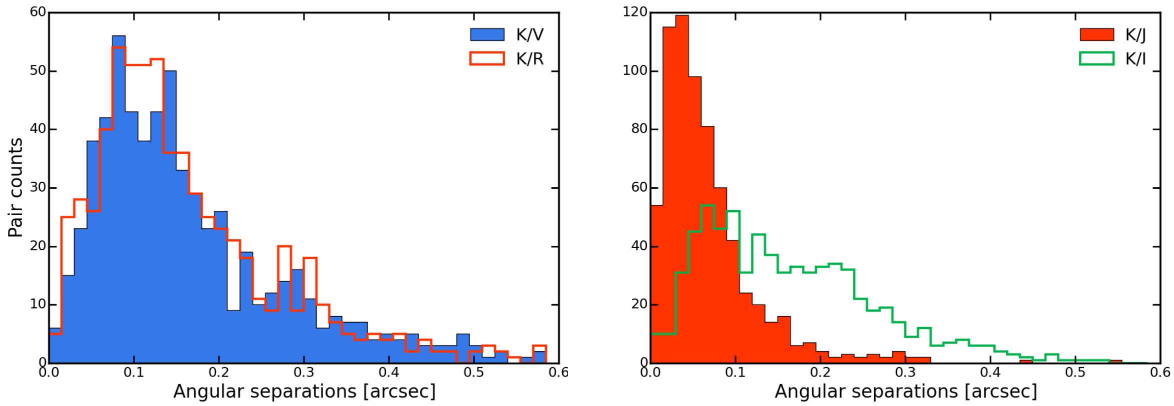

Figure 3.2: Histograms of the angular separations between sources detected in the Ks-band and their counterparts in V, R, I and J, after correcting the frame relative alignment with SCAMP and SWarp. Although these distributions concern the field-of-view toward G244.8 observed with the VLT, we obtain a similar degree of precision in our CFHT images.

Image reduction and astrometric calibration

For each source observed at the CFHT, the resulting dataset includes the individual frames combining the 40 CCDs of MegaCam in r and z bands, and the J and Ks images from WIRCam limited to the single CCD that matches the position of the source (i.e. a field-of-view of $14.1' \times 14.1'$). I first use SExtractor, SCAMP and SWarp (Bertin & Arnouts 1996; Bertin 2010a,b) to perform a consistent astrometric calibration between the four bands. For each GEMS, we decide to register the r, z and Ks frames relative to the J-band image and calibrate the latter relative to an external catalog which we consider as our astrometric reference. Since our nine fields-of-view are falling on the sky area covered by the Sloan Digital Sky Survey (SDSS), I follow the recommendation of Bertin (2010a) and use the SDSS-DR7 catalog as reference instead of 2MASS or USNO because this survey contains a higher number density of sources. To this end, I match the SDSS-DR7 catalogs with original J-band catalogs from SExtractor to find a large number of associations (typically about 800 pairs), and search for the astrometric solution with SCAMP. Correcting for the field distorsions with a fifth-order polynomial, the software finds adequate solutions with average shifts across the CCD below $0.15''$ and I generate the definitive J-band images with SWarp. The resulting positional uncertainty is about $0.10''$ at most.

In order to correct the distortions of MegaCam CCDs I perform a similar astrometric calibration on the individual frames in r and z, taking once again the SDSS-DR7 as reference. I focus on the CCD which contains the source of interest in order to reduce the calculation time and to avoid dealing with tricky edge effects between the detectors. Performing this calibration on the individual frames instead of the final stacked images enables to account for possible variations of the Point Spread Function (PSF) along the night and above all to better correct possible pointing errors. The MegaCam frames in r and z-bands are then coadded by SWarp.

I finally use SWarp to match the r, z and Ks band astrometry with the J-band and resample the optical frames to the nominal scaling of WIRCam, namely $0.30\ ''$/pix. This results in a suitable relative alignment between the four bands, with positional uncertainties of $0.1 - 0.6''$. I compute the angular separations between a given source in the Ks-band image and its counterparts in r, z, and J, build the distributions of these separations across each field, and summarize the peak values in Table 3.2. These distributions are nicely peaked, with FWHM $< 0.2''$, and we find almost no outlier with angular separations above $1''$. The frames are eventually cropped to $5' \times 5'$ fields-of-view centered on the position of the high redshift sources, in order to avoid masking the CCD edges. In a first approach, the resulting frames are large enough to include the bulk of galaxies within the lensing structures toward the high-redshift GEMS and provide statistics on the surrounding field.

The relative astrometry of FORS2 and HAWK-I images is calibrated in the same way, taking again the SDSS-DR7 catalog as external reference. Fig.3.2 shows the angular separations between sources detected in the Ks-band in the field of G244.8 and their counterparts in V, R, I and J, after correcting the frame alignment. Here I use the entire CCD mosaics and crop fields-of-view of $5.7' \times 5.7'$ covered by the two instruments. Since I oversample the optical images to the pixel scale of HAWK-I, about $0.106\ ''$/pix, the final sampling differs from the CFHT reduced images.

Absolute photometric calibration

To calibrate our absolute photometry from MegaCam and WIRCam, we need to derive robust magnitude zero-points in the r, z, J and Ks photometric bands. In a first stage, I compared our Sextractor aperture magnitudes with archival data from the ninth data release of the Sloan Digital Sky Survey (SDSS-DR9, Ahn et al. 2012) and from the Two Micron All Sky Survey (2MASS, Cutri et al. 2003). SDSS is a large scale survey covering about one third of the sky and comprising multi-band imaging and spectroscopy in the optical and NIR. In particular, the survey contains photometric data in the five u, g, r, i, z filters for nearly 500 million sources, with limiting magnitudes between 20 and 22. 2MASS includes the J, H and Ks NIR wavebands with an average limiting magnitude of 14 and provides consistent photometry both for point-sources and extended sources. Fortunately, the filter sets used in these surveys and in our CFHT program have similar transmissions.

For a proper comparison, I extracted dedicated catalogs using the same photometric estimators as in SDSS-DR9 and 2MASS, respectively. In the optical, I used SExtractor AUTO magnitudes as the best match with the model magnitudes of SDSS catalogs. For the NIR calibration, given the atmospheric seeing of about $1''$ in our images I applied the 2MASS standard aperture of $8''$ diameter without any additional curve-of-growth correction. I also converted 2MASS Vega magnitudes to the AB system with the coefficients of Blanton et al. (2005). I subsequently compared this r, z, J and Ks photometry with the reference catalogs, for objects non-saturated and brighter than the limiting magnitudes of SDSS and 2MASS. For each field-of-view and each band I obtained tight correlations with slopes near unity and with intercepts providing the required magnitude zero-points.

In a second stage, I completed a relative calibration between the available bands to remove the possible systematics in the magnitude zero-points, for each line-of-sight. To this end, I selected a sample of non-blended and non-saturated stars from the Guide Star Catalog II (GSC-II, Lasker et al. 2008) and with counterparts in SDSS-DR9 and 2MASS catalogs. I chose the stars with a SED peaking between SDSS optical bands and therefore with a better constrained temperature. In this way I obtained between 3 and 6 stars per field-of-view with Planck functions peaking in the range $5000 - 8000$ Å ($T \sim 4000 - 6000$ °K). I fitted their SDSS and 2MASS photometry with a blackbody SED and then derived zero-point offsets for each CFHT band. This multi-wavelength calibration thus provided final zero-points with absolute uncertainties generally below 0.05 mag (Table 3.1).

Concerning the VLT images in V, R, I broadband filters, I applied the photometric calibration computed by ESO pipeline via observations of standard stars from the catalog of Landolt (1992), and from an updated version of Stetson (2000) standard fields. I followed the recipe of Mignani et al. (2011) and used the suitable gain to convert the extinction-corrected magnitude zero-points released in the quality-control database from electrons/s to ADU/s. I finally corrected these normalized zero-points to the proper exposure times, and to AB magnitudes with the coefficients of Fukugita et al. (1995). In HAWK-I bands, an absolute accuracy of 0.05-0.10 mag should be reasonable for the purpose of this work and I therefore derived the J and Ks zero-points from the 2MASS photometry. I eventually isolated the three non-blended and non-saturated stars over the fields-of-view to fit a blackbody function and validate the relative calibration between the five bands.

Source	Band	Observing run	t_{exp} $^{(1)}$ [min]	Seeing [arcsec]	δpos$^{(2)}$ [arcsec]	Magnitude zero-point	Mag-limit
G045.1	r	Mar. 2014	40	0.97	0.6	32.05 ± 0.01	24.7
	z	Feb. 2014	44	0.84	0.5	30.94 ± 0.02	23.4
	J	Mar. 2014	28	0.97	0.3	28.98 ± 0.04	22.6
	Ks	Mar. 2014	16	0.76	—	28.41 ± 0.05	22.1
G080.2	r	Mar. 2013	65	1.0	0.5	32.20 ± 0.01	24.9
	z	Mar. 2013	44	0.78	0.4	31.10 ± 0.01	23.2
	J	Apr. 2013	64	0.88	0.2	28.81 ± 0.02	22.5
	Ks	Mar. & Apr. 2013	14	0.87	—	27.86 ± 0.05	21.3
G092.5	r	Mar. 2014	45	1.1	0.1	32.00 ± 0.01	24.7
	z	Feb. 2014	44	0.77	0.1	30.94 ± 0.01	23.4
	J	Mar. & May 2014	51	1.1	0.2	29.01 ± 0.05	22.8
	Ks	May 2014	28	0.68	—	20.00 ± 0.05	21.4
G113.7	r	Mar. 2014	35	0.86	0.1	32.03 ± 0.04	24.6
	z	Feb. 2014	44	0.74	0.1	30.96 ± 0.04	23.5
	J	Mar. 2014	59	0.87	< 0.1	29.02 ± 0.05	22.9
	Ks	May 2014	29	0.57	—	28.39 ± 0.02	21.7
G138.6	r	Mar. 2014	35	0.84	0.3	31.99 ± 0.02	24.7
	z	Dec. 2013	44	0.77	0.3	30.95 ± 0.02	23.6
	J	Dec. 2014	85	0.93	0.2	29.15 ± 0.08	23.3
	Ks	Dec. 2014	85	0.92	—	28.64 ± 0.01	22.4
G145.2	z	Nov. 2013	59	1.3	0.4	30.89 ± 0.03	23.4
	J	Dec. 2013	107	1.2	0.4	29.12 ± 0.07	22.8
	Ks	Nov. 2014	18	0.69	—	28.48 ± 0.03	21.5
G165.7	r	May 2014	40	0.81	0.3	31.73 ± 0.02	24.5
	z	Mar. 2014	49	0.94	0.2	30.59 ± 0.01	22.8
	J	Mar. 2014	93	1.1	0.2	28.80 ± 0.04	23.1
	Ks	Mar. 2014	13	0.69	—	28.48 ± 0.03	22.3
G200.6	r	Mar. 2013	55	1.1	0.1	31.87 ± 0.04	24.8
	z	Nov. 2013	44	1.2	0.1	30.88 ± 0.01	23.1
	J	Oct. & Dec. 2013	19	0.87	0.3	29.21 ± 0.05	22.4
	Ks	Dec. 2013 & Oct. 2014	7	0.56	—	28.56 ± 0.03	21.7
G231.3	r	Jan. 2015	39	0.79	0.3	32.20 ± 0.01	24.9
	z	Dec. 2013	44	0.88	0.3	30.74 ± 0.01	23.2
	J	Dec. 2013	73	1.1	0.1	28.59 ± 0.01	22.9
	Ks	Nov. 2014	6	0.59	—	28.37 ± 0.01	21.9

Table 3.1: Observing log for the GEMS observed at CFHT, with MegaCam and WIRCam. We also summarize the results of the astrometric and photometric calibrations and the 3σ limiting magnitudes of the photometric catalogs. — (1): The total on-source integration time. — (2): Peak values of the angular separations between a given source in the Ks-band image and its counterparts in r, z, and J.

Source detection and photometry

I measured the optical-to-NIR fluxes within a common circular aperture for all bands, as previously done in the COSMOS field (Ilbert et al. 2009). For each square patch of $5' \times 5'$ observed at CFHT or VLT, I estimated the atmospheric seeing in the different bands to find the optimal aperture size for point-source photometry. To this end, I identified a small set of unresolved sources including the non-blended and non-saturated stars from GSC-II and measured their FWHM with SExtractor. For

Source	Band	Observing date	t_{exp} $^{(1)}$ [min]	Seeing [arcsec]	δpos$^{(2)}$ [arcsec]	Magnitude zero-point	Mag-limit
G244.8	V	8 May 2013	23	1.1	0.1	26.00 ± 0.09	27.4
	R	8 May 2013	9.3	0.88	0.1	26.37 ± 0.06	26.9
	I	8 May 2013	13	1.1	0.2	21.70 ± 0.10	26.2
	J	12 May 2013	26	0.44	< 0.1	29.87 ± 0.10	24.2
	Ks	13 May 2013	30	0.45	—	30.08 ± 0.10	23.6

Table 3.2: Observing log for the GEMS observed at VLT, with FORS2 and HAWK-I. We also summarize the results of the astrometric and photometric calibrations and the 3σ limiting magnitudes of the photometric catalogs. — (1): The total on-source integration time. — (2): Peak values of the angular separations between a given source in the Ks-band image and its counterparts in V, R, I and J.

CFHT images, I chose fixed apertures of $3.4'' - 4.0''$ diameter depending on the highest stellar FWHM found among the optical/NIR bands. On the one hand, such sizes are convenient to limit both the flux loss outside the apertures and the number of blended sources and, on the other hand, they are high enough to derive NIR fluxes with IRAC (see §3.2.2). However since the atmospheric seeing in VLT images is $\sim 1.0''$ in optical bands and extremely good in J and K ($\sim 0.45''$), I decided to fix smaller apertures of $2.5''$ diameter to include only a moderate fraction of the background sky.

Using the dedicated zero-points I subsequently computed these aperture magnitudes with SExtractor (Bertin & Arnouts 1996), applying a 3σ detection threshold with respect to the local background. The Ks images were used as references to favour the detection of faint red sources and to keep a homogeneous selection in the ten fields-of-view. Photometric errors were estimated by measuring the background sky around each detected source, within circular rings of external diameter up to $6.5''$. I also removed the image artifacts such as cosmic rays by requesting at least 15 pixels above threshold for each detection.

Since the bright and spatially resolved galaxies are indispensable to characterize the foreground structures toward the GEMS, I also computed isophotal fluxes with SExtractor, applying detection isophotes at the 3σ threshold. This estimator provides consistent photometry for these extended sources whereas our apertures would induce significant losses of flux. However we warn that these isophotal magnitudes may suffer from additional uncertainties, such as a source blending in individual isophotes or surface brightness biases across the detector.

Defining the 3σ limiting magnitude of a given frame as the magnitude of a source with flux SNR of 3.0, we obtained about 24.8, 23.5, 22.8, 22.0 mag in r, z, J and Ks bands, respectively, while VLT images are about one order of magnitude deeper (Table 3.1 and Table 3.2).

3.2.2 Spitzer/IRAC NIR photometry

The Spitzer telescope and its infrared imager

The Spitzer Space Telescope operates in the infrared regime and was launched in 2003 on a heliocentric orbit, as the fourth and last space-based telescope of NASA's Great Observatories program (Werner et al. 2004). It is made of a primary mirror of 85 centimeters in diameter and three scientific instruments which were all cryogenically cooled to 5.5°K during the first 6 years of the mission. The observatory includes an imager working between 3 and 160 μm (IRS, Houck et al. 2004), a spectrometer observing between 5 and 38 μm (IRAC, Fazio et al. 2004) and an imaging spectrometer for the 50-100 μm range (MIPS, Rieke et al. 2004). Liquid helium reservoirs maintained the nominal temperature of the system until the coolant was depleted in 2009. Since then, Spitzer is operating at the equilibrium temperature of the system, around 30 °K, with very limited use of its instruments. This mode is expected to extend the telescope lifetime for about a decade.

The infrared camera IRAC that was used in this thesis is the only instrument still operating in the "Spitzer warm mission". With its four different detectors, IRAC was observing simultaneously in four wavelength channels at 3.6, 4.5, 5.8 and 8.0 μm during the optimal phase of the mission. These detectors comprise 256 × 256 pixels corresponding to fields-of-view of $5.12' \times 5.12'$ and as described below, the telescope optics is limiting the images spatial resolution to $\lambda/20$. Among the four channels, the 3.6 and 4.5 μm detectors use a semiconductor device with indium and antimony (InSb) that remains operational at 30 °K. These two short-wavelength channels are therefore able to observe in the "warm mission" with appropriate sensitivities, whereas the 5.8 and 8.0 μm channels became useless without helium cooling.

IRAC was notably designed to study the primordial universe and to detect ULIRGs and AGNs at high redshifts. Its sensitivity and wavelength regime are perfectly suited to probe the near-infrared emission of the GEMS and to detect the stellar populations of the foreground galaxies belonging to the lensing structure. But the wide field-of-view of the camera also make it particularly suitable for multi-wavelength extragalactic surveys such as the Extended Groth Strip (Barmby et al. 2008; Davis et al. 2007).

Observations and image reduction

The GEMS were followed-up at 3.6 and 4.5 μm with IRAC between 2013 and 2014 as part of programs ID 90111 (PI : H. Dole) and ID 10014 (PI : N. Nesvadba) (see the observing log on Table 3.3). A fainter lensed source from the parent sample, G242.3 was imaged with IRAC in program ID 80238 but is not included in the overall follow-up program. Integration times per pixel were chosen to detect point sources of 23.5-24.0 mag and 23.1-23.6 mag at 3.6 μm (channel 1) and at 4.5 μm (channel 2), respectively (1σ sensitivities). Individual observation sequences of 100 seconds produced a total exposure of about 1200s per pixel at the centre of each frame, but the coverage dropped to 500s per pixel at the edges.

Basic Calibrated Data (BCD) were released after a preliminary processing conducted by the Spitzer Science Center standard pipeline. The dark currents and flatfields were automatically calibrated and substracted during this stage. In both channels the frames were flux calibrated, combined into mosaics with 0.60 $''$/pix sampling, corrected for cosmic ray artifacts and astrometrically calibrated with external 2MASS catalogs. The delivered post-BCD images are expressed in true surface brightness units (MJy/sr).

The optical distorsions affecting the pixels far from the telescope optical axis are already corrected in the post-BCD images with $0.1''$ accuracy. We nonetheless refine the astrometric projections with respect to our optical and NIR images in order to get concordant positions in each photometric band, for detections all over the fields-of-view. For each GEMS I apply these corrections with SWarp and resample the IRAC mosaics to the pixel scale of our NIR images, either from WIRCam or from HAWK-I. I carefully check that the process preserves the image surface brightness and eventually crop the frames to $5' \times 5'$ fields-of-view. The SWarp corrections also enables to get rid of the varying size of pixels associated with different projected solid angles. Angular separations between the source positions in the Ks-band and their counterparts in channel 1 and channel 2 exhibit broader distributions than in §3.2.1 that peak between $0.1''$ and $0.5''$ (peak separations are itemized in Table 3.3).

Calibrating the magnitude zero-points

Before extracting the source photometry, I compute the magnitude zero-points of IRAC images in order to directly work with flux densities and AB magnitudes in the SExtractor output catalogs. The absolute flux references estimated from standard stars provide flux calibrations accurate to $\sim 3\%$ in the post-BCD images (Reach et al. 2005). Zero magnitude flux densities of F_0 of 280.9 ± 4.1 Jy/pixel at 3.6 μm and 179.7 ± 2.6 Jy/pixel at 4.5 μm are then derived from this calibration (see IRAC Instrument

Source	Observing date	Band	δpos [arcsec]
PLCK_G045.1+61.1	25 May 2014	[3.6]	0.3
		[4.5]	0.4
PLCK_G080.2+49.8	11 Apr. 2013	[3.6]	0.5
		[4.5]	0.4
PLCK_G092.5+42.9	5 Jun. 2014	[3.6]	0.1
		[4.5]	0.2
PLCK_G102.1+53.6$^{(*)}$	7 Jun. 2014	[3.6]	—
		[4.5]	—
PLCK_G113.7+61.0	19 Jun. 2014	[3.6]	0.5
		[4.5]	0.5
PLCK_G138.6+62.0	24 Jun. 2014	[3.6]	0.5
		[4.5]	0.4
PLCK_G145.2+50.9	6 Jun. 2014	[3.6]	0.3
		[4.5]	0.4
PLCK_G165.7+67.0	8 Jul. 2014	[3.6]	0.4
		[4.5]	0.5
PLCK_G231.3+72.2	23 Aug. 2014	[3.6]	0.5
		[4.5]	0.4
PLCK_G244.8+54.9	28 Aug. 2014	[3.6]	0.2
		[4.5]	0.2

Table 3.3: Observing log for the GEMS observed with IRAC on-board the Spitzer satellite and results of the astrometric calibration. δpos indicates the peak values of the angular separations between a given source in the Ks-band image and its counterparts in channels 1 and 2, respectively. — (*) : G102.1 was not followed-up at CFHT and, since our Palomar imaging is too shallow, it is not included in the multi-wavelength data set.

Handbook[1]).

For a given IRAC channel the magnitude of an astronomical source, m, is therefore expressed as

$$\mathrm{m} = -2.5 \times \log\left(\frac{\mathrm{C} \times \mathrm{S}}{\mathrm{F}_0}\right) = \mathrm{z}_{\mathrm{mag}} - 2.5 \times \log\left(\mathrm{S}\right) \tag{3.1}$$

where S is the source surface brightness in MJy/sr measured in the given IRAC image, C is a conversion factor from MJy/sr to Jy/pixel and F_0 is the zero magnitude flux density in Jy/pixel ($\mathrm{m} = 0$ for $\mathrm{C} \times \mathrm{F} = \mathrm{F}_0$).

The magnitude zero-point $\mathrm{z}_{\mathrm{mag}}$ therefore becomes $\mathrm{z}_{\mathrm{mag}} = +2.5 \times \log\left(\mathrm{F}_0/\mathrm{C}\right)$. I use the pixel scale of the resampled mosaics and the tabulated zero magnitude flux densities to compute the conversion factor C for each field-of-view and each channel. For instance, I obtain $\mathrm{z}_{\mathrm{mag}} = 20.27 \pm 0.02$ mag in channel 1 and $\mathrm{z}_{\mathrm{mag}} = 19.79 \pm 0.02$ mag in channel 2 for the IRAC images that were resampled to the pixel scale of WIRCam.

Source extraction and aperture photometry

Since the background is not strongly varying in our IRAC images, we use aperture photometry to estimate point source fluxes. This recipe is the most straightforward to derive the photometry of point sources but is not applicable for extended sources and for the most crowded areas. Moreover the

---

[1] http://irsa.ipac.caltech.edu/data/SPITZER/docs/irac/iracinstrumenthandbook/17/

resolution of IRAC images are limited by the diffraction pattern of the telescope primary mirror. Since the resulting FWHM of the Point Response Functions (PRFs) reach 1.66″ and 1.72″ in channel 1 and 2, respectively, we expect that most galaxies relevant to our study will remain unresolved. Taking all of this into consideration, I extract the 3.6 and 4.5 μm photometry with SExtractor using the optimal apertures of optical and NIR bands and applying the magnitude zero-points. These apertures are small enough to avoid blending between adjacent point sources, but obviously miss a portion of their flux.

It is therefore mandatory to apply aperture corrections in order to recover the total fluxes of unresolved galaxies across the fields. I use the correction factors derived by Martinache et al. (2016, in prep.) from the Extended Groth Strip (EGS) mosaics, as done in Barmby et al. (2008). Following a classic approach, this study derives aperture corrections by comparing fluxes integrated within several small apertures to fluxes within an IRAC standard calibration aperture of 12.2″. This comparison subsequently provides the curves of growth of channels 1 and 2 presented in Fig.3.3. For the GEMS observed at the CFHT, our optimal apertures in the range 3.4″-4.0″ correspond to correction factors of 1.44-1.63 in channel 1, and 1.48-1.68 in channel 2. We remind that smaller apertures were used for the southern GEMS observed at the VLT, and the large correction factors will likely introduce substantial uncertainties.

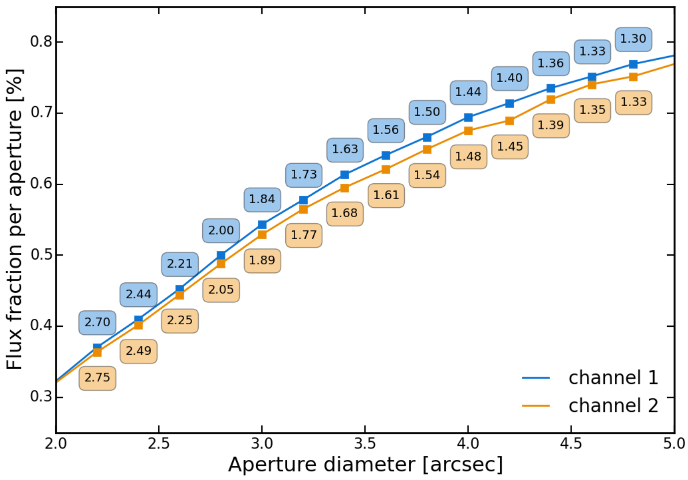

Figure 3.3: Spitzer/IRAC curves of growth computed by C. Martinache for channel 1 (*blue points*) and channel 2 (*orange points*), using the Point Response Function from the Extended Groth Strip. The fraction of the total point source fluxes (measured within a standard calibration aperture of 12.2″) are plotted as a function of the selected aperture. The correction factors to be applied on the extracted fluxes are displayed for aperture diameters starting at 2.2″ and increasing by +0.2″.

Estimating the photometric errors

The fluctuations of the background sky is the main source of photometric errors in channels 1 and 2. For a given aperture, SExtractor computes photometric uncertainties with the following equation

$$\sigma^2 = \sigma_{\rm SE}^2 {\rm N_{pix}} + {\rm F_{aper}}/{\rm g} \tag{3.2}$$

where $\sigma_{\rm SE}^2 {\rm N_{pix}}$ is the background noise estimated by SExtractor, $\rm F_{aper}$ is the aperture flux of the detected source in counts, and g is the local gain. However, Gawiser et al. (2006) notes that SExtractor estimates the background noise without accounting for correlated noise between pixels within the aperture. I therefore replaced the $\sigma_{\rm SE}^2 {\rm N_{pix}}$ term by dedicated measurements of the background sky. After masking the sources in each band, I distributed 500-1000 apertures at random positions. This provided adequate statistics to measure directly the variance of the background sky within our optimized apertures. Finally, I multiplied these uncertainties by the associated correction factors to deduce final errors on the aperture corrected fluxes.

Several systematics are also involved in addition to these photometric errors. Firstly, the surface brightness images in channels 1 and 2 contain a calibration uncertainty usually evaluated at 3%. Secondly, IRAC PRF slightly varies across the post-BCD mosaics. Since we do not account for this effect, the IRAC handbook suggests that our aperture corrections contain 1-2% additional uncertainties.

3.2.3 Band-merged catalogues in the optical and NIR

As stated below I merged the photometric catalogs with respect to the Ks-band detections with the aim of performing a consistent selection in the ten fields-of-view and keeping preferentially the red sources. I do not fix the prior in IRAC NIR bands because of Spitzer lower resolution and considering the higher confusion in IRAC images. The sky areas covered by IRAC channels 1 and 2 match the $5' \times 5'$ fields-of-view of our CFHT and VLT imaging, and we therefore use the same apertures in the subsequent analysis. All magnitudes in these multi-band catalogs are expressed in the AB system. The sources non-detected in a given band have magnitudes set to 99 and I used their 3σ limiting magnitudes as lower limits.

We obtained between 260 and 700 detected sources per field-of-view, depending on the depth of NIR images. This corresponds to 1.2 μm surface densities ranging between 10.4 and 24.0 sources per square arcmin.

3.2.4 IRAM 30-m telescope/GISMO imaging at 2 mm

Description of the instrument

Constraining the Rayleigh-Jeans tail of the dust emission requires to observe the two-millimeter continuum of the GEMS. In our project such observations were carried out with the Goddard-IRAM Superconducting two-Millimeter Observer (GISMO, Staguhn et al. 2012), a bolometer camera mounted on IRAM 30-m telescope since 2011. GISMO includes a 8×16 pixels array of Transition Edge Sensors (TES) and is entirely cryogenically cooled to offer a nominal bandpass FWHM of 140-162 GHz. The cameras offers a relative flux density stability of about 8%. The field-of-view of individual on-the-fly scans is $1.8' \times 3.7'$, with a pixel scale of 3.0 $''$/pix. However a Lissajous mode is also available at the 30-m telescope and offers a scanning pattern mapping areas of up to $4' \times 4'$.

Observing strategy, data reduction and photometry

We fitted the Herschel/SPIRE photometry of the GEMS with SED templates of NGC520 and Arp220 to predict 2-mm flux densities, and we used GISMO expected sensitivity of about 14mJysqrt(sec) to derive integration times per source. We expect all lensed SMGs in our sample to be unresolved point sources in the $21'' \times 21''$ beam of the 30-m telescope at 2-mm. We therefore chose small Lissajous maps of $2' \times 2'$ which are optimal to detect our faint point sources with a stable SNR and a limited number of bad channels over the maps. The sources were observed during the 3rd and 4th GISMO pools in late April 2013 and between 29 October and 5 November 2013, respectively (programs 222-12 and 100-13, PI : H. Dole). The former was observed by S. König under good or moderate weather conditions with 1.7-9.9 mm precipitable water vapour. I conducted the second run with an excellent precipitable water vapour almost exclusively below 2.0 mm. I corrected the flux calibration and the telescope pointing – either after 2 hours of integration or after moving the antenna to a new target – using nearby planets or radio-loud quasars. I also focused the telescope every 4 hours.

Then I reduced, calibrated and coadded individual scans from these two runs with the CRUSH software package (Kovacs 2013). Before combining the scans of November 2015 I used an updated version of the software that takes into account instant pointing corrections of $\sim 2''$. I used the "faint" option which is dedicated to extract integrated signals of about 10 mJy, detected at signal-to-noise ratios of less than 10 per scan. Finally, I computed SNR maps to mask the frame edges and keep only the pixels with high and stable SNR. As shown in Fig.3.4, the 12 GEMS are detected as point sources, with SNR between 3.1 and 16 (Table 3.4). Since our final images are expressed in flux density per beam, the total flux of our point sources is almost equal to their peak flux. We nonetheless perform aperture photometry in order to account for possible flux losses and to estimate the photometric uncertainties. I use circular apertures of $31''$ diameter, 1.5 times the beam FWHM of the 30-m telescope, and estimate the photometric errors from the local background measured in concentric rings of $31'' - 62''$ diameter.

During the November 2015 pool I also observed 6 overdensities of high-redshift galaxies from the Planck/Herschel catalogue, with on-source exposures of 2-3 hours and Lissajous maps of $3' \times 3'$. Since these targets are much fainter than the GEMS, we only obtained one marginal detection for G237.1 (SNR $\sim$ 4) with a GISMO peak flux associated with the Herschel/SPIRE contours.

Source	Observing run	$t_{\rm exp}$ $^{(1)}$ [min]	rms [mJy/beam]	SNR$^{(2)}$	$S_{\rm 2mm}$ [mJy]
PLCK_G045.1+61.1	19 Apr. 2013	37	1.1	8.5	13 ± 2
PLCK_G058.5+64.6	01/02/04 Nov. 2013	90	0.53	4.0	2.2 ± 0.4
PLCK_G080.2+49.8	15 Apr. 2013	24	1.4	3.1	7 ± 2
PLCK_G092.5+42.9	15 Apr. 2013	36	1.1	7.0	8.4 ± 0.6
PLCK_G102.1+53.6	29 Oct./04 Nov. 2013	71	0.73	6.9	5.5 ± 0.7
PLCK_G113.7+61.0	19 Apr. 2013	37	1.4	3.6	4 ± 1
PLCK_G138.6+62.0	15 Apr. 2013	36	1.4	4.6	7 ± 1
PLCK_G145.2+50.9	12 Apr. 2013	29	1.4	16	38 ± 4
PLCK_G165.7+67.0	12 Apr. 2013	28	1.1	4.5	8 ± 1
PLCK_G200.6+46.1	02 Nov. 2013	45	1.0	5.4	7 ± 2
PLCK_G231.3+72.2	27 Apr. 2013	36	1.0	6.4	9 ± 1
PLCK_G244.8+54.9	31 Oct. 2013	10	2.4	5.9	19 ± 2

Table 3.4: 30-m telescope/GISMO observing log for the run of April 2013 (observer : S. König) and the run I observed between October and November 2013. (1): The total on-source integration time. (2): The Signal-to-Noise Ratio (SNR) defined between the peak flux in the original image expressed in Jy/beam, and the map rms in source-free regions.

3.3 Spectroscopy

3.3.1 IRAM 30-m telescope/EMIR

Description of the instrument

The 30-m telescope of IRAM is a single dish antenna observing (sub)-millimeter waves in four atmospheric windows at 0.9, 1, 2 and 3 millimeters. It is located on the Pico Veleta in Spain and considered as one of the largest and most sensitive telescopes operating in the radio regime. Along with the continuum cameras, the 30-m includes monopixel heterodyne receivers offering high resolution spectroscopy. In particular, the Eight MIxer Receiver (EMIR, Carter et al. 2012) is a wideband receiver observing in four different frequency bands: E090 at 73-117 GHz, E150 at 125-184 GHz, E220

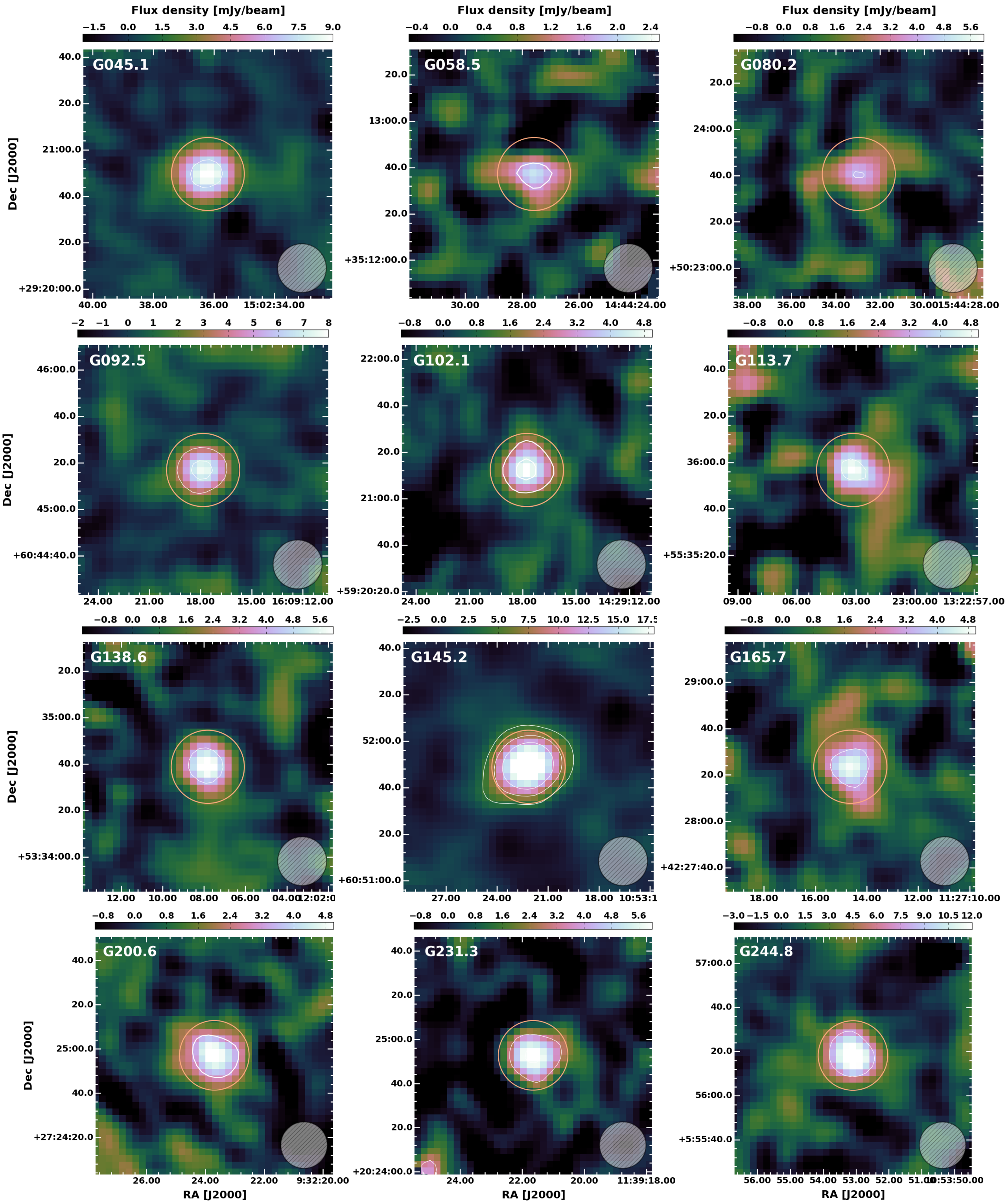

Figure 3.4: The 2-mm continuum of the 12 GEMS observed with GISMO on the IRAM 30-m telescope. The maps are expressed in flux densities per beam and white contours show the SNR isocontours starting at $+3\sigma$ and increasing by 3σ. The telescope beam at 2-mm is plotted in the lower-right corners and shows that the GEMS are indeed unresolved point sources. Orange circles indicate the apertures I used to extract the total fluxes.

at 202-274 GHz and E330 at 277-350 GHz. EMIR offers dual-band observations for a total bandwidth of up to 16 GHz in each of the two orthogonal polarizations. The receiver separates the individual sidebands of 4 GHz and operates in dual-sideband mode with common tuning frequencies between the two polarizations.

Observing the GEMS with EMIR

The high resolution spectra of the brightest atomic and molecular lines from the GEMS were obtained with EMIR as part of an extensive line survey conducted in the millimeter and sub-millimeter bands. The deep spectroscopic observations were carried out between March 2013 and June 2014 in several observing programs (PI : N. Nesvadba).

The first observing runs in 2013 were dedicated to perform a blind redshift search in the 2-mm and 3-mm bands, using the maximal bandwidth of 16 GHz available with EMIR. Following the same strategy as in the pilot program 82-12 and Director's Discretionary program D05-12, we used the photometric redshifts derived from the Herschel/SPIRE SED fitting as a prior to detect at least two emission lines and infer robust spectroscopic redshifts for the 11 GEMS. The whole redshift survey was conducted as part of the Director's Discretionary program D09-12 and the regular program 094-13 in April and June 2013, for a total observing time of 75 hours. The complete description of the methodology is postponed to §4.1. During the following observing runs (programs 223-13 and 108-14), we used these reliable redshifts to detect most of the brightest emission lines in the 2-mm and 3-mm windows. We probed the CO ladder from $J = 3-2$ and up to highly excited levels ($J = 11-10$ for the most extreme source), and detected the [CI](1-0) and [CI](2-1) transitions as well as several low-excitation emission lines from H_2O. The search for molecular gas tracers in the brightest GEMS, G244.8, resulted either in marginal detections or 3σ flux upper limits and required deeper observations. The final dataset includes between 2 and 10 lines per source. We defer the full description of the lines used in this thesis to Chapters 4 and 7.

During the integration, the sky emission was efficiently substracted using a Wobbler switching of 60" above the telescope primary beam (from ~ 7.5" at 340 GHz to ~ 29" at 86 GHz) and above extension of the (sub)-millimeter source. We calibrated the pointing every 2 hours using radio-loud quasars at small angular separation from the GEMS, to obtain pointing accuracies better than $1''$. The telescope focus is expected to change especially during the significant variations of the atmospheric temperature. We therefore calibrated the focus after each sunrise and sunset, and every $\sim$4 hours in stable conditions.

We used either the FTS or WILMA backend, covering 8 and 16 GHz bandwidth respectively, with a spectral resolution of 195 kHz and 2 MHz. When we observed faint emission lines and when the atmospheric precipitable water vapor was high (typically for pwv > 6 mm), we favored the WILMA backend in order to increase the baseline stability in our spectra. The brute individual scans were 30 s long, and we observed successive sets of 12 scans.

Reduction of the spectra and baseline corrections

The data were automatically calibrated during the observations, every 6 minutes. I subsequently reduced the spectra using the CLASS software package from the GILDAS[2] (Gildas Team 2013) distribution delivered by IRAM. I selected the individual scans of 30 seconds falling below our pwv threshold and smoothed the coadded spectra to suitable resolutions. I found that adding the scans observed at higher pwv did not improve the line signal-to-noise ratio or the baseline stability. We therefore decided to leave them aside. We took advantage of a dedicated routine provided by C. Kramer to individually correct the baselines in each sub-band. These baseline were then substracted in each individual scan, using first degree polynomials fitted in spectral windows with no emission line. Where appropriate,

---

[2] http://www.iram.fr/IRAMFR/GILDAS

a refined correction was performed with second or third degree polynomials, and I carefully checked that integrated fluxes were not altered by more than 5% in the process.

I list the specific tuning frequency, integration time and rms noise for each spectrum in Tables 4.1 and 7.1.

Fitting the emission line profiles

Considering that the atomic and molecular emission lines detected in the millimeter are produced by interstellar gas and assuming that this medium is approximately in the local thermodynamic equilibrium (LTE), the line profiles are set by thermal Doppler broadening. In these circumstances, the random motion of particles produce a distribution of velocities following the Maxwell-Boltzmann law. However, the radial velocity component $\mathrm{v_r}$ which can be observed along the line-of-sight follows a Gaussian distribution. Photons emitted by a particle of velocity $\mathrm{v_r}$ toward or away from the observer are Doppler-shifted according to $\nu = \nu_{\mathrm{rest}}(1 \pm \mathrm{v_r}/\mathrm{c})$. Thus, the combined emitted radiation has a Gaussian profile of FWHM related to the gas temperature. Moreover, turbulence induces additional velocity components which are generally Maxwellian in molecular star-forming regions. Turbulence and pure thermal motions therefore produce similar line profiles. Finally, in highly pressurized environments collisions can perturb the rotational levels and broaden the molecular lines independently from the particle velocities.

Given the small-to-intermediate SNR of the individual lines detected with EMIR, I approximate their profiles by single gaussians and fit these components with the GILDAS software. I adopt a specific approach in the rare cases highlighting significant deviations from a single gaussian, generally due to substantial movements of the interstellar gas at macroscopic scales. The presentation of the resulting parameters (uncorrected for lensing magnification) and the interpretation of the line profiles are postponed to Chapters 4 and 7. The observing frequencies mentioned in these Chapters correspond to the line frequencies expected from the redshift measurements, themselves inferred from the two lower-J CO transitions. I convert the line fluxes from apparent brightness temperatures to milli-Jansky using the telescope efficiencies, $\mathrm{S/T_a^*}$, taken from the most recent commissioning and I also correct the line FWHMs for spectral binning. The quoted parameter uncertainties are provided by the fitting routines from the GILDAS package.

In order to quantify the amount of energy dissipated per radiative transition I derive the line luminosities L, in $\mathrm{L_\odot}$, using the relation from Solomon et al. (1992)

$$\frac{\mathrm{L_{line}}}{[\mathrm{L_\odot}]} = 1.04 \times 10^{-3}\ \mathrm{S_{line}}\Delta\mathrm{v}\ \mathrm{D_L^2}\ \nu_{\mathrm{obs}} \tag{3.3}$$

where $\mathrm{S_{line}}\Delta\mathrm{v}$ is the integrated flux in Jy km $\mathrm{s^{-1}}$, ν_{obs} the observed frequency of the line in GHz and $\mathrm{D_L}$ the luminosity distance in Mpc. Converting these luminosities into K km $\mathrm{s^{-1}}$ $\mathrm{pc^2}$ enables to directly associate the luminosity ratio between two lines to the ratio of their intrinsic brightness temperatures (Solomon et al. 1997), provided that the emission from both lines is co-spatial. This second definition reduces to

$$\frac{\mathrm{L'_{line}}}{[\mathrm{K\ km\ s^{-1}\ pc^2}]} = 3.25 \times 10^{7}\ \mathrm{S_{line}}\Delta\mathrm{v}\ \frac{\mathrm{D_L^2}}{\nu_{\mathrm{obs}}^2\ (1+\mathrm{z})^3} \tag{3.4}$$

Using L' can be much more intuitive for some interpretations since, for instance, it will provide roughly constant luminosities for the different rotational levels of a given molecule when the emitting region is thermalized (Carilli & Walter 2013). Moreover, in order to plot the emission lines with my own routines I convert the frequency range of the brute EMIR spectra to a velocity range, by applying the simple Doppler shift

$$\mathrm{v} = \frac{\mathrm{c}\Delta\nu}{\nu_0} \tag{3.5}$$

where $\Delta\nu = \nu - \nu_{\rm rest}$ is the interval between a given observed frequency ν, and the observed systemic frequency ν_0 (i.e. the redshifted frequency of the line set as reference), and c is the speed of light. v is the velocity of the emitter with respect to the systemic velocity $\rm v_0$, defined by $\rm v_0 = 0$ km s^{-1} for $\nu = \nu_0$.

For the spectra showing a marginal or non-detection at the expected frequency of a given line, I compute a flux upper limit following the approach adopted in Rowlands et al. (2015). To this end, I derive the statistical uncertainty on the integrated flux, $\sigma_{\rm S_{line}\Delta v}$ (in Jy km s^{-1}), with the following relation

$$\sigma_{\rm S_{line}\Delta v} = (\Delta \rm v)^2 \; \sigma^2 \; N_l \left(1 + \frac{N_l}{N_b}\right) \tag{3.6}$$

where Δv is the line width which is set, in the case of a non-detection, to a plausible value suggested by other lines detected in the same source (typically $\sim 200 - 400$ km s^{-1}, Young et al. 2011). In this equation, σ is the rms noise of the spectrum expressed in mJy and measured over the baseline, $\rm N_l$ is the number of spectral channels expected to cover the line profile, and $\rm N_b$ is the number of line-free baseline channels. Finally, I assume that the flux upper limit of the corresponding line is equal to $4 \times \sigma_{\rm S_{line}\Delta v}$.

3.3.2 VLT/X-Shooter observations of the brightest GEMS

We use X-Shooter on the Very Large Telescope to measure the spectroscopic redshift of the lensing galaxy that produces the brightest sub-mm source in our sample, G244.8, at a precision of about 10^{-3} or better.

Overview of the spectrograph

X-Shooter (Vernet et al. 2011) is a multi-wavelength spectrograph covering, in a single exposure, the UV to NIR regime from 300 to 2500 nm. The instrument contains three independent arms with their own shutters, slit masks, dispersive elements and detectors. These arms named UVB, VIS and NIR, cover the wavelength ranges 300-559.5 nm, 559.5-1024 nm and 1024-2480 nm respectively, with intermediate spectral resolution. The ultraviolet (UV) cutoff is due to the drop in atmospheric transmission, while the thermal emission becomes a major constraint in the NIR side. The length of X-Shooter slits is fixed to $11''$ but their width can vary from $0.4''$ to about $1.5''$ in each arm. The spectrograph reaches higher resolving powers using more narrow slits, in which case the sampling of UVB, VIS and NIR spectra is only about 2-3 pix/FWHM.

An acquisition and guiding optical camera of $1.5' \times 1.5'$ field-of-view is installed on the fourth arm of X-Shooter. In the meantime, differential atmospheric refraction is corrected since the spectroscopic arms span broader wavelengths than the guiding system. Finally, X-Shooter also offers an Integral Field Unit (IFU) spectroscopic mode with $4.0'' \times 1.8''$ fields-of-view. The interested reader is referred to X-Shooter science case document[3] or to the user manual[4] for more complete information.

Observations and spectrophotometric calibration

Our optical/NIR photometry with FORS2 and HAWK-I previously showed that the lensing galaxy is red and faint, and we therefore needed a 8-meters class telescope to detect spectral features such as the 4000 Å break or strong absorption and emission lines. Moreover the blending of the background GEMS and the lens itself made our preliminary photometric redshift very degenerate. An optical/NIR spectrograph with very large redshift coverage such as X-Shooter was therefore required to identify one of the main lines in the lensing galaxy, up to $z \sim 2 - 3$.

---

[3] https://www.eso.org/sci/facilities/paranal/instruments/xshooter/doc/Xshooter_ScienceCase.pdf

[4] https://www.eso.org/sci/facilities/paranal/instruments/xshooter/doc.html

Our X-Shooter spectroscopy covers a wavelength range from 390 to 2500 nm through DDT program 295.A-5017 (PI : N. Nesvadba). We obtained a total of 4 hours of one-source exposure under good and stable conditions (seeing below 1″), and with slit widths of 1.2″ in the two optical arms, and 1.3″ in the NIR arm, respectively. A first X-Shooter observation taken in June 2015 was not usable because of a bright foreground continuum emitter found in parts of the frames, which is not associated with G244.8. Data were reduced in the standard way with IRAF for the imaging, and with the ESO X-Shooter pipeline (Modigliani et al. 2010) for the spectroscopy.

Analysis of the 1-D spectrum and discussion

X-Shooter shows two emission lines in the NIR H-band at 1.6566 ± 0.0005 μm and 1.6617 ± 0.005 μm (Fig.3.5), which we identify as Hα and [NII]λ6583 at a common redshift $z = 1.525 \pm 0.001$. We detect no other line in either the UV, optical, or NIR arm. As an alternative, these lines could be Paβ and FeIIλ1257 at $z = 0.319$, but this would imply [OIII]λ5007 and Hα falling at wavelengths of 6602 Å and 8654 Å, respectively. These lines should be bright (the intrinsic decrement of Paα/Hα is 0.08), but are not detected. Additional lines in the NIR, like FeIIλ1294, are also missing. Moreover, the equivalent widths of the detected lines are high, $\mathrm{EW_{obs}} > 70$ Å, whereas rest-frame NIR lines typically have low equivalent widths. This all suggests that G244.8 is lensed by a massive high-redshift galaxy at $z = 1.525$.

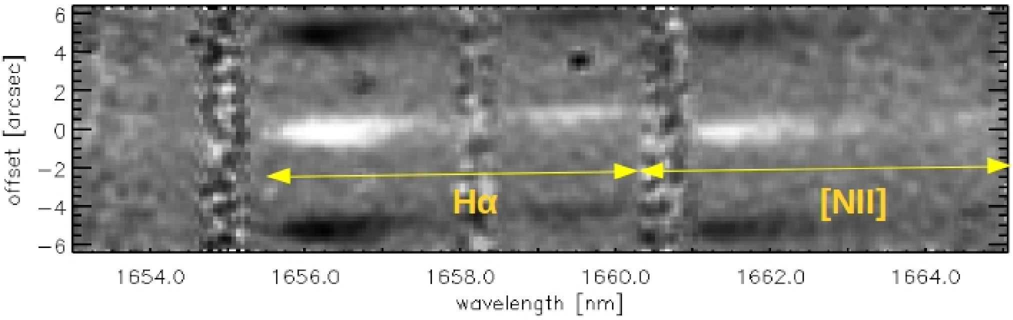

Figure 3.5: The VLT/X-Shooter 2-D spectrum of G244.8 suggesting a surprisingly high-redshift of $z = 1.52$ for the main deflector. The y-axis represents the positional offset along the spectrograph slit while the x-axis shows a zoomed-in view of the spectrum in wavelength or velocity offset units. The detected emission lines are marked with yellow arrows, with Hα lying at shorter wavelengths and [NII] showing fainter emission on the right. Light vertical features are the night-sky lines that were masked during the analysis.

3.4 Interferometry

3.4.1 PdBI/NOEMA

Brief presentation of the interferometer

The IRAM Plateau de Bure Interferometer (PdBI) is a radiotelescope including six antennas of 15 meters diameter arranged in baselines of up to 760 and 368 meters in the East-West axis and North-South axis, respectively. This instrument has the great advantage to provide spectroscopic information simultaneously for a complete field-of-view, with angular resolutions depending on the sampling of the uv-plane offered by each interferometric configuration. The most compact configuration (D) yields the highest sensitivity and results in typical resolutions of 3″ at 230 GHz. More extended configurations (A or B) resolve the most compact sources with resolutions of up to 0.3″ at 230 GHz. Moreover, it is also possible to combine two of these configurations to improve the sampling of the uv-plane.

Four dual-polarization receivers are mounted in each antenna of the array and observe in the 0.8 mm (277-371 GHz), 1.3 mm (201-267 GHz), 2 mm (129-177 GHz) and 3 mm (80-116 GHz) bands which cover the main atmospheric windows. They provide a total bandwidth of 3.6 GHz in each polarization and are used successively during the observations. The receivers then transmit the signal to one of the two available correlators. Firstly, the wide-band correlator (WideX) can process the complete bandwidth of 3.6 GHz delivered by the receivers at a given time, with a constant spectral resolution of 1.95 MHz. Secondly, the narrow-band correlator analyses two sub-bands of 1 GHz width within the available 3.6 GHz. It combines four spectral units and finally yields a total bandwidth of 1 GHz in both polarizations or 2 GHz in one polarization, with resolutions varying between 0.039 and 2.5 MHz. For a complete track of 10 hours integration and typical winter conditions, the PdBI reaches point source sensitivities of about 0.03-0.04 mJy at 90 GHz and 0.06-0.08 mJy at 115 GHz in band 1, or 0.08-0.14 mJy at 230 GHz (c.f. the instrument manual[5]).

A seventh antenna was commissioned in early 2015, as part of the NOrthern Extended Millimeter Array (NOEMA) project. The number of antennas is indeed designed to increase from 6 to 12 by 2019, for an extended baseline reaching up to 1600 meters, in order to increase the sensitivity of the interferometer by a factor of two and its angular resolution by a factor of four.

Observations of molecular lines in single GEMS

We also obtained PdBI interferometry for at least one CO line and, for some targets, additional lines from [CI] and dense gas tracers. I will outline the analysis of these data sets on the example of one of our first targets, G080.2, with which I worked myself in the context of this thesis (see §7.1).

For this source, we obtained high-resolution observations of the redshifted CO(3-2) emission with the PdBI in the most extended configuration (A), which offers an angular resolution of $\sim 0.9''$. This GEMS was observed during a complete track of 10 hours integration on 29 January 2013, with baselines ranging from 136 to 760 meters. Assuming a redshift of $z = 2.5987$ from the independent line search with EMIR, the CO(3-2) line was expected to fall at a frequency of 96.088 GHz. The observations were therefore conducted in the 3 mm window using the WideX correlator which offered a bandwidth of 3.6 GHz centered at the line frequency. The phase was calibrated with observations of the nearby quasars 1547+507 and 1636+473, while 3C279 and MWC 349 were used as band pass and flux calibrators, respectively. The data were subsequently calibrated with a standard procedure using the CLIC software, and the image processing and analysis were performed with GILDAS package from IRAM. Further details can be found in Nesvadba et al. (2016, in prep.).

The original 3-dimensional PdBI data cube has a spectral resolution of about 2 MHz and a rms noise of 0.15 mJy beam^{-1} (or 2.0×10^{-17} erg s^{-1} cm^{-2}), measured in regions around G080.2 without sub-mm emission. I smooth the spectral axis of this cube and lower its resolution to 4 and 6 MHz, respectively, in order to increase the SNR of the faintest emission line regions across the source and to determine whether or not the most narrow spectral features are spurious. Finally, the synthesized beam measures precisely $0.72'' \times 0.95''$ with a position angle of 42.2°, and this data cube provides spectral information over a $2.9' \times 2.9'$ field-of-view sampled with a pixel scale of 0.17 ″/pix.

Detailed spectroscopic analysis

I analyze the calibrated data cubes with a dedicated IDL routine focusing on each pixel with a SNR above 3σ at the frequency of the redshifted CO(3-2) line. I verify that the continuum emission is negligible in the spectral bins covering the baseline. Then, the channels around the emission line are preserved and the weight of all other spectral bins are set to zero. For each pixel (x,y) above the flux threshold, I fit the emission line with the mpfit IDL routine[6] as follows. According to the arguments

---

[5] http://vizier.u-strasbg.fr/doc/man/gildas/pdf/pdbi-intro.pdf

[6] http://www.physics.wisc.edu/ craigm/idl/down/mpfit.pro

presented below, I first assume a single gaussian profile of central velocity $\mathrm{v_c}$, line width σ, and peak flux $\mathrm{S_{peak}}$

$$\mathrm{F_{(x,y)}(v) = S_{peak}(x,y)e^{-\frac{(v-v_C(x,y))^2}{2\sigma(x,y)}}} \tag{3.7}$$

The routine estimates the fitting uncertainties on these three parameters. I subsequently convert the peak fluxes from mJy beam^{-1} to mJy arcsec^2 with the size of the synthetized beam, and express the line integrated flux $\mathrm{S_{line}}$ with

$$\mathrm{S_{line}} = \sqrt{2\pi}\sigma \mathrm{S_{peak}} \tag{3.8}$$

The gaussian line width optimized during the fit corresponds to the velocity dispersion of the gas material. For a gaussian profile, it can be related to the line FWHM by FWHM $= 2\sqrt{2\ln(2)}\ \sigma$. But more importantly, the measured line width σ_{obs} has to be deconvolved from the instrumental resolution σ_{instru}. Intrinsic value can be obtained with

$$\sigma_{\mathrm{int}} = \sqrt{\sigma_{\mathrm{obs}}^2 - \sigma_{\mathrm{instru}}^2} \tag{3.9}$$

I then plot the original spectrum and the best-fitting gaussian along with the corresponding residual, and compute a reduced χ^2 to determine the validity of the fit

$$\chi^2_{\mathrm{(x,y)}} = \frac{1}{\mathrm{N_b - N_p}} \sum_{\mathrm{i=1}}^{\mathrm{N}} \left(\frac{\mathrm{F_{spectrum}[i] - F_{fit}[i]}}{\sigma[\mathrm{i}]} \right)^2 \tag{3.10}$$

where the sum includes the spectral channels used for the fit (with weights not equal to zero), and $\mathrm{N_b}$ designates the number of these spectral bins. $\sigma[\mathrm{i}]$ is the flux error in channel i, estimated by $\sqrt{\mathrm{F_{spectrum}[i]}}$, and $\mathrm{N_p}$ is the number of free parameters. The routine finally produces velocity offset, line width, peak flux and integrated flux maps.

However, this simple approach is not representative of the effective line profile in the majority of pixels because G080.2 also exhibits large-scale motions along the line-of-sight, as usually observed in actively star-forming galaxies at high-redshift. I find that three independent components are systematically detected across the source, either with a spectral resolution of 2 MHz or with the rebinned data cubes for the lines-of-sight with lower SNR. The challenge is therefore to disentangle properly each spectral component with the algorithm, despite the large number of parameters involved. This requires to develop an efficient method which avoids to converge to nonsensical results. Since the most redshifted component is not blended with the two others, I begin by fitting its profile with a single gaussian. The two other components are fitted independently, firstly by obtaining an initial guess for their velocity offsets in the pixels with higher SNR, and secondly by fitting their velocity, width and peak flux simultaneously. I finally derive individual maps for each parameter of the three spectral components.

3.4.2 SMA imaging at 850 μm

The Sub-Millimeter Array

The Sub-Millimeter Array (SMA) is an interferometer operating in the sub-millimeter with eight single dish antennas of 6-meter diameter. This telescope is located at the top of Mauna Kea in Hawaii and offers interferometric configurations with baselines ranging from 16 to 508 meters. The most extended configuration therefore provides sub-arcsecond angular resolutions whereas the primary beam of each antenna is $\sim$ 38" at the observed wavelength. SMA receivers operate at radio frequencies between 180 and 700 GHz and probe the continuum emission from dust grains heated by young stars. Two receivers can be combined at the same time to offer a nominal bandwidth of 4 GHz with thousands of spectral channels. Thus, the SMA is also optimal to observe rotational transitions of ISM molecules, in nearby or distant galaxies.

The SMA also works in an extended interferometric configuration (eSMA) with the James Clerk Maxwell Telescope and the Caltech Submillimeter Observatory as the ninth and tenth elements. In this case, the instrument reaches baselines up to 780 meters and operates in the 230 and 345 GHz bands.

Observing the dust continuum of the GEMS

The 850 μm continuum (353 GHz) of the GEMS was observed with the SMA between June 2013 and January 2015, with total integration times per source between 2 and 7 hours. These data were taken under good to excellent conditions with precipitable water vapor below 2 mm and using the shared-track mode to obtain a good coverage in the uv-plane. All sources but one were observed through program 2013B-S050 (PI : N. Nesvadba) in the compact (COM) configuration, with a maximum baseline of 70 meters and spatial resolutions of about $2''$. G080.2 was observed through DDT programme 2013A-S075 in the extended (EXT) configuration, with a beam of $0.8'' \times 0.5''$. Finally, a small set of 4 sources including G244.8 have been observed at the highest possible resolution of $0.3''$ (VEX), in program 2014B-S018. These angular scales reach the typical size of individual star forming regions in our bright sub-mm emitters.

G. Petitpas reconstructed the multi-channel images and calibrated the fluxes with the MIR package. He then used the Image Analysis and Display software package MIRIAD (Sault et al. 1995) to invert the uv visibilities and to deconvolve the maps. A comparison between the COM maps and the single-dish flux densities from SCUBA-2 suggests that we recover at least 80–90% of the total flux density at 850 μm. This implies that our interferometric data are probably recovering most of the fainter, more extended components. However this ratio is probably not as good in the two extended configurations.

The 850 μm maps taken in the COM configuration trace the dust reservoirs in the GEMS and were pivotal to demonstrate that these are indeed strongly gravitationally lensed galaxies (see Chapter 4). We are currently complementing these COM data with new observations in the EXT and VEX configurations, for a second part of the sample. With these high resolutions we expect to resolve the dust emission at least partially in the GEMS. This enables to measure properly the star formation intensities and to probe the local star formation mechanisms. For instance, G244.8 was observed in the VEX configuration in early 2015, with a synthetized beam of $0.24'' \times 0.30''$ at a position angle (PA) of 60.7° measured North through East. The very high resolution reveals a small partial Einstein ring of $1.5''$ diameter, down to a rms noise of 2.01 mJy beam^{-1}. This target and the SMA VEX observations are further described in §7.3.

3.5 Additional data in the mid-infrared to radio regime

3.5.1 IRAS upper limits at 60 and 100 μm

The Infrared Astronomical Satellite (IRAS) was launched in 1983 and performed the first all-sky infrared survey from space, in four different bands. IRAS observed at central wavelengths of 12, 25, 60 and 100 μm with resolutions between $30''$ at 12 μm and $2'$ at 100 μm limited by the size of the detectors. Among other scientific goals, this instrument was optimal to probe the peak of dust thermal emission from nearby starburst galaxies. However since the GEMS exhibit peak fluxes between 300 and 1100 mJy, their exceptional brightness bring them close to the sensitivity limits of IRAS point-source catalog. In particular, the 60 and 100 μm bands correspond to rest-frame wavelengths of about 15-40 μm for the GEMS. They are therefore associated with the blue tail of the dust emission and allows to search for a possible hotter component that would indicate an AGN.

We searched for counterparts in the IRAS faint source survey (Moshir et al. 1992) but found no detection associated with the GEMS. We therefore constrained the SED fitting presented in §4 with the 90% completeness limit of this catalog, namely 120 mJy and 440 mJy at 60 μm and 100 μm, respectively.

3.5.2 WISE photometry at 22 μm

Despite its moderate depth and low spatial resolution of $6 - 12''$, the WIde Field Survey Explorer (WISE, Wright et al. 2010) has successfully identified dust obscured AGNs at high-redshift (Yan et al. 2013). Its all-sky survey in the 3.4, 4.6, 12 and 22 μm infrared bands (channels 1-4) will therefore help us to better constrain the SED of the background GEMS and to quantify the contribution of a possible AGN to the overall dust heating. The 5σ sensitivities of WISE measured in unconfused regions on the ecliptic plane are 0.048, 0.10, 0.73 and 5.4 mJy at 3.4, 4.6, 12 and 22 μm, respectively. In particular WISE is 1000 times more sensitive than IRAS at 22 μm, in the fourth band which covers rest-frame wavelengths between 4 and 7 μm for the GEMS. This band is therefore particularly interesting to probe the blue tail of the dust emission and to determine whether or not the GEMS contain a hot dust component of 70-100 K heated by a powerful AGN.

I searched for counterparts in the four WISE channels, in the lines-of-sight toward our sub-mm emitters. In front of each GEMS, I found at least one source bright enough in one band to be part of the photometric catalog. I used the point-source photometry of this archival catalog and converted the Vega magnitudes to flux densities. For the fainter sources I treated the 5σ sensitivities of this catalog as upper limits.

In all but one line-of-sight, WISE detected nearby sources in the first three channels with blue spectra dropping steeply between 3.4 and 12 μm. Their colours suggest that these are low-to-intermediate-redshift objects, which we consider part of the intervening lensing structures. These spectra generally fall too steeply to contribute significantly to the 22 μm flux densities, but we nonetheless see an enhanced emission in channel 4 for two GEMS, G138.6 and G165.7. It is therefore necessary to pay close attention to these targets when determining the AGN contamination in the high-redshift components (§4.4). A last source, G102.1, has a mid-infrared rising spectrum which makes the deblending between the foreground and high-redshift components more complicated. To derive properly its photometry, I applied the color corrections computed in Wright et al. (2010) for sources showing red spectra in the WISE bands. Individual flux densities in the fourth band are listed in Table 3.5.

Source	S_{22} [mJy]	S_{60} [mJy]	S_{100} [mJy]	S_{250} [mJy]	S_{350} [mJy]	S_{500} [mJy]	S_{850} [mJy]
PLCK_G045.1+61.1	< 5.4	< 120	< 440	161 ± 5	328 ± 6	397 ± 6	130 ± 13
PLCK_G080.2+49.8	< 5.4	< 120	< 440	220 ± 9	340 ± 6	314 ± 6	87 ± 5
PLCK_G092.5+42.9	< 5.4	< 120	< 440	765 ± 7	865 ± 8	696 ± 7	191 ± 16
PLCK_G102.1+53.6	8.1 ± 0.7	< 120	< 440	327 ± 4	410 ± 5	339 ± 5	—
PLCK_G113.7+61.0	6.0 ± 0.7	< 120	< 440	672 ± 7	603 ± 6	373 ± 5	108 ± 10
PLCK_G138.6+62.0	6.2 ± 0.8	< 120	< 440	619 ± 6	664 ± 8	474 ± 6	123 ± 14
PLCK_G145.2+50.9	< 5.4	< 120	< 440	453 ± 5	719 ± 7	781 ± 8	360 ± 23
PLCK_G165.7+67.0	10.4 ± 0.9	< 120	< 440	867 ± 8	753 ± 6	472 ± 5	90 ± 9
PLCK_G200.6+46.1	< 5.4	< 120	< 440	209 ± 4	294 ± 4	273 ± 5	110 ± 10
PLCK_G231.3+72.2	< 5.4	< 120	< 440	299 ± 4	401 ± 5	341 ± 6	111 ± 12
PLCK_G244.8+54.9	< 5.4	< 120	< 440	1050 ± 10	1054 ± 10	777 ± 7	198 ± 11

Table 3.5: Additional mid-infrared to sub-millimeter photometry of the GEMS. The columns contain : WISE 22 μm flux density or 5σ sensitivites; IRAS 90% completeness limit at 60 μm; IRAS 90% completeness limit at 120 μm; Herschel-SPIRE 250 μm flux density; Herschel-SPIRE 350 μm flux density; Herschel-SPIRE 500 μm flux density; JCMT/SCUBA-2 850 μm flux density.

3.5.3 FIRST counterparts at 1.4 GHz

The Faint Images of the Radio Sky at Twenty-centimeters (FIRST, Becker et al. 1995) is a large-scale radio survey conducted with the Very Large Array (VLA) and covering $\sim$ 10000 square degrees in the same Northern and Southern regions as the SDSS, in order to search for optical counterparts to each radio source. Observations target frequencies around 1.4 GHz, with a bandwidth of 2 × 21 MHz and 3 MHz spectral channels (or 2 × 128 MHz and 2 MHz spectral channels for the most recent data). The publicly available images from the survey have a sampling of 1.8″ per pixel and a rms of 0.13-0.15 mJy which is slightly varying with the position. Since the interferometric observations are performed in the B configuration of the VLA, the synthetized beam provides angular resolutions of 5.4″. Moreover, the FIRST reduction pipeline provides a nominal astrometric accuracy of 1″ for the faintest sources and otherwise in the range $0.5 - 1.0''$.

We search for radio counterparts of the GEMS to determine their position relative to the far-infrared radio correlation. To this end, we use the complete catalog of December 2014, which includes integrated fluxes and sizes (White et al. 1997). For the GEMS, the observed frequency of this survey corresponds to 4.5-6.4 GHz in the rest-frame. Given their outstanding brightness in the FIR/mm regime, we expect that at least some of them will exceed the detection threshold of 1 mJy. We find that six sub-mm sources are indeed associated to 1.4 GHz detections in the FIRST catalog. Since their angular separation from the center of our high-resolution 850 μm imaging is systematically below 5″, these radio sources are most likely direct counterparts of the high-redshift GEMS. Given the beam size of the FIRST survey, this emission could be partially or totally due to a radio-loud AGN in the main foreground lensing galaxies at $z \lesssim 1$ (see e.g. the samples of, White et al. 2003; McGreer et al. 2009). However, further indications on the nature of these foreground objects presented in Chapter 5 will rule out this scenario and we will assume that the 1.4 GHz signal comes exclusively from the background component. In Table 4.3, we present the integrated flux density, $\mu_{1.4}\ \mathrm{S}_{1.4}^{\mathrm{int}}$, of these six sources using the rms at their position as photometric uncertainty. We subsequently convert these flux densities to radio luminosities, $\mu_{1.4}\ \mathrm{L}_{1.4}$, without correcting for the gravitational magnification of the radio component, $\mu_{1.4}$, and by applying the following relation

$$\mu_{1.4}\ \mathrm{L}_{1.4} = \frac{4\pi \mathrm{D}_{\mathrm{L}}^{2}\ \mu_{1.4}\ \mathrm{S}_{1.4}^{\mathrm{int}}}{(1+\mathrm{z})^{(1+\alpha_{1.4})}} \tag{3.11}$$

where $\mathrm{D_L}$ is the luminosity distance to redshift z, and $\alpha_{1.4}$ is the spectral index set at the nominal value for star-forming regions $\alpha_{1.4} = -0.8$ (Condon 1992). After deconvolution of the synthetized beam, the sources appear to be marginally resolved in the FIRST catalog with sizes between 1.5″ and 7.0″. This range is in broad agreement with their resolved dust continuum observed with the SMA. In Table 4.3, we also quote the rms noise from the FIRST catalog for the five other GEMS with no significant detection at 1.4 GHz. We then use a flux upper limit at 3σ to infer upper limits on the radio luminosity of these sources and deduce a range of positions with respect to the far-inrared radio correlation (see Chapter 4 for a complete discussion of this correlation).

Another public radio survey with the VLA, the NRAO VLA Sky Survey (NVSS, Condon et al. 1998), was conducted at 1.4 GHz following a different approach. However, it is shallower than FIRST and therefore less suited to search for counterparts of distant SMGs such as the GEMS. The rms of NVSS images is ranging between 0.29 and 0.45 mJy, about two or three times higher than our flux upper limits, which encourages the use of FIRST to probe the radio emission of the GEMS. Moreover, NVSS has a much larger beam FWHM of 45″ which makes it even more complicated to correctly identify the counterpart of our compact sources smaller than 15″.

3.5.4 Complementary follow-up observations

Between September 2012 and May 2014, Canadian collaborators observed the 850 μm continuum of the GEMS with the SCUBA-2 camera (Holland et al. 2013) on the James Clerk Maxwell telescope (JCMT), with the aim of better sampling the Rayleigh-Jeans tail of their dust emission. In this observing band, the 15 meters diameter single dish antenna offers a spatial resolution of 13″ of the same order of magnitude as the beam of Herschel in SPIRE bands and the beam of the IRAM/30-m antenna at 2-mm. SCUBA-2 therefore detected most of the GEMS as point sources, and the most extended targets were only marginally resolved. The resulting 850 μm flux densities are listed in Table 3.5 and used in the analysis of §4. Further details on the reduction, flux calibration and photometric uncertainties can be found in Cañameras et al. (2015).

Chapter 4

Signatures of strong lensing, dust content and integrated star formation law in the GEMS

Contents

4.1 Secure spectroscopic redshifts in the millimeter

4.1.1 Blind redshift search

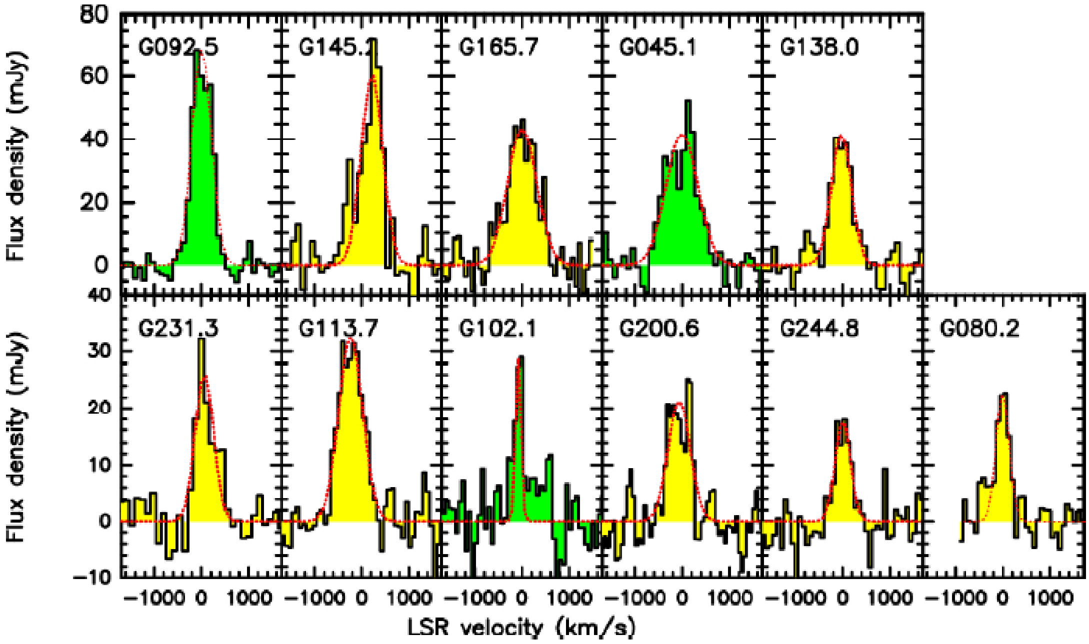

Figure 4.1: Lowest-J CO emission line in each GEMS obtained with the EMIR receiver mounted on the IRAM 30-m telescope. CO(3-2) and CO(4-3) lines are indicated in yellow and green, respectively. Red dotted lines show simple single-Gaussian fits.

In sub-mm bright galaxies such as the GEMS, the optical emission lines commonly used to infer spectroscopic redshifts are unreachable because of the strong dust obscuration. We rather take advantage of the wide-band heterodyne receiver EMIR to directly measure the spectroscopic redshifts from bright emission lines in the millimeter. This technique was previously applied with success to ALMA follow-up of DSFGs from the SPT survey (Weiß et al. 2013). Conducting our follow-up at the IRAM 30-m telescope has the great advantage to provide a similar beam size as Herschel (about 20" at 100 GHz), which makes the identification of the GEMS straightforward.

To obtain a spectroscopic redshift for each source, we perform a blind line search in the 3-mm atmospheric transmission window covered by the E0 band of EMIR (73-117 GHz). We first determine an optimal setup to scan a maximum portion of the band, using the WILMA and FTS backends in parallel. Thanks to their respective bandwidth of about 4 GHz and 8 GHz, we can cover the 77.7-109.1 GHz frequency range with only two tunings centered at 89.4 GHz and 97.4 GHz, respectively (with small overlaps around 85.5, 93.4 and 101.2 GHz). In each of these tunings, the FTS backend has indeed a significant frequency coverage with two sidebands of 7.8 GHz divided into four 3.9 GHz wide spectral windows. Finally, we observe in the dual polarization mode.

The illustration of Figure 4.2 shows that this setup probes the CO(1-0) line for $0.00 < z < 0.50$ and several other CO transitions at higher rotational levels. The spectral coverage includes at least one of these lines for $z > 1.10$, except in the small gap between $z \sim 1.9$ and $z \sim 2.1$. According to the plot, if one single line is detected in the 3-mm spectrum, this suggests that we are probably probing the redshifted CO(2-1) or CO(3-2) transitions. The CO(4-3) and CO(5-4) lines are in principle adjacent to CI(1-0), but the neutral carbon can reach various emission regimes (20 to 80% of the CO(4-3) line luminosity, Alaghband-Zadeh et al. 2013) and this transition could also remain undetected. At high rotational levels, the CO transitions are necesarily observed in pairs. We can show that the same holds for other mm-bright emission lines, from [CI] or H_2O. Lastly, detecting a faint structure line at 3-mm would imply a very high redshift which is ruled out by our SPIRE data.

With these two tunings we detect one emission line per source (Fig.4.1), leaving scope for a small set of possible redshifts. To determine the frequency of the CO line with the next upper rotational level, we combine these results with independent photo-z derived from our SPIRE photometry. Since our fields-of-view were not covered by ancillary multi-wavelength imaging programs at the time of the redshift survey, the poor spectral sampling obtained with SPIRE does not allow to use detailed SED templates. In fact, more constraints would be required to determine a photo-z from the correct star formation rate and history, and level of extinction. We rather use a fixed SED with a concordant temperature of 30 K, as measured in the Cosmic Eyelash (Ivison et al. 2010b). Since this alternative method is very sensitive to SED variations among the SMG population, our individual photo-z can not be more accurate than $\Delta z \sim 1$ (Chapman et al. 2005). Nevertheless, they yield correct predictions in all but two GEMS with high dust temperatures. These photo-z indicate that the second lines fall typically in the 2-mm band and require a separate tuning. Their detection also confirm the preliminary identification of the lowest-J CO transitions. Our follow-up spectroscopy with EMIR therefore provides secure spectroscopic redshifts for the 11 targets, in the range $z = 2.2 - 3.6$ (Table 4.1), with at least two lines detected per source (the lower-J CO lines being either CO(3-2) and CO(4-3), or CO(4-3) and CO(5-4)).

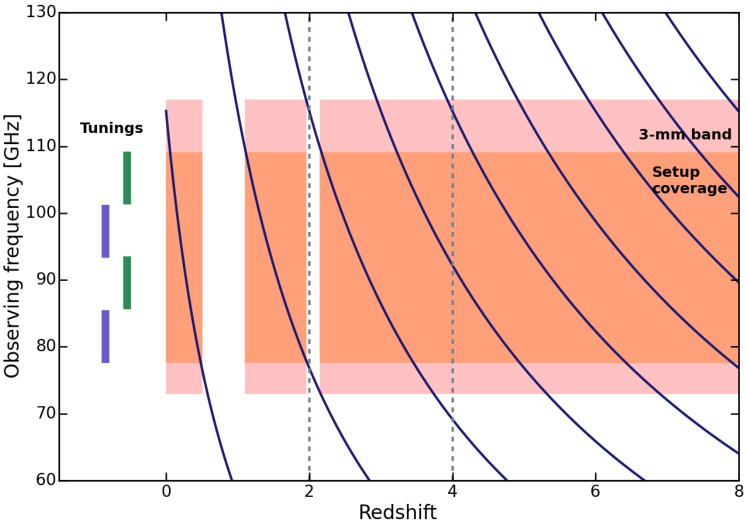

Figure 4.2: Redshift frequency of the CO emission lines from the $J = 1 - 0$ rotational transition on the left to the $J = 9 - 8$ transition on the extreme right. The two frequency tunings are plotted on the left in blue and green, respectively, along with the individual sidebands of 7.8 GHz. We show the 3-mm band of EMIR (light orange region) and the total spectral coverage of our observing setup (dark orange region). The latter indicates the redshifts where at least one CO line is observable. Vertical dotted lines mark the broad redshift range suggested by the SPIRE photometric redshifts.

4.1.2 Comparison with external redshift distributions

The selection of the GEMS in the Planck maps is based on color criteria between the 350 μm, 550 μm and 850 μm spectral bands. It results in a final sample of 11 sources with spectro-z ranging between 2.2 and 3.6, and an average value of $z = 2.9 \pm 0.4$. Such a small sample is not designed to derive robust statistics. In this section, I rather compare the GEMS with ancillary studies of SMGs.

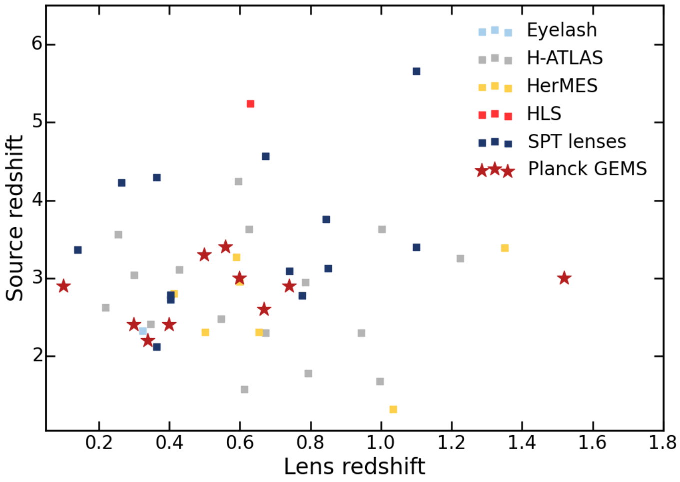

Figure 4.3: Lens and source redshifts for the GEMS and other strongly lensed SMGs selected in recent FIR/sub-mm surveys (more details are given in the text). The main reason for the absence of sources at z < 2 are the color criteria used for the initial selection.

The redshift distribution of the SMG population was first explored by Chapman et al. (2005), in a sample of 73 sources selected in SCUBA fields at 850 μm, with radio counterparts. The limited positioning accuracy from the single dish imaging at JCMT is improved by these higher-resolution observations in the radio. The redshift was then measured in the optical, usually through the detection of the [OII], [OIII], Hα and Hβ emission lines, or Lyα for the most distant sources. This spectroscopic follow-up at Keck Observatory provide a median redshift of 2.2 and a maximum value of 3.6, comparable to the redshift range observed for the GEMS. However, these results suffer from several limitations. First, optical spectrographs often involve redshift deserts, i.e. redshift windows that do not include any bright emission line. Secondly, the redshift distributions based on the identification of radio counterparts are generally biased in the high redshift regime where the 1.4 GHz continuum tend to fall below the detection threshold. This method obviously underestimates the number of very distant SMGs selected at 850 μm and, similarly, it disfavors the intermediate redshift SMGs with very cold dust reservoirs. At similar sub-mm wavelengths, the photo-z of sources selected in the ECDFS with LABOCA (Wardlow et al. 2011) and a complementary analysis with high-resolution interferometric observations (Simpson et al. 2014) overcome these issues. These distributions peak in the redshift range $z = 2.0 - 2.5$.

Going to higher wavelengths, the SMGs detected at 1.1 mm with the AzTEC instrument exhibit a higher median redshift than the 850 μm population, from $z = 2.6 \pm 0.1$ in the GOODS-S field (Yun et al. 2012) to $z = 3.1 \pm 0.3$ in a small sample from COSMOS (Smolčić et al. 2012). In this case, again, the overall redshift distributions are covering the same regime as the GEMS despite the longer-wavelength selection. By contrast, the millimeter redshifts of the gravitationally lensed galaxies from the SPT survey differ significantly (Vieira et al. 2013; Weiß et al. 2013). The reason is probably that these 23 targets confirmed spectroscopically are selected at 1.4 and 2.0 mm, namely at much longer wavelengths than the Planck candidates (350-850 μm). However, we also stress that our parent sample includes HATLAS J114637.9-001132 at $z = 3.259$ (Fu et al. 2012; Herranz et al. 2013; Bussmann et al. 2013) and a much more distant source, HLS 091828.6+514223 at $z = 5.243$ (Combes et al. 2012; Rawle et al. 2014). Both were formally excluded from the Planck's Dusty GEMS subset which only includes newly discovered sources.

Other surveys like BLAST, H-ATLAS and HerMES have imaged large portions of the sky between 250 and 500 μm, in a similar regime as the Planck selection although the latter is somewhat extended

Source	Transition	Redshift	Integ. line flux μ I_{CO} [Jy km s^{-1}]	Line luminosity μ L$'$ [10^{11} K km s^{-1} pc^2]	Line FWHM [km s^{-1}]
G045.1	4-3	3.4	22.9 ± 0.3	6.9 ± 0.1	213 ± 11
G080.2	3-2	2.6	9.2 ± 0.5	3.2 ± 0.2	265 ± 12
G092.5	4-3	3.3	34.3 ± 0.2	9.7 ± 0.1	453 ± 3
G102.1	3-2	2.9	5.7 ± 1.8	2.4 ± 0.7	252 ± 10
G113.7	3-2	2.4	16.5 ± 0.2	5.0 ± 0.1	528 ± 5
G138.6	3-2	2.4	22.0 ± 1.1	6.8 ± 0.3	514 ± 40
G145.2	3-2	3.6	21.9 ± 0.8	12.7 ± 0.6	685 ± 17
G165.7	3-2	2.2	25.4 ± 0.3	6.8 ± 0.1	576 ± 4
G200.6	3-2	3.0	11.2 ± 0.1	4.9 ± 0.1	458 ± 9
G231.3	3-2	2.9	9.4 ± 0.2	3.9 ± 0.1	257 ± 8
G244.8	3-2	3.0	7.4 ± 1.0	3.3 ± 0.4	382 ± 10

Table 4.1: Properties of the lower-J CO emission lines obtained with EMIR on the IRAM 30-m telescope. These quantities are not corrected for the lensing magnification. The line luminosities are expressed in brightness temperature units.

toward longer wavelengths. Proper comparisons obviously depend on the size and depth of each survey, but the GEMS nevertheless cover similar redshifts to that of gravitationally lensed sub-mm galaxies in H-ATLAS ($z = 2.1 - 3.5$, Harris et al. 2012; Bussmann et al. 2013). Moreover, Negrello et al. (2007) predict number counts of lensed sources between 250 and 850 μm, using a combination of physical and phenomenological models. They find a distribution well peaked around $z \sim 2$ for the strongly lensed galaxies brighter than 100 mJy in the SPIRE band at 250 μm, and a mean redshift shifted toward $z \sim 3 - 4$ in the two other SPIRE channels. Their predictions for bright lensed galaxies at 350 and 500 μm perfectly match the redshift range of the GEMS. On the other hand, the redshift distributions of unlensed galaxies selected in this regime has not reached a consensus yet. Studies have used the BLAST observations (e.g., Chapin et al. 2011) or galaxies detected with Herschel/SPIRE (e.g., Casey et al. 2012), but some of them are based on optical follow-up spectroscopy and may therefore include selection biases. In the meantime, other studies have taken advantage of the higher angular resolution of the JCMT/SCUBA-2 camera at 450 μm (e.g., Roseboom et al. 2013).

4.1.3 Profiles of the low-J CO lines

The lower-J CO lines detected in the 3-mm band are shown in Figure 4.1. A large portion of the GEMS exhibit complex line profiles with, for instance, multiple velocity components in G045.1, G080.2, G138.6 or G145.2. Similar non-trivial profiles can be seen in the higher frequency spectra that will be further discussed for G244.8 in Chapter 7. These results suggest either that the lensing configuration allows to observe several regions in individual galaxies, or that these features directly trace rich gas kinematics within single star-forming regions. In the latter case, the line profiles could in principle be a direct consequence of the interplay between global rotation, turbulent motions or stellar/AGN feedback[1]. Alternatively, since the beam of the IRAM 30-m telescope reaches about 20$''$ at these frequencies, it could cover several interacting galaxies. Assuming a fiducial magnification factor of 20 in the overall sample (based on the detailed models for individual sources in Chapter 6 and empirical evidence in §4.3 for the full sample), we would need angular resolutions in the range $0.20 - 0.40''$ to probe scales down to 100 pc in the source plane of the high-redshift dusty GEMS, akin to their individual star-forming regions. This requires high-resolution sub-mm interferometry, as done for example in Tacconi et al. (2006). These follow-up observations at sub-arcsec resolution were obtained with the ALMA and PdBI interferometers and we will present several examples in Chapter 7.

---

[1] We will show below that we have little evidence for powerful AGN activity in these galaxies

Given the challenging interpretation of the emission lines of Figure 4.1, we perform a single Gaussian fit to measure their FWHMs and integrated fluxes. The results are listed in Table 4.1 and show integrated fluxes of $\mathrm{I_{CO}} = (7 - 34)$ Jy km $\mathrm{s^{-1}}$, for FWHM $= 213 - 685$ km $\mathrm{s^{-1}}$. In the following, we will use the spectroscopic redshifts and the profiles of the CO(3-2) or CO(4-3) line in each GEMS to characterize their astrophysical nature.

4.2 Probing the dust reservoirs in the GEMS

4.2.1 SED fitting in the far-infrared and the millimeter

To characterize the dust reservoirs in the GEMS, I perform a direct parametrized fit to the broadband FIR-to-millimeter photometry rather than a SED fitting based on modeled (e.g. with radiative transfer codes) or empirical template libraries. In these extremely bright sources, the dust thermal emission results from the reprocessing of the energetic radiation, coming either from the youngest and most massive stars or from a central AGN. However, this emission can not be modeled with simple blackbody function becauses the overall galaxies contain an extended range of dust temperatures and a spatial gradient in opacity, and one has to account for an additional emissivity term. I therefore use modified blackbody (or greybody) distributions that express the flux densities via

$$\mathrm{S}(\nu, \mathrm{T}) \propto \left(1 - \mathrm{e}^{-\tau(\nu)}\right) \times \mathrm{B}(\nu, \mathrm{T}) \tag{4.1}$$

with $\tau(\nu)$ the optical depth and $\mathrm{B}(\nu, \mathrm{T})$ the Planck function defined as

$$\mathrm{B}(\nu, \mathrm{T}) = \frac{2\mathrm{h}\nu^3}{\mathrm{c}^2} \frac{1}{\mathrm{e}^{\mathrm{h}\nu/\mathrm{kT}} - 1} \tag{4.2}$$

The multiplication factor in Eq.4.1 reflects the fact that a greybody does not absorb the total incident radiation and, because the radiative transfer reduces this incident radiation by a factor $\mathrm{e}^{-\tau(\nu)}$, it emits less energy than a perfect blackbody. The optical depth $\tau(\nu)$ is defined as the product of the dust opacity $\kappa(\nu)$ by the dust surface density Σ_{dust}. I use the frequency-dependent power-law description $\tau(\nu) = (\nu/\nu_0)^\beta$ (e.g., Blain et al. 2003), with β the spectral emissivity index and ν_0 the critical frequency where $\tau(\nu_0) = 1$ (Draine 2006).

For each GEMS, I fit the Herschel/SPIRE, JCMT/SCUBA-2 and IRAM/GISMO photometry with these modified blackbody functions using the Python curve fit routine from the scipy package[2] and plot the results in Figure 4.4. The three instrument involve similar beam sizes, between 15″ and 30″, and the GEMS are always detected as isolated point sources. We therefore believe that our counterpart identification is robust and that the source blending and confusion are not introducing major uncertainties in this data set. Moreover, as further explored in §4.4 through the WISE colors, the emission from the foreground lensing sources is expected to drop significantly below 1-2 μm and to cause very little contamination above 1-5 μm in the rest-frame. Figure 4.4 shows that our data points straddle the peak of the SED generally between the SPIRE bands, and that the Rayleigh-Jeans tail is well sampled by SCUBA-2 and GISMO. We particularly constrain the thermal emission from the coldest dust component which dominate the overall dust mass budget.

I fit the SEDs in the observed frame and derive accurate dust temperatures, thanks to the available spectro-z that break the temperature-redshift degeneracy. I use a single temperature T, representing the big grains in thermal equilibrium. In spite of a small offset between the 500 and 850 μm points[3], the long-wavelength regime is correctly fitted without a second colder component. At shorther wavelengths, even though a MIR excess is commonly observed in SMGs due to the thermal emission from

---

[2] http://docs.scipy.org/doc/scipy/reference/generated/scipy.optimize.curve$_f$*it.html*

[3] This underestimate of the 850 μm flux density, or alternatively, slight overestimate at 500 μm may be partly explained by a significant contamination from bright emission lines (Smail et al. 2011).

warm dust in small clumps (Ivison et al. 2010a), our sparse sampling of the Wien tail (60-80 μm in the rest-frame) does not constrain an additional warmer component. In addition to this single temperature assumption, I model the optical depth with an emissivity index $\beta = 2.0$ and a critical wavelength of $\lambda_0 = 100$ μm (corresponding to $\nu_0 = 3$ THz, Blain et al. 2003). This choice of β is somewhat arbitrary given that the literature usually gives the range $\beta = 1.5 - 2.0$ (Casey et al. 2014). However, I will demonstrate in the next subsection that, given the moderate frequency sampling of the FIR/mm SEDs, the choice of the emissivity index in this interval has only a minor impact.

I perform the fits both for optically thin and optically thick dust reservoirs. In general, modeling the dust emission in SMGs by an optically thin modified blackbody is correct in the long-wavelength regime, where dust absorption is very low and $\tau(\nu) \ll 1$. In Figure 4.4, the two curves are indeed indistinguishable in the Rayleigh-Jeans tail. Given the extreme brighteness of our sources, we nevertheless suspect that most of their FIR/mm radiation comes from dense star-forming clouds. I will therefore rely on the optically thick case in the subsequent discussions. From this fitting process, I will deduce the bolometric FIR luminosity, the dust temperature and mass, and the obscured star formation rate in the GEMS. It is worth reminding that it is made possible by the multi-wavelength FIR/mm photometry and the millimeter spectro-z, while previous studies with fewer available constraints needed to assume a specific dust temperature and were much more sensitive to SED variations between the individual SMGs.

4.2.2 Measuring dust temperatures and dust masses

From the best-fitting distributions I can determine the wavelengths where the modeled SEDs reach their peak, $\lambda_{\rm max}$, and the corresponding flux densities, $S_{\rm max}$. The values presented in Table 4.2 confirm that the dust continuum systematically peak between the SPIRE bands. The SED of G113.7 and G165.7 is not clearly decreasing at 250 μm and it will be particularly worthwhile to further characterize the MIR emission in these two GEMS. Moreover, our sample probes outstanding flux densities of up to 1054 mJy.

Our fits correspond to dust temperatures of $T_{\rm d} = 33 - 50$ K (Table 4.2). More distant SMGs with dust reservoirs associated to intense star formation exhibit hotter temperatures, but here we find no significant trend with redshift. I derive the uncertainties with a 1000-repetition Monte Carlo simulation, by randomly varying the flux density in each band from a normal distribution with mean and standard deviation deduced from the photometric errorbars. I then fit the SED for each data set and deduce the relevant quantities, such as the dust temperatures. The resulting uncertainties are reported in Table 4.2 and can be compared with the influence of different assumptions. To begin, I ignore successively the 500 μm and the 850 μm points to determine whether the observed gap has a major impact on the dust temperatures. In the first case I find a slight increase of 1-2 K, while in the second case I observe a more substantial decline of 1-4 K. Then, I vary the emissivity index in the range $\beta = 1.5 - 2.0$ to probe the degeneracy between $T_{\rm d}$ and β, and find typical offsets in dust temperature of $\Delta T_{\rm d} \sim 1 - 2$ K. Moreover, it has been shown that the choice of an optically thin or thick dust emission and the assumed critical wavelength have a greater influence than the exact value of the spectral emissivity index (again, in the range 1.5-2.0, see the Figure 20 of Casey et al. 2014). I indeed note that with an optically thin modified blackbody, our fits suggest temperatures $T_{\rm d} = 30$ K and 41 K, lower by 3 K to 11 K in each individual source.

The temperature range is in good agreement with previous studies of lensed or unlensed dusty galaxies at $z \gtrsim 2$ selected in the FIR and (sub-)mm, and with SEDs well constrained in this regime (Casey et al. 2012; Magdis et al. 2012; Greve et al. 2012; Weiß et al. 2013). Figure 4.7 illustrates this comparison for samples of strongly lensed sources. In particular, our temperatures are consistent with high-redshift sources ranging from star-forming galaxies along the main sequence (~ 30 K, e.g., Elbaz et al. 2011) to typical starbursts (40-50 K, e.g., Danielson et al. 2011; Riechers et al. 2013). They are slightly lower than the temperatures derived for some local ULIRGs (66 K for Arp220, Rangwala et al.

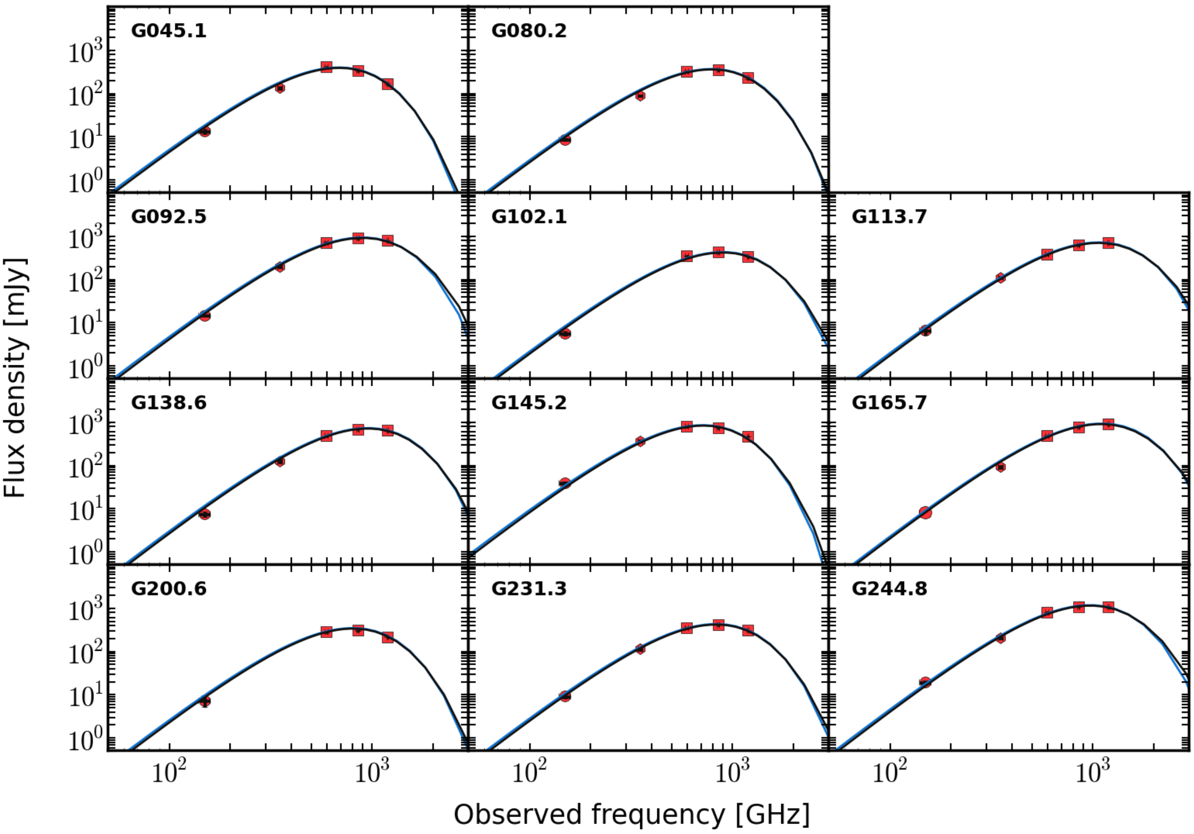

Figure 4.4: Modified black-body fit to the FIR-to-millimeter photometry of the 11 dusty GEMS. We obtained our broadband observations with Herchel/SPIRE at 250, 350 and 500 μm, JCMT/SCUBA-2 at 850 μm and IRAM/GISMO at 2mm (orange points). The dust continuum is therefore sampled with five data points for all but two GEMS that were not observed with SCUBA-2. Black errorbars indicate the photometric uncertainties and are generally smaller than the points. The light and dark blue curves show the best fitting modified blackbody functions for optically thin and optically thick dust, respectively.

2011). We obtain a slightly warmer range than measured for the 850 μm selected SMGs of Chapman et al. (2005) – for which Kovács et al. (2006) rather find 20-40 K – because their selection has proven to favour colder dust components.

I estimate the dust masses from flux densities in the 500 μm band of SPIRE, where the optically thin case remains valid. Using this approximation, I follow Greve et al. (2012) in estimating the observed dust mass of each GEMS with the relation

$$\mathrm{M_d} = \frac{\mathrm{D_L^2\ S_{\nu_{obs}}}}{(1+\mathrm{z})\ \kappa_{\nu_{\mathrm{rest}}}} \frac{1}{\mathrm{B}(\nu_{\mathrm{rest}}, \mathrm{T_d}) - \mathrm{B}(\nu_{\mathrm{rest}}, \mathrm{T_{CMB}(z)})} \tag{4.3}$$

where $\mathrm{D_L}$ is the luminosity distance to redshift z, $\mathrm{T_{CMB}}$ is the CMB temperature at redshift z, and $\mathrm{B}(\nu_{\mathrm{rest}}, \mathrm{T}$ the Planck function at temperature T. I use the fitted dust temperature $\mathrm{T_d}$ and correct for the CMB temperature which proved to affect the dust masses by about 2% (Papadopoulos et al. 2000). $\mathrm{S_{\nu_{obs}}}$ is the flux density at the observed frequency $\nu_{\mathrm{rest}}/(1+\mathrm{z})$, which we set to 600 GHz (corresponding to the 500 μm[4]). I define the dust mass absorption coefficient by $\kappa_{\nu_{\rm rest}} = \kappa_0 \, (\nu_{\rm rest}/\nu_0)^\beta$, with $\kappa_0 = 0.045$ m^2 kg^{-1} (Hildebrand 1983). I assume $\beta = 2.0$, as above, and a similar critical frequency ν_0 of 250 GHz. With this approach and these assumptions, I find dust masses of $\rm M_d = (3.5 - 11) \times 10^9 \; \mu^{-1} \; M_\odot$, before correcting for the unknown gravitational magnification factor μ. Results for individual sources are listed in Table 4.2. This range is very similar to the dust masses measured in the SPT sample (Greve et al. 2012).

4.2.3 Deriving far-infrared luminosities and star formation rates

Source	$\lambda_{\rm max}$ [μm]	$\rm S_{max}$ [mJy]	$\mu \; \rm L_{FIR}^{BB}$ [10^{13} $\rm L_\odot$]	$\mu \; \rm L_{FIR}^{TPL}$ [10^{13} $\rm L_\odot$]	μ SFR [$\rm M_\odot$ yr^{-1}]	$\rm T_d$ [K]	$\mu \; \rm M_d$ [10^9 $\rm M_\odot$]	$\mu \; \rm M_g$ [10^{11} $\rm M_\odot$]
G045.1	420 ± 10	360 ± 10	8.4 ± 0.1	12.1 ± 0.1	14462 ± 172	36.0 ± 0.5	6.5 ± 0.1	5.6 ± 0.1
G080.2	370 ± 10	345 ± 5	4.6 ± 0.1	7.1 ± 0.1	7920 ± 172	33.0 ± 0.5	7.2 ± 0.2	2.6 ± 0.2
G092.5	322 ± 5	900 ± 10	24.8 ± 0.2	34.8 ± 0.2	42698 ± 344	50.1 ± 0.4	5.3 ± 0.1	7.8 ± 0.2
G102.1	333 ± 4	410 ± 5	7.9 ± 0.1	11.9 ± 0.1	13601 ± 172	41.1 ± 0.3	4.3 ± 0.1	2.0 ± 0.2
G113.7	255 ± 20	700 ± 30	9.9 ± 0.2	12.6 ± 0.1	17044 ± 344	45.0 ± 0.4	3.5 ± 0.1	4.0 ± 0.2
G138.6	305 ± 10	690 ± 5	9.0 ± 0.1	13.5 ± 0.1	15495 ± 172	38.7 ± 0.3	6.4 ± 0.1	5.4 ± 0.1
G145.2	400 ± 10	785 ± 30	21.8 ± 0.2	30.1 ± 0.2	37533 ± 344	40.5 ± 0.4	11.0 ± 0.1	10.2 ± 0.2
G165.7	265 ± 2	875 ± 3	10.3 ± 0.1	13.4 ± 0.1	17733 ± 171	42.5 ± 0.3	5.1 ± 0.1	5.4 ± 0.1
G200.6	350 ± 3	295 ± 2	5.7 ± 0.1	8.2 ± 0.1	9813 ± 172	37.5 ± 0.5	4.3 ± 0.1	3.8 ± 0.1
G231.3	350 ± 10	402 ± 5	7.5 ± 0.1	10.7 ± 0.1	12913 ± 172	39.3 ± 0.4	4.7 ± 0.1	3.0 ± 0.1
G244.8	300 ± 2	1135 ± 2	26.5 ± 0.2	36.3 ± 0.2	45625 ± 344	50.0 ± 0.4	5.7 ± 0.1	2.6 ± 0.2

Table 4.2: Physical properties of the dust continuum and gas masses in the GEMS.

Using the best fitting modified black-body functions from the Monte-Carlo simulations of §4.2.1, I derive far-infrared flux densities, $\rm S_{FIR}$, by integrating the SEDs over the mid and far-infrared range 8-1000 μm as suggested by Kennicutt (1998). Then I convert these integrated fluxes to far-infrared luminosities according to

$$\rm L_{FIR} = \frac{4\pi \; D_{lum} \; S_{FIR}}{1+z} \tag{4.4}$$

where $\rm D_{lum}$ is the luminosity distance to redshift z, defined by $\rm D_{lum} = (1+z) \; D_H \int_0^z \frac{dz'}{E(z')}$ in the Friedmann-Lemaitre-Robertson-Walker metric and assuming a flat ΛCDM cosmology ($\Omega_{\rm k} = 0$, Planck Collaboration et al. 2014c). $\rm D_H = c/H_0$ is the Hubble distance with c, the speed of light and $\rm H_0 = 69.6$ km s^{-1} Mpc^{-1}, the Hubble parameter today (Planck Collaboration et al. 2014c). $\rm E(z) = \sqrt{\Omega_M (1+z)^3 + \Omega_\Lambda}$ is a dimensionless quantity that depend on $\Omega_{\rm M}$, the matter energy density and $\Omega_\Lambda = 1 - \Omega_{\rm M}$, the dark energy density. We may notice that this integration range was initially selected to include the entire emission of interstellar dust and is the most widely used in the literature. However in starburst galaxies most of the emission from dust heated by star formation is expected to fall in the rest-frame 10-120 μm (Kennicutt 1998). The 8-1000 μm window therefore also includes the cold diffuse dust component at high wavelengths and the PAH emission in the mid-infrared regime which are usually poorly constrained at high-redshifts, but which are unlikely to play a large role here.

For each GEMS, I compute the mean and standard deviation of $\rm L_{FIR}$ from the 1000 Monte-Carlo realisations. I find luminosities in the range $\rm L_{FIR} \sim (4.6 - 26.5) \times 10^{13} \; \mu^{-1} \; L_\odot$ without correcting for the gravitational magnification factor μ (see § 4.8, Cañameras et al. 2015). Thanks to the available spectroscopic redshifts and to the proper sampling of the dust continuum peak, I get small relative uncertainties of $\sim 1 - 2\%$. However, it is unlikely that the true SEDs of our galaxies consist only of a single "big grain" dust population with a single modified blackbody. We will further discuss these correction factors in §4.4.

---

[4] At this observed wavelength, the dust masses are less dependent on the dust temperatures than in the Wien tail.

These results are of the same order of magnitude as other samples of bright high-redshift lensed galaxies selected in (sub)-millimeter wavelengths. For instance, using the same definition of the far-infrared luminosities Greve et al. (2012) find $L_{FIR} \sim (1.8-6.5)\times 10^{13}\ \mu^{-1}\ L_\odot$ for the SPT lensed galaxies, and the extreme Herschel lenses with Planck counteparts of Fu et al. (2012) and Combes et al. (2012) exhibit $L_{FIR} \sim 1.1\times 10^{14}\ \mu^{-1}\ L_\odot$ and $L_{FIR} \sim 1.4\times 10^{14}\ \mu^{-1}\ L_\odot$ respectively. On the other hand the brightness unlensed HyLIRGs in the literature typically reach up to a few $10^{13}\ L_\odot$ (Farrah et al. 2002). Since Bussmann et al. (2013) derives intrinsic far-infrared luminosities of $\sim (2-20)\times 10^{12}\ L_\odot$ for a sample of Herschel-selected lensed galaxies at $z > 1.5$, the extreme brightness of the GEMS in the image plane suggest that their delensed intrinsic luminosities also fall in the ULIRG regime (i.e. $L_{FIR} > 10^{12}\ L_\odot$). We nevertheless caution that firm conclusions depend on the detailed lens modeling toward each source.

Several methods allow to estimate star formation rates with short wavelength observations. One can use emission lines and correct for dust extinction using SED fitting, or measure the light budget from the young massive stars in the UV/optical (also correcting for fust extinction). It is also possible to rely on MIR fluxes or to convert radio luminosities into the FIR regime with the FIR-radio correlation. However, in dusty galaxies, the application of attenuation laws to the rest-frame UV luminosities strongly underestimates the SFRs above 50 $M_\odot\ yr^{-1}$ (Rodighiero et al. 2014; Lee et al. 2015). Similarly, the MIR tracers prove to be less reliable in bright galaxies at high redshifts (Papovich et al. 2007; Elbaz et al. 2011). On the other hand, measuring the SFR of dusty galaxies directly in the FIR regime only relies on the thermal reradiation of the light from young stars, and avoids to fully understand the dust obscuration mechanisms. We therefore use our FIR/sub-mm photometry and apply the relation of Kennicutt (1998) to measure the SFRs in the GEMS,

$$SFR_{FIR}\,(M_\odot\ yr^{-1}) = 1.71\times 10^{-10}\ L_{FIR}\,(L_\odot) \qquad (4.5)$$

We find star formation rates SFR = 8000–46000 $\mu^{-1}\ M_\odot\ yr^{-1}$ suggesting both high intrinsic values and high magnification factors in the GEMS.

Although this conversion was initially estimated for local star forming galaxies and may be dependent on environment, it has been widely used for more luminous SMGs at high-redshifts (Swinbank et al. 2010; Ivison et al. 2010b). A major drawback of the 8-1000 μm integration window is that its low wavelength portion below 40 μm may include heating processes which are not related to the star formation activity in the host galaxy. In particular, the external heating from Active Galactic Nucleus (AGNs) has proven to become dominant in several extreme sources where it skews the luminosity values by up to 25% (Casey et al. 2014). In our case, the simple greybody curves from which we measure the integral do not include such processes. I will further describe the issues arising from AGN contaminations and the way they are adressed in §4.4.

4.3 How can we claim that the GEMS are strongly lensed ?

In this section, I will describe the empirical evidence used prior to the detailed lens modelling with LENSTOOL to demonstrate that the GEMS suffer strong gravitational magnifications.

4.3.1 Flux densities and morphologies in the (sub)-millimeter

Herschel/SPIRE low-resolution imaging

Before gathering the complete follow-up observations to identify the foreground intervening structures through optical/NIR imaging and to probe the resolved morphology of the background component through high resolution millimeter interferometry, the Herschel/SPIRE detection of the GEMS provided first evidence of their nature. As already described in Chapter 2, their selection in the parent

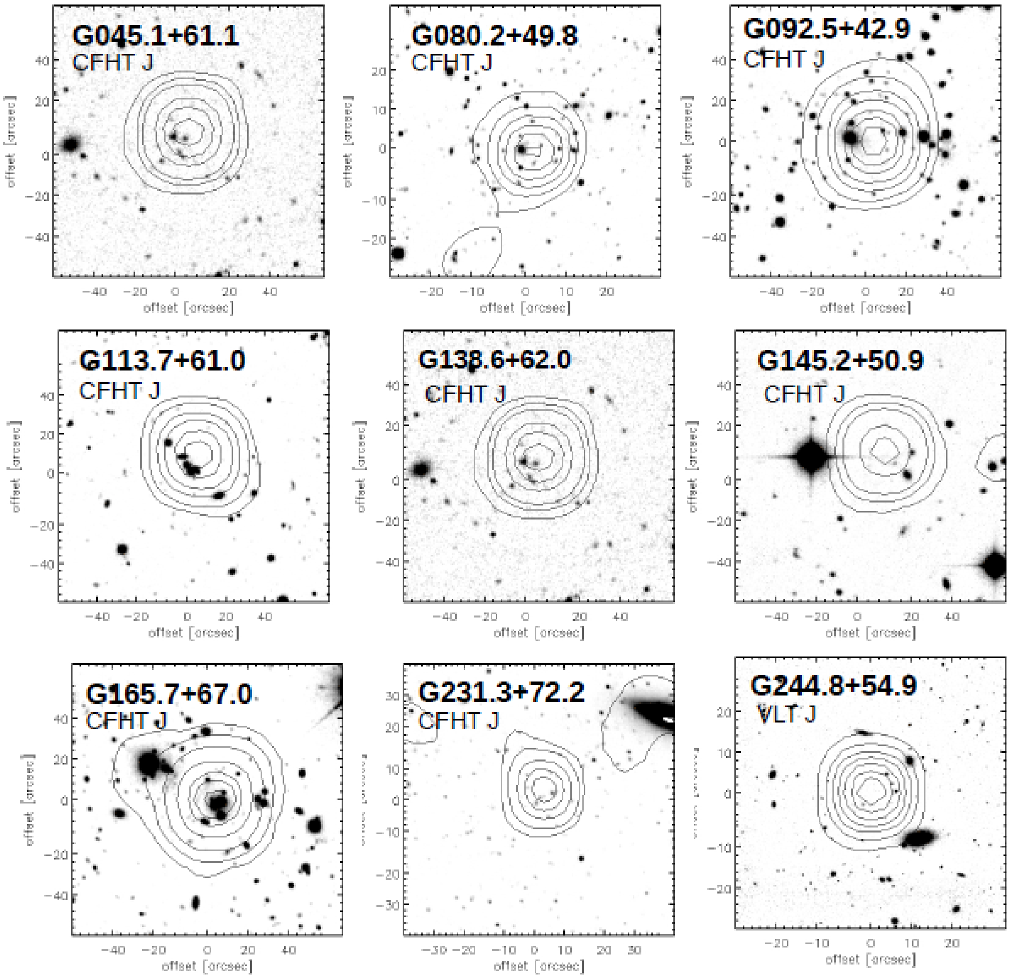

Figure 4.5: Near-infrared J-band images of the nine GEMS for which we obtained optical/NIR imaging and millimetre interferometry before 2015 (Fig.4.6). Contours show the Herschel/SPIRE morphology at 250 μm.

sample require a tremendous flux density at 350 μm exceeding a threshold of 300 mJy and optimal red colors.

Our sample covers the flux regime $S_{500} = 270 - 780$ mJy and most of the GEMS even exceed 100 mJy at 850 μm (Table 3.5). Even though it is based on another SPIRE band, our selection therefore satisfies the thresholds of Negrello et al. (2007). Moreover, the GEMS exhibit small angular sizes below 18″ in the SPIRE imaging shown in Figure 4.5. For their flux densities ($S_{350} > 300$ mJy), the empirical model of Béthermin et al. (2012) predicts about 18 times more lensed than unlensed sources at $z > 2$, in a given solid angle, and further validates our selection. The flux densities of few 10s mJy observed in typical high-z galaxies in the field suggest magnification factors $\mu \gtrsim 10$ for our sources, even if they are intrinsically amongst the most luminous sources on the sky. For more moderate intrinsic flux densities, the gravitational magnification would be accordingly higher. However, we also caution that the magnification factors deduced from the number counts of field SMGs are much higher than obtained with detailed lensing models, due to persisting uncertainties in the luminosity function of SMGs (Bussmann et al. 2013).

Finally, despite our spectroscopic identification, multiple unlensed high-redshift galaxies can potentially contaminate our selection (see, e.g., Ivison et al. 2013). These concentrated sources would lie within projected distances of a few tens of kpc (to remain unresolved at the highest frequency

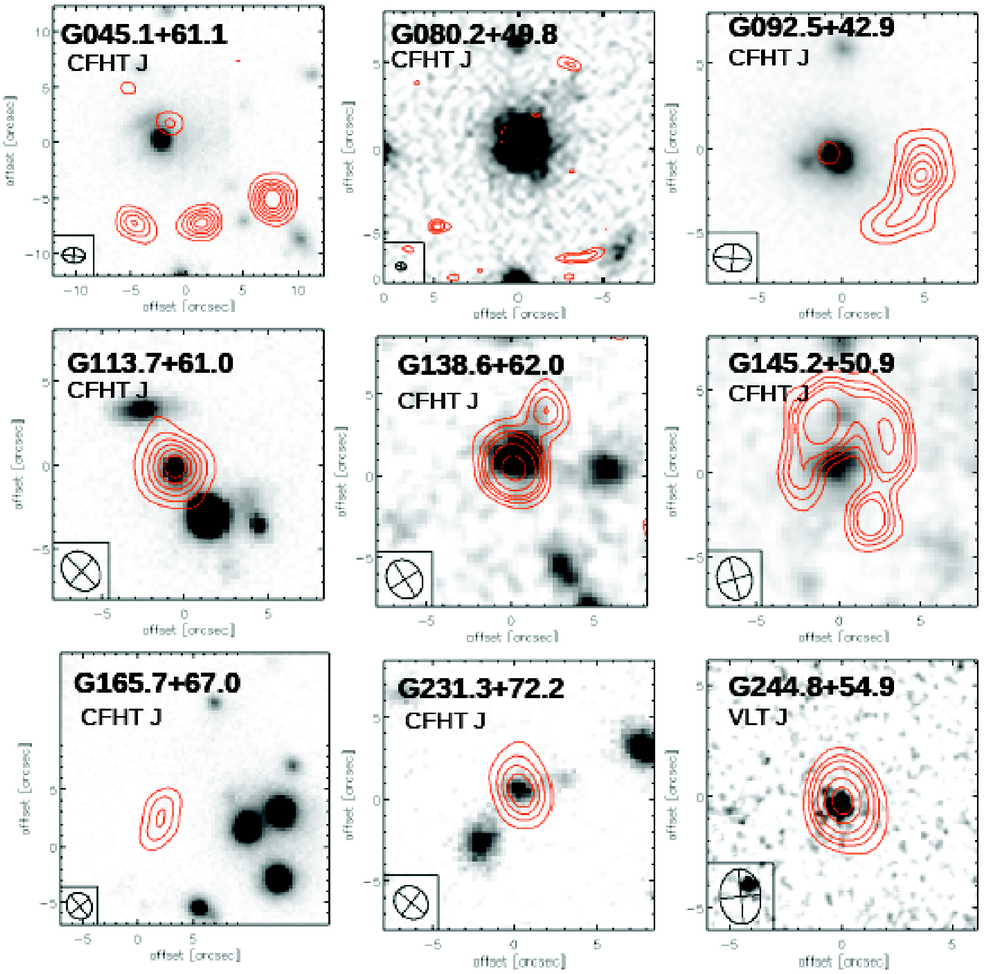

Figure 4.6: Near-infrared J-band images of the nine GEMS with high-resolution millimeter interferometry. Contours show the SMA morphology at 850 μm. The FWHM beam size of all SMA data is shown in the bottom left corner of each panel. It is about 2″ for eight of the nince GEMS and 0.8″ for G080.2.

band of SPIRE), which corresponds to about 120 kpc at z $\sim$ 2. In such volumes it would most likely correspond to mergers between obscured sources. Although higher resolution observations in the sub-mm will further explore these possibilities, the J-band images presented in Figure 4.5 already suggest intervening foreground objects and favour the lensing nature.

High-resolution interferometry

The spatially-resolved sub-mm morphologies of the GEMS provide more evidence of their nature. Strongly gravitationally lensed galaxies should indeed exhibit very characteristic morphologies, either single or multiple images with large distorsions. In the image plane, these sources can form small arclets or extended arcs of up to several arcseconds, either with small distortions or in partial or complete Einstein ring configurations (Vieira et al. 2013; Bussmann et al. 2013). The latter are the most outstanding and correspond to typical fold or cusp catastrophes. According to previous studies of Herschel or SPT samples, as well as other samples selected at shorter wavelengths such as SLACS (Bolton et al. 2008) or CASTLeS (Muñoz et al. 1998), this requires angular resolutions below $1-2''$. This can be obtained with deep follow-up imaging in the optical or NIR or with (sub-)mm interferometry for highly obscured sources such as the GEMS.

The SMA interferometer is one of the few instruments dedicated to map the dust morphologies at suitable resolutions. Figure 4.6 shows our follow-up observations at 850 μm, for all but two GEMS. In the COM configuration, with a synthetized beam of about $2''$, only G113.7, G138.6, G231.3 and G244.8 appear as isolated, unresolved point sources. G045.1 exhibits four distinct components, while G092.5 and G165.7 form small arclets. Moreover, the J-band images plotted in Figure 4.6 show that these three GEMS are aligned with multiple foreground galaxies, as further demonstrated in Chapter 5. G145.2 and G080.2 form extended arcs in a horseshoe and partial Einstein ring configuration, respectively. A reliable lens redshift is still missing for G145.2, mostly because the single foreground source detected in the J-band is very red, and our complete optical/NIR photometry has only been completed recently. However, the distorded arc of $\sim 10''$ diameter seen in the sub-mm is an indisputable proof of its lensing nature.

For their part, G244.8 and G138.6 lie at redshifts of 2.4 and 3.0, respectively. In this range, the $2''$ beam would correspond to intrinsic sizes below 16 kpc in the source plane, assuming no gravitational magnification. This scale is similar to the FWHM of the CO(1-0) spatial distribution in single high-redshift DSFGs (Ivison et al. 2011) and is unlikely to contain a small group of galaxies. Thus we suspect that their peak flux densities of 1054 ± 10 and 664 ± 8 mJy, respectively, can not correspond to individual high-redshift galaxies without benefitting from an additional boost from strong gravitational lensing. To get an independent confirmation, an additional SMA program is currently extending the follow-up in the EXT and VEX configurations for the small set of GEMS unresolved at $2''$. With a beam size of about $0.30''$, G244.8 is resolved as a partial Einstein ring of $\sim 1.5''$ diameter which makes its lensing nature unambiguous (see Fig.6.1). A thorough analysis of the lensing configuration of G244.8 will be presented in Chapter 6 and we defer the complete discussion of its (sub-)mm properties to §7.3. The characterization of the last sources with the SMA is still on-going. However, G231.3 was also observed with high-resolution interferometry of the CO(5-4) line at the PdBI. At a resolution of $0.7 - 0.9''$, this GEMS also forms a near-complete Einstein ring of $\lesssim 2.0''$ diameter, with two distorded arcs of different brightness facing each other.

Moreover, in each case, our optical/NIR photo-z and/or spectro-z indicate a lens redshift significantly lower than the redshift of the background source. The detailed characterizations in Chapter 5 will provide several pieces of evidence that only three GEMS are associated with foreground group or clusters of intermediate-to-high masses. In our sample, the majority of sources are rather behind isolated galaxies or a small handful of galaxies.

In the near future, the advent of the ALMA interferometer and its higher sensitivities will allow us to collect resolved morphologies for the small set of GEMS marginally resolved in the VEXT configuration of the SMA. Pending these complementary observations, the GEMS with resolved morphologies already probe a wide range of separations between the sub-mm components compared to the $1 - 3''$ found in the ALMA 870 μm imaging of the SPT sample (Vieira et al. 2013; Hezaveh et al. 2013). Moreover, our foregroud potential wells probe Einstein radii going from $0.5 - 2.0''$ like the SPT and Herschel lensed galaxies (Hezaveh et al. 2013; Bussmann et al. 2013), to $5 - 10''$. In the rest of this section, I will present additional empirical evidence to illustrate that all of our sample consists of strongly gravitationally lensed galaxies, including the four sources for which we do not yet have morphological constraints (G102.1, G113.7, G138.6 and G200.6).

4.3.2 Bolometric far-infrared emission compared to field galaxies

The FIR/mm properties of the GEMS can be illustrated in the $\mathrm{L_{FIR}} - \mathrm{T_{dust}}$ diagram plotted in Figure 4.7. Greve et al. (2012) adopted this approach to characterize their sample of lensed candidates from the SPT survey. They compared these targets with dedicated samples of SMGs and AGNs from the literature, either lensed or unlensed and selected for their high apparent brightness. Their lensed galaxies have dust temperatures between 34 and 67 K placing them in the same regime as the GEMS,

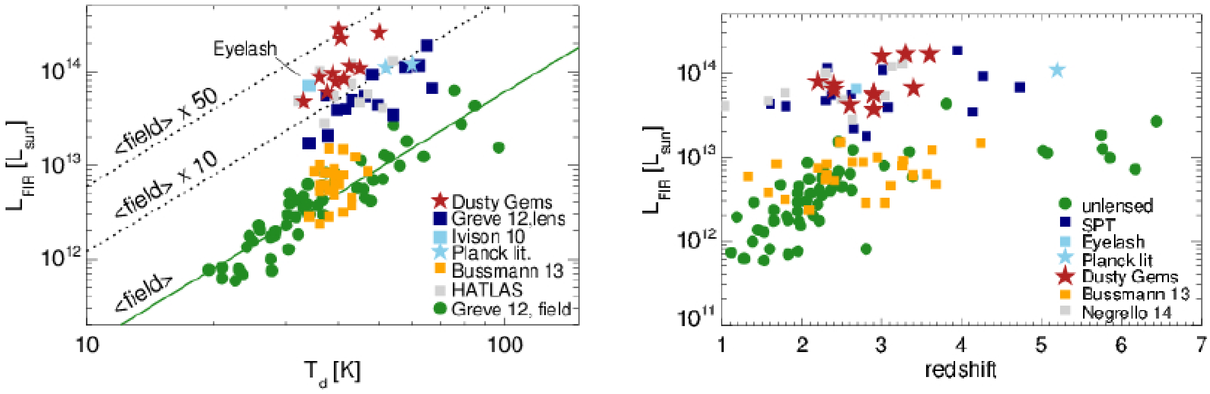

Figure 4.7: *Left :* The diagram of FIR luminosities versus dust temperatures demonstratees that the GEMS are offset towards high amplifications (red stars), compared to the published samples of unlensed and lensed SMGs and AGNs from Greve et al. (2012) (green points and dark blue squares), delensed galaxies from Herschel samples (yellow squares, Bussmann et al. 2013), the Eyelash (light blue square, Ivison et al. 2010b) and the two Planck galaxies found prior to our study and excluded from the current sample (Combes et al. 2012; Fu et al. 2012, light blue stars,). The green solid line is the best power-law fit to the intrinsic properties of the field galaxies and the dotted lines show the same relationship multiplied by 10 and 50, respectively. *Right :* FIR luminosities as a function of redshift for our GEMS and the same samples as in left panel. Our sources fall near the most luminous gravitationally lensed galaxies at similar redshifts.

while a lower range have been subsequently measured for the SPT sources due to their selection at longer wavelengths (i.e. 1.4 and 2.0 mm, Weiß et al. 2013). Moreover, the dust temperatures increase with $\mathrm{L_{FIR}}$ in their population of field galaxies – in agreement with other unlensed high-redshift DSFGs (Magnelli et al. 2012) – implying that the shorter wavelength emission is enhanced in the brightest sources. In Figure 4.7, I compare the position of the GEMS with the samples of Greve et al. (2012), the Herschel-selected lensed galaxies of Bussmann et al. (2013) corrected for the gravitational magnification, and the observed properties of other lensed sources from the literature.

The GEMS are significantly brighter at a given temperature than the unlensed population and even brighter than most of the previously known gravitationally lensed galaxies. Although this plot does not indicate fundamental differences between the properties of unlensed SMGs and the intrinsic properties of lensed SMGs (Harris et al. 2012; Bussmann et al. 2013), it easily reveals strong gravitational magnifications in samples of dusty high-redshift sources. Modeling their dust emission with an isotropic greybody and assuming that the emitting surface is a sphere of radius R, the Stefan-Boltzmann law indeed predicts a power-law relationship between the intrinsic $\mathrm{L_{FIR,int}}$ and $\mathrm{T_d}$,

$$\mathrm{L_{FIR,int}} = 4\pi \mathrm{R}^2 \sigma \mathrm{T_d^4} \tag{4.6}$$

where σ is the Stefan-Boltzmann constant. For a given temperature, the apparent luminosity $\mathrm{L_{FIR,app}}$ should therefore only depend on the size of the emitting surface, the emissivity and the magnification factor. Consequently, the strongly lensed galaxies are expected to lie on a similar power-law relationship with a zero point increasing proportionally with μ. In Figure 4.7 we plot the best fit to the samples of field galaxies instead of the dedicated Stefan-Boltzmann law. We then show the same relations shifted for apparent luminosities enhanced by factors of 10 and 50, respectively, to further prove that the GEMS indeed fall into the regime of strongly gravitationally lensed galaxies. The diagram suggests that μ is systematically greater than 10 in our sample. At the same time, the position of the Eyelash – whose detailed lensing model suggest a range of magnifications of 20-60 and $\mu = 32.5$ on average (Swinbank et al. 2011) – broadly confirms these empirical predictions.

However, these estimates should be treated with caution because the tight empirical relations are based on several assumptions. Firstly, they assume a common emissivity and dust opacity for high-redshift DSFGs discovered with various selection criteria and which probably cover a wide range of environments. Secondly, our observational constraints do not allow a proper modelisation of multiple dust components with different temperatures. Finally, these targets could suffer from significant differential magnifications (Blain et al. 1999), in particular if the lensed samples trace more compact regions in the source plane and warmer environments due to the intense star formation or the proximity of an AGN (Greve et al. 2012).

4.3.3 Profile of the molecular gas lines

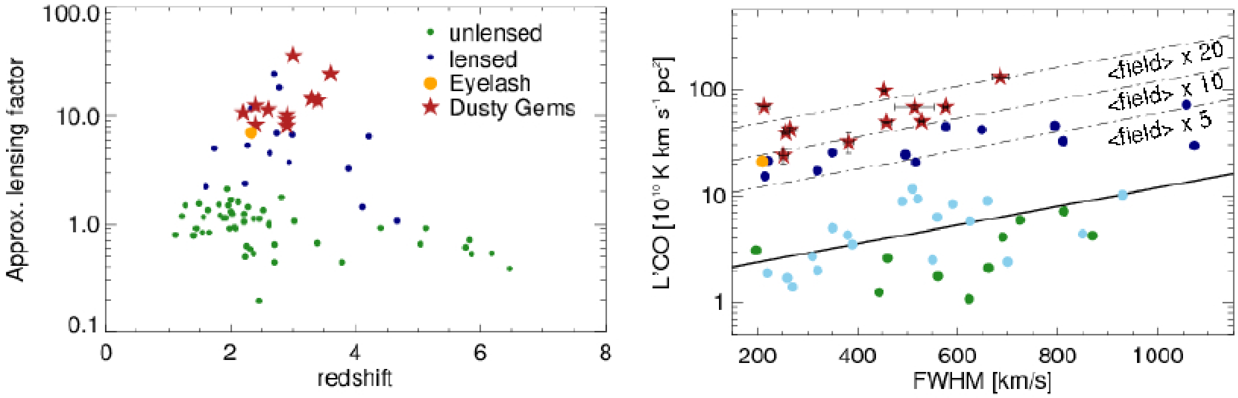

Figure 4.8: *Left :* Order-of-magnitude of the gravitational magnification factors toward the GEMS (red stars) deduced from the relationship between dust temperature and FIR luminosity shown in Fig.4.7. We compare with the factors obtained for bright and gravitationally lensed SMGs in the literature. *Right :* Line luminosities $\mathrm{L}'_{\mathrm{CO}}$ as a function of the FWHMs for the lowest-J CO transitions detected in each GEMS (red stars) compared to the Eyelash (yellow dot, Ivison et al. 2010b) and the GBT observations of lensed galaxies from the H-ATLAS survey (dark blue dots, Harris et al. 2012), without correcting for lensing magnification. The field galaxies are unlensed sources with published CO(1-0) lines or with higher-J lines converted to CO(1-0), and without strong AGN (light blue and green dots, Harris et al. 2010; Carilli et al. 2010; Ivison et al. 2011; Riechers et al. 2011). The black line is the best power-law fit to these typical galaxies and the dotted lines show the same relationship multiplied by factors of 5, 10 and 20. Error bars indicate the 1σ uncertainties of our single-component Gaussian fits.

Without detailed lens models for the sources, we can also use the properties of the spectrally-resolved CO emission lines measured with EMIR to show additional evidence for strong gravitational magnifications. It has been shown that the CO(1-0) line intrinsic luminosities exhibit a sufficiently homogeneous distribution in field SMGs to form a broad trend in the CO(1-0) luminosity-FWHM plot (Bothwell et al. 2013). For minor intrinsic variations in SMGs, Harris et al. (2012) state that significant departures from this relationship can be directly attibuted to gravitational magnifications. Using the parametrization of Bothwell et al. (2013), the CO(1-0) line luminosities accordingly provide a rough estimate of the magnification factors with the ratio $\mu = \mathrm{L}'_{\mathrm{obsersed}}/\mathrm{L}_{\mathrm{intrinsic}}$. Harris et al. (2012) follow these steps to demonstrate that galaxies from the H-ATLAS survey are indeed strongly gravitationally lensed and to derive approximate magnification factors. Their galaxies stand out by 1-2 orders of magnitude above the power-law relationship and suggest $\mu \sim 3 - 20$. Moreover, in this plot, the line FWHMs in lensed galaxies are not expected to evolve in the same way. The lines should rather remain as broad as in field galaxies, or sometimes narrower because lensing allows to zoom in on smaller regions of the large-scale velocity fields. When probing these small scales, the rotation curve indeed becomes partially sampled and the observable turbulent motions are also smaller, which decreases the observed linewidths.

Following the same procedure, I plot in Figure 4.8 the unlensed DSFGs presented in Bothwell et al. (2013) and other field galaxies with published CO(1-0) lines or with higher-J lines converted to CO(1-0), and show the best power-law fit. After converting our low-J line luminosities to $\mathrm{L}'_{\mathrm{CO}}$, the GEMS obviously probe the high luminosity regime and span a large range in FWHM in this diagram. We find a moderate tilt which is nonetheless steeper than for the SPT DSFGs (Aravena et al. 2016). Compared to Ivison et al. (2013), the largest measured FWHMs are nearly as large as those of overdensities of multiple high-redshift sources that are at best moderately gravitationally lensed. However, the GEMS are firmly above the field galaxies in this diagram, within the regime of gravitationally lensed sources also indicated by the Eyeslash and the lensed galaxies from the H-ATLAS survey. Unlike the H-ATLAS sample, even the GEMS with the highest FWHM linewidths are significantly brighter than the most extreme unlensed sources. The 11 GEMS are therefore unambiguously placed in the lens regime.

We multiply the best-fitting relationship by magnification factors of 5, 10 and 20, respectively, and the observed line luminosities of the GEMS suggest a broad magnification regime of $\mu \sim 10 - 50$. The example of the Cosmic Eyelash, which has a magnification factor of 20-60 shows however that the lensing factor derived from the position of a source in this diagram can only be an approximate indicator. This limitation was also demonstrated in Aravena et al. (2016), by the comparison of magnification factors obtained with the empirical CO luminosity-linewidth relationship and more reliable factors deduced from detailed lensing models. Firstly, we do not correct the CO spectra for inclination although such corrections may become significant for galaxies with low FWHM (Harris et al. 2012). Secondly, our low-J CO(3-2) and CO(4-3) transitions may probe a larger variety of intrinsic linewidths than CO(1-0) due to diverse physical conditions.

4.4 Quantifying the AGN contribution to dust heating

The characterization of large samples of high-redshift star-forming galaxies have proven that these systems frequently host a powerful AGN contributing to the dust heating. For instance, Alexander et al. (2003) detect X-ray emission from an AGN in about 30-50% of a sample of bright SMGs with $\mathrm{S}_{850} > 5$ mJy. Similarly, Alexander et al. (2005) find that a vast majority of SMGs detected in SCUBA surveys host AGN activity (about 75%), with a major contribution in about 30% of the sample. Lower AGN fractions have been subsequently reported in other samples, about 15-30 % in Johnson et al. (2013) or about 20% from an ALMA survey in the Chandra Deep Field-South (Wang et al. 2013). These fractions have also proven to increase with SFR and therefore with $\mathrm{L}_{\mathrm{FIR}}$ (Kartaltepe et al. 2010). In particular, they emit in the infrared bands and they can contaminate the FIR luminosities by up to 25% in the 8-1000 μm integration window, or even more for the most obscured QSOs.

The presence of an obscured AGN in the GEMS would add a second hotter blackbody component to their dust thermal emission, with a minor or major effect of the total infrared luminosity budget. Since the dust temperatures in quasars are usually far above 70 K, our results of $\mathrm{T}_{\mathrm{dust}} \lesssim 50$ K seem at first sight to point toward pure starbursts. However, despite the fact that the three SPIRE points cover the emission peak, our fit to the FIR/sub-mm SED lacks observational constraints in the MIR regime. AGNs emit predominantly below 90 μm and their contribution could therefore bias our estimates towards lower temperatures. Moreover, this potential additional component would lower the FIR luminosity budget tracing pure star formation, so that the exceptional apparent brightness could also be reached with lower magnification factors. These reasons make it worthwhile to quantify their AGN content with the best possible accuracy.

4.4.1 Standard AGN detection methods

Deep X-ray observations are a direct probe of the AGN content in high-redshift dusty galaxies which was widely used in the above studies. This technique can be very time-consuming and becomes less efficient for high dust extinctions. The usual optical diagnostics from emission line ratios (Kewley et al. 2006) are often not appropriate to measure the AGN content in SMGs, again because their massive dust reservoirs attenuate the optical regime. Thus imaging observations in the NIR and MIR (below 100 μm in the rest-frame) are probably the most convenient probe of AGN activity in DSFGs, as shown for example with Spitzer data (Lacy et al. 2004). With a good sampling of the Wien tail of the dust greybody emission, it is indeed possible to highlight the presence or absence of warm components above 100 K. At these wavelengths, a power-law slope would very likely indicate a strong AGN heating. Deep photometry from Herschel/PACS would meet these requirements but this instrument was no longer available when we started our follow-up. Ideally, MIR spectroscopy would also help determining the strength of the PAH spectral features relative to the warm dust component and stellar continuum in the host galaxy.

In this thesis, we seek to build on both WISE photometry at 22 μm and IRAS upper limits of non-detection to measure the AGN contribution to the overall dust heating in the GEMS, in comparison with the effect of the star formation activity. Our sparse data points will likely make it impossible to derive tight constraints on the presence of weak AGN activity, but our main goal is rather to show that AGN radiation is not energetically dominant in these sources. Such configurations would have important implications for the estimated star formation rates, plausible ranges of intrinsic infrared luminosities, and gas excitation.

4.4.2 The DecompIR software

I disentangle the contributions from the starburst and AGN components to the infrared bolometric luminosity with the DecompIR software (Mullaney et al. 2011) and our own IR/mm photometry combined with the WISE imaging at 22 μm. These data points are all summarized in Table 3.5. They correctly sample the peak and Rayleigh-Jeans tail of the FIR/mm SED and, thanks to the available spectro-z, our dataset allows a robust characterization of the coldest dust component below 50 K. However, we only sample the Wien tail with the 22 μm data point from WISE because the IRAS upper limits will only test the consistency of the best-fit a posteriori. Fortunately, the SPIRE band at 250 μm covers wavelengths near or below the dust continuum peak and, more importantly, the emission from warm dust heated by an AGN (50-80 μm in the rest-frame). The AGN torus templates (Polletta et al. 2007; Nenkova et al. 2008) as well as the observed SEDs of powerful AGN host galaxies at high redshifts are peaking in this infrared regime (e.g., Sajina et al. 2012).

DecompIR is a publicly available package which performs a χ^2 fit to these six photometric points, using a combination of empirical templates of host star-forming galaxies and AGNs. The code requires robust constraints for the host component to avoid strong degeneracies between the pure star-forming templates and the templates combining both the host and AGN contributions. In our case, this criterion is met by the good sampling of the peak and Rayleigh-Jeans tail of the dust continuum. Under this condition, DecompIR searches for the best fitting normalization of the host component and then determines whether an additional AGN component substantially improves the χ^2. If so, it releases the approximate contribution of the AGN component compared to the host starburst.

Before fitting the SED of each GEMS, I start building the template library with the host starburst component. The DecompIR software package already includes empirical templates derived from nearby starburst galaxies which are unfortunately not representative of the dust temperatures found in the GEMS. These templates would not adequately fit the FIR-to-mm dust emission and make the characterization of the mid-to-FIR regime much more uncertain. To overcome this discrepancy, I use the well constrained temperatures of the cold dust components to build a dedicated starburst template in accordance with the following steps. Among the five host templates of DecompIR, I select the SB2

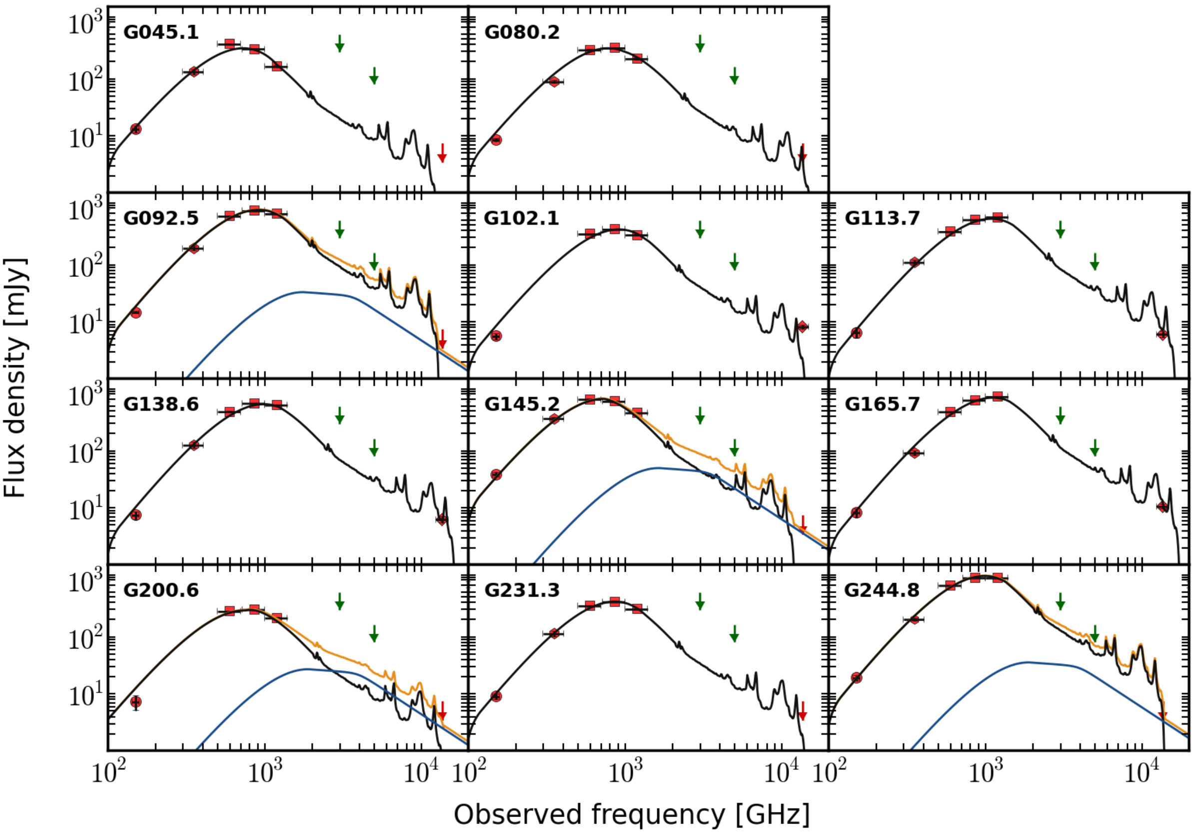

Figure 4.9: Our SED modeling with DecompIR in the infrared-to-millimeter regime rules out a major AGN contribution to the bolometric infrared emission of the GEMS. The red dots show our data points and the error bars along the x-axis indicate the width of each photometric band. On the y-axis, the flux uncertainties are often smaller than the symbols. The green downward arrows show the 90% completeness limit of the IRAS all-sky survey at 60 and 100 μm, respectively. The red downward arrows at 22 μm show the 5σ upper limits provided by the WISE catalogs, where the counterparts were fainter than the 5.4 mJy flux limit. Our single starburst component is plotted in black lines (see the description in the text), while the AGN torus template from Polletta et al. (2007) and the composite output SED from DecompIR appear in solid blue and yellow lines, respectively.

(corresponding to the SED of NGC7252, Mullaney et al. 2011) because it provides the best match to our FIR/mm photometry with no regard of the goodness-of-fit of the 22 μm constraint. For each GEMS, I fit the normalization of this template in the observer frame and then correct for the mismatch in dust temperatures. To this end, I remove the modified blackbody emission in the FIR/mm from the SB2 SED and obtain a residual in the MIR/FIR regime. Then, I connect this residual to the modified blackbody emission previously fitted, applying the suitable dust temperature for each source. Secondly, to model the AGN component I use the type-2 QSO template of Polletta et al. (2007) which was derived to fit the observed photometry of SWIRE J104409.95+585224.8 (Polletta et al. 2006). This torus-only template is already included in the DecompIR package and the lack of photometric constraints blueward to the dust peak does not allow enough flexibility to test other spectral classes of AGN.

Our independent template fitting with DecompIR includes warmer dust components compared to the modified blackbody fits, both for the pure starbursts and for the few sources with a small AGN

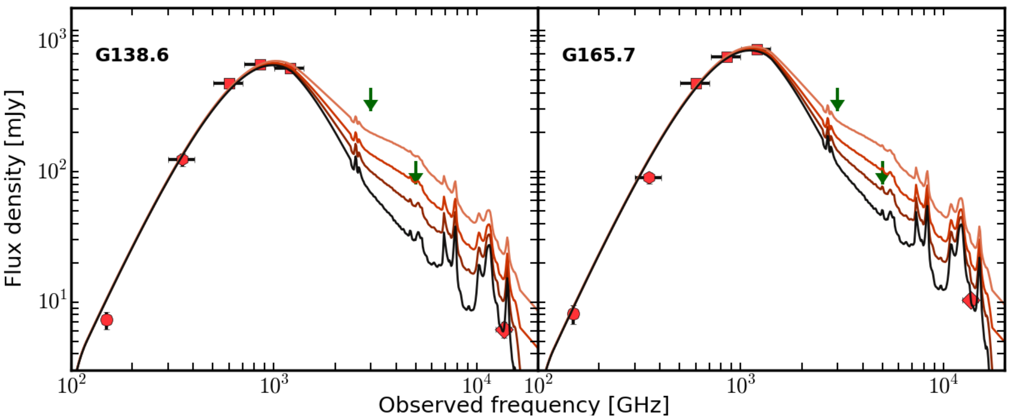

Figure 4.10: The impact of 10, 30 and 50% AGN contaminations to the bolometric FIR luminosity. We illustrate how these components modify the shape of the SED in the MIR regime, for two GEMS poorly constrained by the SPIRE point at 250 μm. For G138.6 and G165.7, the small plateau between 250 and 350 μm indeed leaves the SED slope shortward 100 μm free.

contribution. It therefore provides fiducial correction factors to the FIR luminosities, suggesting that the simple modified blackbody functions underestimate these luminosities by 10-30%. These new results are presented in Table 4.2 for the individual GEMS.

4.4.3 AGN contributions in the GEMS

Figure 4.9 shows that we can rule out a bolometrically dominant AGN contribution from buried quasars, in all cases. Only three galaxies have best-fit results formally inconsistent with pure starbursts. In G092.5 and G244.8, the putative AGN contribution to the FIR luminosity is below 10%, and it is below 30% in G145.2. In all other cases, DecompIR finds the best fit for a pure starburst SED. Figure 4.9 also shows the 90% completeness limits of the IRAS faint source survey, 120 mJy and 440 mJy at 60 μm and 100 μm, respectively. Although these limits are not constraining for the SED fits that we obtained with SPIRE, SCUBA-2, GISMO, and WISE (and were therefore not included in our DecompIR fits) they do illustrate that a hypothetical bright quasar component would have led to a 60 μm detection at least in our brightest targets. In Figure 4.10 I illustrate the impact of fiducial AGN contribution of 0.1, 0.3, and 0.5 × L_{FIR} on the example of G138.6, a source with rather average FIR brightness and 250-to-350 μm colour in our sample. Obviously, these fits are uncertain, given that they cover the far blue wing of the dust SED expected from bright AGN, and a spectral range that has important contributions from rich mid-IR spectral features, in particular from Polycyclic Aromatic Hydrocarbons (PAH), which dominate the infrared SEDs of starburst galaxies between about 3 μm and 10 μm (e.g., Armus et al. 2007).

The equivalent widths of the PAH bands have a wide dispersion in high-redshift galaxies (Fiolet et al. 2010), and are generally larger than those measured in low-redshift ULIRGs, including NGC 7252, which I used as template in our DecompIR fits. Additional uncertainties come from the stellar continuum, which reaches comparable strength to the dust continuum in the wavelength range covered by the 22 μm observations, about 5-7 μm, and whose shape depends strongly on the specific star formation rate, star formation history, and geometry of dust obscuration in the host galaxy. Compared to the average MIR SED of starburst galaxies (Brandl et al. 2006), the stellar continuum in NGC 7252 seems relatively faint, and (Sajina et al. 2012) also found that the MIR continuum of high-redshift starburst galaxies seems to be brighter than in low-redshift galaxies. Other spectral features might also contribute to boosting the observed 22 μm flux density. For example, Fiolet et al. (2010) report the detection of warm H_2 line emission at 6.9 μm in the rest-frame. Moreover, the foreground galaxies may also contribute to the 22 μm flux, given the 12″ beam of WISE. However, all these uncertainties would only act to lower the putative intrinsic contribution of AGN heating relative to what we observe.

Finally, I find that the contribution from obscured AGNs to the bolometric infrared luminosities does not exceed in 30% in the whole sample. On the spatial scales probed by the lensing configurations and by our unresolved photometry, dust heating appears to be largely dominated by the intense star formation with at most a minor AGN contribution. Furthermore, the majority of these extremely bright high-redshift sources are even compatible with pure starbursts. We remind that these conclusions are only drawn for the most magnified regions, whose positions and intrinsic sizes are entirely dependent on the strong lensing effect. However, the global energy budget of AGN and star formation in each galaxy may be different, in particular if the AGN lies along a line of sight that is not strongly magnified (Serjeant 2012).

4.5 Deriving molecular gas masses

4.5.1 Converting the CO luminosities to molecular gas masses

Gas accounts for 99% of the interstellar medium (ISM) mass budget in high redshift galaxies. Measuring the gas content of the GEMS is therefore primordial to characterize their overall properties and to determine the influence of such high gas masses on the star formation mechanisms. Measurements of the molecular gas mass of distant galaxies are usually deduced from a conversion between the CO(1-0) luminosities and the total mass of H_2. Hydrogen amounts to 73% of the mass of interstellar gas, with 25% coming from Helium and about 2% from metals. This requires an empirical CO-to-H_2 conversion factor, $\alpha_{\rm CO}$, which is defined for high-redshift galaxies by the ratio of the integrated molecular mass to the integrated CO line luminosity,

$$\frac{\alpha_{\rm CO}}{[{\rm M}_\odot/({\rm K\ km\ s^{-1}\ pc^2})]} = \frac{{\rm M}_{\rm H_2}}{{\rm L}'_{\rm CO}} \tag{4.7}$$

However, since resolved observations of GMCs are available for the Milky Way and low-redshift spiral galaxies, these studies rather use the ratio of the H_2 column density to the velocity-integrated intensity of the CO transition with, $X_{\rm CO} = N_{\rm H_2}/W_{\rm CO}$. To simplify the discussion, I will however use only the definition using integrated quantities, $\alpha_{\rm CO}$. Measurements of the H_2 masses through a wide range of techniques (e.g., through measurements of gas-to-dust ratios, see a comprehensive summary in Bolatto et al. 2013) have shown that the conversion factor falls in the range $\alpha_{\rm CO} = 3 - 6\ {\rm M}_\odot/({\rm K\ km\ s^{-1}\ pc^2})$ for these nearby GMCs.

Furthermore, Downes & Solomon (1998) discovered that the CO-to-H_2 conversion factor decreases by factors 4-20 in high gas surface density environments. Applying a galactic conversion to their sample of dense and nearby ULIRGs would provide gas masses higher than the independently estimated dynamical masses. In this context, a canonical value of $\alpha_{\rm CO} = 0.8\ {\rm M}_\odot/({\rm K\ km\ s^{-1}\ pc^2})$ (Downes & Solomon 1998) have been adopted for active nearby galaxies (from circumnuclear starbursts to LIRGs and ULIRGs) and for high-redshift DSFGs with evidences of enhanced star formation rate surface densities (Greve et al. 2005; Tacconi et al. 2006).

Although $\alpha_{\rm CO}$ clearly depends on the local physical conditions in the ISM, its value has been heavily debated in the literature in particular to determine the main cause of this bimodality (Glover & Mac Low 2011; Narayanan et al. 2012; Papadopoulos et al. 2012). Recently, several studies also investigated whether a single conversion factor may be appropriate to use for all high-redshift galaxies (Daddi et al. 2010; Genzel et al. 2010). To further constrain these results, an empirical approach applied for instance in Magdis et al. (2011) draws on the robust dust masses obtained from SED fitting. Under the assumption that high-redshift galaxies fall onto a similar relationship between gas-to-dust mass ratios (GDR) and metallicities than the local ones (Leroy et al. 2008), a GDR can be adopted to convert these dust masses to gas masses. Recently, Aravena et al. (2016) have used this method and a constant GDR of 100 (as measured in field SMGs by Santini et al. 2010; Ivison et al. 2011) to confirm that most of the lensed galaxies in the SPT samples are consistent with $\alpha_{\rm CO} \sim 1$. This work provides an independent constrain for a lensed sample that can be affected by differential magnification between the dust and CO(1-0) components. However, we mentioned above that the GDR is much better constrained in the Milky Way and local ULIRGs, and other methods are therefore required. By way of example, Magdis et al. (2011) also constrain α_{CO} from dynamical mass estimates.

4.5.2 The molecular gas masses in the GEMS

Here, to compute the molecular gas masses we also rely on the brightest molecular gas tracer at high redshift which was detected either in the CO(3-2) or the CO(4-3) transition, and estimate the CO-to-H_2 conversion factor for each GEMS. To this end, we first derive the $L'_{\rm CO}/M_{\rm d}$ ratios and use the Figure 3 of Magdis et al. (2011) to obtain a rough estimate of the metallicities. Since this scaling is based on the CO(1-0) transition, we adopt a ratio $r_{32/10} = 1$ (or also $r_{43/10} = 1$) to convert the luminosities of the observed lower-J CO lines to $L'_{\rm CO}$. This factor is expected for optically thick gas (Solomon & Vanden Bout 2005) and assumes that the differential lensing between the CO(3-2) (or CO(4-3)) and CO(1-0) components does not play a significant role. For instance, Danielson et al. (2011) measure $r_{32/10} = 0.7$ in the strongly lensed Cosmic Eyelash. The range $L'_{\rm CO}/M_{\rm d} = 40 - 140$ found among the sample corresponds to gas-phase metallicities of $12 + \log({\rm O/H}) \sim 8.9 - 9.3$, for the same emissivity index as the one assumed throughout this thesis ($\beta = 2.0$).

Moreover, $\alpha_{\rm CO}$ has proven to increase in galaxies with lower metallicity, probably due to less efficient dust shielding (Leroy et al. 2011). On the contrary high gas-phase metallicities lead to $\alpha_{\rm CO} < 1.0$ $M_\odot$/ (K km s^{-1} pc^2). For galaxies with $L'_{\rm CO}/M_{\rm d}$ ratios and metallicities as high as in the GEMS, the linear fit between $\alpha_{\rm CO}$ and metallicity of Genzel et al. (2012) predicts $\alpha_{\rm CO} \sim 0.4$ $M_\odot$/ (K km s^{-1} pc^2) in spite of large uncertainties. Likewise, Magdis et al. (2011) suggest $\alpha_{\rm CO} < 1.0$ $M_\odot$/ (K km s^{-1} pc^2). We therefore assume that a ULIRG conversion factor is more appropriate for the GEMS than the higher values previously adopted for the high-redshift galaxies with disk-like morphologies and quiescent star formation. Using a common conversion factor of $\alpha_{\rm CO} = 0.8$ $M_\odot$/(K km s^{-1} pc^2) for the 11 sources, we find molecular gas masses of $(2 - 10) \times 10^{11}$ μ^{-1} $M_\odot$ (see Table 4.2), without correcting for the gravitational magnification. We stress that, depending on the lensing configurations, these results are probably measured in small regions of the background sources and are not necessarily representative of their average values (Serjeant 2012). We also caution that estimates relying on CO lines at intermediate excitation levels may result in gas masses smaller by factors 1.5-2.0 compared to estimates based on direct measurements of the CO(1-0) line luminosities (Harris et al. 2010).

4.6 The FIR-radio correlation

4.6.1 Physical principle

There is considerable evidence that local SFGs show a tight correlation between their total far-infrared emission, $S_{\rm IR}$, and their monochromatic radio continuum flux at 1.4 GHz, $S_{1.4}$, parametrized as follows (Helou et al. 1985; Ivison et al. 2010b):

$$q_{\rm IR} = \log\left(\frac{S_{\rm IR}}{3.75 \times 10^{12}\ {\rm W\ m^{-2}}}\right) - \log\left(\frac{S_{1.4\ \rm GHz}}{{\rm W\ m^{-2}\ Hz^{-1}}}\right) \tag{4.8}$$

where the far-infared flux density $S_{\rm IR}$ is integated in the range $8 - 1000$ μm in the rest-frame, and the monochromatic radio continuum $S_{1.4}$ is measured at the rest-frame frequency of 1.4 GHz, and k-corrected assuming $S_\nu \propto \nu^{\alpha_{1.4}}$ with $\alpha_{1.4} = -0.8$.

This FIR-radio correlation (FIRRC) was first detected in the Virgo Cluster (Helou et al. 1985). Their sample indicates that quiescent disks, late-type spirals and galaxies hosting a nuclear starburst residing either within or outside the cluster follow a common relation. Observational studies of samples of nearby galaxies confirmed this discovery (de Jong et al. 1985; Yun et al. 2001) and subsequently showed that the relationship is nearly linear and holds on several orders of magnitude in luminosity (Condon et al. 1991), gas surface density, and photon energy density. The FIR-radio correlation was also observed on spatial scales ranging from $\sim$ 100 pc, i.e. the typical sizes of Giant Molecular Clouds (GMCs), to the overall galaxies.

The physical mechanisms that set up the correlation in SFGs are still debated. However it is commonly accepted that FIR emission is dominated by dust absorbing the UV and optical photons in HII regions, and then thermally re-radiating this energy in the FIR (Harwit & Pacini 1975). In these SFGs, the free-free emission from HII regions is low and the synchrotron emission from relativistic electrons accelerated in supernova (SN) shocks dominates the radio regime (Yun et al. 2001). The relation therefore emerges naturally because UV and optical ionizing photons are mainly produced by young, massive stars, the same population that explode as SNe. An equilibrium is achieved between the two processes if the star formation timescale is longer than $\sim 10^7$ yr, the time limit of the first SNe explosions.

Several mechanisms describing larger and lower $q_{\rm IR}$-values (IR and radio excesses) are found in the literature. In particular, Thomson et al. (2015) probes the correlation in three star forming clumps within the Eyeslash and suggests that the $q_{\rm IR}$ parameter evolves with time during a starburst episode. When the star formation is turned on, the thermal FIR emission from dust heating arises nearly instantly whereas the non-thermal synchrotron emission is delayed. Before the first SNe explosions thermal emission from HII regions should indeed dominate the weak radio emission of the proto-starburst, and synchrotron emission should increase subsequently during the starburst evolution. This scenario therefore suggests that higher values of $q_{\rm IR}$ in powerful starbursts could trace dense gas regions with very young stellar populations (Bressan et al. 2002).

4.6.2 Interpretation of the correlation for the GEMS

Source	Distance [arcsec]	$\mu_{1.4}$ $S_{1.4}^{\rm int}$ [mJy]	$\mu_{1.4}$ $L_{1.4}$ [10^{25} W Hz^{-1}]	q
PLCK_G045.1+61.1	–	<0.135	<3.2	>2.4
PLCK_G080.2+49.8	–	<0.135	<1.8	>2.4
PLCK_G092.5+42.9	0.9	1.50 ± 0.16	11.2	2.35 ± 0.11
PLCK_G102.1+53.6	–	<0.149	<2.5	>2.5
PLCK_G113.7+61.0	3.0	1.9 ± 0.14	6.9	2.2 ± 0.08
PLCK_G138.6+62.0	2.7	2.01 ± 0.16	7.3	2.1 ± 0.08
PLCK_G145.2+50.9	–	<0.144	<3.9	>2.8
PLCK_G165.7+67.0	4.1	3.41 ± 0.15	10.1	2.0 ± 0.04
PLCK_G200.6+46.1	1.1	1.23 ± 0.14	6.9	1.9 ± 0.11
PLCK_G231.3+72.2	–	<0.151	<2.5	>2.5
PLCK_G244.8+54.9	3.2	2.26 ± 0.14	13.6	2.3 ± 0.06

Table 4.3: Radio continuum properties of the GEMS extracted from the publicly available catalogues of the FIRST all-sky survey at 1.4 GHz.

In Figure 4.11 we show where our sources fall relative to the local FIR-radio correlation, assuming that differential lensing between the FIR and radio synchrotron emission does not play a major role in our case. Four of our sources are brighter by up to about 0.4 dex in the radio, and fall outside the

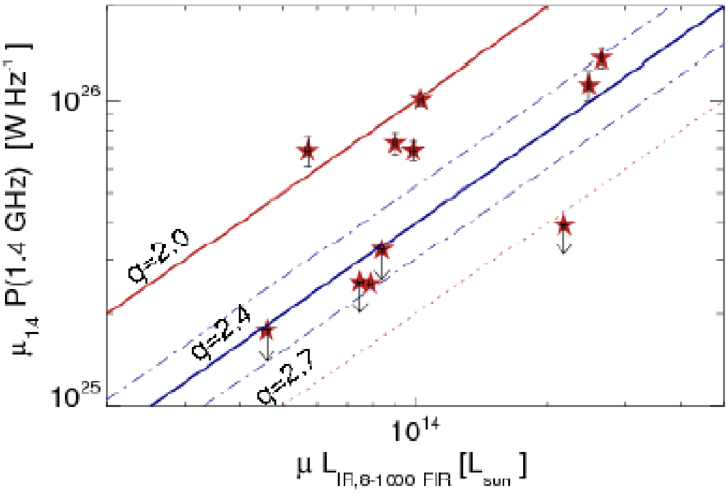

Figure 4.11: The FIR-radio correlation for the GEMS. The diagram shows the observed radio luminosities at 1.4 GHz as a function of the infrared luminosities. $\mu_{1.4}$ and μ correspond to the magnification factors appropriate for the dusty and 1.4 GHz synchrotron emission, respectively. The solid and dot-dashed blue lines show the relationship for q = 2.4 and its 1σ scatter, as found in the local universe by (Jarvis et al. 2010). The red solid line shows the same relationship for q = 2.0, either indicating radio-enhanced emission from an AGN or different ISM conditions in the host galaxies (see the text for further details). The red dotted line indicate the upper range of q parameters measured in higher redshift samples out to z $\sim$ 2.

1σ scatter around the distribution of q parameters of low-redshift galaxies. Six galaxies fall within 1σ from this relationship, however, three of these galaxies only have upper limits on q, and would fall outside the 1σ scatter if we had adopted 1σ, instead of 3σ upper limits. One galaxy has q $>$ 2.7 at 3σ.

If the 1.4 GHz emission is caused by star formation, then the lower q values cannot be caused by our assumption of the spectral index $\alpha_{1.4} = -0.8$. Only for flat radio SEDs ($\alpha_{1.4} = -0.2$ or above, which would only be possible for an AGN) would our highest-q sources be consistent with the FIR-correlation and q = 2.4. If this were the case, our sources with the highest q parameters (i.e., the brightest sources in the FIR relative to the radio) would fall well above q = 3.

One way of obtaining lower q-values, as has been pointed out several times before (Vlahakis et al. 2007; Bourne et al. 2011), is through radio emission from a central AGN. This has an interesting theoretical aspect, since it has been proposed (e.g., Silk & Norman 2009) that gas compression caused by expanding radio sources in massive high-redshift galaxies may in fact contribute to boosting the star formation efficiency in intense high-redshift starbursts. However, although contamination with nuclear radio emission may be a particular concern for stacking analyses (where one or a few relatively bright radio sources may affect the average result of the overall sample), in our case this explanation seems to be less likely. First, the radio sources are spatially resolved in FIRST, suggesting they are extended, just like the star formation. Even if the Dusty GEMS have extended radio sources, the gravitational lensing would need to amplify the radio emission by similar amounts to that of the star formation in most of our sources; this appears relatively unlikely, given that the AGN radio morphologies of high-z galaxies are very different from those of the dust and stellar components (Sajina et al. 2007).

As a second counter argument, our SED fits have already disfavoured the presence of very luminous AGN. Although galaxies are known to host central radio sources without bright bolometric emission, the host galaxies of such AGN tend to have little dust, gas, and on-going star formation. And although relatively faint AGN may be present without leaving strong signatures in the dust SEDs, only a subset of those should be radio loud. Even optimistic results (e.g., from Sajina et al. 2007), imply that only up to about 30% of dusty high-z starburst galaxies may host moderately bright ($P_{1.4} \sim 10^{25}$ W Hz^{-1}, comparable to our sources for magnification factors of order 10) nuclear radio sources that are as bright as or brighter than the star formation itself. In addition, these sources are classified as AGN in the mid-IR. We note that we have not found any obvious trends between the q-parameter and possible probes of AGN contamination like dust temperature or $L_{\rm FIR}$. We also do not find a correlation between the flux density at 22 μm and the 1.4 GHz radio emission.

As an alternative, the offsets towards larger and smaller q-parameters may be caused by the star-forming environments themselves. Lacki & Thompson (2010) suggest that enhanced synchrotron emission from cosmic rays in star-forming galaxies at high redshift could be one outcome of the strong turbulence observed in these galaxies (Förster Schreiber et al. 2009; Lehnert et al. 2009; Swinbank et al. 2011), which enhances the scale height of the gas, and lowers their volume density. In this case, energy loss of cosmic rays through synchrotron radiation, bremsstrahlung, and other processes could be either enhanced or diminished, depending on the local magnetic fields and density distribution of the ISM; this could either decrease or increase the energy losses of the cosmic rays, making our sources either brighter or fainter (Murphy 2009). Other possible explanations, which might also involve the sources with unusually high q-parameters, include evolution in the dust properties, the age of the starburst (the radio should not probe starbursts with ages of less than a few times 10^7 yr or greater than a few times 10^8 yr, because of the timing of core-collapse supernovae, Bressan et al. (2002), and a top-heavy initial mass function (Baugh et al. 2005). It will be interesting to obtain high-resolution centimetrewave maps of these sources, along with our gas and dust interferometry, to constrain the potential impact of differential lensing and to further elucidate how the q-parameter depends locally on the ISM properties in our sources.

4.7 Probing the integrated Schmidt-Kennicutt law in the GEMS

4.7.1 Integrated star formation law in the GEMS

We probe the integrated starvformation law in the GEMS through the relationship between the FIR luminosities and the CO line luminosities. This diagram only uses empirical quantities and can be directly related to the integral form of the Schmidt-Kennicutt law for the following reasons. Firstly, the FIR luminosity is a robust proxy of the star formation rate because it traces the warm dust heated by the most recent generation of newly born stars (Kennicutt 1998). Secondly, we saw in §4.5 that the CO line luminosity is commonly used as proxy of the total molecular gas mass. Our integrated values of $L_{\rm FIR}$ and $M_{\rm H_2}$ are shown in Figure 4.12 and compared with the two correlations found by Daddi et al. (2010) and Genzel et al. (2010) for low and high-redshift starburst and main-sequence galaxies. Considering the observed properties uncorrected for gravitational magnification, the 11 GEMS fall closer to the upper starburst line than the lower main-sequence one. Moreover, we illustrate the influence of the lensing magnification by showing the intrinsic luminosities expected for fiducial magnification factors $\mu = 10$ and $\mu = 50$. This broad range is supported by the results of our first lensing models and should cover the whole spectrum of magnification factors in the sample. Given that both quantities in the diagram depend linearly on μ, the position of our sources relative to each correlation is not altered. We even observe that, after correcting for the strong lensing effect, the GEMS slightly deviate from the average position of ordinary, but nonetheless very intensely star-forming galaxies on the main-sequence (Elbaz et al. 2011). Their intrinsic integrated quantities therefore suggest star formation rates and intensities typical of high-redshift starbursts.

This conclusion is reinforced by the low AGN contribution measured with our unresolved photometry, from the MIR to the radio (§4.4). Consequently, powerful AGNs do not seem to play a dominant role for the dust heating, at least in the most strongly magnified regions. We therefore expect that this component does not substantively bias the results. Moreover, since several studies have suggested

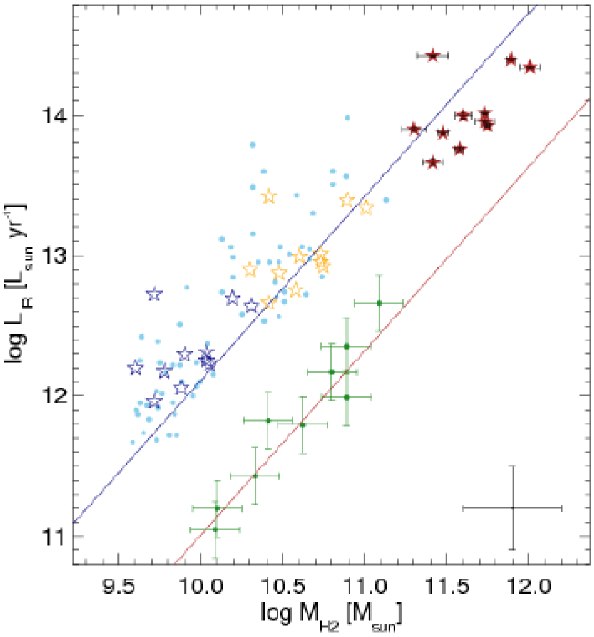

Figure 4.12: Infrared luminosities as a function of molecular gas mass for our sources. Red, yellow, and purple stars indicate the brute measurements (before delensing), and the same values corrected by fiducial magnification factors of 10 and 50, respectively. The gas masses are derived with the classical ULIRG conversion factor $\alpha_{CO} = 0.8$ $M_{\odot}/(\text{K km s}^{-1}\text{ pc}^2)$. The blue and red line indicate the relationships for low and high-redshift starbursts and main-sequence galaxies from Daddi et al. (2010) and Genzel et al. (2010). The light blue dots show low and high-redshift ULIRGs and SMGs, and the filled dark green dots with error bars are BzK galaxies at z $\sim$ 2 (both from the samples of Daddi et al. 2010). Error bars on the lensed quantities include the measurement uncertainties.

similar spatial distributions for the dust and mid-J CO emission in high-redshift intense starbursts, our L_{FIR} and M_{H_2} estimates should not be significantly affected by differential lensing effects. However, we remind that the integrated quantities measured in this chapter necesarily correspond to small, particularly magnified regions in the source plane of our high-redshift galaxies. These regions are selectively amplified according to the lensing configurations. Thus, the integrated gas and dust properties may not represent the global, large-scale properties of the galaxies (Serjeant 2012).

Exploring the resolved Schmidt-Kennicutt law between the molecular gas mass surface density and the star formation rate surface density requires high-resolution interferometry, both for the dust continuum and for a set of CO transitions. On-going follow-up programs will extend this characterization to the most interesting sources in the sample. In particular, this will provide more detailed constraints to determine whether the "starburst" classification suggested by the integrated law is unique, or whether each individual GEMS involve a wide range of star formation efficiencies. In Chapter 7, I will focus on the resolved properties and star formation mechanisms of G244.8, the brightest source in the sample.

4.7.2 Gas consumption timescales and star formation efficiencies

Our FIR luminosities and gas masses allow to constrain the gas depletion timescale in the GEMS, defined as $t_{dpl} = M_{gas}/SFR$ if we neglect the gas fraction returned to the ISM by stars at the end of their life. This quantity determines the approximate time during which the star formation can be maintained with the current intensity, before consuming the molecular gas reservoirs. It is independent from the magnification factor μ. Assuming that the measured SFRs are constant, we find gas depletion timescales of $t_{\mathrm{dpl}} = 5 - 60$ Myr. This is significantly shorther than the values of ∼100 Myr derived in the resolved molecular clumps of the intensely star-forming lensed source SDP.81 (Hatsukade et al. 2015). In addition, Genzel et al. (2010) find a timescale increasing from 0.5 Gyr to 1.5 Gyr between $z \sim 2$ and $z \sim 0$ in a representative sample including both normal star-forming galaxies and starbursts. Furthermore, Greve et al. (2005) place a lower limit of 40 Myr on the gas depletion timescale of unlensed SMGs. We obtain significantly lower results, which are also significantly lower than the typical stellar age of DSFGs (a few times 10^8 yr, Smail et al. 2004; Lapi et al. 2012).

We also define the star formation efficiencies (SFE) as the inverse of the gas depletion timescales (Young et al. 1996)[5], to describe the rate at which the stars form out of a given gas content. This quantity is fundamental to have better a understanding of the single or multiple modes of star formation. The SFE of local ULIRGs lies in the interval 180 ± 160 $L_{\odot}$ $M_{\odot}^{-1}$ (Danielson et al. 2011). Moreover, observational studies suggest that the SFE of starbursting local ULIRGs and high-redshift SMGs is about 4-10 times greater than in normal star-forming disks (Bouché et al. 2007; Genzel et al. 2010). This enhanced efficiency would mean that, during a short period, stars would form at a significantly higher rate in starbursts, for the same gas mass surface density. Genzel et al. (2010) suggest that it is either due to a top-heavy IMF or star formation driven by major mergers. In the latter scenario, global dynamics would compress the gas clouds much more than in normal disks. This would lead to an increase of the fraction of dense gas and of the resulting SFE, with a fundamental limit of ~ 500 $L_{\odot}$ $M_{\odot}^{-1}$ (Scoville 2004). This again confirms that our sources have the characteristics of genuine dusty starburst galaxies placed under particularly powerful cosmic microscopes.

4.8 Related personal publication

---

[5] Some studies prefer to directly use the molecular gas mass instead of the total gas mass (Greve et al. 2005)

A&A 581, A105 (2015)
DOI: 10.1051/0004-6361/201425128

Astronomy & Astrophysics

Planck's dusty GEMS: The brightest gravitationally lensed galaxies discovered with the *Planck* all-sky survey[⋆]

R. Cañameras[1,2], N. P. H. Nesvadba[2,1,⋆⋆], D. Guery[1,2], T. McKenzie[4], S. König[5], G. Petitpas[6], H. Dole[1,2,3], B. Frye[7], I. Flores-Cacho[8,9], L. Montier[8,9], M. Negrello[10], A. Beelen[1,2], F. Boone[9,10], D. Dicken[1,2,11], G. Lagache[1,2,12], E. Le Floc'h[11], B. Altieri[13], M. Béthermin[14], R. Chary[15], G. de Zotti[10], M. Giard[8,9], R. Kneissl[16,17], M. Krips[5], S. Malhotra[18], C. Martinache[1,2], A. Omont[19], E. Pointecouteau[8,9], J.-L. Puget[2,1], D. Scott[4], G. Soucail[8,9], I. Valtchanov[13], N. Welikala[20], and L. Yan[13]

(Affiliations can be found after the references)

Received 8 October 2014 / Accepted 5 June 2015

ABSTRACT

We present an analysis of CO spectroscopy and infrared-to-millimetre dust photometry of 11 exceptionally bright far-infrared (FIR) and sub-mm sources discovered through a combination of the *Planck* all-sky survey and follow-up *Herschel-SPIRE* imaging – "*Planck*'s Dusty Gravitationally Enhanced subMillimetre Sources". Each source has a secure spectroscopic redshift $z = 2.2$–3.6 from multiple lines obtained through a blind redshift search with EMIR at the IRAM 30-m telescope. Interferometry was obtained at IRAM and the SMA, and along with optical/near-infrared imaging obtained at the CFHT and the VLT reveal morphologies consistent with strongly gravitationally lensed sources, including several giant arcs. Additional photometry was obtained with JCMT/SCUBA-2 and IRAM/GISMO at 850 μm and 2 mm, respectively. The SEDs of our sources peak near either the 350 μm or 500 μm bands of SPIRE with peak flux densities between 0.35 and 1.14 Jy. All objects are extremely bright isolated point sources in the 18″ beam of SPIRE at 250 μm, with apparent FIR luminosities of up to $3 \times 10^{14}\,L_\odot$ (not correcting for the lensing effect). Their morphologies, sizes, CO line widths, CO luminosities, dust temperatures, and FIR luminosities provide additional empirical evidence that these are amongst the brightest strongly gravitationally lensed high-redshift galaxies on the sub-mm sky. Our programme extends the successful wide-area searches for strongly gravitationally lensed high-redshift galaxies (carried out with the South Pole Telescope and *Herschel*) towards even brighter sources, which are so rare that their systematic identification requires a genuine all-sky survey like *Planck*. Six sources are above the ≃600 mJy 90% completeness limit of the *Planck* catalogue of compact sources (PCCS) at 545 and 857 GHz, which implies that these must literally be amongst the brightest high-redshift FIR and sub-mm sources on the extragalactic sky. We discuss their dust masses and temperatures, and use additional WISE 22-μm photometry and template fitting to rule out a significant contribution of AGN heating to the total infrared luminosity. Six sources are detected in FIRST at 1.4 GHz, and the others have sensitive upper limits. Four have flux densities brighter than expected from the local FIR-radio correlation, but in the range previously found for high-z sub-mm galaxies, one has a deficit of FIR emission, and 6 are consistent with the local correlation, although this includes 3 galaxies with upper limits. We attribute this to the turbulent interstellar medium of these galaxies, rather than the presence of radio AGN. The global dust-to-gas ratios and star-formation efficiencies of our sources are predominantly in the range expected from massive, metal-rich, intense, high-redshift starbursts. An extensive multi-wavelength follow-up programme is being carried out to further characterize these sources and the intense star formation within them.

Key words. galaxies: high-redshift – galaxies: star formation – galaxies: starburst – submillimeter: galaxies – gravitational lensing: strong – galaxies: formation

1. Introduction

The brightest, most strongly gravitationally lensed galaxies in the high-redshift Universe have an extraordinary potential to advance our understanding of the processes that regulate the growth of the most massive galaxies we see today. In particularly fortuitous cases, gravitational lensing from massive, intervening galaxies, or galaxy clusters not only boosts the apparent integrated brightness of high-redshift galaxies by factors up to 20–60, but also magnifies their images by similar factors while conserving surface brightness. Thereby, they allow us to study the fine spatial details of intensely star-forming high-redshift galaxies at scales much below 1 kpc, down to around 100 pc (e.g., Swinbank et al. 2010, 2011). This is more akin to the scales of individual star-forming regions in nearby galaxies than the galaxy-wide scales (of order a few kpc) with which we must otherwise content ourselves at cosmological distances.

Since the discovery of the first gravitationally lensed galaxy in the optical (Soucail et al. 1987; the first gravitationally lensed quasar had already been discovered by Walsh et al. 1979), strongly gravitationally lensed galaxies have been identified and studied in all wavebands from the ground and in space. Strongly gravitationally lensed sub-mm galaxies provide an extraordinary possibility to probe individual star-forming regions in the most intensely star-forming high-redshift galaxies. They are also very promising sources for increasing our understanding of how the deep gravitational potential well of high-redshift galaxies, their high gas fractions and gas-mass surface densities, and feedback from star formation and perhaps active galactic nuclei (AGNs) are setting the stage for the intense star formation at fine spatial

---

[⋆] Based on observations collected with the *Herschel* and *Planck* satellites, IRAM, SMA, JCMT, CFHT, and the VLT.

[⋆⋆] Corresponding author: N. Nesvadba,
e-mail: `nicole.nesvadba@ias.u-psud.fr`

detail (e.g., Danielson et al. 2011; Swinbank et al. 2011; Combes et al. 2012).

Massive, dust-enshrouded and relatively evolved high-redshift galaxies are characterized by the bright thermal infrared emission from dust heated by intense star formation during their rapid primordial growth phase. These galaxies have typical stellar and dynamical masses of a few times 10^{10-11} $M_\odot$ (Smail et al. 2004; Swinbank et al. 2006; Nesvadba et al. 2007) and form stars at prodigious rates of up to about 1000 $M_\odot$ yr^{-1}, which are unparallelled in the nearby Universe. As a population, dusty starburst galaxies may have contributed as much as about half of the total energy production from star formation at these cosmic epochs (e.g., Hauser & Dwek 2001; Dole et al. 2006).

Unfortunately, given their importance for our understanding of high-redshift star formation and galaxy growth, the high stellar and dynamical masses and short evolutionary timescales of these galaxies make them very rare on the sky. The densities of far-infrared (FIR) and submillimetre (sub-mm) selected galaxies that are bright enough to be good candidates for strong gravitational lensing are only around one every few square degrees for sources with $S_{500} \approx 100$ mJy, with large uncertainties. For example, Lapi et al. (2012) predict about 0.003–0.1 deg^{-2} for sources with $S_{500} \geq 400$ mJy on the sky, for expected maximum gravitational magnification factors of 20–30 adopted in the models. Consequently, we may expect to find only a few of these sources on the entire extragalactic sky, in accordance with models of the diffuse infrared background light (Béthermin et al. 2012). Nonetheless, at luminosities above about 10^{13} $L_\odot$ (corresponding to $S_{500} \approx 100$ mJy), they are expected to dominate the integrated FIR and sub-mm luminosity function (Negrello et al. 2007).

A major breakthrough has been the recent discovery by *Herschel*[1] and the South-Pole Telescope (SPT) of sizeable sets of strongly gravitationally lensed submillimetre galaxies, with typical magnification factors of a few. These are using the new generation of wide-field surveys (several thousand square degrees), probing in particular the range in FIR and sub-mm flux density between 100 and 200 mJy (e.g., Negrello et al. 2010; Harris et al. 2012; Vieira et al. 2013; Wardlow et al. 2013; Bussmann et al. 2013). Most gravitationally lensed sources identified in these surveys are magnified by individual massive galaxies at intermediate redshifts, producing partial Einstein rings of a few arcsec in diameter and magnification factors up to about 10. However, the number of sources identified in these surveys above flux densities of 200–300 mJy remains rather small. For example, Bussmann et al. (2013) list 30 sources with FIR fluxes in this range, with six sources above $S_{350} = 350$ mJy. So far, to our knowledge only one source with $S_{350} > 500$ mJy at 350 μm has been published by the SPT collaboration (Vieira et al. 2013). Meanwhile, the brightest source in the Bussmann et al. (2013) sample has $S_{350} = 484$ mJy.

The extragalactic *Herschel* and SPT surveys together cover about 4% of the sky, which highlights the importance of having an all-sky survey to identify high-redshift FIR and sub-mm galaxies above the 100–300 mJy regime in a systematic way. These sources are likely to be amongst the most strongly gravitationally lensed galaxies on the sky. *Planck* is the first all-sky survey in the submillimetre with the depth and spatial resolution necessary to probe the brightest, and presumably most strongly gravitationally lensed high-redshift infrared galaxies observable to us. The 90% completeness limit of the *Planck* Catalogue of Compact Sources (PCCS) corresponds to $L_{\rm IR} \approx 6 \times 10^{13}$ $L_\odot$ at $z = 2$ (Planck Collaboration XXVIII 2014). At these luminosities, even all-sky surveys may reveal only few sources (Negrello et al. 2010; Béthermin et al. 2012; Lapi et al. 2012). For example, Herranz et al. (2013) find only very few high-redshift sources in the Early Release Catalogue of Compact Sources (ERCSC) from *Planck* (Planck Collaboration VII 2011), primarily blazars. Most extragalactic sources in the ERCSC are low-redshift galaxies.

We used photometry derived from *Planck*-HFI (described in Planck Collaboration I 2014; Planck Collaboration VI 2014) to identify all compact sources in the *Planck* maps that have colours consistent with being exceptionally bright, dusty, intensely star-forming high-redshift galaxies. We then obtained FIR photometry of the most promising candidates (the "HPASSS" programme, Planck Collaboration Int. XXVII 2015, hereafter Paper I), using the Spectral and Photometric Imaging Receiver (SPIRE) on-board the *Herschel* space telescope. This sample, obtained through *Herschel* "Must-Do" Director's Discretionary Time, includes 234 of the brightest, rarest sources in the sky (one source per several tens of square degrees, Planck Collaboration, in prep.). The sample was deliberately selected to only include sources that do not fall into the large *Herschel* survey fields, and which are new to the literature. SPIRE confirms that these sources have the typical sub-mm colours of high-z infrared and sub-mm galaxies. Most of the 234 sources of the HPASSS sample are overdensities of multiple galaxies with the typical FIR colours of high-z galaxies, and only four are Galactic cirrus clouds. Another small subset are bright individual, isolated point sources in the 20″ beam of SPIRE, consistent with being exceptionally bright, presumably strongly gravitationally lensed high-redshift galaxies. An overview of the HPASSS sample is given in Paper I.

Here we present the first results of our multi-wavelength follow-up of the 11 brightest of these isolated HPASSS sources ("*Planck*'s Dusty GEMS"), which can be observed from the northern hemisphere. All have flux densities at 350 μm measured with SPIRE that are at least $S_{350} \approx 300$ mJy, well above the typical range probed by the SPT and wide-field *Herschel* surveys. The brightest source has $S_{350} = 1050$ mJy. Welikala et al. (2015) discuss another set of weaker gravitational lenses observed with *Planck* and the SPT; however, the 11 sources we discuss here were previously unknown and are substantially brighter. Another source, PLCKERC857 PLCK_G270.59+58.52, taken from the ERCSC, which also satisfies our selection criteria and fortuitously falls into the H-ATLAS survey area, has already been discussed by Fu et al. (2012), Herranz et al. (2013), and Bussmann et al. (2013). HLS 091828.6+514223 at $z = 5.2$ (Combes et al. 2012; Rawle et al. 2014) behind the galaxy cluster Abell 773, has been discovered independently from our survey as part of the *Herschel* Lensing Survey (Egami et al. 2010), but is also included in our *Planck* parent sample (Paper I). It forms a 1.5″, near-complete Einstein ring with a magnification factor of 9 ± 2 (Rawle et al. 2014).

Our present analysis has three main goals. Firstly, we determine spectroscopic redshifts and provide empirical evidence from millimetre photometry and spectroscopy that these are indeed high-redshift sources, which owe their exceptional brightness in the submillimetre to strong gravitational lensing. We also show ground-based near-infrared (NIR) imaging, illustrating that the sub-mm sources lie behind overdense regions in the intermediate-redshift Universe. Secondly, we characterize their global dust and star-formation properties and show that their observed FIR emission is dominated by star formation, not by

---

[1] *Herschel* is an ESA space observatory with science instruments provided by European-led Principal Investigator consortia and with important participation from NASA.

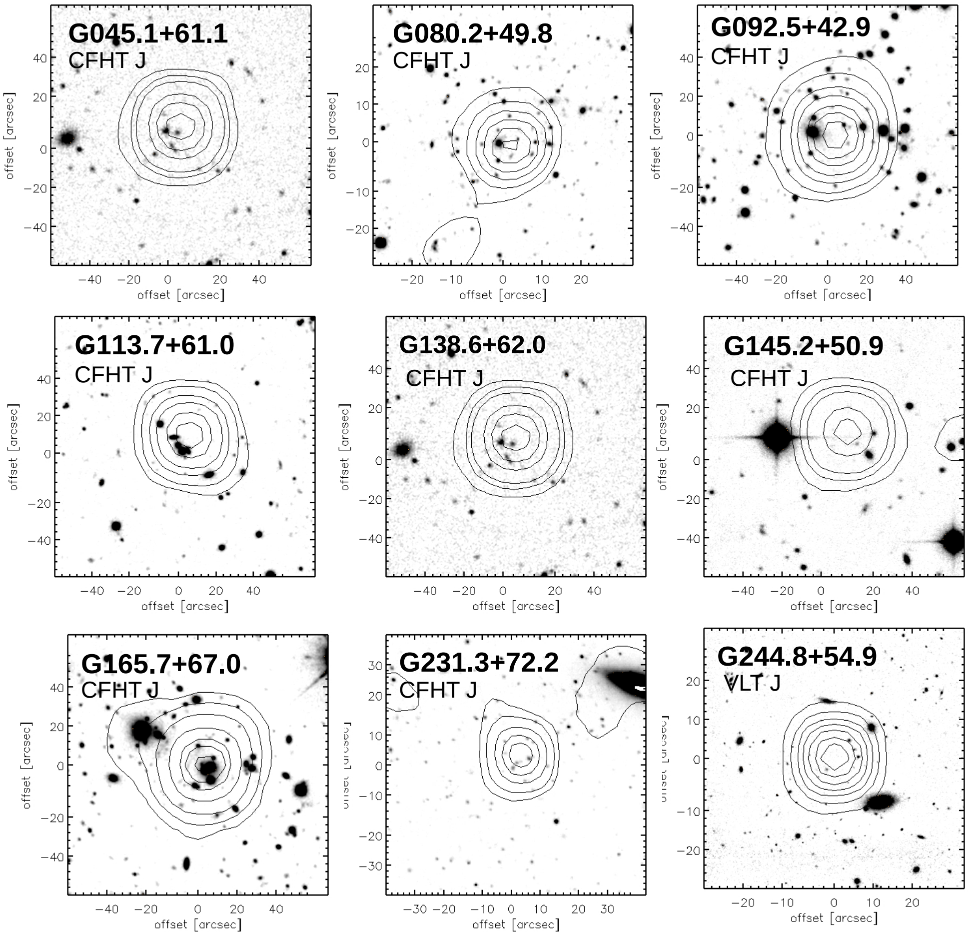

Fig. 1. Near-infrared *J*-band images of the nine sources for which we already have optical/NIR imaging and millimetre interferometry (Fig. 2). Contours show the *Herschel-SPIRE* morphology at 250 μm.

powerful obscured quasars. Thirdly, we estimate molecular gas masses from their CO line emission, calculate dust-to-gas mass ratios, and use their FIR luminosities and molecular gas mass estimates to show that they are more akin to very rapidly forming "starburst" galaxies, than the more gradually, but still intensely star-forming high-redshift galaxies on the "main sequence" (e.g., Elbaz et al. 2011). This is the first in a series of papers about "Planck's Dusty GEMS", and for this analysis we only use parts of the comprehensive data sets we already have in hand. Subsequent publications will provide lensing model solutions, discuss the spatially-resolved properties of our sources in a number of wavebands, and use the multiple millimetre line detections to investigate the detailed gas and star-formation properties of these systems.

The outline of the paper is as follows. After the descriptions of our sample selection in Sect. 2, and our follow-up observations and data reduction in Sect. 3, we provide the redshifts in Sect. 4.2, and the FIR luminosities, dust masses and temperatures in Sect. 5. In Sect. 6 we present the evidence that our sources are very strongly gravitationally lensed galaxies, including arcsec-resolution sub-mm and millimetre interferometry of the dust emission, as well as NIR/optical imaging. In Sect. 7 we impose additional constraints from the *Wide*-field Infrared Survey Explorer, WISE and the VLA FIRST survey to demonstrate that the FIR spectral energy distributions (SEDs) of our sources are not dominated by radiation from powerful AGN, before turning to their gas and star-formation properties in Sects. 9 and 10, respectively. We summarize our results in Sect. 11. Throughout the paper we adopt a flat H_0 = 70 km s^{-1} Mpc^{-1} concordance cosmology with $\Omega_{\rm M}$ = 0.3 and Ω_Λ = 0.7.

2. Sample selection

In Fig. 1 we show 9 of our 11 newly discovered gravitational lens candidates, which are the brightest amongst our sources selected from the nominal data release of the *Planck* all-sky survey. The parent sample consists of two subsets that were identified with similar colour cuts in the 857-GHz to 545-GHz flux density ratio of $S_{857}/S_{545} < 1.5$–2. This is well-matched to the expected spectral shape of the FIR continuum of dusty starburst galaxies at redshifts $z \gtrsim 2$. Six of our sources were taken from the PCCS, which includes all sources with $S/N > 4$ at 545 GHz on the cleanest 52% of the sky (Planck Collaboration XXVIII 2014). Five sources come from a dedicated, blind search for high-redshift candidates in the *Planck* maps, which probes fainter sources in the cleanest 35% of the sky after subtracting estimates of the cosmic microwave background and Galactic cirrus emission. Table 1 lists the origin

Table 1. Mid-IR to millimetre photometry.

Source	Survey	RA (J2000)	Dec (J2000)	$z_{\rm source}$	$z_{\rm fg,sdss}$	S_{22} [mJy]	S_{250} [mJy]	S_{350} [mJy]	S_{500} [mJy]	S_{850} [mJy]	S_{2000} [mJy]
PLCK_G045.1+61.1 . .	OT2	15:02:36.04	+29:20:51	3.4	0.56^{a,b}	<5.4	161 ± 5	328 ± 6	397 ± 6	130 ± 13	13 ± 2
PLCK_G080.2+49.8 . .	OT2	15:44:32.40	+50:23:46	2.6	0.5	<5.4	220 ± 9	340 ± 6	314 ± 6	87 ± 5	7 ± 2
PLCK_G092.5+42.9 . .	PCCS	16:09:17.76	+60:45:21	3.3	0.5	<5.4	765 ± 7	865 ± 8	696 ± 7	191 ± 16	8.4 ± 0.6
PLCK_G102.1+53.6 . .	OT2	14:29:17.98	+59:21:09	2.9	0.74^{a}	8.1 ± 0.7	327 ± 4	410 ± 5	339 ± 5	. . .	5.5 ± 0.7
PLCK_G113.7+61.0 . .	PCCS	13:23:02.88	+55:36:01	2.4	0.3	6.0 ± 0.7	672 ± 7	603 ± 6	373 ± 5	108 ± 10	4 ±1
PLCK_G138.6+62.0 . .	PCCS	12:02:07.68	+53:34:40	2.4	0.4	6.2 ± 0.8	619 ± 6	664 ± 8	474 ± 6	123 ± 14	7 ±1
PLCK_G145.2+50.9 . .	PCCS	10:53:22.56	+60:51:49	3.6	. . .	<5.4	453 ± 5	719 ± 7	781 ± 8	360 ± 23	38 ±4
PLCK_G165.7+67.0 . .	PCCS	11:27:14.60	+42:28:25	2.2	0.34^{a,b}	10.4 ± 0.9	867 ± 8	753 ± 6	472 ± 5	90 ± 9	8 ±1
PLCK_G200.6+46.1 . .	OT2	09:32:23.67	+27:25:00	3.0	0.6	<5.4	209 ± 4	294 ± 4	273 ± 5	110 ± 10	7 ±2
PLCK_G231.3+72.2 . .	OT2	11:39:21.60	+20:24:53	2.9	0.1	<5.4	299 ± 4	401 ± 5	341 ± 6	111 ± 12	9 ± 1
PLCK_G244.8+54.9 . .	PCCS	10:53:53.04	+05:56:21	3.0	0.13	<5.4	1050 ± 10	1054 ± 10	777 ± 7	198 ± 11	19 ± 2
HLS-J0918^{c}		09:18:28.6	+51:42:23	5.2			85 ± 8	168 ± 8	203 ± 9	125 ± 8	15 ± 7
HATLAS-J1146^{d}		11:46:37.9	−00:11:32	3.3			323 ± 24	378 ± 28	298 ± 24	93 ± 12	38 ± 6

Notes. The columns are: source name; indication of whether the sources come from the PCCS or our own high-z selection (OT2, see Sect. 2); RA and Dec coordinates; redshift of the high-z source; SDSS redshift of the intervening foreground source; WISE 22-μm flux density; *Herschel-SPIRE* 250-μm flux density; *Herschel-SPIRE* 350-μm flux density; *Herschel-SPIRE* 500-μm flux density; JCMT/SCUBA-2 850-μm flux density; and IRAM 30-m/GISMO 2-mm flux density. (a) Spectroscopic redshift of intervening foreground source from the SDSS. (b) Multiple foreground sources at a common spectroscopic redshift near the line of sight. (c) This source has been found with the *Herschel* Lensing Survey and has previously been discussed by Combes et al. (2012) and Rawle et al. (2014). The last column lists the 1.2-mm flux density measured with MAMBO on the IRAM 30-m telescope. (d) This source from the ERCSC (Planck Collaboration VII 2011) falls serendipitously into the HATLAS field and has been previously discussed by Fu et al. (2012). The last column lists the 1.2-mm flux density measured with MAMBO on the IRAM 30-m telescope.

of each target. The second subsample will be described in detail by Planck Collaboration (in prep.). A comprehensive summary of the selection and in particular the cleaning algorithm adopted to identify this subsample is given in Paper I.

All sources were followed up with *Herschel-SPIRE* photometry at 250 μm, 350 μm, and 500 μm as part of the HPASSS survey, mostly during "Must-Do" Director's Discretionary Time, and is a subset of the sample presented in Paper I. SPIRE has about 10 times greater depth and 20 times higher spatial resolution than *Planck*, with beam FWHMs of 18″, 24″, and 35″ at 250 μm, 350 μm, and 500 μm, respectively[2]. Therefore, SPIRE can be used to identify and localize the counterparts of *Planck* sources in the same wavelength regime. We identified all potential gravitationally lensed galaxies as bright, isolated point sources in the SPIRE images, with SEDs peaking at flux densities above 300 mJy in either the 350 μm or the 500 μm band as observed with SPIRE (in the final calibration of our SPIRE maps, one source has S_{350} = 294 mJy). This is well matched to the 90% completeness limit of the PCCS of about 600 mJy (Planck Collaboration XXVIII 2014), and purposefully excludes similar sources already identified in other surveys.

We find a total of 15 gravitational lens candidates. For the purposes of this paper, we exclude the two already described in the literature (Fu et al. 2012; Combes et al. 2012, see Sect. 1), and another two that are in the far South. The source described by Combes et al. (2012) is at a higher redshift (z = 5.2) than the sources we discuss here. Apart from that, including those other sources would not change our general conclusions.

In the present analysis we discuss the 11 Northern sources that are already spectroscopically confirmed to be at high redshifts. It is worth noting that by focusing on single, very bright sources in the *Herschel* images, we may have missed sets of multiple, but fainter gravitationally lensed objects behind the same intervening structures; these we would have identified as overdensities of high-redshift infrared galaxies in the overall HPASSS sample (Paper I). Irrespective of this, given the extraordinary sky coverage of our parent sample and the brightness of our targets, six of which reach or even exceed the completeness limits of the PCCS in the 353, 545, and 857 GHz bands of 330, 570, and 680 mJy, respectively (Table 1 of Planck Collaboration XXVIII 2014), the 11 sources discussed here are likely to be amongst the brightest individual high-redshift galaxies on the sky.

3. Photometry

3.1. Herschel-SPIRE FIR photometry

We base our analysis on the *Herschel-SPIRE* photometry at 250 μm, 350 μm, and 500 μm, as well as on ground-based JCMT/SCUBA-2 850-μm and IRAM/GISMO 2-mm single-dish photometry. For sources in the range z = 2.2–3.6, this corresponds to a wavelength range 50–80 μm and 400–600 μm in the rest-frame, which cover the expected peak and Rayleigh-Jeans tail, respectively, of the warm dust emission heated by intense star formation.

Herschel-SPIRE observations were carried out between December 2012 and March 2013. The *Herschel-SPIRE* photometry was obtained using `STARFINDER` (Diolaiti et al. 2000) as part of the HPASSS survey, and is discussed in detail in Paper I. `STARFINDER` integrates over the point spread function obtained directly from the image, and is therefore more suitable for data dominated by confusion noise than classical aperture photometry. Measured flux densities are between 294 mJy and 1054 mJy at 350 μm and between 270 mJy and 800 mJy at 500 μm, respectively (Table 1). Typical uncertainties are of the order of 5–10 mJy, which is close to the confusion level in the

---

[2] See the SPIRE Handbook 2014, `http://herschel.esac.esa.int/Docs/SPIRE/spire_handbook.pdf`

maps (Nguyen et al. 2010), but only includes the measurement error, not the systematic uncertainty of 7% inherent in the SPIRE photometry. However, this has no impact on our results.

3.2. JCMT/SCUBA-2 photometry at 850 μm

The SCUBA-2 (Holland et al. 2013) data were taken between September 2012 and May 2014 in moderate conditions with individual observing times of 15 min per source. The data were reduced using a configuration file optimized for point-source calibrators using the `smurf` data reduction software package for SCUBA-2 (Chapin et al. 2013). Flux densities were extracted using aperture photometry with a 30″ diameter aperture, where the background was estimated within an annulus with inner and outer diameters of 37.5″ and 60″, respectively. Uncertainties are between 4 mJy and 21 mJy per beam. These flux densities are then corrected for missing flux density due to the aperture size by dividing by 0.85, as described by Dempsey et al. (2013). An 8% calibration uncertainty is added in quadrature to the photometric errors. The resulting 850 μm flux densities are listed in Table 1.

3.3. SMA 850 μm interferometry

All sources were also observed in the continuum with the SMA in the 850 μm band. Observations were carried out between June 2013 and June 2014. Data were taken under good to excellent conditions with $pwv < 2$ mm in shared-track mode to obtain good *uv* coverage, in spite of observing each source with less than one track; this was made possible by their extraordinary brightness in the submillimetre. Integration times per source are between 2 and 7 h. All sources but PLCK_G080.2+49.8 were observed through programme 2013B-S050 in the compact configuration, with a beam of about 2″ × 2″. PLCK_G080.2+49.8 was observed through DDT programme 2013A-S075 in the extended configuration, giving a beam of 0.8″ × 0.5″. Data were calibrated in IDL using the `MIR` package, and analysis and imaging utilized the `MIRIAD` package. A full discussion of the interferometry is beyond the scope of the present analysis, and will be presented in a subsequent publication. Here we only use the 850 μm morphologies to illustrate that these are indeed strongly gravitationally lensed galaxies. Comparison with the single-dish flux densities from SCUBA-2 suggests that we recover at least 80–90% of the total flux density, implying that we have typically not missed fainter, more extended components.

3.4. IRAM-30-m /GISMO 2-mm photometry

Two-mm continuum observations were carried out with the 30-m telescope of IRAM between 17 and 23 April with 1.3–1.7 mm of precipitable water vapour, and between 29 October and 5 November 2013, with 3.4–8.6 mm of preciptable water vapour (programmes 222-12 and 100-13).

We used the 8 × 16 pixel bolometer camera GISMO, which covers a frequency range of 140–162 GHz (Staguhn et al. 2012) in the 2-mm band. At the 30-m telescope of IRAM, GISMO covers a 1.8′ × 3.7′ field of view with a 21″ × 21″ beam. We used 2′ × 2′ Lissajous maps with a relative flux density stability of about 8%, which is optimized to obtain high signal-to-noise ratios of relatively faint objects like ours, with only a small number of bad channels. Total integration times per source were between 10 and 100 min, depending on the expected flux density of the target.

We used the `CRUSH` software package (Kovacs 2013) to reduce and calibrate individual scans, and to combine them into the final image. We used the "faint" option, which is well adapted to signals around 10 mJy, detected at signal-to-noise ratios of less than 10 per scan. We detected all targets as point sources, with S/N between 3.4 and 14.8.

3.5. CFHT and VLT optical/NIR photometry

In order to identify and broadly characterize the foreground lensing structure, we also obtained NIR optical imaging of our sample using Megacam and WIRCAM on the Canada-France-Hawaii Telescope (CFHT), and with HAWKI and FORS on the Very Large Telescope (VLT) of the European Southern Observatory (ESO). Here we use the optical imaging to highlight that our sources lie behind massive intervening structures, either galaxy groups or clusters. Observations of the overall sample are still on-going, but have already provided us with optical or NIR imaging of all but one target in at least one band. We used the `scamp` and `swarp` software (Bertin 2010a,b) to register our images relative to the USNO-B2 catalog, with a typical positional uncertainty of 0.2″–0.5″. A full discussion of these data and what they imply more quantitatively for the lensing configuration will be presented in a subsequent publication.

4. Blind spectroscopic redshift survey in the millimetre

4.1. IRAM 30 m/EMIR spectroscopy

We performed a blind redshift search in the 3-mm and 2-mm bands for all 11 targets using the wide-band heterodyne receiver EMIR at the 30-m telescope of IRAM. Following a pilot programme to measure a spectroscopic redshift of our first source, PLCK_G080.2+49.8, through regular programme 82-12 and Director's Discretionary programme D05-12, we obtained another 75 h of observing time through Director's Discretionary programme D09-12 and the regular programme 094-13 in April and June 2013. For all sources we used the WILMA and FTS backends during good to variable conditions.

Individual scans were 30 s long, and we observed sets of 12 scans followed by a calibration. Data were reduced using `CLASS` (Gildas Team 2013). We took advantage of a dedicated routine kindly provided by C. Kramer to individually correct the baselines in each of the sub-bands of the FTS backend. The full set of lines will be discussed in a subsequent publication; here we only use the lowest-J CO transition available in each source, which provides additional empirical evidence that these are strongly gravitationally lensed galaxies. The redshifts are also derived from these lines, and found to be consistent with the full set of available lines per galaxy.

4.2. Spectroscopic redshifts

To obtain a spectroscopic redshift for each source, we started with a blind line search in the 3-mm atmospheric window, which we cover almost entirely with two interleaved tunings of EMIR centred at 89.4 GHz and 97.4 GHz, respectively. We used the WILMA and FTS backends in parallel, which have band widths of about 4 GHz and 8 GHz, respectively.

We discovered a bright emission line in each source in one of the tunings in the 3-mm band (Fig. 3). Subsequently we calculated all possible redshifts compatible with the observed frequency of the line, and tested our redshift hypothesis by

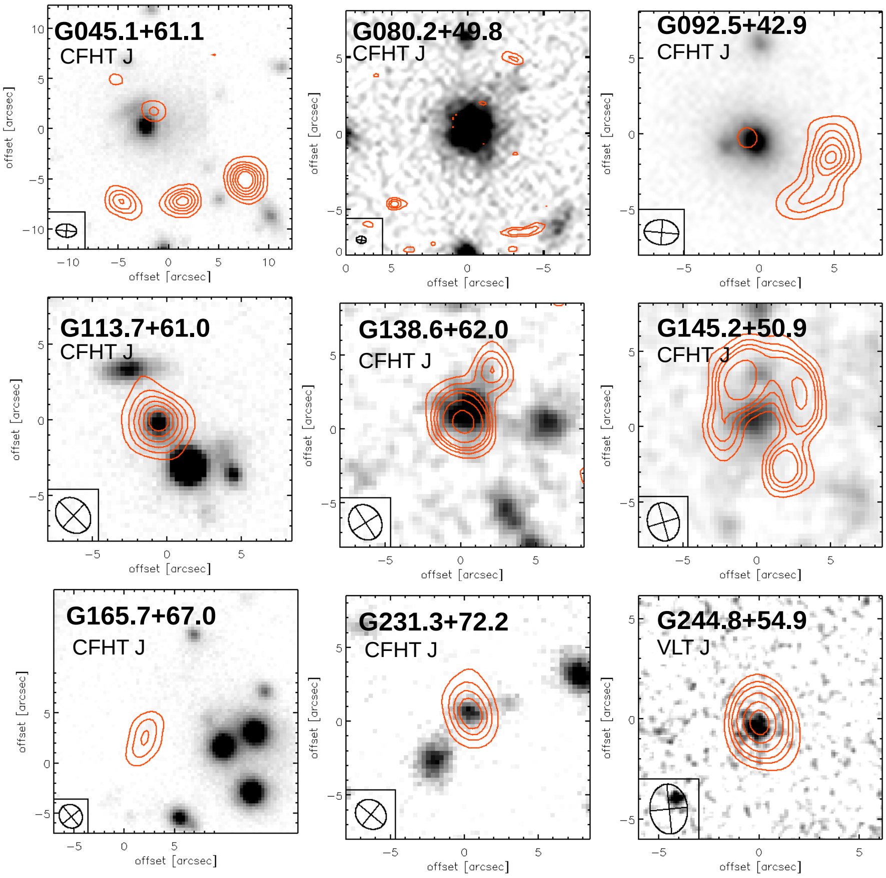

Fig. 2. Near-infrared *J*-band images of the nine sources from Fig. 1. Contours show the SMA morphology at 850 μm. The FWHM beam size of all SMA data is about 2″ (the FWHM beam size is shown in the bottom left corner of each panel), except for PLCK_G080.2+49.8, where it is 0.8″.

searching for a second line (typically CO(5–4) or CO(4–3)) at the predicted higher frequency. This required a separate frequency tuning, with the choice depending on each redshift hypothesis (typically lying in the 2-mm band). We started with the redshift that was closest to the photometric redshift derived from our SPIRE photometry, assuming a dust temperature of $T_{\rm d}$ = 30 K, which is the temperature of the dust component that dominates the FIR SED of the Cosmic Eyelash (Ivison et al. 2010b). This yielded the correct redshift in all but the two galaxies, specifically those with the highest dust temperatures (Table 2). In the end, our EMIR follow-up spectroscopy led to accurate and secure spectroscopic redshifts for all 11 targets, with 2–8 lines detected per source; this provides a wide range of constraints on the physical properties of the gas in these galaxies, which we will discuss in more detail in forthcoming papers.

Planck's Dusty GEMS fall in the redshift range of $z = 2.2$–3.6, comparable to that of radio-selected submillimetre galaxies in the field (Chapman et al. 2005), and very similar to that of gravitationally lensed sub-mm galaxies in the H-ATLAS survey ($z = 2.1$–3.5; Harris et al. 2012; Bussmann et al. 2013). The average redshift of *Planck*'s Dusty GEMS, $z = 2.9 \pm 0.4$ (we give the width of the distribution here), is somewhat lower than the redshift range of the bright gravitationally lensed sub-mm galaxies from the SPT survey. The SPT sample has a mean redshift of $z = 3.5$, obtained from at least two lines for 12 of their 26 targets, and a combination of single-line detections and FIR photometric constraints for the remaining targets (Vieira et al. 2013; Weiß et al. 2013). One reason that we probe somewhat lower redshifts may be that we select our sources at shorter wavelengths (350–850 μm, compared to 1.4 and 2.0 mm for the SPT). However, we stress that our parent sample from *Planck* does include sources with higher redshifts, such as HLS 091828.6+514223 at $z = 5.2$ (Combes et al. 2012; Rawle et al. 2014), a source we selected independently from its confirmation as a high-z source through the HLS survey. We also note that the *Planck* selection is based on 350 μm, 550 μm, and 850 μm measurements, covering somewhat longer wavelengths than the blind *Herschel* surveys. The *Planck* high-z sample has a range of FIR colours, and the redshift distribution derived from the subsample of very bright gravitational lenses does not necessarily correspond to the redshift distribution of the overall *Planck* high-z sample (HLS 091828.6+514223 at $z = 5.2$ being a case in point).

4.3. Line profiles and luminosities

Figure 3 shows the lines we detected in the 3-mm band. Many sources exhibit complex line profiles, which can also be seen in the higher frequency data (Canameras et al., in prep.). These may either originate from several, gravitationally lensed regions in the same galaxy that are blended in the large (20″) beam of

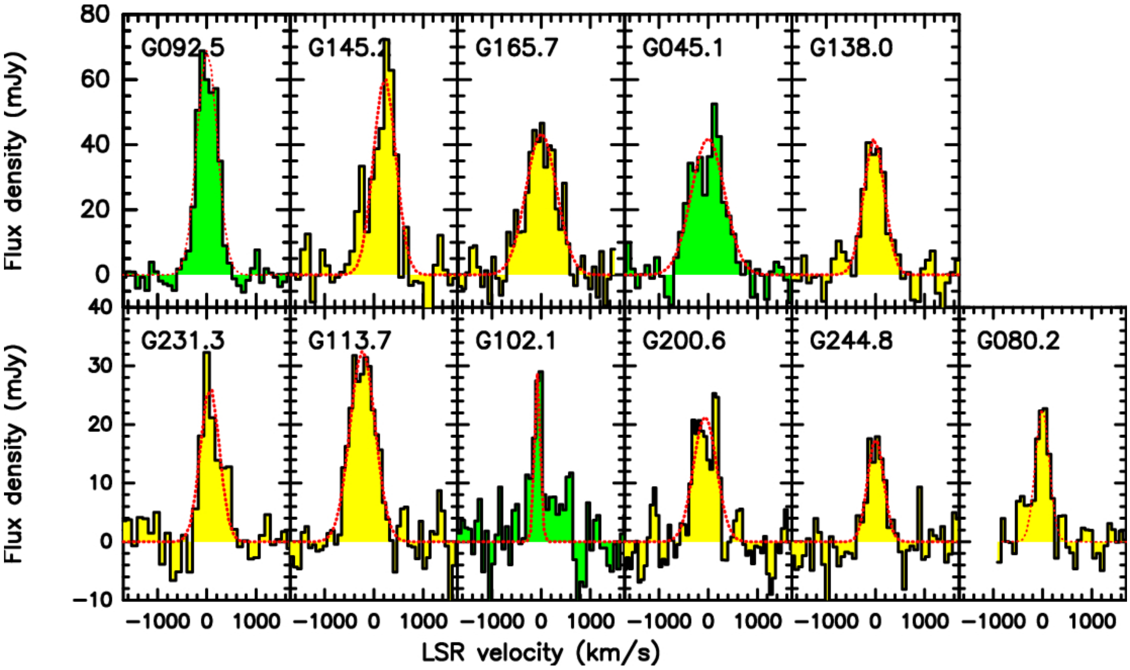

Fig. 3. Lowest-J CO emission line in each of our targets. CO(3–2) and CO(4–3) are indicated in yellow and green, respectively. Red dotted lines show simple single-Gaussian fits.

Table 2. Fitted parameters to the FIR dust continuum and dust properties.

Source	$\lambda_{\max}$ [μm]	$S_{\max}$ [mJy]	$\mu\, L_{\rm FIR}$ [$10^{13}\ L_\odot$]	$\mu\, L_{\rm FIR}^{\rm TPL}$ [$10^{13}\ L_\odot$]	$\mu\, SFR$ [$M_\odot\ {\rm yr}^{-1}$]	$T_{\rm d}$ [K]	$\mu\, M_{\rm d}$ [$10^9\ M_\odot$]	$L_{\rm FIR,AGN}/L_{\rm FIR,tot}$ [%]
PLCK_G045.1+61.1	420 ± 10	360 ± 10	8.4 ± 0.1	12.1 ± 0.1	14 462 ± 172	36.0 ± 0.5	6.5 ± 0.1	
PLCK_G080.2+49.8	370 ± 10	345 ± 5	4.6 ± 0.1	7.1 ± 0.1	7920 ± 172	33.0 ± 0.5	7.2 ± 0.2	
PLCK_G092.5+42.9	322 ± 5	900 ± 10	24.8 ± 0.2	34.8 ± 0.2	42 698 ± 344	50.1 ± 0.4	5.3 ± 0.1	10
PLCK_G102.1+53.6	333 ± 4	410 ± 5	7.9 ± 0.1	11.9 ± 0.1	13 601 ± 172	41.1 ± 0.3	4.3 ± 0.1	
PLCK_G113.7+61.0	255 ± 20	700 ± 30	9.9 ± 0.2	12.6 ± 0.1	17 044 ± 344	45.0 ± 0.4	3.5 ± 0.1	
PLCK_G138.6+62.0	305 ± 10	690 ± 5	9.0 ± 0.1	13.5 ± 0.1	15 495 ± 172	38.7 ± 0.3	6.4 ± 0.1	
PLCK_G145.2+50.9	400 ± 10	785 ± 30	21.8 ± 0.2	30.1 ± 0.2	37 533 ± 344	40.5 ± 0.4	11.0 ± 0.1	33
PLCK_G165.7+67.0	265 ± 2	875 ± 3	10.3 ± 0.1	13.4 ± 0.1	17 733 ± 171	42.5 ± 0.3	5.1 ± 0.1	
PLCK_G200.6+46.1	350 ± 3	295 ± 2	5.7 ± 0.1	8.2 ± 0.1	9813 ± 172	37.5 ± 0.5	4.3 ± 0.1	22
PLCK_G231.3+72.2	350 ± 10	402 ± 5	7.5 ± 0.1	10.7 ± 0.1	12 913 ± 172	39.3 ± 0.4	4.7 ± 0.1	
PLCK_G244.8+54.9	300 ± 2	1135 ± 2	26.5 ± 0.2	36.3 ± 0.2	45 625 ± 344	50.0 ± 0.4	5.7 ± 0.1	9

Notes. The columns are: best-fit wavelength of the peak of the blackbody in the FIR; peak flux density at $\lambda_{\max}$ of the blackbody; FIR luminosity integrated from 8–1000 μm, including the magnification factor μ from our modified blackbody fit, and neglecting the possible presence of additional, hotter dust components; FIR luminosity derived from `DecompIR`, and including the fiducial mid-IR flux from star formation (see Sect. 7); star-formation rate, including magnification factor μ; dust temperature; dust mass, including the magnification factor μ; and AGN contribution to the FIR luminosity as obtained with `DecompIR`, where such a component was found.

the IRAM 30-m telescope, or else they represent sets of nearby, perhaps interacting galaxies. Alternatively, they may represent intrinsically complex gas kinematics in single star-forming environments, driven by the interplay of galaxy rotation, feedback, or perhaps turbulent motion within star-forming regions. High-resolution follow-up interferometry is currently being analysed to further elucidate their nature.

We fitted the emission lines shown in Fig. 3 with single Gaussian profiles to obtain the line FWHMs and integrated fluxes listed in Table 3. Integrated fluxes are $I_{\rm CO} = (7{-}34)\ {\rm Jy\ km\ s^{-1}}$, for $FWHM = 213{-}685\ {\rm km\ s^{-1}}$. A detailed analysis of the spectral properties of our sources that uses all our full sets of spectral line observations and that takes into account changes in line ratios in individual, kinematically distinct emission line regions into account will be presented elsewhere. Here we only use the spectroscopic redshifts, and the fluxes and FWHM line widths of the lowest-J CO transition observed in each source in order to demonstrate that these are indeed gravitationally lensed galaxies with extreme magnification factors.

In Table 3 we also compile luminosity estimates for the CO lines that we detect. We follow Solomon et al. (1997) in translating the integrated line fluxes into CO luminosities (in brightness temperature units), setting

$$L' = 3.25 \times 10^7\ I_{\rm CO} \left(\frac{\nu}{1+z}\right)^{-2} D_L^2 (1+z)^{-3}. \quad (1)$$

Table 3. CO line properties obtained with EMIR on the IRAM 30-m telescope.

Source	Transition	Line flux $\mu\, I_{\rm CO}$ [Jy km s^{-1}]	Line luminosity $\mu\, L'$ [10^{11} K km s^{-1} pc^2]	$\mu\, M_{\rm mol}$ [$10^{11}\, M_\odot$]	*FWHM* [km s^{-1}]
PLCK_G045.1+61.1	4–3	22.9 ± 0.3	6.9 ± 0.1	5.6 ± 0.1	213 ± 11
PLCK_G080.2+49.8	3–2	9.2 ± 0.5	3.2 ± 0.2	2.6 ± 0.2	265 ± 12
PLCK_G092.5+42.9	4–3	34.3 ± 0.2	9.7 ± 0.1	7.8 ± 0.2	453 ± 3
PLCK_G102.1+53.6	3–2	5.7 ± 1.8	2.4 ± 0.7	2.0 ± 0.2	252 ± 10
PLCK_G113.7+61.0	3–2	16.5 ± 0.2	5.0 ± 0.1	4.0 ± 0.2	528 ± 5
PLCK_G138.6+62.0	3–2	22.0 ± 1.1	6.8 ± 0.3	5.4 ± 0.1	514 ± 40
PLCK_G145.2+50.9	3–2	21.9 ± 0.8	12.7 ± 0.6	10.2 ± 0.2	685 ± 17
PLCK_G165.7+67.0	3–2	25.4 ± 0.3	6.8 ± 0.1	5.4 ± 0.1	576 ± 4
PLCK_G200.6+46.1	3–2	11.2 ± 0.1	4.9 ± 0.1	3.8 ± 0.1	458 ± 9
PLCK_G231.3+72.2	3–2	9.4 ± 0.2	3.9 ± 0.1	3.0 ± 0.1	257 ± 8
PLCK_G244.8+54.9	3–2	7.4 ± 1.0	3.3 ± 0.4	2.6 ± 0.2	382 ± 10

Notes. The columns are source name; CO transition; integrated line flux; line luminosity $\mu\, L'$ (in brightness temperature units) derived using Eq. (1); molecular gas mass (see Sect. 9 for details); and full width at half maximum of the emission lines.

Here the measured frequency ν is given in GHz, z is the redshift, D_L is the luminosity distance, the CO luminosity L' is measured in K km s^{-1} pc^2, and the integrated CO line flux is in Jy km s^{-1}. In Sect. 9 we will also derive molecular gas mass estimates and compare with the dust masses obtained from our SED fitting.

5. Dust properties

To further characterize our sources, we fitted their FIR-to-millimetre photometry with modified blackbody distributions between 250 μm and 2000 μm, using the Python `curve_fit` routine from the scipy package[3]. The results are shown in Fig. 4. Most photometry points were observed with roughly similar beam sizes between 15″ and 30″, and we only see single, very bright components in each image, which makes us confident that uncertainties related to confusion and multiple sources within the same beam do not dominate our photometry. We do see the foreground lensing sources at short wavelengths, between the optical and NIR, including the blue channels of WISE. However, their relatively blue colours and locations suggest that they do not contribute significantly to the long-wavelength emission.

In the restframe of our targets, our data cover the peak of the SED and extend well into the Rayleigh-Jeans tail of the dust emission, which is a particularly clean probe of the thermal emission of the coldest dust component, dominating the overall mass budget. We followed, e.g., Blain et al. (2003) to allow for a frequency-dependent optical depth of the FIR emission, which we model in the standard way through a power law with emissivity index $\beta = 2.0$ and a critical wavelength of 100 μm, at which the dust opacity becomes unity. This specific choice of β is somewhat arbitrary, but at the signal-to-noise ratio and sparse frequency sampling of our SEDs, the precise value has a minor impact (for plausible values of β between 1.5 and 2.0) for our study. For example, we find typical offsets in dust temperature $\Delta T_{\rm d} \approx 2$ K between $\beta = 1.5$ and $\beta = 2.0$, comparable to our other uncertainties.

These fits correspond to dust temperatures of $T_{\rm d}$ = 33–50 K, with no significant trend with redshift (Table 2). Uncertainties were derived from Monte Carlo simulations, where we varied the measured flux density in each band 1000 times within the measurement uncertainties, before fitting the SED in the same way as for the data.

The high infrared luminosities and dust temperatures of *Planck*'s Dusty GEMS suggest that most of the radiation in our sources comes from dense star-forming clouds, which is why we consider the optically thick case more relevant to our analysis. We note, however, that had we fit for optically thin emission, we would have derived temperatures between $T_{\rm d}$ = 30 K and 41 K, lower by 3 K to 11 K in each individual source. Figure 4 shows that all sources are adequately fit with a single temperature component, in spite of a slight, systematic underestimate of the 850 μm, or alternatively, slight overestimate of the 500-μm flux density.

The temperature range we find does not differ significantly from those of other strongly lensed samples of high-redshift dusty star-forming galaxies selected in the FIR and (sub-)mm. This is illustrated in Fig. 5. It is interesting that the temperature range of our sources includes those of typical starburst galaxies at high redshift, as well as the lower temperatures of more gradually, but still intensely, star-forming galaxies along the main sequence (e.g., Elbaz et al. 2011). We do not find an obvious trend of dust temperature with redshift. This may either be due to the small number of targets observed over a relatively small redshift range, or because we are sampling environments with a range of properties within individual galaxies.

We derive infrared luminosities by integrating over our best-fit single-component modified blackbody SEDs between 8 μm and 1000 μm in the rest-frame, using the flux densities given in Table 1 and dust temperatures in Table 2. Luminosities thus obtained are in the range $L_{\rm FIR} = (4.6{-}26.5) \times 10^{13}\, \mu^{-1}\, L_\odot$, including the unknown gravitational magnification factor μ. Following Kennicutt (1998) we set $SFR[M_\odot\, {\rm yr}^{-1}] = 4.5 \times 10^{-37}\, L_{\rm FIR}$ [W], finding star-formation rates SFR = 8000–46 000 $\mu^{-1}\, M_\odot\, {\rm yr}^{-1}$, suggesting high intrinsic star-formation rates and high magnification factors. Corresponding apparent dust masses are $M_{\rm d} = (3.5{-}11) \times 10^9\, \mu^{-1}\, M_\odot$ (Table 2).

Figure 4 shows that we cover the peak of the dust SED for most sources, but nonetheless our sensitivity to warmer dust components probed in the FIR shortwards of 250 μm (60–80 μm in the rest-frame) is limited, and we are likely to miss emission from warmer dust components. Through template fitting with `DecompIR` (Mullaney et al. 2011), which we will further discuss in Sect. 7, we derived fiducial correction factors between the modified blackbody fits obtained here, and the templates

---

[3] http://docs.scipy.org/doc/scipy/reference/generated/scipy.optimize.curve_fit.html

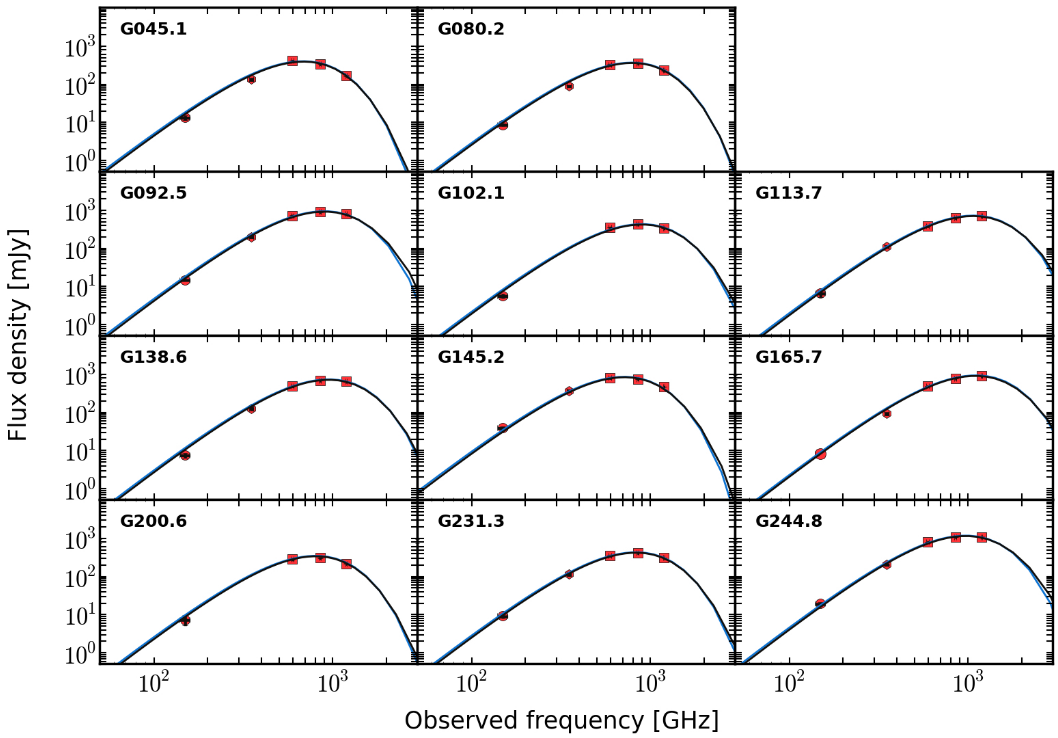

Fig. 4. Modified blackbody fits to the FIR-to-millimetre photometry of our sources as obtained with *Herschel-SPIRE* at 250, 350, and 500 μm, with JCMT/SCUBA-2 at 850 μm (for eight sources), and with IRAM/Gismo at 2 mm. The light and dark blue curves show the blackbody curves for optically thin and optically thick dust, respectively. Error bars are printed in black, and are smaller than the symbols showing the photometric data points.

we used to accommodate our FIR-to-submillimetre photometry (and constraints from WISE at 22 μm within the same SED fit). We thus find that our modified blackbody fits may underestimate the IR luminosity of our targets by 10–30%. We also list the respective values obtained from `DecompIR` in Table 2. Taken together, the direct estimate from the modified blackbody fits, and those from the templates, set a plausible range of luminosities. These luminosities would need to be corrected towards larger values if an additional warmer dust component was found with infrared constraints shortward of 250 μm.

We follow, e.g., Greve et al. (2012) in estimating dust masses, $M_{\rm d}$, by setting

$$M_{\rm d} = \mu^{-1} \frac{D_L^2 S_{\nu_0}}{(1+z)\kappa_{\nu_{\rm r}}} \left(B_{\nu_{\rm r}}(T_{\rm d}) - B_{\nu_{\rm r}}(T_{\rm CMB}(z))\right)^{-1} \qquad (2)$$

where D_L is the luminosity distance to redshift z, S_{ν_0} the flux density at the observed frequency $\nu_{\rm r}(1+z)^{-1}$, which we set to 600 GHz (corresponding to the 500 μm band of `SPIRE`). $T_{\rm CMB}$ is the CMB temperature at redshift z. We used $\kappa_{\nu_{\rm r}} / \left(m^2\,{\rm kg}^{-1}\right) = 0.045 \times (\nu_{\rm r}/\ 250\ {\rm GHz})^{\beta}$, with $\beta = 2.0$ as already stated above. With this approach and these assumptions, we find dust masses of $M_{\rm d} = (3.5-11)\times 10^9\ \mu^{-1}\ M_{\odot}$, with the unknown gravitational magnification factor μ. Results for individual sources are listed in Table 2.

6. Signatures of gravitational lensing

6.1. Flux densities and morphologies

The first observational hint that our targets might indeed be strongly gravitationally lensed galaxies is their sheer brightness and small angular size below 18″ (the FWHM of the SPIRE point spread function at the highest frequency, 250 μm), whereas 90% of the 234 Planck high-z candidates with *Herschel-SPIRE* follow-up consist of multiple sources. Unlensed high-redshift galaxies with FIR flux densities as high as those of our sources are very rare. For example, for flux densities $S_{350} >$ 400 mJy at 350 μm and near the peak of the FIR SEDs of most GEMS, the Béthermin et al. (2012) models predict 3 sources sr^{-1} at $z \geq 2$ that are not, and 53 sources sr^{-1} that are gravitationally lensed. For a given source at these flux densities, it is therefore much more likely to find a gravitationally lensed galaxy than a galaxy in the field. We emphasize that this is true only for galaxies with confirmed high redshifts like the GEMS. The overall population of bright FIR galaxies is at much lower redshifts and has bluer FIR colours.

Given that more typical high-z galaxies in the field have FIR flux densities of few 10s mJy, the observed flux densities of our sources make us expect magnification factors of at least a few and perhaps greater than 10, even if these were intrinsically amongst the most luminous sources on the sky. For more moderate, more typical intrinsic flux densities, the gravitational magnification would be accordingly higher. The one alternative interpretation could be that these are multiple, highly concentrated galaxies within projected distances of a few tens of kpc, so that they are not resolved into individual galaxies by the SPIRE beam, which corresponds to about 120 kpc at $z \approx 2$ (for an example see Ivison et al. 2013).

More direct evidence that our sources indeed have a lensing nature comes from their morphologies. Strongly gravitationally lensed galaxies may either be single or multiple compact images seen near the intervening foreground lensing source, giant arcs extending over several arcseconds, or even partial or complete Einstein rings. However, reaching the required spatial resolutions of about 1–2″ or better requires either deep optical or NIR imaging for sources that are not too heavily obscured, or, alternatively, sub-mm or millimetre interferometry.

Figure 1 shows the *Herschel* image as contours overlaid on optical imaging, and Fig. 2 the dust morphology obtained with the SMA at 850 μm. These figures clearly show that our sources are either single, compact objects at 2″ resolution (as is the case for, e.g., PLCK_G244.8+54.9 and PLCK_G138.6+62.0), or giant arcs (e.g., PLCK_G145.2+50.9 and PLCK_G080.2+49.8). PLCK_G244.8+54.9 and PLCK_G138.6+62.0 have flux densities of 1054 ± 10 and 664 ± 8 mJy, respectively, making it implausible that these are individual high-redshift galaxies if not benefitting from a strong boost from gravitational lensing through a massive foreground source. At a 2″ beam, intrinsic source sizes of unlensed galaxies would be at most 16 kpc, making it implausible to see a small group of high-redshift galaxies within a single beam.

Our sources are associated with overdensities of massive intervening galaxies at intermediate redshift, either galaxy groups or clusters. Table 1 lists the redshifts of the brightest intervening galaxies along the line of sight to our targets, which were taken from the SDSS. They are either photometric redshifts or (in a few individual cases highlighted in Table 1), spectroscopic redshifts. A detailed analysis of the lensing structure based on our own proprietary optical/NIR photometry obtained at the CFHT and the VLT is on-going. The only target associated with a foreground object for which we currently have no good redshift estimate is G145.2+50.9, which forms a near-complete Einstein ring with a diameter of 10″ around a very red foreground source, which we currently only detect in the J-band. For this galaxy, our optical/NIR photometry is not yet complete, and we must therefore defer a detailed analysis of the foreground source to a later publication.

In the rest of this section we will present additional empirical evidence to illustrate that all of our sample consists of strongly gravitationally lensed galaxies, including those for which we do not yet have morphological constraints.

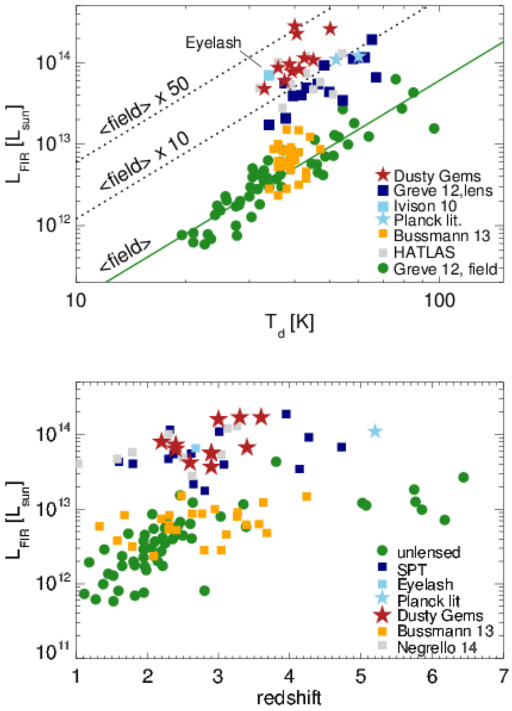

Fig. 5. Characterizing our sources by their FIR luminosities, dust temperatures, and redshifts. *Top*: FIR luminosities versus dust temperatures. The Dusty GEMS targets are shown as red stars on top of the comparison samples of strongly lensed sources taken from the literature (see Greve et al. 2012, and references therein), lens candidates from the SPT survey (Vieira et al. 2013), the Eyelash (Ivison et al. 2010b), and the two *Planck* lenses that were discovered prior to our work (Combes et al. 2012; Fu et al. 2012). The solid line shows a fit to the general population, while the dotted lines show magnification factors of 10 and 50. *Bottom*: FIR luminosity as a function of redshift. In the lower panel, our sources fall near the most luminous gravitationally lensed galaxies at similar redshifts; however, these are strongly dominated by AGN, like APM 08279+5255, whereas our sources are bona fide starbursts, at least in the image plane. This explains the greater luminosities at lower dust temperatures seen in the top panel.

6.2. FIR dust continuum

Greve et al. (2012) suggested the use of the relationship between T_d and L_{FIR} as an empirical indicator of whether a source is strongly gravitationally lensed. According to the Stefan-Boltzmann law, the luminosity emitted by a modified blackbody at a given temperature depends only on the size of the emitting surface and the emissivity. Therefore, if our galaxies form a subset of the generic population of dusty, intensely star-forming high-redshift galaxies, the gravitational magnification factor should lead to an apparent increase in dust luminosity at a given temperature for gravitationally lensed galaxies, compared to unlensed galaxies.

In Fig. 5 we show where our sources fall on a plot of dust temperature versus FIR luminosity, compared to the galaxies of Greve et al. (2012) and other sources from the literature. It is immediately clear that our sources are significantly brighter at a given temperature than galaxies in the field, and even brighter than most of the previously known gravitationally lensed galaxies. The dashed lines illustrate luminosities that are 10 times and 50 times brighter than expected from a simple least square fit to the population of field galaxies (green solid line). We highlight the Cosmic Eyelash of Swinbank et al. (2010) and the two previously confirmed gravitationally lensed galaxies with *Planck* counterparts (Fu et al. 2012; Combes et al. 2012).

For a more explicit, although not necessarily very precise estimate that exploits this relationship between dust temperature, luminosity, and source size, we can use the Stefan-Boltzmann law directly to infer the magnification factor from the observed luminosity and dust temperature. The approach is described in detail in Greve et al. (2012). Given the somewhat higher dust temperatures of our lens candidates compared to the SPT sources of Greve et al. (2012), we have a larger range of “effective” Stefan-Boltzmann constants (which correct for the lower emissivity of a modified relative to a genuine blackbody), $\sigma_{\rm eff}/\sigma = 0.5$–$0.65$, and apparent emitting surfaces that are between 8 and 40 times larger than those of typical FIR galaxies, implying magnification factors that are roughly similar. These results are also shown in Fig. 6. We note that the estimates are very uncertain, since they assume that each high-redshift galaxy has a similar emissivity, that the dust becomes optically thick at similar wavelengths, and that the interstellar medium (ISM) of the galaxies is dominated by a uniform dust component with a single temperature. Each of these assumptions can only be approximately true, and this will lead to uncertainties of at least factors of a few in this estimate. This is illustrated by the magnification factor of about 10 of the "Cosmic Eyelash," which we constrained with the same approach, and which falls into a very similar region of the diagram as our sources. The "Cosmic Eyelash" has intrinsic magnification factors of 20−60 (Swinbank et al. 2011), with an average factor of 32.5. In spite of these caveats, Fig. 5 provides additional indirect support that our sources are indeed strongly gravitationally lensed galaxies.

6.3. Molecular gas lines

More empirical evidence for strong gravitational magnification of our galaxies comes from the emission-line properties that we measured with EMIR on the IRAM 30-m telescope. To demonstrate that their galaxies discovered through the H-ATLAS survey are indeed strongly gravitationally lensed, Harris et al. (2012) compared the CO(1–0) line luminosities L' and FWHMs of their galaxies with the sources of Bothwell et al. (2013), who had found a broad trend between luminosity and line width in galaxies in the field (Fig. 6). The galaxies of Harris et al. (2012) and other strongly gravitationally lensed galaxies from the literature stand out by 1–2 orders of magnitude above this relationship, owing to the boost in line luminosity by the gravitational lens. In contrast, lines are expected to be as broad as in field galaxies (or narrower, because smaller regions of the large-scale velocity field of the galaxy are being observed). If a small region in a galaxy is magnified by strong gravitational lensing, then only parts of the rotation curve will be sampled, and turbulent motion will also be smaller. Therefore, observed line widths should be narrower than if galaxy-wide radii are probed, as in field galaxies.

Figure 6, inspired by Fig. 7 of Harris et al. (2012), shows where our sources fall relative to the Harris et al. sample and those in the literature. Our sources span a large range in FWHM in this diagram, but are all clearly within the regime of gravitationally lensed galaxies. The FWHMs of some of our targets may be as large as those of overdensities of multiple lensed sources that are at best moderately gravitationally lensed like the example in Ivison et al. (2013). Their luminosities are factors of a few brighter, placing them firmly above the field galaxies, and into the lens regime. The example of the Cosmic Eyelash, which has a magnification factor of 20–60 shows however that the lensing factor derived from the position of a source in this diagram can only be an approximate indicator. The line luminosities and profiles provide additional evidence in support for the lensing hypothesis.

7. Dust heating and AGN content

Many dusty high-z starburst galaxies host powerful AGN. For example Alexander et al. (2005) find that 75% of submillimetre galaxies have AGN detected at X-ray wavelengths (but see also Laird et al. 2010, who find significantly lower fractions of 10–20%). Powerful, obscured AGN could contribute significantly to $L_{\rm FIR}$, which would lower the magnification factors that are needed to explain the extraordinary apparent brightness of our targets. The inferred dust temperatures of our sources are akin to those of other high-z starburst galaxies and would be very low compared to those of obscured quasars, which are typically above 70 K, often far above. However, our estimates may be biased towards low temperatures because of the absence of mid-IR constraints shortward of 50–80 μm in our data sets. This makes it worthwhile to investigate in more depth what the possible AGN contribution might be to the infrared luminosity budget of our targets.

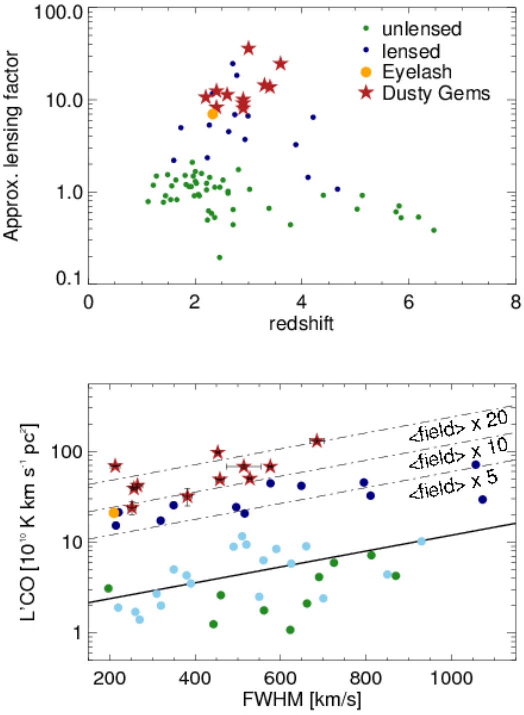

Fig. 6. *Top*: order-of-magnitude estimate of the gravitational magnification factor derived from the dust temperature and FIR luminosity of our sources compared to FIR and sub-mm galaxies in the field (see Sect. 6.2 for details). *Bottom*: CO emission-line luminosity as a function of FWHM line width, using the same symbols as in the top panel, with additional light blue dots showing those sources of Bothwell et al. (2013), which are neither gravitationally lensed nor AGN hosts. The solid and dashed lines show the best linear fit to the sample of field galaxies, as well as shifts of this line corresponding to magnification factors of 5, 10, and 20. Error bars show the 1σ uncertainties of our single-component Gaussian line fits.

Not all AGN play a significant role for the total infrared luminosity budget of their host galaxies. Ideally, searching for obscured AGN activity in our targets would require PACS or at least deep *Spitzer* 24-μm photometry, to sample the dust SED shortward of about 100 μm in the rest-frame. Since our sample was only discovered with SPIRE in the last weeks of the *Herschel* mission, such data sets are not available. Additionally, in spite of their exceptional brightness (for high-redshift targets), they are still too faint to obtain robust mid-IR photometric constraints with SOFIA. We might therefore not be able to give tight constraints on the presence of weak AGN activity in all of our sources, however, most important for our purposes here is to show that AGN radiation is not energetically dominant in our sources (i.e., they do not contribute >0.5 $L_{\rm bol}$), which would have important implications for the estimated star formation rates, plausible ranges of intrinsic infrared luminosities, and gas excitation.

7.1. WISE 22 μm photometry

WISE in the 22-μm band covers rest-frame wavelengths between 4 and 7 μm for our sources, i.e., the far blue tail of hot dust emission from powerful AGN. Consequently, WISE has been successfully used to identify heavily obscured AGN at high-z (e.g., Yan et al. 2013). All of our sources are bright enough to be detected in WISE imaging at 22 μm, and seven are included in the WISE catalogues. The remaining four can be seen as very faint sources in the WISE images, but are not bright enough to obtain robust flux measurements. We will in the following use the flux measurements from the WISE catalogs and treat the 5σ rms of this catalog at 5.4 mJy as upper limit for the fainter sources. Individual flux densities are listed for all sources in Table 1.

Although we do detect nearby bluer sources in each case at 3.4 μm, 4.6 μm, and 12 μm, the SED in all but one source falls off too steeply in the three blue WISE bands to contribute significantly to the 22 μm detections. Their colours suggest that these are low-to-intermediate-redshift objects, which we consider part of the intervening lensing structure.

7.2. Constraining AGN dust heating with `DecompIR`

We used the publicly available package `DecompIR` (Mullaney et al. 2011) to constrain the potential contribution from AGN emission to the infrared SED, using our six available data points between 22 μm and 2 mm, as listed in Table 1. `DecompIR` performs χ^2 fits to infrared SEDs using composites of empirically constructed templates of starburst galaxies and AGN. We only have six photometric data points, but we sample the Rayleigh-Jeans tail and the peak of the SED of the emission from the coldest dust component, and therefore constrain the most abundant dust component well. We have spectroscopic redshifts and hence can estimate robust dust temperatures, and therefore we consider this part of the SED to be well constrained. Our main uncertainties are blueward of the dust peak, which we only sample with the 22 μm data point from WISE and the 250 μm data point from SPIRE. The 250 μm band corresponds to 50–80 μm in the rest-frame for our targets, is slightly blueward of the peak of the dust emission in most of our sources (Fig. 4), and falls near the expected peak of the infrared emission from hot dust in the AGN torus in most templates (e.g., Polletta et al. 2007; Nenkova et al. 2008). The SEDs of powerful AGN host galaxies at high redshifts are typically dominated by AGN emission at these wavelengths (e.g., Sajina et al. 2012; Drouart et al. 2014).

The `DecompIR` software package provides a small set of SED templates, derived from nearby starburst galaxies. One complication in using these templates for our sources is that we find a range of dust temperatures, which are not all well represented by existing templates. This would lead to considerable (but somewhat artificial) discrepancies in the template fitting that would be hard to overcome without a self-consistent model of the mid-to-far-IR SED of high-redshift galaxies, which does not yet exist. To avoid such mismatches, while make optimal use of our existing constraints without overinterpreting the mid-IR data, we therefore constructed a simple starburst template for each of our galaxies from the "SB2" template of `DecompIR` (corresponding to the SED of NGC 7252, Mullaney et al. 2011), but correcting for the mismatch in dust temperatures. We therefore fitted and removed from the template the modified blackbody contribution from cold dust in the FIR. The residual is a template of the SED in the mid-IR only, to which we added the modified blackbody emission obtained from our FIR fits, using the measured temperature for each source. We selected this particular template, because it provided the best match to the FIR and submillimetre measurements of the dust peak and Rayleigh-Jeans tail, with no regard of the goodness of fit of the 22 μm observations. For the AGN component, we simply used the Polletta et al. (2007) type-2 QSO template which is already part of `DecompIR`.

Figure 7 shows that we can rule out a bolometrically dominant AGN contribution from buried quasars, in all cases. Only three galaxies have best-fit results formally inconsistent with pure starbursts. In PLCK_G092.5+42.9 and PLCK_G244.8+54.9, the putative AGN contribution to the FIR luminosity is below 10%, and it is below 30% in PLCK_G145.2+50.9. In all other cases, `DecompIR` finds the best fit for a pure starburst SED.

Figure 7 also shows the 90% completeness limits of the IRAS faint source survey (Moshir et al. 1992), 120 mJy and 440 mJy at 60 μm and 100 μm, respectively (green downward arrows). Although these limits are not constraining for the SED fits that we obtained with SPIRE, SCUBA-2, GISMO, and WISE (and were therefore not included in our `DecompIR` fits) they do illustrate that a hypothetical bright quasar component would have led to a 60 μm detection at least in our brightest targets. In Fig. 8 we illustrate the impact of fiducial AGN contribution of 0.1, 0.3, and 0.5 × $L_{\rm FIR}$ on the example of G138.6+62.0, a source with rather average FIR brightness and 250-to-350 μm colour in our sample.

Obviously, these fits are uncertain, given that they cover the far blue wing of the dust SED expected from bright AGN, and a spectral range that has important contributions from rich mid-IR spectral features, in particular from Polycyclic Aromatic Hydrocarbons (PAH), which dominate the infrared SEDs of starburst galaxies between about 3 μm and 10 μm (e.g., Armus et al. 2007).

The equivalent widths of the PAH bands have a wide dispersion in high-redshift galaxies (e.g., Fiolet et al. 2010), and are generally larger than those measured in low-redshift ULIRGs, including NGC 7252, which we used as template in our `DecompIR` fits. Additional uncertainties come from the stellar continuum, which reaches comparable strength to the dust continuum in the wavelength range covered by the 22 μm observations, about 5–7 μm, and whose shape depends strongly on the specific star-formation rate, star-formation history, and geometry of dust obscuration in the host galaxy. Compared to the average mid-IR SED of starburst galaxies (Brandl et al. 2006), the stellar continuum in NGC 7252 seems relatively faint, and Sajina et al. (2012) also found that the mid-IR continuum of high-redshift starburst galaxies seems to be brighter than in low-redshift galaxies. Other spectral features might also contribute to boosting the observed 22 μm flux density. For example Fiolet et al. (2010) report the detection of warm H_2 line emission at 6.9 μm in the rest-frame. Moreover, the foreground galaxies may also contribute to the 22 μm flux, given the 12$''$ beam of WISE. However, all these uncertainties would only act to lower the putative intrinsic contribution of AGN heating relative to what we observe. It will of course be very interesting to study the mid-IR spectral properties of our sources in depth once that JWST/MIRI will become available.

Relying upon these arguments, we conclude that the dust heating in our sources is not dominated by heavily obscured quasars, but that the *Planck* Dusty GEMS are genuine starburst galaxies with at most a minor contribution of AGN heating to the dust emission and the bolometric energy budget of our sources. Of course this only refers to the regions that we are seeing under the gravitational microscope of the foreground lensing systems. The global energy budgets of AGN and star formation in these

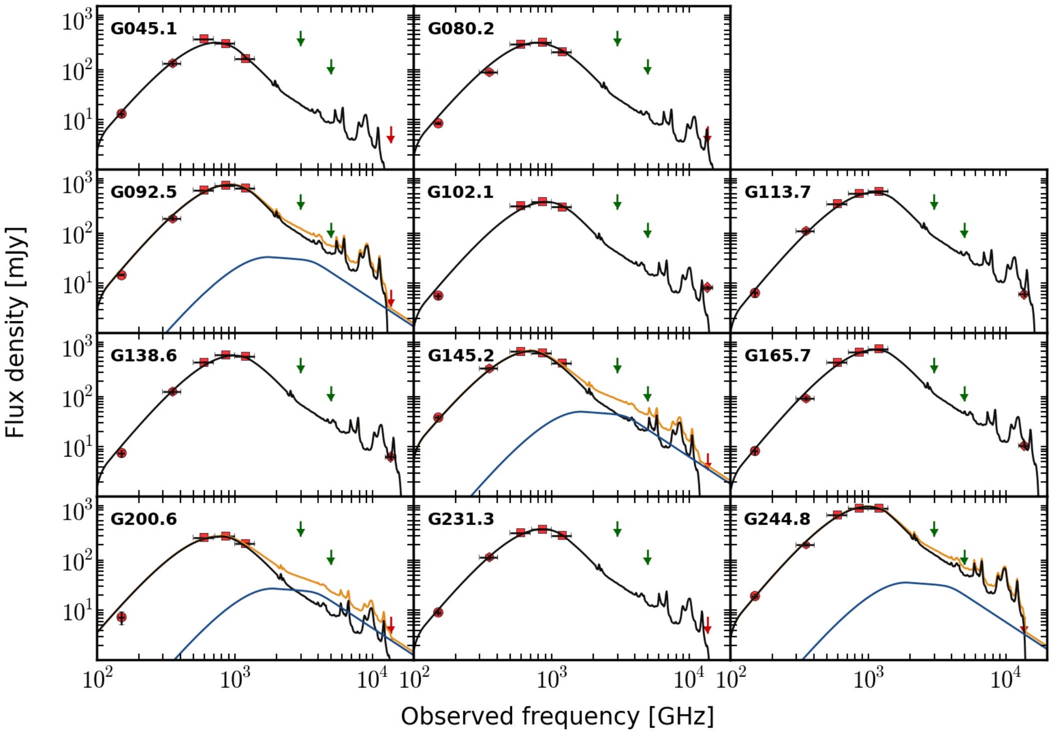

Fig. 7. Infrared-to-millimetre SEDs of all of our 11 sources obtained using `DecompIR` (Mullaney et al. 2011). Red dots show our data points, where the error bars along the abscissa indicate the width of each band. The error bars along the ordinate are often smaller than the symbol size. Green downward arrows show the 90% completeness limit of the IRAS all-sky survey at 60 and 100 μm, respectively. Red downward arrows at 22 μm show the 5σ upper limits provided by the WISE catalogs, where the counterparts were fainter than the 5.4 mJy flux limit of the WISE catalog. Black, blue, and yellow lines show the starburst and AGN component (if an AGN was fitted), and the sum of both, respectively.

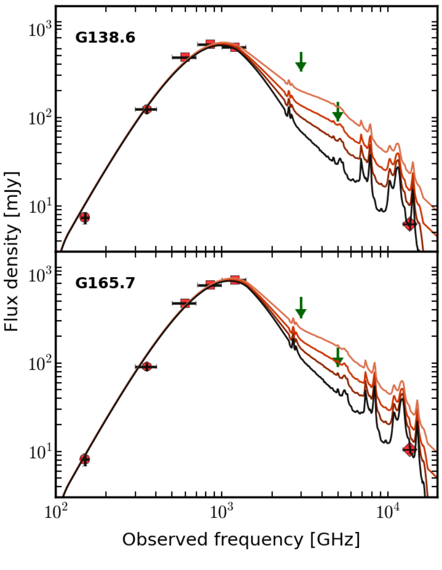

Fig. 8. A schematic illustrating the impact of 0.1, 0.3, and 0.5 × $L_{\rm FIR}$ of AGN contamination to the shape of the SED of our sources, on the example of G138.6+62.0 and G165.7+67.0.

galaxies may be different, if the AGN lies along a line of sight that is not strongly magnified (see also Serjeant 2012).

8. FIR-radio correlation

Given the extraordinary brightness of our targets on the sky, we can use the 1.4 GHz VLA survey of the northern sky, FIRST (Becker et al. 1995), to search for counterparts of our sources at an observed frequency of 1.4 GHz (between 4.5 and 6.4 GHz in the rest-frame). We find that six of our sources have counterparts within 5″ of a source in the FIRST catalogue, and the other five have sensitive upper limits (see Table 4). Here 5″ corresponds to the beam size of FIRST. We assume a radio spectral index $\alpha_{1.4} = -0.8$ (as is appropriate for star-forming regions, Condon 1992) to convert these flux densities to a monochromatic radio flux density at rest-frame 1.4 GHz, as well as to estimate a radio power. For galaxies without detections we use the 3 σ upper limits implied by the rms given in the FIRST catalogue. Results for individual sources are listed in Table 4. All sources are listed in the FIRST catalog as marginally resolved, with deconvolved sizes between 1.5″ and 7″. The 5″ beam of FIRST is not always sufficiently small to rule out contamination from a radio nucleus in the foreground lensing galaxy. However, most sources are isolated enough to conclude that the radio counterpart is at the position of the high-redshift galaxy, and not coincident with a massive, intermediate-redshift galaxy that could host a radio-loud AGN. This is particularly the case for PLCK_G244.8+54.9.

The FIR radio correlation is commonly parametrized as $q = \log L_{\rm IR}/(3.75\times10^{12}\,{\rm W}) - \log L_{1.4}/({\rm W\,Hz^{-1}})$, where $L_{\rm IR}$ is measured in the range 8–1000 μm in the rest-frame, and the centimetre continuum at a rest-frame frequency of 1.4 GHz. Early *Herschel* results suggest $\langle q\rangle = 2.4 \pm 0.12$ in the local Universe (Jarvis et al. 2010), although values can change

Table 4. Radio continuum properties extracted from the FIRST catalogue.

Source	Dist. [arcsec]	$\mu_{1.4}\,S^{\rm int}_{1.4}$ [mJy]	$\mu_{1.4}\,L_{1.4}$ [10^{25} W Hz^{-1}]	q
PLCK_G045.1+61.1		<0.135	<3.2	>2.4
PLCK_G080.2+49.8		<0.135	<1.8	>2.4
PLCK_G092.5+42.9	0.9	1.50 ± 0.16	11.2	2.35 ± 0.11
PLCK_G102.1+53.6		<0.149	<2.5	>2.5
PLCK_G113.7+61.0	3.0	1.9 ± 0.14	6.9	2.2 ± 0.08
PLCK_G138.6+62.0	2.7	2.01 ± 0.16	7.3	2.1 ± 0.08
PLCK_G145.2+50.9		<0.144	<3.9	>2.8
PLCK_G165.7+67.0	4.1	3.41 ± 0.15	10.1	2.0 ± 0.04
PLCK_G200.6+46.1	1.1	1.23 ± 0.14	6.9	1.9 ± 0.11
PLCK_G231.3+72.2		<0.151	<2.5	>2.5
PLCK_G244.8+54.9	3.2	2.26 ± 0.14	13.6	2.3 ± 0.06

Notes. The columns are: source name; relative distance between the SPIRE position at 250 μm and the position of the FIRST counterpart, if detected within 5″; integrated flux density at 1.4 GHz from the FIRST catalogue and gravitational magnification factor of the radio component, $\mu_{1.4}$; radio luminosity at 1.4 GHz in the rest-frame and gravitational magnification factor of that component, $\mu_{1.4}$, for sources without 1.4 GHz detections, the luminosities are derived from 3× the rms given in column 3; the Ratio between radio and FIR luminosity (see Sect. 8), i.e. the q-parameter.

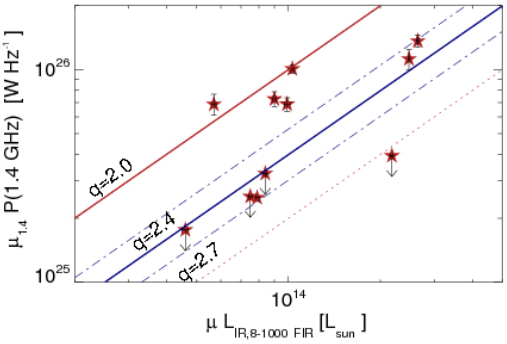

Fig. 9. Far-infrared radio correlation of our sources, as discussed in Sect. 8. $\mu_{\rm FIR}$ and $\mu_{1.4}$ correspond to the magnification factors appropriate for the dusty and 1.4 GHz synchrotron emission, respectively. Solid blue and red lines show the relationship for $q = 2.4$ and 2.0, respectively, while the red dotted line is for $q = 2.7$. The dot-dashed lines show the $\pm 1\sigma$ scatter about $q = 2.4$ at low redshift from Jarvis et al. (2010).

considerably even within individual galaxies (e.g., Tabatabaei et al. 2013). Towards higher redshifts, results show less of a consensus. Kovács et al. (2006), Vlahakis et al. (2007), Michałowski et al. (2010), and Bourne et al. (2011) report an increase in radio power at a given FIR luminosity at $z \gtrsim 1$, with $\langle q \rangle = 2.0$. However, several studies (e.g., Ivison et al. 2010a,b; Sargent et al. 2010; Thomson et al. 2014) find average values in the range $q = 2.4$–2.7, out to $z \approx 2$. Most of these studies use stacking analyses to overcome the inherent faintness of high-redshift galaxies in the FIR and sub-mm and in the radio, and are based on ground-based data that do not sample the FIR dust SED very well. In the Cosmic Eyelash, a single, strongly lensed galaxy at $z = 2.4$ with *Herschel-SPIRE* coverage, Ivison et al. (2010b) find $q = 2.4$.

In Fig. 9 we show where our sources fall relative to the local FIR-radio correlation, assuming that differential lensing between the FIR and radio synchrotron emission does not play a major role in our case. Four of our sources are brighter by up to about 0.4 dex in the radio, and fall outside the 1σ scatter around the distribution of q parameters of low-redshift galaxies. Six galaxies fall within 1σ from this relationship, however, three of these galaxies only have upper limits on q, and would fall outside the 1σ scatter if we had adopted 1σ, instead of 3σ upper limits. One galaxy has $q > 2.7$ at 3σ.

If the 1.4 GHz emission is caused by star formation, then the lower q values cannot be caused by our assumption of the spectral index $\alpha_{1.4} = -0.8$. Only for flat radio SEDs ($\alpha_{1.4} = -0.2$ or above, which would only be possible for an AGN) would our highest-q sources be consistent with the FIR-correlation and $q = 2.4$. If this were the case, our sources with the highest q parameters (i.e., the brightest sources in the FIR relative to the radio) would fall well above $q = 3$.

One way of obtaining lower q-values, as has been pointed out several times before (e.g., Vlahakis et al. 2007; Bourne et al. 2011) is through radio emission from a central AGN. This has an interesting theoretical aspect, since it has been proposed (e.g., Silk & Norman 2009) that gas compression caused by expanding radio sources in massive high-z galaxies may in fact contribute to boosting the star-formation efficiency in intense high-z starbursts. However, although contamination with nuclear radio emission may be a particular concern for stacking analyses (where one or a few relatively bright radio sources may affect the average result of the overall sample), in our case this explanation seems to be less likely. First, the radio sources are spatially resolved in FIRST, suggesting they are extended, just like the star formation. Even if the Dusty GEMS have extended radio sources, the gravitational lensing would need to amplify the radio emission by similar amounts to that of the star formation in most of our sources; this appears relatively unlikely, given that the AGN radio morphologies of high-z galaxies are very different from those of the dust and stellar components (e.g. Sajina et al. 2007).

As a second counter argument, our SED fits have already disfavoured the presence of very luminous AGN. Although galaxies are known to host central radio sources without bright bolometric emission, the host galaxies of such AGN tend to have little dust, gas, and on-going star formation. And although relatively faint AGN may be present without leaving strong signatures in the dust SEDs, only a subset of those should be radio loud. Even optimistic results (e.g., from Sajina et al. 2007), imply that only up to about 30% of dusty high-z starburst galaxies may host moderately bright ($P_{1.4} \approx 10^{25}$ W Hz^{-1}, comparable to our sources for magnification factors of order 10) nuclear radio sources that are as bright as or brighter than the star formation itself. In addition, these sources are classified as AGN in the mid-IR. We note that we have not found any obvious trends between the q-parameter and possible probes of AGN contamination like dust temperature or $L_{\rm FIR}$. We also do not find a correlation between the flux density at 22 μm and the 1.4 GHz radio emission.

As an alternative, the offsets towards larger and smaller q-parameters may be caused by the star-forming environments themselves. Lacki & Thompson (2010) suggest that enhanced synchrotron emission from cosmic rays in star-forming galaxies at high redshift could be one outcome of the strong turbulence observed in these galaxies (e.g., Förster Schreiber et al. 2009; Lehnert et al. 2009; Swinbank et al. 2011), which enhances the scale height of the gas, and lowers their volume density. In this case, energy loss of cosmic rays through synchrotron radiation, bremsstrahlung, and other processes could be either enhanced or diminished, depending on the local magnetic fields and density distribution of the ISM; this could either decrease or increase the energy losses of the cosmic rays, making our sources either brighter or fainter (e.g., Murphy 2009). Other possible explanations, which might also involve the sources with unusually high q-parameters, include evolution in the dust properties, the age of the starburst (the radio should not probe starbursts with ages of less than a few times 10^7 yr or greater than a few times 10^8 yr, because of the timing of core-collapse supernovae, Bressan et al. 2002), and a top-heavy initial mass function (e.g., Baugh et al. 2005). It will be interesting to obtain high-resolution centimetre-wave maps of these sources, along with our gas and dust interferometry, to constrain the potential impact of differential lensing and to further elucidate how the q-parameter depends locally on the ISM properties in our sources.

9. Gas masses and gas-to-dust ratios

To determine the molecular gas mass (which is dominated by H_2) from the CO luminosity, we have to assume an empirical conversion factor, which is notoriously difficult to justify from first principles, and which is therefore still heavily debated in the literature, in particular for high-redshift galaxies (e.g., Daddi et al. 2010; Genzel et al. 2010; Glover & Mac Low 2011; Narayanan et al. 2012). The canonical value adopted for most high-z galaxies is $\alpha \approx 0.8\, M_\odot/(\mathrm{K\,km\,s^{-1}\,pc^2})$. This value was first derived by Downes & Solomon (1998) for the dense, circumnuclear, optically thick molecular gas discs in nearby ULIRGs, and is commonly adopted also for dusty starburst galaxies in the early Universe.

However, several studies in recent years (starting with Daddi et al. 2010 and Genzel et al. 2010) have called into question whether a single CO(1–0)-to-H_2 conversion factor may be appropriate to use for all high-z galaxies. Several attempts have therefore been undertaken to constrain $\alpha_{\rm CO}$ either from dynamical mass estimates, or on theoretical grounds. One empirical approach suited for galaxies with well constrained dust mass measurements like ours, is to assume that high-z galaxies fall onto a similar relationship between gas-to-dust mass ratios and metallicities as found for SINGs galaxies in the local Universe (Leroy et al. 2008). Magdis et al. (2011) used this approach to confirm their $\alpha_{\rm CO}$ determinations, which they previously obtained from dynamical mass estimates.

We can use our measurements of the dust mass, $M_{\rm d}$ (Sect. 6.2 and Table 2), and the CO line luminosity, L' (Sect. 4.3 and Table 3), to estimate ratios of $L'/M_{\rm d}$, which scale with gas-phase metallicity (Leroy et al. 2008; Magdis et al. 2011). Using Fig. 3 of Magdis et al. (2011), we find that our measured range $L'/M_{\rm d} = 40$–140 corresponds to gas-phase metallicities $12 + \log(\mathrm{O/H}) \sim 8.9$–$9.3$. These values are appropriate for $\beta = 2.0$ (Sect. 6.2). Furthermore, we adopted a ratio $r_{32/10} = 1$ to convert from the luminosities of the observed mid-J CO lines to CO(1–0). This factor is expected for optically thick gas (e.g., Solomon & Vanden Bout 2005). In the Cosmic Eyelash, Danielson et al. (2011) measured $r_{32/10} = 0.7$.

High gas-phase metallicities correspond to small values of $\alpha_{\rm CO}$ of ≤ 1.0. For example, if we use the linear fit between $\alpha_{\rm CO}$ and metallicity of Genzel et al. (2012), we find conversion factors of about 0.4 at face value, although with large uncertainties. Likewise, Fig. 3 of Magdis et al. (2011) suggests $\alpha_{\rm CO} < 1.0\, M_\odot/(\mathrm{K\,km\,s^{-1}\,pc^2})$ for galaxies with $L'/M_{\rm d}$ ratios and metallicities as high as in our sources. This suggests that using the ULIRG conversion factor of $\alpha_{\rm CO} = 0.8\, M_\odot/(\mathrm{K\,km\,s^{-1}\,pc^2})$ is more appropriate than much higher factors of 3–5 $M_\odot/(\mathrm{K\,km\,s^{-1}\,pc^2})$, as previously adopted for more moderately star forming, disk-like high-redshift galaxies and the Milky Way. We stress that these results are measured in small regions of high-z galaxies, and are not necessarily representative of the average values in these galaxies (Serjeant 2012).

When using a common conversion factor $\alpha_{\rm CO} \approx 0.8\, M_\odot/(\mathrm{K\,km\,s^{-1}\,pc^2})$, we find molecular gas masses of 2–$10 \times 10^{11}\, \mu^{-1}\, M_\odot$ for *Planck*'s Dusty GEMS (including the gravitational magnification factor μ). Results for individual galaxies are listed in Table 3.

10. Integrated star-formation law

The tight correlation between molecular gas mass surface density and star-formation intensity over scales of around 100 pc to entire galaxies highlights how star formation depends on the available molecular gas reservoirs (i.e., the Schmidt-Kennicutt law, Schmidt 1959; Kennicutt 1998), although there is no consensus about a unique physical mechanism putting this relationship in place.

However, starting with, e.g., Daddi et al. (2010) and Genzel et al. (2010), several studies have emphasized in recent years that not all high-redshift galaxies may strictly obey the same empirical star-formation law, but that at a given gas surface density, starburst galaxies may be more efficient in turning their gas into stars. The reasons for this are still unclear, with possibilities ranging from changes in the stellar initial mass function (Baugh et al. 2005) to different star-formation efficiencies. For example, there may be more star-forming clouds in their ISM than in more quiescent high-z galaxies (Lehnert et al. 2013), or the star-formation efficiency per free-fall time could be higher (Dekel et al. 2009). What we can confidently assert (given the absence of dust with $T \gg 50$ K, faint 22-μm flux density, or excess radio emission) is that AGN do not play a dominant role in boosting the FIR continuum in the strongly amplified regions that we are seeing in our galaxies (Sect. 7). Given the close astrophysical connection between dust and gas in star-forming regions, we see no reason to believe that differential lensing plays an important role for our analysis of the gas conditions in the regions, which are amplified by the gravitational lenses. Of course, we must keep in mind that the gas and dust measurements obtained in small, selectively amplified regions of these galaxies are not necessarily representative of the average gas and dust properties in these galaxies on global scales (Serjeant 2012).

The relationship of FIR luminosity with CO line luminosity is a simple, empirical, and robust way of investigating this "star-formation law". It is directly related to the integral form of the Schmidt-Kennicutt law, because the FIR luminosity probing the emission from warm dust is an excellent tracer of star formation. CO line emission is mainly excited through collisions with H_2 and is the most commonly adopted proxy of the total molecular gas mass (e.g., Omont 2007).

In order to investigate whether our sources are representative of star formation in high-z starburst galaxies or more ordinary, but nonetheless very intensely star-forming galaxies on the "main sequence" (e.g., Elbaz et al. 2011), we use the molecular gas masses estimated from the CO luminosities ($M_{\rm H2}$) and FIR luminosities ($L_{\rm FIR}$), shown in Fig. 10, and compare with the correlations found by Daddi et al. (2010) and Genzel et al. (2010) for starburst galaxies, together with the more gradually, but nonetheless intensely star-forming high-z galaxies on

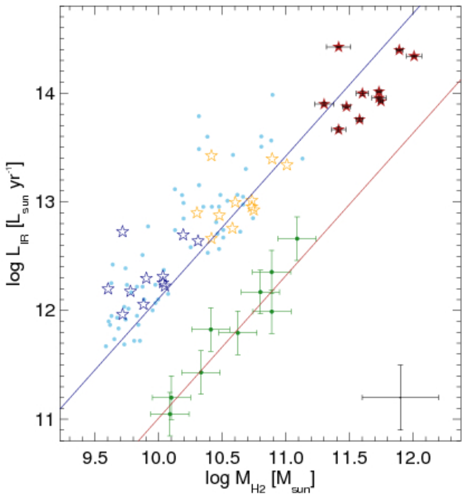

Fig. 10. Infrared luminosities ($L_{\rm IR}$) as a function of molecular gas mass for our sources. Red, yellow, and purple stars indicate the measured values (uncorrected for gravitational amplification), and the same values corrected by fiducial lensing factors of 10 and 50, respectively. In agreement with the dust-to-gas ratios discussed in Sect. 9 we adopt the classical "ULIRG" conversion factor $\alpha_{\rm CO} = 0.8\,M_\odot/({\rm K\,km\,s^{-1}\,pc^2})$ for all sources. The blue and red line indicate the relationships for starbursts and "main-sequence" galaxies emphasized by Daddi et al. (2010). Small dots show the low- and high-z samples of Daddi et al. (2010) for comparison. Light blue dots along the upper line show low- and high-z ULIRGs and SMGs, respectively. The filled dark green dots (with error bars) are BzK galaxies at $z \sim 2$; for details of these samples see Daddi et al. (2010). All error bars include the measurement uncertainties. The black cross in the lower right corner of the plot shows a fiducial factor 2 in statistical uncertainty.

the "main sequence". For this comparison, we use the integrated star-formation rates and molecular gas masses, adopting $\alpha_{\rm CO} = 0.8\,M_\odot/({\rm K\,km\,s^{-1}\,pc^2})$ as justified in Sect. 9.

We find that all sources fall closer to the upper "starburst" than the lower "main sequence" lines in Fig. 10. To illustrate the effects of lensing, i.e., how these sources might appear in the image plane, we plot not only the observed luminosities (red filled stars), but also the luminosities for fiducial magnification factors $\mu = 10$ and $\mu = 50$ (orange and light blue empty stars in Fig. 10). Even without the detailed lens modelling their position in the diagram relative to typical starburst or main-sequence galaxies does not depend sensitively on the precise magnification factor.

We stress that in the present study, we only show integrated measurements, whereas the relationship that underlies the Schmidt-Kennicutt diagram is between the surface density of molecular gas mass and the star-formation rate. Our on-going interferometric follow-up programme will enable us to derive more detailed constraints, and to investigate whether the "starburst" and "main sequence" classifications are unique for each source, or whether each individual Dusty GEM will show a range in star-formation efficiency.

FIR luminosities and gas mass estimates also provide simple, rough constraints on the gas depletion timescale, $t_{\rm dpl} = M_{\rm gas}/{\rm SFR}$, and hence the time during which the current star formation intensity can be maintained without replenishing the molecular gas reservoirs. Assuming that star-formation rates are constant, we find short gas depletion timescales, $t_{\rm dpl} = (0.5{-}6) \times 10^7$ yr, significantly less than the typical stellar age of a FIR or sub-mm galaxy (a few times 10^8 yr, Smail et al. 2004; Lapi et al. 2012), and also somewhat, but not dramatically, shorter than the gas depletion timescales found for unlensed sub-mm galaxies (e.g., Greve et al. 2005). This highlights again the fact that our sources have all the hallmarks of being "ordinary" dusty starburst galaxies placed under particularly powerful cosmic microscopes.

11. Summary

We have presented a first analysis of an extensive multi-wavelength follow-up campaign of a new sample of the brightest high-redshift FIR and sub-mm galaxies, discovered through the unique synergy of the *Planck* and *Herschel* satellites. *Planck*'s all-sky nature and multi-frequency coverage allows us to select rare peaks in the sub-mm background and *Herschel* observations lead to subsample of strongly lensed candidates – *Planck*'s Dusty GEMS. Their FIR peak flux densities are up to $S_{350} = 1130$ mJy at 350 μm, including six sources that are above the completeness limit of *Planck* at the highest frequencies. Our sample extends the very successful searches for gravitationally lensed high-z galaxies already carried out with *Herschel* and the SPT towards the brightest, rarest targets on the FIR and sub-mm sky, which emphasized the need for a genuine all-sky survey to systematically probe such exceedingly uncommon sources.

All sources in our sample are bright, isolated point sources in SPIRE 250-μm maps (18″ FWHM), and have the typical FIR-to-mm SEDs of dusty, intensely star-forming galaxies at high redshift. They have redshifts in the range $z = 2.2$–3.6, based on multiple bright millimetre emission lines obtained with EMIR at the IRAM 30-m telescope. Their dust and gas properties provide firm evidence that they are indeed gravitationally lensed galaxies, as is further supported through interferometric observations of their dust and gas morphologies, already obtained for most sources.

We used the WISE survey at 22 μm and the 1.4 GHz VLA FIRST survey to show that the FIR continuum of the Dusty GEMS is not dominated by the radiation of powerful AGN. In particular, we find that buried quasars cannot make a dominant contribution to their observed FIR SEDs. All SEDs are well fitted with a single modified blackbody distribution with temperatures $T_{\rm d} = 33$–50 K, covering the range of high-redshift starburst galaxies, as well as more gradually, but still intensely star-forming, high-z galaxies on the "main sequence". They show a wide scatter about the local FIR radio correlation, with q-parameters ranging from 2.0, as has previously been found for high-z galaxies by some authors, to above 2.7, which suggests a considerable excess of FIR relative to synchrotron emission. One plausible interpretation is that this is probably a consequence of their turbulent ISM, but this needs to be confirmed through more detailed studies comparing the resolved radio emission with other source properties. All galaxies have gas-to-dust ratios of 40–140, consistent with a low CO-to-H$_2$ conversion factor, as expected for massive, dusty starburst galaxies with metallicities above solar. A full analysis of the spatially resolved properties of these galaxies, as well as detailed lens modelling, is on-going.

Strongly lensed high-redshift sub-mm galaxies represent an excellent opportunity to study gas heating and acceleration, and the mechanism driving star formation in the most vigorous starbursts in the early Universe. Detailed observations of the dust, stellar populations, and multiple emission and absorption lines, in particular with sub-mm and millimetre interferometry have already been obtained and will be discussed in future papers.

Acknowledgements. We would like to thank the staff at the IRAM 30-m telescope, in particular N. Billot and S. Trevino, for their excellent support during observations. We are also very grateful to the former director of IRAM, P. Cox, the director of the SMA, R. Blundell, the director of the CFHT, D. Simons, and the director of ESO, T. de Zeeuw, for the generous allocation of Director's Discretionary Time. We thank the referee, S. Bussmann, for constructive comments that helped improve our manuscript. We would also like to thank A. Sajina and several other colleagues unknown to us and solicited by the Planck collaboration as external referees for their valuable comments on an earlier version of the paper. We would also like to thank C. Kramer for having made his `CLASS` routine FTSPlatformingCorrection5 available to us. We thank B. Partridge and the Planck Editorial Board for ensuring that our manuscript is in accordance with the internal Planck publication rules and standards. R.C. wishes to acknowledge support from the École Doctorale Astronomie & Astrophysique de l'Île de France. M.N. acknowledges financial support from ASI/INAF agreement 2014-024-R.0 and from PIRN-INAF 2012 project "Looking into the dust-obscured phase of galaxy formation through cosmic zoom lenses in the *Herschel* Astrophysical Large Area Survey". I.F.C., L.M. and E.P. acknowledge the support of grant ANR-11-BS56-015. The largest part of this work is based on observations carried out with the IRAM 30-m Telescope and the IRAM Plateau de Bure Interferometer. IRAM is supported by INSU/CNRS (France), MPG (Germany) and IGN (Spain). The Submillimeter Array is a joint project between the Smithsonian Astrophysical Observatory and the Academia Sinica Institute of Astronomy and Astrophysics and is funded by the Smithsonian Institution and the Academia Sinica. Based in part on observations obtained with MegaPrime/MegaCam, a joint project of CFHT and CEA/DAPNIA, at the Canada-France-Hawaii Telescope (CFHT), which is operated by the National Research Council (NRC) of Canada, the Institute National des Sciences de l'Univers of the Centre National de la Recherche Scientifique of France, and the University of Hawaii. Based in part on observations obtained with WIRCam, a joint project of CFHT, Taiwan, Korea, Canada, France, and the Canada-France-Hawaii Telescope (CFHT). The development of *Planck* has been supported by: ESA; CNES and CNRS/INSU-IN2P3-INP (France); ASI, CNR, and INAF (Italy); NASA and DoE (USA); STFC and UKSA (UK); CSIC, MICINN, JA, and RES (Spain); Tekes, AoF, and CSC (Finland); DLR and MPG (Germany); CSA (Canada); DTU Space (Denmark); SER/SSO (Switzerland); RCN (Norway); SFI (Ireland); FCT/MCTES (Portugal); and PRACE (EU). A description of the Planck Collaboration and a list of its members, including the technical or scientific activities in which they have been involved, can be found at[4]. The *Herschel* spacecraft was designed, built, tested, and launched under a contract to ESA managed by the *Herschel*/*Planck* Project team by an industrial consortium under the overall responsibility of the prime contractor Thales Alenia Space (Cannes), and including Astrium (Friedrichshafen) responsible for the payload module and for system testing at spacecraft level, Thales Alenia Space (Turin) responsible for the service module, and Astrium (Toulouse) responsible for the telescope, with in excess of a hundred subcontractors. We acknowledge the use of the Galaxies, INterstellar mater & COsmology (GINCO) archive for the Integrated Data & Operation Centre (IDOC) at Institut d'Astrophysique Spatiale and Observatoire des Sciences de l'Univers de l'Université Paris Sud (OSUPS). Support for IDOC is provided by CNRS & CNES.

References

Alexander, D. M., Bauer, F. E., Chapman, S. C., et al. 2005, ApJ, 632, 736
Armus, L., Charmandaris, V., Bernard-Salas, J., et al. 2007, ApJ, 656, 148
Baugh, C. M., Lacey, C. G., Frenk, C. S., et al. 2005, MNRAS, 356, 1191
Becker, R. H., White, R. L., & Helfand, D. J. 1995, ApJ, 450, 559
Bertin, E. 2010a, SCAMP: Automatic Astrometric and Photometric Calibration, Astrophysics Source Code Library [`record ascl:1010.063`]
Bertin, E. 2010b, SWarp: Resampling and Co-adding FITS Images Together, Astrophysics Source Code Library [`record ascl:1010.068`]
Béthermin, M., Daddi, E., Magdis, G., et al. 2012, ApJ, 757, L23
Blain, A. W., Barnard, V. E., & Chapman, S. C. 2003, MNRAS, 338, 733
Bothwell, M. S., Smail, I., Chapman, S. C., et al. 2013, MNRAS, 429, 3047
Bourne, N., Dunne, L., Ivison, R. J., et al. 2011, MNRAS, 410, 1155
Brandl, B. R., Bernard-Salas, J., Spoon, H. W. W., et al. 2006, ApJ, 653, 1129
Bressan, A., Silva, L., & Granato, G. L. 2002, A&A, 392, 377
Bussmann, R. S., Pérez-Fournon, I., Amber, S., et al. 2013, ApJ, 779, 25
Chapin, E. L., Berry, D. S., Gibb, A. G., et al. 2013, MNRAS, 430, 2545
Chapman, S. C., Blain, A. W., Smail, I., & Ivison, R. J. 2005, ApJ, 622, 772
Combes, F., Rex, M., Rawle, T. D., et al. 2012, A&A, 538, L4
Condon, J. J. 1992, ARA&A, 30, 575
Daddi, E., Elbaz, D., Walter, F., et al. 2010, ApJ, 714, L118
Danielson, A. L. R., Swinbank, A. M., Smail, I., et al. 2011, MNRAS, 410, 1687
Dekel, A., Sari, R., & Ceverino, D. 2009, ApJ, 703, 785
Dempsey, J. T. Friberg, P., Jenness, T., et al. 2013, MNRAS, 430, 2534
Diolaiti, E., Bendinelli, O., Bonaccini, D., et al. 2000, A&AS, 147, 335
Dole, H., Lagache, G., Puget, J.-L., et al. 2006, A&A, 451, 417
Downes, D., & Solomon, P. M. 1998, ApJ, 507, 615
Drouart, G., De Breuck, C., Vernet, J., et al. 2014, A&A, 566, A53
Egami, E., Rex, M., Rawle, T. D., et al. 2010, A&A, 518, L12
Elbaz, D., Dickinson, M., Hwang, H. S., et al. 2011, A&A, 533, A119
Fiolet, N., Omont, A., Lagache, G., et al. 2010, A&A, 524, A33
Förster Schreiber, N. M., Genzel, R., Bouché, N., et al. 2009, ApJ, 706, 1364
Fu, H., Jullo, E., Cooray, A., et al. 2012, ApJ, 753, 134
Genzel, R., Tacconi, L. J., Gracia-Carpio, J., et al. 2010, MNRAS, 407, 2091
Genzel, R., Tacconi, L. J., Combes, F., et al. 2012, ApJ, 746, 69
Gildas Team. 2013, GILDAS: Grenoble Image and Line Data Analysis Software, astrophysics Source Code Library [`record ascl:1305.010`]
Glover, S. C. O., & Mac Low, M.-M. 2011, MNRAS, 412, 337
Greve, T. R., Bertoldi, F., Smail, I., et al. 2005, MNRAS, 359, 1165
Greve, T. R., Vieira, J. D., Weiß, A., et al. 2012, ApJ, 756, 101
Harris, A. I., Baker, A. J., Frayer, D. T., et al. 2012, ApJ, 752, 152
Hauser, M. G., & Dwek, E. 2001, ARA&A, 39, 249
Herranz, D., González-Nuevo, J., Clements, D. L., et al. 2013, A&A, 549, A31
Holland, W. S., Bintley, D., Chapin, E. L., et al. 2013, MNRAS, 430, 2513
Ivison, R. J., Alexander, D. M., Biggs, A. D., et al. 2010a, MNRAS, 402, 245
Ivison, R. J., Magnelli, B., Ibar, E., et al. 2010b, A&A, 518, L31
Ivison, R. J., Swinbank, A. M., Smail, I., et al. 2013, ApJ, 772, 137
Jarvis, M. J., Smith, D. J. B., Bonfield, D. G., et al. 2010, MNRAS, 409, 92
Kennicutt, Jr., R. C. 1998, ARA&A, 36, 189
Kovacs, A. 2013, CRUSH: Comprehensive Reduction Utility for SHARC-2, astrophysics Source Code Library [`record ascl:1308.011`]
Kovács, A., Chapman, S. C., Dowell, C. D., et al. 2006, ApJ, 650, 592
Lacki, B. C., & Thompson, T. A. 2010, ApJ, 717, 196
Laird, E. S., Nandra, K., Pope, A., & Scott, D. 2010, MNRAS, 401, 2763
Lapi, A., Negrello, M., González-Nuevo, J., et al. 2012, ApJ, 755, 46
Lehnert, M. D., Nesvadba, N. P. H., Le Tiran, L., et al. 2009, ApJ, 699, 1660
Lehnert, M. D., Le Tiran, L., Nesvadba, N. P. H., et al. 2013, A&A, 555, A72
Leroy, A. K., Walter, F., Brinks, E., et al. 2008, AJ, 136, 2782
Magdis, G. E., Daddi, E., Elbaz, D., et al. 2011, ApJ, 740, L15
Michałowski, M., Hjorth, J., & Watson, D. 2010, A&A, 514, A67
Moshir, M., Kopman, G., & Conrow, T. A. O. 1992, IRAS Faint Source Survey, Explanatory supplement version 2
Mullaney, J. R., Alexander, D. M., Goulding, A. D., & Hickox, R. C. 2011, MNRAS, 414, 1082
Murphy, E. J. 2009, ApJ, 706, 482
Narayanan, D., Krumholz, M. R., Ostriker, E. C., & Hernquist, L. 2012, MNRAS, 421, 3127
Negrello, M., Perrotta, F., González-Nuevo, J., et al. 2007, MNRAS, 377, 1557
Negrello, M., Hopwood, R., De Zotti, G., et al. 2010, Science, 330, 800
Nenkova, M., Sirocky, M. M., Nikutta, R., Ivezić, Ž., & Elitzur, M. 2008, ApJ, 685, 160
Nesvadba, N. P. H., Lehnert, M. D., Genzel, R., et al. 2007, ApJ, 657, 725
Nguyen, H. T., Schulz, B., Levenson, L., et al. 2010, A&A, 518, L5
Omont, A. 2007, Rep. Prog. Phys., 70, 1099
Planck Collaboration VII. 2011, A&A, 536, A7
Planck Collaboration I. 2014, A&A, 571, A1
Planck Collaboration VI. 2014, A&A, 571, A6
Planck Collaboration XXVIII. 2014, A&A, 571, A28
Planck Collaboration Int. XXVII. 2015, in press, DOI: 10.1051/0004-6361/201424790
Polletta, M., Tajer, M., Maraschi, L., et al. 2007, ApJ, 663, 81
Rawle, T. D., Egami, E., Bussmann, R. S., et al. 2014, ApJ, 783, 59
Sajina, A., Yan, L., Lacy, M., & Huynh, M. 2007, ApJ, 667, L17
Sajina, A., Yan, L., Fadda, D., Dasyra, K., & Huynh, M. 2012, ApJ, 757, 13
Sargent, M. T., Schinnerer, E., Murphy, E., et al. 2010, ApJ, 714, L190
Schmidt, M. 1959, ApJ, 129, 243
Serjeant, S. 2012, MNRAS, 424, 2429
Silk, J., & Norman, C. 2009, ApJ, 700, 262
Smail, I., Chapman, S. C., Blain, A. W., & Ivison, R. J. 2004, ApJ, 616, 71
Solomon, P. M., & Vanden Bout, P. A. 2005, ARA&A, 43, 677
Solomon, P. M., Downes, D., Radford, S. J. E., & Barrett, J. W. 1997, ApJ, 478, 144
Soucail, G., Fort, B., Mellier, Y., & Picat, J. P. 1987, A&A, 172, L14
Staguhn, J. G., Benford, D. J., Fixsen, D. J., et al. 2012, in SPIE Conf. Ser., 8452
Swinbank, A. M., Chapman, S. C., Smail, I., et al. 2006, MNRAS, 371, 465
Swinbank, A. M., Smail, I., Longmore, S., et al. 2010, Nature, 464, 733
Swinbank, A. M., Papadopoulos, P. P., Cox, P., et al. 2011, ApJ, 742, 11
Tabatabaei, F. S., Schinnerer, E., Murphy, E. J., et al. 2013, A&A, 552, A19
Thomson, A. P., Ivison, R. J., Simpson, J. M., et al. 2014, MNRAS, 442, 577
Vieira, J. D., Marrone, D. P., Chapman, S. C., et al. 2013, Nature, 495, 344

---

[4] `http://www.rssd.esa.int/index.php?project=PLANCK&page=Planck_Collaboration`

Vlahakis, C., Eales, S., & Dunne, L. 2007, MNRAS, 379, 1042
Walsh, D., Carswell, R. F., & Weymann, R. J. 1979, Nature, 279, 381
Wardlow, J. L., Cooray, A., De Bernardis, F., et al. 2013, ApJ, 762, 59
Weiß, A., De Breuck, C., Marrone, D. P., et al. 2013, ApJ, 767, 88
Yan, L., Donoso, E., Tsai, C.-W., et al. 2013, AJ, 145, 55

---

[1] Institut d'Astrophysique Spatiale, UMR 8617, Université Paris-Sud, Bât. 121, 91405 Orsay, France
[2] CNRS, 91405 Orsay, France
[3] Institut Universitaire de France, Paris, France
[4] Department of Physics & Astronomy, University of British 66 Columbia, 6224 Agricultural Road, Vancouver, British Columbia, 58 Canada
[5] Institut de Radio Astronomie Millimétrique (IRAM), 300 rue de la Piscine, Domaine Universitaire, 38406 Saint-Martin d'Hères, France
[6] Harvard-Smithsonian Center for Astrophysics, Cambridge, MA 02138, USA
[7] Steward Observatory, University of Arizona, Tucson, AZ 85721, USA
[8] Université de Toulouse, UMS-OMP, IRAP, 31028 Toulouse Cedex 4, France
[9] CNRS, IRAP, 9 Av. colonel Roche, BP 44346, 31028 Toulouse Cedex 4, France
[10] INAF, Osservatorio Astronomico di Padova, Vicolo dell'Osservatorio 5, 35122 Padova, Italy
[11] CEA-Saclay, 91191 Gif-sur-Yvette, France
[12] Aix-Marseille Université, CNRS, LAM (Laboratoire d'Astrophysique de Marseille) UMR 7326, 13388 Marseille, France
[13] ESAC, ESA, PO Box 78, Villanueva de la Cañada, 28691 Madrid, Spain
[14] Infrared Processing and Analysis Center, California Institute of Technology, Pasadena, CA 91125, USA
[15] European Southern Observatory, Karl-Schwarzschild Str. 2, 85748 Garching, Germany
[16] European Southern Observatory, ESO Vitacura, Alonso de Cordova 3107, Vitacura, Casilla 19001, Santiago, Chile
[17] Atacama Large Millimeter/submillimeter Array, ALMA Santiago Central Offices, Alonso de Cordova 3107, Vitacura, Casilla 763-0355, Santiago, Chile
[18] School of Earth and Space Exploration, Arizona State University, Tempe, AZ 85287, USA
[19] UPMC Univ. Paris 06, UMR 7095, Institut d'Astrophysique de Paris, 75014 Paris, France
[20] Department of Physics, University of Oxford, Denys Wilkinson Building, Keble Road, Oxford OX1 3RH, UK

Chapter 5

Intervening mass distributions along the lines-of-sight

Contents

5.1 Overview of the methodology

In this chapter we aim at characterizing the mass distribution along the lines-of-sight toward our Planck Dusty GEMS, before computing detailed models of the strong lensing magnification. This study is based on the rest-frame optical/NIR imaging obtained at CFHT and VLT, and also uses additional spectroscopy from the SDSS publicly available catalogs and from our own follow-up observations. On the whole, the components of the foreground amplifying mass are analyzed in three steps. We first compute number densities with a dedicated algorithm to identify the most significant overdensities of sources in the K-band. Then we combine spectroscopic redshifts with our independent photometric redshifts to analyze individual foreground galaxies and to identify genuine three-dimensional structures. We finally use the galaxy red sequence as a probe of the densest environments in order to search for the most massive foreground clusters. We perform a blind search of this red sequence at $z < 1.0$ and deduce cluster redshifts with a reasonable accuracy ($\Delta z \sim 0.05$). Based on this analysis, will finally show that all sub-mm sources have nearby intervening structures lying almost exclusively at intermediate redshifts ($z < 1.0$).

Since the GEMS are exceptionally bright sources we will have to ensure we account for the possibility of multiple lenses at different redshifts. As a matter of fact, the sub-mm sources would be associated with multiple potential wells which could play a major role in the strong lensing models due to extrenal shear components. In addition, we will also have to rule out the presence of multiple source planes behind a primary lens. These type of configurations involve secondary arcs at intermediate redshifts, between the lens and the sub-mm emitter, and were previously encountered in systems such as SDSSJ0946+1006 (Gavazzi et al. 2008). They could also make the lens modeling more challenging.

5.2 Number densities using galaxy number counts in the near-infrared

We first derive the overall surface densities of NIR sources and the number density fields from number counts in the K-band. Using these quantities, we search for projected overdensities of galaxies with respect to the field and measure their peak position and significance. This step enables us to identify the GEMS directly associated with overdensities of galaxies, which are therefore probably gravitationally lensed by foreground groups or clusters. But in other cases, it rules out the presence of massive and extended structures in the gravitational lensing potentials. We note that such surface densities are nevertheless subject to chance alignments. For this reason, further analysis will be required to determine the physical nature of the lensing structures and to account for the possibility of multiple lenses at different redshifts.

5.2.1 The Adaptive Kernel Density Estimate

Overview of the method

To quantify the mean number density fields and search for overdensities of NIR sources I use the non-parametric Adaptive Kernel Density Estimation (AKDE) method recommended in Ferdosi et al. (2011). The AKDE algorithm of I. Valtchanov (applied in Valtchanov et al. 2013) allows us to characterize the spatial distribution of these overdensities and to quantify their significance with respect to the background rms. The procedure is exclusively based on the positions of sources detected in the K-band, which we take from the photometric catalogs presented in §3.2.1.

In the general case, if we consider N points at the positions $\tilde{r}_i$ ($i = 1, ..., N$), the AKDE $\rho(\tilde{r})$ introduced in Pisani (1996) will be expressed as

$$\rho(\tilde{r}) = \frac{1}{N}\sum_{i=1}^{N} K_2(\tilde{r}_i, \sigma_i; \tilde{r}) \qquad (5.1)$$

where the σ_i ($\mathrm{i} = 1, ..., \mathrm{N}$) are the kernel widths of each point and $\mathrm{K_2}(\tilde{\mathrm{r}}_\mathrm{i}, \sigma_\mathrm{i}; \tilde{\mathrm{r}})$ defines the two-dimensional Gaussian kernels.

Since adopting the correct $\sigma_{\mathrm{i}=1,...,\mathrm{N}}$ is a crucial step of the calculation, the AKDE algorithm follows the iterative method of Pisani (1996) to find the optimal Gaussian kernel at the position of each point, according to the local density of sources. This is achieved by minimizing a local quantity – the integrated squared error – between the true and estimated number density fields. Densities are then derived at each point, i.e. at the position of each K-band detection, and the algorithm uses kernel-smoothed catalogues to deduce a density map for each NIR photometric catalogue. As further described below, the AKDE finally computes the standard deviation of each number density field as well as SNR density maps. The latter depict the center and morphology of each overdensity which describes, for example, the concentration of sources toward the center of the structure. Consequently, the significance of each overdensity is naturally defined as the SNR density peaks.

In this method, using a locally adaptive kernel enables to properly account for possible clustered structure in the field-of-view. In such a case, the minimal distance between individual members of the structure indeed drops. Thus, if a global solution was computed, the optimization would provide an incorrect kernel with too small size and significantly overestimate the densities (Ferdosi et al. 2011).

Standard deviation of the number density fields for the background sky

The standard deviation of the number density fields, σ_ref, should not be biased by the potential high density peaks in the fields themselves. Using the AKDE calculated in our K-band frames centered on the GEMS to infer this standard deviation could thereby significantly overestimate σ_ref. As a consequence the SNR density peaks found over the maps would be biased. To overcome this issue we could derive the standard deviation over the background sky from Monte Carlo simulations as done in Planck Collaboration et al. (2015d). This would require to generate random positions for the sources detected in our K-band images, and then deduce σ_ref from the resulting number density field.

We rather follow a more empirical approach and characterize the background sky in WIRCam or HAWK-I fields with similar depth as our $5' \times 5'$ optimal fields-of-view. Choosing frames of identical sizes is also necessary to avoid any bias from structures extended to larger scales. For the GEMS imaged at CFHT, this method is indeed appropriate given that the depth of K-band images is comparable for all sources (3σ limiting magnitudes of ~ 22, see Table 3.1). The basic idea is to use independent frames without significant overdensities in the three remaining WIRCam quadrants. I use the three CCDs around G165.7 and select several frames of $5' \times 5'$ typically centered 3 Mpc away from the position of the GEMS, for a fiducial lens plane at $\mathrm{z} = 0.35$. Since we have no clear evidence for an extremely massive cluster of $\mathrm{M} > 10^{14}\ \mathrm{M}_\odot$ in front of G165.7, these frames are necessarily decoupled from any overdensity toward the sub-mm source. I perform precisely the same source extraction on each of them, applying the same flux threshold and extraction procedure and using the zero-point of §3.2.1. With the resulting catalogs of source positions I then run the AKDE and keep the five frames without SNR density peaks above 3σ, in order to avoid potentially significant structures. For the selected frames, I compute the number density field and its standard deviation, σ_ref. For consistency between the WIRCam catalogs, the final σ_ref of the number density field of the background sky (σ in the following) is taken as the median of these five standard deviations computed around G165.7. This common value is applied to each of the nine fields observed with WIRCam. A similar procedure is followed for G244.8.

Significant overdensities of NIR sources toward the GEMS

I compute the AKDE using the galaxies detected with $\mathrm{SNR} > 3$ in the K-band, inside our ten fields-of-view of about $5' \times 5'$. Hence, I do not apply any color cut that would favour the selection of galaxies at intermediate redshifts, but rather perform a blind density estimate. The AKDE provides the NIR number density fields toward each GEMS and extracts the peak and mean values over these fields, in

Source	AKDE peak[(1)] Significance	Peak offset[(2)]	Significance toward the GEMS[(3)]
PLCK_G045.1+61.1	4.4σ	$\sim 20''$	$\sim 4.0\sigma$
PLCK_G080.2+49.8	6.3σ	$\sim 25''$	$\sim 5.5\sigma$
	4.2σ	$\sim 1.2'$	—
PLCK_G092.5+42.9	5.3σ	$\sim 34''$	$\sim 4.0\sigma$
PLCK_G113.7+61.0	4.0σ	$\sim 2.6'$	$\sim 2.5\sigma$
PLCK_G138.6+62.0	$<4.0\sigma$	$\sim 50''$	$\sim 3.0\sigma$
PLCK_G145.2+50.9	5.4σ	$< 10''$	$\sim 5.0\sigma$
	5.2σ	$\sim 2.0'$	—
	4.7σ	$\sim 2.1'$	—
PLCK_G165.7+67.0	5.5σ	$\sim 10''$	$\sim 5.5\sigma$
	5.3σ	$\sim 1.2'$	—
	5.3σ	$\sim 1.7'$	—
PLCK_G200.6+46.1	4.0σ	$\sim 1.8'$	$\sim 1.5\sigma$
PLCK_G231.3+72.2	$<4.0\sigma$	$\sim 2.7'$	$\sim 3.5\sigma$
PLCK_G244.8+54.9	6.1σ	$\sim 1.0'$	$\sim 2.0\sigma$
	8.9σ	$\sim 2.9'$	—

Table 5.1: (1): The AKDE peaks above 4σ significance, listed from the closest to the GEMS to the more distant. (2): Angular offset between the AKDE peak and the position of the GEMS. (3): Approximate value of the SNR density of K-band sources at the position of the high redshift emitter.

addition to the standard deviation of the background sky, σ. Using the densities and Gaussian kernels at the position of each input galaxy, I divide by σ and compute significance maps of 500×500 pixels, in order to identify the overdensities more easily. The significance of each overdensity is then defined as its peak SNR.

As reported in Table 5.1, the ten maps contain at least one high density peak with significance ranging from 3.8 to 11.2σ. Secondary overdensities with lower peak SNR are also detected and we quote those above 4σ. To illustrate the position of these overdensities relative to the high redshift emitter and their morphology, I plot the AKDE contours inferred from the SNR maps in Fig.5.1 & 5.2. It turns out that many of these features are not centered in front of the sub-mm sources. I present the angular offsets between the AKDE peaks and the position of the GEMS in Table 5.1. To determine the significance of these overdensities in the lines-of-sight toward each high redshift background emitter, I also quote the SNR of the density maps at these specific coordinates.

G045.1, G080.2 and G145.2 are clearly associated with overdensities of NIR sources, with peak AKDE of 4.4, 6.3 and 5.4σ significance, respectively, located within $30''$ of the GEMS. The corresponding 4σ isodensity contours show irregular morphologies with major axis between $\sim 1.0'$ and $\sim 1.5'$. Moreover, the SNR density of K-band sources remains above 4σ at the position of the high redshift sources. For G045.1, G080.2 and G145.2, the overdensity regions used in the following analysis and lens modeling (§5.4, §5.3 and §6) are defined with the same 4σ contours. G165.7 present the most significant peak AKDE over the ten fields, showing another overdensity of K-band detections in the lensing potential. As seen in Fig.5.2, the contours suggest an elongated filament from the North-East to the South-West of the frame.

The AKDE of G092.5 shows a peak of 5.3σ significance, $\sim 34''$ towards the East. However, because the density contours are off-centre and because the SMA morphology of the GEMS shows a single sub-mm arclet, it is difficult to conclude whether or not this highlights a physical cosmic structure. The clear overdensity South-East of G113.7 suggests an elongated structure close to the edge of the frame which is probably unrelated to the lensed source. Concerning G138.6, G200.6 and G244.8, the

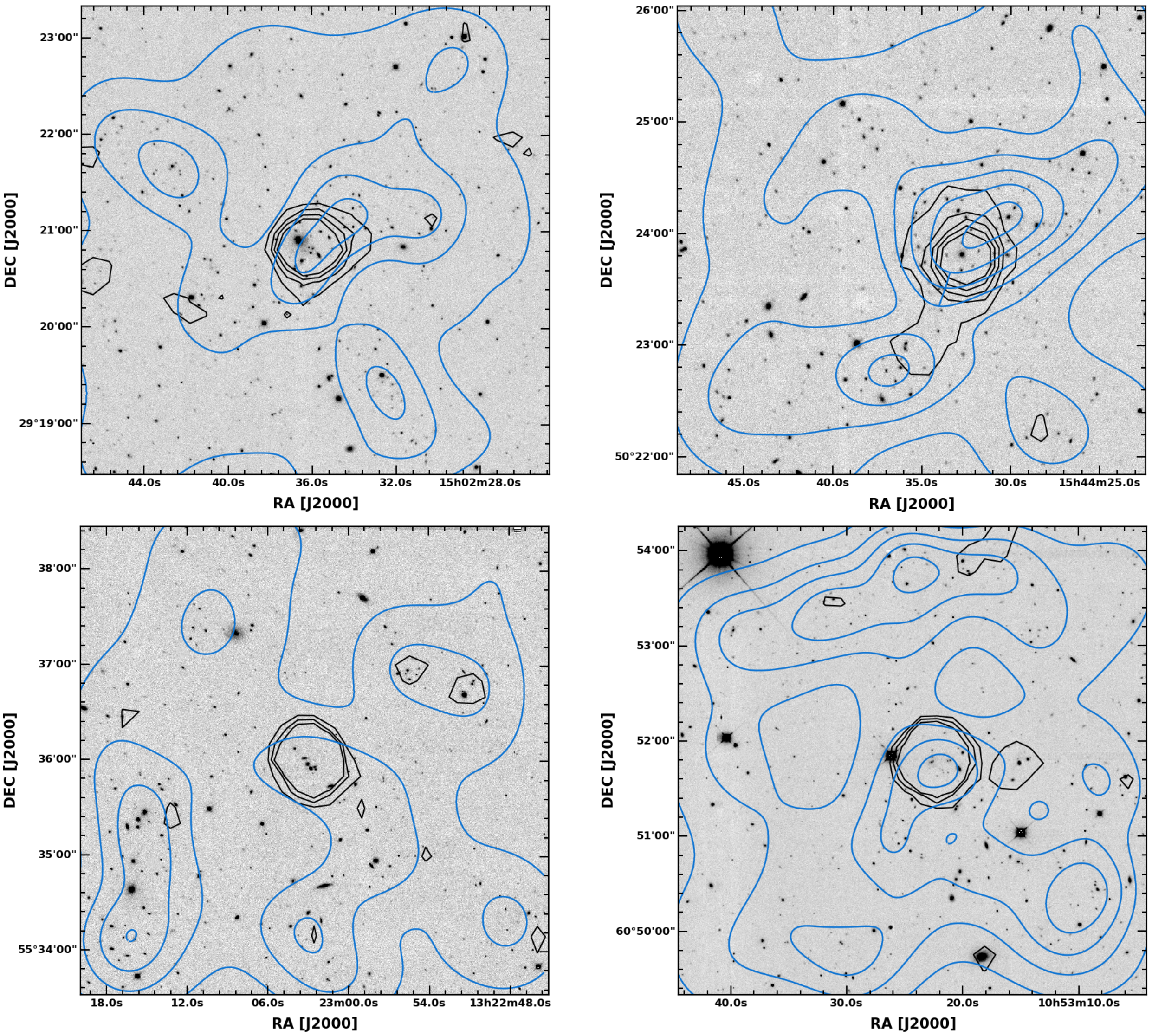

Figure 5.1: CFHT/WIRCam or VLT/HAWK-I K-band images of G045.1, G080.2, G113.7 and G145.2, from top-left to bottom-right, respectively. We show the entire fields-of-view of about $5' \times 5'$ used in the AKDE. Blue contours show the AKDE of galaxies detected in the K-band inside these areas, starting at $+1\sigma$ and increasing by $+1\sigma$. These overdensities are measured with respect to the background standard deviation derived in an independent region (see text). The black lines delineate the Herschel/SPIRE emission at 350 μm and show the position of the background GEMS, with contour levels starting at $+3\sigma$ and increasing by $+3\sigma$. On these maps, North is up and East is on the left.

AKDE algorithm seems to rule any massive group or cluster of galaxies along the direct sight lines. In the foreground of G231.3, a secondary peak between 3 and 4σ is well aligned with the sub-mm source, around a small group of 4-5 galaxies (not presented in Table 5.1). Although this detection is only tentative in the current AKDE, precautions must be taken to model this lensing potential. Finally, the secondary AKDE peaks found within our $5' \times 5'$ fields-of-view are systematically off the GEMS by more than $1'$, which corresponds to a projected distance of ~ 400 kpc in a fiducial lens plane at $z = 0.50$. They are therefore ignored when modeling the foreground lensing potential.

As mentioned below, the AKDE maps and peak values could be significantly affected by chance alignments and, if the worst comes to the worst, some overdensities could result exclusively from this

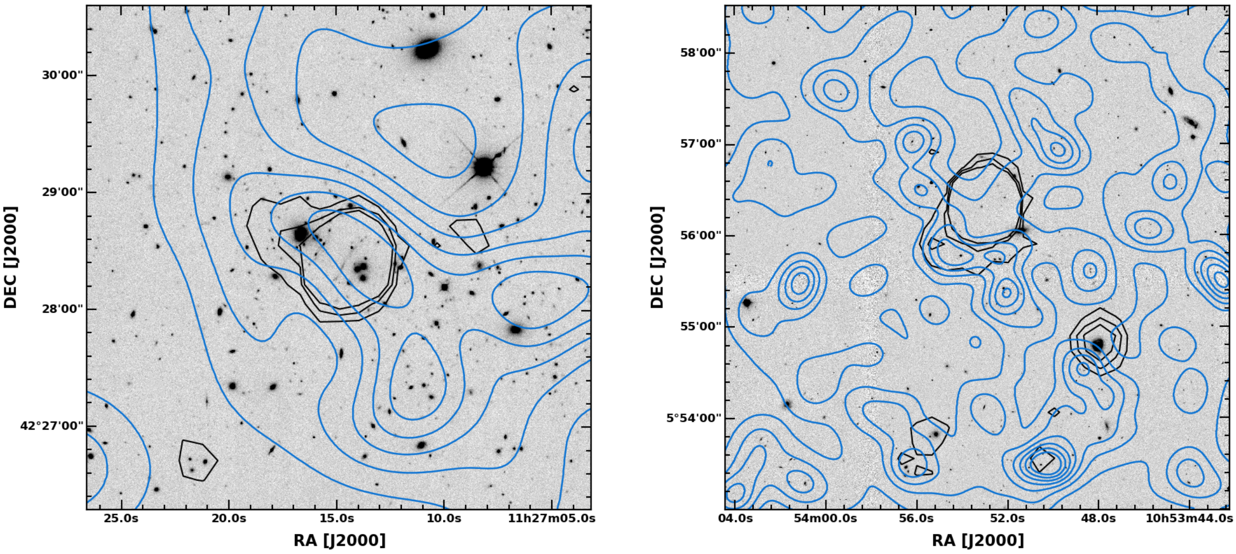

Figure 5.2: Same as Fig.5.1, for G165.7 and G244.8.

spurious effect. Valtchanov et al. (2013) quantifies the probability of finding an overdensity of the same significance after randomly distributing the same number of galaxies over an equivalent area. Instead, we rely on the red sequence and photometric redshifts analysis to further probe the physical nature of these AKDE peaks.

However, we aim at testing the influence of the image size on our AKDE to determine whether or not the density peaks detected in our $5' \times 5'$ fields-of-view are in fact substructures of larger overdensities. This is particularly important for G165.7 because the elongated filament seems to be cut at the edges of our WIRCam K-band frame (Fig.5.1). Since additional photometric criteria suggest that these overdensities all lie at $z < 0.8$ and mostly contain early-type galaxies, they should also be detected with SDSS imaging.

I therefore reproduce the AKDE on shallower SDSS r-band images of $14' \times 19'$ centered on the GEMS. For this purpose, I extract my own catalogs of sources using the same 3σ threshold and derive the standard deviation of the number density field, $\sigma_{\rm ref}$, in the same control field around G165.7. Each overdensity quoted in Table 5.1 is found in these optical data, generally with higher significance. For instance, the most significant peak found for G113.7 and G165.7 is at 7 and 6σ, respectively. We caution that for G231.3, the two AKDE peaks toward the GEMS and in the North-West reach about 5σ, suggesting they could be more significant than expected with our NIR imaging (the third peak in the South-West stays at 3σ. The shape of the new overdensity contours is slightly different but apparently do not extend outside the WIRCAM and VLT fields-of-view, except for G113.7. For this source, however, the r-band detections suggest that the density peak identified with WIRCam is indeed the most significant over $14' \times 19'$. This GEMS is centered at about $2.1'$ from the AKDE peak and since only cluster cores act a strong gravitational lenses (Kovner 1987; Limousin et al. 2007b), this hypothetical massive structure should not affect the lens model of G113.7 at all. In the subsequent parts of the analysis, we therefore suppose that this GEMS is rather magnified by a group of 3-4 galaxies within about $5''$.

5.3 Measuring the redshifts of foreground galaxies

Gathering precise redshift measurements for the foreground galaxies aligned with the dusty GEMS is a major step to characterize the three dimensional shape of the potential wells producing the gravitational magnification. With secure redshifts we can account for chance alignments and characterize the astrophysical nature of lenses to identify the background sources associated with three dimensional overdensities of galaxies at intermediate redshifts. From this analysis, we will select the intervening isolated galaxies, or the group/cluster members to infer the spatial distribution of the underlying dark matter halos and better constrain the strong lensing models. Lastly, this allows us to ensure we account for the possibility of multiple lenses at different redshifts. In the following we present the spectroscopic redshifts of particular interest to our study, which are either publicly available or derived from our follow-up observations. We also describe the methodology used to measure photometric redshifts for the remaining sources in our multi-wavelength catalogs.

5.3.1 The foreground galaxies with spectroscopic redshifts

Public spectro-z from the SDSS

Some of the brightest foreground galaxies have SDSS optical spectra publicly available through the DR12 Science Archive Server (SAS) (Alam et al. 2015). These spectra were obtained as part of the SDSS Baryon Oscillation Spectroscopic Survey (BOSS) or included in the first SDSS Data Release. The SDSS and BOSS spectrographs cover $3800 - 9200$ Å and $3650 - 10400$ Å, respectively, with a resolution of 1500 at ~ 4000 Å and of 2500 at ~ 9000 Å. In these instruments, each fiber has a diameter projected on the sky of 3 and $2''$, respectively. The resulting spectra are calibrated in flux and wavelength.

In BOSS, the targets classified as galaxies by the spectroscopic pipeline and with a robust spectro-z are then processed by independent codes to derive their main physical properties (Bolton et al. 2012). In the Portsmouth pipeline, the broad-band ugriz photometry is fitted with the stellar population models of Maraston (2005) and Maraston et al. (2009) that include both passive or active star formations with various laws, Salpeter (1955) or Kroupa (2001) IMFs, and that test the influence of stellar mass losses. Several galaxy properties such as their age, metallicity and star formation history are derived from the best-fitting SEDs and the stellar masses and star formation rates are then computed accordingly. In addition, the results from two other SED-fitting procedures based on Bruzual & Charlot (2003) and Conroy et al. (2009) models are also provided.

The properties of the spectral lines and stellar continuum and the stellar kinematics are derived from the BOSS spectra without accounting for the internal reddening of the Milky Way, as described in Thomas et al. (2013). This analysis measures the emission line fluxes and equivalent widths and derives the gas kinematics, stellar velocity dispersions and reddening.

In Table 5.2 we present the main properties of the bright foregroud galaxies in our $5' \times 5'$ fields-of-view with spectra from the SDSS. In particular these data indicate a group of two evolved galaxies at a common spectroscopic redshift of 0.348 in front of G165.7. In combination with an additional galaxy at $z = 0.337$, this denotes a small group of galaxies physically connected in a single dark matter halo. As warned in the SDSS release, the stellar mass of the massive elliptical in the field-of-view of G231.3 is probably very underestimated due to photometric issues.

Independent spectro-z from our follow-up

Our X-Shooter spectrum shows that the main deflector toward G244.8 is an optically faint very distant galaxy, with a secure spectroscopic redshift of 1.52 derived from two emission lines (see §3.3.2). To our knowledge, the redshift of this strong lens is nearly matching previous record holders with unambiguous configurations. van der Wel et al. (2013) recently discovered a galaxy at $z = 1.53 \pm 0.09$ magnifying a low-mass starbursting galaxy at $z = 3.417$. This object covers a similar cosmic epoch as the most distant lens found to date, a brightest cluster galaxy at a spectro-z of 1.62 with a nearby companion, both magnifying a two-component source at $z = 1.62$ (Wong et al. 2014).

Distant lensing galaxies of this kind provide oustanding opportunities to infer the total mass of high-redshift galaxies, and to measure precisely their dark matter budget. van der Wel et al. (2013)

Source	SDSS Object					
	RA (J2000)	Dec (J2000)	Spectro-z	σ_{stellar} [km/s]	M_* [10^{11} $M_\odot$]	SFR [$M_\odot$ yr^{-1}]
G045.1	15:02:36.62	+29:20:53.94	$0.55419 \pm 0.00018^{(1)}$	375 ± 53	–	–
	15:02:36.49	+29:20:41.68	$0.55955 \pm 0.00013^{(2)}$	233 ± 30	1.3-2.5	0
	15:02:31.67	+29:20:50.56	0.48306 ± 0.00010	306 ± 29	1.7-2.0	1.7-2.5
G080.2	15:44:32.74	+50:23:48.94	$0.67253 \pm 0.00024^{(3)}$	303 ± 63	6.0-6.3	0
	15:44:20.35	+50:20:56.29	0.51163 ± 0.00010	291 ± 30	1.4-4.0	0.0-2.7
G092.5	16:09:13.07	+60:46:16.09	0.65478 ± 0.00022	–	–	–
	16:09:18.24	+60:45:22.23	$0.44805 \pm 0.00009^{(4)}$	275 ± 21	5.6-5.8	0
G113.7	13:23:08.37	+55:37:19.65	0.17597 ± 0.00006	128 ± 19	0.2-0.3	0
	13:23:16.11	+55:34:38.23	0.27418 ± 0.00004	284 ± 13	1.4-1.9	0
G145.2	10:53:14.41	+60:51:48.24	1.19084 ± 0.00031	–	–	–
G165.7	11:27:13.13	+42:31:09.48	0.50974 ± 0.00018	319 ± 48	0.9-2.1	0.5-2.6
	11:27:10.77	+42:30:14.14	0.03348 ± 0.00001	174 ± 3	0.4-0.5	0
	11:27:16.59	+42:28:41.01	$0.34788 \pm 0.00007^{(5)}$	323 ± 22	4.2-5.6	0
	11:27:16.69	+42:28:38.17	$0.33767 \pm 0.00004^{(6)}$	307 ± 14	2.1-6.0	0.0-1.1
	11:27:13.75	+42:28:22.61	$0.34770 \pm 0.00012^{(7)}$	271 ± 35	1.6-2.7	0
	11:27:06.69	+42:27:50.27	0.27524 ± 0.00009	290 ± 23	1.0-3.7	0
	11:27:16.98	+42:27:32.76	2.22477 ± 0.00052	–	–	–
G200.6	09:32:28.41	+27:25:50.82	1.07176 ± 0.00043	–	–	–
	09:32:24.92	+27:22:44.75	0.10693 ± 0.00002	98 ± 6	0.1-0.3	0
G231.3	11:39:13.44	+20:26:55.78	0.16246 ± 0.00003	172 ± 9	1.4-2.2	0
	11:39:16.19	+20:25:39.49	$0.02581 \pm 0.00001^{(8,*)}$	157 ± 3	~ 0.7	0
G244.8	10:53:43.89	+05:57:13.86	$0.18383 \pm 0.0006^{(*)}$	182 ± 20	1.1-1.6	0
	10:53:51.41	+05:56:02.94	$0.13068 \pm 0.00003^{(9)}$	225 ± 11	1.7-2.3	0
	10:53:55.42	+05:55:08.00	0.49103 ± 0.00014	140 ± 37	1.0-1.2	2.0-4.9
	10:53:45.25	+05:55:01.32	0.06970 ± 0.00001	45 ± 42	~ 0.003	0.3-0.4
	10:53:48.03	+05:54:47.82	0.06929 ± 0.00001	134 ± 9	0.2-0.4	2.3-5.7
	10:54:01.71	+05:54:09.26	0.13036 ± 0.00001	63 ± 20	0.07-0.2	0.8-1.7
	10:53:55.14	+05:53:49.51	0.37041 ± 0.00010	260 ± 24	1.6-4.9	0.0-3.3
	10:53:47.63	+05:53:54.97	$0.06919 \pm 0.00001^{(*)}$	–	~ 0.01	0.0-0.2

Table 5.2: Publicly available spectroscopic redshifts and physical properties of foreground galaxies from the Sloan Digital Sky Survey. The stellar masses and the star formation rates are derived from the best-fitting models from the Portsmouth pipeline. We quote the 68% confidence intervals deduced from their PDF. We choose either the passive or star forming templates according to the reduced χ^2. (1-9): Identify the objects in the sight lines toward the GEMS which are directly relevant for the strong lensing analysis, either because they are within $10''$ of the background emitters or given their high stellar masses. The SDSS spectra of these sources are reproduced in annex. (*): Warning concerning the photometric quality.

find an enclosed mass of 7.6×10^{10} $M_\odot$ within the near-complete Einstein radius of $\overset{\circ}{0}.35''$ formed by the gravitational arcs. They combine this result with the stellar mass obtained from SED fitting to establish an upper limit on the contribution of dark matter within the background arcs of about 60%. Similarly, the system studied by Wong et al. (2014) comprises an integrated mass of 1.8×10^{11} $M_\odot$ within $0.38''$, suggesting a lower dark matter fraction, between 0 and 30% of the total mass depending on the choice of IMF. Since these discoveries require specific alignments which are extremely unlikely, they also enable to tune the predicted number counts of intermediate mass galaxies at high-redshift and to better constrain the galaxy evolution models.

5.3.2 Deriving photometric redshifts in the optical/NIR

Photometric redshifts (photo-z) are widely used to measure the distance of large sets of faint galaxies detected in deep multi-wavelength surveys, as a complement of specto-z which are more time consuming. Photo-z are usually derived using large band photometry and require to identify strong spectral features such as sharp discontinuities (either the 4000 Å break or the Lyman break at 912 Å). These features should indeed remain apparent in the low resolution spectra obtained after convolving the theoretical SED with the filter transmission functions, to allow a robust comparison with the observations. The accuracy of photo-z measurements depends on the number of available filters and their bandpass – i.e. the resolution of the observed spectra – and on the absolute photometric uncertainties. With our multiband imaging sampling the optical-to-NIR wavelengths with four or five bands, we probe the 4000 Å break for galaxies at redshifts above 0.4-0.6 which limits the degeneracies. Moreover our relative calibration provides robust zero-points and the flux extraction process offers relative photometric uncertainties almost always below 10%. In the following I will take advantage of this careful analysis to derive a photo-z for each galaxy selected in the multi-wavelength catalogs of §3.2.1.

Brief overview of the photo-z estimators

Before developing the steps taken to derive the photo-z, I briefly introduce the two main approaches reported in the literature and compare their reliability and general performances.

The SED fitting method (Koo 1985; Pello et al. 1996; Sawicki et al. 1997) uses a library of template spectra, either empirical or derived from synthetic stellar populations models, to predict colors for several galaxy types and different redshifts. In practice, the individual spectra are corrected for dust extinction and redshifted, and then convolved with the response functions of the available filters. The resulting set of modeled colors is fitted to the observed SEDs using a standard χ^2 minimization, in order to determine the most likely redshift (e.g., the hyperz public code, Bolzonella et al. 2000). In spite of its simplicity, this method is based on the strong assumption that a given color corresponds to a single redshift. The reliability of the derived photo-z therefore depends heavily on the completeness and representativity of the underlying template grid (Sawicki et al. 1997). In a given study, one should caution that the reference set indeed describes most of the detected galaxies, with a reasonable number of SEDs to avoid the color/redshift degeneracies particularly challenging for faint sources. If, despite these precautions, a wrong template is assigned to a galaxy, either because of random photometric errors or because the template library is incomplete, the resulting photo-z will be affected by a minor or catastrophic error. The latter errors are due to ambigious assocations in color space and generally affect significant fractions of samples characterized with pure SED fitting (up to 10%).

To strengthen these estimates and minimize the number of catastrophic failures, one can use Bayesian marginalization to include relevant knowledge in prior probabilities (Benítez 2000). The resulting photo-z are less affected by color/redshift degeneracies than in frequentist approaches, even for large template libraries, but Bayesian inference can also introduce misleading effects. We decided to use this technique in our study and our motivations are further described in the next subsection.

The training set approach (Connolly et al. 1995; Brunner et al. 1997) is empirical and requires to identify a large subsample of galaxies with spectroscopic redshifts and, at least, apparent magnitude and color measurements (the so-called training set). From these targets we assess the probability of finding a given redshift z for a galaxy in the training set, given its observed magnitudes and colors. In particular, the magnitudes of reference galaxies are crucial since they help break the color/redshift degenaracies. The probabilities are parametrized with polynomial fits (see e.g. Connolly et al. 1995), or using more advanced algorithms (e.g., the Artificial Neural Network code ANNz of Collister & Lahav 2004). This provides empirical calibrations that fit properly the reference spectroscopic redshifts and that can be used as priors to deduce photo-z for the remaining galaxies. In addition, some studies have introduced other observational parameters such as the angular size or the concentration index to better constrain these redshift priors with machine learning algorithms (Collister & Lahav 2004). In conclusion, the training set approach is providing robust photo-z for large and shallow surveys – ideally probing up to $z \sim 1$ (Brunner et al. 1997) – with a partial spectroscopic coverage. Nowadays, machine learning algorithms also provide very accurate magnitude/color and magnitude/redshift calibrations for substantial training sets. However the method is not valid beyond the ranges of redshift and spectral type covered by the training set since any extrapolation of the empirical relations would be very inaccurate. It therefore becomes impractical for faint galaxy samples without spectro-z.

Moreover, Abdalla et al. (2011) compare several photo-z codes using >10000 galaxies with spectro-z in the 2SLAQ sample. They observe that the training set indeed reduces the scatter for redshifts close to the reference galaxies (although their comparison is exclusively based on a sample of luminous red galaxies). Nevertheless this approach remains inapplicable in our study since we lack consistent training samples with spectro-z.

The Bayesian formalism and the BPZ code

As already mentioned, Bayesian inference is appropriate to include relevant knowledge in prior probabilities (Kodama et al. 1999; Benítez 2000). If we assume that a given survey provides observed magnitudes and colors, Bayesian marginalization seeks to quantify $\mathrm{p(z|C,m)}$, the probability that a galaxy of apparent magnitude m and color C will have a redshift z. In the formalism of Benítez (2000), it is expressed as

$$\mathrm{p(z|C,m)} = \frac{\mathrm{p(z|m)p(C|z)}}{\mathrm{p(C)}} \propto \mathrm{p(z|m)p(C|z)} \tag{5.2}$$

where $\mathrm{p(C)}$ is a normalization factor, and the likelihood $\mathrm{p(C|z)}$ corresponds to the probability of finding a galaxy with color C at a given redshift z. The prior probability is encoded in the $\mathrm{p(z|m)}$ term and weights each template considering a set of observed properties. In this basic example, it corresponds to probability of a galaxy having redshift z given its magnitude m. Generally, a wide range of priors can be introduced to reduce the color/redshift degeneracies and the number of catastrophic errors. One can use the redshift distribution expected for a given template, for example to favour low redshifts for bright and elliptical galaxies. Alternately, expected redshift limits, galaxy type fractions, shapes or angular sizes can be encoded in prior probabilities.

The Bayesian Photometric Redshifts code (BPZ, Benítez 2000) applies this formalism by taking a multiband photometric catalog, the transmission functions of the corresponding filters and a template library as inputs. The multi-wavelength catalogue should include the magnitude and error of each target, as well as a specific flag for the non-detections and the 3σ detection limit of each band. The software is able to find systematic differences between template and observed colors and to compute zero point corrections in each photometric band. In output, BPZ yields the most likely redshift and spectral type together with the complete Probability Distribution Function (PDF). Possible multiple solutions are indicated in the ODDS parameter. To select galaxies with a nicely peaked redshift PDF we can apply the criteria ODDS > 0.90, or increase the threshold up to 0.99 to keep only the most robust photo-z. For the most likely template/redshift combination, a χ^2 indicates the reliability of the fit

$$\chi^2 = \sum_{\mathrm{i=1}}^{\mathrm{n}} \left(\frac{\mathrm{F_{observed,i}} - \mathrm{A} \times \mathrm{F_{template,i}}}{\sigma_{\mathrm{i}}} \right)^2 \tag{5.3}$$

where $\mathrm{F_{observed,i}}$ and σ_{i} are the observed flux in filter i and its uncertainty, $\mathrm{F_{template,i}}$ is the flux of the most likely template at the appropriate photo-z, and A is a scaling factor applied on the normalized

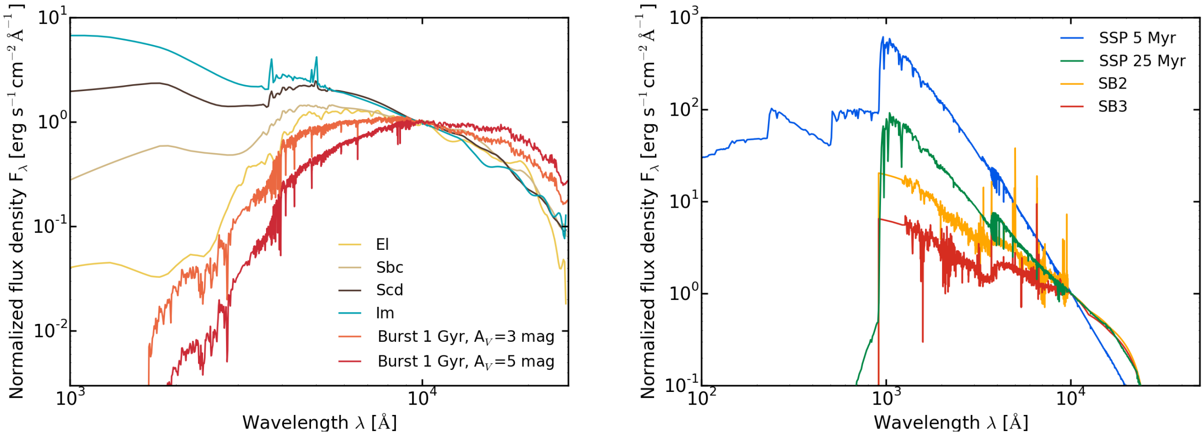

Figure 5.3: The reference templates chosen in the input library of BPZ. *Left :* Empirical templates from the CWW library (El, Sbc, Scd, Im, Coleman et al. 1980) and our additional strongly reddened spectra (orange and red curves). *Right :* The four templates with bluer colors, including the starburst spectra of Kinney et al. (1996) (red and yellow lines) and the young SSPs from Bruzual & Charlot (2003) evolutionary synthesis models (green and blue lines). The SEDs are normalized to $F_\lambda = 1$ at $\lambda = 10^4$Å.

templates.

The code also provides individual plots for each SED fit.

The photometric redshift calibration and estimate

I apply BPZ to the optical/NIR photometric catalogs from our follow-up imaging at CFHT and VLT. Since IRAC photometry involves inherent uncertainties and probes rather flat portions of the template SEDs, the 3.6 and 4.5 μm bands are not helpful in the process and are set aside.

As stated in Sawicki et al. (1997), the set of input templates should be representative and complete. However – although this issue is minimized in the Bayesian approach – one should not increase too much the number of templates to avoid bringing in new color/redshift degeneracies. Taking account of this will limit the situations where a given set of observed colors can be associated with several templates at different photo-z, therefore leading to catastrophic failures. The original template library of BPZ contains the four empirical templates of Coleman et al. (1980) (CWW) recalibrated in Benítez et al. (2004), along with the two starburst templates of Kinney et al. (1996) representing the blue galaxies observed in the Hubble Deep Field North (HDF-N). The latter two are crucial to refine our photo-z, in particular at $z > 2$ where the population of actively star forming galaxies becomes dominant (Benítez 2000). As stated in Coe et al. (2006), even bluer SEDs composed of Single Stellar Populations (SSP) of 5 and 25 Myr from the BC03 synthesis models (Bruzual & Charlot 2003) are mandatory to reproduce the youngest galaxy types . For their part, the CWW standard templates cover the most common spectral types found in the local universe. Finally, we augment this library with strongly reddened SEDs ($A_V = 3$ and 5 mag) to probe the degeneracy between dust attenuation and redshift. Each one of these SED cover wavelengths between 500 and ~ 26000 Å, with a sharp discontinuity at 912 Å modeling the Lyman break (Fig.5.3). We do not interpolate the model colors between these templates. We also remind that evolution with cosmic time is not taken into account, except requiring that the age of the galaxy is below the age of the universe at a given redshift.

The continuum emission of galaxies between 912 Å and a few microns is dominated by the emission from their stellar populations and the most significant color variations from type to type appears in the UV/optical domains. As shown by the right panel of Figure 5.3, the youngest stellar populations of less than 100 Myr dominate the UV regime in the bluest late-type galaxies with active star formation. More evolved galaxies presented in the left panel contain very little young stars and their SED is rather dominated by the intermediate age (about 1 Gyr) and oldest ($>$ 10 Gyr) populations, in the optical and NIR regimes, respectively. Since their emission peaks between 6000 and 12000 Å, these early-type elliptical or lenticular galaxies exhibit redder colors.

Moreover, the radiation from stars can be severely affected by the ISM of the host galaxy, as illustrated with the two reddened additional templates. The gas and dust reservoirs scatter and absorb the continuum emission, in particular from the most massive populations emitting at shorter wavelengths. It then reprocesses this energy in the infrared resulting in a global reddening of the spectrum. In particular, in late-type galaxies, neutral hydrogen gas around star forming regions absorbs the UV photons with energies greater than the Lyman limit at 912 Å. The absorption by the diffuse hydrogen gives rise to the Lyman break, a very prominent feature seen in the right panel of Figure 5.3 which is nevertheless falling at shorter wavelengths than our photometric bands.

Spectral breaks due to absorption features in the stellar atmospheres are usually observed in evolved galaxies with older and more metal rich stellar populations. For instance the Balmer, MgII and Fe decrements at 3646 Å, $\sim$ 2800 Å and 2635 Å, respectively, are more or less prominent given the physical conditions in these atmospheres, namely their spectral type (see e.g. Binney & Merrifield 1998, for more details). The Balmer cutoff appears below 3646 Å and comes from the absorption of photons more energetic than the Balmer limit by hydrogen electrons in the first excited state. Since a majority of photons from very massive stars ionize the surrounding hydrogen atoms in the chromospheres, this process is more efficient in stars of intermediate effective temperature (type A). It is more easily detected in the continuum emission of early-type galaxies where it can serve as a proxy for the age of the stellar populations. In the UV, the strong absorption doublet of the ionized magnesium MgII and additional weak metal lines produce a continuum break around 2800 Å (Kondo et al. 1970). FeII absorption multiplets in F and G type stars produce a nearby cutoff just below 2640 Å (Morton et al. 1977; Cimatti et al. 2004) and a top-hat shaped feature therefore appears inbetween (Spinrad et al. 1997).

However, the strongest spectral feature most frequently used to determine the photo-z of galaxies at $z \lesssim 1$ is the $D_n(4000)$ discontinuity at 4000 Å (Connolly et al. 1995). It arises from several absorption lines extremely close to each other and probes the age of the stellar populations from the last episode of star formation, mainly through variations of atmospheric opacity in O and B stars (Kauffmann et al. 2003). Metals are multiply ionized in the atmospheres of these young and hot stars which reduces the opacity of the environment and also decreases the intensity of absorption lines. The $D_n(4000)$ feature is therefore moderately pronounced in spiral and irregular late-type galaxies where these massive stars are dominant but becomes prominent in quiescent early-types (Boselli 2011). The four star-forming templates on the right panel of Fig.5.3) are classified from the youngest populations (blue line) to the oldest (red line). They illustrate that the amplitude of the $D_n(4000)$ feature indeed decreases in younger types with bluer SEDs. On the other hand, this discontinuity also increases with metallicity (Gallazzi et al. 2005) (see also Fig.5.8).

Our photometry covers the optical/NIR regimes between the r (or V) and K bands and therefore probes the 4000 Å sharp break in principle from $z \sim 0.5$ up to the highest redshifts ($z \sim 4$). The Lyman break is redshifted in our bluest band for very distant sources lying at $z > 6$ which are obviously inaccessible with the depth of our CFHT and VLT images. This avoids incorrect identifications of these major spectral discontinuities, one of the main source of catastrophic errors.

I use the BPZ default priors derived from the HDF-N and the CFRS which have proven to be efficient for 90% of the galaxies with spectroscopic redshifts in the HDF-N, over a broader magnitude range than our photometry (Benítez 2000). These priors are based on the K-band magnitudes. I avoid

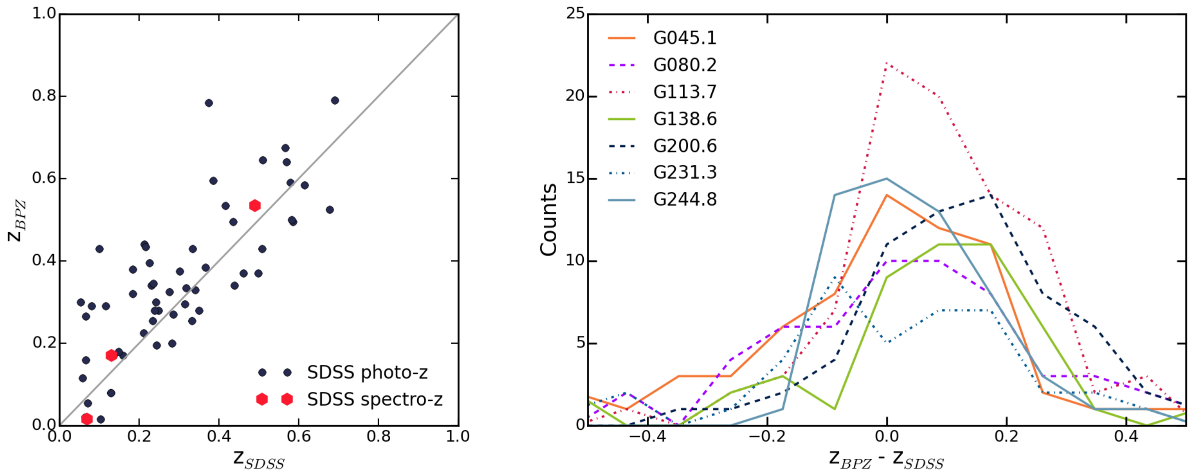

Figure 5.4: *Left* : BPZ photometric redshift of the galaxies in the field-of-view toward G244.8 plotted against the photometric and spectroscopic SDSS ones, in the range $0 < z < 1$. Objects with reliable BPZ estimates are selected, namely with $\chi^2 < 10$ and ODDS > 0.9. The continuous line displays the 1:1 relation and the 1σ scatter defined as $\left\langle (z_{\rm BPZ} - z_{\rm SDSS})^2 \right\rangle^{1/2}$ is about 0.13. *Right* : Histograms of the difference between our photometric redshift measurements and SDSS photo-z from the public archive, for subsets of galaxies matching the above reliability criteria. We overplot 7 representative curves among the 10 fields-of-view included in our BPZ analysis.

deriving priors from the avaible spectro-z because these calibrators are too rare, and do not favour any redshifts for the galaxy groups or clusters suggested, for example, toward G165.7. To avoid skewing the results, I rather perform a blind characterization with a broad photo-z upper limit of 5.0.

I implement the appropriate filter transmission functions and carefully indicate the photometric uncertainties and calibration errors in the input catalogs and parameter files for BPZ, as advised in (Margoniner & Wittman 2008). Including either the SDSS-DR12 ugriz photometry or its 3σ detection limits for each galaxy significantly increases the number of sources with robust photo-z. For instance, 35 new reliable photo-z are found in the field toward G244.8. SDSS data indeed extend the optical constraints down to about 3500 Å – with however larger photometric uncertainties in SDSS u-band – which, in some cases, breaks the redshift/type degeneracies and rules out multiple redshift solutions. The bluest u and g bands notably offer a better sampling of the SED on both sides of the $\rm D_n(4000)$ discontinuity for sources between $z = 0$ and $z = 0.5$. In doing so, we reduce the significant bias between BPZ and SDSS photo-z to obtain the distributions of Figure 5.4.

Among the 10 fields-of-view characterized with BPZ, the algorithm finds very few systematic offsets between the observed magnitudes and the magnitudes of the best fit models. This strengthens the validity of our photometric calibration in the VLT and CFHT bands. Only K-band magnitudes for G080.2, z-band magnitudes for G138.6 and G200.6, and J-band magnitudes for G231.3 proved to be too bright by 0.05, 0.10, 0.15 and 0.30 mag, respectively. In these cases, the additional adjustments suggested by BPZ overcome our zero-point uncertainties and are probably due to the low number of stars available for the relative calibration. I apply these four zero-point offsets in the corresponding bands to reduce the dispersion on the output photometric redshifts.

Comparison with public photometric and spectroscopic redshifts from the SDSS

I use the ODDS parameter and the χ^2 returned by BPZ to select the targets with robust photo-z estimates. In Figure 5.4, I then compare the public photo-z from the SDSS with our independent results from BPZ, for galaxies with $\chi^2 < 10$ and ODDS > 0.90. After including the galaxies with reliable

Source	σ	bias
PLCK_G045.1+61.1	0.204	-0.010
PLCK_G080.2+49.8	0.272	0.089
PLCK_G113.7+61.0	0.195	0.102
PLCK_G138.6+62.0	0.193	0.067
PLCK_G200.6+46.1	0.165	0.122
PLCK_G231.3+72.2	0.207	0.006
PLCK_G244.8+54.9	0.118	0.051

Table 5.3: The average 1σ scatter between SDSS and BPZ photo-z and the corresponding bias, for the 7 representative fields-of-view presented in Fig.5.4.

photo-z toward G244.8, I plot histograms of the differences between z_{BPZ} and z_{SDSS} for 7 representative fields-of-view among the 10 included in our BPZ analysis. The deviations are substantial and highlight that many sources have $z_{\mathrm{BPZ}} - z_{\mathrm{SDSS}} > 0.2$. To compare properly each of these distributions we can compute their bias and average 1σ scatter, given respectively by

$$\mathrm{b} = \langle (z_{\mathrm{BPZ}} - z_{\mathrm{SDSS}}) \rangle \tag{5.4}$$

$$\sigma = \sqrt{\langle (z_{\mathrm{BPZ}} - z_{\mathrm{SDSS}})^2 - \mathrm{b}^2 \rangle} \tag{5.5}$$

Assuming this definition of the 1σ scatter enables to suppress the influence of outliers which would otherwise dominate. As shown in Table 5.3, these quantities confirm significant discrepancies between the two methods, notably through the scatter values ranging from 0.12 to 0.27. To understand the origin of this dispersion, one should disentangle the impact of the photometry accuracy from the effect of the algorithm. To this end, I first quantify the dispersion induced by the method by downloading the SDSS primary photometric catalog associated with each $5' \times 5'$ field-of-view and deriving the corresponding photo-z with BPZ, adopting the same method and priors as below. I download the photo-z computed with the SDSS pipeline and derive the 1σ scatter between these two estimates. σ ranges between 0.08 and 0.14 showing that the algorithm partly explains the scatter of Figure 5.4.

Furthermore, while the average biases quoted in table 5.3 remain moderate, they turn out to be almost systematically positive. The Data Release 12 uses the empirical training set approach combined with a machine learning algorithm. Its training set is built from three independent surveys and comprises $1,976,978$ galaxies. However, this substantial sample efficiently covers the redshift space only out to $z \sim 0.6$ (the set extends to $z \sim 0.8$ but with a partial coverage, Beck et al. 2016). Besides being calibrated on optical photometry, the SDSS photo-z are therefore reliable in a small redshift range. For this reason, the biases are probably mostly due to the galaxies beyond $z \sim 0.6$, for which our NIR bands are essential. They show that our additional WIRCam/HAWK-I photometry probes redder or higher redshift SEDs that are poorly constrained with the SDSS. Alternatively the biases may indicate that our photo-z are overestimated for the bluest galaxies because our tempate library is not optimal for these sources. A few catastrophic failures with $z_{\mathrm{BPZ}} - z_{\mathrm{SDSS}} > 1.0$ were found in this comparison but do not appear in the plots of Figure 5.4.

In addition, to properly check the accuracy of our Bayesian SED fitting method we need a reference sample with true spectro-z. Since we have little or no galaxy with available spectroscopy in each line-of-sight and since the BPZ analysis used an identical procedure for the 10 GEMS, I use the calibration galaxies of §5.3.1 without distinguishing between the fields-of-view. In this way, I obtain a combined sample of 11 sources with reliable redshifts from the SDSS and showing nicely peaked P(z) in BPZ with no evidence for multiple redshift solutions (all exhibit $\chi^2 < 10$ and ODDS > 0.90). Fig.5.5 shows the comparison between these spectro-z and the photo-z from the BPZ SED fitting code. The 95% confidence intervals indicate a very good agreement with the 1:1 relation, for the whole sample.

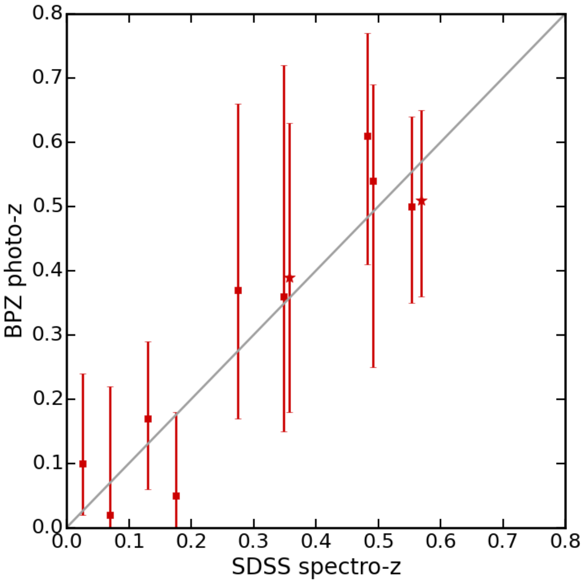

Figure 5.5: Validation of our photo-z derived with the BPZ fitting algorithm, through a comparison with the spectro-z available from the SDSS archive (see Tab.5.2). We plot the 1:1 relation as reference (grey line). For convenience, the two galaxies marked with stars were manually shifted by $\Delta z = +0.01$ horizontally. The errorbars show the 95% confidence intervals computed by BPZ. Each one of the 11 selected targets show a nicely peaked PDF, and no evidence for multiple redshift solutions.

Despite our photo-z showing large uncertainties due to broad redshift PDFs, the mean dispersion of this calibration uncertainty – defined by $|z_{\rm spectro} - z_{\rm photo}| / (1 + z_{\rm spectro})$ – is as good as $\sim 4.8\%$. Compared to similar calibrations performed in large scale surveys (e.g. Coe et al. 2006), this value is reasonable. Another reassuring point is that we find no catastrophic failures in this test sample, i.e. no target with $|\Delta z| / (1 + z_{\rm spectro}) > 0.15$.

This good agreement indicates that our photometry does not require additional systematic corrections (i.e. new zero-point offsets) to match the template SEDs. This also suggests that our input template library represents conveniently the galaxy types, at least in the redshift range covered by this subsample. Nevertheless, we caution that the performance of our method is tested with a subset of galaxies with spectroscopic data available in the SDSS. These sources are relatively bright and generally associated with higher SNR and lower uncertainties in our catalogs. As cautioned by Margoniner & Wittman (2008), the dispersion quoted below may therefore be too optimistic for the expected performance of BPZ in the totality of our multiband catalogs.

Photo-z of individual foreground galaxies and global redshift probability distributions

In the following plots and discussions, I rely on subsamples of galaxies with ODDS > 0.90 and $\chi^2 < 10$ that include between 30% and 50% of the input catalogs. In this way, I identify the sources for which the most likely redshift found by BPZ is unreliable, either because of a wide PDF or multiple solutions, and the sources with low goodness-of-fit. These thresholds are then associated with several flags reproduced in our multiband catalogs to indicate the reliability of each photo-z derived with BPZ. However, we warn that the lowest χ^2 from BPZ do not necessarily indicate reliable redshifts because the uncertainties on the model magnitudes are not taken into account (Benítez 2000; Coe et al. 2006). The brightest galaxies with more robust photometry will actually provide more accurate redshifts but the associated χ^2 will be higher due to the small errorbars. On the other hand, the

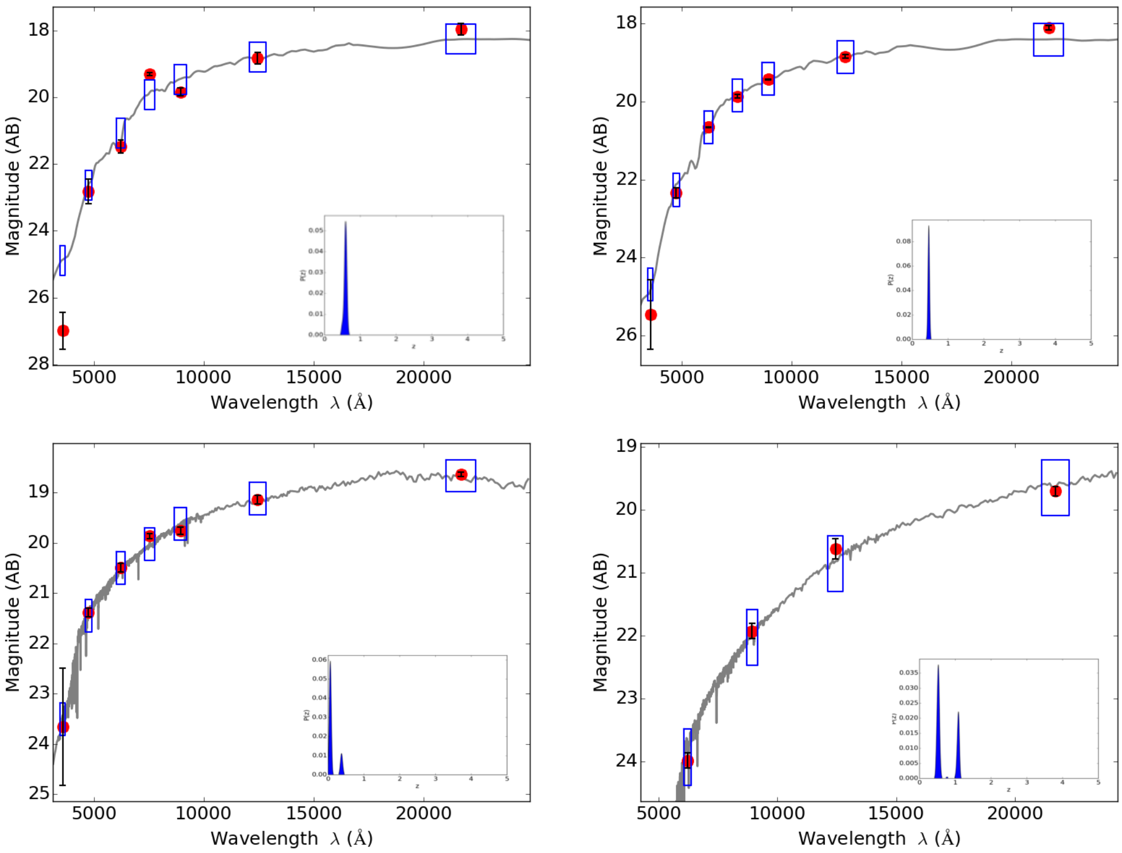

Figure 5.6: Best-fitting SED of four foreground galaxies with robust photo-z estimated with BPZ. The observed AB magnitudes are plotted in red dots, with their uncertainties indicated through the black errorbars. For each target, the redshifted best fitting SED from our input library is plotted as a grey line. It is convolved with the filters transmission functions to find the model magnitudes and their uncertainties, shown as blue rectangles. A good match between the red dots and the blue rectangles warrants the quality of the fit. The insets show the probability histograms P(z) from BPZ. *Top-left :* The brightest source in front of G080.2 with $z_{\rm best} = 0.60$, ODDS = 1.00 and $\chi^2 \sim 8.9$. *Top-right :* The main lensing galaxy toward G092.5 with $z_{\rm best} = 0.47$, ODDS = 1.00 and $\chi^2 \sim 3.0$. Bottom panels show the optical sources aligned with G113.7 (*bottom-left*) and G231.3 (*bottom-right*) for which we obtain $z_{\rm best} = 0.08$, ODDS = 0.83, $\chi^2 \sim 2.1$ and $z_{\rm best} = 0.53$, ODDS = 0.67, $\chi^2 \sim 0.4$, respectively. The last two estimates are less certain since BPZ finds secondary peaks in the PDFs. However, the main peaks suggest photo-z of 0.07 and 0.53, respectively, which have 83% and 67% chances of being correct.

faintest galaxies have much larger photometric uncertainties and ensure low χ^2 values for wide ranges of template SEDs.

The updated version of BPZ also provides a complete redshift PDF P(z) for each galaxy and plots the best-fitting SED. An example of these outputs is shown in Fig.5.6 for the main lensing galaxies toward G080.2, G092.5, G113.7 and G231.3 for which we obtain best fit photo-z of 0.60, 0.47, 0.08 and 0.53, respectively. For some targets P(z) highlights degeneracies between different redshift/type combinations, as seen for example in the two bottom panels of Fig.5.6. By adding all these PDFs in a given field-of-view we then obtain the corresponding redshift probability histogram.

I compute the full probability distribution histograms in the three fields-of-view where local over-densities of NIR galaxies have been identified with the AKDE, i.e. G045.1, G080.2 and G145.2. In

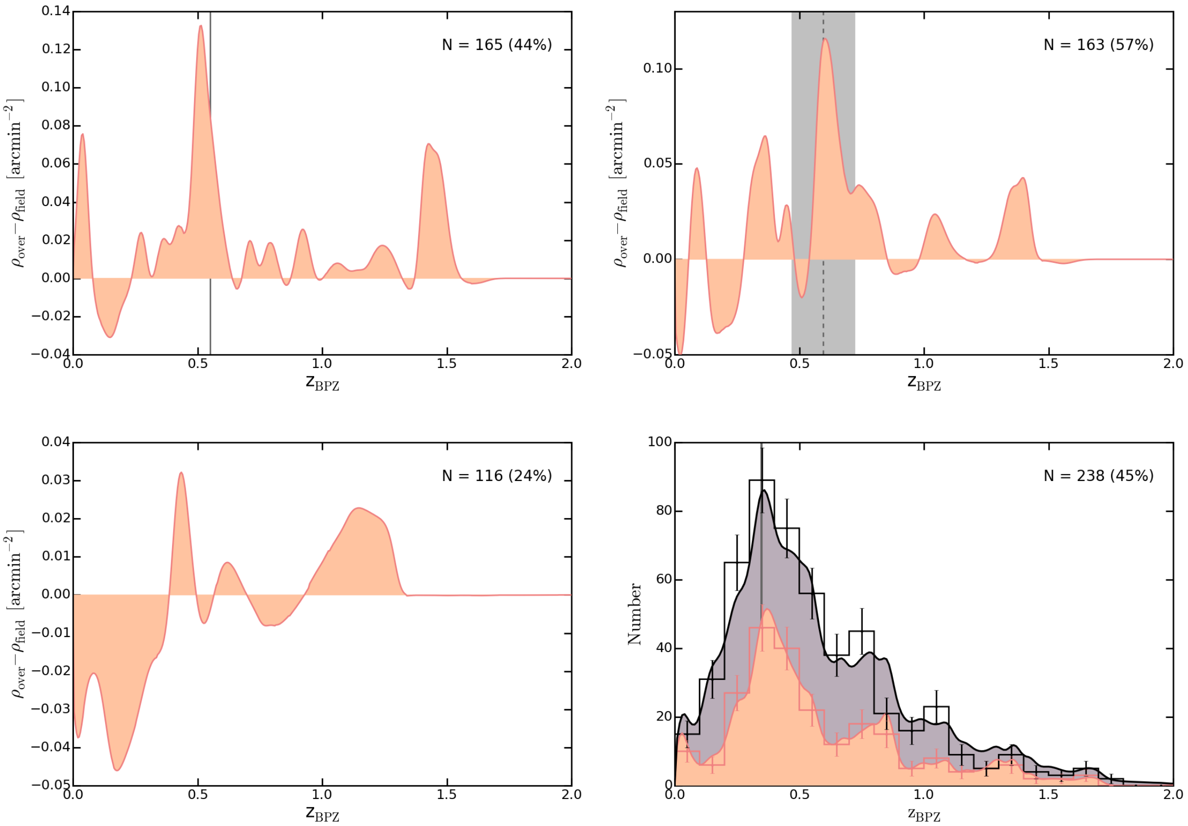

Figure 5.7: The first three plots show the difference between the BPZ probability histogram of galaxies within the K-band overdensities and the corresponding histograms of sources outside these regions. The P(z) in the two regions are normalized to the same unit area and the differences are plotted with redshift bins of 0.005. The most uncertain SED fits with ODDS < 0.90 and $\chi^2 > 10$ are removed and the proportions of reliable photo-z among the whole samples are quoted in the upper-right corner of each plot. (*Top-left :*) Field-of-view toward G045.1, with the vertical line showing the SDSS spectro-z of two galaxies aligned with the GEMS. (*Top-right :*) Field-of-view toward G080.2. The grey shaded region indicates the best-fitting photo-z of the central galaxy dominating the lensing potential and its 95% confidence interval. (*Bottom-left :*) Galaxies in the foreground of G145.2. (*Bottom-right :*) BPZ redshift probability histogram for galaxies in the $5' \times 5'$ field-of-view toward G165.7 plotted in black, and the most robust estimates shown separately as the red filled region. These histograms are compared with the histograms of the single best-fitting redshifts for each galaxy, using redshift bins of 0.1 (the two step lines with a similar color code). The errorbars are Poissonian. The P(z) are rescaled for greater clarity and the vertical grey line shows the SDSS spectro-z of two galaxies in the small clumps near the background arcs.

order to compare properly the P(z) in these specific lines-of-sight with the distribution of the surrounding fields, I select the potential overdensity members in circular regions centered on the AKDE peak and of $1.5'$ diameter (see Fig.5.11). This conservative selection does not rely on the exact AKDE contours that could be affected by several systematic effects. For G145.2 I reduce the diameter to $1.0'$ to match the apparent concentration of sources in the AKDE. After rescaling both regions to the same area, I compute the global P(z) in the two regions and plot the difference between these distributions to highlight any excess of galaxies at a given redshift in front of the GEMS. As shown in Fig.5.7, G045.1 is clearly located behind a structure at z $\sim$ 0.5, in agreement with the SDSS spectro-z of the two galaxies in the overdensity region (see §5.3.1). A dozen of galaxies are associated with this peak whereas only two others are responsible for the second peak around 1.5. We find a similar excess of sources at intermediate redshift around G080.2, between $\sim z \sim 0.55$ and z ~ 0.75. The peak observed in Fig.5.7 is well centered on the best fitting photo-z of the central galaxy which dominates the lensing potential and whose SED is plotted in Fig.5.6. In front of G145.2, while the excess at redshift beyond 1.0 is not significant enough, the excess at z ~ 0.45 could trace a physical structure. However since the z-band was initially missing for this target, few sources have a reliable single photo-z and less than ten of them are responsible for this peak. The large uncertainties of the current photo-z estimates are therefore limiting the interpretation of this distribution.

Since the extended overdensity of K-band sources toward G165.7 is more extended, I rather plot the raw redshift probability histogram for all the galaxies in the $5' \times 5'$ field and for the ones with more reliable photo-z. In Figure 5.7, these distributions are compared with two other histograms showing the single best-fitting redshifts for each galaxy. The latter reproduce quite well the shape of the redshift probability histograms although minor differences are seen for the full sample. A strong peak of sources at $\mathrm{z_{BPZ}} \sim 0.3 - 0.4$ is detected, in good agreement with the SDSS spectra of two foreground galaxies near the gravitational arcs. The Poissonian errorbars demonstrate that this peak is indeed significant which provides further evidence that G165.7 lies behind a filament at z ~ 0.35. The definitive membership of individual galaxies will be addressed with complementary follow-up in spectroscopy and, for the time being, we plot each candidate on the sky in the next section to compare with our current photometric constraints. In addition, the work of Coe et al. (2006) in the UDF shows that BPZ should be sensitive to massive overdensities with high redshift peaks. As stated in this study, smaller redshift peaks induced by few galaxies would probably be deleted by the photo-z uncertainties, but the groups or clusters with a few tens of members should appear as broad peaks in the probability histograms. The feature at z ~ 0.35 in Figure 5.7 might therefore indicate a massive lensing structure toward G165.7, either an extended filament or a virialized cluster.

Combining the P(z) of galaxies in the six other fields-of-view did not reveal significant excesses of sources in the redshift space that could be associated with the GEMS. The high AKDE peak found in the same K-band image as G113.7 is well detected in the global probability distribution of BPZ, as an excess of galaxies at z ~ 0.1.

Thanks to the overall output from BPZ we also analyze the most common spectral types in our fields-of-view, i.e. the proportion of galaxies associated with each template from the input library. The best-fitting SED prove to be either the El or the Sbc for a vast majority of galaxies. The reddened templates are particularly relevant toward G080.2, where they are involved in about 40% of the best fits and shift the peak of the global P(z) histogram by Δz ~ -0.2. However, the four bluer spectral types seem rather uncommon in sharp contrast with the analysis of deeper Hubble fields such as the UDF (Coe et al. 2006). They never exceed 10 to 15% of the full BPZ catalogs. This suggests that these ten sight lines are mainly populated with red populations of evolved early-type galaxies with, in some cases, tentative clues for dusty obscured sources. A detailed study of the stellar populations within individual foreground galaxies will be further developed below, for specific targets of primordial interest to the strong lensing analysis.

5.4 The color red sequence as a probe of galaxy clusters

Although the overall properties of galaxy clusters obviously evolve with cosmic time, all the massive clusters identified so far at z < 1 contain a significant population of red, early-type galaxies. These sources are mainly concentrated in the cluster cores, while the outskirts are more subject to environmentals disruptions such as infalling gas flows from the intercluster medium.

The color-magnitude diagrams (CMD) of galaxies collected in large fields-of-view distinguish two broad populations, the red sequence and the blue cloud. This bimodal color distribution was predicted in 1961 by the morphological analysis of G. Vaucouleurs and first detected with the SDSS. The blue cloud traces spiral galaxies with young stellar populations revealing a current or recent star formation activity, and an intermediate space in the color distribution – the 'green valley' – is populated by more dusty and red spirals. The red sequence mainly contains evolved ellipticals and but is also populated by some of these red spirals. As emphasized below, in the presence of a massive cluster in the targeted field-of-view, the red sequence will form a very tight feature in the CMDs, thereby providing a powerful probe of three-dimensional structures of galaxies (Gladders & Yee 2000). This technique is an excellent complement to the time-consuming spectroscopic observations since it merely requires the detection of significant overdensities in the color space. It is reliable since, to our knowledge, no signature from very reddened star forming galaxies has so far been misidentified as a red sequence.

The detection of the red sequence in the CMDs is associated with the $D_n(4000)$ discontinuity in the characteristic spectra of relatively evolved stars. At a given redshift and in a given CMD, the red sequence is therefore better defined if the broad-band photometry covers this feature. The $D_n(4000)$ is more prominent in galaxies without young stellar populations that would smooth the overall continuum. In galaxies experiencing a violent burst of star formation at high redshift followed by a passive evolution, this spectral break is therefore expected to become more and more prominent over time.

In this section, I first provide basic elements to understand how the red sequence is set up in massive clusters. Then I present our method to model its slope and intercept at a given redshift and for a given set of broad-band filters. Finally I apply these predictions to the CMDs observed in the fields-of-view toward the GEMS, to seek additional clues of evolved clusters.

5.4.1 The early-type population in galaxy clusters

Observational properties

Massive clusters contain a population of red galaxies with elliptical or lenticular morphologies which are gas and dust poor. This type is particularly dominant in the core of local clusters but only represents below 20% of the field galaxies. They exhibit very uniform properties in these nearby clusters as observed, for instance, through the well-defined relation between their colors and magnitudes (Kodama et al. 1998). This implies that the overall properties of cluster ellipticals can be derived via power-law scaling relations. Their similar colors suggest that they experienced similar star formation histories, probably involving a violent star formation episode right after their collapse, followed by a long phase of passive evolution (Bower et al. 1998). For this reason, these galaxies are called 'early-types'. Without accounting for the dust processing, they initially had blue stellar populations which became redder and redder during the passive phase (Bower et al. 1999).

Within the ΛCDM framework, cluster early-type galaxies can follow different evolutionary paths (Poggianti et al. 2006). Some of them were necessarily formed in the original peaks of the dark matter fluctuations, in synchronization with the formation of the clusters themselves. These galaxies indeed assembled most of their stellar mass at high redshift, during violent and short bursts of star formation (Springel et al. 2005) and are probably the descendants of the bright sub-millimeter or Lyman-break galaxies. The remainder were probably accreted from the cluster envionments and underwent intense interactions that quenched their star formation. Today they are either virialized in the cluster cores or located on the outskirts.

Although early-type galaxies are clearly evolved and dominated by old stellar populations, some studies have attempted to assign more realistic SFHs. Young and intermediate age stellar populations are indeed detected in few cluster members, as a result of a weak star formation activity driven by interactions (Bower et al. 1998). Unfortunately such characterizations are strongly limited by the degeneracy between age and metallicity in the most evolved templates.

In term of mass profiles, strong lensing systems show little evidence for dark matter in the center of bright early-type galaxies and the discrepancy between visible and total mass appear in their outter regions (Sanders 2014). We defer a more comprehensive analysis of these mass components to Chapter 7.

The buildup of the red sequence

The red sequence between galaxy colours and magnitudes turns out to be suprisingly homogeneous in local clusters, even though their high redshift progenitors contain active star formation and diverse stellar populations. Since this relation is well defined in the CMDs and widely characterized in the literature, it has become a fundamental probe of galaxy clusters and of their population of early-types. In cluster cores, lenticulars follow the red sequence, albeit with a slightly larger scatter than for ellipticals alone (Mei et al. 2009).

Its slope, intercept and scatter provide essential constrains to the properties of early-type galaxies. Firstly, the small redshift variations of the slope can be used to date the formation of galaxies in the cluster cores Gladders et al. (1998); Blakeslee et al. (2003). Secondly, its scatter traces the variations of the stellar population age between the cluster members. The low intrinsic scatter observed down to the low mass regime implies very homogeneous stellar populations and suggest that these galaxies should either be formed almost simulatenously, or made up of very old stellar populations (Bower et al. 1998; Eisenhardt et al. 2007). The red sequence therefore places a lower limit on the redshift of the last star formation episode. Finally, its intercept allows to determine the redshift of the cluster from blind imaging only (see §5.4.3).

The red sequence is also a robust tracer of the last mergers occuring between galaxies in cluster cores, especially during their passive evolution phase. After a given number of consecutive mergers, the red sequence scatter indeed tends to increase, while its tilt decreases because the process make the overall population more homogeneous. In the model of Bower et al. (1998), the values of scatter to slope ratios implies that early-types in clusters only grow by a factor of 2-3 mass after their last major star formation phase.

The origin of this feature is probably a variation of metal abundances rather than different stellar ages (Kodama & Arimoto 1997). It seems to be a consequence of the mass-metallicity relation which can be established after a short or extended star formation period in the hierarchical galaxy formation model (Bower et al. 1999).

It is apparently well defined in galaxy groups of intermediate mass, if one considers only the brightest elliptical members (Zepf et al. 1991). A rather small scatter is even obtained with this selection. This can be surprising because these structures have shorter dynamical timescales and we could thus expect their properties to be less homogeneous.

A tight red sequence is detected at $z \gtrsim 1$ with similar properties and a slight increase in scatter compared to $z = 0$ (Stanford et al. 1997; Blakeslee et al. 2003; Mei et al. 2006, 2009). This proves that the population of evolved ellipticals was already in place in the most overdense regions at these redshifts. Such red sequences in distant clusters are properly described by the passive evolution of an old stellar population with an initial burst at $z > 3$ (Stanford et al. 1997). From a direct photometric selection of red galaxies in proto-clusters, Kodama et al. (2007) claim that the red sequence is settled a bit later, between $z \sim 3$ and $z \sim 2$. However the increasing population of active galaxies in clusters at $z > 1$ generally make the analysis more challenging. In particular, we observe more galaxies bluer than the red sequence in the cores of high-redshift clusters (up to 25% at $z = 0.5$), a global magnitude drift and a larger photometric scatter (Butcher & Oemler 1984).

5.4.2 Modeling the galaxy red sequence

I model the properties of the color red sequence by following several steps. After calibrating the red sequence slope and intercept at $z = 0$, I simulate its redshifts evolution and compare the results with spectroscopically confirmed clusters in the literature. This recipe was validated in several studies (Tran et al. 2007; Song et al. 2012a) and the resulting red sequence models are also helpful to prepare imaging observations, that is say to predict the average color of cluster galaxies at a given redshift accessible with a given filter set and integration time.

A library of mock early-type SEDs

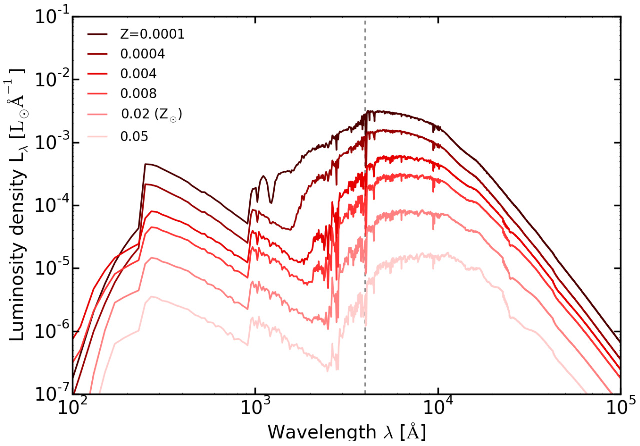

Figure 5.8: A subset of the BC03 templates modeling the population of early-type galaxies with a single burst of star formation at $z = 3$ followed by a passive evolution during a few Gyr. These templates have a common age of 11.50 Gyr and are rescaled arbitrarily for ease of view. We represent the six different metallicities used to reproduce the tilt and zero-point of the red sequence observed in the Coma cluster. The vertical dotted lines indicate the position of the $\mathrm{D_n}(4000)$ spectral break, essential to detect the galaxy red sequence.

The detection of the galaxy red sequence in a wide range of environments indicate that early-type galaxies in the most evolved cluster cores should have fairly homogeneous properties. In particular, their similar color indicate that they probably share common star formation histories. Modeling the SED of red, early-type galaxies is thereby quite straightforward. The prevailing, albeit simplistic, approach in the literature is to model a single burst of star formation at high redshift followed by a passive evolution during a few billion years. Conversely, bluer galaxies are more difficult to model because they are much more sensitive to the recent star formation history.

In this thesis, I build evolutionary models for the early-type population using the GALAXEV library of stellar population synthesis templates from Bruzual & Charlot (2003). I choose an exponentially declining star formation history (SFH) of e-folding time $\tau = 50$ Myr starting at $z = 3$, as done in Song et al. (2012a). This represents a single a burst of star formation about 2.2 Gyr after the Big-Bang followed by a passive evolution until $z = 0$. The models use the Padova 1994 evolutionary tracks and are based on a Chabrier (2003) IMF truncated at 0.1 $M_\odot$ and 100 $M_\odot$. I do not include dust attenuation in the models given that dust reservoirs in these early-type galaxies are supposed to be heavily depleted.

I use the publicly available routines from GALAXEV to extract the individual spectra in units of luminosity per unit wavelength ($L_\odot$Å^{-1}) and at different ages. These ages are choosen to reproduce the time intervals between the burst at $z = 3$ and the redshifts where we place our mock red sequences, namely from $z = 0.0$ to $z = 1.0$ with steps of $\Delta z = 0.05$. For each age, GALAXEV provides six independent templates covering a large range in metallicity ($Z = 0.0001$, 0.0004, 0.004, 0.008, 0.02 ($Z_\odot$) and 0.05). Since a mass-metallicity relation holds in star-forming (Tremonti et al. 2004) and early-type galaxies (Faber 1973; Burstein et al. 1988), these templates correspond to different masses and luminosities. I briefly checked that the choice of SFH had a minor effect on the output spectra for ages above 3.50 Gyr, corresponding to $z < 1$. As expected, the passive evolution erases any trace from the initial active stage, making it impossible to constrain more detailed SFHs including, for instance, secondary bursts. In Figure 5.8, we plot six SEDs showing the full range of metallicities, for an age of 11.50 Gyr. Applying an arbitrary rescaling, we highlight that the 4000 Å break becomes more and more prominent with increasing metallicity.

For the selected SFH, before we rescale them to the appropriate stellar mass, the brute BC03 models are normalized to a total stellar mass of gas turned into stars approaching 1 $M_\odot$ at increasing ages (Bruzual & Charlot 2003). They are however not normalized in luminosity. The spectra are originally covering the wavelength range 91 Å – 160 μm with a constant resolution of 3 Å between 3200 and 9500 Å. Since the spectral sampling is varying outside this range, I rebin each SED to a resolution of 20 Å.

I compute the mock magnitudes and colors from the rest-frame or redshifted spectra, using my own codes instead of the GALAXEV output catalogs. For this purpose, I first gather the transmission functions for the appropriate broadband filters, including the transmission of the telescope optics, and normalize their maximum response to unity. I also resample the filter transmission functions to a resolution of 20 Å and then convolve the spectra with each filter using a dedicated routine kindly provided by C. Martinache.

Calibration with the Coma cluster

The red sequence can be modeled with this set of mock SEDs by setting a reference at redshift $z \sim 0$. Eisenhardt et al. (2007) collected UBVRIzJHKs photometry for hundreds of galaxies in/around the core of the Coma cluster at $z = 0.023$, one of the most massive clusters in the nearby universe. They focus on a field-of-view of about $29' \times 23'$ and gather spectroscopic observations of the brightest 111 galaxies from former studies. From this outstanding dataset, they compute the colors between eight filter pairs and plot these colors with respect to the apparent magnitudes in the H-band. After having identified the cluster members and non-members and removed a few galaxies with ambiguous morphological types, they identify the red sequence in each CMD and search for the best-fitting slope, intercept and scatter.

These robust observational results are used to calibrate our models. I consider the BC03 templates with an age of 11.50 Gyr to build the mock red sequence at $z \sim 0$. For the comparison to be meaningful, I compute the magnitudes and colors in the filters of the Kitt Peak National Observatory (KPNO) 2.1 m telescope whose response functions are provided in the supplement tables of Eisenhardt et al. (2007). I use the six metallicities of BC03 templates to derive the eight CMDs. Since the slope of the red sequence directly depends on the metal abundances, I follow Song et al. (2012a) and select the suitable range of metallicity and template rescaling to reproduce the color and tilt measured on the Coma cluster. The best-fitting combination of metallicities and scaling factors is found by minimizing the difference between the modeled and observed linear relations. The calibration rules out the two less enriched BC03 templates. The results are presented in Table 5.4 for the eight CMDs. We see that our models better reproduce the observed slope and intercept in the most extreme opt./NIR bands such as (V-K), but that there is also a good agreement in the NIR bands where the red sequence flattens. However, significant discrepancies appear in the CMDs involving the U or B photometric bands centered below 5000 Å (first four lines). The calibration is therefore less reliable at lower wavelengths, an effect which we nonetheles consider as minor in our analysis because the CFHT/VLT imaging does not probe this regime.

In principle, it should be more realistic to account for an intrinsic scatter of the red sequence due to the non-unique stellar populations in early-type galaxies within the cluster cores. Barkhouse et al. (2006) suggests an intrinsic scatter of 0.075 mag which shall be added to the dispersion induced by the photometric accuracy to reproduce the measured scatter.

Color	Slope		Intercept	
	Coma	Model	Coma	Model
(U-B)	-0.079 ± 0.007	-0.047	1.386 ± 0.089	0.892
(U-V)	-0.122 ± 0.010	-0.083	2.929 ± 0.123	2.474
(B-V)	-0.042 ± 0.004	-0.036	1.543 ± 0.049	1.582
(B-R)	-0.055 ± 0.006	-0.063	2.259 ± 0.074	2.499
(V-I)	-0.029 ± 0.005	-0.028	1.540 ± 0.066	1.643
(V-K)	-0.109 ± 0.017	-0.109	4.455 ± 0.209	4.451
(I-K)	-0.080 ± 0.013	-0.082	2.915 ± 0.164	2.807
(J-K)	-0.025 ± 0.009	-0.028	1.232 ± 0.111	1.154

Table 5.4: Red sequence slope and intercept modeled with our BC03 templates and measured in the Coma cluster by Eisenhardt et al. (2007).

Redshift evolution of the red sequence models

In a first instance, we assume that the most massive structures in front of the GEMS will fall typically at redshifts below 1.0 and we model the red sequence from $z = 0.0$ to $z = 1.0$. In this way, we impose a lookback time above 3 Gyr until the burst and we avoid the uncertain transition phase during which the red sequence is being implemented.

To model the redshift evolution of the red sequence in bins of $\Delta z = 0.05$, I use the set of BC03 templates with different ages, all rescaled with the factors derived from the Coma cluster. For a given redshift bin, I choose the age corresponding to the correct look-back time until the burst, redshift the template accordingly, and finally convolve the SED with the suitable filters. I therefore obtain the mock CMDs at each redshift from which I can deduce a best-fitting red sequence. The resulting relations appear to be offset from each other in the CMDs and, as expected, the slope shows very little variations.

In the rest-frame, the 4000 Å discontinuity emerges between our optical bands (either r and z or V and R) and the feature is shifted in the NIR filters for redshifts above 1.3. In a first stage I therefore model the red sequence slope and zero-point between the most extreme bands available in our catalogs that offer a maximal probability of detection when the redshift is unknown (either r and K or V and K). Secondly, I derive an additional set of models intended to reproduce several CMDs in the literature and to validate our predictions at $z \neq 0$.

For instance, Kodama et al. (1998) characterized the redshift evolution of the red sequence in clusters at $0.3 < z < 1.3$, a crucial step to understand the formation of the massive gravitationally bound structures and the evolution of the stellar populations and structure of ellipticals, closer to their active phase. Our modeled slope and zero-points correspond perfectly to the predictions of this study, in the redshift bins below $z = 0.8$. Above this threshold, the intercepts are more sensitive to the differing values applied for the redshift of the burst.

Validation with known clusters at $z < 1$

To begin, I compare the red sequence with the blind CMDs of Gladders et al. (1998) which combine several Abell clusters at $z < 0.15$ to overcome the contamination from foreground and background interlopers. The slope and intercept in our (B-R)-R diagrams are in excellent agreement both with their large dataset arranged in five redshift bins and with their own models. In figure 5.9, I illustrate the comparison for the highest of these bins by overplotting our red sequence models on the KPNO 0.9 m photometric points.

The position of the galaxy red sequence strongly depends on the photometric estimator applied and therefore varies with the aperture size. With smaller apertures, it should exhibit redder colors in the CMDs (i.e. a higher intercept) because early-type galaxies involve color gradients, with redder colors

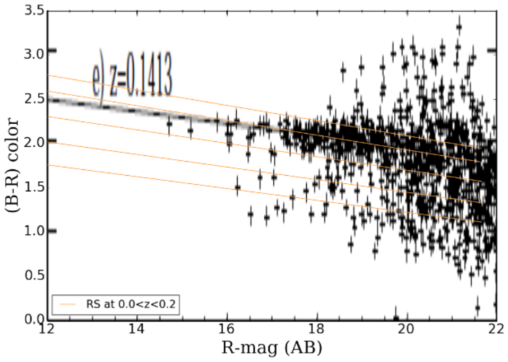

Figure 5.9: Illustration of the good agreement between our red sequence models and the color magnitude diagram published in Gladders et al. (1998) for an Abell cluster at spectroscopic redshift z = 0.14. The text provides further details on the extensive comparison with the colors of spectroscopically identified galaxy clusters, and with other red sequence templates from the literature.

at lower radii (Boroson et al. 1983). This effect might explain why our models calibrated with the 6.2” aperture of Eisenhardt et al. (2007) predict a lower zero-point in the (J-K) CMD than Valentinuzzi et al. (2009), in their analysis of nearby clusters at z $\sim$ 0.05 from the WINGS sample. On its side, the slope of the red sequence remains nonetheless little sensitive to the aperture size.

The validity of the modeled intercepts is crucial to deduce a reliable redshift from the observed CMDs, but the slopes can be severely affected by age variations during the build up of the red sequence. We test our models with the compilation of massive clusters from the MACS and LARCS samples presented by Stott et al. (2009). These structures probe up to z = 1 and were previously identified spectroscopically. Accordingly, they offer a convenient reference sample to determine whether or not our models can recover the correct redshift. After modeling the red sequence in the same BVRI broadband filters, we find an excellent agreement between our predictions and the observationnal points in the (B-R)-R and (V-I)-I CMDs. However our slopes are marginally inconsistent with the fits of Stott et al. (2009), probably because the redshift of the burst is incorrect for these clusters (Gladders et al. 1998).

5.4.3 Identifying lensing groups or clusters toward the GEMS

Blind search of the red sequence

In a last stage, I use these models to search for a galaxy red sequence in the $5' \times 5'$ field-of-view toward each GEMS. I compute the colour histograms for all possible combinations of broad-band filters and plot the CMDs, always displaying the magnitude in the reddest band on the x-axis. In the CMDs between the most extreme bands shown in Figure 5.10, G113.7 and G165.7 show a significant excess of red sources of about 3.5 and 5.0 σ, respectively. This excess turns out to be less prominent in the remaining filters and we therefore decide to focus on the (r-K) diagrams in the first instance. None of the eight other GEMS exhibit a significant color excess in the blind histograms compared to the Poisson errors.

I compare the slope and intercept of the red sequence models with the galaxies falling within the K-band overdensities toward G045.1 and G080.2 (Fig.5.10), without obtaining a clear detection. The most interesting results are obtained for the sources showing color excesses in the blind search, namely G113.7 and G165.7. The observed red sequences for these two GEMS are fully consistent with the models plotted in the (r-K) versus K color magnitude diagrams of Figure 5.10, and with the independent spectro-z or photo-z. The overdensity of red sources detected toward G165.7 is clearly concentrated between the models at z = 0.30 and z = 0.40, in excellent agreement with the SDSS

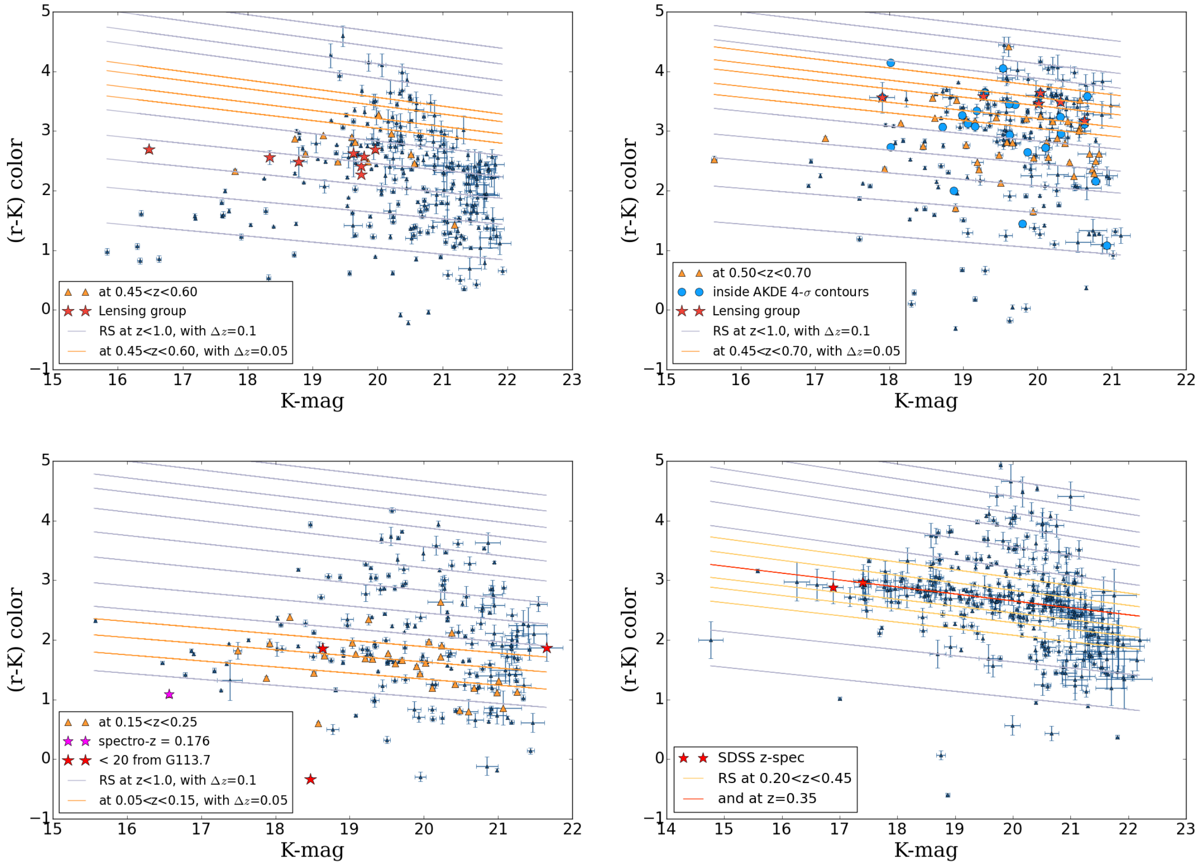

Figure 5.10: (r-K) versus K color-magnitude diagrams for the fields-of-view including significant excesses of red galaxies, namely G045.1 (*Top-left*), G080.2 (*Top-right*), G113.7 (*Bottom-left*), and G165.7 (*Bottom-right*). Orange triangles show the galaxies with photo-z falling in the same range as our best redshift estimate for the main foreground structure. The individual galaxies in the line-of-sight toward the GEMS (red stars), and the small set of sources with available spectro-z (magenta or red stars) are both identified. For G080.2, galaxies plotted in blue fall within the blue circle of Figure 5.11, which corresponds to the average size of clusters (1-2 Mpc) at the redshift of the lensing structure. I overplot the red sequence models for the redshift range $0.0 < z < 1.0$. Yellow lines indicate the position of this red sequence for the most probable redshifts derived either from our photo-z distributions or from the publicly available spectro-z.

spectro-z of two members ($z = 0.348$).

We remind that our blind search for the red sequence is necessarily biased by some late-type outliers in front of or behind the structures, especially concerning the more distant ones (Mei et al. 2009). We could reduce this side effect and increase the SNR of the red sequence with a morphological classification isolating the early-type galaxies from other contaminants such as reddened spirals. However, this requires higher resolution imaging from the HST (Gladders et al. 1998; Blakeslee et al. 2003) and, in §5.5, we will account for these interlopers with an alternative approach.

The red sequence as redshift estimator

The red sequence can be considered as an efficient and time-saving photometric redshift estimator for galaxy clusters that only requires wide field-of-view imaging in two optical/NIR bands. Instead, the usual SED-fitting codes need a few more bands to obtain reliable redshifts for individual objects as seen in §5.3.2. Given that this standard relation is tight in massive clusters, the typical accuracy of redshift estimates based on the red sequence reach $\Delta z \sim 0.05$ and $\Delta z \sim 0.1$ for clusters below and beyond $z = 0.8$, respectively (Fassbender et al. 2008, 2011; Song et al. 2012a). For $z > 0.8$, the 4000 Å discontinuity is indeed shifted towards redder wavelengths where the photometric bands (J, H or K) are broader. Song et al. (2012b) provide an analytical recipe to extract the redshift of overdense and structured regions from the identification and analysis of red sequence galaxies and obtain an accuracy of $\Delta z/(1+z) \sim 0.02$. They apply this method to characterize a cluster discovered by Sunyaev-Zel'dovich effect on the SPT.

Such an approach requires the presence of a significant overdensity of red sequence galaxies in the targeted field-of-view. In this configurations the colour distribution of red cluster galaxies can be unambiguously distinguished from the field population. Song et al. (2012b) propose to identify these significant color excesses and to compare them with red sequence models derived from BC03 templates, as done in this thesis. The cluster redshift is then deduced from the mock red sequence that best fits the color peak. I therefore use this technique to estimate the redshift of the two overdense structures toward the GEMS that show the most significant color excesses in the (r-K)-K CMDs, namely G165.7 and G113.7. For G165.7, our models and the scatter observed in Fig.5.10 show that the filament lies between $z = 0.30$ and $z = 0.40$, in good agreement with the redshift of the two members obtained from the SDSS spectra. For G113.7, the color excess is less significant and we therefore need to combine different CMDs to derive a robust redshift range. Fig.5.10 shows one of these CMDs which favours the models between $z = 0.10$ and $z = 0.15$. However, the remaining diagrams point toward a higher upper-limit and we conclude that the AKDE overdensity in the South-East of the GEMS is lying at $0.10 < z < 0.20$.

5.5 What types of structure are magnifying the GEMS ?

5.5.1 The nature of the lensing potentials

To conclude, about half of the GEMS in our overall sample are associated with isolated foreground galaxies. Such is the case of G092.5, G113.7, G138.6, G200.6, G231.3. and G244.8. The first of them, G092.5, is behind a luminous red galaxy at a spectro-z of 0.448 measured in BOSS. Although this source is expected to dominate the lensing potential given the radial distorsion of the background arc (see the SMA morphology in Fig.4.6), the AKDE contours suggest a possible contribution of two additional galaxies within $5''$. These are faint sources in the K-band with a BPZ photo-z of about 0.25. The AKDE peak of 7σ and the red sequence detected in the field-of-view of G113.7 are apparently not related to the sub-mm emitter, but the potential well is rather comprised of a galaxy at a photo-z of 0.08 (Fig.5.6). Two other galaxies with similar apparent magnitudes in the NIR and a photo-z of ∼0.25 and ∼0.15 are also close enough to G113.7 to produce local distorsions. The configurations of G138.6 and G200.6 are similar and involve two foreground galaxies blended in our photometric apertures and in SDSS catalogs. We therefore caution that the photo-z of these lens planes – of ∼0.4 for G138.6 and ∼0.6 for G200.6 – is probably significantly biased. For their part, G231.3 and G244.8 are behind optically-faint isolated sources. We obtain a robust photo-z of 0.53 for the one toward G231.3 (Fig.5.6) and ∼0.1, ∼0.3 and ∼0.7 for its nearby companions within $5''$. As mentioned above, we use the X-Shooter spectrum to deblend the foreground and background components of G244.8 and find a spectro-z of 1.52 for the lensing galaxy. Very massive ($M_* \sim (1-2) \times 10^{11}\ M_\odot$) elliptical galaxies are also observed a few tens of arcsec away from G231.3 and G244.8, at spectro-z of $z = 0.026$ and $z = 0.131$, respectively. These sources are therefore closer to the observer than the main lens planes and their strong lensing effect could be non-negligible.

G145.2 is apparently associated with an overdensity of NIR sources but its horseshoe-shaped dust continuum rather suggests that a single foreground source dominates the strong lensing magnification. We currently detect this objects with WIRCam but we are lacking a robust redshift estimate due to

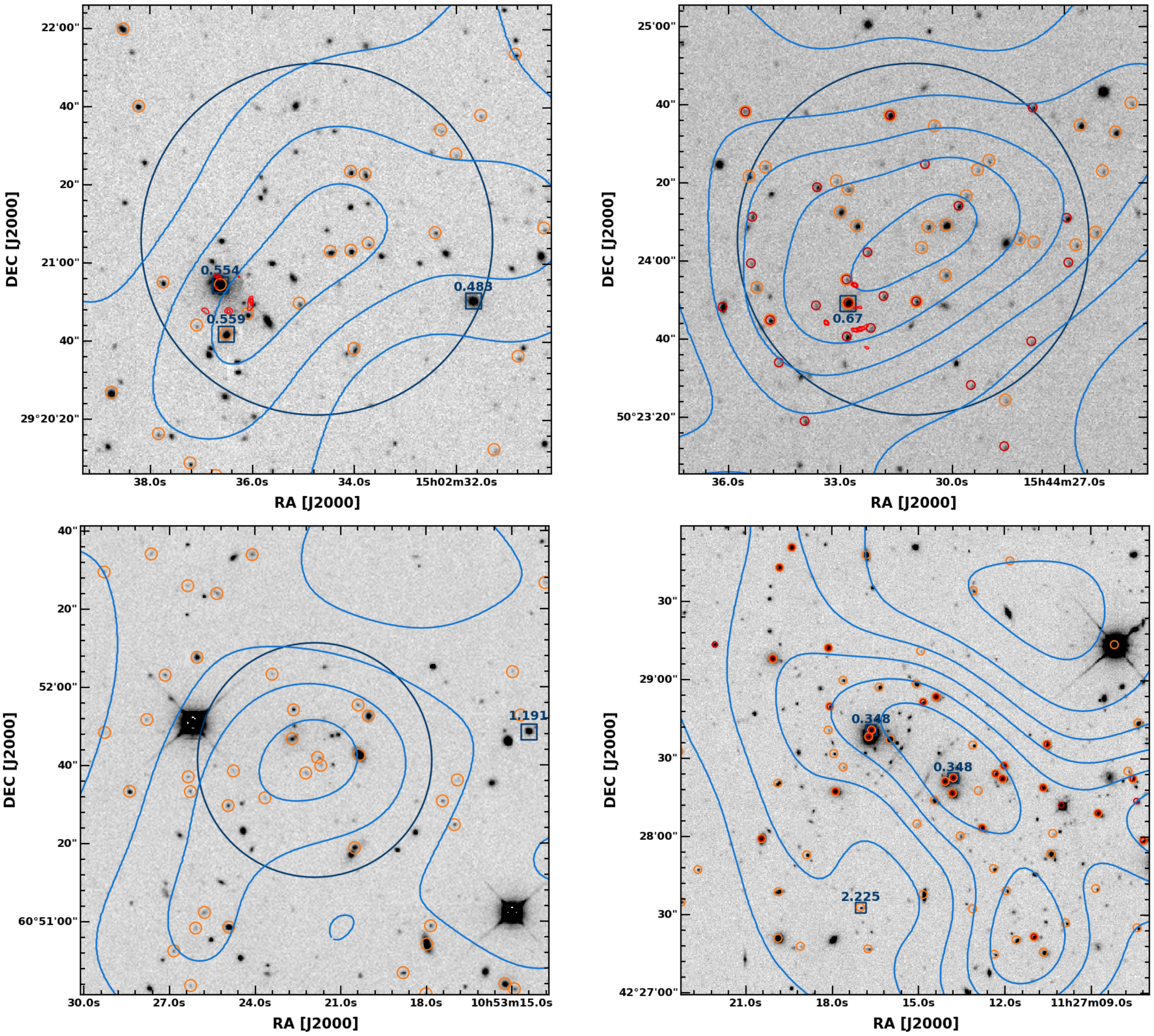

Figure 5.11: Morphology of the lensing structures for the four GEMS magnified by three-dimensional mass overdensities, namely G045.1 (*Top-left*), G080.2 (*Top-right*), G145.2 (*Bottom-left*), and G165.7 (*Bottom-right*). AKDE contours are shown in light blue and the overdensity regions considered in this analysis are plotted in dark blue. The latter are centered on the peak of the AKDE map. Yellow circles indicate the position of galaxies with photo-z consistent with the most probable redshift of each structure (deduced either from the overall photo-z distribution or from the publicly available spectro-z). Red circles show the sources selected with the red sequence models, for G080.2 and G165.7 only. Both selections highlight a clear filamentary structure toward G165.7, passing through the position of the background GEMS and including the two concentrations of 3-4 early-type galaxies. The small set of sources with publicly available spectro-z from the SDSS are shown as blue squares. For G045.1 and G080.2, the dust continuum from the background GEMS observed with the SMA appears as red contours, while the sub-mm emitter falls exactly in the center of the frame for G145.2 and G165.7.

the strong blending with the background GEMS in NIR bands. To overcome this issue, spectroscopic follow-up observations are scheduled with Hectospec on the Multiple Mirror Telescope (MMT).

Only G045.1, G080.2, and G165.7 are clearly lensed by galaxy groups or clusters according to the AKDE contours and to the distribution of sources in the redshift space. A red sequence agreeing with our predicted slope and intercept is also identified for G080.2 and G165.7 (see Fig.5.10). As shown in §5.3.1, spectroscopic redshifts are available for a few galaxies in these three structures, either from the SDSS or from our follow-up. Figure 5.11 shows that these spectro-z are compatible both with the excess in the distribution of photo-z, and with the redshift of the red sequence templates.

Some GEMS therefore appear to be more or less clearly associated with multiple lenses at different redshifts. A detailed analysis of the strong lensing effect is required to determine the relative contribution of each components to the overall magnification. Moreover, we are not able to highlight configurations with multiple source planes, neither with our deep optical/NIR imaging nor with our sub-mm interferometry.

5.5.2 Selection of the group/cluster members

To build accurate models of the mass distribution toward G045.1, G080.2 and G165.7, we need to identify the foregound early-type galaxies that belong to the overall clusters. For G080.2 and G165.7, I extract the sources falling on the red sequence in the (r-K)-K and (r-J)-J CMDs, in the polygons limited by our models at different redshifts. For G080.2, the members are selected between the modeled red sequences at $z = 0.55$ and $z = 0.70$, and I use thresholds at $z = 0.30$ and $z = 0.40$ for G165.7. I also apply a cutoff at K-band magnitudes beyond 22 to reject the fainter sources with higher photometric uncertainties and which are expected to evolve toward the red sequence with longer timescales.

After extracting the red sequence galaxies in this way, I examine their respective redshifts and their best-fitting spectral type to refine the selection of cluster members. I exclude the objects with reliable BPZ photo-z derived fromlate-type templates. Since G165.7 shows a significant color excess in the blind CMDs, I also exclude the interlopers with a robust photo-z inconsistent with the redshift of the red sequence. Finally, I remove the red sequence members that reside in under-dense regions outside the 2σ contours of AKDE maps, and I include the galaxies falling outside the red sequence but with a spectro-z consistent with the redshift of the cluster.

Concerning G045.1, our red sequence template for $z = 0.55$ is significantly offset from the colours of galaxies within the AKDE contours. Thus, I rely on the AKDE 4σ contours to determine the cluster membership of galaxies in front of this GEMS. I refine this two-dimensional selection by assuming that the lensing structure is located at the spectro-z of the two bright early-types (i.e. $z = 0.55$) and removing the sources with inconsistent photo-z.

Chapter 6

Modeling the strong gravitational lensing effect toward the GEMS

Contents

6.1 General methodology

Strong gravitational lensing, contrary to the weak lensing regime, probes strong shear fields in the non-linear regime. It can be produced by foreground objects massive and dense enough such as the cores of massive ellipticals or the central regions of clusters filled with dark matter. Models are generally based on identifying and localizing multiple images. This approach has its own limitations and uncertainties, but it has been well tested by independent teams in specific system such as, for instance, multiply imaged strongly lensed supernova SN Refsdal behind the massive cluster MACSJ1149.5+2223 (Sharon & Johnson 2015; Oguri 2015; Grillo et al. 2016; Treu et al. 2016). In this chapter, I focus on the lens modeling performed in collaboration with M. Limousin, for the four GEMS with the most complete set of observational constraints.

6.1.1 The global modeling approach

We use a parametric approach that draws on the observational results to decompose the lensing structures into different halos and to model the surface brightness of the sources. These models are based on physically motivated descriptions of the gravitational potentials and attempt to minimize the number of free parameters. They have amply demonstrated their efficiency, not only to constrain the profiles of the deflectors but also to recover the main intrinsic properties of the background objects. This approach constrasts with "grid-based" techniques that directly pixelize the light maps with multi-scale grids to better describe the potential well of complex clusters (see further details in Warren & Dye 2003; Treu & Koopmans 2004; Vegetti & Koopmans 2009; Rybak et al. 2015a).

Moreover, competing groups using interferometric observations of lensed SMGs have previously advocated fitting models in the uv-plane rather than the reconstructed, Fourier transformed images. They argue that this approach allows to reconstruct the source plane properties more accurately, either assuming a parametric description of the intrinsic light profiles (Hezaveh et al. 2013; Bussmann et al. 2013) or using a pixelisation of the source to recover the extended emission (Rybak et al. 2015a). The partial sampling of the uv-plane is indeed leading to several uncertainties when deriving the surface brightness distribution in the image plane. A given weighting results in a given synthetized beam, which in turn will possibly involve significant sidelobe effects creating unphysical structures in the reconstructed images. For instance, this approach is widely used to compute the intrinsic surface brightness distribution of high-redshift lensed sources from the SPT or H-ATLAS samples with available interferometric data. In particular, the main lensing models of SDP.81 are derived both in the image plane (Dye et al. 2015; Swinbank et al. 2015) and in the visibility plane (Rybak et al. 2015a,b). They illustrate that the reconstruction of the source intrinsic properties are quite different between the two approaches. The three compact regions in the source plane continuum maps have varying positions and flux ratios (e.g. compare Fig.2 of Rybak et al. 2015a with Fig.1 of Swinbank et al. 2015) and the visibility-plane method seems to recover more extended emission in the CO maps.

However, in this thesis the observational constraints on the background emitters are rather diverse. We therefore decide to work systematically in the image plane and to fit the Fourier transform of the visibilities for the GEMS with sub-mm interferometry available from SMA, PdBI or ALMA. Although for the latter the noise between nearby pixels is necessarily correlated due to the instrumental beam, our models are exclusively based on the local peaks of the emission maps. These maxima are either identified in our high resolution molecular and dust continuum interferometry or in our deep infrared imaging. Since the image plane morphologies derived from interferometric observations can be misleading, in particular at large spatial scales, our approach only relies on the position of the most significant clumps. Uncertainties on these positions are solely due to the beam size but they are not related to surface brightness variations. In this way, fitting in the image plane is much more efficient and allows to focus on the lensed source without considering the large set of visibilities that correspond to the background sky (Dye et al. 2015).

6.1.2 The LENSTOOL code

In this thesis, I use the publicly available LENSTOOL software to optimize the foreground potential wells (Kneib 1993; Jullo et al. 2007). The code follows a parametric approach and adopts the Bayesian formalism to quantify the uncertainties of each model and to assign their likelihood. After performing a MCMC sampling of the parameter space, it provides a posterior probability distribution function for each fitted parameter, allowing us to derive the related uncertainties. Finally, LENSTOOL finds the most likely model from its evidence (Jullo et al. 2007).

To constrain the foreground mass distribution, we measure the apparent position of each background arclet in the image plane and its redshift. This determines the angular diameter distances and then allows to recover the profile of the lensing potential by inverting the lens equation. However, LENSTOOL does not allow to fit the morphology of the background component in the image plane. This algorithm is therefore less straightforward to model the gravitational magnification towards extended background sources than towards point sources. A number of n multiply imaged arclets with known redshift will therefore provide $2 \times (\mathrm{n} - 1)$ constraints for the optimization and leave the opportunity to fit as many parameters.

6.1.3 Identifying the multiply imaged systems

In a first stage, the mass modeling therefore requires to correctly identify the distorded arclets, to determine their apparent substructure and to figure out how to group them into systems of multiple images. Given their very nature, the multiple images of our sources stand out from their surroundings by their red colors. They are identified either in deep three-color optical/infrared images from our follow-up or with the help of the high-resolution sub-mm interferometry. On the one hand, for instance, G244.8 is not detected in our optical data and seems, at first sight, to be strongly blended with the foreground lens in the infrared. However the sub-mm regime nicely covers the background Einstein-ring like source without any contribution from the lens, allowing an unambiguous identification of the distorded arclets. On the other hand, the GEMS associated with foreground groups or clusters and showing more extended configurations in the image plane are conveniently detected in three-color images between bands of extreme wavelength (e.g., between r or V-bands from the CFHT or the VLT and IRAC channel 2). In these systems, several counter images are also detected around the sub-mm bright GEMS and deblended from the local foreground galaxies.

While awaiting for the complementary spectroscopic follow-up of these counter images which is currently scheduled at MMT and Gemini, we associate multiple images of the same source using empirical arguments. First, we consider that the number of multiple images in a given system is expected to be odd, with a de-amplified component in the center that will most probably remain undetected. Although firm identifications require a complete census of the spectroscopic redshifts of each candidate, we sometimes need to rely on photometric motivations. In such cases we require that, for a given background source, the multiple images produced by the lensing potential have similar colors and morphologies. Moreover, they must be arranged in a plausible configuration that complies with the expected parities in the image plane.

The misidentification of some images in a given multiply imaged system or their non-detection can severely affect the reconstruction of the foreground mass distributions. To overcome this issue we carefully test different scenarios in our lensing models.

LENSTOOL allows to force the position of the critical lines when observations unambiguously identify the parities between multiple images, therefore indicating where these lines should be located (Jullo et al. 2007). We do not use this option and carefully check a posteriori if the position of the simulated critical lines is relevant. Moreover, flux ratios between the multiple images could also be implemented but we rather await the availability of deep HST imaging to improve the photometric accuracy.

6.1.4 Density profile of the dark matter components

The standard profiles

In the parametric approach, the gravitational potential of individual galaxies or overall galaxy clusters is described with a combination of standard density profiles. Taken individually, these profiles simultaneously represent both the dominant dark matter component and the overall distribution of baryonic matter, and remain valid for all sources residing in the same type of gravitational potential. The detection of gravitationally lensed arcs is ideal to determine which one of them best describes each class of astrophysical object acting as a lens. It therefore offers an outstanding window on the spatial distribution of dark matter and its interplay with baryons.

For instance, the Navarro, Frenk and White profile (NFW, Navarro et al. 1997) is widely used to model the density profiles of dark matter halos in large-scale cosmological simulations. Alternatively, Navarro et al. (2004) propose to assume a Sérsic (Sérsic 1963) profile to model their gravitational potential in the three-dimensional space. In this context, the help of gravitational lensing is crucial to further test the validity of these universal descriptions, which are both derived from purely theoretical Λ-CDM simulations. This requires to focus on observations of massive galaxy clusters in the local or more distant universe. Strong lensing is particularly important to probe the density profiles at intermediate radii, between 10 and 100 kpc. Generally, it complements other observational constraints, such as the direct measurement of velocity dispersions in the inner regions of the clusters, and the collection of X-ray imaging or the weak lensing studies in the outer regions. The Sersic, the NFW and other profiles have been widely compared at cluster scales in several studies (e.g., Jullo et al. 2007).

The total – projected or three-dimensional – density profiles of lensing structures are conveniently parametrized by a logarithmic slope γ', given by $\mathrm{d}\log\rho/\mathrm{d}\log\mathrm{r} = -\gamma'$. The most simple description arises with the singular isothermal spheres or ellipsoids (SIS or SIE, Keeton 2001), where $\gamma' \sim 2$. The first mass models of lensing clusters were not constrained enough to consider sophisticated parameterizations and were fitted with SIS profiles. But more importantly, the profiles of individual lensing galaxies are usually approximated by this simple isothermal model because it conveniently matches other observables such as the rotation curves of spiral galaxies (Rubin et al. 1978), or the X-ray luminosity distribution of ellipticals (Fabbiano 1989). It is today well established that early-type lensing galaxies have highly homogeneous properties at $z < 1$, with total mass density profiles roughly isothermal in their inner ~ 10 kpc (Kochanek 1995). The ellipticity of their total potential is not negligible (with $\epsilon > 0.7$ in some cases, Koopmans et al. 2006), and they are preferentially modeled with isothermal ellipsoids. They are fully compatible with a perfect alignment between the observed light distribution and the modeled lensing mass distribution, as found by Koopmans et al. (2006) in 15 sources of the SLACS survey. However, this does not necesarily mean that the stellar and dark matter components in early-type galaxies have exactly the same slope (Treu & Koopmans 2004).

Unfortunately, in many cases this simple isothermal model turns out to be unsatisfactory. First, N-body simulations indicate that the distribution of dark matter in the cluster-scale mass concentrations is not homogeneous. Several studies based on the extremely deep imaging of massive clusters (e.g. from the Hubble Frontier Field program) indeed highlight complex dark matter substructures, proving the necessity to refine the parametrization of their mass profiles. Secondly, for single galaxy lenses, γ' depends on the environment because their density profiles are truncated by tidal stripping. This effect remains poorly understood because the observational constrains from strong lensing generally lie below the effective radius, $\mathrm{R_e}$, but it neverteless suggests that a universal slope $\gamma' \sim 2$ is not appropriate. In conclusion, these considerations lead us to adopt a different description of the lensing potentials from galaxy to cluster scales, in order to account for external shear and for various radial profiles.

The Pseudo Isothermal Elliptical Mass Distribution

The Pseudo Isothermal Elliptical Mass Distribution (PIEMD) can be used to derive the gravitational deflection, distortion, amplification and time delay in an analytical way for mass distributions of arbitrary ellipticity (Elíasdóttir et al. 2007). This description was first introduced by Kassiola & Kovner (1993) in order to provide a physically motivated description where the total mass remains finite when the radius goes towards to infinity. Actually, it generalizes the single isothermal sphere and ellipsoid to a cored and truncated radial profile. The PIEMD has been successfully used to model galaxy-scale dark matter haloes containing early-type ellipticals (Natarajan et al. 1998, 2002a,b; Limousin et al. 2007b). I adopt this mass distribution to model the lensing potentials in front of the GEMS, from the individual galaxies to the large-scale components.

The projected 2-dimensional shape of the PIEMD is described by its angular position on the sky, redshift $\mathrm{z_{lens}}$, ellipticity ϵ, and position angle θ. The ellipticity is given by $\epsilon = \frac{\mathrm{a^2-b^2}}{\mathrm{a^2+b^2}}$, with semi-major axis, a, and semi-minor axis, b. The radial density distribution of the PIEMD $\rho(\mathrm{r})$ is expressed as a function of radius, r, as (Jullo et al. 2010),

$$\rho(\mathrm{r}) = \frac{\rho_0}{\left(1+\mathrm{r}^2/\mathrm{r}_{\mathrm{core}}^2\right)\left(1+\mathrm{r}^2/\mathrm{r}_{\mathrm{cut}}^2\right)} \tag{6.1}$$

The PIEMD radial profile is therefore characterised by the following set of parameters : firstly, a central density ρ_0 which is related to σ_{PIEMD}, the central velocity dispersion of the mass potential. Secondly, the core radius $\mathrm{r_{core}}$, and the cut-off radius $\mathrm{r_{cut}}$, the two characteristic scales where the slope of the density profile changes :

- $\mathrm{r} < \mathrm{r_{core}}$: in the inner region the profile is flat, corresponding to a core of central density ρ_0
- $\mathrm{r_{core}} < \mathrm{r} < \mathrm{r_{cut}}$: the profile corresponds to the isothermal sphere and varies as $\rho \propto \mathrm{r}^{-2}$
- $\mathrm{r} > \mathrm{r_{cut}}$: the distribution declines steeply $\rho \propto \mathrm{r}^{-4}$

Where about half of the mass is contained below $\mathrm{r_{cut}}$ (Limousin et al. 2007a). σ_{PIEMD} is a parameter of the PIEMD description that should be related to the physical velocity dispersion using the calibration of Elíasdóttir et al. (2007). Precautions must therefore be taken when comparing σ_{PIEMD} with the velocity dispersions of isothermal spheres.

6.1.5 Optimization of the mass models

For the reasons given above, we optimize our models in the image plane (also called ”lens plane” in the following) in order to be able to quantify the underlying uncertainties (as done, for instance, in Jauzac et al. 2014, 2015). This approach requires to invert the lens equations in order to reconstruct the positions of the arclets in the image plane, according to the lensing potential. It can become very time consuming for large sets of multiple images. To overcome this issue, some studies have performed their optimization in the source plane by minimizing the offsets between each image of a given multiple system in this plane. However, this faster approach is unable to estimate the uncertainties and produces several biases in the output parameters (Jullo et al. 2007).

The configurations of the GEMS do not imply excessive computing times. LENSTOOL thus determines the best-fitting mass model by minimizing the offsets between the reconstructed and input images in the lens plane, for each system. Then, the most straightforward way to determine the accuracy of a given model is to compute the overall rms of these offsets in the image plane according to

$$\mathrm{rms_i} = \sqrt{\frac{1}{\mathrm{n}}\sum_{\mathrm{j=1}}^{\mathrm{n}} \left(\tilde{\mathrm{r}}_{\mathrm{j,obs}} - \tilde{\mathrm{r}}_{\mathrm{j}}\right)^2} \tag{6.2}$$

where n is the total number of lensed arclets, $\tilde{\mathrm{r}}_{\mathrm{j,obs}}$ their observed position in the telescope images and $\tilde{\mathrm{r}}_{\mathrm{j}}$ their position in the lens plane predicted by LENSTOOL. The smaller the $\mathrm{rms_i}$, the better the modeling of the strong lensing mass distribution. For each GEMS, we select the robust models by requiring that $\mathrm{rms_i}$ remains below the positioning uncertainties from our astrometry.

I also consider the χ^2 computed by LENSTOOL

$$\chi^2 = \sum_{\mathrm{j}=1}^{\mathrm{n}} \frac{[\tilde{\mathrm{r}}_{\mathrm{j,obs}} - \tilde{\mathrm{r}}_{\mathrm{j}}]^2}{\sigma_{\mathrm{j}}^2} \tag{6.3}$$

In this equation, σ_{j} are the positioning uncertainties of each image. In particular, the ones lying close to the critical lines may have uncertain positions which can strongly affect their χ^2.

6.2 Galaxy-galaxy strong gravitational lensing toward the brightest GEMS

The following section presents the procedure followed to derive the lensing model of G244.8, the brightest GEMS in the sample.

6.2.1 Simple mass model with LENSTOOL

Constraining the strong lensing magnification toward the dense star-forming regions in G244.8 requires to quantify the relative contribution of the bright foreground elliptical and the faint central galaxy to the overall lensing. The spherical symmetry of the background emission detected with the SMA and ALMA suggests that the main lensing potential is located in the center of the sub-mm clumps. I therefore start by assuming that the main deflector responsible for the magnification of G244.8 is associated with the red Ks-band source seen with HAWK-I. The X-Shooter spectrum shows that this foreground source is at redshift $z = 1.52$ (see §3.3.2).

6.2.2 Constraining the foreground potential well

As stated below, I use LENSTOOL to model the foreground mass distribution of the single clump. Reconstructing the lensing potential and the intrinsic morphology of the source in the source plane requires as input parameters the structural properties of the mass distribution as well as the position and multiplicity of the lensed arclets. In the case of G244.8 such preliminary constraints arise from the symmetric distribution of the sub-mm clumps either observed in the SMA 850 μm continuum map, or in the CO(4-3) flux map from ALMA (with spatial resolutions of $\sim 0.30''$ and $< 0.10''$, respectively, Fig.6.1).

According to the resolved velocity offsets measured from the CO(4-3) emission line in Chapter 7, these background clumps detected in the (sub)-mm lie at a common spectroscopic redshift of $z = 3.005$. Using the dust morphology from the SMA and additional PdBI spectroscopy of the CO(6-5) line in the C-array ($2''$ beam), we detect four individual clumps associated with two velocity maxima and minima marginally resolved with the PdBI (left panel of Fig.6.1). This hypothesis is confirmed and refined by ALMA since our highest-resolution map of G244.8 at $0.14''$ resolution recovers these four components and resolves the Southern arclet into three smaller knots (right panel of Figures 6.1 and 6.3 below). The high-redshift source is therefore composed of six distinct clumps which I associate in multiple imaged systems to constrain the foreground mass distribution.

To carry out a correct identification, I take into account the expected position, multiplicity and morphology of the gravitational images produced by an elliptical potential as a function of the source position relative to the caustic lines (see diagrams in J.-P. Kneib PhD thesis, Kneib 1993, and Figure 3.8 in M. Meneghetti lecture notes[1]). In Figure 6.3, the velocity offsets of the CO(4-3) line span

---

[1] http://www.ita.uni-heidelberg.de/~massimo/sub/Lectures/gl_all.pdf

different ranges in each arclet and therefore cannot represent six images of a single star-forming knot. However these offsets are very sensitive to the image parity in the lens plane and to differential lensing effects (e.g. see the CO(8-7) emission in SDP.81 for comparison, ALMA Partnership et al. 2015). To avoid a wrong identification, I rather place the clumps at the peak of the integrated flux map from ALMA. I subsequently test ten different associations that seem reasonable and keep the three of them providing consistent LENSTOOL outputs. The most likely configuration involves two separate systems with two and four counter images, respectively, as labeled in the right panel of Figure 6.1.

These multiple image systems are in good agreement with the position and multiplicity of gravitational arcs in other galaxy-galaxy or galaxy-group strong lensing systems with similar configurations, from the SLACS (Gavazzi et al. 2008), SL2S (Tu et al. 2009; Limousin et al. 2009), RCS-2 (Bayliss et al. 2011) or independent samples (Grillo et al. 2008). I also checked that varying the position of the clumps within the ALMA beam did not significantly affect the model outputs. In the following the two other plausible scenarios are examined as well, in order to evaluate the uncertainties induced by the choice of our input constraints.

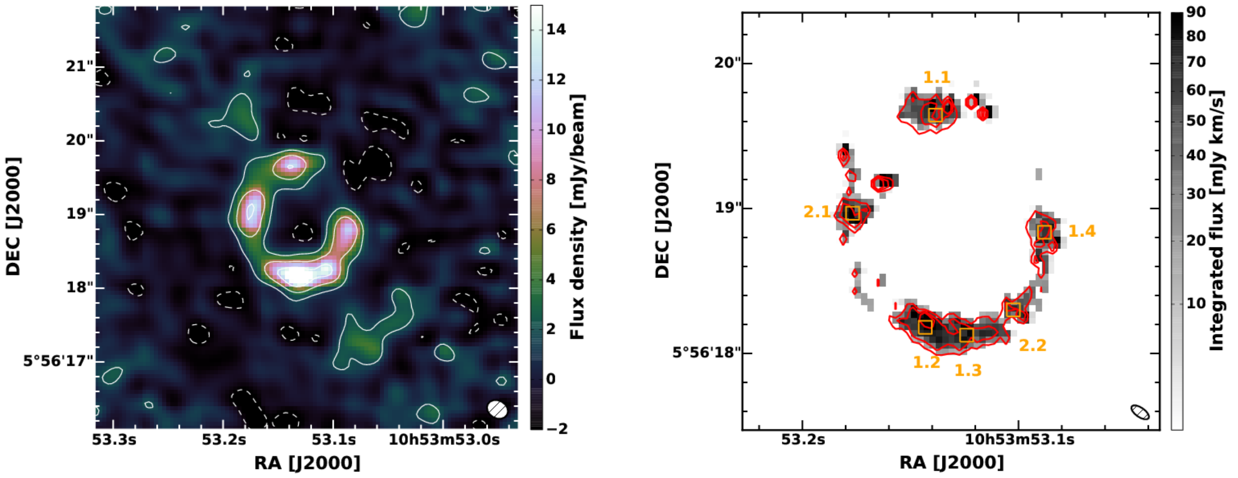

Figure 6.1: *Left :* The high resolution dust continuum of G244.8, obtained with the SMA in the VEXT configuration. The dust emission at 850 μm exhibits a near complete Einstein ring morphology with a diameter of ~ 1.4". The synthetized beam ellipse is shown in the lower-right corner. I overplot the contours at -3,-1,+1,+3,+6σ (with negative contours in dashed lines), where the rms σ reaches 2.01 mJy beam^{-1}. *Right :* The ALMA flux map of the CO(4-3) line (greyscale) and its contours starting at +20 mJy km s^{-1} and increasing by 40 mJy km s^{-1}. The orange squares identify the six clumps and show the most likely combination of multiple images, namely two separate systems with two and four counter images, respectively.

In this single lens plane model, the mass profile of the foreground dark matter clump is computed with a parametric description (Richard et al. 2010), using the truncated PIEMD. The positions of multiply-imaged arclets constrain the location of the critical curve, without considering their morphology and orientation. Since our optimal configuration comprises two systems with $\mathrm{n_1} = 2$ and $\mathrm{n_2} = 4$ multiple images, it provides $\sum 2 \times (\mathrm{n_i} - 1) = 8$ constraints to the Bayesian algorithm and can be used to determine as many parameters.

We place our PIEMD at the geometric center of the clumpy dust emission, and set the redshift of the lens to the spectro-z $\mathrm{z_{lens}} = 1.52$, measured with X-Shooter. The center, position angle and ellipticity of the distribution are left as free parameters since dark matter halos are apparently far from being spherical (Limousin et al. 2013; Bonamigo et al. 2015). I then adopt the following strategy concerning the characteristic radii of the density profile.

The cut radius is known to be highly degenerate with $\sigma_{\rm PIEMD}$ because the total galaxy mass is proportional to $\sigma^2_{\rm PIEMD} r_{\rm cut}$ (see 6.2.3). Moreover, our model shows that the reconstruction of the multiple images is little sensitive to the value of $r_{\rm cut}$ for $r_{\rm cut} > \theta_e$ (i.e. for $r_{\rm cut} > 6.2$ kpc at $z_{\rm lens} = 1.52$). This is much smaller than the typical truncation radius of galaxy scale dark matter halos, usually spanning a few tens of kpc. Likewise, the constraints are falling at much larger radii than the typical values of $r_{\rm core}$ which is therefore also poorly constrained in our model. Under these circumstances, I decide to fix the core radius and to optimize the truncation radius only, as done for example in Limousin et al. (2012). I use a typical core radius of 0.15 kpc as generally assumed for individual galaxies (Limousin et al. 2007b; Brainerd & Specian 2003; Richard et al. 2014). Concerning the truncation radius, isolated galaxies generally exhibit $r_{\rm cut}$ of about 100 kpc (Elíasdóttir et al. 2007), about two times larger than the bulk of cluster members which have lost a large portion of their dark matter halos (Limousin et al. 2007a; Natarajan et al. 2009). Since we have no clear indication of the presence of a larger structure at $z = 1.52$ around the main lensing galaxy, I test different initial values of $r_{\rm cut}$ between 50 and 100 kpc.

As mentioned in §6.1.2, LENSTOOL determines the best-fitting model by minimizing the offsets between the reconstructed and input images in the lens plane, which I take here from our ALMA flux map. I select a set of suitable models by requiring that $\rm rms_i$ remains below the positional uncertainties from our astrometry, ~ 0.10". Since our mass profile contains many degree of freedom, the rms of individual images in our best-fitting model drops in the range $0.02 - 0.10$". Combining the 6 clumps together, I obtain an image plane rms of 0.07". The two other multiple image configurations explored in our analysis provide similar accuracies, namely $\rm rms_i = 0.05$ and 0.09.

LENSTOOL performs 2000 MCMC realisations to compute the probability distribution functions (PDF) of each input parameter and their degeneracies, in particular from the $r_{\rm cut} - \sigma_{\rm PIEMD}$ relationship. In Figure 6.2, I show the 1D histograms of these PDFs, for each individual parameter. The probability densities are nicely peaked, except for the cut radius for which secondary solutions are appearing given its strong degeneracy with the velocity dispersion of the PIEMD. This optimization therefore provides a highly constrained gravitational potential compared to the ancillary model based on SMA 850 μm imaging. The reason is probably that we better sample the external critical line with more resolved clumps in the ALMA flux map. Hence the best-fitting mass model used below to compute the gravitational magnification and the source plane morphology corresponds to the following parameters :

- right ascension offset $\Delta \rm RA = -0.054$ arcsec
- declination offset $\Delta \rm Dec = -0.028$ arcsec
- ellipticity $\epsilon = 0.112$
- position angle $\theta = 2.7$ degrees
- cut radius $r_{\rm core} = 95.5$ kpc in the lens plane
- fiducial velocity dispersion $\sigma_{\rm PIEMD} = 261.5$ km s^{-1}

We note that these results perfectly match the peak values of the individual PDFs in Figure 6.2. This is due to the maximum likelihood method used by LENSTOOL to extract the best fit model (inverse 4). This set of optimized parameters is summarized in Table 6.1 along with the 68% confidence intervals. In our three different scenarios and regardless of the initial value of $r_{\rm cut}$, the PIEMD systematically converges to a truncation radius between 95 and 115 kpc. This result therefore suggests that the main galaxy responsible for the light deflection toward G244.8 is indeed isolated.

Figure 6.3 shows our best-fitting lens model. The left panel shows a comparison between the integrated flux map of the CO(4-3) line from ALMA (red contours starting at +20 mJy km s^{-1} and

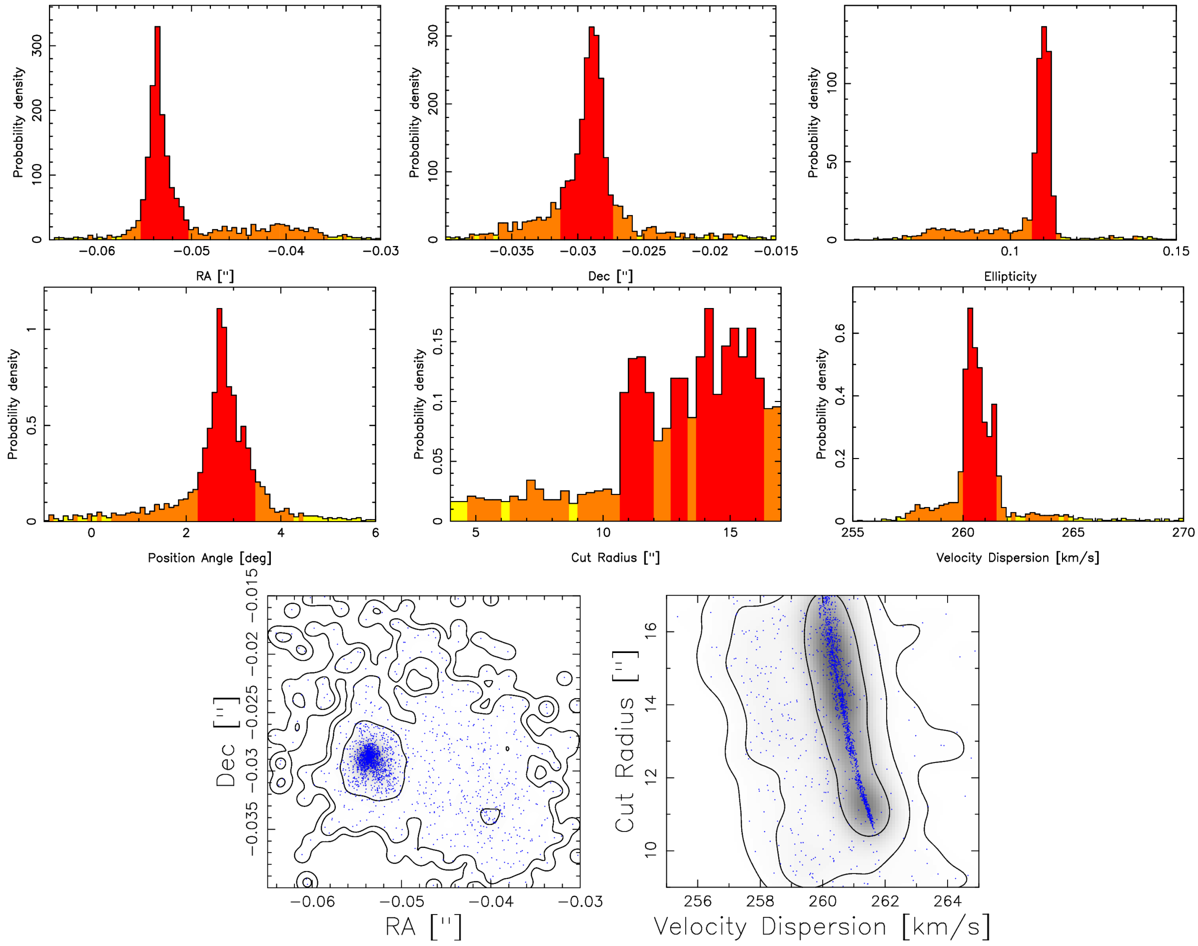

Figure 6.2: *Top/Middle* : 1D histograms of the individual probability distribution functions, for each parameter of the PIEMD optimized with LENSTOOL. *Bottom* : Examples of 2D relationships between weakly and highly degenerate couple of parameters, ΔRA $-$ ΔDec and $r_{\rm cut} - \sigma_{\rm PIEMD}$, respectively. The contours contain 68%, 95% and 99% of the full sample.

increasing by 40 mJy km s^{-1}), and the computed surface-brightness map from our best-fitting model (grayscale). The reconstructed image plane morphology is convolved with the ALMA beam and is a good match to the position of the observed molecular clumps. Although the regions associated with the Southern and Northern arclets (1.1 and 1.2) are slightly brighter, the predicted surface brightness intensity poorly reproduces the clumpiness of the sub-mm emission and reveals a more homogeneous Einstein ring.

In Figure 6.3, I also overlay the tangential (outer) and radial (inner) critical lines at $z = 1.52$. These lines clearly show that the bright sub-mm emission arises from external images with tangential distortion. The bar in the upper right corner shows a scale of 0.5" corresponding to ~4.3 kpc in the image plane at $z = 1.52$. The symmetries of the multiple images with respect to the critical lines of the mass model are illustrated in Figure 6.3. We observe the expected relative position between critical lines and images, for instance with the external critical line falling between images 1.2 and 1.4, and between images 1.4 and 1.1. This arrangement conveniently explains the parity change observed in the velocity map of the CO(4-3) emission between the Southern, Western and Northern clumps, respectively. This figure also shows the position of the magnified images predicted by LENSTOOL using the best-fitting mass model. There is a good match with the input constrains displayed as white squares, and several additional images are predicted along the critical line without obvious counterparts in the ALMA flux and continuum maps. Finally, LENSTOOL also predicts demagnified

	ΔRA [10^{-2} arcsec]	ΔDec [10^{-2} arcsec]	ϵ	θ [deg]	r_{core} [kpc]	r_{cut} [kpc]	σ_{PIEMD} [km s^{-1}]
DM clump	$-5.4^{+0.5}_{-0.1}$	$-2.8^{+0.2}_{-0.2}$	$0.112^{+0.002}_{-0.006}$	$2.7^{+0.6}_{-0.7}$	[1.3]	96^{+18}_{-32}	$261.5^{+1.0}_{-0.7}$

Table 6.1: Results of LENSTOOL optimization. Numbers in square brackets are not allowed to vary during the fit and position angles are expressed clockwise from North. I quote the peak of the individual probability distribution functions and asymmetric errorbars associated with the 1σ confidence levels for each parameter of the PIEMD optimized by LENSTOOL.

images aligned with the center of the potential well.

Our other two configurations converge to similar, nearly circular mass profiles with small positional offsets. They yield the same relative positions of critical lines and observed arclets. However, in those cases, one of the clumps is either not predicted by LENSTOOL or offset from its observed position.

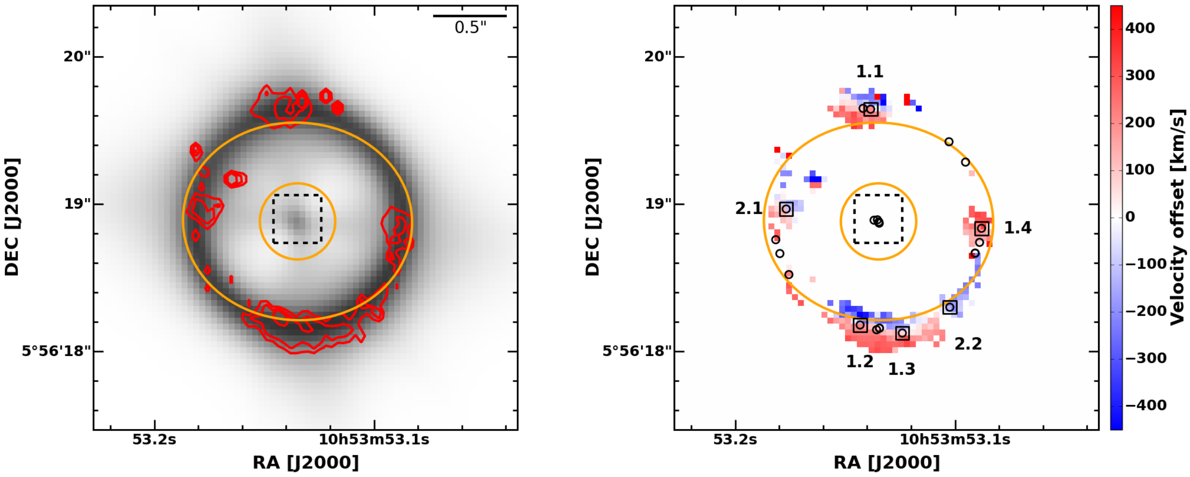

Figure 6.3: Our best-fitting lens model. *Left* : Comparison between the ALMA flux map of the CO(4-3) line (red contours starting at +20 mJy km s^{-1} and increasing by 40 mJy km s^{-1}), and the computed surface-brightness map from our best-fitting model (grayscale). The reconstructed image is convolved with the ALMA beam shown in Fig.6.1. I also overlay the tangential (outer) and radial (inner) critical lines for z = 3.005. A scaling bar in the upper right shows a scale of 0.5" corresponding to 4.30 kpc in the image plane at z = 1.52. *Right* : Velocity offsets of the CO(4-3) line with respect to its average frequency over G244.8. I show the position of the six clumps combined into multiple systems in our model (black square) and the position of the 16 magnified images predicted by LENSTOOL with the best-fitting mass model (black circles). The figure also illustrates the symmetries of the multiple images with respect to the critical lines of the mass model (orange lines).

6.2.3 Mass estimate of the foreground lensing galaxy

Gravitational lensing provides the most accurate estimates of the enclosed mass within the Einstein radius, with 5-10 % uncertainties. For the PIEMD, Limousin et al. (2005) shows that the enclosed mass within an aperture of radius R is :

$$M_{aper}(R) = \frac{\pi \sigma^2_{PIEMD} r_{cut}}{G} \left(1 - \frac{\sqrt{r^2_{cut} + R^2} - \sqrt{r^2_{core} + R^2}}{r_{cut} - r_{core}} \right) \quad (6.4)$$

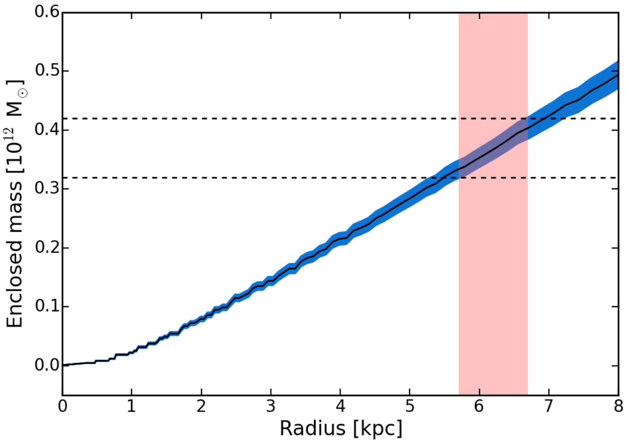

Figure 6.4: Mass profile of the best-fitting PIEMD corresponding to the total projected mass enclosed within a given aperture, with 1σ errorbars derived from the MCMC realizations (blue shaded area). The radii are expressed relative to the center of the gravitational potential, in the lens plane at $z_{\rm lens} = 1.52$. The red shaded area shows the region where the sub-mm arclets are found and inside which I integrate the total lensing mass.

with the gravitational constant, G. Moreover in the PIEMD profile, the total dynamical mass $M_{\rm TOT}$ is finite and scales with $\sigma^2_{\rm PIEMD} r_{\rm cut}$ as :

$$M_{\rm tot} = \frac{\pi\sigma^2_{\rm PIEMD} r_{\rm cut}}{G} \tag{6.5}$$

Since gravitational lensing is only sensitive to the mass enclosed within the position of the background clumps, these relations illustrate why strong degeneracies are expected between the characteristic radii of the mass distribution and $\sigma_{\rm PIEMD}$. LENSTOOL uses the optimized parameters of the PIEMD to compute the integrated mass along each line of sight, and displays the values in a regular grid at $z_{\rm lens}$. To derive the total lensing mass in front of G244.8, I use the mean radial profile of the lensing potential shown in Fig.6.4, and its errorbars derived from the MCMC realizations. I find an enclosed mass of $M_{\rm aper}(\theta_e) = (3.7 \pm 0.5) \times 10^{11} M_\odot$ ($\frac{\delta M}{M} \sim 13\%$) within the radial range covered by the sub-mm arclets, i.e. within an Einstein radius of $\theta_e = 0.72 \pm 0.06$ arcsec corresponding to 6.2 ± 0.5 kpc at $z = 1.52$. This result proves to be very stable, regardless of the input constraints chosen among our three plausible scenarios (variations below 1%).

We can also derive a mass without accounting for ellipticity by using the following relation,

$$\frac{M_{\rm lensing}}{M_\odot} = \frac{10^{11.09}}{M_\odot} \times \frac{\theta_e^2}{\rm arcsec^2} \times \frac{d_L d_S / d_{LS}}{\rm Gpc} \tag{6.6}$$

where D_L, D_S, D_{LS} are the angular diameter distances to the lens, to the source, and between the lens and the source, respectively. The quantity θ_e^2 is related to the area within which the background sources are expected to be strongly amplified and distorted. This simple relation assumes a spherical symmetry of the potential, and provides $M_{\rm lensing} = (3.7 \pm 0.6) \times 10^{11}$ $M_\odot$. Both results are consistent within the uncertainties. This makes us confident that our PIEMD description is reliable in spite of the unavoidable degeneracies.

6.2.4 Quantifying the gravitational magnification

I use the absolute magnification factors μ computed by LENSTOOL from the best-fitting PIEMD to quantify the amplification regime towards each star-forming clump. Their FWHMs and near-circular

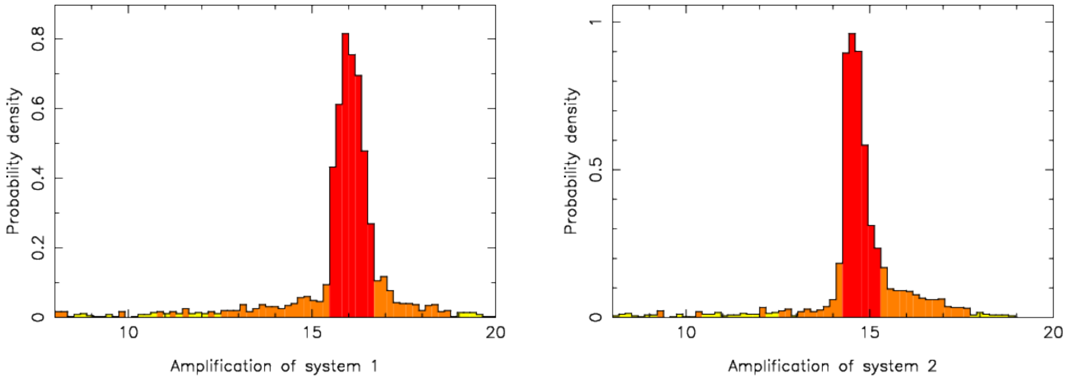

Figure 6.5: Statistical distributions of the total magnifications for systems 1 and 2, respectively, combining all their multiple images together. I use the 2000 realisations of the Monte Carlo Markov Chain and display the 68% confidence intervals in red.

morphologies indicate that they are at best marginally resolved. I therefore extract their magnification factors in beam-like apertures centered on the peaks of the CO(4-3) flux map. The resulting regimes are summarized in Table 6.2, along with the values of μ at the center of each clump provided by LENSTOOL. I also present the clump sizes found by the clumpfind algorithm and the source plane dimensions corrected for gravitational lensing using the values of μ at the maximum fluxes. The quoted errorbars are obviously dominated by the uncertainties on μ. In what follows, these results and the global amplification map computed by LENSTOOL will be used to correct the fluxes, luminosities and star formation rates of each individual sub-mm knot.

The amplification regimes across the beam of ALMA indicate that μ is actually poorly constrained toward the clumps very close to the external critical line, such as 1.2 and 2.2. In the lines-of-sight with more stable magnifications, these results seem nonetheless to be consistent with the observed variations in surface brightness. For instance, I find a ratio of about 1.5 between 1.2 and 1.1 in the integrated flux map and a magnification significantly higher for 1.2. Assuming that these two clumps are indeed multiple images of the same star forming regions in the source plane, our lensing model might justify their different SNRs in the image plane.

Using the two alternative scenarios, I obtain a rough estimate of the additional uncertainties induced by the choice of the input constraints. Even if the images are very close to the critical line, I find that the magnifications quoted in the third column of Table 6.2 are rather stable (variations below 35%).

Clump	μ (across the beam)	μ (at the flux peak)
1.1	8-18	11 ± 1
1.2	12-120	27 ± 5
1.3	8-17	11 ± 1
1.4	10-17	13 ± 2
2.1	10-16	14 ± 2
2.2	12-56	21 ± 5

Table 6.2: Magnification factor toward each clump estimated either in beam-like apertures or at the peak of the CO(4-3) flux map.

Finally, the 2000 realisations of the Monte Carlo Markov Chain enable to derive the statistical distributions of the total magnifications factors, for the two systems of multiple images. I plot these distributions in Figure 6.5. The histograms are nicely peaked and suggest $\mu = 16.2 \pm 0.7$ and

$\mu = 14.7 \pm 0.5$ for systems 1 and 2, respectively.

6.2.5 Source plane reconstruction

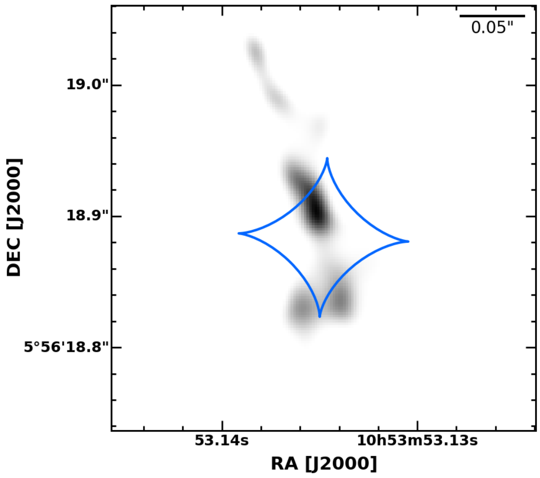

Figure 6.6: The delensed source plane morphology of G244.8 reconstructed with the cleanlens algorithm using our best fit model (greyscale). I zoom in onto the black dashed box delineated in Fig.6.3. The blue line shows the internal caustic curve in the source plane, where the amplification is maximal, while the external caustic falls outside the map.

In LENSTOOL the source-plane reconstruction is done by ray-tracing the observed frame pixel by pixel through the gravitational potential of the best-fitting lens model. While inverting the lens equation, the cleanlens algorithm (Sharon et al. 2012) preserves the spatial information by allowing delensed pixels to have arbitrary shapes and sizes. I subsample the original CCD frame by a factor of 10 (each pixel is subdivided into 10 × 10 smaller pixels) to calculate the source plane morphology at higher spatial sampling. On the other side, the reconstructed frame in the source plane is also subsampled by the same factor to avoid undefined pixels. I extract the six arclets within six individual polygonal contours enclosing each clump in the image plane and compute their independent reconstructions. A final delensed image is obtained by combining the six segments of the source into a single frame.

Figure 6.6 shows this reconstruction by zooming onto the galaxy in the source plane, in a region corresponding to the black dashed box in Figure 6.3. The scaling bar in the upper right corner shows a scale of 0.05" corresponding to about 390 pc in the source plane at $z = 3.005$. The greyscale map shows the intrinsic source plane morphology of the CO(4-3) emission, reconstructed with the cleanlens algorithm. The angular position of the emission peak illustrates that G244.8 is well aligned with the magnifying potential. The blue line shows the internal caustic curve in the source plane, where the amplification is maximal.

The source delensed morphology reveals three main components with compact spatial profiles. We shall note that the delensing process assumes gaussian profiles for the source components and therefore tends to smooth the likely complexity of the system. Assuming the effective half-light radius definition from Erb et al. (2004) and masking the unphysical components, I find that the source plane knot extends to $R_{1/2} \sim (1.8 \times 10^{-2})$" correponding to $R_{1/2} \sim 130$ pc at $z_{\rm source} = 3.005$. The ratio of the median FWHM of the clumps in the image plane to this half-light radius provides an average magnification factor of $\mu = 16 \pm 1$. This estimate averaged over the four components broadly agrees with the range of individual magnifications quoted in §6.2.3. The lines of sight shifted from the external critical line are indeed less amplified and lower the average value across the SMA beam.

The location of the source galaxy with respect to the source plane caustics determines the geometry, multiplicity, and parity of each of its lensed images. Unfortunately we can not improve the sampling of the source plane image without introducing undefined pixel values, making the interpretation difficult. Nevertheless, the position of the three components near the sharp portions of the diamond-like caustic is related to the formation of highly distorted arcs in the image plane, around the quasi-circular critical line. Consequently, the position of the source plane components on the opposite sides of this caustic curve naturally explain the separation of the source into the Southern/Northern arcs observed in our sub-mm interferometry.

6.3 Focus on the GEMS associated with galaxy groups or clusters

In this section, I present the strong lensing models of the GEMS associated with groups and clusters of foreground galaxies, which therefore involve intermediate-scale dark-matter halos.

6.3.1 Strong lensing by overdensities of foreground galaxies

Similarly to the configurations found in the SL2S samples of Limousin et al. (2009), the gravitational arcs in G045.1, G080.2 and G165.7 are separated by moderate angular offsets with respect to each other. Their configuration translates into critical lines radii of about $5 - 15''$, as a function of the angular diameter distance ratio, and the enclosed mass. These GEMS thereby cover intermediate lensing regimes, between galaxy lensing ($\theta_{\rm e} < 1''$) and cluster lensing ($\theta_{\rm e} \sim 1'$) (Belokurov et al. 2009). They are amplified by a mix of cluster scale dark matter halos and galaxy members, akin to the strong lensing cluster cores of Bayliss et al. (2011). Other targets with arclets similarly distributed in the image plane were previously reported in the literature, the most famous being probably the Cosmic Horseshoe (Belokurov et al. 2007), a near-complete Einstein ring of $5''$ lensed by a red galaxy within a group at $z = 0.44$.

Representation of the mass components

The mass distribution in front of these GEMS is parametrized with two distinct mass components. The overall dark matter halos surrounding the galaxy overdensities are modeled by large scale components, henceforth simply referred to as ”halos”. I superimpose individual galaxy-scale ”clumps” bringing together both the baryonic and dark matter masses of each early-type galaxy, so that the global potentials are expressed as follows (Kneib et al. 1996),

$$\Phi_{\rm tot} = \Phi_{\rm halo} + \sum_{\rm i} \Phi_{\rm clumps,i} \tag{6.7}$$

For a given overdensity, I assume that all galaxies near the line-of-sight are at the same redshift as the main dark matter halo. I only include the clumps of bright galaxies with $K < 20$ and consider that the fainter and less massive sources will have a minor gravitational lensing effect (Elíasdóttir et al. 2007). In these models, the position, ellipticity and orientation angle describing their PIEMD are matching the observed distribution of light, in agreement with the results of Koopmans et al. (2006) for galaxies in less dense environments. Nevertheless, it is worth mentioning that the weak lensing study of early-type field galaxies suggest that dark matter components can be marginally rounder (Hoekstra et al. 2004). Moreover, if present, misalignments between the two components in individual cluster members would significantly affect the predicted position of multiple images (Harvey et al. 2016). It remains nonetheless acceptable to center each clump at the position of the corresponding peak in the K-band image. I convert the ellipticities and orientation angles from the source morphologies measured by SExtractor. On the other hand, the characteristic radii and the velocity dispersion of the PIEMD are fixed or optimized in a common way to reduce the number of free parameters. Assuming that all cluster galaxies have a constant mass-to-light ratio[2], the following scaling relations then allow to infer their mass profiles from the rest-frame K-band luminosities $\mathrm{L_K}$ (Brainerd et al. 1996; Limousin et al. 2007b),

$$\mathrm{r_{core}} = \mathrm{r^*_{core}} \left(\frac{\mathrm{L_K}}{\mathrm{L^*_K}}\right)^{1/2} \tag{6.8}$$

$$\mathrm{r_{cut}} = \mathrm{r^*_{cut}} \left(\frac{\mathrm{L_K}}{\mathrm{L^*_K}}\right)^{1/2} \tag{6.9}$$

$$\sigma_{\mathrm{PIEMD}} = \sigma^*_{\mathrm{PIEMD}} \left(\frac{\mathrm{L_K}}{\mathrm{L^*_K}}\right)^{1/4} \tag{6.10}$$

where $\mathrm{r^*_{core}}$, $\mathrm{r^*_{cut}}$ and $\sigma^*_{\mathrm{PIEMD}}$ are the only parameters considered. They represent the PIEMD of a fiducial $\mathrm{L^*}$ galaxy, namely a galaxy that exhibits a K-band luminosity identical to the characteristic luminosity of the Schechter function. Since luminosity functions vary for different populations of galaxies and depending on the environments, they obviously also evolve with redshift. de Propris et al. (1999) express the relation between the characteristic magnitude[3] $\mathrm{K^*}$ and the redshift in galaxy clusters out to $\mathrm{z} \sim 1$, by fitting a Schechter function to the number counts of cluster members. I use this relation to derive $\mathrm{K^*}$ at the redshift of the lens plane for these three GEMS.

I only optimize the value of σ_{PIEMD}. The $\mathrm{r^*_{core}}$ parameter is set at the typical value of 0.15 kpc in several studies of rich clusters (Brainerd & Specian 2003; Limousin et al. 2007b; Richard et al. 2014). Elíasdóttir et al. (2007), for their part, directly fit the single galaxy profile of Brainerd et al. (1996) on the individual members of Abell 2218. I adopt their estimate of $\mathrm{r^*_{core}} = 0.25$ kpc. I also fix the $\mathrm{r^*_{cut}}$ parameter in the models to 50 kpc, a standard value for galaxies in clustered regions which takes into account the tidal stripping suffered by the outskirts of individual dark matter halos (Natarajan et al. 1998; Limousin et al. 2007a). The latter effect is responsible for the decline of the truncation radius compared to isolated galaxies where $\mathrm{r_{cut}}*$ reaches about 100 kpc. Richard et al. (2014) also use $\mathrm{r^*_{cut}} = 45$ kpc[4] to model dark matter subhalos hosting a typical $\mathrm{L^*}$ early-type galaxy. We caution that these scaling relations do not include any scatter, even though Ziegler et al. (2001) show that this scatter may be significant in the members of Abell 2218 due to age variations in the early-type population. In the PIEMD, the total mass of each clumps can be expressed as (Kneib et al. 1996),

$$\mathrm{M_{tot}} = \frac{\pi}{\mathrm{G}} \sigma^2_{\mathrm{PIEMD}} \mathrm{r^2_{cut}} = \frac{\pi}{\mathrm{G}} \left(\sigma^*_{\mathrm{PIEMD}}\right)^2 \mathrm{r^*_{cut}} \left(\frac{\mathrm{L_K}}{\mathrm{L^*_K}}\right) \tag{6.11}$$

I tested several scenarios for these three GEMS, assuming a given set of constraints, and concluded that combining both components is mandatory to deduce consistent models where the critical lines reproduce the symmetries observed between counter images (Natarajan & Kneib 1997). The galaxy-scale clumps alone are not able to provide a good enough rms in the image plane. Moreover, it is sometimes worthwhile to optimize the parameters of individual cluster members independently when they are massive enough and sufficiently close to the angular position of the high-redshift arclets. Such individual clumps – often associated with the BCGs in the inner region of overdense structures – may indeed perturb the local light paths and heavily influence the image reconstruction (Meneghetti et al. 2007).

---

[2] This description seems reasonable since we carefully identified and rejected some late-type galaxies with BPZ and our red sequence selection should in principle provide a clean sample of early-types

[3] i.e. the characteristic luminosity converted into an absolute magnitude

[4] as motivated by the study of galaxy-galaxy weak lensing effects in the central regions of clusters, in Natarajan et al. (2009)

6.3.2 LENSTOOL mass models

Constraining the strong lensing magnification toward the star-forming regions in G045.1 and G080.2, and toward the red arclets forming G165.7, requires initial assumptions about the foreground structures responsible for the light deflection. I search for the best-fitting mass models assuming that the potential wells systematically include a cluster-scale mass component and individual galaxy components accounting for the cluster members.

Identifying the multiple images to constrain the mass distributions

Figure 7.7 shows that G045.1 forms a typical "cusp" configuration. Three multiply imaged sub-mm clumps are distributed along a curved line on the south of the main deflector, and a fourth counter image is detected on the northern side. For the sake of simplicity, we consider that these four images are associated to a single background emitter.

G165.7, together with the additional counter images found in our optical/infrared imaging, form two elongated arcs illustrated in Figure 6.8 through the IRAC contours at 4.5 μm. Both arcs exhibit distorded morphologies and their orientation indicates that the two groups of early-type galaxies selected with the red sequence are indeed dominating the light deflection. Each one of them include three different clumps with similar colours, which we associate into two systems of multiple images.

In the following discussions we will mainly focus on G080.2 which comprises three main components identified in the PdBI CO(3-2) interferometry of Figure 7.3. The velocity map highlights three extended molecular regions, at a common spectroscopic redshift of $z = 2.599$. The first component consists of two double imaged clumps in the north, A1 and A2, with a common velocity gradient of ~ 600 km s^{-1}. Since A1 and A2 are resolved with the PdBI, we split their extreme ends in four independent double imaged systems : the two redshifted ends on one side and the two blueshifted ones on the other. In this way, we account for the orientation of the velocity gradient in the model. The second component is the extended arc in the south-west, labeled B. This arc is blueshifted at both ends and is problably revealing two double images of a single star-forming region. In LENSTOOL we fix our constraints at the position of the maximal blueshift, namely at the position where the velocity reaches about -50 km s^{-1}.

Choosing the multi-scale components : the example of G080.2

In this section, I provide further details on the parametrization of the lensing potential toward G080.2.

We assume that the main deflector responsible for the magnification toward this GEMS is a single cluster-scale DM halo. We only optimize the parameters describing the cluster halo, since this component plays a crucial role for recovering the position of A1, A2 and B in the lens plane. The critical curves are relatively poorly sampled by the sub-mm arclets and we are therefore unable to optimize the parameters of the PIEMD for individual cluster galaxies. However, we stress that the southern pair of galaxies aligned with both ends of B are strongly affecting its shear and magnification in the image plane.

As a first guess, the position of the cluster halo is set to the barycenter of BCG emission in the K-band. During the optimization process we allow its center to vary within $\pm 5''$ assuming that the distribution of dark matter can be shifted with respect to the peak of the light emission. We also let the ellipticity, ϵ, and position angle, θ, free during the optimization. Among the seven parameters fully describing the PIEMD we only keep the cut radius, $\mathrm{r_{cut}}$, fixed. Models of group and cluster halos in the literature typically use $\mathrm{r_{cut}} >> 100$ kpc corresponding to $\mathrm{r_{cut}} >> 15$" at $z = 0.670$, the redshift of our lens plane. However, such an angular scale goes well beyond the position of our sub-mm background clumps. Thus, as stated in Limousin et al. (2007b), the spatial configuration of G080.2 is not ideal to constrain properly the truncation radius. Fortunately, this parameter has a negligible impact on the reconstruction of G080.2, and we set $\mathrm{r_{cut}}$ to 500 kpc.

G045.1	χ^2	rms$_{\rm i}$ [$''$]
1.1	0.6	0.30
1.2	0.5	0.28
1.3	3.1	0.70
1.4	4.2	0.41
Combined	5.2	0.51

G080.2	χ^2	rms$_{\rm i}$ [$''$]
1.1	0.02	0.02
1.2	0.02	0.02
2.1	0.05	0.11
2.2	0.09	0.11
3.1	0.02	0.05
3.2	0.09	0.15
Combined	0.20	0.09

G165.7	χ^2	rms$_{\rm i}$ [$''$]
1.1	2.6	0.64
1.2	4.6	0.85
1.3	0.9	0.38
2.1	1.2	0.44
2.2	9.0	1.20
2.3	2.5	0.64
Combined	20.8	0.74

Table 6.3: Goodness-of-fit and rms in the lens plane for the individual background arclets in G045.1, G080.2, and G165.7.

In addition, the selection of cluster members results in 38 sources. We include this subset of individual galaxies without adding free parameters in the model by applying the scaling relations, with $K^* \sim 17.5$ at $z \sim 0.65$ (de Propris et al. 1999). It is more challenging to find an independent criterion to constrain $\sigma^*_{\rm PIEMD}$. However, using the $\sigma^*_{\rm PIEMD} - r^*_{\rm cut}$ relations from Natarajan et al. (2009) for a mass-to-light ratio in the V-band ∼15, we find $\sigma^*_{\rm PIEMD} \sim 250$ km s^{-1}, and we fix this value during the optimization.

Results of the optimization with LENSTOOL

While performing the optimization, LENSTOOL determines the best-fitting model by minimizing the offsets between the reconstructed and input images in the lens plane. For G045.1 and G080.2, the latter are taken from our dust continuum from the SMA and from our CO(3-2) line flux map from the PdBI, respectively. For G165.7, the input constraints are derived from the combination of CO(5-4) interferometry with the PdbI and NIR imaging with WIRCam. From these offsets, the algorithm then computes a rms in the image plane for each independent clump. I select the suitable lensing models by applying the criterion that rms$_{\rm i}$ should remain below the positional uncertainty from our sub-mm or NIR astrometry, which ranges between 0.2$''$ and 1.0$''$. The rms of the best-fitting models are summarized in Table 6.3 for each individual image of the lensed GEMS. For G165.7, the image in the middle of the Western arc which is responsible for most of the sub-mm emission is also the most poorly fitted. However, even though its rms exceeds the positional accuracy, this high value is also expected given the very elongated morphology observed with the PdBI. In addition, when combining the six arclets, I obtain a much lower rms of about 0.74$''$ for G165.7. For G080.2, I obtain rms$_{\rm i}$ ∼ 0.02" for A, and rms$_{\rm i}$ ∼ 0.11" on the opposite ends of arc B.

For these three sources, depending on the total computational time, LENSTOOL performs either 2000 or 3000 MCMC realisations to calculate the posterior probability distribution functions (PDF) of each input parameter and their degeneracies. The 1D histograms of the individual PDFs and the 2D relationships are shown in Figures C.1, C.2, C.3, C.4 and C.5 reported in Annex. They point out that the individual parameters of the lensing models of G045.1 and G080.2 are difficult to constrain accurately. I nevertheless obtain a consistent picture with limited degeneracies and multiple peaks in the posterior PDFs. In contrary, the strategy adopted to model the mass distribution toward G165.7 with a limited number of free parameters results in very well constrained PIEMDs. For this GEMS, the spatial distribution of the lensed arclets is also a great advantage because it constrains the position of the critical line quite robustly and helps breaking some degeneracies.

I present the optimized parameters resulting from the analysis of the posterior PDFs in Table 6.4, along with the 68% confidence intervals. For a few parameters with flatter PDFs, I find large discrepancies between these values and the parameter of the best-fitting mass model. This is not unexpected since LENSTOOL selects the output set of parameter from a joint posterior PDF. The velocity dispersion of the L* galaxy in front of G165.7 is significantly different from the results found in Ziegler et al. (2001) for Abell 2218. Their value of $\sigma^* = 195 \pm 35$ km s^{-1} remains higher, even after accounting for the different redshifts of the lensing potentials.

Figure 6.7 shows the best-fitting lens model for G080.2. The left panel shows the comparison of the CO(3-2) fluxes from our PdBI interferometry at $0.8''$ resolution presented in Chapter 7 (red contours starting at $+2\sigma$ and increasing by 4σ), and the surface-brightness map computed from our best-fitting model (grayscale). This reconstructed image is convolved with the synthetized beam of the PdBI and is a good match to the position and clumpiness of the Northern A1 and A2 counterparts. However the position of the large Southern arc appears to be shifted with respect to the molecular emission. I also overlay the tangential (outer) and radial (inner) critical lines for $z = 0.670$. They clearly show the bright sub-mm emission arising from B corresponds to an external image with tangential distortion. A scaling bar in the upper right shows a scale of 5" corresponding to 35.5 kpc in the image plane at $z = 0.670$. I show a similar comparison for G165.7 in Figure 6.8.

Source	Component	ΔRA ["]	ΔDec ["]	ϵ	θ [deg]	r_{core} [kpc]	r_{cut} [kpc]	σ_{PIEMD} [km s^{-1}]
G045.1	DM halo	$2.41^{+0.07}_{-0.04}$	$-8.15^{+0.11}_{-1.76}$	$0.20^{+0.03}_{-0.03}$	72^{+1}_{-2}	$4.6^{+1.8}_{-0.1}$	[500]	545^{+54}_{-6}
	L* galaxy	...	...	...	...	[0.25]	[50]	[250]
G080.2	DM halo	$1.12^{+0.08}_{-0.14}$	$1.06^{+0.29}_{-1.48}$	$0.53^{+0.08}_{-0.42}$	80^{+3}_{-5}	$0.7^{+4.0}_{-0.2}$	[500]	555^{+95}_{-10}
	L* galaxy	...	...	...	...	[0.25]	[50]	[250]
G165.7	DM halo	[31.2]	[-18.8]	$0.504^{+0.017}_{-0.020}$	$-27.6^{+0.4}_{-0.4}$	[100]	[500]	$958.7^{+2.1}_{-2.0}$
	L* galaxy	...	...	...	...	[0.25]	[50]	$363.4^{+4.0}_{-3.3}$

Table 6.4: Results of the final optimizations with LENSTOOL, for the three GEMS associated with groups and clusters of foreground galaxies. Numbers in square brackets are not allowed to vary during the fit and position angles are expressed clockwise from North. I present the peak of the individual probability distribution functions and asymmetric errorbars associated with the 1σ confidence levels for each fitted parameter.

Estimates of the foreground lensing masses

As stated below, LENSTOOL uses the $M_{aper}(R)$ relation together with the optimized parameters of the PIEMD to compute the integrated mass along each line of sight. For G080.2, the algorithm provides the output frames shown in Figure 6.9. To derive the lensing mass in front of this GEMS and the two others considered in this section I sum over the pixels in these frames, within a range of apertures illustrated in the right panel of Figure 6.9. I fix these apertures at the angular position of cluster-scale PIEMD. For G080.2, their radii measure 4.2, 7.0 and 9.9", corresponding to 30, 50 and 70 kpc respectively in the image plane at $z = 0.670$. The corresponding enclosed masses are $M(< 30 \text{ kpc}) \sim 6.8 \times 10^{12}\ M_\odot$, $M(< 50 \text{ kpc}) \sim 1.1 \times 10^{13}\ M_\odot$, and $M(< 70 \text{ kpc}) \sim 1.4 \times 10^{13}\ M_\odot$.

We can also derive a mass without accounting for ellipticity by using the following relation,

$$\frac{M_{aper}(\theta_e)}{M_\odot} = \frac{10^{11.09}}{M_\odot} \times \frac{\theta_e^2}{\text{arcsec}^2} \times \frac{d_L d_S / d_{LS}}{\text{Gpc}} \tag{6.12}$$

where D_L, D_S, D_{LS} are the angular diameter distances to the lens, to the source, and between the lens and the source, respectively. The quantity θ_e^2 is related to the area within which the background sources are expected to be strongly amplified and distorted. Since this simple relation assumes a spherically symmetric potential, I measure the Einstein radius of G080.2 from the barycenter of the sub-mm arcs detected with the PdBI. For $\theta_e = 6.4 \pm 0.8$ arcsec, we find $M_{aper}(\theta_e) = (1.2 \pm 0.3) \times 10^{13}\ M_\odot$. This result is consistent with the regime of mass enclosed within 50-70 kpc, the typical radius where the

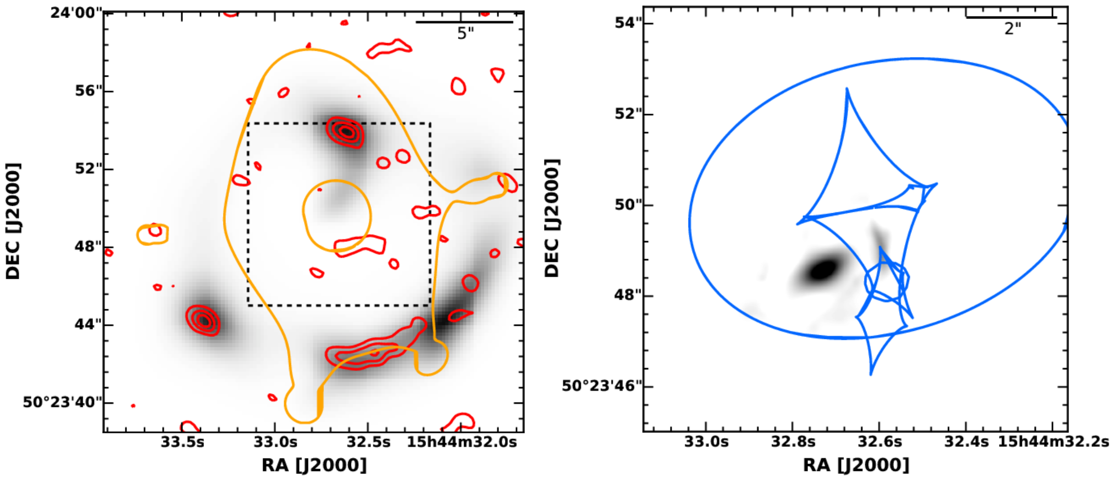

Figure 6.7: Our best-fitting lens model for G080.2. *Left* : Comparison of the integrated CO(3-2) fluxes from our PdBI interferometry at 0.8″ resolution (red contours starting at $+2\sigma$ and increasing by 4σ), and the surface-brightness map computed from our best-fitting model (grayscale). The reconstructed image is convolved with the PdBI beam shown in Fig.7.1. We also overlay the tangential (outer) and radial (inner) critical lines for z = 0.670 (orange lines). A scaling bar in the upper right shows a scale of 5", which corresponds to 35.5 kpc in the image plane at z = 0.670. *Right* : The intrinsic source plane morphology reconstructed with the cleanlens algorithm is shown as greyscale. We zoom in onto the black dashed box delineated in left panel. Blue lines show the internal and external caustic lines in the source plane, where the amplification is maximal.

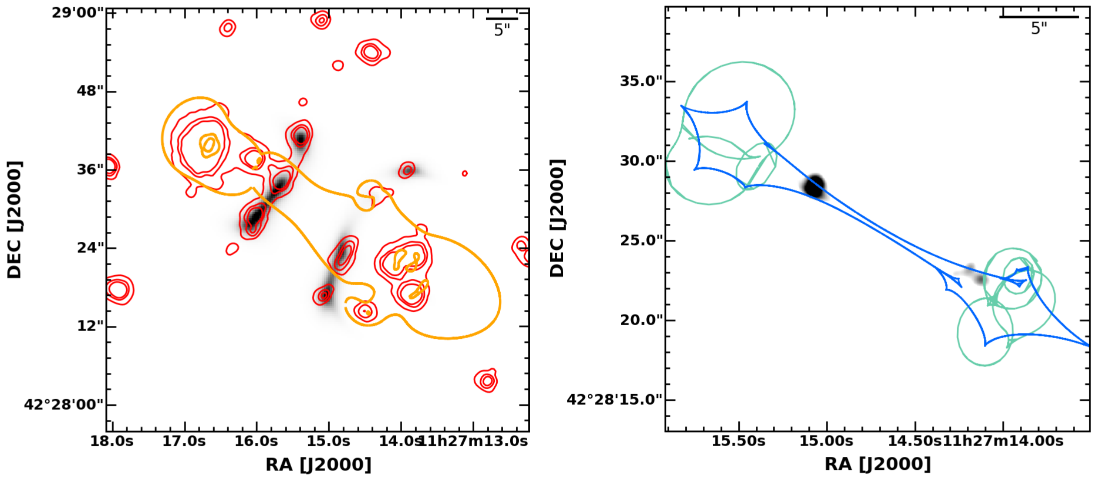

Figure 6.8: Our best-fitting lens model for G165.7. *Left :* Comparison of the IRAC contours at 4.5 μm and the image plane morphology predicted by LENSTOOL (grayscale). I also overlay the tangential and radial critical lines for z = 2.236. *Right :* The delensed source plane morphology of G165.7 reconstructed with the cleanlens algorithm using our best fit model (greyscale). The green and blue lines show the internal and external caustic curves, respectively, indicating the positions in the source plane where the amplification is maximal.

molecular gas emission is detected. This makes us confident that our description of the foreground mass distribution is reliable in spite of the unavoidable degeneracies.

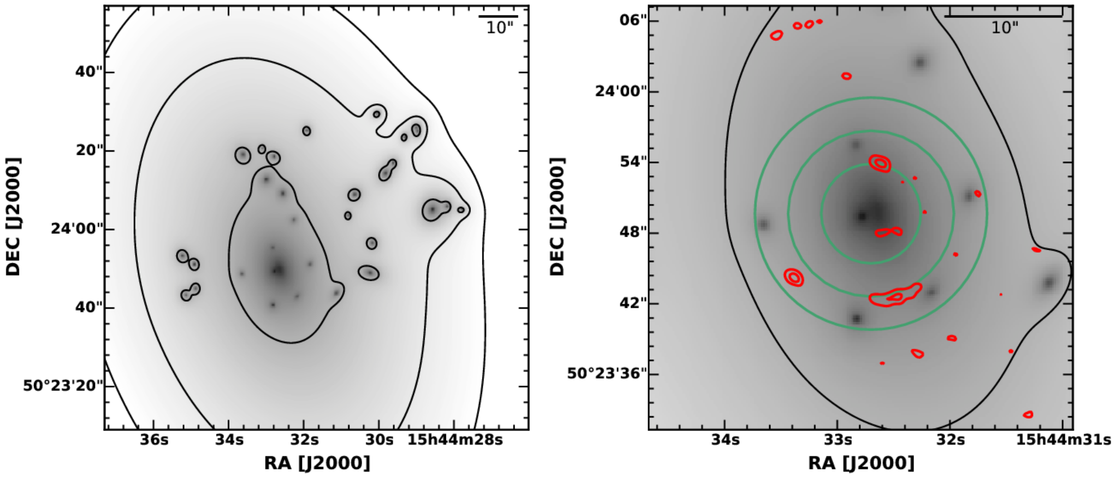

Figure 6.9: *Left* : The integrated and projected mass-density map computed by LENSTOOL from our best-fitting model. The pixel scaling of 0.17 ″/pix matches the sampling of the PdBI data cube. The projected mass densities are expressed in units of 10^{12} $M_\odot$ pix^{-1}. The contours show pixels with mass densities beyond 5×10^7 $M_\odot$, 1×10^8 $M_\odot$ and 5×10^8 $M_\odot$ from the outside to the inside, respectively. A bar in the upper right corner shows a scale of 10″, which corresponds to ∼70 kpc in the image plane at z = 0.670. *Right* : Zoom onto the center of the dark matter halo, with red contours showing the surface brightness map from the SMA at 850 μm (starting at $+3\sigma$ and increasing by 6σ). I display the three circular apertures used to derive the enclosed masses responsible for the strong lensing effect. They correspond to radii of 30, 50 and 70 kpc respectively, in the image plane at z = 0.670.

Quantifying the gravitational magnification

I use the absolute magnification factors μ computed by LENSTOOL from the best-fitting mass distribution to quantify the amplification regime towards each star-forming clump in G045.1, G080.2 and G165.7. In G080.2, A1, A2, and B are resolved with the PdBI and I therefore extract their magnification factors within the 3σ contours of the CO(3-2) flux map. The resulting ranges are summarized in Table 6.5, along with the gravitational magnifications obtained for G165.7. These results will be later used to correct the sizes, luminosities and star formation rates of each individual arclet.

In Figure 6.10, I also present the distribution of the total magnification factor toward each system of multiple images from the 2000 or 3000 realisations of the Monte Carlo Markov Chains.

G080.2 Component	$\mu_{\mathrm{CO(3-2)}}$
A1	2.0-2.5
A2	2.5-3.0
B	10-100

G165.7 Clump	$\mu_{4.5\mu\mathrm{m}}$	μ_{peak}
1.1	8-15	9.0 ± 1.0
1.2	5-25	12.0 ± 1.0
1.3	4.0-4.5	4.0 ± 0.2
2.1	8-18	10.5 ± 1.5
2.2	3-10	6.0 ± 1.5
2.3	3.5-4.5	3.7 ± 0.2

Table 6.5: Regime of gravitational magnification toward each background emitter of G080.2 (left) and G165.7 (right), and obtained from the best-fitting mass distributions. For G080.2, μ is estimated within the 3σ contours of the CO(3-2) flux map. For G165.7, it is derived either within the IRAC 6σ contours at 4.5 μm, or at the peak of the K-band emission.

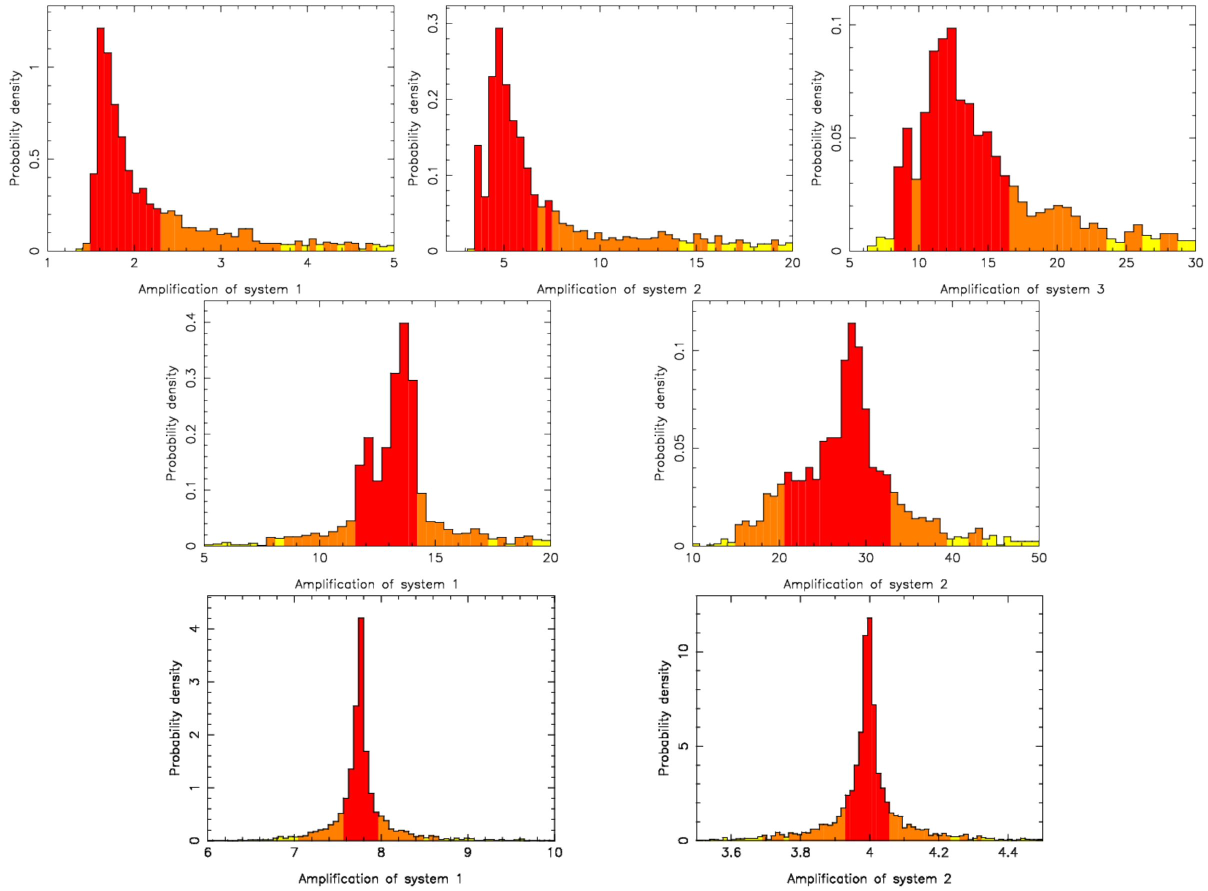

Figure 6.10: Statistical distributions of the total magnification factors toward each system of multiple images. I use the 2000 or 3000 realisations of the Monte Carlo Markov Chains and display the 68% confidence intervals in red. The top panels show these distributions for the three multiply imaged systems of G080.2, while the middle panels correspond to the two systems identified in G045.1. The bottom panels show the two components that form the western and eastern arcs in G165.7, from left to right, respectively.

Reconstruction of the intrinsic properties in the source plane

I also perform the source plane reconstruction of G045.1, G080.2 and G165.7 with the cleanlens algorithm, using the optimized mass distributions. I extract each individual arclet in the image plane with polygonal contours. As previously, I will essentially discuss the results obtained for G080.2, while the reconstruction of G165.7 is illustrated in Figure 6.8.

I derive the independent reconstructions of A1 and A2 on one side, and of the two ends of B on the other, and find a good agreement in the source plane. A final delensed image is obtained by combining the segments of the source into a single frame. The right panel of Figure 6.7 shows this reconstruction by zooming onto the high-redshift system, in a region corresponding to the black dashed box in the left panel. The intrinsic delensed morphology reconstructed with the cleanlens algorithm is shown as greyscale, with A and B located behind the peak of the magnifying potential. The centroids of these two components are offset by $\sim 1.4''$ and this spatial distribution shows that our systems are independent emitters in the source plane. I tested alternative representations of the lensing potential, in order to further demonstrate that A and B are intrinsically segregated in the source plane regardless of the delensing process. In particular, I tried to assume a circular PIEMD for the main halo, I tested the effect of fixing $r_{\rm core}$ and $r_{\rm cut}$, and I fixed the center of the PIEMD at the barycenter of the sub-mm arclets. Each one of these configurations resulted in a reasonable rms in the image plane, but the angular offset between A and B remained systematically greater than $1''$ (i.e. more than $\sim$8 kpc at $z = 2.599$).

In Figure 6.7, blue lines show the internal and external caustic lines in the source plane, where the amplification is maximal. As expected, the internal caustic from the cluster dark matter halo is very close to each component (A and B) and it is likely to dominate their shear and magnification. However we can see in the middle of the panel that two secondary caustics – resulting from the faint foreground galaxies on both sides of B – are also crucial to interpret the observed magnification and multiplicity of the extended arc B in the image plane.

Assuming the definition of the half-light radius from Erb et al. (2004) and masking the unphysical components, I find that the source plane reconstruction of A extends over $R_{1/2} \sim 0.28$" corresponding to $R_{1/2} \sim 2.28$ kpc at $z = 2.599$. The ratio of the median FWHM of A1 and A2 in the image plane to this half-light radius provides a total magnification factor of $\mu \sim 1.7$. This estimate broadly agrees with the range of individual magnifications quoted in §6.3.2. For B, I find $R_{1/2} \sim 76$ mas (~ 620 pc at $z = 2.599$). However the magnification toward B is poorly estimated with our simplistic ratio because its large distorsion in the image plane makes any measurement of its FWHM highly uncertain. We typically find $\mu > 10$ which confirms that A is indeed much less amplified than B.

Chapter 7

Properties of the most remarkable Planck's Dusty GEMS

Contents

7.1 Spatially-resolved gas and dust properties of G080.2 at z = 2.6

7.1.1 Properties of the sub-millimeter source

The Planck Dusty GEMS G080.2, hereafter referred to as "the Malachite", was identified as a gravitationally lensed source in 2012, before the large follow-up program with Herschel/SPIRE, and is detected as a single point source in our FIR/mm photometry with Herschel/SPIRE, JCMT/SCUBA-2 and IRAM/GISMO. With a peak flux density of 345 ± 5 mJy at 370 ± 10 μm derived from the modified blackbody fit, G080.2 is one of the faintest GEMS. This same fit provides a dust temperature $\mathrm{T_d} = 33.0 \pm 0.5$ K, a dust mass $\mathrm{M_d} = (7.2 \pm 0.2) \times 10^9$ μ^{-1} $\mathrm{M_\odot}$ and a star formation rate $\mathrm{SFR} = 7920 \pm 172$ μ^{-1} $\mathrm{M_\odot}$ $\mathrm{yr^{-1}}$, before correcting for the magnification factor μ (Chapter 4). Moreover, the steep decrease of the SED between 350 and 250 μm and the flux upper limit from WISE at 22 μm also indicate that the IR-to-mm SED of this source is consistent with a pure starbursting galaxy without a significant AGN contribution. The spectroscopic redshift of G080.2 was obtained during our blind search in the 3-mm band with EMIR on the IRAM 30-m telescope (see §4.1.1). The first detected line was identified as CO(3-2) ($\nu_{\mathrm{rest}} = 345.796$ MHz in the rest-frame), suggesting a redshift $\mathrm{z} = 2.5987 \pm 0.0003$ which was subsequently confirmed by the detection of the CO(5-4) transition in the 2-mm band.

Later, G080.2 was observed with the SMA in the EXT configuration with a reconstructed beam of $0.77'' \times 0.54''$ and a position angle of 88.1° (see Fig.7.1). Compared to the overall sample, the 850 μm dust continuum in the Malachite exhibits a very peculiar morphology. It is composed of three components in the image plane, two similar compact and bright clumps in the North and North-East (named A1 and A2) and an elongated more diffuse arc (named B). These components have high angular separations compared to the other GEMS plotted in Figure 4.6 or to the typical separations of SPT lensed SMGs ($2 - 3''$, Vieira et al. 2013), and are distributed along a quasi-circular line of $12.5''$ diameter. The most magnificent example of a lensed galaxy forming a circular Einstein ring with similar size is perhaps the "Cosmic Horseshoe", a strongly lensed Lyman-break galaxy at $\mathrm{z} = 2.379$ amplified by a massive red galaxy at $\mathrm{z} = 0.444$ (Belokurov et al. 2007). Moreover, the dust continuum has apparent sizes of $0.6'' \times 1.3''$, $0.7'' \times 1.2''$ and $0.6'' \times 2.9''$ in A1, A2 and B, respectively, according to the 3σ isophotal contours (Nesvadba et al. 2016, in prep.). The two compact clumps are therefore resolved in the SMA beam.

These three components have been subsequently confirmed with the high-resolution CO(3-2) interferometry from the PdBI as further described in the next subsection. In a nutshell, this datacube also resolves the redshifted molecular gas emission and allows to characterize its morphology and kinematics as well as the overall gas mass surface densities. It shows that the arc extends to 4.0 ± 0.2" and 1.4 ± 0.2" along the major and minor axis, respectively. In addition, the bright [CII] line was detected in G080.2 with the Herschel/HIFI spectrometer and PdBI interferometry of the [CI](1-0) line was obtained as part of the follow-up observations (Nesvadba et al. 2016, in prep). Although resolved emission from atomic carbon is a powerful probe of the bulk of the gas reservoir in the Malachite and its physical conditions (Alaghband-Zadeh et al. 2013), these data are not further discussed in this thesis.

The components of the Malachite are distributed around the bright foreground early-type galaxy at $\mathrm{z} = 0.670$ which is clearly detected in the optical/NIR images of Figure 7.1. In Chapter 5, I demonstrated that this source is the brightest member of a foreground overdensity of red early-type galaxies at $\mathrm{z} \sim 0.6 - 0.7$ and I needed to include faint nearby companions in the strong lensing model of Chapter 6 to reproduce adequately the background arclets. The zoomed region of $30'' \times 30''$ presented in Figure 7.1 includes this small set of foreground galaxies causing significant deflections toward G080.2. Moreover, the sub-mm emitter is below the sensitivity limits of the optical/NIR imaging and it is detected as a faint source in both IRAC channels. The 3-color image shows that it is extremely red compared to other sources detected near this line-of-sight.

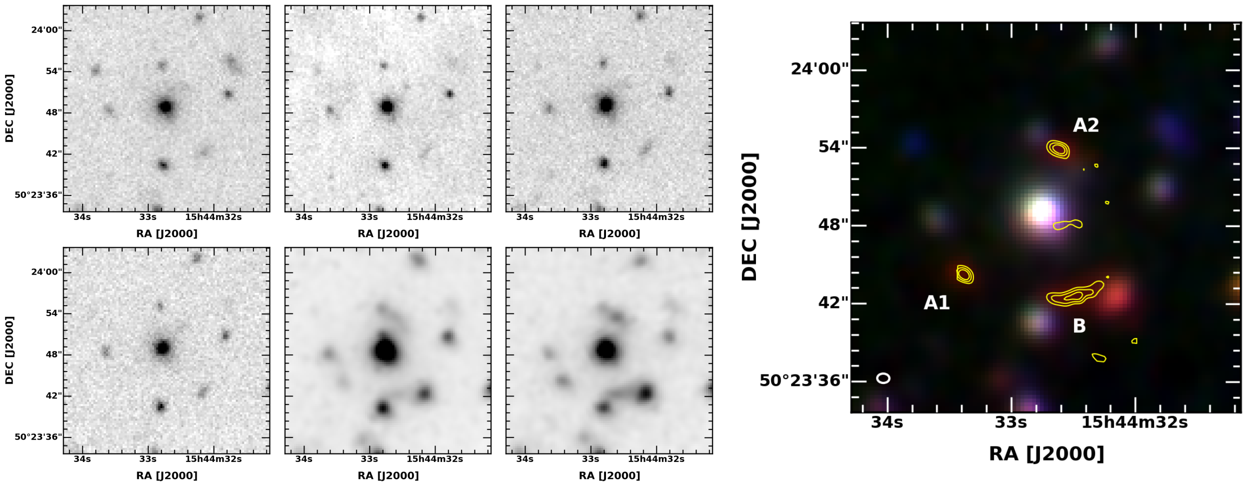

Figure 7.1: *Left :* Single band images of G080.2 obtained in the r, z, J and K bands with MegaCam and WIRCam and at 3.6 and 4.5 μm with IRAC, from top-left to bottom-right respectively. *Right :* 3-color image in the r, K and 4.5 μm bands of a $30'' \times 30''$ region centered at the peak of single dish (sub-)mm emission. The resolution of the two optical and NIR images have been matched to the PSF of IRAC channel 2. The yellow contours indicate the morphology of the CO(3-2) emission obtained with the PdBI, from the integrated flux map. Contours start at $+3\sigma$ and increase in steps of $+3\sigma$. The beam FWHM of the PdBI is also shown in the lower-left corner.

Line	$\nu_{\rm rest}$ [GHz]	Project ID	$\nu_{\rm tuning}$ [GHz]	Beam FWHM [arcsec]	$t_{\rm obs}$ [hr]	Binning [MHz]	3σ rms [mK]	S/T_a^* [Jy K^{-1}]
CO transitions								
^{12}CO(7-6)	806.652	223-13	224.400	$\sim$ 11	3.2	30	0.82	7.8
Atomic gas lines								
[CI](1-0)	492.161	223-13	136.749	$\sim$ 18	2.4	10	2.35	6.7
[CI](2-1)	809.343	223-13	224.400	$\sim$ 11	3.2	30	0.82	7.8

Table 7.1: Observations of the atomic and molecular emission lines in G080.2 with EMIR on the IRAM 30-m telescope. The binning column indicates the spectral binning applied in Fig.7.2. The 3σ rms is derived with GILDAS in line-free regions of each baseline. The point source sensitivities of the 30-m telescope used to convert the peak antenna temperatures to flux densities through the factor S/T_a^* were taken from the instrument commissioning of April 2015[2].

7.1.2 Integrated profiles of the spectral lines observed with EMIR

EMIR observations of the Malachite were performed through different runs between November 2012 and February 2014. In addition to the CO(3-2) and CO(5-4) transitions detected during our redshift search, other lines were targeted as part of our extensive spectroscopic survey of the GEMS (see Table 7.1). Firstly, we detected the CO(7-6) transition, the third and last mid-J line of ^{12}CO observable from the ground for z $\sim$ 2.6. Secondly, we detected the [CI]($^3P_1$-$^3P_0$) and [CI]($^3P_2$-$^3P_1$) fine structure lines of atomic carbon. I present their integrated profiles in Figure 7.2 and quote the results of the single gaussian fits in Table 7.2. At the redshifted frequencies of low-J CO and [CI](1-0) transitions, the three spatial components of G080.2 are included in the beam of the IRAM 30-m antenna. However, at higher frequencies the beam FWHM decreases as low as the spatial extent of the dust continuum from the SMA or the PdBI. Hence, the integrated fluxes of CO(7-6) and [CI](2-1) are probably missing extended emission. In Figure 7.2, the lower-J CO transitions suggest a double-peaked profile and this spectral feature is also marginally detected in [CI](2-1).

Line	$\nu_{\rm obs}$ [GHz]	Redshift	FWHM [km s^{-1}]	$T_{\rm peak}$ [mK]	Line flux [Jy km s^{-1}]	$L_{\rm line}$ [10^8 $L_\odot$]	10^{-11} $L'_{\rm line}$ [K km s^{-1}pc^2]
CO transitions							
^{12}CO(7-6)	224.170 ± 0.015	2.5984 ± 0.0002	248 ± 42	2.13	4.40 ± 0.61	4.87 ± 0.68	0.29 ± 0.04
Atomic gas lines							
[CI](1-0)	136.767 ± 0.008	2.5985 ± 0.0002	316 ± 60	3.93	8.85 ± 1.09	5.98 ± 0.74	1.57 ± 0.19
[CI](2-1)	224.848 ± 0.022	2.5995 ± 0.0003	393 ± 67	1.99	6.50 ± 0.81	7.22 ± 0.90	0.43 ± 0.05

Table 7.2: Properties of three atomic and molecular lines detected in the Malachite with EMIR on the IRAM 30-m telescope. The central frequency, full width at half maximum, peak temperature and flux of each line are obtained with a single gaussian fit, using the routines from the GILDAS package. The values are not corrected for gravitational magnification. Line luminosities are expressed either in K km s^{-1} pc^2 or in solar luminosities.

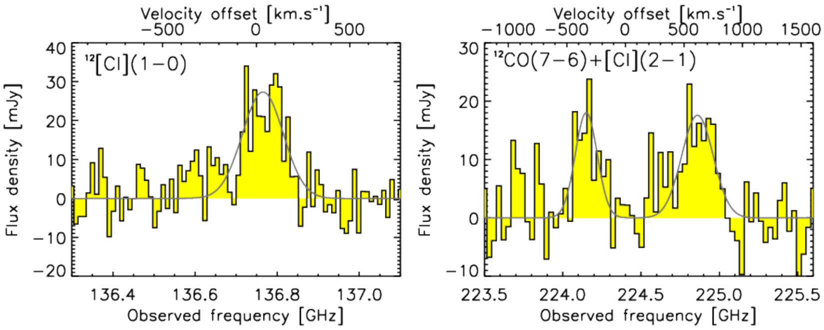

Figure 7.2: Spatially-integrated spectra of the atomic and molecular lines in G080.2 obtained with EMIR. The continuum-subtracted spectra are fitted with a single Gaussian-profile overlaid in grey. The reference velocities are fixed to the line frequencies which are themselves deduced from the CO(3-2) detection.

7.1.3 Resolved gas kinematics from the CO(3-2) emission line

To probe the gas kinematics in the Malachite from the CO(3-2) interferometry, I first rely on a single gaussian fit to each pixel of the 2 MHz resolution data cube, as described in §3.4.1. In Figure 7.3, I show the resulting maps of the line fluxes, velocity offsets and gaussian widths, σ. The tuning frequency and, accordingly, the reference velocity are deduced from the redshift z = 2.5987, which was initially measured on the EMIR CO(3-2) detection.

Firstly, the sub-mm clumps A1 and A2 resolve in two kinematically distinct regions with the PdBI beam of $0.72'' \times 0.95''$. The first one is significantly redshifted by ~ 500 km s^{-1} compared to the systemic velocity and the second one is blueshifted by about -100 km s^{-1}. However, these regions are at best marginally resolved individually with the PdBI/A-array. More importantly for the lensing model, these strong velocity offsets and the line width map highlight a clear change in parity between A1 and A2. The velocity dispersions deduced from their integrated line profiles are also systematically above 50 km s^{-1}. Secondly, the gas kinematics in arc B exhibit a strong symmetry with both ends bluedshifted by $\lesssim 100$ km s^{-1}. Figure 7.3 provides a preliminary indication of the velocity dispersion in this extended component from a single gaussian fit, suggesting a rather homogeneous and quiescent gas material with $\sigma \sim 40 - 70$ km s^{-1}. Nevertheless, a more thorough analysis of the spectral components resolved with the PdBI is required to fully characterize the gas kinematics in this arc. Finally these simplistic single gaussian fits result in high residuals, especially in A1 and A2 (see Fig.7.3), and poor

---

[2] http://www.iram.es/IRAMES/mainWiki/EmirforAstronomers?action=AttachFiledo=gettarget=new-optics-commissioning-apr2015-v0.9.4.pdf

normalized χ^2 of up to ~ 5 in some pixels. In the following, I seek to improve the quality of the fit and to determine whether the parities observed in the velocity offsets are due to spectral sub-structures. I first show that the integrated spectra of A1, A2 and B resolve into multiple components, and I then use a detailed fitting routine to disentangle each one of these velocity components and to compute individual maps.

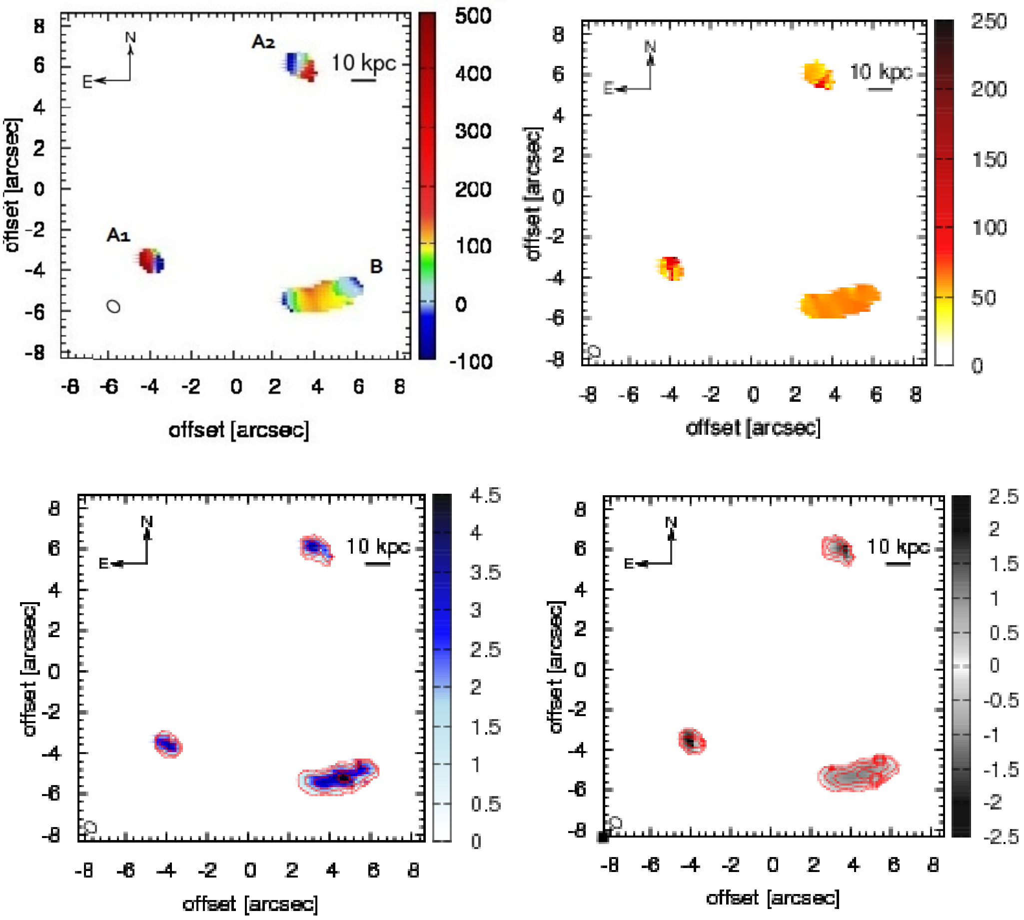

Figure 7.3: Profile of the CO(3-2) emission line measured in the Malachite with the PdBI in the A-array. The line profile has been fitted with a single gaussian for each pixel within the spatially-resolved components A1, A2, and B. Individual maps show the velocity offsets (top-left), gaussian line widths (top-right), both expressed in km s^{-1}, along with the peak fluxes (bottom-left) and residuals (bottom-right), both expressed in mJy beam^{-1}. The reconstructed beam of the PdBI is shown as a black ellipse in the lower-left corner of each panel. The red contours indicate constant fluxes, starting at 3σ and increasing by $+9\sigma$. A rms noise of 2.0×10^{-17} erg s^{-1} cm^{-2} is measured in line-free spectral channels of pixels with high signal-to-noise ratio. The scale bar in top-right corners indicate the apparent angular size of a 10 kpc wide structure at z $\sim$ 2.6, without considering any gravitational magnification.

In Figure 7.4, I show the integrated CO(3-2) lines in the three main components of the Malachite obtained by stacking the spectra of individual pixels within the 3σ flux contours (taken from the single gaussian fit). The data cube of 12 km s^{-1} (i.e. 6 MHz) spectral resolution reveals non-trivial line profiles in A1, A2 and B, with multiple components separated by different velocity offsets and with variable peak fluxes. A1 and A2 exhibit a double-peaked profile with velocity offsets of about 415 km s^{-1} and 395 km s^{-1} between the two bright components, respectively. These relative offsets are consistent with the results of the single gaussian fits, under the condition that the respective peak fluxes vary spatially within the clumps. There is also a tentative detection of a third component between the main two peaks, which has a higher signal-to-noise ratio in the integrated spectrum of A1 and prove to be particularly prominent in specific lines-of-sight. I illustrate these substructures by stacking the spectra of high SNR regions, within individual apertures of the size of the synthetized beam (bottom panels of Fig.7.4). The arc also reveals a complex profile with two or three components resolved at 2 MHz and which become blended at lower spectral resolutions into a single line of FWHM $\gtrsim 250$ km s^{-1} (top panel of Fig.7.4). Similarly, I highlight the complex line profiles in B using the high-resolution data cube and a dedicated aperture matching the size of the beam. The stacked spectrum indicates two main components with a relative velocity offset of 150 km s^{-1}. Generally, we resolve extremely narrow profiles both in the compact clumps and the extended arc, with intrinsic velocity dispersions corrected for the instrumental resolution systematically below 90 km s^{-1} and decreasing down to $\sim$ 30 km s^{-1} in A1 and B, and down to $\sim$ 25 km s^{-1} in A2. Finally, combining all the pixels within the 3σ flux contours of G080.2 results in a double-peaked profile with a major contribution from the most blueshifted component, while the narrower sub-structures become fully blended. I find a relative velocity offset of about 345 km s^{-1} between the two peaks, which broadly agrees with our preliminary characterization of the low and mid-J CO line profiles with EMIR single dish spectroscopy (Fig.7.2). The properties of the multiple spectral components in the integrated spectra of A1, A2, B, and the entire sub-mm source are listed in Table 7.3, while the narrower components detected with individual apertures are presented in Table 7.4.

Component	LSR velocity [km s^{-1}]	Gaussian width σ [km s^{-1}]	Peak flux [mJy]	Integrated flux [Jy km s^{-1}]
Individual				
A1 blue	-44.6	109.0	4.15	1.13
A1 red	371.8	118.1	2.77	0.82
A2 blue	-36.7	106.1	4.64	1.23
A2 red	358.6	[118.1]	1.24	0.37
B	-0.8	108.0	9.91	2.68
Total				
G080.2 blue	-29.3	103.1	17.7	4.59
G080.2 red	314.3	182.2	3.79	1.73

Table 7.3: Spatially-integrated profiles of the CO(3-2) emission line in the spatial components A1, A2 and B, and for the complete source. The gaussian width of the most redshifted component in A2 is fixed to the value optimized in A1 in order to avoid poor-quality fits.

Component	LSR velocity [km s^{-1}]	Gaussian width σ [km s^{-1}]	Peak flux [mJy]	Integrated flux [mJy km s^{-1}]
A1	-88.2	33.1	0.71	58.6
A1	115.0	59.5	0.54	79.9
A1	403.0	88.9	0.55	123.4
A2	-23.7	45.5	0.35	40.5
A2	143.1	26.8	0.50	33.6
A2	378.0	66.7	0.20	33.3
B	-70.1	30.6	1.52	116.5
B	79.2	43.2	3.23	349.7

Table 7.4: Properties of the high-resolution spectra stacked within three individual apertures toward A1, A2 and B, as large as the synthetized beam. The gaussian widths, σ, are intrinsic line widths corrected for the instrumental resolution and can be assimilated to line-of-sight velocity dispersions.

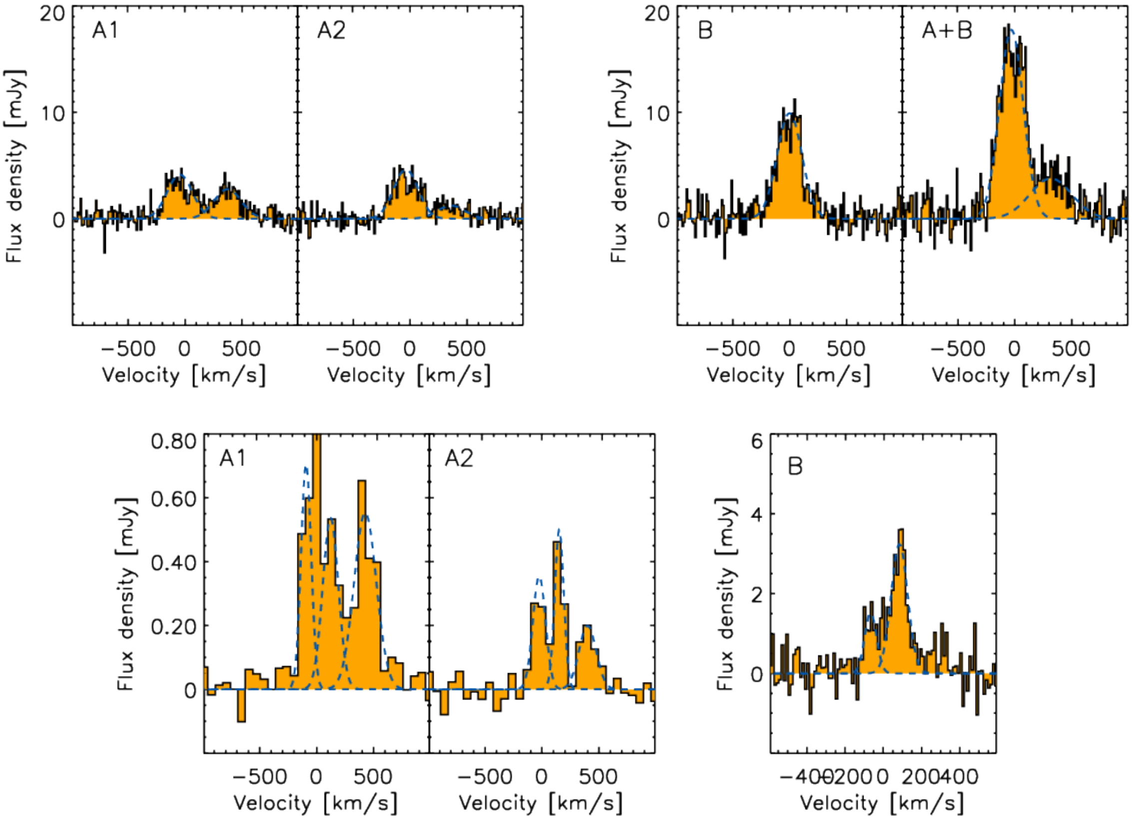

Figure 7.4: *Top :* Spatially-integrated profiles of the CO(3-2) emission line for the three main components of G080.2 and for the complete source. I obtained these four plots by stacking the spectra of individual pixels within the 3σ flux contours. The blue dotted lines show single or double gaussian fits. *Bottom :* High-resolution spectra extracted with individual apertures of size of the beam toward A1, A2 and B, respectively.

When looking more closely at the data cube with the nominal spectral resolution of 2 MHz, the CO(3-2) emission of individual pixels in A1 and A2 indeed reveal three narrow spectral components. In fact, the third fainter component turns out to be less blended than in the integrated profiles of Figure 7.4. Since these observations motivate a three gaussian fit, I use the advanced fitting algorithm described in §3.4.1 to derive the parameters of each component in A1 and A2, respectively. The resulting velocity offset, gaussian width and line flux maps are shown in Figure 7.5. The first component is blueshifted with velocity offsets distributed in a wide range from -150 to 0 km s^{-1}, with respect to the systemic velocity. Similarly to the single gaussian fit, the most blueshifted pixels highlight a clear change in parity between A1 and A2. Moreover, the maps show highly homogeneous velocity dispersions of about 70 km s^{-1} and similar fluxes in the two clumps. The second component is redshifted with peak velocities offset by 60-180 km s^{-1}, and slightly lower velocity dispersions of $\sim$ 60 km s^{-1} suggesting a second molecular cloud with less turbulent kinematics. Its peak fluxes vary significantly between A1 and A2. This is most likely due to different magnification factors along the two lines-of-sight, even if our lensing model with LENSTOOL only indicates a slightly higher μ in A2 (mostly due to the faint red galaxy located within $2''$ of the sub-mm clump). Eventually, the third component is also redshifted with velocity offsets around 400 km s^{-1}, and gaussian widths of $40-60$ km s^{-1}. The fact that only one of these components shows different peak fluxes in A1 and A2 suggests significant differential lensing effects between the gas reservoirs. It is also worth mentioning that, globally, the symmetry between A1 and A2 is blurred in these separate maps. Moreover, such mean velocity offsets of -80, 150 and 400 km s^{-1} could trace ordered rotation within a molecular disk. This range is compatible with the upper limit of 575 ± 100 km s^{-1} obtained in GN20, a well-studied luminous starburst at $z = 4.05$ with high gas surface densities (Carilli et al. 2010). It is however more extended than the rotation velocity of the Cosmic Eyelash measured by Swinbank et al. (2011) (320 ± 25 km s^{-1}), using a disk model with gas kinematics supported by the overall rotation. At somewhat lower redshifts ($z \sim 1 - 2$), Tacconi et al. (2010) find double-peaked CO(3-2) line profiles in a small set of typical star-forming galaxies, which they consider evidence of ordered rotation in extended disks. Their maximum rotation velocities corrected for disk inclination are below 350 km s^{-1} which is much lower compared to the compact clumps of the Malachite, probably because this sample probes a different mass regime.

Concerning the extended arc, the third component is only firmly detected in individual pixels and for a spectral resolution degraded to 6 MHz. Given that the width of each component is comparable to the relative velocity offsets, they are blended in several pixels and can hardly be fitted independently over the entire arc. Instead of mapping each component as was done for A1 and A2, I therefore characterize its kinematics by fitting multiple gaussians to the spectra stacked within dedicated apertures. An example of such line profiles is shown in Figure 7.4, for a spectral resolution of 12 km s^{-1}. I find that the gaussian line widths are extremely narrow, from 30 km s^{-1} to about 45 km s^{-1}, implying that the arc probes lower velocity dispersions than A1 and A2. Moreover, although it is not fitted in Figure 7.4, the third component of intermediate velocity offset appears to be extended over a few resolution elements. Since it is also detected in all individual pixels with SNR > 5, I conclude that this feature is not spurious.

As a comparison, the single dish spectroscopy of the GEMS show much broader CO line profiles with gaussian widths above 100 km s^{-1}, even for the lowest-J transitions. In the literature, on the one hand, Tacconi et al. (2006) present high-resolution CO(3-2) interferometry in eight SMGs at $z \sim 2.0 - 3.4$. With the PdBI and a beam of about $1''$, they obtain broad line profiles – sometimes resolved into multiple components – which translate into gaussian line widths of $\sigma \sim 150 - 350$ km s^{-1}. Bothwell et al. (2010) observe three ULIRGs at $z \sim 2$ with higher spatial resolutions ($\sim 0.4''$) and only find velocity dispersions below 100 km s^{-1} for one component of one of their source identified as a late-stage merger. On the other hand, the models of Narayanan et al. (2009) also predict broad CO lines for SMGs formed in galaxy mergers, probably due to turbulent motions triggered by the interaction. Our strongly magnified arc at $z = 2.5987$ observed at high angular resolution with the PdBI therefore suggests that such broad CO line profiles trace diverse gas kinematics, at least in specific regions of SMGs.

Finally, I compare these results with the integrated flux of the CO(3-2) line measured with our EMIR single-dish spectroscopy, in order to determine the proportion of extended emission filtered out by the interferometric configuration of the PdBI. On the one hand, EMIR provides a total flux of 9.2 ± 0.7 Jy km s^{-1} (Nesvadba et al. 2016, in prep.) which should correspond to the entire sub-mm emission from G080.2 given that the beam FWHM of the 30-m telescope at 350 GHz is about twice the angular separation between A1, A2 and B (Tab.7.1). One the other hand, I use the integrated spectra from the PdBI data cube, obtained by stacking all the pixels of above a 3σ flux threshold in the three spatial components of the Malachite. I then fit the line profile with two components, as in Figure 7.4, and deduce a total flux of 6.3 ± 0.5 Jy km s^{-1}. This result is significantly lower than the EMIR line flux and suggests that the extended A configuration from the PdBI is missing about 30% of extended CO emission.

7.1.4 Intrinsic nature of G080.2

To summarize, the Malachite comprises a doubly imaged compact molecular region at $z = 2.5987$, resolved into three spectral components of gaussian width $\sigma = 40 - 70$ km s^{-1}. These two clumps are only marginally resolved spatially in the $0.9'' \times 0.7''$ beam of the PdBI. G080.2 also includes an

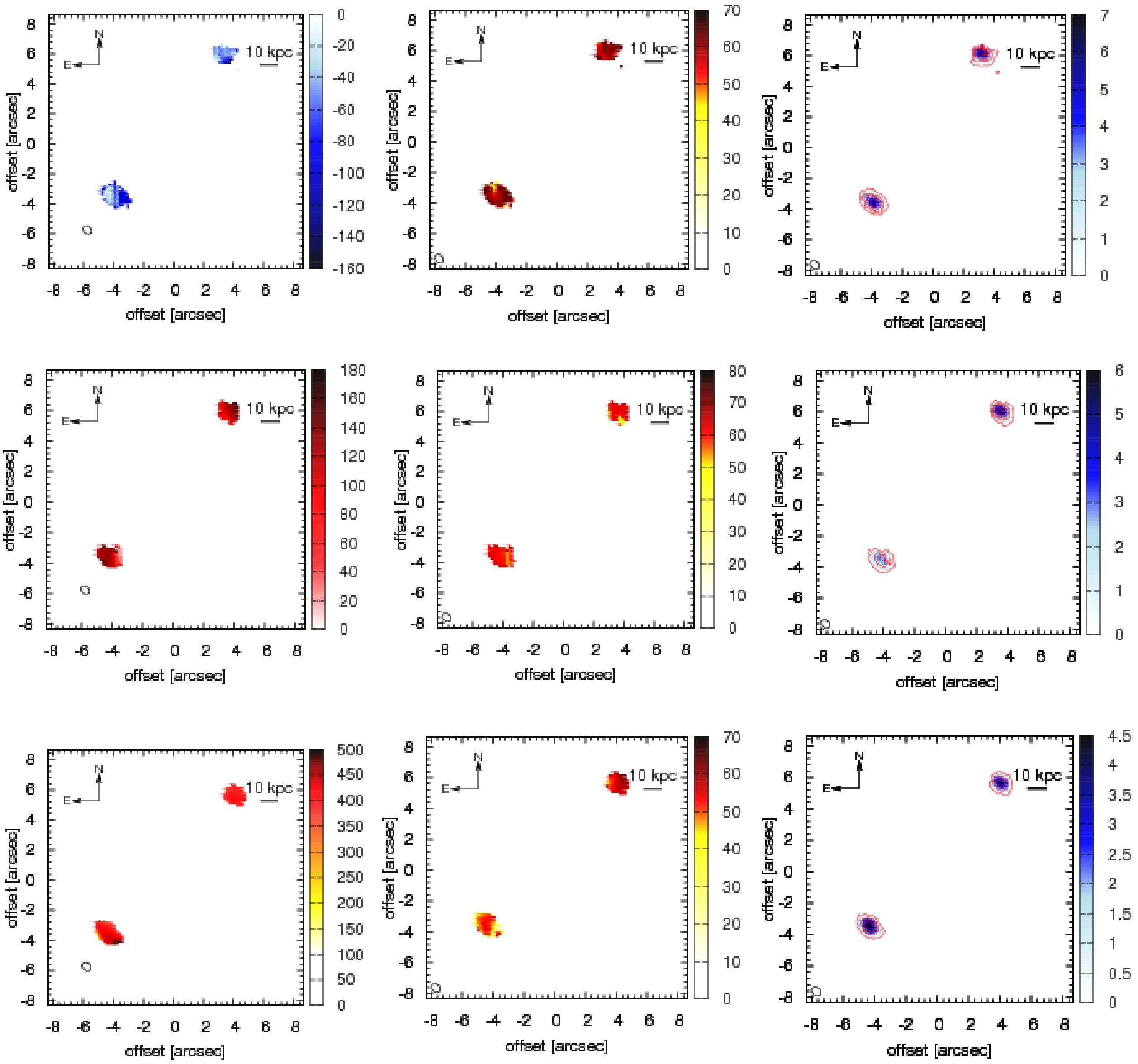

Figure 7.5: Velocity offset (left), gaussian line width σ (center) and peak flux (right) maps of the three CO(3-2) spectral components detected in A1 and A2, from the most blueshifted (top) to the most redshifted (bottom). These narrow components are also identified in the spatially integrated spectra. The velocities are expressed in km s^{-1} and the peak fluxes in mJy beam^{-1}. The reconstructed beam of the PdBI is shown as a black ellipse in the bottom-left corner of each panel. In the flux maps, red contours indicate constant line fluxes, starting at 3σ and increasing by +9σ. The scale bar in the top-right corner of each panel indicates the apparent angular size of a 10 kpc wide structure at z $\sim$ 2.6, without considering the boost in spatial resolution provided by strong gravitational amplifications.

extended arc of about 4$''$ folded back onto itself, with more quiescent kinematics. The substantial velocity offsets of up to 600 km s^{-1} detected between both sides of A1 and A2 seem to rule out that the underlying molecular gas reservoirs originate from the same galaxy. If these CO maps were tracing ordered rotational motions in an isolated disk, such offsets would imply an implausibly high dynamical mass. The kinematics of A1 and A2 may rather trace an overlap region between two interacting galaxies, as already found in other SMGs by Tacconi et al. (2006). The similar brightness of the redshifted and bluedshifted components in A1 and A2 suggests that they are magnified by similar factors, and that they lie within a few kpc of one another in the source plane. The gaussian width of these components points toward a strong interaction, probably a galaxy merger, with a line broadening most likely caused by the kinetic energy released in the process, as commonly accepted for SMGs (Swinbank et al. 2006).

The arc B shows three spectral components with relative velocity offsets below 200 km s^{-1}, in agreement with the velocity gradient observed between its center and extreme edges. This smooth gradient has an amplitude of 105 km s^{-1} which I attribute to rotation (Tacconi et al. 2010). The most interesting property of B is the very narrow gaussian width of its individual components which probe down to about 30 km s^{-1}, comparable to the line-of-sight velocity dispersions observed in the molecular clouds of the Milky Way and other nearby galaxies (Fig.9 of Heyer & Dame 2015). These values are quite unexpected in high-redshift galaxies where the larger line widths are usually associated with strong turbulence, although the underlying physical mechanisms remain poorly understood. It has been suggested that these turbulent motions in the molecular gas reservoirs could be related to the high star formation surface densities found in distant SMGs with high gas surface densities. Turbulence is probably a key process determining the star formation efficiency in these environments, if interstellar shocks convey the energy injected at large spatial scales down to the smaller scales where it can be radiated. But, in contrast, turbulence also produces an internal pressure in molecular clouds which slows down the gravitational collapse and should reduce the star formation.

For instance, Swinbank et al. (2011) find line widths about 3-4 times higher in the Eyelash and conclude that it could favour a different mode of star formation in the distant universe. The lower velocity dispersions found in the Malachite therefore suggest that this argument does not hold, at least in specific regions of SMGs where star formation would rather be similar to nearby galaxies. I use the plot of Swinbank et al. (2011) reproduced in Figure 7.6 to confirm that these gaussian widths indeed probe intrinsically small, highly magnified regions in the arc. The plot shows the scaling relation between the velocity dispersion, σ, and the intrinsic radius, R, of several molecular clouds by comparing the star-forming regions in the Eyelash to their counterparts in the local universe. A relation for the nearby universe is derived from Galactic Giant Molecular Clouds (GMCs, Larson 1981) and parametrized as $\sigma \propto \mathrm{R}^{\mathrm{p}}$, with $\mathrm{p} \sim 1/2$. The GMCs resolved in the Eyelash or near the Galactic center are significantly offset due to strong turbulence. Comparing the most narrow spectral components in the CO(3-2) data cube ($\sim$ 25 km s^{-1}) with this relation suggests that the PdBI resolves molecular regions of order 100 pc in the Malachite.

It is far less evident to determine how A and B are related. One possibility would be that the arc corresponds to a second star-forming region within one of the two interacting galaxies seen in images A1 and A2, but B may also originate from a third galaxy. In this case, given their common spectroscopic redshift, the three separate components would be within the same potential well. The source plane reconstruction with LENSTOOL presented in §6.3.2 indeed results in intrinsic angular separations below $1.2''$, in 90 out of 100 MCMC realizations. This corresponds to a projected distance of about 10 kpc in the source plane at $z \sim 2.6$, roughly the dimension of a single galaxy dark matter halo.

Strong gravitational lensing conserves the surface brightness of the CO(3-2) emission making its properties independent of the detailed model. In these circumstances, it is interesting to note that most of the CO emission in the arc is fairly diffuse and regular, with the exception of an unresolved knot of high surface brightness. This distribution is quite different to the morphology of the Eyelash, where the 870 μm dust continuum in the arc is dominated by a linear chain of bright knots (Swinbank et al. 2010). However, these results were obtained with a smaller beam of $0.33'' \times 0.21''$ and higher sensitivity. Thus, we might also detect such star-forming clumps in the Malachite with observations at higher spatial resolution and lower rms noise level, for instance with ALMA. Moreover, we also note that the arc has a lower surface brightness than A1 and A2. This suggests either that the gas mass surface densities are somewhat lower in B than in A, or that the gas excitation mechanisms are different

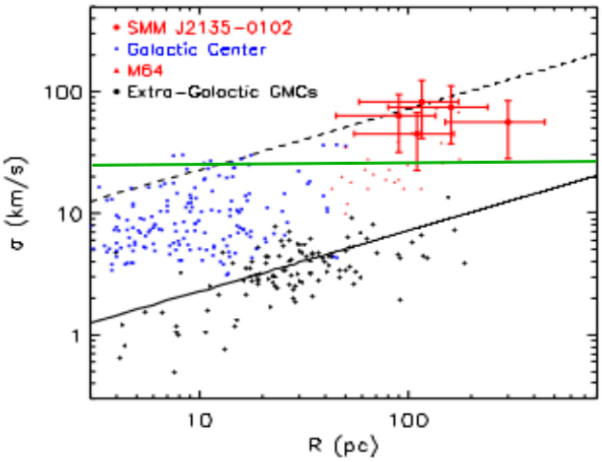

Figure 7.6: Plot from Swinbank et al. (2011) showing the scaling relation between the velocity dispersion and intrinsic radius of several molecular clouds. The star-forming regions in the Eyelash are compared to their counterparts in the local universe. A local relation (black line) is derived from extra-galactic GMCs (Larson 1981). The GMCs resolved in he Eyelash or near the Galactic center are significantly offset due to strong turbulence. If we consider that the most narrow components in the CO(3-2) data cube (~ 25 km s^{-1}) trace quiescent environments, the intrinsic spatial scales resolved in G080.2 should stand around 100 pc (green line).

in the two components (thereby explaining a variable CO(3-2) emission). High resolution observations of the CO(1-0) transition with the VLA should help us further elucidate the latter scenario.

It is interesting to compare the Malachite with the ALMA CO(3-2) interferometry of the overlap region of the local galaxy merger, ”The Antennae” (Herrera et al. 2012). The line profiles of GMCs in this intense starburst are very similar to the components of G080.2. In both cases we observe either double-peaked or irregular profiles with narrow components and, in the Antennae, these features are likely tracing overlapping gas clouds or filaments. Although I already mentioned that the SMA morphology of G080.2 roughly follows that of the CO emission, a detailed comparison between the gas properties and the dust continuum observations at 850 μm will allow us to further characterize the star formation mechanisms in this GEMS.

7.2 An ALMA view on the extended [CII] emission and absorption at z = 3.4

7.2.1 Using the [CII] fine structure line as gas tracer

In the interstellar medium of active galaxies, atomic fine structure lines are radiating significant amounts of energy at the lowest spatial scales and therefore play an important role in the gas cooling (Spitzer 1978). In star-forming galaxies, [CII] at 157.74-μm is the strongest of these lines and turns out to be brighter than all other molecular and atomic transitions in the FIR/(sub)-mm regime (although [OI] can dominate in a few cases). It accounts for 0.1%-1% of the bolometric FIR luminosity (Malhotra et al. 2001), as further described in 7.2.4, which makes it a dominant coolant of the interstellar gas. Since its ionization potential of 11.2 eV is slightly lower than that of HI, [CII] mainly traces the cold neutral medium ($T < 10^4$ K) where hydrogen transitions are not accessible (Bennett et al. 1994). However, it can also arise from warm ionized gas, and the relation between [CII] emission and the star formation mechanisms or the overall gas content is therefore a major subject of discussion. It is generally accepted that this line is optically thin and results from the collisional excitation of C^+

ions with neutral hydrogen atoms (or with free electrons for an ionized medium). The critical density of [CII] is only 2.8×10^3 cm^{-3} (or ~ 50 electrons cm^{-3} if the gas is significantly ionized) (Carilli & Walter 2013) and, combined with the excitation potential of 91 K, it makes this transition easily excited in a broad range of environments. In the nearby universe, it is commonly detected in star-forming regions filled with cold neutral gas, as is the case for the sample of $0.2 < z < 0.8$ ULIRGs of Rigopoulou et al. (2014). But in addition, [CII] is also associated with more diffuse environments in the Milky Way (Gerin et al. 2015).

[CII] is necesarily associated with interstellar regions with physical conditions leading to the ionization of carbon atoms. For this reason, Stacey et al. (1991) argue that about 70% of the [CII] emission in nearby spirals arise from photodissociation regions (PDRs), where the intense UV radiation from massive stars contains photons with energies above 11.3 eV. Consequently, mapping this emission line is a robust way to determine the spatial distribution of these PDRs which themselves trace the surface of molecular clouds and the interstellar radiation field. At $z \sim 1-2$, it is also dominated by PDRs, although X-ray dominated regions (XDRs), cosmic ray dominated regions (CRDRs), HII regions or diffuse HI clouds also have minor contributions (Stacey et al. 2010). [CII] emission therefore arises from very diverse environments covering about an order of magnitude in the UV radiation fields from star formation (Stacey et al. 2010), and a wide range of densities (Goldsmith et al. 2012).

During the last decade Maiolino et al. (2005) presented the first detection of [CII] at high-redshift, more precisely from the ISM surrounding the central AGN of a $z = 6.42$ quasar which was further characterized by Walter et al. (2009). Subsequent studies conducted with ground-based sub-mm interferometers have been able to detect [CII] in several galaxies between $z \sim 1$, the lowest redshift at which [CII] can be observed from the ground, and up to $z = 7.1$ (Venemans et al. 2012). These discoveries both concern lensed (e.g., Rawle et al. 2014; Schaerer et al. 2015; Gullberg et al. 2015) and unlensed sources, and complement the few detections with the Herschel Space Observatory (e.g., Rhoads et al. 2014; Gullberg et al. 2015). More recently, this transition was probed with ALMA in dozens of other high-redshift QSOs, powerful SMGs or more gradually star-forming galaxies, thanks to the combination of the broad spectral coverage and high sensitivity of this interferometer (e.g., Knudsen et al. 2016).

Since this bright fine structure line obviously probes a wide range of gas conditions, it is of prime interest to advance our understanding of its properties at high-redshift. This requires resolved observations of bright and distant star-forming galaxies such as the GEMS with the current day facility that allows the highest spatial resolutions and sensitivities, namely the Atacama Large Millimeter Array. In particular, early studies with Herschel have highlighted spatial offsets between CO and [CII] emission in the Galactic plane (e.g., Rodriguez-Fernandez et al. 2006) and ALMA observations would easily probe the relative spatial distributions of atomic and molecular gas in high-redshift sources. [CII] also presents an opportunity to measure properly their gas kinematics, as done in De Breuck et al. (2014). Finally, it can be combined with other fine structure lines to infer additional diagnostics of the physical state of interstellar gas in distant galaxies as, for example, the [CII]/[NII] ratio which provides a rough estimate of the metallicity (Nagao et al. 2012). In this section, I describe the results of our spatially-resolved ALMA observations of one GEMS which have been obtained during Cycle 2.

7.2.2 Sub-millimeter properties of G045.1

Presentation of the source

The [CII] fine structure line was detected with ALMA in G045.1, subsequently referred to as "the Garnet". According to the modified blackbody fit, G045.1 has a peak flux of 360 ± 10 mJy at 420 ± 10 μm, placing it among the faintest sources in the sample as well as G080.2. It exhibits a dust temperature $T_d = 36.0 \pm 0.5$ K, a dust mass $M_d = (6.5 \pm 0.1) \times 10^9$ μ^{-1} $M_\odot$ and a star formation rate SFR $= 14462 \pm 172$ μ^{-1} $M_\odot$ yr^{-1}, before correcting for the magnification factor μ (Chapter

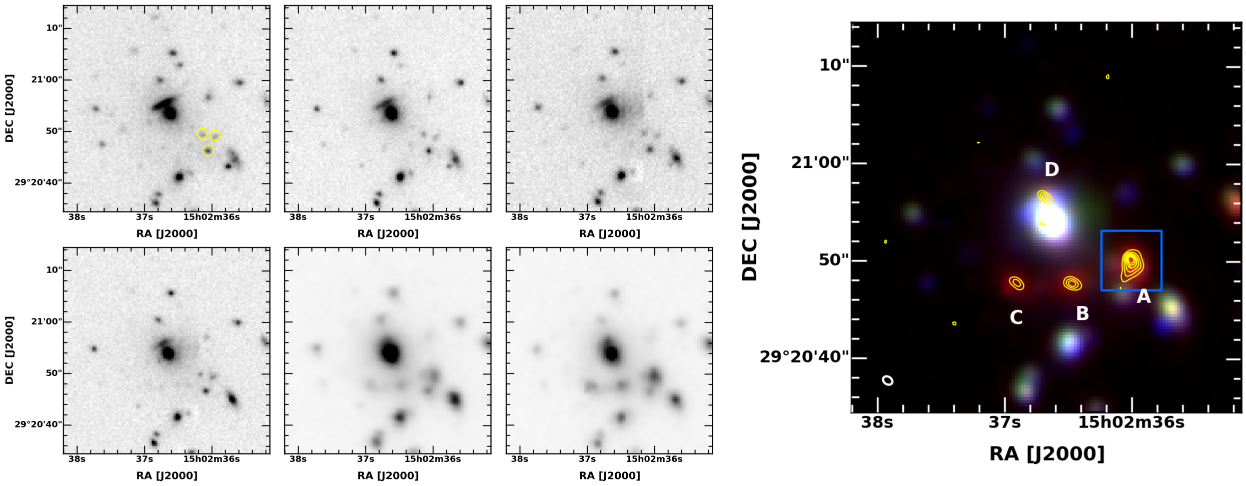

Figure 7.7: *Left :* Images of G045.1 obtained in the r, z, J and K bands with MegaCam and WIRCam at the CFHT and at 3.6 and 4.5 μm with IRAC, from top-left to bottom-right respectively. The yellow circles in the r-band image indicate three foreground galaxies particularly relevant for the lensing model. *Right :* 3-color image in the r, K and 4.5 μm bands of this zoomed region of $40'' \times 40''$ centered at the peak of the single dish (sub-)mm emission. The resolution of the two optical and NIR images have been matched to the PSF of IRAC at 4.5 μm. The yellow contours illustrate the morphology of the CO(5-4) emission, from the line peak map. The rms of this map is 0.1 mJy beam^{-1} and contours start at $+3\sigma$ and increase in steps of $+3\sigma$. The beam FWHM of the PdBI in the AB configuration is also shown in the lower-left corner. The blue rectangle denotes the pointing and total field-of-view of our [CII] observations with ALMA.

4). The dust continuum of the Garnet peaks at higher wavelengths compared to the other GEMS. Consequently, the flux decrease of nearly 250 mJy between 500 and 250 μm and the WISE upper limit at 22 μm do not highlight any AGN contamination to the bolometric FIR luminosity. This source has a spectroscopic redshift $z = 3.4266 \pm 0.0005$, first derived from the CO(4-3) emission line and then confirmed with the detection of CO(5-4), both with EMIR.

The FIR/sub-mm continuum in the Garnet was also imaged with the SMA in the COM configuration (as shown in Fig.4.6), recovering about 90% of the total flux measured with JCMT/SCUBA-2. This suggests that our interferometric observations are not missing significant amounts of extended emission. These data indeed reveal four counter images of the single point source detected with Herschel/SPIRE, which are nevertheless unresolved in the synthetized beam of about $2''$. Three of them are distributed along a fictive arc in the South of a bright foreground galaxy at a spectroscopic redshift $z = 0.554$, while the fourth image is located on the other side. These components have relative angular separations between $5''$ and $10''$, suggesting that the Garnet probes a foreground lensing mass similar to the Malachite (c.f. the complete models in Chap.6). The three southern components have comparable integrated fluxes at 850 μm, with a slight increase from the eastern to the western clumps, respectively. On the contrary, the northern one is significantly fainter. In this section, we focus on the [CII] emission from the brightest counter image, which is labelled as A in Figure 7.7 and produces 46% of the total flux at 850 μm measured by the SMA.

The CO(5-4) emission from G045.1 was also observed with the PdBI in the AB configuration. At redshifted frequencies of about 130 GHz, this corresponds to a synthetized beam of about $1.03'' \times 0.78''$, with a position angle of 56.8°. The CO(5-4) peak flux contours are shown in Figure 7.7. At these higher spatial resolutions, the molecular gas emission confirms the presence of four separate clumps. In addition, it resolves an extended tail of CO(5-4) emission on the South-East of component A. The background emitter is not detected in our optical/NIR imaging, where the light peaks rather trace the foreground lensing potentials producing a gravitational deflection. Given its extremely red colour, the high-redshift sub-mm component is only detected in IRAC channels.

These four components are distributed around the massive early-type galaxy detected in our optical/NIR imaging from the CFHT, and which has a spectroscopic redshift of $z = 0.554$ measured by the SDSS. This produces a similar configuration to the Malachite, with the brightest foreground source surrounded by a group of evolved galaxies at $z \sim 0.5 - 0.6$. This overall lensing group is responsible for the light deflection toward the Garnet and multi-scale mass components were needed to reproduce the observed morphology of the dust continuum and the CO(5-4) emission. A few members visible in the zoomed region of Figure 7.7 turn out to contribute significantly to the strong lensing magnification toward G045.1. Unfortunately, three faint early-type galaxies aligned with A – and indicated with yellow circles in the r-band panel – are strongly affecting the magnification factors derived for this clump. The following results involving delensed physical quantities are therefore subject to large systematics. Follow-up spectroscopy and high-resolution imaging of these foreground galaxies are on-going with the NOT and the HST, respectively, in order to refine our lensing model and to overcome this limitation.

Spectral lines observed with EMIR

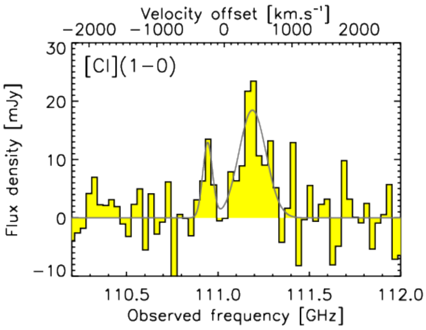

Figure 7.8: Spatially-integrated spectrum of the [CI](1-0) emission line from G045.1 obtained with EMIR on the IRAM 30-m telescope. The continuum-subtracted spectrum is fitted with a double Gaussian profile (grey line). The reference velocity is fixed to the line frequency, which is itself deduced from the CO(4-3) transition.

Our spectroscopic follow-up of the Garnet with EMIR resulted in the detection of several emission lines, including CO(4-3) and [CI]($^3P_1$-$^3P_0$)[3]. I report in Table 7.5 the observing log of the runs during which these two lines have been detected. At the observing frequencies, the beam of the 30-m telescope exceeds 20″ and encompasses the four spatial components. This means that we indeed obtain integrated fluxes for both emission lines. Their profiles and the results of single or double Gaussian fits are shown in Figure 7.8 and Table 7.6. These transitions are particularly pertinent to probe the molecular and atomic gas reservoirs in G045.1.

Firstly, CO(4-3) was used in Chapter 4 to derive $L'_{CO(1-0)}$ and then deduce a H_2 mass and a total gas mass, including the contribution of He. Its is our lowest-J CO transition and the most appropriate to probe the molecular gas reservoirs for the following reasons. Like local starbursts, distant SMGs such as the Garnet exhibit a moderate or strong excitation of their molecular gas, with a gradual flux increase from the CO transition that falls back down to the ground rotational level, to CO(4-3) or CO(5-4) (Weiß et al. 2007; Danielson et al. 2011; Bothwell et al. 2013). Since the excitation potential and critical density of the CO molecule increase with the upper rotational level, J_{up} (Carilli & Walter 2013), higher-J CO transitions trace the warmer and denser gas components. As already stated in Chapter 4, a brightness temperature ratio is therefore required to convert the luminosity of mid-J

---

[3] The [CI]($^3P_2$-$^3P_1$) line falling at 809 GHz in the rest-frame is inaccessible from the ground for the redshift of G045.1

transitions of ^{12}CO (such as CO(4-3)) to the luminosity of its lowest rotational level, $L'_{CO(1-0)}$, without missing the contribution of colder gas components. However, the excitation mechanisms of CO transitions above the peak of the SLED (typically $J_{up} > 5$) remain poorly constrained. Detailed characterization of this portion of the SLED becomes even more challenging in high-redshift SMGs and its average properties are consequently subject to large uncertainties. Deriving the molecular gas mass in G045.1 from CO(4-3) therefore enables to rely solely on a robust line luminosity ratio $r_{43/10} \sim 0.5$ (Danielson et al. 2011). Using the low CO-to-H$_2$ conversion factor of 0.8 $M_\odot/(\mathrm{K\ km\ s^{-1}\ pc^2})$, we find $M_{mol} = 5.6 \pm 0.1 \times 10^{11}\ \mu^{-1}\ M_\odot$.

Secondly, the observation of [CI](1-0) on 2 March, 2014, under good and stable conditions, confirmed the spectroscopic redshift of the Garnet. EMIR resolves two velocity components offset by about 700 km s^{-1} in this emission line. The faint component has an integrated flux about four times lower than the brighter one. It could trace a powerful gaseous in- or outflow related to the main sub-mm emitter, which would remain undetected in the molecular gas emission. Consequently, I use the peak velocity of the brighter component to compute the spectroscopic redshift. I find $z = 3.4263 \pm 0.0004$, in full agreement with the value of $z = 3.4266 \pm 0.0005$ derived from CO(4-3).

The properties of the [CI](1-0) emission line including its two spectral components result in a luminosity $L'_{[CI](1-0)} = (3.3 \pm 0.7) \times 10^{11}\ \mu^{-1}$ K km s^{-1} pc^2, without correcting for the gravitational magnification μ. This provides a $L'_{[CI](1-0)}/L'_{CO}$ ratio of about 0.45, marginally inconsistent with the value of 0.32 ± 0.13 found in a sample of high-redshift QSOs and SMGs by Walter et al. (2011). This suggests that the [CI] emission in the Garnet is slightly higher than in local star-forming galaxies (Gerin & Phillips 2000), in contradiction with previous studies based on samples of lensed or unlensed high-redshift sources. Alternatively, this result could also highlight a significant differential magnification between the atomic and molecular gas components of G045.1.

Moreover, Papadopoulos et al. (2004) argue that this line can serve as proxy for the H$_2$ mass in several environments of $z > 1$ galaxies, for which a ground-based spectroscopic follow-up is possible. In particular, this study shows that [CI](1-0) together with [CI](2-1) are reliable tracers of the diffuse gas, less sensitive to excitation mechanisms than ^{12}CO. For high-redshift metal-poor and star-forming galaxies, the ionization of large amounts of carbon atoms makes the situation more complicated. However, [CI] remains an interesting probe of the H$_2$ mass in these environments because the intense radiation field from young stars is able to dissociate a part of the CO molecules – the alternative tracer of molecular gas. The following equation presented in Wagg et al. (2006) provides the conversion of the integrated line flux, $S_{[CI]}$ expressed in Jy km s^{-1}, to M_{H_2},

$$\frac{M_{H_2}}{M_\odot} = 1375.8\ \frac{D_L^2}{1+z} \left(\frac{X_{[CI]}}{10^{-5}}\right)^{-1} \left(\frac{A_{10}}{10^{-7}\ s^{-1}}\right)^{-1} Q_{10}^{-1}\ S_{[CI]} \tag{7.1}$$

where D_L is the luminosity distance to the redshift of the source, z, and $X_{[CI]}$ is the abundance of carbon atoms with respect to H$_2$ molecules, with $X_{[CI]} = (8.4 \pm 3.5) \times 10^{-5}$ (Walter et al. 2011). A_{10} refers to the Einstein coefficient, and $Q_{10} = 0.7$ (Papadopoulos et al. 2004) is the dimensionless excitation factor. From this relationship, we find a total gas mass of $(17 \pm 4) \times 10^{11}\ \mu^{-1}\ M_\odot$. This result is a factor of about three larger than our previous estimate based on the CO(4-3) transition. This suggests that, for the Garnet, the CO-to-H$_2$ conversion factor could be higher than previously thought even though it remains inconsistent with the value found in Milky-Way environments. α_{CO} could rather lie in an intermediate regime between the starburst and Milky-Way values as found in a small number of high-redshift SMGs (for instance, the Eyelash, Danielson et al. 2011; Swinbank et al. 2011).

Line	$\nu_{\rm rest}$ [GHz]	Project ID	$\nu_{\rm tuning}$ [GHz]	Beam FWHM [arcsec]	$t_{\rm obs}$ [hr]	Binning [MHz]	3σ rms [mK]	S/T$_{\rm a}^*$ [Jy K^{-1}]
CO transition								
^{12}CO(4-3)	345.795	094-13	78.120	$\sim$ 30	1.8	25	2.82	5.5
Atomic gas line								
[CI](1-0)	492.161	223-13	111.035	$\sim$ 21.5	1.4	10	1.06	6.2

Table 7.5: Observations of the atomic and molecular emission lines in G045.1 with EMIR. I list the spectral binning applied in Fig.7.8 and the 3σ rms derived with GILDAS in line-free regions of each spectral baseline. The beam efficiencies of the 30-m telescope used to derive the conversion factors, S/T$_{\rm a}^*$, between the peak antenna temperatures and the flux densities (i.e. the point source sensitivities) were taken from the instrument commissioning of April 2015[5].

Line	$\nu_{\rm obs}$ [GHz]	Redshift	FWHM [km s^{-1}]	T$_{\rm peak}$ [mK]	Line flux [Jy km s^{-1}]	L$_{\rm line}$ [10^8 L$_\odot$]	10^{-11} L$'_{\rm line}$ [K km s^{-1}pc^2]
CO transition							
^{12}CO(4-3)	78.118 ± 0.011	3.4266 ± 0.0005	213 ± 11	7.64	22.9 ± 0.3	17.2 ± 0.2	13.0 ± 0.2
[CI](1-0) line							
Comp. 1	111.189 ± 0.014	3.4263 ± 0.0004	447 ± 118	2.92	8.64 ± 1.60	9.2 ± 1.7	2.42 ± 0.45
Comp. 2	110.951 ± 0.011	$\oslash$	154 ± 64	2.30	2.33 ± 0.87	2.49 ± 0.93	0.66 ± 0.25

Table 7.6: Properties of the atomic and molecular lines detected in the Garnet with EMIR. The central frequency, full width at half maximum, peak temperature and flux of each line are obtained with a single gaussian fit, using the routines from the GILDAS package. The values are not corrected for gravitational magnification and line luminosities are expressed either in K km s^{-1} pc^2 or in solar luminosities.

7.2.3 Extended [CII] emission and absorption

Detailed analysis of the ALMA data cube

We use our ALMA data cube covering the redshifted frequency of [CII] with a bandwidth of about 1300 km s^{-1}, and three other spectral windows in band 8, to probe the spectral line and continuum emissions in the Garnet. The continuum is measured in the baselines of two line-free spectral windows. For each individual pixel, we fit a first degree polynomial to these baselines and subtract the resulting flux density from each spectral channel, including at the redshifted frequency of [CII]. During this process, we also correct for the evolution of the continuum level between each spectral window. To this end, we simply use the dust temperature of 36.0 K obtained from the point-source photometry of G045.1, and find a maximum difference in the continuum flux density of only 2%. The continuum-subtracted data cube then allows us to extract the channel maps of the [CII] emission in component A (identified in Fig.7.7). The four maps centered at -500 km s^{-1}, 0 km s^{-1}, $+100$ km s^{-1} and $+350$ km s^{-1} with respect to the systemic velocity reveal two extended emission line regions (EELRs) distributed along an axis running from the north-east to the south-west (Fig.7.9). The 3σ isophotal contours of each channel map shows that these EELRs are fully resolved, with different morphologies. The blueshifted region on the south-west measures about $2.2'' \times 2.0''$ and the redshifted one on the north-east extends on about $2.0'' \times 0.9''$. Their major axis are nearly perpendicular to each other. In addition, the continuum resolves into a bright compact clump between these two interstellar clouds and a weak diffuse emission in the south. The diffuse component shows a distorded morphology centered on the position of the western foreground galaxy marked with a yellow cross in Figure 7.7. For the clump, we find a FWHM of $0.66 \pm 0.01''$ and $0.51 \pm 0.01''$ along the major and minor axis, respectively. It is therefore

---

[5] http://www.iram.es/IRAMES/mainWiki/EmirforAstronomers?action=AttachFiledo=gettarget=new-optics-commissioning-apr2015-v0.9.4.pdf

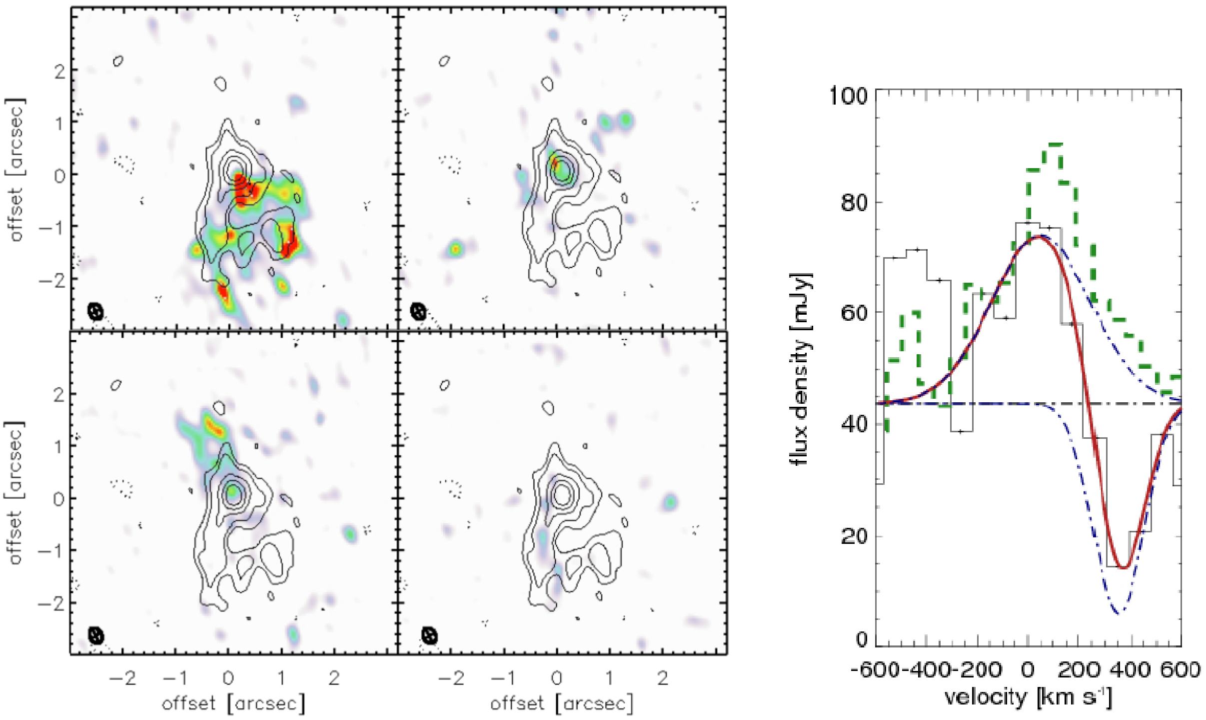

Figure 7.9: *Left :* Channel maps of the [CII] emission in the component A of the Garnet centered on -500 km s^{-1}, 0 km s^{-1}, $+100$ km s^{-1} and $+350$ km s^{-1}, from top-left to bottom-right, respectively. These velocity offsets are expressed with respect to the systemic velocity deduced from the detection of the CO(4-3) transition with EMIR. Each one of these four spectral channel is 87 km s^{-1} wide. Black contours show the continuum emission measured in line-free baseline channels from the ALMA data cube. They correspond to redshifted wavelengths of about 0.7 mm, in band 8. Apart from a negative contour at -3σ (dotted lines) they are given for 3, 5, 10, 15 and 20σ (solid lines). The reconstructed beam of ALMA is plotted in the lower-left corner of each map (plain circle). *Right :* Integrated spectrum of the emission in the center of component A measured with ALMA, for spectral channels of 87 km s^{-1} (solid black line). The spectrum is obtained by collapsing the pixels within an aperture of 1.2$''$ diameter centered on the peak of the continuum emission. We show individual gaussian fits to the absorption and emission features (blue lines), as well as the combined fit (red line). The dashed horizontal line corresponds to the ALMA band 8 continuum, extracted in the same aperture and fitted with a first degree polynomial in two other line-free spectral windows. The green dotted line shows the integrated profile of the [CI](1-0) transition detected with EMIR, for the same systemic velocity as the [CII].

marginally resolved with the beam of ALMA in the C34-3 configuration, which corresponds to about $0.41'' \times 0.27''$.

We extract the flux of this compact continuum source within an aperture of two times the beam FWHM, centered on the emission peak. We find 42.9 μ^{-1} mJy, before correcting for the gravitational magnification. This amounts to about 28% of the total FIR luminosity of G045.1, for a modified blackbody with $T_d = 36$ K and $\beta = 2.0$. In addition to the three other images identified in the lens plane (c.f. Fig.7.7), we find that the diffuse continuum emission extended toward the South also accounts for a significant proportion of L_{FIR} (about 18%).

Table 7.7 lists the observed properties of the integrated [CII] emission in each component, obtained with single gaussian fits. Given the width of ALMA spectral channels of 87 km s^{-1}, we can determine that the two EELRs are offset by about 560 km s^{-1}. The most blueshifted region has a velocity-integrated flux about six times higher than the redshifted one. Moreover, the FWHM of their integrated profile is consistent with the lower range obtained from spatially-unresolved spectroscopy of lensed SMGs from the SPT (FWHM $\sim 200-820$ km s^{-1}) (Gullberg et al. 2015). The observed morphologies of the EELRs in the image plane may be due to the strong gravitational lensing effect given that the faint foreground source lies within $1''$. However, if the shear produced by this perturbation of the overall gravitational potential is negligible at the position of the EELRs, this could also highlight intrinsic gas distributions. Regarless of the gravitational magnification, the velocity offset detected between the four maps is abrupt and larger than the FWHMs found in the integrated spectrum of each EELR. This makes it obvious that the [CII] emission does not probe ordered rotational motions. Table 7.7 also presents the integrated profiles of the [CII] emission at the position of the continuum clump which falls mostly around the systemic velocity.

Component	μ I$_{\rm [CII]}$ [Jy km s^{-1}]	Velocity [km s^{-1}]	FWHM [km s^{-1}]	μ L$'_{\rm [CII]}$ [10^{10} K km s^{-1} pc^2]	μ L$_{\rm [CII]}$ [10^9 L$_\odot$]	μ
Blue EELR	52.4 ± 0.6	-467 ± 15	202 ± 20	9.5 ± 0.7	21 ± 0.2	21
Red EELR	8.3 ± 0.6	97± 36	213 ± 50	1.5 ± 0.2	3.3 ± 0.2	22
Clump Blue	4.8 ± 0.6	-418 ± 47	190 ± 66	0.87 ± 0.1	1.9 ± 0.2	10
Clump Red	8.73 ± 0.8	0 ± 35	274 ± 49	1.5 ± 0.1	3.5 ± 0.3	10
Total	74.2 ± 1.3	—	—	13 ± 0.3	29 ± 0.5	—
Absorber	-0.60 ± 0.15	343 ± 34	124 ± 25	—	—	10

Table 7.7: Properties of the [CII] emission line measured in the integrated spectra of the blueshifted and redshifted EELRs and the continuum clump. The parameters were obtained with single gaussian fits. For the absorption line seen in the integrated spectrum of the continuum source, we present the depth τ instead of the velocity-integrated flux.

Integrated spectrum and [CII] absorption

In Figure 7.9, we also show the integrated spectrum in the center of component A, for spectral channels of 87 km s^{-1}. This spectrum is obtained by collapsing the pixels within an aperture of $1.2''$ diameter centered on the peak of the continuum emission. As already found in Table 7.7 from the analysis of the channel maps, two velocity components are detected in the [CII] emission toward the clump, one very near the systemic velocity and the other between -500 km s^{-1} and -400 km s^{-1}. This [CII] emission toward the continuum source is faint since the aperture only includes a minor portion of the EELRs (see the left panel of Fig.7.9). Moreover, we also detect an absorption line around $+350$ km s^{-1}, as previously found toward massive star-forming regions of the Milky Way (Gerin et al. 2015). To our knowledge, this type of absorption feature has so far never been detected in extragalactic environments. We measure the continuum level by extracting the flux density within the same aperture, in the two line-free spectral windows, and then fit the absorption and emission features with single gaussians. The results are presented in Table 7.7. In particular, the depth of the absorption trough reaches -0.60 ± 0.15.

Considering the results of previous studies with ALMA, this type of spectral feature should be extremely uncommon in high-redshift SMGs. Moreover, the bandwidth of about 1300 km s^{-1} available at the redshifted frequency of [CII] is only large enough to include the red tail of the absorption line, without additional baseline channels. It is therefore mandatory to check whether our detection could be spurious. First, the line covers five spectral channels of 87 km s^{-1} in the integrated spectrum and the two other spectral windows used to derive the continuum emission exhibit a flat spectrum. This makes it very unlikely that the amplitude drop is only due to a baseline instability. Secondly, it is detected for a wide range of aperture diameters that do not exceed the maximal extent of the continuum emission, and it is little sensitive on the choice of the CLEAN parameters during the reduction. Thirdly, the absorption is also seen in the dirty maps. Finally, neither the check source nor the phase calibrator show a similar drop and the field-of-view does not contain other bright emitters in these wavelength regime that could produce negative signals. In conclusion, this set of arguments strongly suggests that the [CII] absorption feature detected toward the continuum clump of G045.1 is real.

Delensed properties of the Garnet

Although some physical parameters such as the surface brightnesses and velocities are not depending on the strong lensing model, it remains crucial to constrain the gravitational magnification toward each spatial component in order to compute the physical quantities in the source plane. The strong lensing model of the Garnet computed with LENSTOOL rely on the position of the four main components in the dust continuum emission, which were initially detected with the SMA at $2''$ resolution. Assuming that components A, B, C, and D are four multiple images of the same star-forming region in the source plane, I obtain reliable magnification factors for each of them. The situation is further complicated when I derive μ at the position of the sub-components of A detected with ALMA, at sub-arcsec resolution. To do this, I rely on the output map from LENSTOOL that provides the absolute magnification factors on a regular grid, according to the best-fitting foreground mass distribution. This provides average values of μ at the position of each spectral component of ALMA data cube. I find $\mu \sim 10$ at the position of the compact continuum source, while the magnification increases to $\mu \sim 21$ and $\mu \sim 22$ toward the blueshifted and redshifted EELRs, respectively. However, we remind that these values are not accounting for the statistics of the MCMC realisations. Even if the analysis of Chapter 6 revealed that the foreground potential well is properly constrained with our parametrization of the mass profile and thanks to the distribution of the four components in the image plane, such statistics would make the regime of amplifications more robust. In addition, the [CII] emission line regions and the star-forming clump are distributed around a faint foreground galaxy which is detected in the six optical-to-infrared bands. This source was included in the model as a perturbation of the large-scale dark-matter halo, but its properties were scaled with the other members of the group. Given the very small angular separation between this single source and the background emission detected with ALMA (below $\sim 1''$), it would be necessary to further constrain its influence on the light deflection. In particular this requires to refine our lensing model by fitting its mass profile independently. Unfortunately, such detailed description needs to await the scheduled Hubble Space Telescope imaging of this galaxy at higher resolution and sensitivity (program GO-14223, PI: Frye).

For now, assuming an average magnification factor $\mu \sim 20$ toward the EELRs translates to an ALMA beam measuring about 150 pc in the source plane at $z = 3.4$. This suggests that the lensing configuration toward component A allows to resolve extremely detailed physical structures, with sizes similar to the giant molecular clouds in the Milky Way (5-200 pc, Murray 2011). In addition, $\mu \sim 10$ provides a delensed flux density of about 4.3 mJy for the star-forming clump. For a modified blackbody of temperature $T_d = 36$ K (Chap.4) and emissivity index $\beta = 2.0$, the integration between 8 μm and 1000 μm gives the intrinsic FIR luminosity of this clump in the source plane. The usual conversion of Kennicutt (1998) results in a star formation rate of about 400 $M_\odot$ yr^{-1}, nearly an order of magnitude above the values found in massive star clusters in the Milky Way and nearby galaxies ($0.1 -$ few $\times$ 10 $M_\odot$ yr^{-1}, Larsen & Richtler 2000). Finally, with the apparent size of the clump ($0.66'' \times 0.51''$), we can deduce a star formation surface density of about 220 $M_\odot$ yr^{-1} kpc^{-2}. This result falls in the same regime as maximal starbursts (Elmegreen 1999), and is also an order of magnitude greater than the star formation intensities of local star clusters (Larsen & Richtler 2000).

7.2.4 Comparison of the [CII]/FIR ratio and astrophysical implications

Deriving the [CII] to FIR luminosity ratio is of particular interest to probe the physical properties of the interstellar regions where this fine-structure line arises. At low-redshift, the resolved studies of late-type disks result in a relatively stable ratio of about 0.003 which drops significantly for very

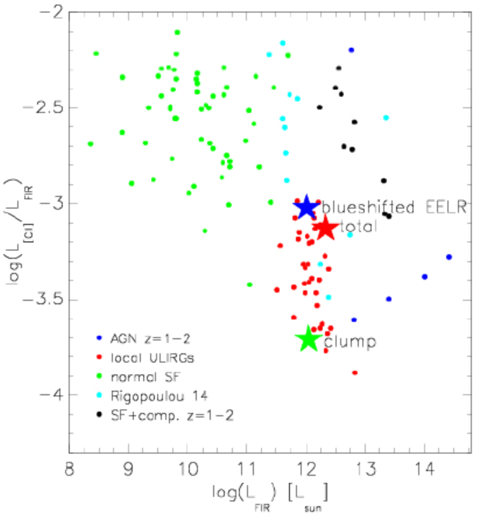

Figure 7.10: $L_{[CII]}/L_{FIR}$ versus L_{FIR} relationship for different regions in the Garnet, compared to populations of low and high-redshift galaxies in the literature. We show the position of the blue emission line region in G045.1 (blue star), as well as the continuum source (green star) and the total source (red star), after correcting for the gravitational magnification. The external samples comprise the intermediate redshift ULIRGs of Rigopoulou et al. (2014) ($0.2 < z < 0.8$) and the actively star-forming or AGN-dominated galaxies of Stacey et al. (2010) ($z \sim 1-2$).

luminous galaxies with $L_{FIR} > 10^{11}$ $L_\odot$ (e.g., Malhotra et al. 1997). Several scenarios have been considered to interpret this trend. Given their high FIR emission, these galaxies are necesarily heated by intense FUV radiation fields from the massive and newly formed stars. It has been suggested that the excitation of ionized carbon could be less efficient in these environments because of an enhanced proportion of charged grains (Farrah et al. 2013). However, these galaxies with $L_{FIR} > 10^{11}$ $L_\odot$ also contain large amounts of dust reprocessing the FUV radiation into the FIR domain. Consequently, an efficient dust shielding could reduce the photoelectric heating of hydrogen atoms and free electrons. This would result in a lower collisional excitation of carbon ions and therefore explain the [CII]-to-FIR deficit. Figure 7.10 shows this trend for samples of low-redshift ULIRGs and moderately star-forming galaxies from the literature (green and red points).

At high-redshift, the [CII]-to-FIR ratios are highly scattered and a broad consensus has not yet emerged. The deficit is not systematically observed in lensed or unlensed sub-mm bright sources (Swinbank et al. 2012; Rigopoulou et al. 2014; Gullberg et al. 2015; Schaerer et al. 2015). For instance, it is detected in the sample of $z \sim 1-2$ galaxies of Stacey et al. (2010) where it appears to be particularly prominent for the sources with bolometric FIR luminosities dominated by an AGN. Given the very broad range of results found in the literature, it becomes particularly interesting to probe the spatially-resolved properties of [CII] emission in distant galaxies such as the Garnet. Figure 7.10 shows the position of G045.1 in the $L_{[CII]}/L_{FIR}$ versus L_{FIR} diagram, together with the low-redshift samples and populations of AGN or star formation dominated sources at $z \sim 1-2$. The galaxies at $z > 1$ are offset in this plot due to their extreme FIR luminosities, systematically above 10^{12} $L_\odot$. Instead, the intermediate redshift sample of Rigopoulou et al. (2014) links the two populations and covers the full range of [CII]-to-FIR ratios. We disentangle the different spatial components probed by the ALMA observations of clump A and correct their apparent luminosities by the above magnification factors. We also remind that the absorption feature is not affecting our continuum FIR luminosities since the latter are deduced from the SED integrated between 8 and 1000 μm in the rest-frame. Firstly, we find $L_{[CII]}/L_{FIR} \sim 10^{-3}$ for the blue emission line region which thereby falls right between the samples of nearby star-forming galaxies and ULIRGs. Secondly, the continuum clump exhibits a strong [CII]-to-FIR deficit comparable to the lowest ratios found in local ULIRGs and in one of the AGN-dominated sources of Stacey et al. (2010). Finally, the overall emission of the Garnet falls very close to the emission line region. This suggests that the [CII]-to-FIR ratios measured in unresolved galaxies are dominated by the properties of star-forming gas clouds and PDRs where the [CII] emission arises, rather than the sites of continuum emission.

The resolved observations of internal regions within our high-redshift strongly lensed source thus demonstrates the variety of intrinsic [CII]-to-FIR ratios. The position of the continuum clump in Figure 7.10 is in line with the deficit particularly pronounced for compact regions in local LIRGs with $L_{FIR} > 10^{11}$ $L_{\odot}$ (in comparison with more extended regions, Díaz-Santos et al. 2014). At also agrees with the ratios found in some high-redshift samples, such as the lensed sources from the SPT survey (Gullberg et al. 2015), where it could result from the [CII] emission becoming optically thick in regions with very dense dust material (Gullberg et al. 2015). It is worth mentioning that local galaxies reveal that the [CII] to FIR luminosity ratio is increasing for a decreasing metallicity (see, e.g., the study of the Magellanic Clouds in Israel & Maloney 2011). With less metals, the dust content and its opacity are necesarily lower which implies that FUV photons can enter more deeply in the star-forming clouds. For a given FIR luminosity, the gas heating therefore becomes more efficient with a lower metallicity, thereby increasing the [CII] luminosity. Conversely, even though the [CII]-to-FIR ratio of the most distant sources detected in [CII] is highly dispersed, it suggests a decrease in metallicity at $z > 5$. This trend suggests that the ISM in G045.1 is quite enriched by recent bursts of star formation, at least in the continuum component.

7.2.5 Astrophysical nature of [CII] in G045.1

Kaufman et al. (1999) present a grid of PDR models for various ISM conditions and environments. They also predict the values of the most common line luminosity ratios for different combinations of interstellar radiation fields and gas densities. We use these models together with the spatially-integrated luminosities of the [CII], [CI](1-0) and CO(4-3) transitions (c.f. Chap.4) to derive the average gas properties in component A of the Garnet. Since the luminosities of the two lines detected with EMIR on the 30-m telescope also include the contribution of components B, C and D, we apply a correction factor of 0.46 – as suggested by the flux ratios measured with the SMA – to focus on clump A. This correction assumes that the emission of each transition is co-spatial with the dust continuum at 850 μm. We obtain $L_{CII}/L_{CI} = 72.5 \pm 13$ and $L_{CII}/L_{CO} = 23 \pm 1$. These ratios suggest that the gas material in G045.1 is on average exposed to a radiation field 200 times greater than in the solar neighbourhood, in good agreement with the high star formation surface density found in the continuum source. We also find a gas density of about 10^4 cm^{-3}.

The other spectral component of [CII] consists of a strong absorption feature, which proves to be unique with respect to previous high-redshift studies. Generally, [CII] absorption serves as a tracer of the diffuse interstellar medium in the Milky Way (e.g. Gerin et al. 2015). It is detected toward bright continuum sources (i.e. star-forming regions) and allows to probe the physical conditions of the ambient diffuse gas. Our detection in the Garnet opens a new window to study this gas component in very distant galaxies that benefit from an additional boost from strong gravitational lensing.

It is mandatory to constrain the spatial configuration that gives rise to such absorption feature. Our integrated spectrum shows that the [CII] emission and absorption extends over at least 1200 km s^{-1} in the velocity space, and within a small region of $\lesssim 1$ kpc in the source plane (for $\mu \geq 10$). The absorption line appears to be significantly redshifted with respect to the systemic velocity. This proves that the reservoir of absorbing gas is located between the observer and the continuum source, and falls toward the starbursting clump. In principle, the intense radiation field from the clump can easily produce multiple ionizations of the surrounding carbon atoms. Our detection of the [CII] absorption line from singly ionized carbon therefore guarantees that the absorbing gas is efficiently shielded, and most probably located several kpc away from the clump. For this reason, the Garnet provides a rare opportunity to study the gas in a high-redshift galaxy, outside of intense star-forming regions. Furthermore, the FWHM of the absorption line is large (120 km s^{-1}) and could result from the combination of multiple narrow components tracing, for instance, multiple clouds in an infalling cosmic filament. This scenario is indeed observed in our Galaxy where [CII] absorption lines reach FWMHs of $70 - 80$ km s^{-1} despite the lower velocity dispersions measured in the ISM (about 10 km s^{-1} in average).

According to Gerin et al. (2015), [CII] absorption and [CI] emission can arise from gas with similar physical conditions, at least in the Milky Way. By analogy, we assume that both features are associated to the same emitting regions in the Garnet and we derive the total mass of absorbing gas through the profile of the [CI](1-0) emission line. Figure 7.9 shows that the red wing of [CI](1-0) covers the same velocity offset as the [CII] absorption. We first determine the proportion of the integrated flux of [CI](1-0) located in this wing, and subtract the contribution of components B, C and D. The equation of Papadopoulos et al. (2004) then provides a conversion into a gas mass. Assuming the a magnification factor $\mu \sim 10$, this results in a delensed molecular gas mass of 3.2×10^{10} $M_{\odot}$, comparable to the overall reservoirs in high-redshift starbursts (Tacconi et al. 2008).

There is considerable evidence that the [CII] emission line is an efficient tracer of the gas kinematics in the ISM of the most distant galaxies (Casey et al. 2014). This bright transition has a great potential to replace the search for low-J CO lines which is sometimes challenging, either because of the lack of observing facility covering their redshifted frequency or due to their intrinsic faintness in low-metallicity galaxies. Moreover, several studies have demonstrated the outstanding contribution of ALMA to characterize the [CII] emission in a wide range of high-redshift environments (e.g., Carniani et al. 2013).

As stated below, the [CII] emission in the Garnet probes two interstellar clouds which are obviously unrelated in the velocity space given the strong offset of about 560 km s^{-1} measured in the channel maps. These EELRs are blueshifted and redshifted on the opposite sides of a bright star-forming clump detected in the continuum. It is therefore natural to wonder whether the [CII] emission could trace powerful winds induced by the central starburst. This hypothesis can be tested with the approach followed by Heckman et al. (2015), to analyse galactic winds driven by star formation in local galaxies. This study recommends to use a critical quantity, R_{crit}, that depends on the column density, N_C, and the circular velocity, v_{circ}, to determine the type of outflow induced by the total momentum from a given starburst. More precisely, R_{crit} allows to measure the momentum threshold above which the powerful star formation can produce an outflow escaping the gravitational potential of the host galaxy. For G045.1, the average velocity of the absorbing gas can be used as a proxy of the circular velocity. This allows us to derive a star formation momentum associated with the star formation surface density measured in the continuum clump of component A (more details are given in Nesvadba et al. 2016). According to the criterion of Heckman et al. (2015) the resulting value should, in principle, produce a galactic wind above the escape velocity. However, we remind that the high gas surface densities in high-redshift SMGs such as the Garnet result in higher column densities than the low-redshift sample of Heckman et al. (2015). Consequently, higher thermal pressures are expected in the ISM of G045.1. The presence of a large-scale wind regulating the star formation in the continuum clump therefore becomes very unlikely. We rather favour the scenario where the EELRs are associated with different clouds, either in the same star-forming region as the continuum source or in separate ones overlapping along the line-of-sight. However, the relative position of the two components in the source plane remains poorly constrained by the lensing model and, alternatively, the EELRs could arise from a merger. Finally, our results do not rule out the presence of weaker gas outflows as found, for instance, in Maiolino et al. (2012).

7.2.6 Related personal publication

A&A 593, L2 (2016)
DOI: 10.1051/0004-6361/201629037
© ESO 2016

Astronomy & Astrophysics

LETTER TO THE EDITOR

Planck's Dusty GEMS

II. Extended [CII] emission and absorption in the Garnet at $z = 3.4$ seen with ALMA[⋆]

N. Nesvadba[1,2,3,4], R. Kneissl[5,6], R. Cañameras[1,2,3,4], F. Boone[7], E. Falgarone[8], B. Frye[9], M. Gerin[8], S. Koenig[10], G. Lagache[11], E. Le Floc'h[12], S. Malhotra[13], and D. Scott[14]

(Affiliations can be found after the references)

Received 1 June 2016 / Accepted 20 July 2016

ABSTRACT

We present spatially resolved ALMA [CII] observations of the bright (flux density S_{350} = 400 mJy at 350 μm), gravitationally lensed, starburst galaxy PLCK G045.1+61.1 at z = 3.427, the "Garnet". This source is part of our set of "*Planck*'s Dusty GEMS", discovered with the *Planck's* all-sky survey. Two emission-line clouds with a relative velocity offset of ~600 km s^{-1} extend towards north-east and south-west, respectively, of a small, intensely star-forming clump with a star-formation intensity of 220 $M_\odot$ yr^{-1} kpc^{-2}, akin to maximal starbursts. [CII] is also seen in absorption, with a redshift of +350 km s^{-1} relative to the brightest CO component. [CII] absorption has previously only been found in the Milky Way along sightlines toward bright high-mass star-forming regions, and this is the first detection in another galaxy. Similar to Galactic environments, the [CII] absorption feature is associated with [CI] emission, implying that this is diffuse gas shielded from the UV radiation of the clump, and likely at large distances from the clump. Since absorption can only be seen in front of a continuum source, the gas in this structure can definitely be attributed to gas flowing towards the clump. The absorber could be part of a cosmic filament or merger debris being accreted onto the galaxy. We discuss our results also in light of the on-going debate of the origin of the [CII] deficit in dusty star-forming galaxies.

Key words. galaxies: high-redshift – Galaxy: formation – galaxies: ISM – galaxies: starburst – galaxies: kinematics and dynamics – infrared: galaxies

1. Introduction

The bright 158 μm line of singly ionized carbon, [CII]158, is one of the most versatile tracers of the interstellar gas in star-forming galaxies. With a low ionization potential, C$^+$ is a probe of the cold neutral gas in galaxies, and can be associated with intensely star-forming environments (e.g., Stacey et al. 2010; Rigopoulou et al. 2014) and diffuse gas (e.g. Langer et al. 2010; Gerin et al. 2015). It is the main coolant of the cold neutral medium (Bennett et al. 1994), and the most luminous line of gas heated by UV photons from star formation over wide ranges of density and UV intensity (e.g., Goldsmith et al. 2012; Le Petit et al. 2006; Kaufman et al. 1999), but can also be bright in shocked gas (Appleton et al. 2013). The diversity of environments and gas conditions probed by [CII] (Rawle et al. 2014; Boone et al. 2014; Schaerer et al. 2015; Knudsen et al. 2016) entail that many empirical properties of [CII] are not yet very well understood, especially at high redshift.

Here we present spatially resolved ALMA cycle 2 observations of [CII] in a strongly gravitationally lensed dusty starburst galaxy at z = 3.427, G045.1+61.1 ("the Garnet"), which was discovered using th *Planck* all-sky survey, and was subsequently confirmed with SPIRE imaging (Planck Collaboration Int. XXVII 2015), and through ground-based observations (Cañameras et al. 2015, C15 hereafter). The Garnet consists of four counter-images seen behind a small group of galaxies at a spectroscopic redshift of z = 0.56 (C15), which together reach a peak flux density of 400 mJy at 350 μm as seen with SPIRE. The spectral energy distribution (SED) of the dust is consistent with star formation, without obvious signs of AGN contamination (C15). Here we focus on the brightest of the four counter-images, which contributes 46% of the total flux at 850 μm seen with the SMA (C15). The SMA recovers over 90% of the total flux measured with SCUBA-2 at the same wavelength. Our ALMA data resolve the [CII] emission into two clouds at different velocities, around an intensely star-forming clump, against which [CII] is seen in absorption. To our knowledge, no such absorption line has previously been found outside the Milky Way, where it is seen against massive star-forming clouds and is a tracer of the diffuse interstellar medium (ISM, Gerin et al. 2015). Throughout the paper we adopt a flat H$_0$ = 70 km s^{-1} Mpc^{-1} concordance cosmology with $\Omega_{\rm M}$ = 0.3 and Ω_Λ = 0.7.

2. Observations and data reduction

ALMA observed our Cycle 2 project with 37 antennae on 6 June, 2015 and obtained 27 min of band 8 data in the C34-3 configuration, tuned to the [CII] line (428.775 GHz sky frequency) in one spectral window. Three more windows were placed on the line-free continuum. The intrinsic channel width was 15.6 MHz in all spectral windows, yielding a total bandwidth of 1.856 GHz per window after flagging the edge channels. This corresponds to about 1300 km s^{-1} at z = 3.4, sufficient to cover all [CII] emission, assuming a line profile similar to CO(4−3), which we used as reference. One spectral window had four times higher noise levels on average, which is due to the nearby telluric oxygen line at 424.8 GHz and was ultimately not used in the analysis.

[⋆] Based on data obtained with ALMA in program 2013.1.01230.S, and with EMIR on the IRAM 30 m telescope in program 223-13.

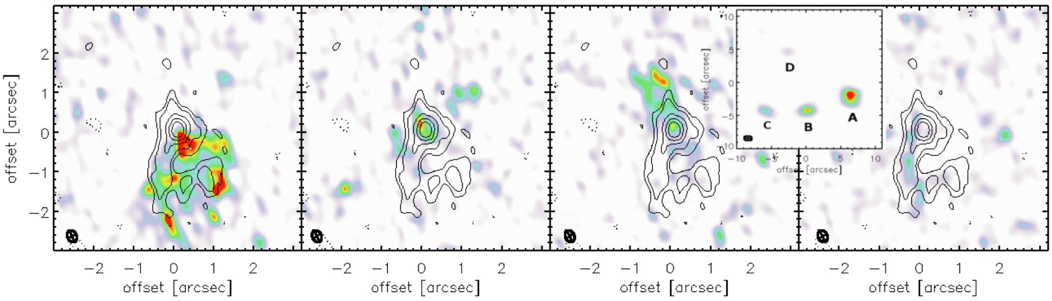

Fig. 1. *Left to right*: [CII] channel maps centered on −500 km s^{-1}, systemic velocity, +100 km s^{-1}, and +350 km s^{-1}, respectively, all relative to $z = 3.427$ and with a channel width of 87 km s^{-1}. Contours show the continuum in the line-free spectral windows and are given for 3, 5, 10, 15, and 20σ. Negative contours are −3σ. The *inset* shows the SMA 850 μm image with all counter images; the gray circle is the primary beam of ALMA. The *other panels* show image A. The ALMA beam size in the lower left corner of each map corresponds to 150 pc at $z = 3.4$ (for $\mu = 20$).

Table 1. Emission-line properties for the redshifted and blueshifted EELRs and the two line components seen against the clump.

Component	$\mu\, I_{\rm CII}$ [Jy km s^{-1}]	Velocity [km s^{-1}]	*FWHM* [km s^{-1}]	$\mu\, L'_{\rm CII}$ [10^{10} K km s^{-1} pc^2]	$\mu L_{\rm CII}$ [$10^9\, L_\odot$]	μ
Blue EELR	52.4 ± 0.6	–467 ± 15	202 ± 20	9.5 ± 0.7	21 ± 0.2	21
Red EELR	8.3 ± 0.6	97 ± 36	213 ± 50	1.5 ± 0.2	3.3 ± 0.2	22
Clump	4.8 ± 0.6	–418 ± 47	190 ± 66	0.87 ± 0.1	1.9 ± 0.2	10
	8.73 ± 0.8	0 ± 35	274 ± 49	1.5 ± 0.1	3.5 ± 0.3	10
Absorber	–0.60 ± 0.15	343 ± 34	124 ± 25	···	···	10

Notes. For the absorption line, we list the depth τ of the flux-normalized spectrum instead of the flux.

We used the standard manual scripts for ALMA reduction with the Common Astronomy Software Application `CASA`, and `CLEAN` to construct the synthesized beam-deconvolved images of the frequency data cubes. The spectral channels were rebinned to a width of 50 km s^{-1}. The major and minor axis size of the beam is 0.41″ × 0.27″ along PA = 13.5°, The largest angular scale is 3.9″, and the primary beam size 12″. The rms is 1.3 mJy in each 50 km s^{-1} channel, and 0.46 μJy in the averaged continuum image extracted from spectral windows 1 and 2.

In addition, we also used the CO(4−3) line from C15 and the [CI] line corresponding to the $^3P_1$–$^3P_0$ transition of atomic carbon at 492.16 GHz in the rest frame, which we observed during the same campaign with EMIR on the IRAM 30 m telescope with a 20″ beam. Our [CI] detection also confirmed the redshift of the Garnet. At $z = 3.4266 \pm 0.0005$, the line falls at (111.183 ± 0.015) GHz. Observations were carried out on 2 March, 2014, under good and stable conditions, for a total observing time of 81 min. Observations and the data reduction are described in C15. The integrated apparent line flux of [CI](1−0) is (8.6 ± 1.6) Jy km s^{-1}, with a peak brightness temperature of 3.3 mK, and *FWHM* = (420 ± 120) km s^{-1}. The integrated [CI] luminosity is $\mu L' = (3.3 \pm 0.7) \times 10^{11}$ K km s^{-1} pc^2, and we estimate a gas mass of $(17.4 \pm 4) \times 10^{11} \mu^{-1}\ M_\odot$, a factor of 2 higher than previously estimated in C15 from CO(4−3), and broadly confirming our previous choice of a low CO-to-H$_2$ conversion factor in C15. All values are uncorrected for the gravitational magnification factor μ. The $^3P_2$–$^3P_1$ [CI](2−1) line at 809 GHz is inaccessible from the ground at $z = 3.43$. We made this estimate using the relation reported in Papadopoulos et al. (2004) and Wagg et al. (2006), $M^{\rm [CI]}({\rm H_2}) = 1375.8 \frac{D^2}{1+z} X_{\rm [CI,-5]^{-1}} A_{10,7}^{-1} Q_{10}^{-1} S_{\rm [CI]} [M_\odot]$, where D^2 is the luminosity distance at redshift z, $X_{\rm [CI,-5]} = 5$ the abundance of atomic carbon in the ISM in units of 10^{-5}, and A_{10} the Einstein coefficient in units of 10^{-7} s^{-1}. $Q_{10} = 0.7$ captures the population of the upper and lower level of the transition (Papadopoulos et al. 2004)

3. Observed morphologies and spectrum

We used the line-free continuum image from spectral windows 1 and 2 to estimate the continuum flux density in each spaxel of the [CII] cube and subtracted this value from every spectral bin. We also corrected for the (insignificant) brightening of the dust continuum by 2% between the line and continuum windows expected for an apparent dust temperature, $T_{\rm d} = 36$ K (C15).

Figure 1 shows the channel maps of the two extended emission line regions (EELRs) as seen in the image plane, which are offset by 564 km s^{-1} from each other (redshifted and blueshifted channels, respectively), and centered on a small continuum clump with high surface brightness. The integrated spectral properties of each region are listed in Table 1. Each EELR extends about ∼2″ radially from the continuum source, but the southwestern region is much wider in tangential direction, 2.2″ instead of 0.9″ measured for the northeastern region (all sizes are 3σ isophotal sizes).This might either represent differences in the intrinsic gas properties or in the gravitational magnification. In either case, the strong sudden velocity offset, which is larger than the full width at half maximum (FWHM) of the individual clouds, shows that the [CII] lines do not probe large-scale rotational motion, but are two kinematically separated clouds.

We used `Lenstool` (Kneib et al. 1996; Jullo et al. 2007) to construct a gravitational lens model from the positions of the four images seen in Fig. 2 of C15, and calculated the magnification of each image, assuming that all four are multiple images of the same region. The average magnification at the position of the bright star-forming clump is $\mu = 10$, while $\mu = 21$ and $\mu = 22$ for the blueshifted and redshifted gas, respectively. We

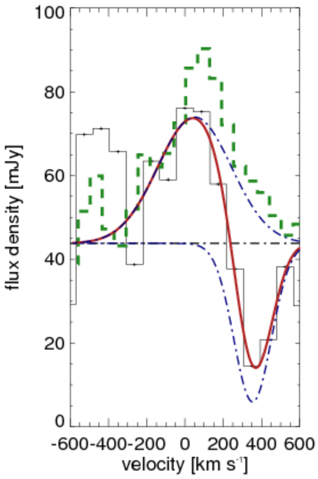

Fig. 2. Integrated spectrum in a $1.2''$ aperture centered on the bright continuum source. The spectrum is shown in black with 87 km s^{-1} channels, blue lines are individual Gaussian fits, the red line plots the combined fit. The continuum (dashed black line) was measured independently from the same aperture in the line-free continuum spectral windows. The dashed green line shows the integrated [CI] 1−0 profile.

will present a more detailed analysis of the lensing configuration when our scheduled *Hubble* Space Telescope imaging has been taken (GO-14223/PI Frye). The present analysis does not strongly depend on the details of the lens modeling, because the most important physical parameters (surface brightnesses, velocities) are not directly affected by the lensing.

The continuum clump is marginally resolved, with a FWHM size of $0.66 \pm 0.01'' \times 0.51 \pm 0.01''$ along the major and minor axis, respectively, compared to a beam size of $FWHM = 0.41 \times 0.27''$. The continuum flux density of the clump within 2× the FWHM beam size is $42.9\,\mu^{-1}$ mJy, corresponding to that expected for a modified blackbody with $\beta = 2.0$ and $T = 36$ K (C15). The clump alone contributes 28% of the total FIR luminosity of G045.1+61.1. Another 18% comes from faint, diffuse emission associated with the two emission-line regions (Fig. 1), the remaining flux comes from the other lensed images shown in the inset of Fig. 1. Adopting a conversion from $L_{\rm FIR}$, integrated between 8 μm and 1000 μm, and star formation rate, SFR, of SFR $[M_\odot\ {\rm yr}^{-1}] = 4.5\times 10^{-37}$ W (Kennicutt 1989), and the apparent size of the clump of $0.66'' \times 0.51''$, this implies an average star-formation intensity of 220 $M_\odot$ yr^{-1} kpc^{-2}, which is in the range of maximal starbursts (Elmegreen 1999).

In Fig. 1 we also show the spectrum extracted from an aperture with $1.2''$ diameter centered on the bright continuum source. As expected from the strong velocity jump in this region (also visible in the channel maps), we see both velocity components, one at +100 km s^{-1} from the systemic redshift of $z = 3.427$ measured at the [CI] peak and one at −500 km s^{-1}. Line emission is faint near the bright star-forming clump; most flux comes from the extended blueshifted and redshifted EELRs (Fig. 1 and Table 1). In addition, we also see an absorption feature around velocities of +350 km s^{-1}. The depth of the absorption trough was measured from the normalized spectrum to be -0.60 ± 0.15, and other fit parameters are listed in Table 1.

We examined whether this feature might be an observational artifact. The line is resolved into at least five spectral channels and does not depend on the specific choice of aperture size or *CLEAN* parameters used in the reduction. It is also apparent in the dirty maps. We do not detect any strongly negative regions in the maps, and our field does not contain bright sources that could cause strong negative signals. The spectra in the continuum spectral windows are flat, and neither the check source nor the phase calibrator show a corresponding amplitude drop. We therefore conclude that there is no evidence that the absorption-line feature in G045.1+61.1 is spurious.

4. Astrophysical nature of [CII] in the Garnet

Our ALMA data show a rich environment with two kinematically offset emission-line clouds around a bright star-forming clump, and another component is seen in absorption. For a magnification factor of $\mu \sim 10$, the FIR luminosity of the clump implies ~400 $M_\odot$ yr^{-1} of star formation, an order of magnitude greater than in massive star clusters in the Milky Way and nearby galaxies (0.1 – few × 10 $M_\odot$ yr^{-1}, Larsen & Richtler 2000).

We used the PDR models of Kaufman et al. (1999) to derive the average gas properties from the [CII] luminosities obtained with ALMA, the CO(4−3) luminosity of C15, and the [CI] 1−0 luminosity (Sect. 2). From the ratios $L_{\rm CII}/L_{\rm CI} = 72.5 \pm 13$ and $L_{\rm CII}/L_{\rm CO} = 23 \pm 1$, we estimate that the gas in the Garnet is on average exposed to a radiation field 200 times greater than in the solar neighborhood, and has a density of about 10^4 cm^{-3}. To derive these line ratios, we corrected the [CI] 1−0 and CO(4−3) luminosities by a factor of 0.46 to take into account that the fainter images are also in the beam, and we assumed that the gas probed by the CO line emission is optically thick.

[CII] emission extends over at least 1200 km s^{-1} in the Garnet, over a small area of $\lesssim$1 kpc in the source plane (assuming $\mu \geq 10$ as suggested by our preliminary lensing analysis, see Sect. 3). It is therefore interesting that the Garnet has only redshifted, and no blueshifted [CII] absorption. Unlike EELRs, where blue- and redshifts may either indicate outflows or inflows from the host galaxy (because the gas may be in front of the galaxy or behind it), redshifted absorption is always found in front of the emitter, and therefore a unique signature of an inflow, not an outflow. The [CI] emission line shows a distinct wing at the same velocity as the [CII] absorption. This is also characteristic of [CII] absorption in the Milky Way. Gerin et al. (2015) have shown that both lines can simultaneously arise from gas with similar conditions. By analogy with the Milky Way, we also assume that the line we see consists of multiple deep narrower absorption components that sample a velocity range of 120 km s^{-1}. This might be the intrinsic velocity range of multiple clouds in a filament or merger debris. Even in the Milky Way, where average velocity dispersions in the ISM are about 10 km s^{-1}, the total width over which absorption is found is known to be up to 70−80 km s^{-1}.

We followed Gerin et al. (2015) to estimate a column density of the absorbing gas. With their Eq. (1) originally taken from Goldsmith et al. (2012) to derive a C$^+$ column density, $N({\rm C}^+) = 1.4 \times 10^{17} \int \tau {\rm d}v [{\rm cm}^{-2}]$, we find $N({\rm C}^+) = 8.2 \times 10^{18}$ cm^{-2}, corresponding to $N({\rm HI}) = 5.9 \times 10^{22}$ cm^{-2} when adopting the Galactic carbon abundance of 1.4×10^{-4}. This choice is reasonable for massive dusty starburst galaxies at high redshift, which have gas-phase metallicities comparable to those in the Milky Way (Takata et al. 2006; Nesvadba et al. 2007), but might be too high for infall of more pristine gas. For solar metallicity, this column density is about a factor of 2 higher than the most extreme values found in the Milky Way, and is accordingly more suitable for lower metallicity gas. The implied total column density of neutral gas is comparable to those estimated for H_2 from the CO emission-line surface brightness (Swinbank et al. 2011; Cañameras et al., in prep.) and also plausible here, given our gas mass estimate from [CI].

It is impossible to estimate a total mass from an absorption line, therefore we constrained the total mass within this region from the flux in the red wing of [CI], that coincides in velocity with the [CII] absorption (Fig. 1). The wing contains 26% of the [CI] 1−0 flux, and 3.2 × 10^{10} $M_\odot$ in mass (for $\mu \sim 10$), comparable to the total molecular gas content of high-z starbursts (e.g., Tacconi et al. 2008). Carbon is easily ionized (e.g., Goldsmith et al. 2012), and the absorber must therefore be effectively shielded from the intense UV radiation of the clump, and cannot be associated with intense star formation. The absorber is most likely located at a large distance from the clump, potentially several kpc. A velocity offset of 350 km s^{-1} is also too large for the gas to be associated with the clump itself, and is comparable to velocity dispersions of massive low-redshift galaxies (Bernardi et al. 2005), suggesting the gas is bound to the host galaxy. The Garnet provides a rare opportunity to study gas in a high-redshift galaxy outside of intense star-forming regions, and possibly even infalling gas from a cosmic filament, merger debris or satellite accretion.

The blue- and redshifted EELRs extend from a massive star-forming clump, which could be probing a wind. We used the recent empirical analysis of Heckman et al. (2015) of momentum-driven winds in intensely star-forming low-redshift galaxies to show that this scenario is unlikely, and alternative explanations, such as overlapping gas clouds in a star-forming region or merger, are more realistic. Heckman et al. (2015) argued that winds will escape if the momentum input from star formation is ≥10× a critical value that depends on the column density, N_C, and circular velocity, υ_c, of the galaxy. We used the 400 km s^{-1} velocity of the absorbing gas to approximate the circular velocity of the Garnet at large distances.

Using Eq. (3) of Heckman et al. (2015), we found $p_{\rm crit} = 2 \times 10^{36}$ dyn, for a fiducial cloud distance of 100 pc from the starburst. The critical momentum increases linearly with increasing distance. We also adopted $N_C = 1 \times 10^{23}$ $\rm cm^{-2}$, $\upsilon_c = 400$ km s^{-1}, and used the mass per H_2 molecule, that is 3.24 × 10^{-24} g. N_C is set by the gas mass surface density estimates of 0.4 and 3.9 × 10^9 $M_\odot$ $\rm kpc^{-2}$ implied by the [CI] line profile, assuming that [CI] and [CII] have the same morphology. Assuming (again following Heckman et al. 2015) that the combined momentum flux from ram and radiation pressure in the star-forming clump is 4.8 × 10^{33} SFR dyn, we find a total momentum input from star formation of 1.9 × 10^{36} dyn for $SFR = 400$ $M_\odot$ $\rm yr^{-1}$. Following Heckman et al. (2015), this may be enough to balance gravity, but not to form a wind that escapes, the main difference to low-redshift galaxies being the high column densities. Of course, this does not rule out the presence of fainter more energetic wind components, as reported for unlensed galaxies (Maiolino et al. 2012; Cicone et al. 2015).

5. Implications for high-z galaxies and conclusions

It is also interesting to investigate how our sources relate to dusty star-forming galaxies at high redshifts in the field, where we have more comprehensive knowledge of the global properties, but lack the detailed spatially resolved information that only strong lensing can provide. Infrared-selected, intensely star-forming galaxies at low redshift show a marked deficit in [CII] luminosity relative to the total FIR luminosity, compared to galaxies with lower star formation rates and less extinction; this is a trend that is rarely found at high redshift (Rigopoulou et al. 2014; Malhotra et al. 2016). We show in Fig. 3 where the Garnet lies relative to other populations of low- and high-redshift galaxies. The absorption does not lower the continuum luminosity, which is derived from the integrated flux between 8 and 1000 μm in the rest-frame. The blue EELR falls into the region of the diagram, in which distant and nearby star-forming galaxies, and local ULIRGs overlap, whereas the aperture centered on the clump lies near the extreme end of the local ULIRG sample. This highlights the fact that unresolved observations of high-redshift galaxies sample wide ranges of intrinsic line ratios. The integrated spectrum of the Garnet lies very close to the blue EELR, suggesting that the global [CII]/FIR ratios are dominated by the global spatial distribution and sizes of gas clouds within star-forming regions, and do not reflect the properties of individual star clusters.

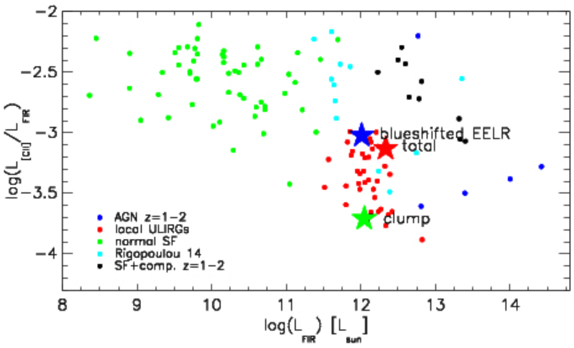

Fig. 3. Ratio of [CII] to FIR luminosity as a function of FIR luminosity for the Garnet and for several samples of low and high-redshift galaxies in the literature. The FIR luminosities have been corrected for average magnification factors of 10, 21, and 21 at the position of the total source, and the blueshifted gas and the continuum source, respectively.

These ALMA data of G045.1+61.1 at $z = 3.43$, the first of *Planck*'s Dusty GEMS, shows that [CII] at high redshift probes a wide range of environments, from the dense gas irradiated by UV photons from maximally star-forming clumps to the diffuse interstellar gas at large distances seen in absorption. Although we found signatures of [CII] spanning at least 1200 km s^{-1}, we did not detect strong evidence for a wind that would regulate star formation by removing the gas reservoirs, as is often suggested in starburst-driven wind scenarios. This might indicate that broad wings of [CII] and other lines in high-redshift galaxies probe a much richer phenomenology than previously thought. Deeper higher-resolution observations spanning a wider spectral range will open an interesting new window to study the cold neutral gas in intense high-redshift starburst galaxies, including the ambient gas outside of the intense star-forming regions.

Acknowledgements. We thank the ALMA staff for carrying out the observations, and the team at the ARC in Grenoble for their help with preparing the data taking. We also thank the referee for suggestions that helped improve the paper. NPHN wishes to acknowledge funding through the JAO within their visiting scientists program, and is grateful for their hospitality during her stay as a science visitor in Vitacura.

References

Appleton, P. N., Guillard, P., Boulanger, F., et al. 2013, ApJ, 777, 66
Bennett, C. L., Fixsen, D. J., Hinshaw, G., et al. 1994, ApJ, 434, 587
Bernardi, M., Sheth, R. K., Nichol, R. C., Schneider, D. P., & Brinkmann, J. 2005, AJ, 129, 61

Boone, F., Combes, F., Krips, M., et al. 2014, in SF2A-2014: Proc. of the Annual meeting of the French Society of Astronomy and Astrophysics, eds. J. Ballet, F. Martins, F. Bournaud, R. Monier, & C. Reylé, 381
Cañameras, R., Nesvadba, N. P. H., Guery, D., et al. 2015, A&A, 581, A105
Cicone, C., Maiolino, R., Gallerani, S., et al. 2015, A&A, 574, A14
Elmegreen, B. G. 1999, ApJ, 517, 103
Gerin, M., Ruaud, M., Goicoechea, J. R., et al. 2015, A&A, 573, A30
Goldsmith, P. F., Langer, W. D., Pineda, J. L., & Velusamy, T. 2012, ApJS, 203, 13
Heckman, T. M., Alexandroff, R. M., Borthakur, S., Overzier, R., & Leitherer, C. 2015, ApJ, 809, 147
Jullo, E., Kneib, J.-P., Limousin, M., et al. 2007, New J. Phys., 9, 447
Kaufman, M. J., Wolfire, M. G., Hollenbach, D. J., & Luhman, M. L. 1999, ApJ, 527, 795
Kennicutt, Jr., R. C. 1989, ApJ, 344, 685
Kneib, J.-P., Ellis, R. S., Smail, I., Couch, W. J., & Sharples, R. M. 1996, ApJ, 471, 643
Knudsen, K. K., Richard, J., Kneib, J.-P., et al. 2016, MNRAS, 462, L6
Langer, W. D., Velusamy, T., Pineda, J. L., et al. 2010, A&A, 521, L17
Larsen, S. S., & Richtler, T. 2000, A&A, 354, 836
Le Petit, F., Nehmé, C., Le Bourlot, J., & Roueff, E. 2006, ApJS, 164, 506
Maiolino, R., Gallerani, S., Neri, R., et al. 2012, MNRAS, 425, L66
Nesvadba, N. P. H., Lehnert, M. D., Genzel, R., et al. 2007, ApJ, 657, 725
Papadopoulos, P. P., Thi, W.-F., & Viti, S. 2004, MNRAS, 351, 147
Planck Collaboration Int. XXVII. 2015, A&A, 582, A30
Rawle, T. D., Egami, E., Bussmann, R. S., et al. 2014, ApJ, 783, 59
Rigopoulou, D., Hopwood, R., Magdis, G. E., et al. 2014, ApJ, 781, L15
Schaerer, D., Boone, F., Jones, T., et al. 2015, A&A, 576, L2
Stacey, G. J., Hailey-Dunsheath, S., Ferkinhoff, C., et al. 2010, ApJ, 724, 957
Swinbank, A. M., Papadopoulos, P. P., Cox, P., et al. 2011, ApJ, 742, 11
Tacconi, L. J., Genzel, R., Smail, I., et al. 2008, ApJ, 680, 246
Takata, T., Sekiguchi, K., Smail, I., et al. 2006, ApJ, 651, 713
Wagg, J., Wilner, D. J., Neri, R., Downes, D., & Wiklind, T. 2006, ApJ, 651, 46

---

[1] Institut d'Astrophysique Spatiale, Bât. 121, 91405 Orsay Cedex, France
e-mail: `nicole.nesvadba@ias.u-psud.fr`
[2] CNRS, France
[3] Université Paris-Sud, France
[4] Université Paris-Saclay, France
[5] European Southern Observatory, ESO Vitacura, Alonso de Cordova 3107, Vitacura, Casilla 19001 Santiago, Chile
[6] Atacama Large Millimeter/submillimeter Array, ALMA Santiago Central Offices, Alonso de Cordova 3107, Vitacura, Casilla 763-0355 Santiago, Chile
[7] Université de Toulouse, UMS-OMP, IRAP, 31028 Toulouse Cedex 4, France
[8] LERMA, UMR 8112 CNRS, École Normale Supérieure and Observatoire de Paris, 75000 Paris, France
[9] Steward Observatory, University of Arizona, Tucson, AZ 85721, USA
[10] Chalmers University of Technology, Onsala Space Observatory, 439 92 Onsala, Sweden
[11] Aix Marseille Université, CNRS, LAM (Laboratoire d'Astrophysique de Marseille) UMR 7326, 13388 Marseille, France
[12] CEA-Saclay, 91191 Gif-sur-Yvette, France
[13] School of Earth and Space Exploration, Arizona State University, Tempe, AZ 85287, USA
[14] Department of Physics and Astronomy, University of British Columbia, 6224 Agricultural Road, Vancouver, 6658 British Columbia, Canada

7.3 Probing the gas, dust and stars down to 100 pc scales in the brightest GEMS

7.3.1 The sub-millimeter source

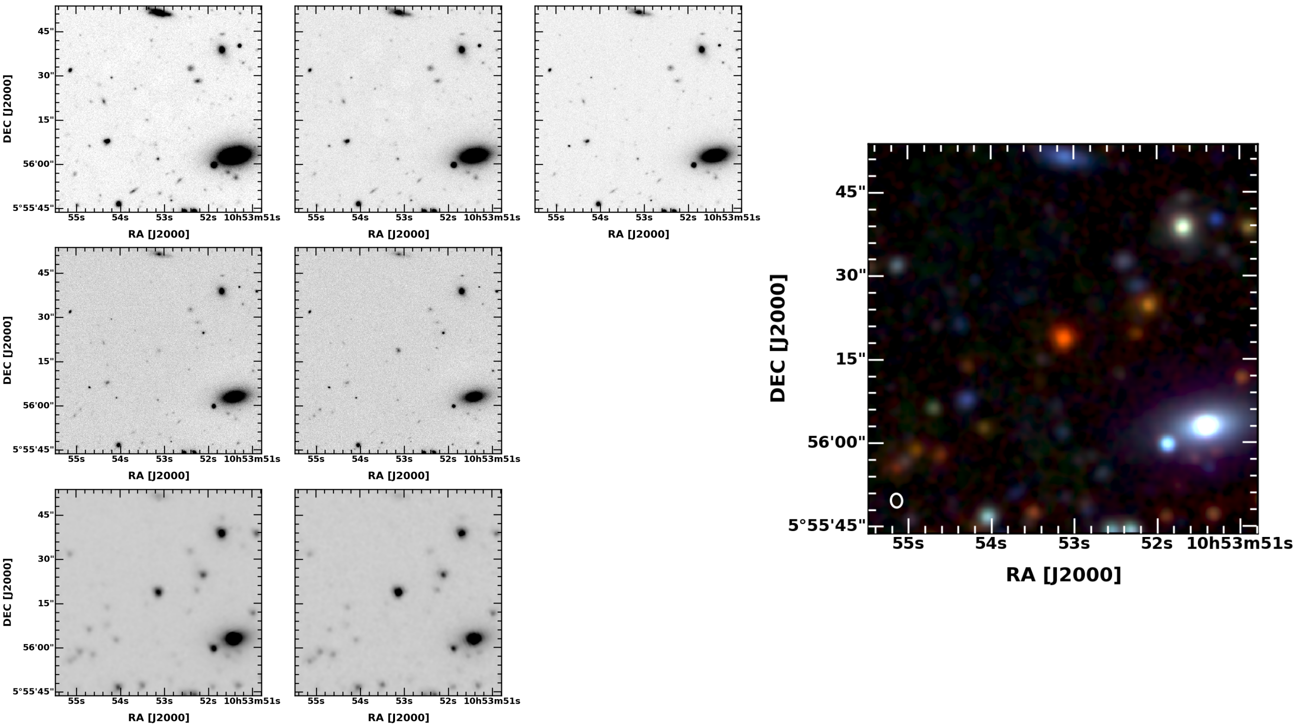

Figure 7.11: *Left :* Single band images of G244.8 obtained in the V, R, I, J and K bands with FORS2 and HAWK-I and at 3.6 and 4.5 μm with IRAC, from top-left to bottom-right respectively. *Right :* 3-color image in the R, K and 4.5 μm bands of this zoomed region of $70'' \times 70''$ centered at the peak of single dish (sub-)mm emission. The resolution of the two optical and NIR images have been matched to the PSF of IRAC at 4.5 μm.

G244.8, also referred to as "the Ruby" hereafter, is the brightest source among the Planck's Dusty GEMS sample and, to our knowledge, the only high-redshift galaxy that reaches an apparent peak flux density above 1 Jy ($S_{350} = 1054$ mJy) in the FIR/submm regime. A robust spectroscopic redshift of $z = 3.0054 \pm 0.0001$ was derived with the identification of the CO(3-2) and CO(4-3) emission lines during our blind redshift search with EMIR. Moreover, G244.8 is detected as a single point source in our FIR-to-mm single dish photometry, consistent with being a strongly gravitationally lensed galaxy, rather than a dense environment with intense star formation.

Our follow-up observations of the dust continuum with SMA in the COM configuration at $2''$ beam size also show a single unresolved, very bright emitter (see Fig.4.6). As I will further discuss below, subsequent observations were required in the VEXT configuration and with ALMA, at $\sim 0.3''$ and $\sim 0.1''$ resolutions, respectively. These data resolve the source and reveal a near complete Einstein ring of about $1.5''$ diameter. This makes it obvious that the Ruby is indeed gravitationally lensed, with the majority of the light deflection attributed to an isolated foreground galaxy at $z = 1.52$ (see §3.3.2 and Chap.6).

Having such an exceptionally bright source raises immediately the question whether an AGN is present. The immense flux density could either be produced by an extreme environment with a moderate lensing magnification, or trace a more average source with an exceptional boost. The SED analysis with DecompIR that I have already presented in §4.4 shows that the AGN contamination of the overall FIR emission in the Ruby must be rather small, below $\sim 10\%$. This estimate is based not only on the WISE upper limit at 22 μm, but also on IRAS upper limits at 60 and 100 μm which become very constraining for a distant source with such an extraordinary brightness in the image plane. I cannot rule out a smaller AGN contribution to the overall FIR luminosity because the dust continuum portion of the SED peaks around 250 μm. However, this SED decomposition ensures that the observed properties of this GEMS are indeed dominated by active star formation instead of a putative AGN, and that the AGN is unlikely to dominate the feedback. This suggests that the Ruby provides indeed an excellent opportunity to study intense star formation in the high-redshift universe, either in a particularly vigorously star-forming source, or – if the brightness is dominated by an outstanding lensing factor – on exceptionally fine spatial scales.

A modified blackbody fit to our FIR/mm photometry indicates that G244.8 has one of the highest dust temperatures in our sample, $\mathrm{T_d} = 50.0 \pm 0.4$, although this value remains in the regime of other actively star-forming galaxies at high-redshift. The overall SED implies $\mathrm{M_d} = (5.7 \pm 0.1) \times 10^9\ \mu^{-1}\ \mathrm{M_\odot}$, and an outstanding luminosity $\mathrm{L_{FIR}} = 2.7 \times 10^{14}\ \mu^{-1}\ \mathrm{L_\odot}$ which makes it the brightest high-redshifted galaxy on the extragalactic sky at sub-millimeter wavelengths. $\mathrm{L_{FIR}}$ translates into an apparent star-formation rate of about $45625 \pm 344\ \mu^{-1}\ \mathrm{M_\odot\ yr^{-1}}$, even though this extreme value needs to be corrected for the gravitational magnification. The detailed lensing model of Chapter 6 suggests a magnification factor $\mu \sim 15$, implying an intrinsic SFR of about 3000 $\mathrm{M_\odot\ yr^{-1}}$. The Ruby is therefore a particularly vigorously star-forming source. It represents a great opportunity to further study the most intense phases of star formation at high-redshift, near the highest possible rates. Elmegreen (1999) coined the term "maximal starburst" for a galaxy that is forming all of its stars within one crossing time, limited only by the available gas supply and the speed at which a signal can propagate within the interstellar gas ("causality limit" Elmegreen 1999). The processes that limit star formation as a galaxy approaches this limit are still not well understood. The effects of the gravity itself – through limiting the gas supply in dense star-forming cores – or the feedback through winds or radiation pressure have been considered.

7.3.2 Analysis of the optical-to-MIR spectral energy distribution

I use the extensive photometry reported in Table 7.8 to deblend the emission from the lensing galaxy and to characterize its stellar populations. The ring-like morphology of the dust and line emission detected in our SMA and ALMA interferometry shows that the FIR-to-mm regime is dominated by the background component, whereas the more centrally concentrated morphology in the near-infrared J and K bands suggests that the foreground lens accounts for the majority of the emission at shorter wavelengths. The emission from the foreground and background sources appear strongly blended, even at the highest spatial resolution data we currently have at these wavelengths ($0.4''$). We therefore need to at least approximately deblend the two sources in order to constrain how much each component may contribute to the overall SED in the optical and IR bands. This eventually allows us to broadly characterize the stellar populations in both components.

As described in §3.2.1, the optical and NIR photometry of the Ruby is extracted using an aperture of 2.5" that covers the PSF in the FORS2 and HAWKI frames as well as putative counterparts to the 850 μm arcs (Fig.7.14). The corresponding magnitudes are $\mathrm{I} = 23.91 \pm 0.09$, $\mathrm{J} = 22.0 \pm 0.1$ and $\mathrm{K} = 20.00 \pm 0.06$, including the calibration zero-point uncertainties. These photometric points are displayed in Figure 7.13 together with the upper limits in the optical, IRAC 3.6 and 4.5 μm and WISE 22 μm points, and show that the overall SED is very red. Fitting this SED requires two distinct components to reproduce the flux increase in the IRAC bands, and I make two rather generic assumptions about the nature of each source to limit the number of possible parameter combinations. Firstly, I assume that the foreground lensing galaxy has relatively evolved stellar populations (from one to a few Gyr), consistent with the absence of bright sub-millimeter emission and the red optical/NIR colors of the combined SED. Secondly, I assume that the high-redshift counterpart has younger stellar populations recently formed from the massive dust and gas reservoirs seen in the sub-millimeter and beyond. I present the observational evidence supporting these assumptions and explore alternative scenarios.

Observed wavelength [μm]	Observed flux density μF_ν [mJy]	Intrinsic flux density F_ν [mJy]	Instrument/ Survey
0.55	$< 8.3 \times 10^{-5}$	–	VLT/FORS2
0.65	$< 1.3 \times 10^{-4}$	–	VLT/FORS2
0.77	$(6.9 \pm 0.7) \times 10^{-4}$	–	VLT/FORS2
1.3	$(5.7 \pm 0.6) \times 10^{-3}$	–	VLT/HAWK-I
2.1	$(3.6 \pm 0.2) \times 10^{-2}$	–	VLT/HAWK-I
3.6	$(5.3 \pm 0.5) \times 10^{-2}$	–	Spitzer/IRAC
4.5	$(1.4 \pm 0.1) \times 10^{-1}$	–	Spitzer/IRAC
12	$(5.8 \pm 1.7) \times 10^{-1}$	$(3.9 \pm 1.4) \times 10^{-2}$	WISE
22	< 5.4	$\lesssim 3.6 \times 10^{-1}$	WISE
60	< 120	$\lesssim 8$	IRAS
100	< 440	$\lesssim 29$	IRAS
250	1050 ± 10	70 ± 5	Herschel/SPIRE
350	1054 ± 10	70 ± 5	Herschel/SPIRE
500	777 ± 7	52 ± 4	Herschel/SPIRE
850	198 ± 11	13 ± 2	JCMT/SCUBA-2
2000	19 ± 2	1.3 ± 0.2	IRAM/GISMO

Table 7.8: Infrared to millimeter photometry of G244.8 combined with the VLT/FORS2, VLT/HAWK-I and Spitzer/IRAC fluxes at lower wavelengths. I also present intrinsic fluxes corrected from the magnification factor $\mu \sim 15$ found in Chapter 6, for the bands only weakly contaminated by the lensing galaxy. Quoted errors include photometric and delensing uncertainties.

Stellar populations in the lensing foreground source

The non detection of a sub-mm source at the geometric center provides a 1σ upper limit on the flux density of the amplifying galaxy at 850 μm. Assuming that the gaseous reservoir within the lens is unresolved in the beam of the SMA in the VEXT configuration, I obtain an upper limit of $S_{850} < 2$ mJy from the SMA 850 μm image. This implies that the foreground does not contribute more than 1% to the 850 μm emission. I then compare this result with the properties of strongly star-forming LIRGs by scaling the SED template of Arp 220 to this upper limit, for $z = 1.52$ (blue curve in Fig.7.12). In this scenario, following Greve et al. (2012), I would find $M_{dust} \sim 5.0 \times 10^7$ $M_\odot$ in the lensing galaxy. The integrated SED would suggest $L_{FIR}(8 - 1000\ \mu m) = 2.3 \times 10^{12}$ $L_\odot$ and a substantial SFR of 400 $M_\odot$ yr^{-1}. However the young, highly reddened stellar populations associated with this dusty star-forming environment are not consistent with the shape of the SED in the optical, in particular the V and R bands. This discrepancy further indicates that the lens contains more evolved and redder stellar populations, further suggesting that it is an early-type galaxy with little FIR emission. As I already discussed in Chapter 6, we can derive a total foreground mass from the lensing configuration itself. In agreement with our other constraints, this lensing mass would also be inconsistent with the stellar mass of a young and strongly reddened stellar population in the lens.

I take this into account and use the stellar population synthesis models of Bruzual & Charlot (2003) (hereafter BC03) in the GALAXEV library to model the emission from the lens. I assume a single burst of star formation followed by an exponentially declining star formation history with e-folding time $\tau = 50$ Myr. The burst starts during the redshift range $z_f = 2 - 5$, which correponds to ages ranging from 1.0 to 3.1 Gyr at $z = 1.52$. I use a Chabrier (2003) initial mass function (IMF), solar metallicity and redden the spectra using the Calzetti et al. (1994) extinction law for typical starburst SEDs (i.e. using $R_V = 4.05$). I then fit the age, scaling factor and stellar continuum reddening $E(B - V)$. As shown in Figures 7.12 and 7.13, these evolved populations are a good fit to the I, J and K data points provided that the effect of dust extinction is modeled. This suggests that the high-redshift component has only a minor contribution below 3 μm, up to 0.1% of the total flux density in the J band and ∼2% in K. The observed NIR colors toward the lens (within an aperture of $1.0''$ diameter), and toward the sub-mm arcs (within an annulus matching the 3σ contours at 850 μm) support this trend. Despite a similar seeing in J and K images I find a redder color in the annulus, $(\mathrm{J}-\mathrm{K})_{\mathrm{annulus}} = 2.00 \pm 0.12$, than in the inner aperture, $(\mathrm{J}-\mathrm{K})_{\mathrm{inner}} = 1.70 \pm 0.12$. Since several studies have shown that the colors of early-type galaxies become bluer from the center to larger radii (red-cored, Boroson et al. 1983; De Propris et al. 2005), we expect the foreground emitter to contribute little to the outskirts of the HAWK-I source.

The best-fitting template that does not overestimate the emission in the optical is 1.5 Gyr old, with $\mathrm{E(B-V)} = 0.2$ corresponding to $\mathrm{A_V} = 0.6$. For the selected template, the mass-to-light ratios computed by GALAXEV in the rest-frame B and V band are 0.7 and 0.6 $\mathrm{M}_\odot/\mathrm{L}_\odot$, respectively. The age derived for these evolved populations is obviously affected by the degeneracy between age and metallicity (Worthey 1994). In fact, an increase in metallicity (with respect to the solar metallicity) can be easily compensated by a lower age of the stellar populations and result in the same optical/NIR colors, and vice versa. Unfortunately, the sparse SED sampling of G244.8 and the strong spectral blending of the lens and the source make it impossible to constrain the metal content of both components. I nevertheless find that adopting a fixed solar metallicity has little effect on the physical parameters deduced from this analysis, such as the stellar masses.

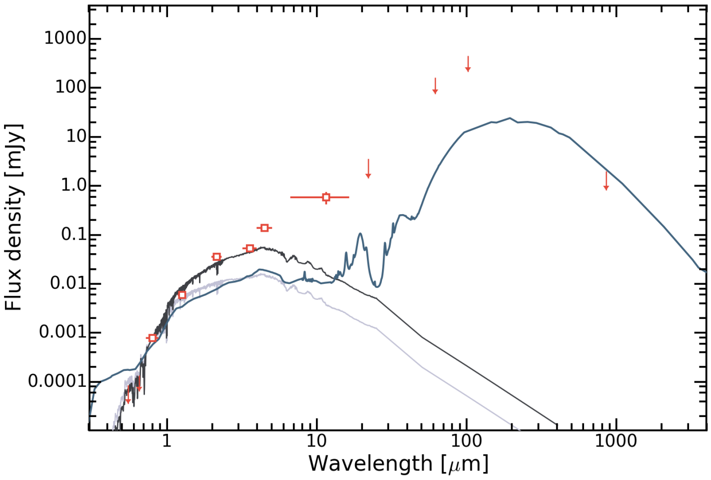

Figure 7.12: SED of the lensing galaxy toward G244.8 including the optical-to-MIR photometric points and the upper limits in the FIR-to-mm regime. This figure only shows the foreground source and missing flux in NIR bands comes from the background source (both components are plotted in Fig.7.13). The modeled SED of Arp 220 is rescaled to the 1σ upper limit from the SMA at 850 μm and plotted in dark blue. The best-fitting template of the foreground source obtained for the I, J and K bands is shown in dark grey. I also plot the same template without dust reddening in light blue.

I use these ratios along with the modeled rest-frame luminosities in the B and V bands to compute the stellar mass of the lens, and account for dust attenuation. I find $\mathrm{M}_* = (2.5-3.0) \times 10^{11}\ \mathrm{M}_\odot$, about the same order of magnitude as the lensing mass found in §6.2.3 ($\sim (3-4) \times 10^{11}\ \mathrm{M}_\odot$). Furthermore, I obtain a stellar mass in the lens about three times lower than this value if no correction for dust extinction is applied. The uncertainties involved in this estimate are therefore comparable to other studies of lensing galaxies at $z > 1$ such as van der Wel et al. (2013). This stellar mass measurement is, of course, affected by several sources of uncertainties which are unavoidable with our observational constraints. Firstly, the choice of the star formation history is not unique and corresponds to one of the simplest possible scenario. Secondly, the adopted IMF can also severely affect the output physical quantities (e.g., Wong et al. 2014) and some studies of early-type galaxies at $z < 1$ have advocated to use a Salpeter law (e.g., Conroy 2013).

The lensed submillimeter galaxy

The IRAC and WISE photometry and the deficit of MIR emission from the foreground early-type galaxy highlight the need for a second component to account for the overall shape of the SED. Given that the high-redshift GEMS selected in the sub-mm is expected to be strongly attenuated, we expect that the IRAC 4.5 μm and WISE 22 μm fluxes will be dominated by the background emission from G244.8. At $z_s = 3.00$ we benefit from the rest-frame 1.6 μm bump, a major spectral feature emerging from stellar populations older than 100 Myr. I therefore fit the MIR emission with younger templates, and measure the age, scaling factor and the required dust extinction. To this end I model a single burst of star formation at $z_f = 3 - 5$ with e-folding time $\tau = 50$ Myr. I adopt ages below 1 Gyr, the time interval between $z = 5$ and $z = 3$. These templates also use a solar metallicity, the Chabrier (2003) IMF and the extinction law from Calzetti et al. (1994).

The best-fitting SED suggests that the Ruby is indeed a young starburst with a ~150 Myr old stellar population, and a dust reddening of $E(B - V) = 2.1$. Combining the SEDs from the lens and the high-redshift source in the MIR results in the fit presented in Figure 7.13. I get a fairly good χ^2 of 3.5, for three degrees of freedom. From this deblending I find that both sources contribute by about the same amount to the overall MIR emission. The template representing the background component amounts to 30% and 55% of the total flux density at 3.6 and 4.5 μm respectively.

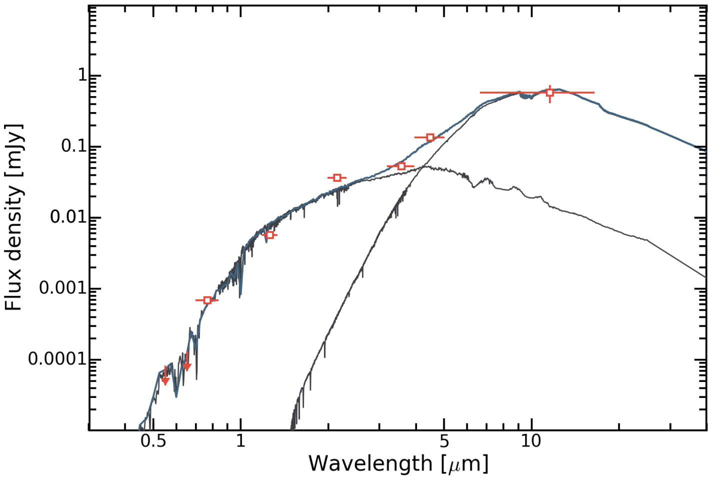

Figure 7.13: The best-fitting SED to the overall optical-to-MIR emission from G244.8 is plotted in dark blue, with flux densities uncorrected for the gravitational magnification. The grey lines represent the deblended components from the lens and the high-redshift source, from left to right, respectively. Further details on the best-fitting stellar populations are presented in the text.

The HAWK-I and IRAC imaging in the NIR do not resolve the spatial morphology of the high-redshift stellar continuum. This limitation combined with the high level of attenuation does not allow to firmly constrain the stellar mass in the Ruby. Nevertheless, adopting the same approach as for the lens, I find an upper limit for the stellar mass in the lensed source of about 1×10^{13} M$_\odot$, without correcting for the lensing magnification. Contamination from the foreground source may also increase this value.

7.3.3 Resolved dust continuum seen with the SMA at 850 μm and 0.3” beam size

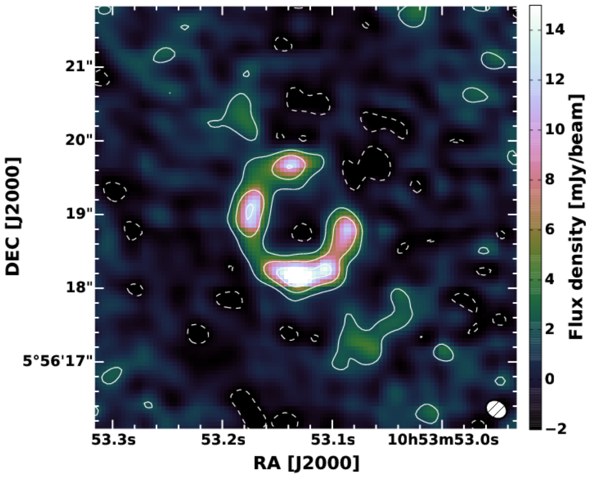

Figure 7.14: The high resolution dust continuum of G244.8, obtained with the SMA in the VEXT configuration. The dust emission at 850 μm exhibits a near-complete Einstein ring morphology with a diameter of about 1.4”. The synthetized beam ellipse is shown in the lower-right corner.

In Figure 7.14, I show the dust continuum of the Ruby resolved with the SMA in the VEXT configuration. The interferometer provides an angular resolution of 0.3″ that would correspond to about 150 pc in the source plane at z = 3.005 without gravitational amplification. Instead, at 850 μm, the dust emission exhibits an Einstein ring morphology with a diameter of about 1.4” that reveals a strong light deflection. The gravitational arc is not continuous but separated into two main components. Each of them contain two bright unresolved clumps.

We can directly measure the intrinsic surface brightness of the four clumps given that this quantity is conserved by strong gravitational lensing. Using the global dust temperatures deduced from our single-dish imaging, these values can be converted to star formation rate densities. On average, we find about 1000 $M_\odot$ yr^{-1} kpc^{-2} and up to 5000 $M_\odot$ yr^{-1} kpc^{-2} in the brightest clump in the south. This extreme star formation activity concentrated in bright and dense regions are reminiscent of the compact sites of star formation found in a majority of high-redshift SMGs (Swinbank et al. 2010). These observations also establish a parallel with the formation of stars in nearby late-type galaxies, which occur in dense cloud cores generally surrounded by a more diffuse ISM.

The ALMA view of the dust continuum at 3-mm is also shown in Figure 7.15. At sub-arcsec angular resolution, the southern clump resolves into two separate knots and the three other components identified with the SMA are associated to a single counterpart. There is also tentative detection of a few more point sources, but their final identification is derived with the CO(4-3) data cube where the additional velocity dimension is much more constraining.

7.3.4 An ALMA view of the gas kinematics and star formation law in G244.8

On the following pages, I summarize the first results of the on-going detailed analysis of molecular gas and star formation in the Ruby with ALMA in cycle 3. Only parts of the program have so far been taken – in particular 0.1″ interferometry of CO(4-3) with a 10-km baseline configuration – and the results will be published as a letter (Cañameras, Nesvadba, Kneissl et al. 2016, in prep). The

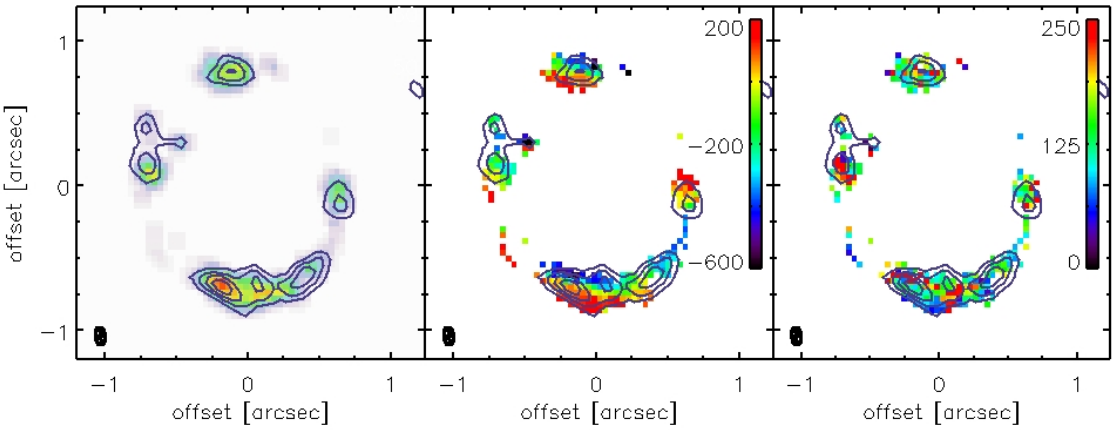

Figure 7.15: Sub-arcsec resolution ALMA observations of the CO(4-3) emission line in the Ruby. I show the line flux map (*left*), the velocity offsets in km s^{-1} (*center*) and the line FWHMs in km s^{-1} (*right*). Contours show the 3-mm dust continuum measured in line-free spectral channels of the data cube.

full analysis will be completed as soon as we have access to the high-resolution HST imaging of this source, which has already been obtained through a program led by my colleague B. Frye and which will allow to finalize the lensing model.

Observations and data reduction

These ALMA Cycle 3 data (2015.1.01518.S) were taken on October 23 2015 in the long baseline configuration C36-8 corresponding to maximum baselines of over 10 km. The target was observed with 35 antennas in excellent conditions with pwv ~ 0.92 mm and high phase stability (99.5 μm rms on baselines of 6500 m). We centered baseband 1 onto the redshifted CO(4-3) line at 114.888 GHz, and the remaining three spectral windows onto the continuum at frequencies of 100.908 GHz, 102.783 GHz, and 112.897 GHz, respectively.

The reduction was performed by R. Kneissl at the ALMA headquarters in Santiago de Chile with the standard manual scripts and the Common Astronomy Software Application (CASA), applying automatic and manual flagging of visibilities, calibrating bandpass, phase and amplitude/flux. The CLEAN algorithm was applied to construct the synthesized beam deconvolved continuum image and CO(4-3) data cube. We used the best estimates of antenna positions available from the entire campaign of baseline monitoring, throughout the long baseline observing period (October and November 2015).

The data were imaged into cubes using the "channel" and "velocity" modes, "Briggs" weighting with robust = 0.5, and custom cleaning masks using 1000 iterations. The rms in the final continuum image is 0.014 mJy beam^{-1} and 0.34 mJy beam^{-1} in the CO(4-3) cube, for a spectral channel width of 24.4 MHz (i.e. 64.3 km s^{-1}). The beam size is $0.14'' \times 0.06''$ along PA = 55°.

The interpolation of the dust SED from Chapter 4 suggests a source-integrated continuum flux density of 2.75 mJy. The ALMA data recovers 73% of this estimate, namely 2.0 mJy. Most of the missing flux is likely coming from the extended diffuse regions along the Einstein ring seen with the SMA at 850 μm (Fig.7.14). This extended component is not relevant for the current analysis since we focus on the brightest and most compact star-forming knots.

Analysis of the CO(4-3) kinematics

I fitted the emission line with the same procedure as that applied to the PdBI data cube of the Malachite and described in Chapter 3. However, I also measured the continuum in the CO(4-3) data cube with a constant value fitted to the measured flux in each spatial pixel, and subtracted the result before deriving the line fluxes. The resulting maps can be seen in Figure 7.15, which shows the gas morphology, velocity offsets, and Gaussian line widths, σ, with the continuum emission overplotted as contours. Most line and dust emission come from a total of 10 clumps, that are each resolved into 2-3 resolution elements. Maximal CO line and continuum surface brightnesses are relatively uniform in all clumps, between 200 and 600 μ Jy km s^{-1} beam^{-1} in CO, and between 45 and 120 μ Jy beam^{-1} for the continuum emission, respectively. Velocity offsets range from -600 to 200 km s^{-1} assuming a redshift $z = 3.005$. The velocity dispersions (Gaussian widths) are between 25 km s^{-1} and about 330 km s^{-1}, and vary rapidly with position.

The velocity gradients are nearly perpendicular to the magnification axis, so that the measured line widths are unlikely to be strongly broadened by bulk motion. This shows that we resolve the source also in the direction perpendicular to the gravitational shear, consistent with the small beam of $0.06''$ along the same direction. The large distances implied by the offsets between the most highly redshifted and blueshifted gas, $0.25''$ or ~ 2 kpc at $z = 3.005$, suggests that we see multiple clouds that are covering larger regions than the small region stretched out by the lens. If the velocity offsets are dominated by gravitational motion, then they suggest a dynamical mass of $\mathrm{M_{dyn}} = \mathrm{v}^2 \sin \mathrm{i}\ \mathrm{R/G}$, with the projected velocity, v, the inclination angle, i, and the gravitational constant, G. For a radius, R, measured perpendicularly to the direction of the shear introduced by the lensing galaxy, the gravitational magnification should be small. Assuming $\mathrm{R} = 0.25''$ corresponding to about 2 kpc in the source plane and $\mathrm{v} = 260$ km s^{-1}, and neglecting the gravitational magnification, we find $\mathrm{M_{dyn}} = 3 \times 10^{10}\ \mathrm{M_\odot}$.

7.3.5 Resolved star formation at the Eddington limit

The Schmidt-Kennicutt diagram in Figure 7.16 shows the local star formation intensities as a function of the local gas-mass surface densities extracted from each spatial pixel (Kennicutt 1989). To estimate the star formation rates, we measured the average continuum flux density in each pixel in the line-free spectral windows 1-3, and used the global temperature and luminosity of $\mathrm{L_{FIR}} = 26.5 \times 10^{13}\ \mathrm{L_\odot}$ and $\mathrm{T_d} = 50$ K, respectively (Cañameras et al. 2015), to translate these flux densities into FIR luminosities. We follow Kennicutt (1989) in estimating star formation rates with the relation $\mathrm{SFR} = 4.5 \times 10^{-44}\ \mathrm{L_{FIR}}$. In this relation, the SFR is given in $\mathrm{M_\odot}$ yr^{-1} and $\mathrm{L_{FIR}}$ is in erg s^{-1}, and integrated between 8 and 1000 μm in the rest frame. This results in local star formation intensities of $10^{3.0-3.7}\ \mathrm{M_\odot}$ yr^{-1} kpc^{-2}.

The linearity of the CO-FIR relationship of high-redshift galaxies suggests that the brightness of the J=4-3 transition is dominated by gas-mass surface density instead of gas excitation (Greve et al. 2014). We follow Solomon et al. (1997) to estimate molecular gas masses from the CO line flux of each spaxel and adopt $\alpha_{\mathrm{CO}} = 0.8\ \mathrm{M_\odot}/[\mathrm{K\ km\ s^{-1}\ pc^2}]$ (in accordance with the global dust-to-gas ratio presented in Cañameras et al. 2015), along with $r_{43/10} = 1$. Resulting gas-mass surface densities are in the range $10^{3.5-4.5}\ \mathrm{M_\odot}$ pc^{-2}.

Harrington et al. (2016) recently repeated our analysis of the Herschel and Planck photometry from Cañameras et al. (2015) for five of the GEMS including the Ruby. They confirmed our previous results within their larger error bars, with the sole but significant difference that they found much higher gas masses by adopting a Galactic $\mathrm{H_2}$-to-CO conversion factor. It is therefore worth stressing that the high gas-mass surface densities we find with ALMA correspond to column densities in the range $2 \times 10^{23-24}$ cm^{-2}. This is akin or even higher than the highest densities inside giant molecular clouds (Könyves et al. 2015) and in nearby ULIRGs (Downes & Solomon 1998), and several orders of magnitude above the average column densities in the Milky Way, $0.1 - 3 \times 10^{20}$ cm^{-2} (Dame et al. 2001). Consequently, this further justifies our choice of a low α_{CO} (see also Bolatto et al. 2013). Adopting a Milky-Way conversion factor would increase the column densities by another factor ~ 5.

The position of the Ruby in the Schmidt-Kennicutt diagram also indicates that the star formation efficiencies in this source are higher than the canonical 1% per free-fall time found in giant molecular clouds in the Milky Way and nearby galaxies (e.g., Krumholz & Tan 2007). The free-fall time for gas

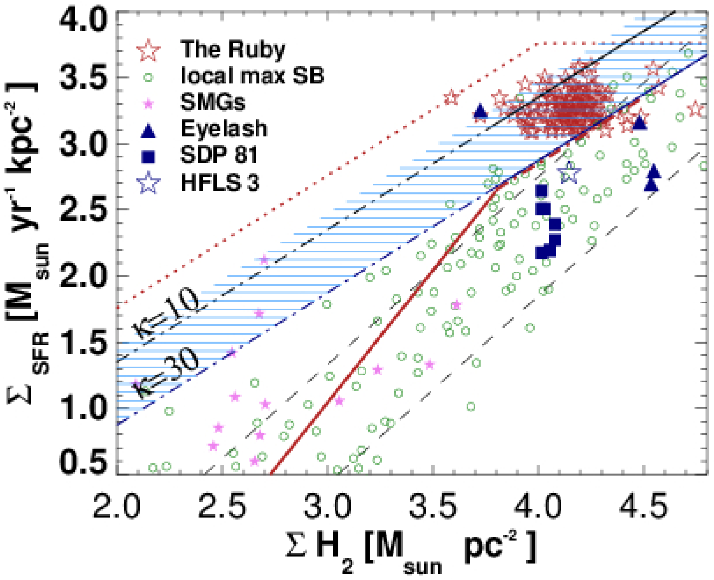

Figure 7.16: Spatially resolved Schmidt-Kennicutt law in G244.8 (red stars). Dark blue lines show the Eddington limit for an optically thick starburst with a range of opacities between 10 and 30 cm^2 g^{-1} (Andrews & Thompson 2011; Ostriker & Shetty 2011). Thin black dashed lines show the position of starburst and main sequence galaxies following Daddi et al. (2010, see also Genzel et al. 2010). The dotted red line shows the maximal star formation intensities that can be reached for the Eddington limit in optically thin gas of Andrews & Thompson (2011), and the solid red line shows the position of the Eddington limit in the model by Ostriker & Shetty (2011). Other symbols indicate: nearby Eddington-limited starbursts (empty purple circles, Andrews & Thompson 2011), sub-millimeter galaxies at z ∼ 2 (light blue squares), spatially-resolved data from the Eyelash (dark blue triangles, Swinbank et al. 2011), SDP.81 (dark blue squares, Hatsukade et al. 2015), and the maximal starburst HFLS 3 at z = 6 (empty blue star, Riechers et al. 2013). The upper and lower black dashed lines indicate the Schmidt-Kennicutt relationship for high-redshift starburst galaxies and main-sequence galaxies, respectively.

with mass surface densities between $10^{3.5}$ and $10^{4.3}$ $M_\odot$ pc^{-2} is between $\sqrt{h}$ and $3\sqrt{h}$ Myr, depending on the cloud sizes in the third dimension, h, given in pc. According to the size of the clumps along the magnification direction, we expect h ∼ 50 − 100 pc and free-fall times between 1 and 5×10^7 yrs. This suggests that about 30% of the gas is turned into stars per free-fall time. This rate is much higher than the star formation efficiencies in other galaxies and in molecular clouds generally. It is however akin to star formation efficiencies within the cores of giant molecular clouds in the Milky Way (Alves et al. 2007), which have similar gas-mass surface densities of few 10^4 $M_\odot$ pc^{-2}. It has been proposed that high-redshift galaxies act like single star-forming regions extending over many kpc (e.g., Stacey et al. 2010). In this sense, the Ruby suggests that star-forming regions within these galaxies might be akin to molecular cloud cores of several tens of pc (see also Swinbank et al. 2011).

7.3.6 What limits star formation ?

In Figure 7.17, we show the gas velocity dispersion as a function of the local gas surface density, measured in each pixel. We also overplot three different values of the virial parameter, α, defined as the ratio of turbulent to gravitational energy of a cloud, $\alpha = 5\sigma^2/(\pi \text{ G } R_{CL} \Sigma_{gas})$ (Bertoldi & McKee 1992). σ is the velocity dispersion, G the gravitational constant, R_{CL} the cloud radius, and Σ_{gas}

the gas-mass surface density. Star-forming clouds in the Milky Way fall near the value $\alpha = 1$. This regime is expected for marginally bound clouds where turbulence roughly balances gravity globally, but where relatively dense cells favour the star formation (Krumholz & McKee 2005). The figure shows that for typical cloud sizes between 30 and 90 pc, the turbulent velocity indicated by the line widths exceeds that which is required to balance gravity. Hence, turbulence appears to be capable to limit star formation in the Ruby.

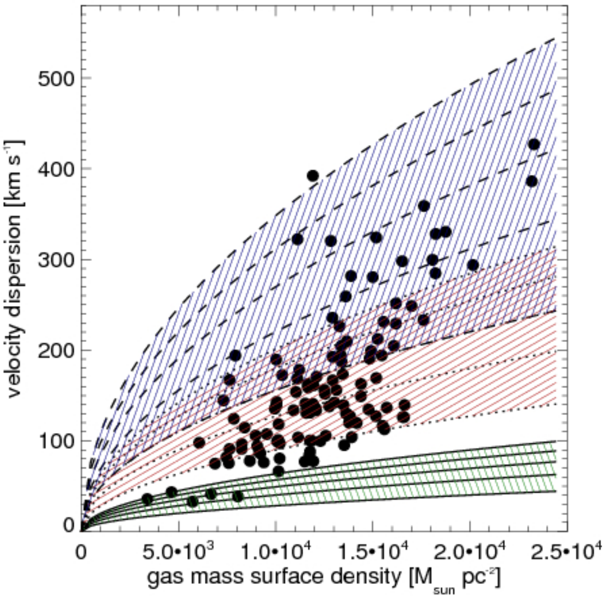

Figure 7.17: Velocity dispersion of CO(4-3) as a function of the local gas surface density. The green, red, and blue shaded areas show the expected dispersions for virial parameters α =1, 10, and 30, respectively, and a range of cloud sizes between 30 and 150 pc.

A number of processes might contribute to producing the turbulence and thus to limiting the star formation in G244.8. This includes gravitational stirring from merging of galaxies or clumps in a fragmenting disk, feedback from the star formation through radiation pressure, ram pressure from thermalized supernova ejecta, or an active galactic nucleus. The latter is unlikely for the Ruby. The AGN indeed contributes at most $< 10\%$ to the bolometric luminosity, suggesting that AGN photons do not dominate the radiative energy budget within the star-forming clump of the Ruby. Since we would be seeing the same photons in the spectral energy distribution, this argument would hold even if a powerful AGN was present in the host galaxy, but hidden through strong differential lensing. We also do not expect a strong effect of feedback from a radio-loud AGN because this GEMS falls onto the FIR-radio correlation with $\mathrm{q_{IR}} = 2.4$ (Cañameras et al. 2015). This implies that the ratio of far-infrared luminosity to monochromatic 1.4 GHz luminosity ($\mathrm{q_{IR}}$ parameter) corresponds to that expected from star formation (e.g., Condon et al. 1991). We therefore discard AGN feedback.

We must defer a more complete analysis until the full ALMA data set has been obtained, which will include additional constraints regarding the presence of outflows, of dense gas tracers, and the gas excitation. HST imaging is also required to finalize our lens modeling so that we can derive intrinsic physical parameters like cloud masses and sizes. Nonetheless, we can already give preliminary, more tentative constraints on several hypotheses.

The overall gas kinematics in the Ruby do not correspond very well to what would be expected from a fragmented gas disk. Only the smaller gradients in the eastern and western clouds are consistent with predictions for internal rotational motion of massive clumps in a fragmented disk (Ceverino et al. 2012) of up to $\mathrm{v_c} = 1/2\ \mathrm{v_{obs}}\ \sin^{-2}\mathrm{i} \sim 120\ \mathrm{km\ s^{-1}}$, and only if we neglect projection and beamsmearing effects. Finding higher velocity gradients may indicate outflows, merging of multiple clumps, or overlapping clouds. If gravity dominates the gas kinematics in the Ruby, a major merger would therefore be a better explanation, lending support to the standard scenario for massive, dusty starburst galaxies at high-redshift from a new perspective. Renaud et al. (2014) show with AMR simulations using RAMSES that merger-induced turbulence may produce a high-density tail in the gas density distribution of mergers. This effect pushes the galaxies about a factor 10 above the starburst sequence in the Schmidt-Kennicutt diagram, comparable to the position of G244.8 in Figure 7.16.

Figure 7.16 however also shows that the Ruby falls into the regime predicted for star formation that is self-regulated by feedback. Dark blue lines show the maximal star formation intensities allowed by the Eddington limit for a maximal starburst regulated by radiation pressure, in optically thick clouds with dust opacity κ (Andrews & Thompson 2011). For spherical symmetry, a starburst at the Eddington limit radiates enough photons for radiation pressure to balance gravity. κ scales with gas mass surface density, and determines how often a FIR photon may scatter on dust particles before it escapes (Andrews & Thompson 2011). With each scatter it transfers momentum corresponding to a fraction of its bolometric luminosity L/c onto the surrounding gas (where c is the speed of light). Figure 7.16 also shows that the star formation intensities in the Ruby exceeds those within the Cosmic Eyelash and SDP.81 by more than an order of magnitude, for comparable gas-mass surface densities.

The two blue dot-dashed lines give the position of galaxies forming stars at the Eddington limit with the assumptions of Andrews & Thompson (2011) and fiducial values of $\kappa = 10$ and 30, plausible for high-redshift galaxies. The dotted red line at higher star formation intensities indicates the maximal possible Eddington limit, which holds for optically thin environments where each photon may scatter at most once on a dust particle before it escapes. In such cases, higher star formation intensities must be reached at a given gas-mass surface density before radiation pressure may limit further gas collapse. The Ruby falls generally below that limit, and well into the range between the two fiducial values of dust opacity.

Radiation pressure as a mechanism limiting star formation has lately been met with some reservation amongst modelers, because high-resolution hydrodynamic simulations found that the photons will easily escape along channels cleared out by the wind created by the radiation pressure itself (e.g., Krumholz 2014; Bieri et al. 2016). However, given the exceptionally high gas-mass surface densities in the Ruby, it is not clear if winds will be very efficient in removing the overlying gas. Ostriker & Naab (2012) argue that radiation pressure should become very effective in regulating star formation at gas mass surface densities around 10^4 $M_\odot$ pc^{-2}, as indicated by the solid red line in Figure 7.16. A more detailed analysis will become possible when we have additional wind tracers at hand, in particular absorption line constraints, which are already scheduled. Likewise, a more detailed analysis of the wind kinematics should enable us to make more detailed statements once we have derived total gas and clump masses from our final lensing model.

Chapter 8

Summary and Outlook

8.1 Summary

My thesis presents a first characterization of the Planck's Dusty Gravitationally Enhanced subMillimetre Sources (GEMS), a small set of extremely bright star-forming galaxies at z $\sim 2-3$. These are eleven of the brightest high-redshift galaxies discovered with the Planck sub-millimeter all-sky survey, with flux densities between 300 and 1000 mJy at 350 μm, factors of a few brighter than the majority of lensed sources previously discovered through the wide-field surveys conducted with Herschel (Eales et al. 2010; Oliver et al. 2012) and the South Pole Telescope (Vieira et al. 2013). This sample therefore offers a great opportunity to characterize the mechanisms underlying the intense star formation in galaxies near the peak of the cosmic star formation rate density (Madau & Dickinson 2014), down to the scales of individual star-forming regions.

After a general introduction into the topic of high-redshift galaxy formation and strong gravitational lensing in Chapter 1, I focused on the selection of this outstanding sample in Chapter 2, based on the search for high-redshift candidates in the all-sky survey of the High Frequency Instrument on-board the Planck satellite. I described how this subset of lensed source candidates was identified with follow-up imaging at higher resolution with the Spectral and Photometric Imaging Receiver on-board the Herschel Space Observatory. The resulting set of 11 targets are located in unexplored areas of the extragalactic sky and directly observable from the northern hemisphere. They are bright, isolated point sources in SPIRE 250 μm maps of $18''$ resolution, and have the typical colours of dusty, intensely star-forming galaxies at high-redshift. Six of them are originally from the Planck Catalog of Compact Sources (PCCS), and exceed its 90% completeness limit of ~600 mJy in the highest-frequency bands. This suggests that they are among the brightest high-redshift sources on the sky selected for the bright dust SEDs produced by their intense star formation. The five others have been detected during a dedicated search of cold sources in the cosmic infrared background in Planck maps.

This thesis includes an analysis of the lensing configurations as well as a characterization of selected high-redshift sources. Thus, in Chapter 3, I presented the observations that were conducted during this thesis with several ground or spaced-based facilities. The characterization of the foreground lensing structures that magnify our high-redshift emitters was performed with optical/near-infrared imaging from the CFHT, the VLT, and IRAC on-board the Spitzer satellite. We also used X-Shooter spectroscopy to probe the main lensing component toward the brightest source in the sample. The characterization of dust emission in the background sources was conducted with single dish imaging from JCMT/SCUBA-2 and IRAM/GISMO at 850 μm and 2-mm, respectively, in addition to the sub-mm photometry from Herschel/SPIRE. I also included the publicly available fluxes or upper limits from IRAS at 60 and 100 μm and WISE at 22 μm. The molecular and atomic emission lines from the interstellar gas associated with star formation were observed in the (sub-)millimeter regime with EMIR on the 30-m telescope. In addition, we were able to resolve the dust emission from the gravitationally magnified and distorded images of the high-redshift emitters via the SMA interferometry, either in the COM or the VEXT configuration. PdBI observations complemented our view of the dust and gas reservoirs in a few sources, revealing their resolved kinematics. Finally, the stellar populations of the high-redshift components were probed by IRAC, in spite of a strong spatial and spectral blending with the foreground lensing galaxies.

In Chapter 4, I determined the global properties of our sample, taken as a whole, as published in Cañameras et al. (2015). I first described the blind redshift search in the 3-mm band with the EMIR broadband receiver on the IRAM 30-m telescope. This follow-up provided secure spectroscopic redshifts in the range z = 2.2 − 3.6, and subsequent observations completed the line survey with between 2 and 10 detections per source. I fitted a modified blackbody to their FIR-to-mm photometry to characterize their cold dust reservoirs. Each source is well fitted with single dust temperatures in the range $T_d = 33 - 50$ K. This covers the range of high-redshift starburst galaxies, as well as more gradually, but still intensely star-forming, high-z galaxies on the "main sequence". I also obtained outstanding far-infrared luminosities of up to 2×10^{14} $L_\odot$, before correcting for the gravitational magnification.

Given their exceptional brightness, I verified that the radiation from powerful active galactic nuclei was not making a dominant contribution to their observed far-infrared spectral energy distributions. To this end, we used the WISE survey and the 1.4 GHz VLA FIRST survey and found that the dust heating in each GEMS is entirely dominated by star formation. I presented a number of empirical arguments in favour of the strongly gravitationally lensed nature of each source, including the resolved dust and gas morphologies, and the relationship between dust temperatures and enhanced far-infrared luminosities. Then, we characterized the far-infrared-radio correlation for the GEMS and found a high scatter in the q-parameters. Some sources exhibit $q \sim 2.7$ which indicates a considerable excess of FIR relative to synchrotron emission. I tentatively interpreted this value as the consequence of turbulent motions in their interstellar medium, also observed in the broad profiles of the CO emission lines. The GEMS have gas-to-dust ratios of 40-140, consistent with a low CO-to-H_2 conversion factor, as expected for massive, dusty starburst galaxies with high metallicities. Finally, the integrated Schmidt-Kennicutt law provides evidence that this sample contains ordinary dusty starburst galaxies benefitting from strong gravitational magnifications.

I performed a detailed analysis of the foreground mass distribution toward each dusty high-redshift emitter in Chapter 5. For that purpose, I derived galaxy number counts in the near-infrared, measured the photometric redshifts and conducted a blind search for the galaxy red sequence in the optical and near-infrared. Together with a small set of publicly available spectroscopic redshifts, these results unambiguously identified the astrophysical structures magnifying the Planck's Dusty GEMS. I found that about half of the GEMS are associated with isolated foreground galaxies. Only three of them are clearly lensed by galaxy groups or clusters according to the AKDE contours and to the distribution of sources in the redshift space. Finally our red sequence models matched the observed slope and intercept for the two GEMS associated with the most significant excess of red foreground sources.

Chapter 6 is dedicated to the detailed modeling of the strong lensing effect with LENSTOOL. I deduced the total masses enclosed in the lensing potentials and accurate magnification factors, for the four GEMS with the most complete set of observational constraints. Firstly, I focused on the galaxy-galaxy strong lensing effect toward the brightest source in the sample, and confirmed that it is located behind a particularly powerful cosmic telescope producing magnifications of $\mu \sim 10 - 20$. I found a total lensing mass of $(3.7 \pm 0.5) \times 10^{11}$ $M_\odot$ within the radial range covered by the sub-mm arclets, and reconstructed the source-plane morphology. Secondly, I presented the strong lensing models of the GEMS associated with groups and clusters of foreground galaxies, which involve intermediate-scale dark-matter halos.

Lastly, in Chapter 7, I focused on the most remarkable properties of three gravitationally lensed sources obtained as part of the full analysis of the sample. Firstly, we used high-resolution interferometry to study the perturbed kinematics of the molecular gas in the Malachite, a gradually star-forming source at $z = 2.599$ showing a particular morphology in the image plane. This GEMS comprises three components along a critical line of $12''$ diameter, including two compact images of a single region in the source plane, and an extended arc of $\gtrsim 5''$ with quiescent kinematics.

Secondly, we used the [CII] fine structure line observed with the ALMA interferometer at $0.3''$ resolution to trace the properties of the interstellar gas in the Garnet. We only studied one of the bright multiply imaged starbursting clump of this source. We presented not only the resolved kinematics of the [CII] emission, but also the first extragalactic detection of a [CII] absorption feature which we attributed to infalling gaseous material. Generally, these results show that detecting this fine structure line at high redshift probes a wide range of environments, from dense interstellar gas to more diffuse and extended reservoirs at large distances from the star-forming regions.

Thirdly, I characterized the brightest source in our sample, referred to as the Ruby. This maximal starburst is magnified by a single foreground galaxy and forms a near-complete Einstein ring of $\sim 1.4''$ diameter in the image plane. We measured outstanding star formation rate surface densities between 1000 and 5000 $M_\odot$ yr^{-1} kpc^{-2} in the different star-forming knots resolved with our SMA dust continuum imaging. Then, I deblended the contribution from the foreground and background stellar populations to the optical-to-MIR spectral energy distribution. This allowed me to derive a stellar mass for the lensing galaxy which falls at a surprisingly high-redshift of $z = 1.52$. I summarized the first results of the molecular gas conditions and star formation processes in this GEMS obtained from the $0.1''$ resolution interferometry of CO(4-3) with ALMA. This data cube showed that most of the line and dust emission come from a total of 10 clumps, with strong velocity offsets and a wide range of velocity dispersions. After deriving a dynamical mass, I discussed the resolved Schmidt-Kennicutt relation, and highlighted an enhanced star-formation efficiency in this source compared to nearby galaxies and similar giant molecular clouds in the Milky Way. I therefore reached the conclusion that star-forming regions in high-redshift galaxies might be akin to molecular cloud cores.

8.2 Future prospects

This thesis presents a number of specific aspects concerning the on-going comprehensive analysis of the Planck's Dusty Gravitationally Enhanced subMillimetre Sources (GEMS). In the near future, many aspects of this analysis could be improved with additional follow-up observations.

For instance, complementary optical/near-infrared imaging and spectroscopy for the three GEMS magnified by overdensities of early-type galaxies will allow us to refine our characterization of the foreground mass distributions. This includes high-resolution imaging with the HST, or spectroscopic observations with the NOT or Gemini. Such additional constrains will be pivotal, either to validate or to refine our existing lensing models. A complementary weak lensing analysis of these systems could shed light on their projected mass distribution, at larger scales than otherwise accessible with strong lensing constraints. In addition, these new data will enable us to model the gravitational magnifications towards the remaining sources in the sample, and open up detailed studies of the intrinsic properties of these individual GEMS.

Concerning the Ruby, our extensive survey with EMIR on the 30-m telescope provided a wide range of atomic and molecular emission lines, in particular several CO transitions for $J_{\rm up} \geq 3$. Generally, these lines are very bright, with integrated fluxes $I_{\rm CO} = 18 - 46$ Jy km s^{-1} and rotational levels of up to $J_{\rm up} = 11$, suggesting that the gas reservoirs in this GEMS are highly excited. The strong gravitational magnification toward this source therefore offers a great opportunity to characterize the gas excitation mechanisms in extremely star-forming environments at high-redshift, and to disentangle the relative contributions of collisional and radiative processes. Accordingly, it would be interesting to determine the peak of the CO SLED (Spectral Line Energy Distribution) in the Ruby and to further interpret the CO line ratios.

To understand the link between the intense star formation and the evolutionary state of these outstanding sources, it is required to probe a wide range in gas densities and temperatures. Observing the dense gas of $n \gtrsim 10^5$ cm^{-3} embedded within the star-forming cloud cores is a pivotal stage to characterize the gas material directly fueling the star formation. I recently obtained PdBI interferometry of the HCO+, HCN and HNC dense gas tracers with WIDEX as principle investigator, either in the $J = 4 - 3$ or $J = 5 - 4$ rotational levels, and for the two brightest GEMS in the sample. A detailed analysis of this data set will be extremely interesting to constrain the most likely density and temperature regime in the densest regions of these starbursts. This will also enable to compare the conditions probed by CO and the dense gas, and to determine whether they trace similar or different environments.

Finally, the new generation of observing facilities such as the James Webb Space Telescope (JWST), the European Extremely Large Telescope (E-ELT) or the Square Kilometre Array (SKA) will open new opportunities in the near or more distant future. For instance, the JWST will enable to derive much more accurate estimates of the AGN contribution in the GEMS, and provide a number of interesting novel constraints on the gas content in these sources from near and mid-infrared lines, and PAH bands. The SKA would be particularly suitable to search for neutral atomic hydrogen (HI), to resolve the radio emission, and to further test our interpretation of the position of the GEMS with respect to the FIR-radio correlation. Given the outstanding brightness of the sources in this sample, and the fine spatial structures that are visible through the gravitational magnification, I believe that the GEMS will represent an important set of sources for the community overall, to test our ideas about the physics of high-redshift star formation in ways that are not possible for other sources. In this sense, they might become benchmarks for our understanding of how galaxies formed and evolved during the most rapid phase of cosmic star formation.

Bibliography

Abdalla, F. B., Banerji, M., Lahav, O., & Rashkov, V. 2011, MNRAS, 417, 1891

Ahn, C. P., Alexandroff, R., Allende Prieto, C., et al. 2012, ApJS, 203, 21

Alaghband-Zadeh, S., Chapman, S. C., Swinbank, A. M., et al. 2013, MNRAS, 435, 1493

Alam, S., Albareti, F. D., Allende Prieto, C., et al. 2015, ApJS, 219, 12

Alexander, D. M., Bauer, F. E., Brandt, W. N., et al. 2003, AJ, 125, 383

Alexander, D. M., Bauer, F. E., Chapman, S. C., et al. 2005, ApJ, 632, 736

Alexander, D. M., Chary, R.-R., Pope, A., et al. 2008, ApJ, 687, 835

ALMA Partnership, Vlahakis, C., Hunter, T. R., et al. 2015, ApJ, 808, L4

Alves, J., Lombardi, M., & Lada, C. J. 2007, A&A, 462, L17

Andrews, B. H. & Thompson, T. A. 2011, ApJ, 727, 97

Appenzeller, I., Fricke, K., Fürtig, W., et al. 1998, The Messenger, 94, 1

Aravena, M., Spilker, J. S., Bethermin, M., et al. 2016, MNRAS, 457, 4406

Armus, L., Charmandaris, V., Bernard-Salas, J., et al. 2007, ApJ, 656, 148

Barkhouse, W. A., Green, P. J., Vikhlinin, A., et al. 2006, ApJ, 645, 955

Barmby, P., Huang, J.-S., Ashby, M. L. N., et al. 2008, ApJS, 177, 431

Baugh, C. M., Lacey, C. G., Frenk, C. S., et al. 2005, MNRAS, 356, 1191

Bayliss, M. B., Hennawi, J. F., Gladders, M. D., et al. 2011, ApJS, 193, 8

Beck, R., Dobos, L., Budavári, T., Szalay, A. S., & Csabai, I. 2016, ArXiv e-prints

Becker, R. H., White, R. L., & Helfand, D. J. 1995, ApJ, 450, 559

Belokurov, V., Evans, N. W., Hewett, P. C., et al. 2009, MNRAS, 392, 104

Belokurov, V., Evans, N. W., Moiseev, A., et al. 2007, ApJ, 671, L9

Benítez, N. 2000, ApJ, 536, 571

Benítez, N., Ford, H., Bouwens, R., et al. 2004, ApJS, 150, 1

Bennett, C. L., Fixsen, D. J., Hinshaw, G., et al. 1994, ApJ, 434, 587

Bertin, E. 2010a, SCAMP: Automatic Astrometric and Photometric Calibration, Astrophysics Source Code Library

Bertin, E. 2010b, SWarp: Resampling and Co-adding FITS Images Together, Astrophysics Source Code Library

Bertin, E. & Arnouts, S. 1996, A&AS, 117, 393

Bertoldi, F. & McKee, C. F. 1992, ApJ, 395, 140

Béthermin, M., Daddi, E., Magdis, G., et al. 2012, ApJ, 757, L23

Bieri, R., Dubois, Y., Silk, J., Mamon, G. A., & Gaibler, V. 2016, MNRAS, 455, 4166

Binney, J. & Merrifield, M. 1998, Galactic Astronomy

Blain, A. W., Barnard, V. E., & Chapman, S. C. 2003, MNRAS, 338, 733

Blain, A. W., Ivison, R. J., & Smail, I. 1998, MNRAS, 296, L29

Blain, A. W., Smail, I., Ivison, R. J., & Kneib, J.-P. 1999, MNRAS, 302, 632

Blain, A. W., Smail, I., Ivison, R. J., Kneib, J.-P., & Frayer, D. T. 2002, Phys. Rep., 369, 111

Blakeslee, J. P., Franx, M., Postman, M., et al. 2003, ApJ, 596, L143

Blandford, R. D. & Narayan, R. 1992, ARA&A, 30, 311

Blanton, M. R. & Roweis, S. 2007, AJ, 133, 734

Blanton, M. R., Schlegel, D. J., Strauss, M. A., et al. 2005, AJ, 129, 2562

Bolatto, A. D., Wolfire, M., & Leroy, A. K. 2013, ARA&A, 51, 207

Bolton, A. S., Burles, S., Koopmans, L. V. E., et al. 2008, ApJ, 682, 964

Bolton, A. S., Burles, S., Koopmans, L. V. E., Treu, T., & Moustakas, L. A. 2006, ApJ, 638, 703

Bolton, A. S., Schlegel, D. J., Aubourg, É., et al. 2012, AJ, 144, 144

Bolzonella, M., Miralles, J.-M., & Pelló, R. 2000, A&A, 363, 476

Bonamigo, M., Despali, G., Limousin, M., et al. 2015, MNRAS, 449, 3171

Boroson, T. A., Thompson, I. B., & Shectman, S. A. 1983, AJ, 88, 1707

Boselli, A. 2011, A Panchromatic View of Galaxies

Bothwell, M. S., Chapman, S. C., Tacconi, L., et al. 2010, MNRAS, 405, 219

Bothwell, M. S., Smail, I., Chapman, S. C., et al. 2013, MNRAS, 429, 3047

Bouché, N., Cresci, G., Davies, R., et al. 2007, ApJ, 671, 303

Boulade, O., Vigroux, L. G., Charlot, X., et al. 1998, in Proc. SPIE, Vol. 3355, Optical Astronomical Instrumentation, ed. S. D'Odorico, 614–625

Bourne, N., Dunne, L., Ivison, R. J., et al. 2011, MNRAS, 410, 1155

Bouwens, R. J., Illingworth, G. D., Bradley, L. D., et al. 2009, ApJ, 690, 1764

Bouwens, R. J., Illingworth, G. D., Oesch, P. A., et al. 2012, ApJ, 752, L5

Bower, R. G., Kodama, T., & Terlevich, A. 1998, MNRAS, 299, 1193

Bower, R. G., Terlevich, A., Kodama, T., & Caldwell, N. 1999, in Astronomical Society of the Pacific Conference Series, Vol. 163, Star Formation in Early Type Galaxies, ed. P. Carral & J. Cepa, 211

Brainerd, T. G., Blandford, R. D., & Smail, I. 1996, ApJ, 466, 623

Brainerd, T. G. & Specian, M. A. 2003, ApJ, 593, L7

Brandl, B. R., Bernard-Salas, J., Spoon, H. W. W., et al. 2006, ApJ, 653, 1129

Bressan, A., Silva, L., & Granato, G. L. 2002, A&A, 392, 377

Brinchmann, J., Charlot, S., White, S. D. M., et al. 2004, MNRAS, 351, 1151

Brunner, R. J., Connolly, A. J., Szalay, A. S., & Bershady, M. A. 1997, ApJ, 482, L21

Bruzual, G. & Charlot, S. 2003, MNRAS, 344, 1000

Burstein, D., Davies, R. L., Dressler, A., Faber, S. M., & Lynden-Bell, D. 1988, in Astrophysics and Space Science Library, Vol. 141, Towards Understanding Galaxies at Large Redshift, ed. R. G. Kron & A. Renzini, 17–21

Bussmann, R. S., Pérez-Fournon, I., Amber, S., et al. 2013, ApJ, 779, 25

Butcher, H. & Oemler, Jr., A. 1984, ApJ, 285, 426

Cañameras, R., Nesvadba, N. P. H., Guery, D., et al. 2015, A&A, 581, A105

Calzetti, D., Kinney, A. L., & Storchi-Bergmann, T. 1994, ApJ, 429, 582

Carilli, C. L., Daddi, E., Riechers, D., et al. 2010, ApJ, 714, 1407

Carilli, C. L. & Walter, F. 2013, ARA&A, 51, 105

Carniani, S., Marconi, A., Biggs, A., et al. 2013, A&A, 559, A29

Carniani, S., Marconi, A., Maiolino, R., et al. 2015, A&A, 580, A102

Carter, M., Lazareff, B., Maier, D., et al. 2012, A&A, 538, A89

Casali, M., Pirard, J.-F., Kissler-Patig, M., et al. 2006, in Proc. SPIE, Vol. 6269, Society of Photo-Optical Instrumentation Engineers (SPIE) Conference Series, 62690W

Casey, C. M., Berta, S., Béthermin, M., et al. 2012, ApJ, 761, 140

Casey, C. M., Narayanan, D., & Cooray, A. 2014, Phys. Rep., 541, 45

Ceverino, D., Dekel, A., Mandelker, N., et al. 2012, MNRAS, 420, 3490

Chabrier, G. 2003, PASP, 115, 763

Chapin, E. L., Chapman, S. C., Coppin, K. E., et al. 2011, MNRAS, 411, 505

Chapman, S. C., Blain, A. W., Smail, I., & Ivison, R. J. 2005, ApJ, 622, 772

Cicone, C., Maiolino, R., Sturm, E., et al. 2014, A&A, 562, A21

Cimatti, A., Daddi, E., Renzini, A., et al. 2004, Nature, 430, 184

Clements, D. L., Rigby, E., Maddox, S., et al. 2010, A&A, 518, L8

Coe, D., Benítez, N., Sánchez, S. F., et al. 2006, AJ, 132, 926

Coleman, G. D., Wu, C.-C., & Weedman, D. W. 1980, ApJS, 43, 393

Collett, T. E. & Auger, M. W. 2014, MNRAS, 443, 969

Collister, A. A. & Lahav, O. 2004, PASP, 116, 345

Combes, F., Rex, M., Rawle, T. D., et al. 2012, A&A, 538, L4

Condon, J. J. 1992, ARA&A, 30, 575

Condon, J. J., Anderson, M. L., & Helou, G. 1991, ApJ, 376, 95

Condon, J. J., Cotton, W. D., Greisen, E. W., et al. 1998, AJ, 115, 1693

Connolly, A. J., Csabai, I., Szalay, A. S., et al. 1995, AJ, 110, 2655

Conroy, C. 2013, ARA&A, 51, 393

Conroy, C., Gunn, J. E., & White, M. 2009, ApJ, 699, 486

Coppin, K., Chapin, E. L., Mortier, A. M. J., et al. 2006, MNRAS, 372, 1621

Cutri, R. M., Skrutskie, M. F., van Dyk, S., et al. 2003, 2MASS All Sky Catalog of point sources.

Daddi, E., Cimatti, A., Renzini, A., et al. 2004, ApJ, 617, 746

Daddi, E., Dickinson, M., Morrison, G., et al. 2007, ApJ, 670, 156

Daddi, E., Elbaz, D., Walter, F., et al. 2010, ApJ, 714, L118

Daddi, E., Renzini, A., Pirzkal, N., et al. 2005, ApJ, 626, 680

Dame, T. M., Hartmann, D., & Thaddeus, P. 2001, ApJ, 547, 792

Danielson, A. L. R., Swinbank, A. M., Smail, I., et al. 2011, MNRAS, 410, 1687

Davis, M., Guhathakurta, P., Konidaris, N. P., et al. 2007, ApJ, 660, L1

De Breuck, C., Williams, R. J., Swinbank, M., et al. 2014, A&A, 565, A59

de Jong, T., Klein, U., Wielebinski, R., & Wunderlich, E. 1985, A&A, 147, L6

De Propris, R., Colless, M., Driver, S. P., Pracy, M. B., & Couch, W. J. 2005, MNRAS, 357, 590

de Propris, R., Stanford, S. A., Eisenhardt, P. R., Dickinson, M., & Elston, R. 1999, AJ, 118, 719

Dekel, A., Sari, R., & Ceverino, D. 2009, ApJ, 703, 785

Díaz-Santos, T., Armus, L., Charmandaris, V., et al. 2014, ApJ, 788, L17

Dickinson, M., Papovich, C., Ferguson, H. C., & Budavári, T. 2003, ApJ, 587, 25

Diolaiti, E., Bendinelli, O., Bonaccini, D., et al. 2000, A&AS, 147, 335

Dole, H., Lagache, G., Puget, J.-L., et al. 2006, A&A, 451, 417

Downes, D. & Solomon, P. M. 1998, ApJ, 507, 615

Draine, B. T. 2006, ApJ, 636, 1114

Dye, S., Furlanetto, C., Swinbank, A. M., et al. 2015, ArXiv e-prints

Eales, S., Dunne, L., Clements, D., et al. 2010, PASP, 122, 499

Eddington, A. S. 1919, The Observatory, 42, 119

Egami, E., Rex, M., Rawle, T. D., et al. 2010, A&A, 518, L12

Einstein, A. 1916, Annalen der Physik, 354, 769

Eisenhardt, P. R., De Propris, R., Gonzalez, A. H., et al. 2007, ApJS, 169, 225

Elbaz, D., Daddi, E., Le Borgne, D., et al. 2007, A&A, 468, 33

Elbaz, D., Dickinson, M., Hwang, H. S., et al. 2011, A&A, 533, A119

Elíasdóttir, Á., Limousin, M., Richard, J., et al. 2007, ArXiv e-prints

Elmegreen, B. G. 1999, ApJ, 517, 103

Elmegreen, B. G. 2007, ApJ, 668, 1064

Engel, H., Davies, R. I., Genzel, R., et al. 2011, ApJ, 729, 58

Engel, H., Tacconi, L. J., Davies, R. I., et al. 2010, ApJ, 724, 233

Erb, D. K., Steidel, C. C., Shapley, A. E., Pettini, M., & Adelberger, K. L. 2004, ApJ, 612, 122

Fabbiano, G. 1989, ARA&A, 27, 87

Faber, S. M. 1973, ApJ, 179, 731

Farrah, D., Lebouteiller, V., Spoon, H. W. W., et al. 2013, ApJ, 776, 38

Farrah, D., Serjeant, S., Efstathiou, A., Rowan-Robinson, M., & Verma, A. 2002, MNRAS, 335, 1163

Fassbender, R., Böhringer, H., Lamer, G., et al. 2008, A&A, 481, L73

Fassbender, R., Böhringer, H., Nastasi, A., et al. 2011, New Journal of Physics, 13, 125014

Fazio, G. G., Hora, J. L., Allen, L. E., et al. 2004, ApJS, 154, 10

Ferdosi, B. J., Buddelmeijer, H., Trager, S. C., Wilkinson, M. H. F., & Roerdink, J. B. T. M. 2011, A&A, 531, A114

Feruglio, C., Fiore, F., Carniani, S., et al. 2015, A&A, 583, A99

Finkelstein, S. L., Papovich, C., Dickinson, M., et al. 2013, Nature, 502, 524

Fiolet, N., Omont, A., Lagache, G., et al. 2010, A&A, 524, A33

Förster Schreiber, N. M., Genzel, R., Bouché, N., et al. 2009, ApJ, 706, 1364

Förster Schreiber, N. M., Genzel, R., Lehnert, M. D., et al. 2006, ApJ, 645, 1062

Fu, H., Jullo, E., Cooray, A., et al. 2012, ApJ, 753, 134

Fukugita, M., Shimasaku, K., & Ichikawa, T. 1995, PASP, 107, 945

Gallazzi, A., Charlot, S., Brinchmann, J., White, S. D. M., & Tremonti, C. A. 2005, MNRAS, 362, 41

García-Burillo, S., Combes, F., Usero, A., et al. 2015, A&A, 580, A35

Gavazzi, R., Treu, T., Koopmans, L. V. E., et al. 2008, ApJ, 677, 1046

Gawiser, E., van Dokkum, P. G., Herrera, D., et al. 2006, ApJS, 162, 1

Geach, J. E., Smail, I., Moran, S. M., et al. 2011, ApJ, 730, L19

Genzel, R., Förster Schreiber, N. M., Rosario, D., et al. 2014, ApJ, 796, 7

Genzel, R., Tacconi, L. J., Combes, F., et al. 2012, ApJ, 746, 69

Genzel, R., Tacconi, L. J., Gracia-Carpio, J., et al. 2010, MNRAS, 407, 2091

Gerin, M. & Phillips, T. G. 2000, ApJ, 537, 644

Gerin, M., Ruaud, M., Goicoechea, J. R., et al. 2015, A&A, 573, A30

Gildas Team. 2013, GILDAS: Grenoble Image and Line Data Analysis Software, Astrophysics Source Code Library

Gladders, M. D., López-Cruz, O., Yee, H. K. C., & Kodama, T. 1998, ApJ, 501, 571

Gladders, M. D. & Yee, H. K. C. 2000, AJ, 120, 2148

Glover, S. C. O. & Mac Low, M.-M. 2011, MNRAS, 412, 337

Goldsmith, P. F., Langer, W. D., Pineda, J. L., & Velusamy, T. 2012, ApJS, 203, 13

Greve, T. R., Bertoldi, F., Smail, I., et al. 2005, MNRAS, 359, 1165

Greve, T. R., Leonidaki, I., Xilouris, E. M., et al. 2014, ApJ, 794, 142

Greve, T. R., Vieira, J. D., Weiß, A., et al. 2012, ApJ, 756, 101

Griffin, M. J., Abergel, A., Abreu, A., et al. 2010, A&A, 518, L3

Grillo, C., Karman, W., Suyu, S. H., et al. 2016, ApJ, 822, 78

Grillo, C., Lombardi, M., Rosati, P., et al. 2008, A&A, 486, 45

Gullberg, B., De Breuck, C., Vieira, J. D., et al. 2015, MNRAS, 449, 2883

Harrington, K. C., Yun, M. S., Cybulski, R., et al. 2016, MNRAS, 458, 4383

Harris, A. I., Baker, A. J., Frayer, D. T., et al. 2012, ApJ, 752, 152

Harris, A. I., Baker, A. J., Zonak, S. G., et al. 2010, ApJ, 723, 1139

Harvey, D., Kneib, J. P., & Jauzac, M. 2016, MNRAS, 458, 660

Harwit, M. & Pacini, F. 1975, ApJ, 200, L127

Hatsukade, B., Tamura, Y., Iono, D., et al. 2015, PASJ, 67, 93

Hauser, M. G. & Dwek, E. 2001, ARA&A, 39, 249

Heckman, T. M., Alexandroff, R. M., Borthakur, S., Overzier, R., & Leitherer, C. 2015, ApJ, 809, 147

Heckman, T. M., Armus, L., & Miley, G. K. 1990, ApJS, 74, 833

Helou, G., Soifer, B. T., & Rowan-Robinson, M. 1985, ApJ, 298, L7

Herranz, D., González-Nuevo, J., Clements, D. L., et al. 2013, A&A, 549, A31

Herrera, C. N., Boulanger, F., Nesvadba, N. P. H., & Falgarone, E. 2012, A&A, 538, L9

Heyer, M. & Dame, T. M. 2015, ARA&A, 53, 583

Hezaveh, Y. D., Dalal, N., Marrone, D. P., et al. 2016, ApJ, 823, 37

Hezaveh, Y. D. & Holder, G. P. 2011, ApJ, 734, 52

Hezaveh, Y. D., Marrone, D. P., Fassnacht, C. D., et al. 2013, ApJ, 767, 132

Hickox, R. C., Wardlow, J. L., Smail, I., et al. 2012, MNRAS, 421, 284

Hildebrand, R. H. 1983, QJRAS, 24, 267

Hoekstra, H., Yee, H. K. C., & Gladders, M. D. 2004, ApJ, 606, 67

Hogg, D. W. 1999, ArXiv Astrophysics e-prints

Holland, W. S., Bintley, D., Chapin, E. L., et al. 2013, MNRAS, 430, 2513

Hopkins, P. F., Hernquist, L., Cox, T. J., et al. 2006, ApJS, 163, 1

Houck, J. R., Roellig, T. L., van Cleve, J., et al. 2004, ApJS, 154, 18

Ilbert, O., Capak, P., Salvato, M., et al. 2009, ApJ, 690, 1236

Israel, F. P. & Maloney, P. R. 2011, A&A, 531, A19

Ivison, R. J., Papadopoulos, P. P., Smail, I., et al. 2011, MNRAS, 412, 1913

Ivison, R. J., Swinbank, A. M., Smail, I., et al. 2013, ApJ, 772, 137

Ivison, R. J., Swinbank, A. M., Swinyard, B., et al. 2010a, A&A, 518, L35

Ivison, R. J., Swinbank, A. M., Swinyard, B., et al. 2010b, A&A, 518, L35

Jarvis, M. J., Smith, D. J. B., Bonfield, D. G., et al. 2010, MNRAS, 409, 92

Jauzac, M., Clément, B., Limousin, M., et al. 2014, MNRAS, 443, 1549

Jauzac, M., Richard, J., Jullo, E., et al. 2015, MNRAS, 452, 1437

Johnson, S. P., Wilson, G. W., Wang, Q. D., et al. 2013, MNRAS, 431, 662

Jullo, E., Kneib, J.-P., Limousin, M., et al. 2007, New Journal of Physics, 9, 447

Jullo, E., Natarajan, P., Kneib, J.-P., et al. 2010, Science, 329, 924

Kartaltepe, J. S., Sanders, D. B., Le Floc'h, E., et al. 2010, ApJ, 709, 572

Kassiola, A. & Kovner, I. 1993, ApJ, 417, 450

Kauffmann, G., Heckman, T. M., White, S. D. M., et al. 2003, MNRAS, 341, 33

Kaufman, M. J., Wolfire, M. G., Hollenbach, D. J., & Luhman, M. L. 1999, ApJ, 527, 795

Keeton, C. R. 2001, ArXiv Astrophysics e-prints

Kennicutt, Jr., R. C. 1989, ApJ, 344, 685

Kennicutt, Jr., R. C. 1998, ARA&A, 36, 189

Kereš, D., Katz, N., Weinberg, D. H., & Davé, R. 2005, MNRAS, 363, 2

Kewley, L. J., Groves, B., Kauffmann, G., & Heckman, T. 2006, MNRAS, 372, 961

Kinney, A. L., Calzetti, D., Bohlin, R. C., et al. 1996, ApJ, 467, 38

Kissler-Patig, M., Pirard, J.-F., Casali, M., et al. 2008, A&A, 491, 941

Kneib, J.-P. 1993, PhD thesis, Ph. D. thesis, Université Paul Sabatier, Toulouse, (1993)

Kneib, J.-P., Ellis, R. S., Smail, I., Couch, W. J., & Sharples, R. M. 1996, ApJ, 471, 643

Knudsen, K. K., Richard, J., Kneib, J.-P., et al. 2016, ArXiv e-prints

Kochanek, C. S. 1995, ApJ, 445, 559

Kodama, T. & Arimoto, N. 1997, A&A, 320, 41

Kodama, T., Arimoto, N., Barger, A. J., & Arag'on-Salamanca, A. 1998, A&A, 334, 99

Kodama, T., Bell, E. F., & Bower, R. G. 1999, MNRAS, 302, 152

Kodama, T., Tanaka, I., Kajisawa, M., et al. 2007, MNRAS, 377, 1717

Kondo, Y., Henize, K. G., & Kotila, C. L. 1970, ApJ, 159, 927

Könyves, V., André, P., Men'shchikov, A., et al. 2015, A&A, 584, A91

Koo, D. C. 1985, AJ, 90, 418

Koopmans, L. V. E., Treu, T., Bolton, A. S., Burles, S., & Moustakas, L. A. 2006, ApJ, 649, 599

Kovacs, A. 2013, CRUSH: Comprehensive Reduction Utility for SHARC-2 (and more...), Astrophysics Source Code Library

Kovács, A., Chapman, S. C., Dowell, C. D., et al. 2006, ApJ, 650, 592

Kovner, I. 1987, ApJ, 312, 22

Kroupa, P. 2001, MNRAS, 322, 231

Krumholz, M. R. 2014, Phys. Rep., 539, 49

Krumholz, M. R., Dekel, A., & McKee, C. F. 2012, ApJ, 745, 69

Krumholz, M. R. & McKee, C. F. 2005, ApJ, 630, 250

Krumholz, M. R. & Tan, J. C. 2007, ApJ, 654, 304

Kurczynski, P., Gawiser, E., Acquaviva, V., et al. 2016, ArXiv e-prints

Lacki, B. C. & Thompson, T. A. 2010, ApJ, 717, 196

Lacy, M., Storrie-Lombardi, L. J., Sajina, A., et al. 2004, ApJS, 154, 166

Landolt, A. U. 1992, AJ, 104, 340

Lapi, A., Negrello, M., González-Nuevo, J., et al. 2012, ApJ, 755, 46

Larsen, S. S. & Richtler, T. 2000, A&A, 354, 836

Larson, R. B. 1981, MNRAS, 194, 809

Lasker, B. M., Lattanzi, M. G., McLean, B. J., et al. 2008, AJ, 136, 735

Lee, N., Sanders, D. B., Casey, C. M., et al. 2015, ApJ, 801, 80

Lehnert, M. D., Le Tiran, L., Nesvadba, N. P. H., et al. 2013, A&A, 555, A72

Lehnert, M. D., Nesvadba, N. P. H., Le Tiran, L., et al. 2009, ApJ, 699, 1660

Leroy, A. K., Bolatto, A., Gordon, K., et al. 2011, ApJ, 737, 12

Leroy, A. K., Walter, F., Brinks, E., et al. 2008, AJ, 136, 2782

Lilly, S., Eales, S., Gear, W., et al. 1999, ArXiv Astrophysics e-prints

Limousin, M., Cabanac, R., Gavazzi, R., et al. 2009, A&A, 502, 445

Limousin, M., Ebeling, H., Richard, J., et al. 2012, A&A, 544, A71

Limousin, M., Kneib, J. P., Bardeau, S., et al. 2007a, A&A, 461, 881

Limousin, M., Kneib, J.-P., & Natarajan, P. 2005, MNRAS, 356, 309

Limousin, M., Morandi, A., Sereno, M., et al. 2013, Space Sci. Rev., 177, 155

Limousin, M., Richard, J., Jullo, E., et al. 2007b, ApJ, 668, 643

Madau, P. & Dickinson, M. 2014, ARA&A, 52, 415

Madau, P., Ferguson, H. C., Dickinson, M. E., et al. 1996, MNRAS, 283, 1388

Magdis, G. E., Daddi, E., Béthermin, M., et al. 2012, ApJ, 760, 6

Magdis, G. E., Daddi, E., Elbaz, D., et al. 2011, ApJ, 740, L15

Magnelli, B., Lutz, D., Santini, P., et al. 2012, A&A, 539, A155

Maiolino, R., Cox, P., Caselli, P., et al. 2005, A&A, 440, L51

Maiolino, R., Gallerani, S., Neri, R., et al. 2012, MNRAS, 425, L66

Malhotra, S., Helou, G., Stacey, G., et al. 1997, ApJ, 491, L27

Malhotra, S., Kaufman, M. J., Hollenbach, D., et al. 2001, ApJ, 561, 766

Maraston, C. 2005, MNRAS, 362, 799

Maraston, C., Strömbäck, G., Thomas, D., Wake, D. A., & Nichol, R. C. 2009, MNRAS, 394, L107

Margoniner, V. E. & Wittman, D. M. 2008, ApJ, 679, 31

McGreer, I. D., Helfand, D. J., & White, R. L. 2009, AJ, 138, 1925

Mei, S., Holden, B. P., Blakeslee, J. P., et al. 2009, ApJ, 690, 42

Mei, S., Holden, B. P., Blakeslee, J. P., et al. 2006, ApJ, 644, 759

Meneghetti, M., Argazzi, R., Pace, F., et al. 2007, A&A, 461, 25

Meylan, G., Jetzer, P., North, P., et al., eds. 2006, Gravitational Lensing: Strong, Weak and Micro

Mignani, R. P., Shearer, A., de Luca, A., et al. 2011, A&A, 533, A101

Mihos, J. C. & Hernquist, L. 1996, ApJ, 464, 641

Miville-Deschênes, M.-A. & Lagache, G. 2005, ApJS, 157, 302

Modigliani, A., Goldoni, P., Royer, F., et al. 2010, in Proc. SPIE, Vol. 7737, Observatory Operations: Strategies, Processes, and Systems III, 773728

Montier, L. A., Pelkonen, V.-M., Juvela, M., Ristorcelli, I., & Marshall, D. J. 2010, A&A, 522, A83

Morton, D. C., Bruzual A., G., Kurucz, R. L., & Spinrad, H. 1977, ApJ, 212, 438

Moshir, M., Kopman, G., & Conrow, T. A. O. 1992, IRAS Faint Source Survey, Explanatory supplement version 2

Muñoz, J. A., Falco, E. E., Kochanek, C. S., et al. 1998, Ap&SS, 263, 51

Mullaney, J. R., Alexander, D. M., Goulding, A. D., & Hickox, R. C. 2011, MNRAS, 414, 1082

Murphy, E. J. 2009, ApJ, 706, 482

Murray, N. 2011, ApJ, 729, 133

Nadeau, D., Yee, H. K. C., Forrest, W. J., et al. 1991, ApJ, 376, 430

Nagao, T., Maiolino, R., De Breuck, C., et al. 2012, A&A, 542, L34

Narayanan, D., Cox, T. J., Hayward, C. C., Younger, J. D., & Hernquist, L. 2009, MNRAS, 400, 1919

Narayanan, D., Krumholz, M. R., Ostriker, E. C., & Hernquist, L. 2012, MNRAS, 421, 3127

Natarajan, P. & Kneib, J.-P. 1997, MNRAS, 287, 833

Natarajan, P., Kneib, J.-P., & Smail, I. 2002a, ApJ, 580, L11

Natarajan, P., Kneib, J.-P., Smail, I., & Ellis, R. S. 1998, ApJ, 499, 600

Natarajan, P., Kneib, J.-P., Smail, I., et al. 2009, ApJ, 693, 970

Natarajan, P., Loeb, A., Kneib, J.-P., & Smail, I. 2002b, ApJ, 580, L17

Navarro, J. F., Frenk, C. S., & White, S. D. M. 1997, ApJ, 490, 493

Navarro, J. F., Hayashi, E., Power, C., et al. 2004, MNRAS, 349, 1039

Negrello, M., Hopwood, R., De Zotti, G., et al. 2010, Science, 330, 800

Negrello, M., Perrotta, F., González-Nuevo, J., et al. 2007, MNRAS, 377, 1557

Nenkova, M., Sirocky, M. M., Nikutta, R., Ivezić, Ž., & Elitzur, M. 2008, ApJ, 685, 160

Nesvadba, N., Kneissl, R., Cañameras, R., et al. 2016, A&A, 593, L2

Nesvadba, N. P. H., Lehnert, M. D., Genzel, R., et al. 2007, ApJ, 657, 725

Newman, S. F., Genzel, R., Förster-Schreiber, N. M., et al. 2012, ApJ, 761, 43

Nguyen, H. T., Schulz, B., Levenson, L., et al. 2010, A&A, 518, L5

Noeske, K. G., Weiner, B. J., Faber, S. M., et al. 2007, ApJ, 660, L43

Oesch, P. A., Brammer, G., van Dokkum, P. G., et al. 2016, ApJ, 819, 129

Oguri, M. 2015, MNRAS, 449, L86

Oguri, M., Inada, N., Pindor, B., et al. 2006, AJ, 132, 999

Oke, J. B. & Sandage, A. 1968, ApJ, 154, 21

Oliver, S. J., Bock, J., Altieri, B., et al. 2012, MNRAS, 424, 1614

Ostriker, E. C. & Shetty, R. 2011, ApJ, 731, 41

Ostriker, J. P. & Naab, T. 2012, Physics Today, 65, 43

Papadopoulos, P. P., Röttgering, H. J. A., van der Werf, P. P., et al. 2000, ApJ, 528, 626

Papadopoulos, P. P., Thi, W.-F., & Viti, S. 2004, MNRAS, 351, 147

Papadopoulos, P. P., van der Werf, P., Xilouris, E., Isaak, K. G., & Gao, Y. 2012, ApJ, 751, 10

Papovich, C., Rudnick, G., Le Floc'h, E., et al. 2007, ApJ, 668, 45

Pello, R., Miralles, J. M., Le Borgne, J.-F., et al. 1996, A&A, 314, 73

Pettini, M., Steidel, C. C., Adelberger, K. L., Dickinson, M., & Giavalisco, M. 2000, ApJ, 528, 96

Pilbratt, G. L., Riedinger, J. R., Passvogel, T., et al. 2010, A&A, 518, L1

Pirard, J.-F., Kissler-Patig, M., Moorwood, A., et al. 2004, in Proc. SPIE, Vol. 5492, Ground-based Instrumentation for Astronomy, ed. A. F. M. Moorwood & M. Iye, 1763–1772

Pisani, A. 1996, MNRAS, 278, 697

Planck Collaboration, Adam, R., Ade, P. A. R., et al. 2015a, ArXiv e-prints

Planck Collaboration, Ade, P. A. R., Aghanim, N., et al. 2014a, A&A, 571, A1

Planck Collaboration, Ade, P. A. R., Aghanim, N., et al. 2014b, A&A, 571, A28

Planck Collaboration, Ade, P. A. R., Aghanim, N., et al. 2013, A&A, 550, A133

Planck Collaboration, Ade, P. A. R., Aghanim, N., et al. 2014c, A&A, 571, A16

Planck Collaboration, Ade, P. A. R., Aghanim, N., et al. 2011a, A&A, 536, A1

Planck Collaboration, Ade, P. A. R., Aghanim, N., et al. 2011b, A&A, 536, A7

Planck Collaboration, Ade, P. A. R., Aghanim, N., et al. 2015b, ArXiv e-prints

Planck Collaboration, Ade, P. A. R., Aghanim, N., et al. 2015c, ArXiv e-prints

Planck Collaboration, Aghanim, N., Altieri, B., et al. 2015d, A&A, 582, A30

Planck HFI Core Team, Ade, P. A. R., Aghanim, N., et al. 2011, A&A, 536, A4

Poggianti, B. M., von der Linden, A., De Lucia, G., et al. 2006, ApJ, 642, 188

Polletta, M., Tajer, M., Maraschi, L., et al. 2007, ApJ, 663, 81

Polletta, M. d. C., Wilkes, B. J., Siana, B., et al. 2006, ApJ, 642, 673

Pope, A., Chary, R.-R., Alexander, D. M., et al. 2008, ApJ, 675, 1171

Puget, P., Stadler, E., Doyon, R., et al. 2004, in Proc. SPIE, Vol. 5492, Ground-based Instrumentation for Astronomy, ed. A. F. M. Moorwood & M. Iye, 978–987

Rangwala, N., Maloney, P. R., Glenn, J., et al. 2011, ApJ, 743, 94

Rawle, T. D., Egami, E., Bussmann, R. S., et al. 2014, ApJ, 783, 59

Reach, W. T., Megeath, S. T., Cohen, M., et al. 2005, PASP, 117, 978

Refsdal, S. 1964, MNRAS, 128, 307

Refsdal, S. 1966, MNRAS, 132, 101

Renaud, F., Bournaud, F., Kraljic, K., & Duc, P.-A. 2014, MNRAS, 442, L33

Rhoads, J. E., Malhotra, S., Allam, S., et al. 2014, ApJ, 787, 8

Richard, J., Jauzac, M., Limousin, M., et al. 2014, MNRAS, 444, 268

Richard, J., Pei, L., Limousin, M., Jullo, E., & Kneib, J. P. 2009, A&A, 498, 37

Richard, J., Smith, G. P., Kneib, J.-P., et al. 2010, MNRAS, 404, 325

Richard, J., Stark, D. P., Ellis, R. S., et al. 2008, ApJ, 685, 705

Riechers, D. A., Bradford, C. M., Clements, D. L., et al. 2013, Nature, 496, 329

Riechers, D. A., Hodge, J., Walter, F., Carilli, C. L., & Bertoldi, F. 2011, ApJ, 739, L31

Rieke, G. H., Alonso-Herrero, A., Weiner, B. J., et al. 2009, ApJ, 692, 556

Rieke, G. H., Young, E. T., Engelbracht, C. W., et al. 2004, ApJS, 154, 25

Rigopoulou, D., Hopwood, R., Magdis, G. E., et al. 2014, ApJ, 781, L15

Rodighiero, G., Daddi, E., Baronchelli, I., et al. 2011, ApJ, 739, L40

Rodighiero, G., Renzini, A., Daddi, E., et al. 2014, MNRAS, 443, 19

Rodriguez-Fernandez, N. J., Braine, J., Brouillet, N., & Combes, F. 2006, A&A, 453, 77

Roseboom, I. G., Dunlop, J. S., Cirasuolo, M., et al. 2013, MNRAS, 436, 430

Rowlands, K., Wild, V., Nesvadba, N., et al. 2015, MNRAS, 448, 258

Rubin, V. C., Thonnard, N., & Ford, Jr., W. K. 1978, ApJ, 225, L107

Rybak, M., McKean, J. P., Vegetti, S., Andreani, P., & White, S. D. M. 2015a, MNRAS, 451, L40

Rybak, M., Vegetti, S., McKean, J. P., Andreani, P., & White, S. D. M. 2015b, MNRAS, 453, L26

Sajina, A., Yan, L., Fadda, D., Dasyra, K., & Huynh, M. 2012, ApJ, 757, 13

Sajina, A., Yan, L., Lacy, M., & Huynh, M. 2007, ApJ, 667, L17

Salim, S., Charlot, S., Rich, R. M., et al. 2005, ApJ, 619, L39

Salpeter, E. E. 1955, ApJ, 121, 161

Sanders, D. B. & Mirabel, I. F. 1996, ARA&A, 34, 749

Sanders, R. H. 2014, MNRAS, 439, 1781

Santini, P., Maiolino, R., Magnelli, B., et al. 2010, A&A, 518, L154

Sault, R. J., Teuben, P. J., & Wright, M. C. H. 1995, in Astronomical Society of the Pacific Conference Series, Vol. 77, Astronomical Data Analysis Software and Systems IV, ed. R. A. Shaw, H. E. Payne, & J. J. E. Hayes, 433

Sawicki, M. J., Lin, H., & Yee, H. K. C. 1997, AJ, 113, 1

Schaerer, D., Boone, F., Jones, T., et al. 2015, A&A, 576, L2

Schawinski, K., Urry, C. M., Simmons, B. D., et al. 2014, MNRAS, 440, 889

Schmidt, M. 1959, ApJ, 129, 243

Scoville, N. 2004, in Astronomical Society of the Pacific Conference Series, Vol. 320, The Neutral ISM in Starburst Galaxies, ed. S. Aalto, S. Huttemeister, & A. Pedlar, 253

Serjeant, S. 2012, MNRAS, 424, 2429

Sérsic, J. L. 1963, Boletin de la Asociacion Argentina de Astronomia La Plata Argentina, 6, 41

Shapiro, K. L., Genzel, R., Förster Schreiber, N. M., et al. 2008, ApJ, 682, 231

Sharon, K., Gladders, M. D., Rigby, J. R., et al. 2012, ApJ, 746, 161

Sharon, K. & Johnson, T. L. 2015, ApJ, 800, L26

Silk, J. & Norman, C. 2009, ApJ, 700, 262

Simpson, J. M., Swinbank, A. M., Smail, I., et al. 2014, ApJ, 788, 125

Smail, I., Chapman, S. C., Blain, A. W., & Ivison, R. J. 2004, ApJ, 616, 71

Smail, I., Ivison, R. J., & Blain, A. W. 1997, ApJ, 490, L5

Smail, I., Swinbank, A. M., Ivison, R. J., & Ibar, E. 2011, MNRAS, 414, L95

Smail, I., Swinbank, A. M., Richard, J., et al. 2007, ApJ, 654, L33

Smolčić, V., Aravena, M., Navarrete, F., et al. 2012, A&A, 548, A4

Solomon, P. M., Downes, D., & Radford, S. J. E. 1992, ApJ, 398, L29

Solomon, P. M., Downes, D., Radford, S. J. E., & Barrett, J. W. 1997, ApJ, 478, 144

Solomon, P. M. & Vanden Bout, P. A. 2005, ARA&A, 43, 677

Song, J., Mohr, J. J., Barkhouse, W. A., et al. 2012a, ApJ, 747, 58

Song, J., Zenteno, A., Stalder, B., et al. 2012b, ApJ, 761, 22

Soucail, G., Fort, B., Mellier, Y., & Picat, J. P. 1987a, A&A, 172, L14

Soucail, G., Mellier, Y., Fort, B., Mathez, G., & Hammer, F. 1987b, A&A, 184, L7

Spinrad, H., Dey, A., Stern, D., et al. 1997, ApJ, 484, 581

Spitzer, L. 1978, Physical processes in the interstellar medium

Springel, V., White, S. D. M., Jenkins, A., et al. 2005, Nature, 435, 629

Stacey, G. J., Geis, N., Genzel, R., et al. 1991, ApJ, 373, 423

Stacey, G. J., Hailey-Dunsheath, S., Ferkinhoff, C., et al. 2010, ApJ, 724, 957

Staguhn, J. G., Benford, D. J., Fixsen, D. J., et al. 2012, in Proc. SPIE, Vol. 8452, Millimeter, Submillimeter, and Far-Infrared Detectors and Instrumentation for Astronomy VI, 84520T

Stanford, S. A., Elston, R., Eisenhardt, P. R., et al. 1997, AJ, 114, 2232

Stetson, P. B. 2000, PASP, 112, 925

Stott, J. P., Pimbblet, K. A., Edge, A. C., Smith, G. P., & Wardlow, J. L. 2009, MNRAS, 394, 2098

Swinbank, A. M., Chapman, S. C., Smail, I., et al. 2006, MNRAS, 371, 465

Swinbank, A. M., Dye, S., Nightingale, J. W., et al. 2015, ApJ, 806, L17

Swinbank, A. M., Karim, A., Smail, I., et al. 2012, MNRAS, 427, 1066

Swinbank, A. M., Papadopoulos, P. P., Cox, P., et al. 2011, ApJ, 742, 11

Swinbank, A. M., Smail, I., Chapman, S. C., et al. 2004, ApJ, 617, 64

Swinbank, A. M., Smail, I., Longmore, S., et al. 2010, Nature, 464, 733

Tacconi, L. J., Genzel, R., Neri, R., et al. 2010, Nature, 463, 781

Tacconi, L. J., Genzel, R., Smail, I., et al. 2008, ApJ, 680, 246

Tacconi, L. J., Neri, R., Chapman, S. C., et al. 2006, ApJ, 640, 228

Tacconi, L. J., Neri, R., Genzel, R., et al. 2013, ApJ, 768, 74

Tauber, J. A., Mandolesi, N., Puget, J.-L., et al. 2010, A&A, 520, A1

Thomas, D., Steele, O., Maraston, C., et al. 2013, MNRAS, 431, 1383

Thomson, A. P., Ivison, R. J., Owen, F. N., et al. 2015, MNRAS, 448, 1874

Toomre, A. 1964, ApJ, 139, 1217

Tran, K.-V. H., Franx, M., Illingworth, G. D., et al. 2007, ApJ, 661, 750

Tremonti, C. A., Heckman, T. M., Kauffmann, G., et al. 2004, ApJ, 613, 898

Treu, T. 2010, ARA&A, 48, 87

Treu, T., Brammer, G., Diego, J. M., et al. 2016, ApJ, 817, 60

Treu, T. & Koopmans, L. V. E. 2004, ApJ, 611, 739

Tu, H., Gavazzi, R., Limousin, M., et al. 2009, A&A, 501, 475

Valentinuzzi, T., Woods, D., Fasano, G., et al. 2009, A&A, 501, 851

Valenziano, L., Sandri, M., Morgante, G., et al. 2007, New A Rev., 51, 287

Valtchanov, I., Altieri, B., Berta, S., et al. 2013, MNRAS, 436, 2505

van der Wel, A., van de Ven, G., Maseda, M., et al. 2013, ApJ, 777, L17

Vegetti, S. & Koopmans, L. V. E. 2009, MNRAS, 392, 945

Venemans, B. P., McMahon, R. G., Walter, F., et al. 2012, ApJ, 751, L25

Vernet, J., Dekker, H., D'Odorico, S., et al. 2011, A&A, 536, A105

Vieira, J. D., Marrone, D. P., Chapman, S. C., et al. 2013, Nature, 495, 344

Vlahakis, C., Eales, S., & Dunne, L. 2007, MNRAS, 379, 1042

Wagg, J., Wilner, D. J., Neri, R., Downes, D., & Wiklind, T. 2006, ApJ, 651, 46

Walsh, D., Carswell, R. F., & Weymann, R. J. 1979, Nature, 279, 381

Walter, F., Riechers, D., Cox, P., et al. 2009, Nature, 457, 699

Walter, F., Weiß, A., Downes, D., Decarli, R., & Henkel, C. 2011, ApJ, 730, 18

Wang, R., Wagg, J., Carilli, C. L., et al. 2013, ApJ, 773, 44

Wardlow, J. L., Cooray, A., De Bernardis, F., et al. 2013, ApJ, 762, 59

Wardlow, J. L., Smail, I., Coppin, K. E. K., et al. 2011, MNRAS, 415, 1479

Warren, S. J. & Dye, S. 2003, ApJ, 590, 673

Weiß, A., De Breuck, C., Marrone, D. P., et al. 2013, ApJ, 767, 88

Weiß, A., Downes, D., Neri, R., et al. 2007, A&A, 467, 955

Weiß, A., Kovács, A., Coppin, K., et al. 2009, ApJ, 707, 1201

Werner, M. W., Roellig, T. L., Low, F. J., et al. 2004, ApJS, 154, 1

White, R. L., Becker, R. H., Helfand, D. J., & Gregg, M. D. 1997, ApJ, 475, 479

White, R. L., Helfand, D. J., Becker, R. H., et al. 2003, AJ, 126, 706

Wolfe, A. M., Gawiser, E., & Prochaska, J. X. 2005, ARA&A, 43, 861

Wong, K. C., Tran, K.-V. H., Suyu, S. H., et al. 2014, ApJ, 789, L31

Worthey, G. 1994, ApJS, 95, 107

Wright, E. L., Eisenhardt, P. R. M., Mainzer, A. K., et al. 2010, AJ, 140, 1868

Yan, L., Donoso, E., Tsai, C.-W., et al. 2013, AJ, 145, 55

Young, J. S., Allen, L., Kenney, J. D. P., Lesser, A., & Rownd, B. 1996, AJ, 112, 1903

Young, L. M., Bureau, M., Davis, T. A., et al. 2011, MNRAS, 414, 940

Yun, M. S., Reddy, N. A., & Condon, J. J. 2001, ApJ, 554, 803

Yun, M. S., Scott, K. S., Guo, Y., et al. 2012, MNRAS, 420, 957

Zepf, S. E., Whitmore, B. C., & Levison, H. F. 1991, ApJ, 383, 524

Ziegler, B. L., Bower, R. G., Smail, I., Davies, R. L., & Lee, D. 2001, MNRAS, 325, 1571

Zwicky, F. 1937a, Physical Review, 51, 290

Zwicky, F. 1937b, Physical Review, 51, 679

Appendix A

Overdensity contours from the adaptive kernel density estimate

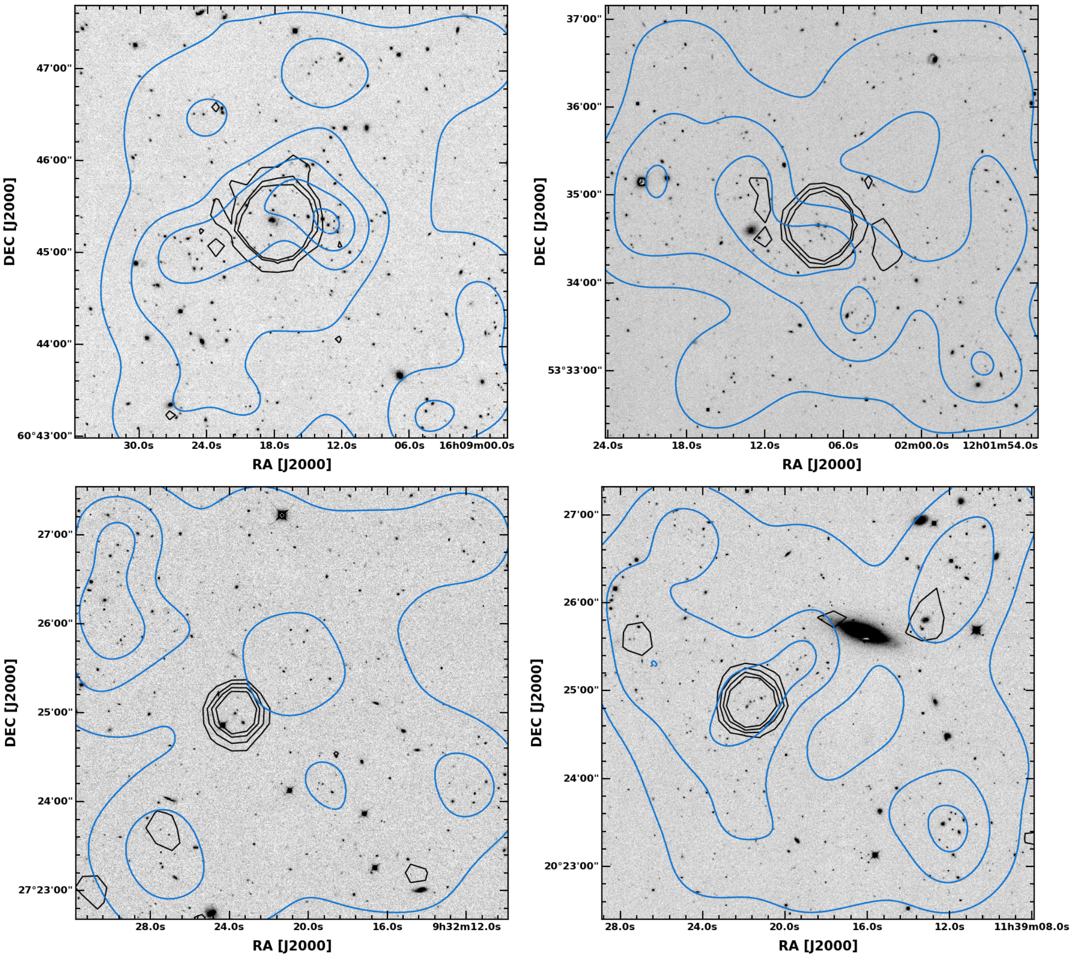

Figure A.1: CFHT/WIRCam K-band images of G092.5, G138.6, G200.6 and G231.3, from top-left to bottom-right, respectively. We show the entire fields-of-view of about $5' \times 5'$ used in the AKDE. Blue contours show the AKDE of galaxies detected in the K-band inside these areas, starting at $+1\sigma$ and increasing by $+1\sigma$. These overdensities are measured with respect to the background standard deviation derived in an independent region (see §5.2.1). The black lines delineate the Herschel/SPIRE emission at 350 μm and show the position of the background GEMS, with contour levels starting at $+3\sigma$ and increasing by $+3\sigma$. On these maps, North is up and East is on the left.

Appendix B

Optical SDSS spectra of lensing galaxies

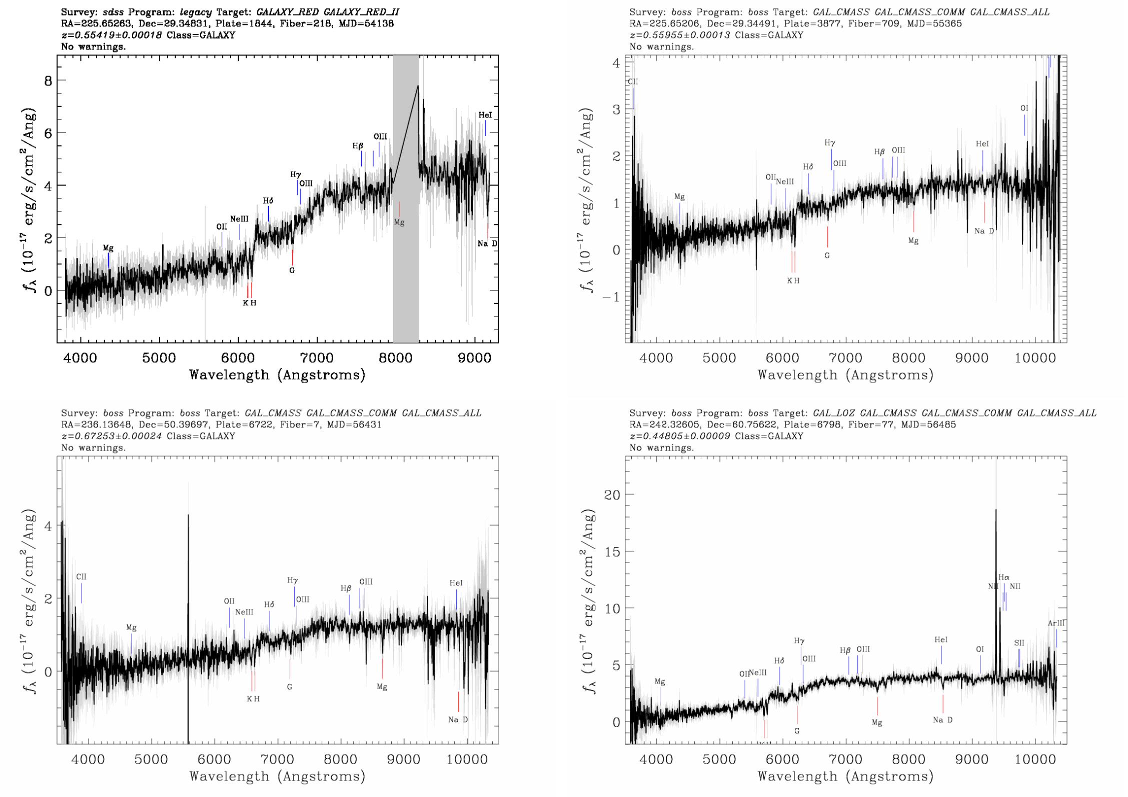

Figure B.1: SDSS spectra of foreground galaxies aligned with G045.1, G080.2 and G092.5 and contributing significantly to the overall lensing magnifications.

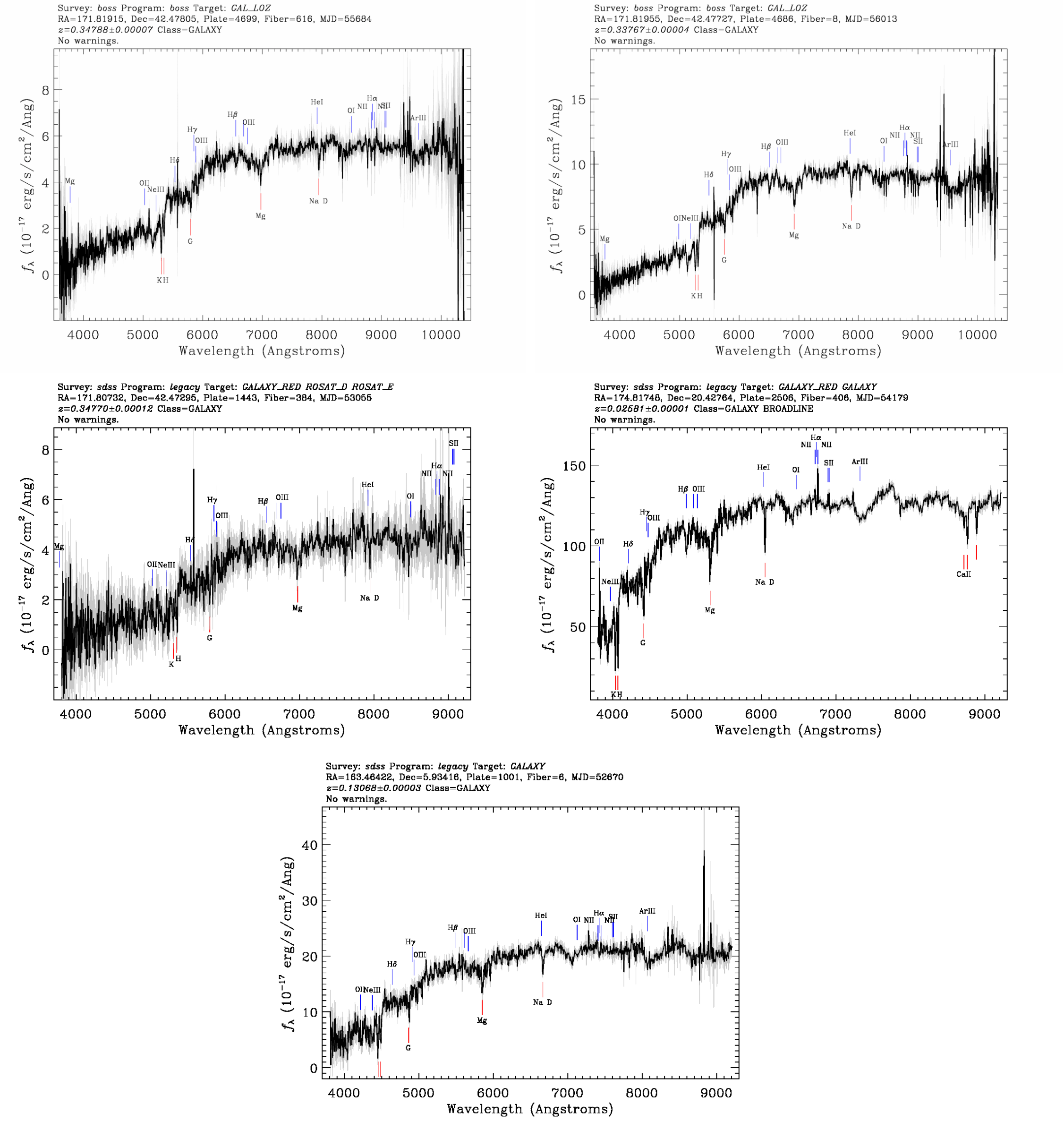

Figure B.2: SDSS spectra of foreground galaxies aligned with G165.7, G231.3 and G244.8 and contributing significantly to the overall lensing magnifications.

Appendix C

Posterior distributions of parameters in the mass models

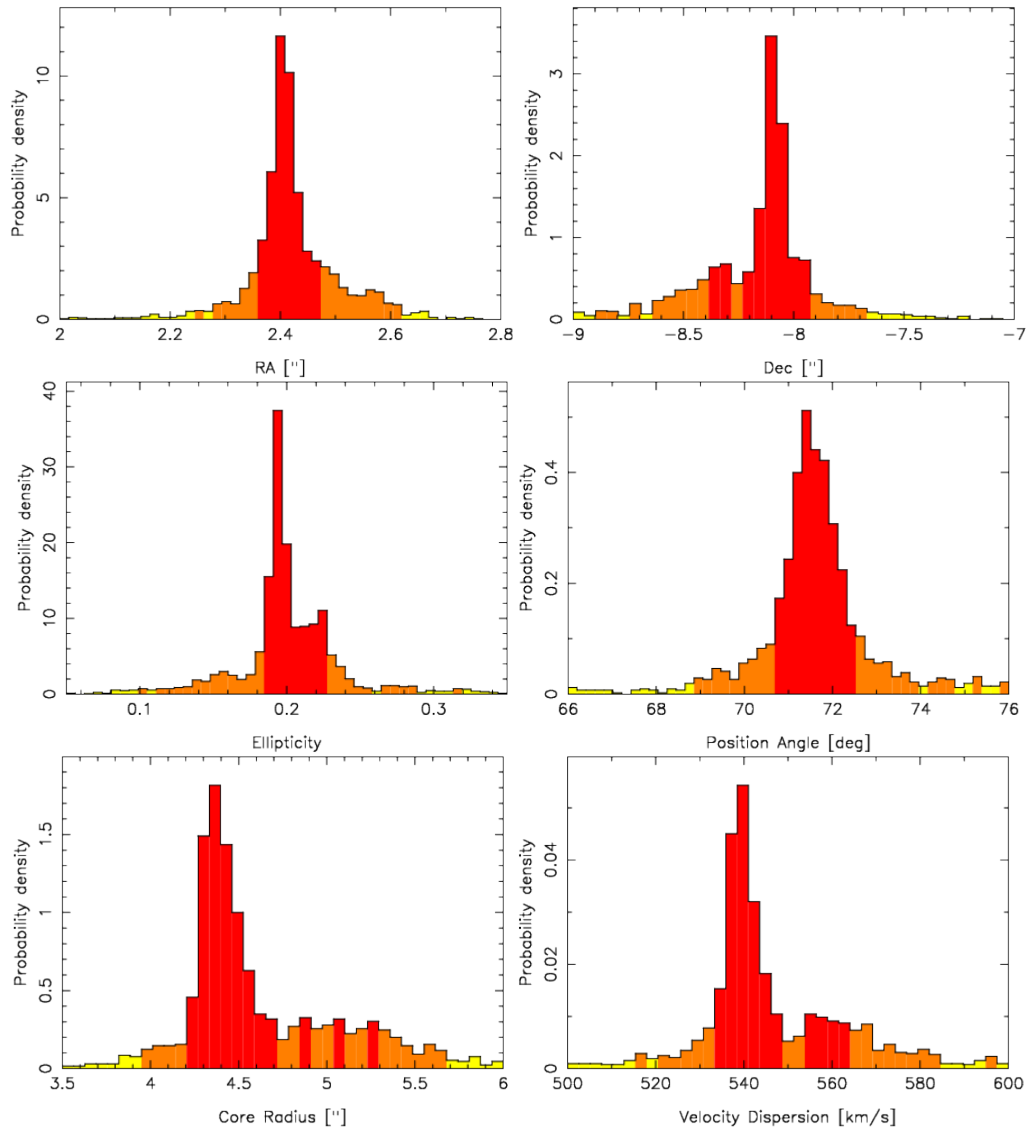

Figure C.1: 1D histograms showing the individual probability distribution function for each parameter involved in the lensing model of G045.1. Red, orange and yellow regions contain 68%, 95% and 99% of the full sample, respectively.

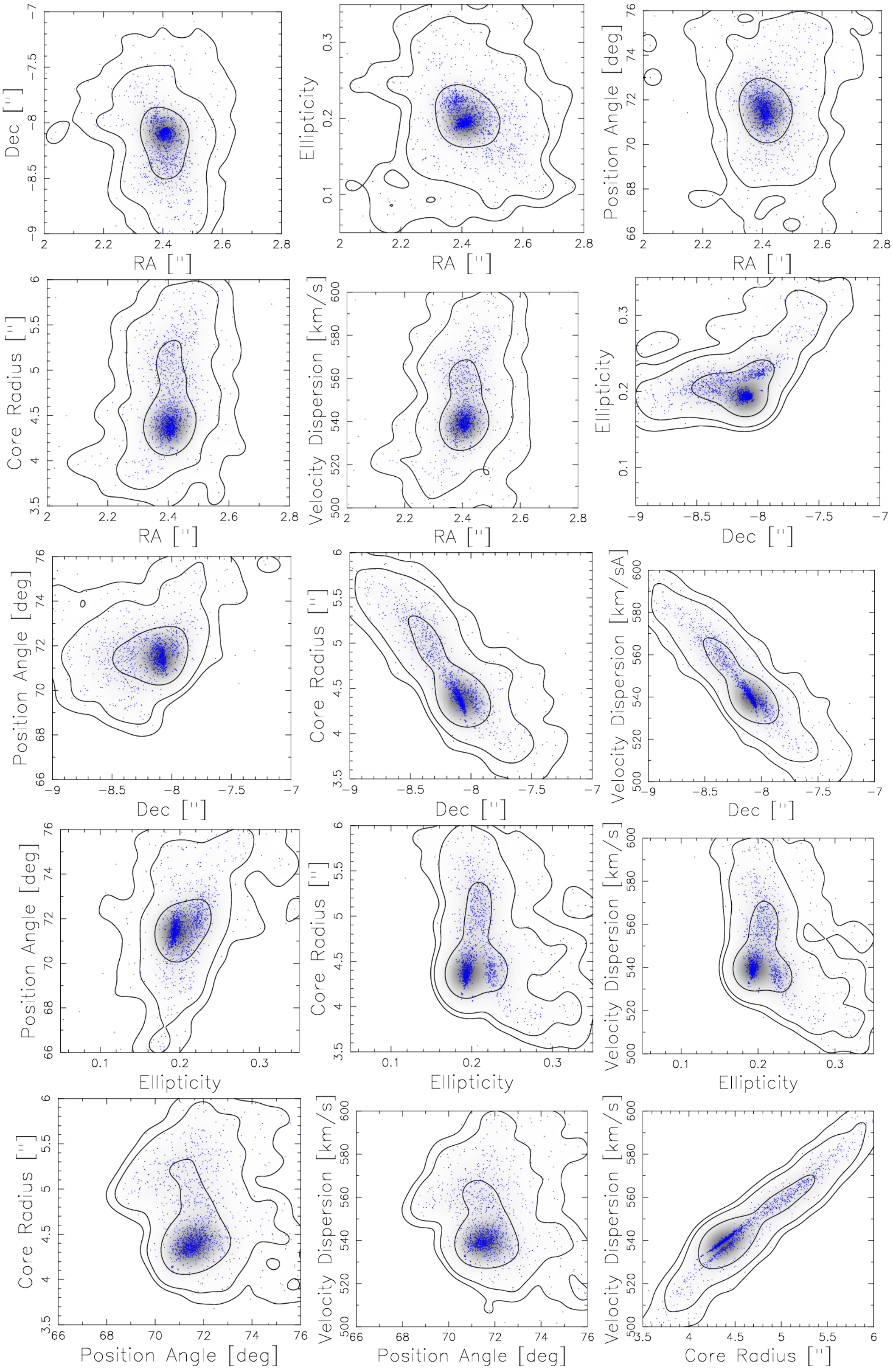

Figure C.2: The 2D posterior distributions between each couple of parameters describing the cluster-scale mass distribution in front of G045.1. The contours delineate the 1σ, 2σ and 3σ confidence levels.

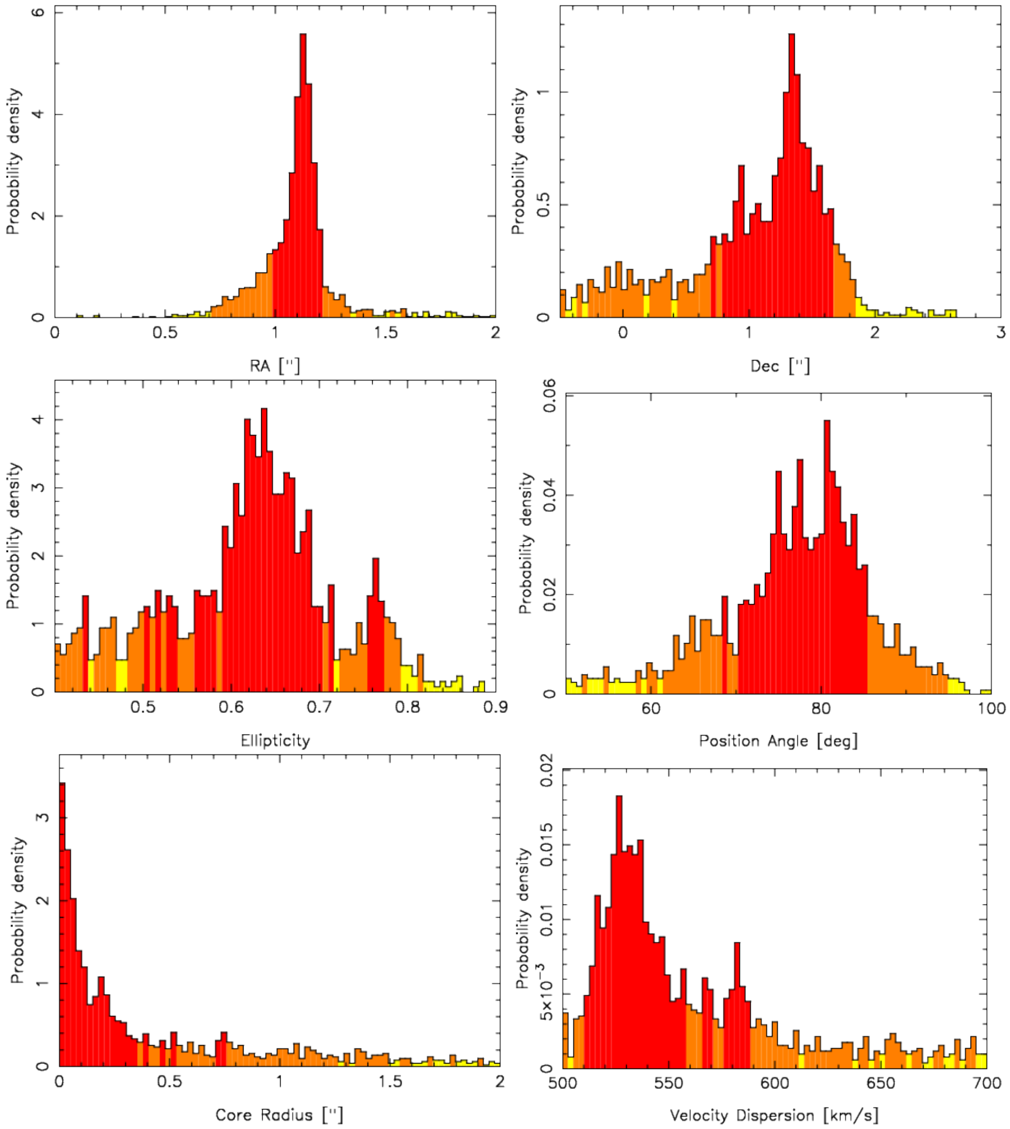

Figure C.3: 1D histograms showing the individual probability distribution function for each parameter involved in the lensing model of G080.2. Red, orange and yellow regions contain 68%, 95% and 99% of the full sample, respectively.

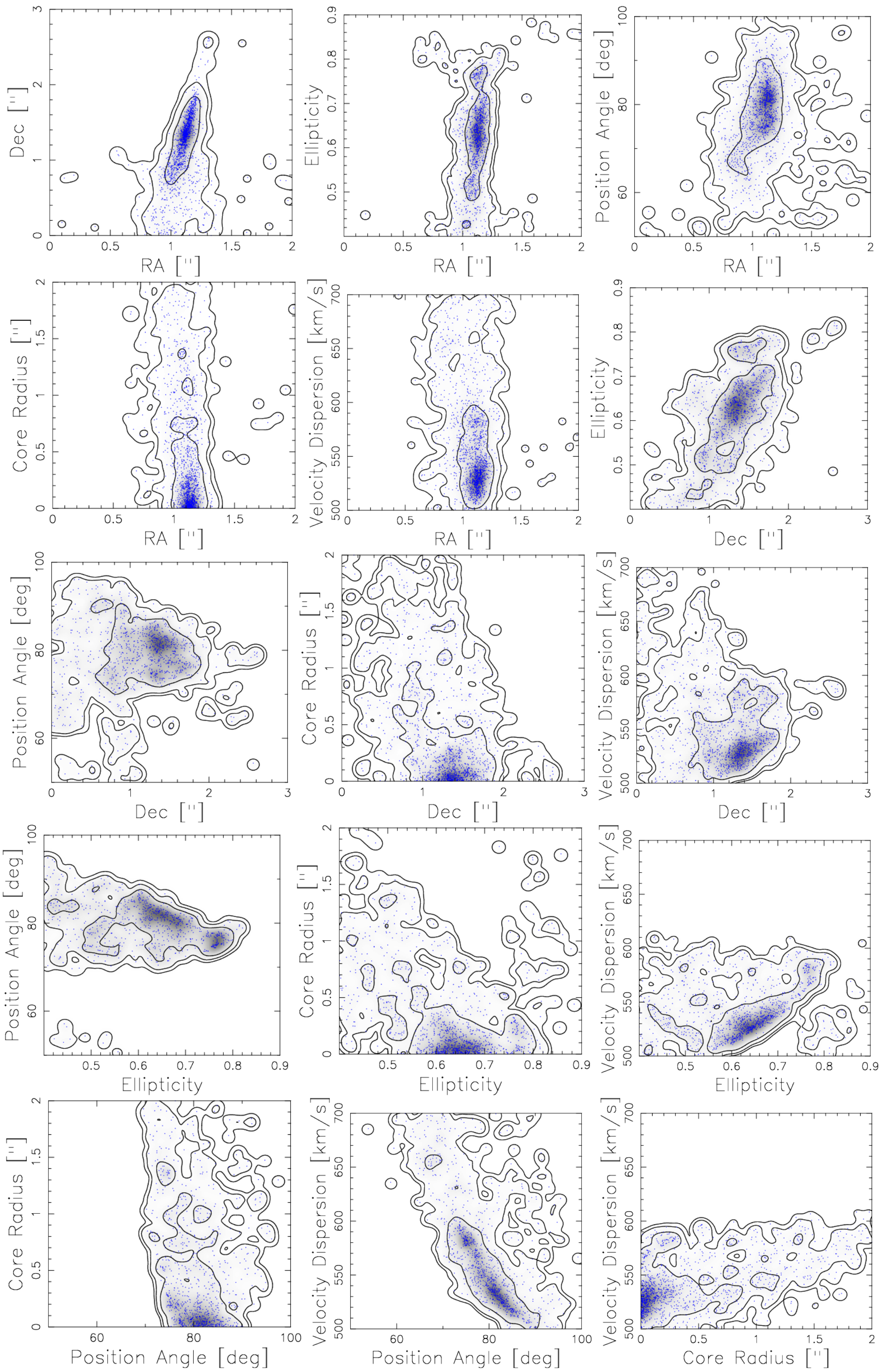

Figure C.4: The 2D posterior distributions between each couple of parameters describing the mass distribution in front of G080.2. The contours delineate the 1σ, 2σ and 3σ confidence levels (68%, 95% and 99% of the sample). In particular, these 2D relationships highlight a strong degeneracy between r_{core} and σ_{PIEMD}.

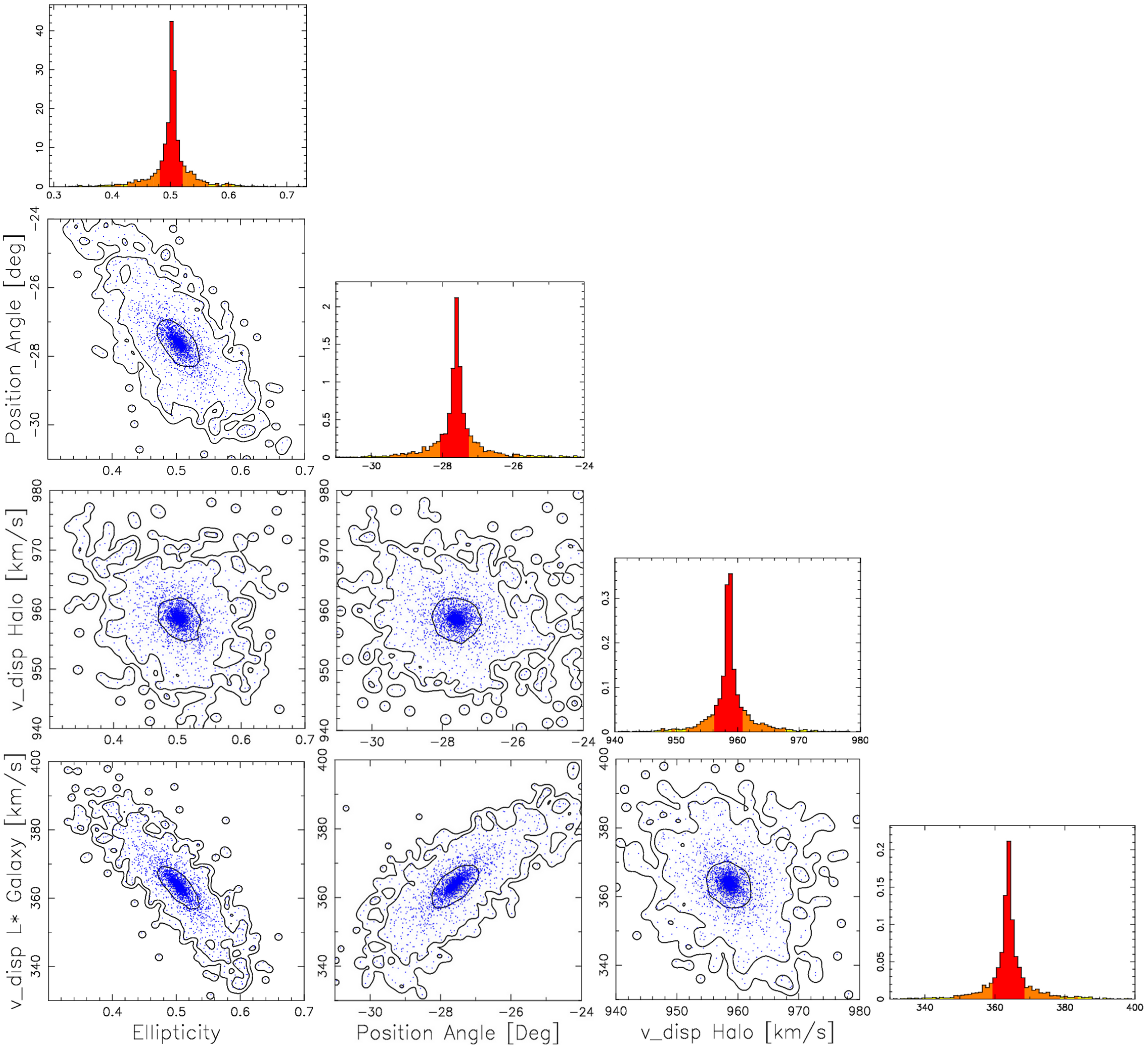

Figure C.5: 2D posterior distributions between each couple of parameters involved in the lensing model of G165.7. Contours delineate the 1σ, 2σ and 3σ confidence levels (68%, 95% and 99% of the sample). I also show the individual probability distribution function for each parameter of the PIEMD. Red, orange and yellow regions contain 68%, 95% and 99% of the full sample, respectively.